Springer Proceedings in Materials

K. Geetha
Francisco M. Gonzalez-Longatt
Hui-Ming Wee *Editors*

Recent Trends in Materials

Select Proceedings of ICTMIM 2022

Springer

Springer Proceedings in Materials

Volume 18

Springer Proceedings in Materials publishes the latest research in Materials Science and Engineering presented at high standard academic conferences and scientific meetings. It provides a platform for researchers, professionals and students to present their scientific findings and stay up-to-date with the development in Materials Science and Engineering. The scope is multidisciplinary and ranges from fundamental to applied research, including, but not limited to:

- Structural Materials
- Metallic Materials
- Magnetic, Optical and Electronic Materials
- Ceramics, Glass, Composites, Natural Materials
- Biomaterials
- Nanotechnology
- Characterization and Evaluation of Materials
- Energy Materials
- Materials Processing

To submit a proposal or request further information, please contact one of our Springer Publishing Editors according to your affiliation:

European countries: **Mayra Castro** (mayra.castro@springer.com)
India, South Asia and Middle East: **Priya Vyas** (priya.vyas@springer.com)
South Korea: **Smith Chae** (smith.chae@springer.com)
Southeast Asia, Australia and New Zealand: **Ramesh Nath Premnath** (ramesh.premnath@springer.com)
The Americas: **Michael Luby** (michael.luby@springer.com)
China and all the other countries or regions: **Mengchu Huang** (mengchu.huang@springer.com)

This book series is indexed in **SCOPUS** database.

K. Geetha · Francisco M. Gonzalez-Longatt ·
Hui-Ming Wee
Editors

Recent Trends in Materials

Select Proceedings of ICTMIM 2022

Springer

Editors
K. Geetha
JCT College of Engineering
and Technology
Coimbatore, India

Hui-Ming Wee
Department of Industrial and Systems
Engineering
Chung Yuan Christian University (CYCU)
Taoyuan City, Taiwan

Francisco M. Gonzalez-Longatt
Department of Electrical Power
Engineering
University of South-Eastern Norway
Notodden, Norway

ISSN 2662-3161 ISSN 2662-317X (electronic)
Springer Proceedings in Materials
ISBN 978-981-19-5394-1 ISBN 978-981-19-5395-8 (eBook)
https://doi.org/10.1007/978-981-19-5395-8

We are honored to dedicate the proceedings of ICTMIM 2022 to all the participants and editors of ICTMIM 2022.

Preface

With an extended gratification, we happily welcome you to the proceedings of 2022 4th International Conference on Trends in Material Science and Inventive Materials (ICTMIM 2022) at Coimbatore, India. The main objective and feature of the conference is to bring together academicians, researchers and industrialists to share and exchange their research experiences and results in different aspects of material science, computational mechanics and innovative materials.

The editorial team of 4th ICTMIM 2022 has mainly preferred the state-of-the-art discussions on the practical challenges encountered in the emerging innovative material science paradigm and solutions adopted to it. The 4th ICTMIM 2022 proceedings has been committed to remain both informative and research stimulating to cope up with the current issues present in innovative materials and general material science domain. Delegates from different countries have made the conference to be truly international in scope. Totally, 4th ICTMIM 2022 has received 197 papers, out of which 43 papers were selected for the conference. It has been strictly followed that each contributed paper has refereed by at least 2–3 international reviewers before being accepted for publication.

The 4th ICTMIM 2022 program consists of technical sessions and discussions on most of the recent material science research topics with eminent session chairs, program chairs, plenary lectures and keynote speakers by covering a wide range of topics. The conference totally had 43 oral presentations, which are delivered by the conference participants by leveraging a great opportunity for the academicians, scholars and industrialists to gain a wider knowledge on the state-of-the-art progress in material science research. Also, we are pleased to extend our gratitude to the review committee members, who have delivered their professional and technical expertise to the fullest to improve the publication quality of the research papers submitted to 4th ICTMIM 2022. Furthermore, we would like to thank the conference organizers, local organizing committee members, faculty and non-faculty members and volunteers for making this technical gathering to be a more enjoyable and informative event.

At last, we would like to extend our gratitude to the publication support delivered by Springer team in this entire journey from conference to publication and our institution JCT College of Engineering and Technology for their continual support in successfully organizing this conference event.

Dr. K. Geetha
Dean Academics and Research
JCT College of Engineering
and Technology
Coimbatore, India

Dr. Francisco M. Gonzalez-Longatt
Professor in Electrical Power
Engineering, Leader of DIgital Energy
System Lab (DIgEnSysLab)
University of South-Eastern Norway
Notodden, Norway

Dr. Hui-Ming Wee
Distinguished Professor, Department
of Industrial and Systems Engineering
Chaplain, Chung Yuan Christian
University (CYCU)
Taoyuan City, Taiwan

Contents

Computation of Properties for a Friction Stir Welded 6082 Aluminum Alloy Using Artificial Neural Network Model 1
Saumil K. Joshi, Dhairya Vyas, and Sheshang Degadwala

Study of Frictional Force and Volumetric Wear Rate of T6 Heat Treated Hypereutectic Al–18Si–3.6Cu–0.36Ce Alloy 17
Krishnaraddi Gangal and K. Devendra

Phased Array Ultrasonic Evaluation for Defect Characterization in Aerospace Grade Maraging Steel MDN250 Weldments 31
M. Prema Kumar, M. V. N. Mohan, V. Malolan, and Nakka Sudarshan

Artificial Cells as Programmable, Micro-/Nano-structured Bio-materials 45
Pasquale Stano

Biosynthesis of PHBs by the Method of Full-Factorial Design for Obtaining PHB/Magnetite Composites 57
A. A. Dudun, V. A. Zhuikov, T. K. Makhina, E. A. Akoulina, V. V. Voinova, A. P. Bonartsev, and G. A. Bonartseva

Validation of the Experimental Results of the Concrete with M-sand Using ABAQUS Software 71
Anup K. Chitkeshwar and P. L. Naktode

A Review on the Use of Industrial Waste and Agricultural Waste in the Production of Alkali-activated Concrete 85
Sonal Thakkar, Abhishek Chanda, and Shivanjali Rawat

Various Geometrical Parameters of the Topography Elements of the Honeycomb Films from PHB and Its Copolymer with 3-Hydroxyvalerate 103
Nikita Belishev, Elizaveta Akoulina, Vera Voinova, Irina Demianova, Garina Bonartseva, Tatiana Makhina, Viktoria Nikalaichuk, Viktoryia Kulikouskaya, and Anton Bonartsev

Effect on Structural Characteristics After Adding Gypsum Wall Waste and Polymer 113
Mukunda D. Bhor and Manendra P. Verma

FEA of Femur Bone Implant of Calcium, PEEK, Ti–6Al–4V Alloy and 316L Steel 127
Jihan Mehra, Kushank Khandelwal, Aditya Jain, Rushikesh Dandagwhal, and Rakesh Chaudhari

Literature Review in Artificial Neural Network for the Strength Calculation of Soil 143
Rahul Ramdas Wankhade and P. V. Durge

Rheological and Tribological Characterization of Completely Biogenic Grease 155
Ravikiran, Srikara Kundargi, S. L. Aravind, V. M. Akhil, and R. Madhusudhana

Piezoelectric Energy Harvesting from Automotive Wheels 163
Vaishak, Roopa Manjunatha, and G. L. Manjunath

Modeling of Graphene Oxide Coated QCM Sensor for E-Nose Application 179
Alisha Das and Roopa Manjunatha

Low-Temperature Reduction Processing of Copper Slag 189
Sokhibjon Turdalievich Matkarimov, Bakhriddin Tilovkabulovich Berdiyarov, Zaynobiddin Turdalievich Matkarimov, Raimkul Rakhmonkulov, and Sevara Dusmuratovna Jumaeva

Dimensionless Bending Rigidity Ratio and Material Dependency of Microbeams with Size Effects 201
R. Resmi, V. Suresh Babu, and M. R. Baiju

Characterization and Slurry Erosion Performance of Plasma Sprayed Ni–Al_2O_3 and Ni–TiO_2–Al_2O_3 Coatings on Turbine Steel 215
Vishal Kumar Rana, Vibhu Sharma, and Sushma Singh

On Complex Loading of Shell of Revolution 233
R. A. Abirov

Analysis of Effect of Pitch Error on Transmission Error and Mesh Stiffness in Spur Gear Using SciLab and Ansys Software 245
Vijay Kumar Karma and Govind Maheshwari

On a Method of Calculating of Continua with an Initial Crack 261
F. F. Adilov

Ultra-Broadband Absorber Based on Metasurfaces in the Infrared Regime 273
Vijay Laxmi, Abida Parveen, Deepika Tyagi, and Zhengbiao Oyuang

Analysis with Platinum for Optimized Performance of Perforated RF MEMS Switch 285
P. Chandini Begum, S. C. H. Kantha Rao, and K. Sravani

Analysis of Micro RF Switches Role in Reconfigurable Antenna Design 303
N. Gopi Chand, N. Durga Parameswara Rao, and Ch. Manasa

Analysis of Elevated Water Tank by Considering Slab, Wall, and Capacity in Seismic Zones 315
Dasari Tirupathi and Kota Srinivasu

Analysis of Machining Parameters of Wire Electric Discharge Machining Process on Polysilicon Material 335
Raminder Singh and Anish Kumar

Gold/ZnO Interface-Based D-Shaped PCF Surface Plasmon Resonance Sensor with Micro-Openings, Analytic Designing, and Some Applications 365
Vinod Singh, Deepak Kumar, and Mukta Sharma

Investigation of Micro-Cracks of Pure Titanium Using Wire Electric Discharge Machining (WEDM) Through Response Surface Methodology 377
Vinod Kumar, Renu Sharma, Jatinder Kumar, Ravinder Pal Singh, and Anish Kumar

Polarization-Independent Broadband Metasurface Absorber for Near Infrared Spectrum 393
Abida Parveen, Vijay Laxmi, Keyu Tao, and Zhengbiao Oyuang

Natural Frequency of Overhead Water Tanks Using Shaking Table 403
M. B. Vikram, G. P. Chandradhara, and J. Abdul Bari

Metamaterial-Based Biomedical Antenna for Low SAR Applications 419
G. V. Naveen Kumar, D. K. Kavitha, and P. Kiran Babu

Performance Investigations of Partially Shaded Solar Photovoltaic Modules with Cell-Level Configurations 427
V. BalaRaju and Ch. Chengaiah

Biocompatibility of Poly(3-Hydroxybutyrate)/Nano-Magnetite Composite Material for Bone Tissue Engineering Applications 445
Daria Travnikova, Dariana Chesnokova, Irina Zharkova, Garina Bonartseva, Tatiana Makhina, Yulia Mukhortova, Artem Pryadko, Roman Chernozem, Maria Surmeneva, Roman Surmenev, and Anton Bonartsev

Angle Detection of Steering in a Self-Driving Car 453
Vipul Devnani, Chandan Panjwani, Navin Kachhela, Abha Tewari, and Neeraj Gwalani

Dielectric Properties of Barium Titanate Using Different Preparation Techniques 463
N. Preetha, S. Padmavathi, and B. Mahalakshmi

Modeling Effective Maintenance Strategy for Rotodynamic System Using RCM and AHP 473
P. T. Elijah and M. Obaseki

About the Editors

Dr. K. Geetha is currently Professor, Dean-Academics and Research in JCT college of Engineering and Technology, Tamil Nadu, India. She a rich experience of teaching and administration for the past 20 years. Her research guidance includes 14 Ph.D. scholars for their doctoral degree. Her research areas include artificial intelligence, optimization techniques, and medical image processing. She has published articles in reputed journals in her area of specialization. She is passionate about continuous teaching-learning processes and involved in research related to student-centric learning methodologies. In 2020 and 2021, she served as the conference chair of the IEEE International Conference on Artificial Intelligence and Smart Systems and the Springer International Conference on Inventive Systems and Control.

Dr. Francisco M. Gonzalez-Longatt is currently a full professor in electrical power engineering and Founder and leader of the DIgEnSys-Lab (Digital Energy Systems Laboratory) at the Department of Electrical Engineering, Information Technology and Cybernetics, University of South-Eastern Norway, Norway. He is a former Lecturer in Electrical Power System at Electrical Power System in School of Electronic, Electrical and Systems Engineering at Loughborough University (2013–2019). He is Vice-President of Venezuelan Wind Energy Association, Fellow of the Higher Education Academy (UK), Senior Member of the IEEE, member of The Institution of Engineering and Technology—The IET (UK) and member of International Council on Large Electric Systems —CIGRE. His research interest includes innovative (operation/control) schemes to optimise the performance of future energy systems.

Dr. Hui-Ming Wee is the Associate Dean, Chaplain and Distinguished Professor in Chung Yuan Christian University. He has received an excellent research award from the Taiwan Ministry of Science and Technology, an excellent life researcher award from CYCU and the Medal for Distinguished Industrial Engineer Award. He has published more than 400 papers in refereed journals, international conferences and book chapters. His papers were cited over 3275 times (Scopus) with h-index: 32. He has co-edited six books and holds two patents; was keynote speaker to a number

of international conferences, Senior Member for Asian Council of Science Editors (ACSE), Board of Directors for International Engineering and Technology Institute (IETI) and Editor/editorial board member for a number of international journals.

Computation of Properties for a Friction Stir Welded 6082 Aluminum Alloy Using Artificial Neural Network Model

Saumil K. Joshi, Dhairya Vyas, and Sheshang Degadwala

Abstract This paper identifies the effect of two different non-consumable tools with different shoulder geometries (Raised and Recced) on aluminum alloy undergoing Friction Stir Welding (FSW) processes. Properties like Ultimate Tensile Strength (UTS) and microhardness of 4-mm-thick 6082 aluminum alloy butt weld joints have been investigated at three different rotation speeds and traverse rates. Tensile and microhardness tests have been carried out on 36 welding joints to find the best combination of tool traverse rate and tool rotation speed for obtaining higher UTS and lower Hardness as compared to the base metal. ANN model has been developed based on BP Neural Network to predict the UTS and hardness of aluminum alloy in FSW. Results show that raised tool geometry gives 6% better desirable properties than the recced tool geometry.

Keywords Friction stir welding · Aluminum alloy · Microhardness · Tensile strength · Artificial Neural Network

1 Introduction

Auto motive industries, railway, the heavy structure of shipbuilding, marine, aerospace, etc., widely consume aluminum material and its alloy. Various series of aluminum from 1 to 9XXX are available on market. Out of which, highly alloyed 2XXX, 6XXX, and 7XXX series aluminum fall in the category of non-weld able materials due to porosity, poor solidification, and mechanical properties as compared to the base metal of weld zone during welding by fusion technology [1, 2]. To counter this problem, friction Stir welding innovation (a solid-state joining technology) was

S. K. Joshi (✉)
Mechanical Engineering Department, Sigma Institute of Engineering, Vadodara, Gujarat, India
e-mail: 14meams03@gmail.com

D. Vyas
Shree Drashti Infotech LLP, Vadodara, Gujarat, India

S. Degadwala
Computer Engineering Department, Sigma Institute of Engineering, Vadodara, Gujarat, India

K. Geetha et al. (eds.), *Recent Trends in Materials*, Springer Proceedings in Materials 18, https://doi.org/10.1007/978-981-19-5395-8_1

designed at The Welding Institute (TWI) of the UK in 1991 as a solid-state joining innovation. This joining technology was at first connected to aluminum composites [2].

In friction stir welding, the non-consumable tool rotates and travels along the mating surface of the two plates [3]. This non-consumable tool consists of (1) Shoulder and (2) Pin. These both have specially designed geometry, which generates required friction for welding. The geometry plays a vital role in material movement during the welding operation. At the starting of the welding process, the tool probe charged into the adjoining edge of plates up to the shoulder surface. Thus, out of the total generated heat, 80% heat generates by the shoulder geometry, and the rest is by pin geometry [4]. During the welding process, the flow of material and flow of workpiece heat are the two primary functions of the FSW tool. Because of localized heating, plastic deformation of work piece occurs, and the material becomes softened around the pin, which leads to the flow of metal from retarding side to the advancing side of the probe. Because of this, solid-state joint is formed [5]. FSW is also significantly considered as a green technology because of its special characteristics like energy efficiency, environment friendly, and versatility. FSW does not require any special type of filler metal and shielding gas or flux to cover the welding. Hence, FSW is a rapidly developing green welding technology. This paper explores FSW in more depth and identifies the influence of two different shoulder geometries on UTS and the hardness of the weld zone of the aluminum 6082 alloy plates.

There have been many types of research on the different aluminum alloy series such as 2XXX, 6XXX, and 7XXX. The aeronautics, automotive, maritime industries have a wide variety of aluminum alloy applications. In addition to that, aluminum replaces steel in the heavy structures of industries due to its higher lightweight to strength ratio. The short survey of literature found that 6xxx aluminum alloys were mainly used in various applications. The Al 6082 has reasonable strength and is the best in the 6-series alloys, taking into consideration its different uses and characteristics. Al 6082, precipitation hardening Alloy, excellently characteristic for corrosion resistance, found its diverse mechanical properties.

Several aspects govern heat generation and metal mixing during the operation, determining the weld's final quality and attributes [6, 7]. The two main variables are tool RPM and welding feed; even so, tool shape and dimensions (i.e., pin diameter, pin length, shoulder diameter, shoulder concavity angle), tool tilt angle, plunge depth, applied load, the thickness of welded plates, weld setup, alloy composition, and preliminary temper all play a key role [8–10]. As a result, many efforts have investigated the FSW process parameters and their impact on weld microstructures and mechanical characteristics. The effect of tool RPM [11–14], welding feed [12–17], welded alloy setup [18, 19], and pin shapes[20–23] on the welding of dissimilar aluminum alloys have been widely researched to date. Very little research is found based on the effect of the FSW tool shoulder profile. So, two different combinations of tool pin profiles and shoulder geometries were analyzed during the research.

In addition to that computer-aided ANN, design is also incorporated in this study due to the increased use of AI (Artificial Intelligence) in the areas of science and engineering [24–26]. ANN is among the most critical aspects of exploration in the

fields of genetics, telecommunications, information systems, engineering, and mathematics. ANN is a "Knowledge-Based Information System." It is a mathematical technique to simulate the biological neural system. So, it is like a human system of thought [27]. The neural network is initially programmed with experience or facts and then used to assess the effects of all problems like that of the nervous system. ANN creates and patterns the complex relationship between inputs and outputs. These relationships tend to solve humanly or statistically complex challenges.

In this study, two FSW tools with two different shoulder geometries (raised and recessed) with round pin profiles are used to friction weld the 6082 aluminum alloy plates. Welding is performed at predefine tool rotation speed and tool travel speed. After welding different quality tests are performed on welded aluminum alloy plate. By using these experimental outputs, ANN creates the relationship between three input variables, namely FSW shoulder geometry, spindle rotation speed (RPM), Spindle Traverse Rate (Feed—mm/min), and two responses or output variables, namely Ultimate Tensile Strength (UTS) and hardness. This relationship helps to predict the responses or outcomes.

2 Experimental Process

The base metal 6082 aluminum alloy plate of 4 mm thickness has been used in experiments. 6082 aluminum alloy consists of magnesium and silicon. Its composition is 0.78% Mg, 0.95% Si, 0.08% Cu, 0.39% Fe, 0.48% Mn, 0.05% Ti, 0.04% Zn, and 0.03% Cr, with the remainder Al [28]. It is highly ductile and tough due to the presence of magnesium. Nowadays, 6082 aluminum has replaced other 6XXX series aluminum alloys. FSW process conducted on 300 × 150 × 4 mm 6082 aluminum alloy plate. Hence, the total weld length available for welding was 300 mm.

During the process, a non-consumable tool made of H-13 dies steel material rotates at three different tool rotation speeds (2300, 2500, and 2700 RPM) and tool travel speed (20, 30, and 40 mm/min). This non-consumable tool is made from H-13 die steel material. During the fabrication of the FSW tool, the ratio of tool shoulder diameter to pin diameter is maintained at 3 as per the observation of many research work [29–31]. Also, the pin length is kept 2 mm less than the thickness of the workpiece plate to avoid direct contact between the rotating tool and base plate [3, 8, 32]. Figure 1 shows the tool dimensions and actual tool geometry.

Planning of experiment is most important for experimentation and analysis. In this study, the Taguchi method has been used as a statistical technique that optimizes and designs the experiments. Tool rotation speed and tool traverse speed have three levels, and shoulder geometry has two levels; therefore, mixed level Taguchi design has been adopted for the design of experiments. The mixed level Taguchi method is performed on Minitab 18 software which gives a total of 36 experiment combinations for both, tool raised and recessed geometry together as given in Table 1.

FSW welding of 6082 aluminum alloy plates of dimension 300 × 75 × 4 mm has been carried out on a CNC milling machine (HASS USA). It has been observed

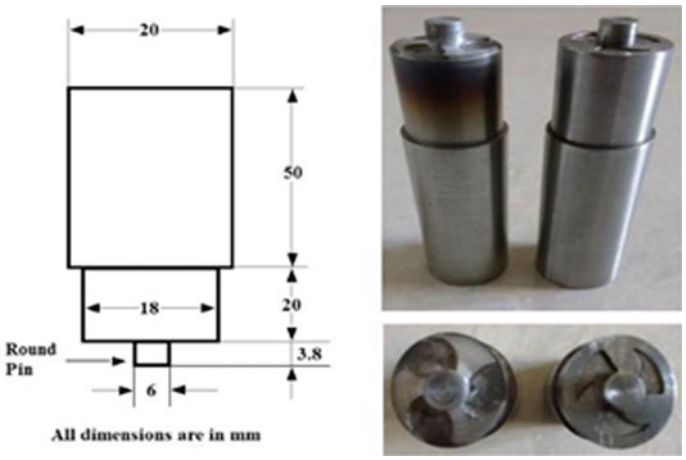

Fig. 1 FSW tool dimension and geometry

Table 1 Design of experiment

No.	Shoulder geometry	Spindle rotation speed (RPM)	Spindle traverse speed (mm/min)	No.	Shoulder geometry	Spindle rotation speed (RPM)	Spindle traverse speed (mm/min)
1	Raised	2300	20	19	Recessed	2300	30
2	Raised	2500	30	20	Recessed	2500	40
3	Raised	2700	40	21	Recessed	2700	20
4	Raised	2300	20	22	Recessed	2300	30
5	Raised	2500	30	23	Recessed	2500	40
6	Raised	2700	40	24	Recessed	2700	20
7	Raised	2300	20	25	Recessed	2300	40
8	Raised	2500	30	26	Recessed	2500	20
9	Raised	2700	40	27	Recessed	2700	30
10	Raised	2300	20	28	Recessed	2300	40
11	Raised	2500	30	29	Recessed	2500	20
12	Raised	2700	40	30	Recessed	2700	30
13	Raised	2300	30	31	Recessed	2300	40
14	Raised	2500	40	32	Recessed	2500	20
15	Raised	2700	20	33	Recessed	2700	30
16	Raised	2300	30	34	Recessed	2300	40
17	Raised	2500	40	35	Recessed	2500	20
18	Raised	2700	20	36	Recessed	2700	30

Fig. 2 FSW experimental setup

that during the FSW process, the tremendous force is developed on plates, leading to, abutting of plates during the process, damage of worktable and workpiece plate. Hence, it is important to fix the plates with special fixtures as shown in Fig. 2. The tool has been positioned in an orthogonal direction to the welding surface during the welding process, as shown in Fig. 2.

Friction Stir Welding experiments were carried out on a 4-mm-thick 6082 aluminum alloy plate. Experiments are conducted using two different FSW tools with circular pin profiles having raised and recessed shoulder geometries as shown in Fig. 1. Tool parameters were kept constant throughout the welding process.

The front and back surfaces of thirty-six welding samples prepared from the CNC milling machine have been noticed. The surface appearance of one of the samples of friction stir weld of 6082 aluminum alloy at 2700 rpm spindle rotation speed and 40 mm/min feed rate by raised shoulder feature tool have been shown in Fig. 3.

Further, as per the ASTM E8M-11 standards, tensile test and Vickers hardness specimens as shown in Fig. 4 were produced perpendicular to weld zone by Abrasive Water Jet Cutting (AWJM) which is displayed in Fig. 4. UTS and Microhardness of each sample were identified through Universal Testing machine and Vickers hardness tester machine, respectively, and encapsulated in Table 2.

Fig. 3 Surface appearance

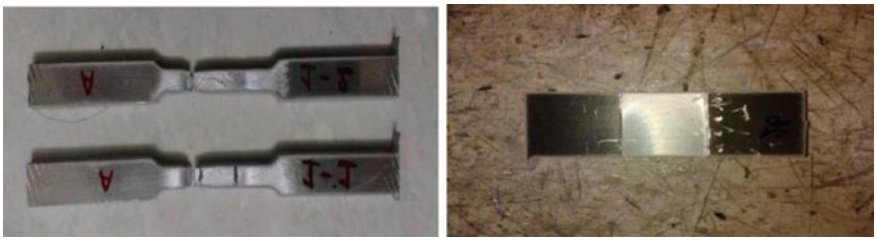

Fig. 4 Tensile and hardness test specimen

Table 2 Experimental result

Sr. No.	RPM	FEED	UTS	Microhardness	Sr. No.	RPM	FEED	UTS	Microhardness
1	2300	20	168	57	19	2300	30	162	57
2	2500	30	168	56	20	2500	40	164	61
3	2700	40	172	61	21	2700	20	115	51
4	2300	20	168	54	22	2300	30	159	58
5	2500	30	171	55	23	2500	40	151	59
6	2700	40	168	60	24	2700	20	116	50
7	2300	20	159	56	25	2300	40	135	49
8	2500	30	171	57	26	2500	20	147	50
9	2700	40	176	58	27	2700	30	145	42
10	2300	20	159	57	28	2300	40	138	50
11	2500	30	165	59	29	2500	20	144	51
12	2700	40	171	61	30	2700	30	146	41
13	2300	30	168	47	31	2300	40	137	49
14	2500	40	164	49	32	2500	20	144	48
15	2700	20	159	44	33	2700	30	147	41
16	2300	30	165	45	34	2300	40	133	50
17	2500	40	171	50	35	2500	20	142	47
18	2700	20	159	48	36	2700	30	144	40

3 ANN Modeling

3.1 Introduction

Artificial Neural Network is a numerical framework in light of the human sensory system, also known as a "Learning-Based Information System." Implies, first, we instruct the network, and then, this network gives the proper answers of any issue simply like a human by utilizing that information. The basic flow diagram of this system is represented in Fig. 5.

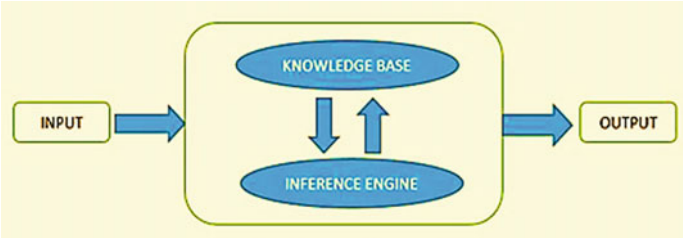

Fig. 5 Knowledge-based information system

It can discover the association between the information and yield values with the goal that it is utilized to foresee the result for further independent info might be non-linear and unpredictable, after preparing of network regardless of the possibility that it is non-clear. ANN has various fields of use like assembling, signal processing, bio-electric signal characterization, pattern recognition, speech recognition, picture handling, correspondences, independent vehicle, and route control of gantry crane to give some examples.

Indeed, even in production, Artificial Neural Network utilized cold forging for anticipating the flow stress in hot deformity, for the forecast of production conduct, for apparatus wear observing and for streamlining of assembling procedures among numerous others, is very much archived and just a couple of examples are recorded here [34–37].

Neurons are non-linear functions. The variable of this function is called as input of the system and the value of this function is called the output of the system. Figure 6 shows the basic structure of the ANN.

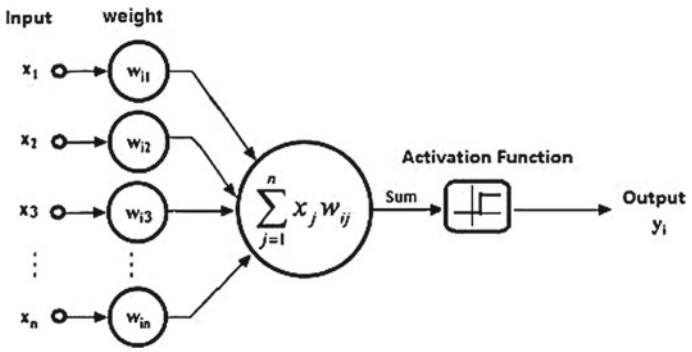

Fig. 6 Basic artificial neurons [33]

3.2 Backpropagation Neural Network

Backpropagation Neural Network is a training and learning model incorporating a feedback-based system. The model measures the gradient of the loss function and passes it to the optimization method to update the weights to decrease the loss functions. Figure 7 indicates the basic architecture of the Backpropagation Neural Network.

Backpropagation is a preparation strategy utilized for a multi-layer neural system. It is additionally called the generalized delta rule. It is an angle plummet technique that limits the aggregate squared mistake of the yield figured by the net.

Any neural system is relied upon to react effectively to the info designs that are utilized for preparing which is named as a remembrance and it ought to react sensibly to include that is like however not the same as the examples utilized for preparing which is called speculation. Figure 8 represents the algorithm of the Backpropagation neural network. Table 3 shows the input data which we use to train the ANN system. During the training, 3 input neurons, 10 hidden neurons, and 2 output neurons (3-10-2) are utilized. Here, we predict the probability as an outcome and probability lies between 0 and 1. Thus, we use the log (Sigmoid) transfer function.

The preparation of a neural system by back spread happens in three phases:

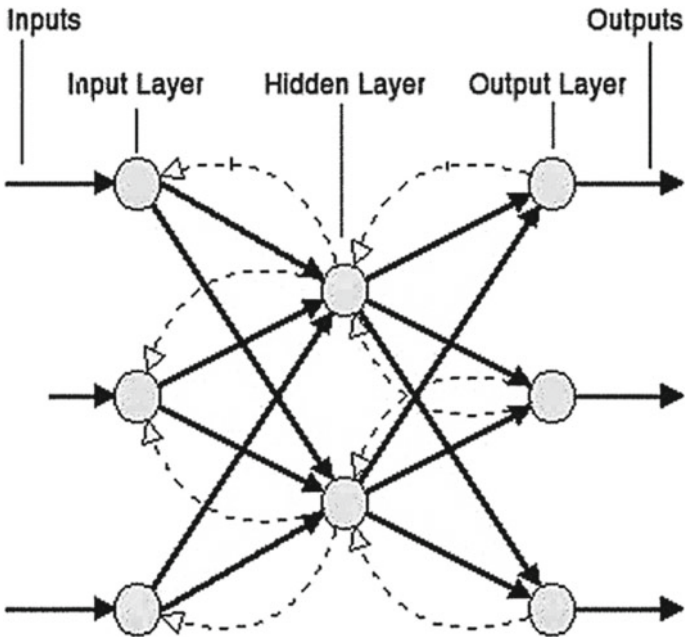

Fig. 7 Back propagation model [33]

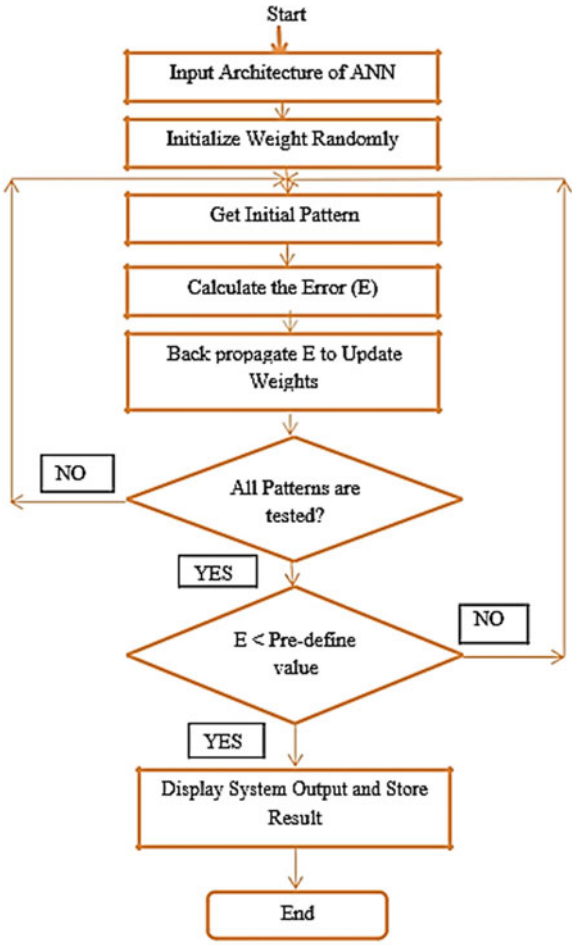

Fig. 8 Backpropagation ANN algorithm

Table 3 ANN training data

1	Network outline	3-10-2
2	No. of hidden layer	1
3	Transfer function utilized	Log (Sigmoid)
4	No. of epochs	1000
5	No. of hidden neuron	10
6	No. of pattern utilized for exercise	100%
7	Max. validation check	1000

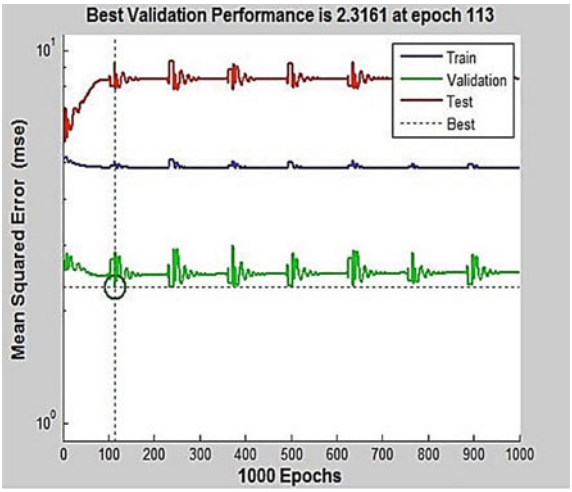

Fig. 9 Mean square error graph

1. Feedforward of the input design
2. Count and Back proliferation of the related fault
3. Alterations of the weights.

Algorithm of Backpropagation Neural Network:

The last MSE is little as appeared in Fig. 9. Both the approval set and the test set error have comparative qualities. No critical overfitting has happened by epoch 113 (The finest endorsement execution). The direct relapse among the system yields and the relating goals appear in Fig. 10. For our situation, the yield tracks the objective extremely well to training, testing, and approval, and the r-esteem is somewhat more than 0.99 for the aggregate reaction.

4 Result

The initial stage to portray the joint is a pictorial assessment of roots and tops. Other than agreeing on this, additionally the leave opening hole was analyzed. A hover of metal plasticized by the tool shoulder continuously exists in the nearby areas. The presence of this material implicates the weld quality. With a decent joint, the hover nearer to the leave opening hole is fully finished. Both tools delivered a total hover in the gap.

A subjective examination of tops and roots has been conveyed out. Every one of the roots has demonstrated no deformities. Figure 11 appears the tops of the weld.

The average properties obtained from the weld UTS tests are condensed in Table 2. Not surprisingly, the weld qualities acquired were lesser than those of ordinary aluminum 6082. Experiment no. 3 displayed the best quality by raised tool shoulder feature, and experiment no. 20 showed the best quality by recessed tool shoulder

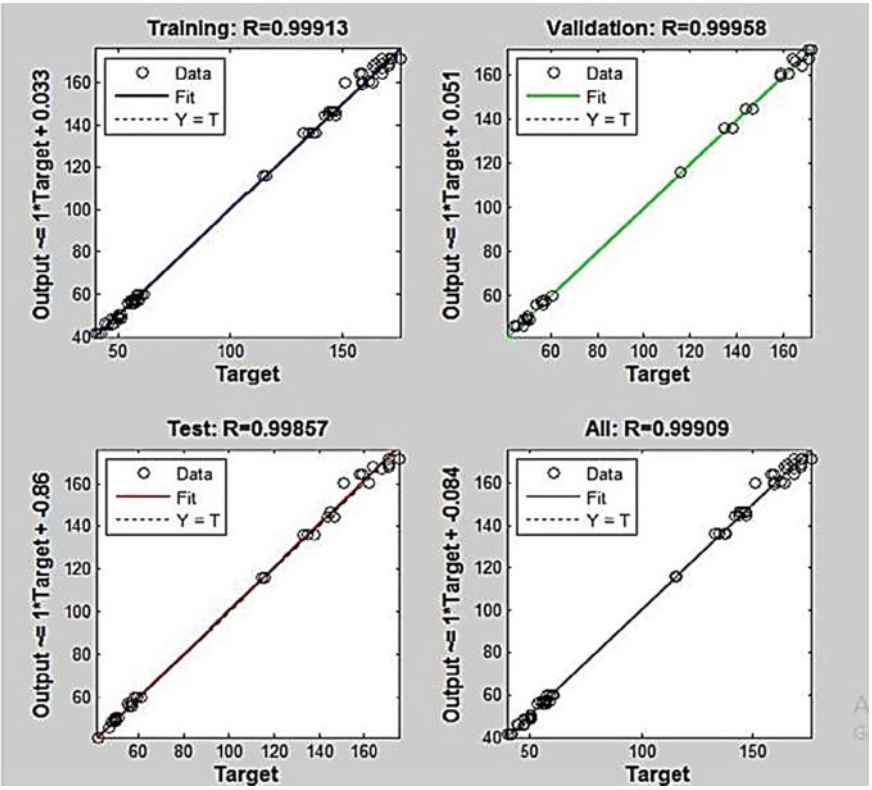

Fig. 10 Regression plot for performance analysis

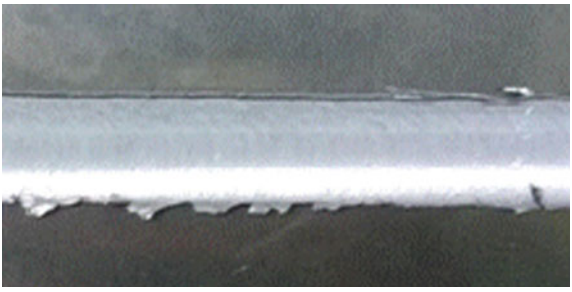

Fig. 11 Crown obtained by tool 1

feature. Figure 12 shows the 3D graph of variation of UTS at different feed and RPM.

Micro Vikers hardness acquired for all the welds are listed in Table 2. Vickers microhardness (HV) was measured along the weld zone on the cleaned cross-segment utilizing 100 gm of the connected load. The outcomes demonstrate that the hardness of the weld zone gained was lower than the standard aluminum 6082 compound.

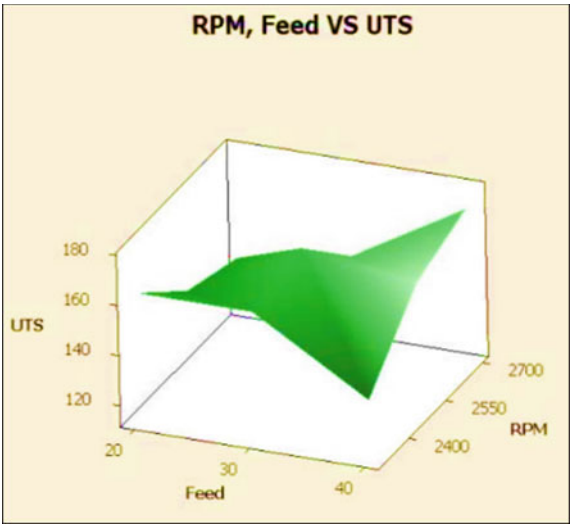

Fig. 12 UTS graph

Figure 13 demonstrates the 3D chart of a variety of micro Vickers hardness at various feed and RPM.

Tables 4 and 5 represent the variation in exploratory outcome and ANN-anticipated after effect of Friction Stir Welding properties. The variety in the exploratory outcome and ANN anticipated outcome is near each other, closer around 2.45% in UTS and 3.66% in Microhardness, which falls in the acceptable range. So prepared system 3-10-2 can be utilized to foresee mechanical properties of the FSW process.

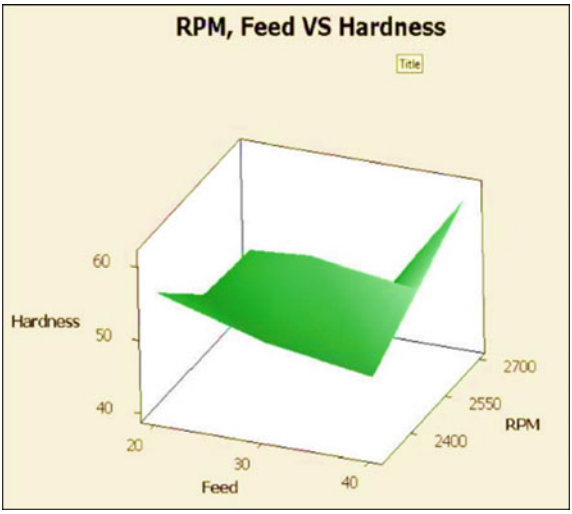

Fig. 13 Micro hardness graph

Table 4 Comparison of experimental result and ANN result for UTS

Sr. No.	Tool	RPM	FEED	UTS	UTS ANN	% Error
1	1	2300	40	174.66	170.37	2.45
2	2	2500	30	148.66	145.91	1.85
3	2	2700	40	145.33	146.03	0.48

Table 5 Comparison of experimental result and ANN result for hardness

Sr. No.	Tool	RPM	FEED	Hardness	Hardness ANN	% Error
1	1	2300	40	51	52.24	2.43
2	2	2500	30	50	51.83	3.66
3	2	2700	40	50	51.84	3.68

5 Conclusion

In the present work, 36 trials of FSW have been completed according to the pre-characterized set of info parameters blend for tensile strength and hardness of FSW weld on 6082 aluminum combination. The accompanying imperative conclusions are as follows:

- The test result demonstrates that tensile strength is increasing with increment in axle revolution speed. Greatest elasticity, 176 N/mm^2 accomplished at 2700 rpm axle revolution speed and 40 mm/min traverse speed of shaft with the utilization of raised device shoulder geometry.
- Almost the same tensile strength was obtained by utilizing both raised and recessed shoulder geometry, raised geometry to give a 6% preferable outcome over recessed apparatus geometry. The hardness of the weld nugget zone is lower at higher spindle rotation speed compared to standard hardness by using raised geometry.
- The created ANN system can be utilized to foresee the UTS and hardness of 6082 aluminum plates welded at the given FSW condition. Comes about shows that the system outcome is exceptionally shut to the experiment result. The examination demonstrates that the most extreme 2.45 and 3.68% variety in UTS and hardness individually.

References

1. Singh G et al (2017) Experimental comparison of friction stir welding process and TIG welding process for 6082-T6 Aluminium alloy. Mater Today: Proc 4(2):3590–3600
2. Terry K (2005) An outsider looks at friction stir welding. Report: ANM-112N-05-06
3. Mishra RS, Ma Z (2005) Friction stir welding and processing. Mater Sci Eng R Rep 50(1–2):1–78

4. Schmidt H, Hattel J, Wert J (2003) An analytical model for the heat generation in friction stir welding. Modell Simul Mater Sci Eng 12(1):143
5. Thomas W et al (2002) Friction based welding technology for aluminum. In: Materials science forum. Trans Tech Publications Ltd
6. DebRoy T, Bhadeshia H (2010) Friction stir welding of dissimilar alloys–a perspective. Sci Technol Weld Joining 15(4):266–270
7. Murr L (2010) A review of FSW research on dissimilar aluminum alloys. J Mater Eng Perform 19:1071–1089
8. Mishra RS et al (2011) Friction stir welding and processing VI. John Wiley & Sons
9. Babu AS, Devanathan C (2013) An overview of friction stir welding. Int J Res Mech Eng Technol 3(2):259–265
10. Pandya S, Menghani J (2013) Friction stir welding of dissimilar 5xxx to 6xxx Al alloys: a review. Appl Mech Mater. Trans Tech Publications Ltd
11. Palanivel R et al (2012) Effect of tool rotational speed and pin profile on microstructure and tensile strength of dissimilar friction stir welded AA5083-H111 and AA6351-T6 aluminum alloys. Mater Des 40:7–16
12. Kasman Ş, Yenier Z (2014) Analyzing dissimilar friction stir welding of AA5754/AA7075. Int J Adv Manuf Technol 70(1–4):145–156
13. Sivachidambaram S, Rajamurugan G, Amirtharaj D (2015) Optimizing the parameters for friction stir welding of dissimilar aluminum alloys AA5383/AA7075. ARPN J Eng Appl Sci 10:5434–5437
14. Mastanaiah P, Sharma A, Reddy GM (2016) Dissimilar friction stir welds in AA2219-AA5083 aluminum alloys: effect of process parameters on material inter-mixing, defect formation, and mechanical properties. Trans Indian Inst Met 69(7):1397–1415
15. Ghosh M et al (2013) Friction stir-welded dissimilar aluminum alloys: microstructure, mechanical properties, and physical state. J Mater Eng Perform 22(12):3890–3901
16. Saravanan V, Rajakumar S, Muruganandam A (2016) Effect of friction stir welding process parameters on microstructure and mechanical properties of dissimilar AA6061-T6 and AA7075-T6 aluminum alloy joints. Metallography, Microstructure, Anal 5(6):476–485
17. Rao S, Naik Y (2018) Understanding the effect of multiple traverse feed during friction stir welding processes. Arch Metall Mater
18. Scialpi A, De Filippis L, Cavaliere P (2007) Influence of shoulder geometry on microstructure and mechanical properties of friction stir welded 6082 aluminum alloy. Mater Des 28(4):1124–1129
19. Guo J et al (2014) Microstructural and mechanical properties of dissimilar friction stir welds between AA6082-T6 and AA7075-T651. Mater Des 56:185–192
20. Kasman Ş (2019) Identification of the pin offset effect on the friction stir welding (FSW) via Taguchi-Grey relational analysis: a case study for AA 7075–AA 6013 alloys. Materialwiss Werkstofftech 50(11):1364–1381
21. Sharma N et al (2018) Material stirring during FSW of Al–Cu: effect of pin profile. Mater Manuf Processes 33(7):786–794
22. Sahlot P et al (2018) Wear-induced changes in FSW tool pin profile: effect of process parameters. Metall and Mater Trans A 49(6):2139–2150
23. Tamadon A, Baghestani A, Bajgholi ME (2020) Influence of WC-based pin tool profile on microstructure and mechanical properties of AA1100 FSW welds. Technologies 8(2):34
24. Eren B, Guvenc MA, Mistikoglu S (2021) Artificial intelligence applications for friction stir welding: a review. Met Mater Int 27(2):193–219
25. Maleki E (2015) Artificial neural networks application for modeling of friction stir welding effects on mechanical properties of 7075-T6 aluminum alloy. In: IOP Conference Series: Materials Science and Engineering. IOP Publishing
26. Yousif Y, Daws K, Kazem B (2008) Prediction of friction stir welding characteristic using neural network. Jordan J Mech Indus Eng 2(3)
27. Graupe D (2013) Principles of artificial neural networks, vol 7. World Scientific

28. Patel UA (2015) Optimization of process parameter in MIG welding process on dissimilar material by using artificial neural network. Ganpat University
29. Rajakumar S, Muralidharan C, Balasubramanian V (2011) Influence of friction stir welding process and tool parameters on strength properties of AA7075-T6 aluminum alloy joints. Mater Des 32(2):535–549
30. Elangovan K, Balasubramanian V (2008) Influences of tool pin profile and tool shoulder diameter on the formation of friction stir processing zone in AA6061 aluminum alloy. Mater Des 29(2):362–373
31. Malarvizhi S, Balasubramanian V (2012) Influences of tool shoulder diameter to plate thickness ratio (D/T) on stir zone formation and tensile properties of friction stir welded dissimilar joints of AA6061 aluminum–AZ31B magnesium alloys. Mater Des 40:453–460
32. Mehta KP, Badheka VJ (2016) A review on dissimilar friction stir welding of copper to aluminum: process, properties, and variants. Mater Manuf Processes 31(3):233–254
33. Yegnanarayana B (2009) Artificial neural networks. PHI Learning Pvt. Ltd
34. Kanti KM, Rao PS (2008) Prediction of bead geometry in pulsed GMA welding using back propagation neural network. J Mater Process Technol 200(1–3):300–305
35. Najafi B, Ardabili SF (2018) Application of ANFIS, ANN, and logistic methods in estimating biogas production from spent mushroom compost (SMC). Resour Conserv Recycl 133:169–178
36. Ghosh S et al (2016) Development of the location suitability index for wave energy production by ANN and MCDM techniques. Renew Sustain Energy Rev 59:1017–1028
37. Renno C, Petito F, Gatto A (2016) ANN model for predicting the direct normal irradiance and the global radiation for a solar application to a residential building. J Clean Prod 135:1298–1316

Study of Frictional Force and Volumetric Wear Rate of T6 Heat Treated Hypereutectic Al–18Si–3.6Cu–0.36Ce Alloy

Krishnaraddi Gangal and K. Devendra

Abstract Current research work is to study the effect of applied loads and the sliding speeds on the tribological behaviors of As-cast and T6 heat treated (cast aged at 1, 3, 5 and 7 h) conditions of the hyper eutectic Al–Si alloy with cerium alloying element. Experiments are conducted for different loads and sliding speeds on pin-on-disk tribometer setup, friction force, weight loss of the test specimen and surface roughness are frequently noted during test for applied loads (9.81–39.24 N) and sliding speeds (1–4 m/s). Experimental results of Al–18Si–3.6Cu–0.36Ce alloy concludes that the volumetric wear rate and the friction force F_n are dominated by applied loads and transition point of wear mechanism than the sliding speeds. Wear rate and F_n are increasing with load and decreased sliding velocity. COF varied in the range of 0.214–0.353; the wear rates are ranging from 0.88 to 6.8 $mm^3/m \times 10^3$. Rare-earth element Ce to Al–Si and T6 treatment noticeably enhances the mechanical and tribological properties of the hypereutectic alloy.

Keywords T6 heat treatment · Tribometer · COF · Wear rate · Transition point · As-cast · Hypereutectic alloy

1 Introduction

Hypereutectic aluminium alloys are abundantly used among the metal matrix alloys in wider range of automobile industrial applications because of their inherent physical properties such as high strength to weight ratio and are the most promising material with the effective tribological performance over the other alloys with fuel-efficient engine components [1–3]. Torabian et al. study reported that Al–Si alloys exhibit lower wear rates for increasing sliding speed up to certain speed and beyond that

K. Gangal (✉)
Department of Mechanical Engineering, Rural Engineering College Hulkoti, Hulkoti 582205, India
e-mail: krishnargangal@gmail.com

K. Devendra
Department of Mechanical Engineering, SKSVMACET, Laxmeshwar, India

K. Geetha et al. (eds.), *Recent Trends in Materials*, Springer Proceedings in Materials 18, https://doi.org/10.1007/978-981-19-5395-8_2

wear rate is high irrespective of the alloy composition and also noticed that the load bearing capacity of the alloy strongly depends on the silicon weight percentage, which increase with increasing silicon content in alloy. The wear process and its nature are strongly depending on compositions of the alloy and the experimental conditions [4, 5]. The T6 heat treatment of hypereutectic Aluminium-Silicon alloy significantly effect on the hardness, COF, microstructure and the wear rate of the alloy, and the fine silicon particles of the alloy reduce the friction, increase the load bearing capacity and reduce the wear rate with abrasion and adhesion wear at lower applied loads and adhesion and oxidative wear at higher loads [6]. The temperature at the sliding surface increases with the sliding speed due to frictional heat; the wear mechanisms also change with the increased sliding speed; during the lower speed, equi-axed wear particles are formed; around the critical speed, compacted particles will get delamination; beyond the critical sliding speed, the flakes are formed due to plastic deformation of the alloy; the critical speed depends on the hardness of the counter face material [5]. Parthasarathi et al. studied dry sliding wear test on AISI type 316L austenite stainless-steel at different operating temperature for 20 N load and 0.8 m/s sliding speed, the worn-out surfaces are used to study the surface roughness, then correlated with the coefficient of friction during wear and concluded that both the Ra and COF are the positive dependents of the operating temperature during the wear test [7].

Menezes et al. investigated the harder surface texture effect and its importance against the softer one throughout wear characterization of aluminum pins on pin-on-plate slide test. Friction force (COF) and the transfer layer formation during the wear of softer surface (aluminum pins) over hard steel plate surface by varying steel plate surface parameters, such as surface texture and roughness, were studied, it was noticed from the test that the friction force and the transfer layer formation are independent of the steel plate (harder) surface roughness and are controlled by surface texture of the steel plate [8], and also the alloys surface roughness (Ra) after the machining is decreased with the addition of copper to the alloy [9]. Addition of rare earth elements like Ce and Sr, individual and combined addition, has great effect on the modification of microstructure, wear and the tensile strength, by grain refinement of the Al–8Si alloy. The heterogeneous nucleation of primary silicon by adding Ce + P as a modifier in Al–21Si alloy also improves the tribological and mechanical properties [10, 11]. Czerwinski et al. studied the review on cerium in aluminum alloys and concluded that the availability of cerium and low cast and the appealing properties of the existing grades of aluminum alloys with cerium as a minor and major alloying element need to be developed with the wider commercial applications [12]. Mahmoud et al. reviewed that the refinement of primary silicon structure was noticed with Ce addition up 1.0 wt%, the nucleation temperature and the growth of Al–Cu phase increase with addition level of Ce, and the formation intermetallic compounds of Al–Si–Ce and Si–Cu–Ce will affect the silicon modification. Cerium addition to the alloy and secondary dendrites arm space will be improved by 36% and also the tensile strength of Al–11Si–Cu–Mg alloy [13].

Table 1 Chemical composition of the ally by weight%

Alloy	Grade	%Si	%Cu	% Ce	%Al
Al–18Si–3.6Cu–0.34Ce	3XXX	17.98	3.66	0.36	Balance

Fig. 1 Cylindrical test sample pins with worn-out surface

2 Experimental Details

2.1 Materials and Their Preparation

In the present investigation the hyper eutectic heat treatable alloy was prepared by conventional gravity casting method with following composition by weight as given in Table 1. Chemical composition of the alloy was examined by Spectro-Spark Emission spectrometer (Model QSN 750-II Panalytical XRD and XRF instrument) and also confirmed with EDS results from Fig. 5. The casting alloy ingots of size 180 mm × 25 mmΦ synthesized are machined on lathe to prepare the wear test sample of cylindrical pins of size 25 mm × 10 mmΦ, as shown in Fig. 1. The ingots are solutionized at 510 °C for 1 h and are water quenched at room temperature; further the different sets of cylindrical pins are subjected to artificial aging at 210 °C for different aging durations of 1, 3, 5 and 7 h in a muffle resistance furnace with a temperature accuracy of ±3 °C. All cylindrical pin surfaces are made flat in order to establish the better contact with counter surface, the edges are chamfered, and the pins are washed with acetone before and after the wear test. Wear tests are conducted at room temperature for different combinations of loads, speeds and aged conditions of test specimens.

2.2 Controlling Parameters and There Levels

Dry sliding wear test is conducted for four levels with the controlling variables such as applied normal load (N) and the sliding speed (m/s) as given in Table 2.

Table 2 Controlling factors and three levels

Controlling variables	Levels			
	I	II	III	IV
Sliding velocity, m/s	1	2	3	4
Normal load, N	1	2	3	4

For each condition of the alloy (As-cast and cast aged), sixteen (L16) combinations of loads and speeds are arranged to carry out the wear performance experiments on pin-on-disk setup.

2.3 Wear Test

Wear test is performed on pin-on-disk wear test machine supplied by DUCOM Instruments, Bangalore, to bring out the wear characteristics of the prepared hyper eutectic alloy against the hard surface of EN-32, having HRC 62-65, with relative humidity of 65% at room temperature. Cylindrical pins of size 25 mm × 10 mmΦ with flat contact surfaces are polished by using polishing disk machine; the polished surfaces are cleaned with acetone. The samples are weighed before and after the wear test using electronic weighing balance machine having accuracy of 10^{-7} kg. Weight loss method is employed to find the volumetric wear loss of the alloy pins using the equation, Volumetric Wear Rate $= [\Delta w \div (\rho L)]$, where $\Delta w = (w_i - w_f)$, w_i and w_f are the weights of cylindrical pin before and after the wear test and "ρ" is the density of the alloy (0.0027 g/mm^3). Wear test is performed for a fixed sliding distance of 2000 m, by varying sliding speed (from 1 to 4 m/s) and applied load (from 1 to 4 kg). During the test, the contact surface temperature and friction force developed between sliding members are noted with the help of digital display of controlling unit. For each condition of the alloy (As-cast and cast aged), experiment is repeated for constant load and constant speed at four levels (L16).

2.4 Metallographic Examinations

To understand the means of wear during the dry sliding test, the optical and/or the scanning electron microscopic examination is done on the worn-out surfaces of the pin samples for the metallographic study. From the images, the effect of heat treatment with Ce addition on the primary silicon and other alloy constituent in the alloy structure before and after the heat treatment is analyzed as listed in Fig. 2, the rare earth element cerium as a minor alloying element will enhance the hardness of the alloy and will play a major role in modifying the primer Si needle like structure in to a fine fibrous structure during the casting, and further T6 heat treatment results

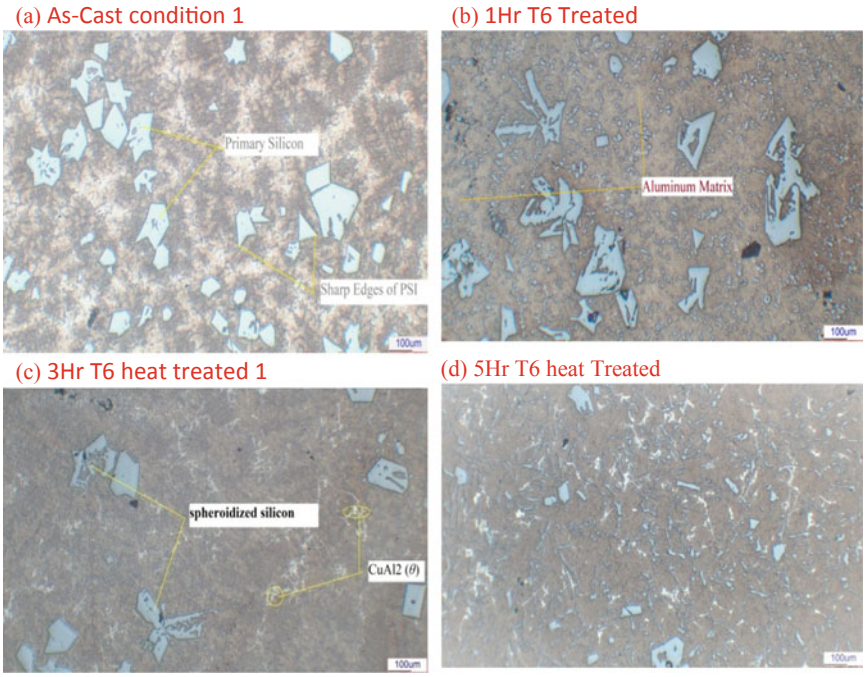

Fig. 2 Optical microscopic images of Al–18Si–3.6Cu–0.36Ce alloy. **a** As-cast condition; **b** 1 h T6 heat treated; **c** 3 h T6 heat treated and **d** 5 h T6 heat treated conditions alloy

in dissolution of left out larger and sharp needle like primary silicon particles into a fine dendrite structure which, in turn, improves the grain boundaries; hence, the mechanical properties such as harness, tensile strength and the wear properties are improved. Figure 5 shows the optical images of the alloy samples of As-cast and cast aged conditions. EDAX technique is used to analyze the elemental chemical characterization of the alloy.

3 Results and Discussions

3.1 Mechanical Properties and Microstructure of the Alloy

Aluminium–silicon alloys are having the most industrial application after the steel in automobile industries, aerospace and marine industries [6]. As these alloys possess the good characteristics such as resistance to wear, hardness, anti-corrosive, heat treatable, low thermal expansion and good strength to weight ratio with increasing the presence of silicon content, the tensile strength of alloy increases with silicon presence but decreases in % of elongation continuously with further addition of

silicon [11, 14–16]. Cu addition to alloy can be in the range of 2–5%; by increasing the hardness, most of the mechanical properties of Al–Si–Cu alloys are turned on with the heat treatment and will lead to the betterment of microstructure of the alloy by forming Al_2Cu stable phase [15].

Solution treatment followed by T6 heat treatment of the Al–18Si–3.6Cu–0.36Ce alloy in the presence 3.6% Cu, the primary α-Si particles of irregular shapes are transformed into spheroidized silicon particles as outcome of precipitation. These changes in the microstructural level bring noticeable improvements in the mechanical properties of the alloy [17, 18] such as tensile, wear and the hardness. Re-precipitation and the redistribution of $CuAl_2$ (θ) are largely formed in the grain boundary. There are no remarkable changes in primary silicon particles seen before and after T6 treatment for lower aging time of 1 h, and the large silicon particles of round dark colored are distributed in aluminium matrix [18]. From Fig. 2, the microstructure of the As-cast and cast aged Al–18Si alloy with 3.6% Cu and 0.36% Ce by weight, coarser primary silicon is formed in this alloy as compared to eutectic Al–Si alloy; Si is the brittle and hard element as compared to Al which is ductile in nature and softer, so in the Al–Si melt, the soft structure of α-Al function as dendrite matrix, eutectic phase was formed by the reaction of partial Si with Al [19]. In the presence of Ce in hypereutectic alloy, the intermetallic compounds are formed due to dissolution of Ce in α-Al. Matrix and needle like dendritic structures of AlCe and $CeAl_{1.2}Si_{0.8}$ are formed; addition of Ce modified the morphology of Si more intensively from coarser eutectic in to fine fibrous [10, 11, 19]. Wang et al. studied that Ce beyond 0.6% to Al-21Si will weaken the refinement effect of primary silicon crystal particles; at 0.6% Ce, the silicon crystal particles sizes are reduced from 66.4 to 23.3 μm with reduced silicon grain size 8.3 to 5.2 μm [11]; hence, the wear characteristics will be improved by adding the Ce to the Al–18Si alloy. In a hypereutectic Al–18Si–4Cu–0.5 Mg alloy, the addition of 0.3 wt% of LaCe has great effect in reducing the primary Si size from 61 to 28 μm, coarse blocky and irregular polygonal silicon shapes into fine lakes. Hence, the structural modification of hypereutectic alloy enhances the UTS by 9%, and elongation also improved by 97% by changing the fracture mode from brittle to ductile [20]. Bevilaqua et al. studied that the effect of Ce (0.3 wt%) and Zr (0.16–0.36 wt%) addition to Al–Si–Cu–Mg alloy is the reason for thermal stability of the alloy due to the intermetallic phases formed with 0.3 wt% Ce and 0.27 wt% Zr, at 275 °C improved the yield strength by 13.8% as compared to the base alloy and concluded that this combination will be the most effective at elevated temperature applications with high yield strength [21]. Zou et al. study on the combined effect of T6 treatment and Pr + Ce addition to Al–Si–Cu–Mg alloy concludes that the corrosion density was reduced immensely, and the micro-hardness of the alloy increased by 27.8% as compared to the base alloy matrix. Fish bone like phase of inter metallic compounds, such as $Al_{12}FeMnSi$ bright block like points, is reformed to long needle structure. Al_2Cu phases are distributed more uniformly after combined effect [22].

3.2 Wear Characterization

3.2.1 Effect of Applied Load

Volumetric wear rate is the measure of weight loss per unit sliding distance; for all combinations of applied loads (1–4 kg) and sliding speeds (1–4 m/s), the wear rates are computed for As-cast and cast aged conditions of the alloy. The wear rate takes place in three different regions in the alloy as mild, intermediate and the severe wear; changing from one region to other is called transition point [15]. During the wear test, the coefficient of friction and the wear rates are observed, are solely dominated by the applied load and are increased with applied load [20, 23] as shown in Fig. 3a, b. Because of the transition of wear from mild wear at low loads and speeds to moderate rate by adhesion wear and severe at higher applied loads. From Fig. 3b, it was observed that the wear rate gradually increases with the load up to 3 kg, and further loading will not have dominating effect on wear rate for 1, 3 and 5 h T6 treated samples, instead they show decrease in wear rates, but As-cast and 7 h treated samples have a tendency of increase in wear rate with further increased loads beyond 3 kg, which may be due to severe wear and delaminating wear by plastic deformation. From Fig. 3a COF for As-cast samples was increased with load; due to the hard particles of primary silicon, abrasive wear was noticed. For 7 h samples, COF was gradually increased with applied load from 1 to 4 kg at 1 m/s. From the experimental observations, the coefficient of friction for all conditions of samples increased with load up to 3 kg at lower speeds and remains flat with further loading.

But COF and wear rates are decreased with increased sliding speed as shown in Fig. 3c, d, due to reduced contact time and the formation of oxidative layer between the two-sliding surface and due to rise in temperature at contact surface during the high speed. 1, 3 and 5 h T6 treated alloy samples show low wear rates as a result of oxidative and mild wear rate by forming equi-axed wear particles as compared to As-cast, and the 7 h T6 treated alloy at high velocity (3–4 m/s) and loads (3–4 kg) results in severe wear rates by forming de lamination and adhesive wear. The different worn-out surface SEM images are shown in Fig. 4.

3.2.2 Effect of Sliding Speed

From the experiment result, the plots of COF and volumetric wear rates are drawn for constant applied load and speed to all conditions of the (As-cast, 1, 3, 5 and 7 h aged) alloy as shown in Fig. 3c, d; it is noticed from the Fig. 3d that the wear rates are reduced initially by increasing the sliding velocity up to certain speed (2.5 m/s) due to adhesive wear (powder like metal particle); beyond 3 m/s sliding velocity, the wear rate of As-cast and 7 h heat treated samples shows high wear rates with sliding speed due to delaminating of surface by transition point noticed from SEM images in Fig. 4; 1, 3 and 5 h treated samples show gradually decrease in wear due to oxidative and mild wear as sliding speed increased. Coefficient of friction also decreased with

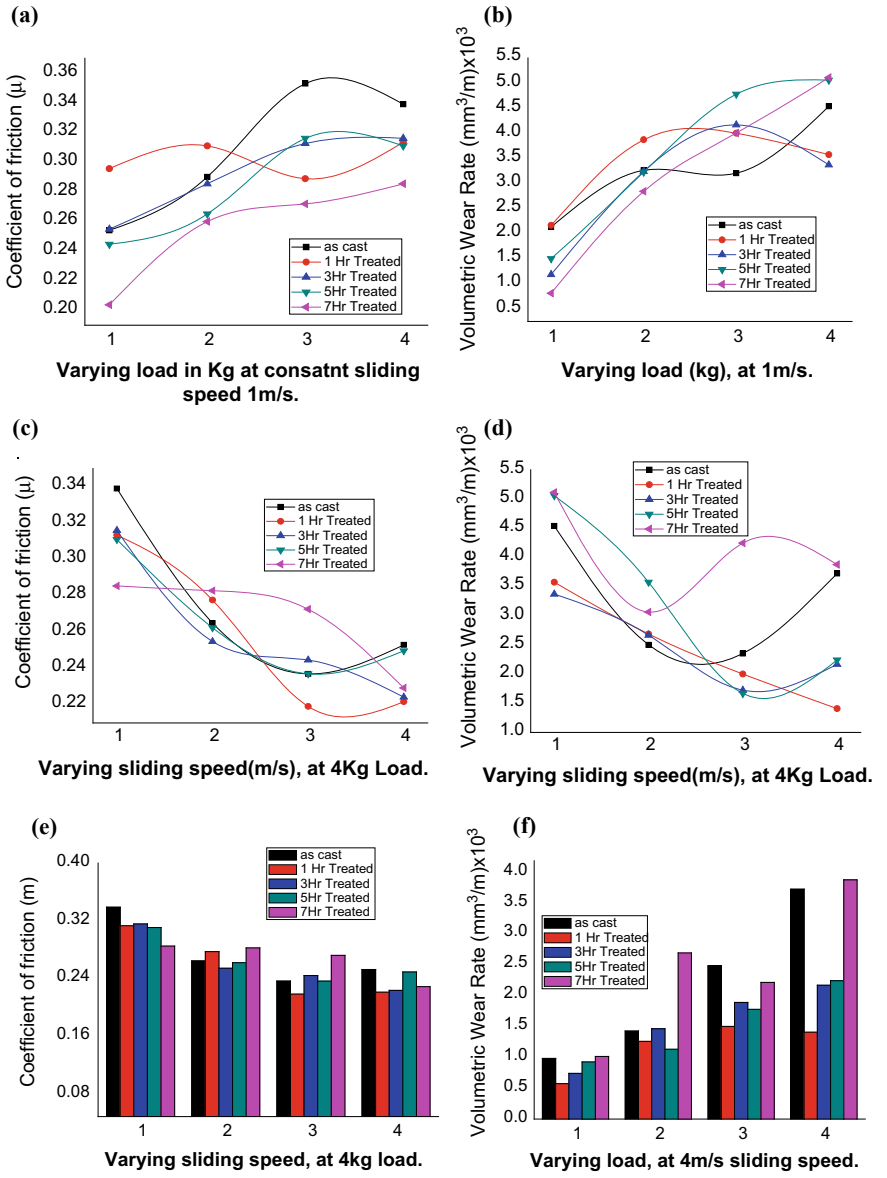

Fig. 3 **a** COF versus load at 1 m/s; **b** VWR versus load at 1 m/s; **c** COF versus speed at 4 kg load; **d** VWR versus speed at 4 kg load; **e** bar chart of COF versus sliding speed at 4 kg load; **f** bar char of VWR versus load at 4 m/s

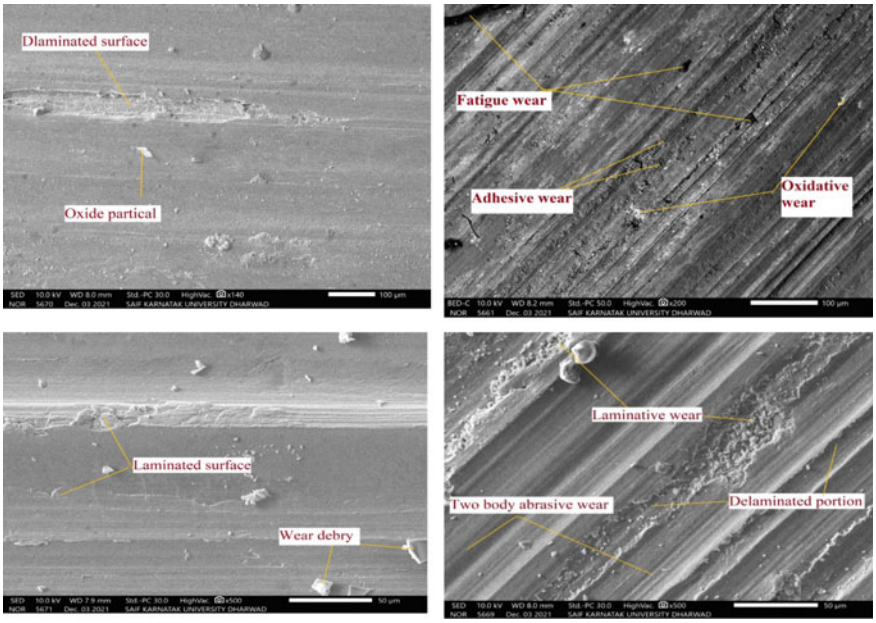

Fig. 4 SEM images of worn-out surfaces, taken at SAIF Karnataka University Dharwad

increasing speed due to skidding and oxidative wear and forming new surface by delaminating surfaces as examined from SEM analysis as shown in Fig. 4.

From Fig. 3e, f, the overall experimental observations show that COF greatly reduced for 1, 3 and 5 h treated samples as the sliding velocity increased from 1 to 4 m/s. During constant speed 4 m/s by varying the load from 1 to 4 kg, 1 h treated samples show a greater wear resistance among all other samples, and 3 and 5 h aged samples also performed better wear resistance as compared to As-cast and the 7 h aged conditions.

3.2.3 Effect of Cerium as a Minor Alloying Element and T6 Treatment

Cerium is an effective rare earth element having superior chemical and the physical properties which will satisfy the recent engineering applications; Ce is a silvery white metal, ductile in nature, softer and having an atomic no-58, which is abundantly available with rank no. 26. Rare earth metal addition to hypereutectic Al–Si alloy will help in many metallurgical aspects such as de-gasifying and de-slagging agent; by reacting with the impurities in the melt, refinement effect on the microstructure results a stable compound with high melting point. Micro-hardness of the alloy is achived by having intermetallic phases of Ce_3Al and $CeAl_{11.2}Si_{0.8}$ compounds [11, 19]. And from the wear test, it is confirmed that the wear properties of Al–Si alloy enhanced. From SEM analysis and the XRD, the intermetallic compounds in the

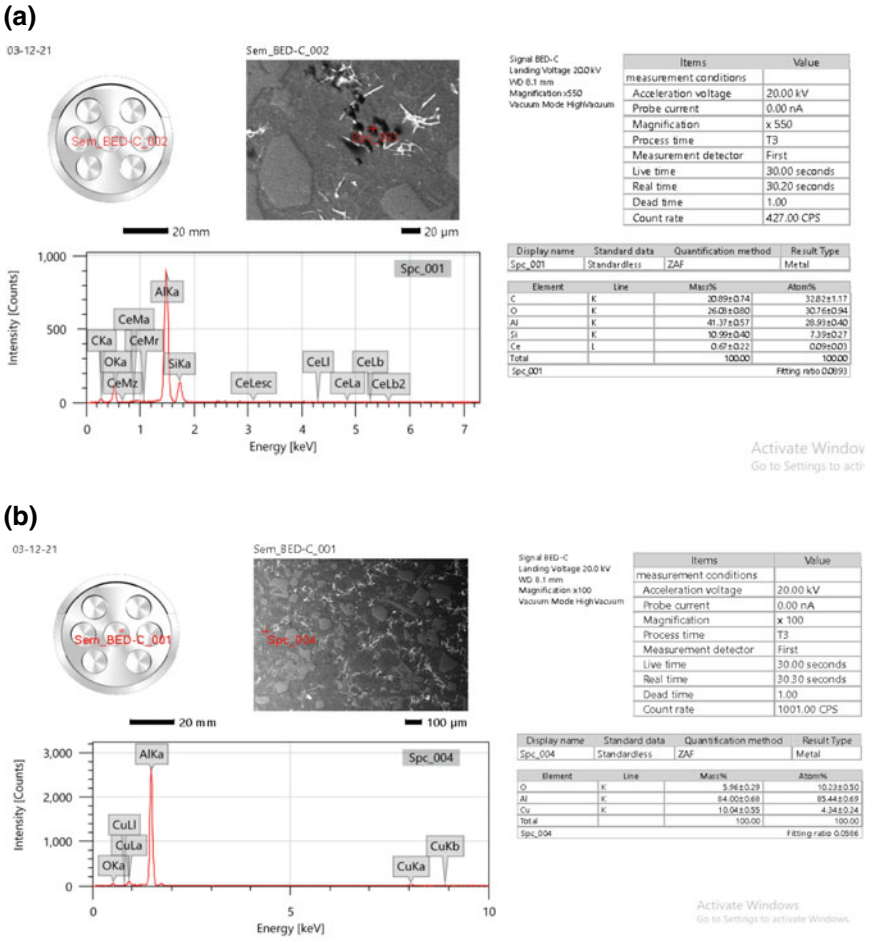

Fig. 5 **a** EDS result_spot1 **b** EDS result_spot2

alloy are restructured with T6 treatment, and Al_2Cu phases are uniformly scattered as shown in optical images in Fig. 2. The grain size of silicon particles are reduced by the combined effect of Ce addition and T6 treatment, the re-rich intermetallic compounds are noticed such as Al3Ce, which will enhance the micro-hardness; intern the wear properties are improved.

3.2.4 SEM and EDAX

Figure 4 shows the worn-out surfaces of pins SEM images taken at SAIF Karnataka University Dharwad, Karnataka.

From the metallographic and visual evidence of worn-out surfaces of the alloy, we can state that Al–18Si–3.6Cu–0.36Ce alloy gets wear under the influences of different wear mechanism as shown in Fig. 4, at different operating conditions such as applied load, sliding speed and the temperature developed between two contact surfaces. The oxidative and two body abrasive moderate wear took place under low and medium loads and sliding speeds; by increasing strain rate in succession, it will increase the flow strength (hardness) of contact surface of pin; during this wear, the smaller metallic particles in the form of dust are produced. As the operating speed increased, the oxide layers will get soften as the frictional temperature directly varies with speed; hence, the contact area is improved, and in turn, it will result in a high wear beyond the critical speed [4]. At higher load and sliding speed, the limitative, metallic and adhesive wear are seen as a result of plastic deformation, and the sub surfaces will get delaminated. Energy dispersive X-ray spectroscopy analysis is made for chemical characterization of the samples as shown in Fig. 5.

4 Conclusion

The overall observations of the dry sliding wear behavior of the As-cast and T6 age hardened hypereutectic Al–Si alloy with addition of Cu and Ce as alloying elements; for varying loads (1–4 kg) and sliding speeds (1–4 m/s) are drawn as follows:

1. Volumetric wear rates are having linear relation with applied load; increasing wear rate is observed for all conditions of the alloy as load increased; at lower loads and speeds, the oxidative wear and adhesive wear occur; as load increased, the wear mechanism changes to medium and then to erosive wear.
2. Age hardening of the alloy for different durations (1, 3, 5 and 7 h) by T6 heat treatment shows a noticeable reduce in wear rates for all combinations of wear test as compared to As-cast alloy. Due to age hardening the temperature generated at contact surfaces during relative motion will not affect much on wear rate of aged samples as compared to As-cast conditions; as the sliding speed increases, the friction temperature also increases which, in turn, softens the surface of the untreated (As-cast) pin surface material, so that more contact surface area of pin will be exposed to wear for un treated (As-cast) condition.
3. Friction force developed during dry sliding of Al–18Si–3.6Cu–0.36Ce alloy has linear relation with applied load and sliding speed, which increases with applied loads and decreases with sliding velocity as a result of increased contact surface area.
4. As-cast and the 7 h aged alloy samples will show higher wear rate compared to 1, 3 and 5 h aged samples at 3 and 4 m/s critical sliding speeds by varying the load combinations of the test, which may be due to low load bearing capacity, the entire metallic particles wear and deforming the subsurface layers.

5. Wear rate also depends upon the nature of wear such as oxidative wear which occurs at lower speed and loads; oxidative and the metallic wear debris will form at moderate loads and the severe metallic wear at higher applied loads.
6. Compared to other hypereutectic Al–Si alloy, Al–18Si–3.6Cu–0.36Ce alloy greatly enhances wear and mechanical performance in the presence of cerium as an alloying element by intensively reducing the eutectic silicon size and refinement of primary Si crystals.

References

1. Aluminium Association (1984) In Hatch JE (ed) Aluminium: properties and physical metallurgy. ASM International, pp 1–24. https://doi.org/10.1361/appm1984p001
2. Kumar KG (2013) Influence of refinement and modification on dry sliding wear behavior of hypereutectic Al–Si cast alloys. Adv Mater Res 685:112–116
3. Rohatgi PK, Pai BC (1974) Effect of microstructure and mechanical properties on the seizure resistance of cast aluminium alloys. Wear 28:353–367
4. Torabian H, Pathak JP, Tiwari SN (1994) Wear characteristics of Al–Si alloys. Wear 172:49–58
5. Subramani C (1991) Effects of sliding speed on the unlubricated wear behaviour of Al–12.3wt.%Si alloy. Wear I51:97–110
6. Naik MP, Padal KTB (2019) A review on friction and wear performance of Al–Si alloy/steel tribopair. Mater Today: Proc 18:5502–5506
7. Parthasarathi NL, Borah U, Albert ShK (2013) 2013, Correlation between coefficient of friction and surface roughness in dry sliding wear of Ai–Si 316 l (n) stainless steel at elevated temperatures. Comp Modell New Technol 17(1):51–63
8. Menezes PL, Kishore, Kailas SV (2009) Influence of surface texture and roughness parameters on friction and transfer layer formation during sliding of aluminium pin on steel plate. Wear 267:1534–1549
9. Saggu HS Dr (2019) To study the influence of slight additions of chromium and copper on surface roughness of Al–Si alloy. JETIR 6(3), March 2019. www.jetir.org. ISSN: 2349-5162
10. Vijeesh V, Prabhu KN (2015) The effect of addition of Ce and Sr on the solidification path of Al–8Si–2Cu alloy. Trans Indian Inst Met 68(6):1119–1123. https://doi.org/10.1007/s12666-015-0656-z
11. Wang A, Zhang L, Xie J (2013) Effects of cerium and phosphorus on microstructures and properties of hypereutectic Al–21%Si alloy. J Rare Earths 31(5):522, May 2013
12. Czerwinski F (2019) Cerium in aluminum alloys. Canmet Materials, Natural Resources Canada, Hamilton, ON, Canada, 28 Aug 2019. https://doi.org/10.1007/s10853-019-03892-z
13. Mahmoud MG, Zedan Y, Samuel AM, Songmene V, Doty HW, Samuel FH (2021) Applications of rare earth metals in Al–Si cast alloys. February 26th 2021. https://doi.org/10.5772/intechopen.96011
14. Elzanaty H (2015) Effect of composition on the microstructure, tensile and hardness properties of Al–xSi alloys. J Mater Sci Surf Eng 2(2):126–129
15. Zeren M, Karakulak E (2009) Study on hardness and microstructural characteristics of sand cast Al–Si–Cu alloys. Bull Mater Sci 32(6):617–620. December 2009. © Indian Academy of Sciences
16. Fathy N (2014) Microstructural evolution of hyper-eutectic Al–18% Si alloy during semi-solid isothermal heat treatment. Int J Res Chem Metall Civil Engg (IJRCMCE) 1(1). ISSN 2349-1442, EISSN 2349-1450
17. Pio LY, Department of Material science and Manufacturing Science, University Tunku (2011) Effect of T6 heat treatment on the mechanical properties of gravity die cast A356 aluminium

alloy. J Appl Sci 11(11):2048–2052, 20: ISSN 1812-5654. https://doi.org/10.3923/jas.2011.2048.2052
18. Heo JY, Gwon JH, Park JK, Lee KA (2018) Effects of heat treatment on the microstructures and high temperature mechanical properties of hypereutectic Al–14Si–Cu–Mg alloy manufactured by liquid phase sintering process. Met Mater Int.https://doi.org/10.1007/s12540-018-0068-9
19. Joy Yii SL, Anas NM, Ramdziah MN, Anasyida AS (2016) Microstructural and mechanical properties of Al-20%Si containing cerium. Procedia Chem 19(2016):304–310
20. Al-Samarai RA, Haftirman AKR, Al-Douri Y (2012) Effect of load and sliding speed on wear and friction of Aluminium–Silicon casting alloy. Int J Scien Res Publ 2(3), March 2012. ISSN 2250-3153
21. Lin G, Li K, Feng D, Feng Y, Song W, Xiao M (2019) Effect of LaCe addition on microstructure and mechanical properties of Al–18Si–4Cu–0.5Mg alloy. Trans Nonferr Met Soc China 29(2019):1592–1600
22. Zou Y, Yan H, Hul Z, Ran Q (2020) Effect of (Pr + Ce) addition and T6 heat treatment on microhardness and corrosion of AlSi5Cu1Mg alloy. Mater Res Express 7(2020):026526. https://doi.org/10.1088/2053-1591/ab6fa7
23. Al-Samarai AR, Haftirman, Ahmad KR, Al-Douri Y (2013) Effect of roughness of hypo- and hyper-eutectic Al–Si piston alloy on wear characteristics under lubrication. Procedia Eng 53(2013):616–623. Elsevier

Phased Array Ultrasonic Evaluation for Defect Characterization in Aerospace Grade Maraging Steel MDN250 Weldments

M. Prema Kumar, M. V. N. Mohan, V. Malolan, and Nakka Sudarshan

Abstract Quality and reliability are of great importance in aerospace industry. The factor of safety (FoS) for the aerospace structures is challenging. To meet the challenging FoS, the materials used for pressure vessels are expected to have a very high specific strength. It is important to critically evaluate the internal discontinuities present in a material. Radiographic testing (RT) and ultrasonic testing (UT) have limitations in precise detection and sizing of flaws. Phased array ultrasonic testing (PAUT) technique overcomes the limitations in RT as well as conventional UT. PAUT is an effective method to detect 'tight cracks' in the weldments irrespective of orientation in materials and weld joints. This paper deals with the PAUT technique for detection and characterization of flaws in a thin (3.8 mm) pressure vessel weld joints of maraging steel MDN250. This paper demonstrates PAUT superiority over RT and conventional UT. Three case studies are presented to substantiate the claim.

Keywords PAUT · NDT · RT · UT defect characterization · Pressure vessel · Weld inspection · Maraging steel · Aerospace structures · Quality

1 Introduction

The high specific strength materials like MDN250 maraging steel is being used in realization of rocket motor casing pressure vessels. Highly fracture-prone MDN250 has brought a change in the design philosophy as well as in quality assurance methodology. PAUT technique is more suitable for the evaluation of weld joints in thin sections. The PAUT technique is implementing in various industries such as in the field of medical, low-thickness pressure vessels, and aerospace industry. This technique increases the quality and reliability in inspection. The probe with small foot print can inspect the weldment without moving the probe. This technique is also suitable for inspection where there is inadequate access to scanning. PAUT has overcome the limitations in conventional UT and RT with demonstrating its defect

M. P. Kumar (✉) · M. V. N. Mohan · V. Malolan · N. Sudarshan
Advanced Systems Laboratory, DRDO, Hyderabad, India
e-mail: premakumarscientist@gmail.com

K. Geetha et al. (eds.), *Recent Trends in Materials*, Springer Proceedings in Materials 18, https://doi.org/10.1007/978-981-19-5395-8_3

detection capabilities in foremost areas such as weld inspection, hidden crack detection, and internal discontinuities in thin sections. Extensive welding is the prime source of defects. Complete elimination of defects is not warranted and uneconomical. Complex geometrical structures can be simply inspected with this technique. Weld inspection can be done easier with single-element probe. Multiple angles can be projected from single-element crystal which increases the possibility in detection of defect. NDE is used as an effective tool to identify and to take a judicious decision for repair. Conventional radiographic testing complimented with ultrasonic testing is very effective in detecting the flaws in welding and heat-affected zones. Convectional UT and RT methods are used to demonstrate geometry and orientation of the defects in the welding and heat-affected zones. Certain tight cracks in a brittle weldment may go undetected by these methods due to either the limitations of the technique or fatigue of the operator.

2 Literature Review

Erhard et al. [1] have applied PAUT for in-service inspection of nuclear components. Parker and Zimmermann [2] have studied theory and architectures of phased arrays. Moles and Ginzel [3] have applied PAUT in inspection of thin-walled pipes and the components with smaller cross-section in diameter. Xiao et al. [4] have studied the grain noise in ultrasonic for interpretation of post-signal data. Gowri Shankar et al. [5] have studied the quality evaluation in motor casings for detection of crack while hydraulic pressurization. Thakur and Chapgaon [6] have studied the effects that caused by using of gas tungsten arc welding technique and the details of the weld parameters. Prema Kumar et al. [7] have applied PAUT for the inspection of welds in pressure vessels used in rocket industry. Dheeraj et al. have applied PAUT technique over conventional UT for inspection of weldments in single-sided access. Kutelu et al. [9] have studied the welding parameters which may affect mechanical properties and corrosion that caused due to GTA welding. Li et al. [10] have applied PAUT technique for fast and accurate inspection of butt-welded components. Pei et al. [11] have applied PAUT technique for detection of internal cracks in metal specimens. Sumana et al. [12] have applied PAUT for inspection detection of narrow gaps between the dissimilar metals and finding out the planar defects in forgings. Introduction to phased array ultrasonic technology applications [13] by OLUMPUS NDT has briefed the theory of PAUT. Zhang [14] has applied PAUT for inspection of weld seams in various industries. Society for automotive engineers (SAEs), aerospace material standards—SAE AMS 2632B for reference standard [15]. Lei et al. [16] have applied PAUT in inspection of side-drilled hole (SDH) for evaluation of focusing various depths. Kumar et al. [17] have applied PAUT in inspection of nuclear reactor components for evaluation of lack of side-wall fusion in welding. Vithanage et al. [18] have applied PAUT for inspection of side-drilled hole (SDH) and artificial defects which are implanted in multipass of welding for evaluation and further usage in industries. Liu et al. [19] have applied PAUT for inspection of small diameter tubes

Table 1 Mechanical properties of material

Parameter	Parent material specimens	Weld specimens
Ultimate tensile strength	1758 MPa (minimum)	1582 MPa (minimum)
0.2% Proof stress	1689 MPa (minimum)	1520 MPa (minimum)
% Elongation for GL of 50.8 mm	4% (minimum)	3% (minimum)

in power plant and power station boilers. Šimeková et al. [20] have applied PAUT for inspection in thin weld joints for evaluation of the detection capabilities in location and sizing of defects in weld joints.

3 Materials and Method

The current work is aimed at demonstration of superiority of PAUT over conventional NDT techniques. For experimental demonstration real case studies, pertaining to aerospace industry using maraging steel, GTA welding are taken. The details of the materials and methods are given below.

3.1 Materials

High specific strength maraging steel is used for construction of pressure vessel. The base metal used in this study is in aging condition. The material is heat treated and quenched. The filler metal chosen is MDN250-W2 for GTA welding. The specified mechanical properties of the base metal are listed in Table 1. The mechanical properties of the weld specimen and parent specimen are subjected to tensile testing as per ASTM A 370 with 50.8 mm gauge length (GL).

3.2 Method

Welding. The welding technique used in fabrication of pressure vessels is gas tungsten arc welding (GTAW). GTAW is especially suited for welding of thin metals, metals ranging from sheet metal up to ¼ in including expansion bellows, transistor cases, instrument diaphragms and can-sealing joints. The microstructural changes that occurs during welding and at weld joint are still a major challenge today as it affects the corrosion resistance and mechanical properties of the material.

The following weld parameters are chosen for current work.

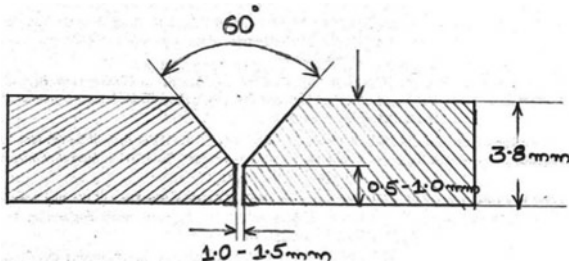

Fig. 1 Weld configuration

(a) Weld design: Single V with 60º angle.
(b) Root gap: 1.0–1.5 mm
(c) Base height: 0.5–1.0 mm as shown in Fig. 1.
(d) Welding current: In root weld, current is DC negative, peak current is 130–150 and back ground current 40–50%. In final weld, DC negative, peak current is 120–140 and back ground current 40–50%.
(e) Welding voltage: In root welding layer and final welding layer, the voltage 15–18 eV is maintained.
(f) Welding speed: In root welding layer, the welding speed is maintained as 80–120 mm/min and for the final weld layer, the welding speed is maintained as 50–90 mm/min.
(g) Shielding gases: Shielding gas used in welding of maraging steel MDN250 is ARGON—IOLAR Gr I. The flow rate of the shielding gas is 10–13 l/min, and backing 6–9 l/min is maintained for MDN250 welding.
(h) Filler Metal: In welding of maraging steel, the filler metal used is MDN250-W2. Two different filler metal diameters used in welding of root weld layer and final layer. In welding of root layer, 1.6-mm-diameter filler metal is used, and for final weld layer, 2.5-mm-diameter filler metal is used.

A detailed step-by-step workflow is mentioned in block diagram. Starting from the stage of raw material to the activities carried out, post-welding is shown in Fig. 2.

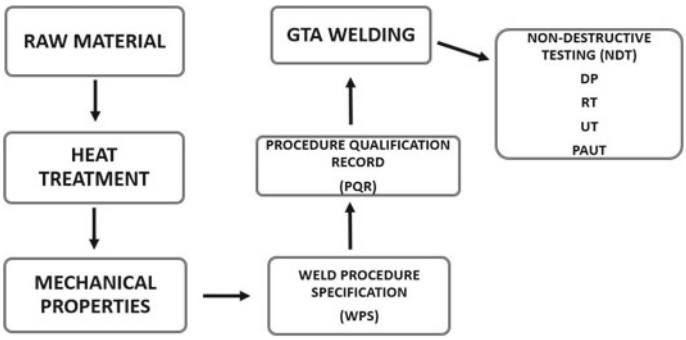

Fig. 2 Schematic block diagram

Type of Flaws in GTA Welding

- Lack of penetration
- Excessive penetration
- External and internal undercut
- Lack of fusion
- Porosity
- Tungsten inclusions
- Transverse and longitudinal cracks.

4 Evaluation Method

The phased array ultrasonic testing was performed on solid rocket motor casings fabricated using maraging steel. Welding is a dominant process in fabricating the solid motor casing. GTAW was during the fabrication. The PAUT equipment used is OLYMPUS® make, MX model, and 4 MHz and 16 element probe.

4.1 Phased Array Ultrasonic Testing

In recent years, use of PAUT for aerospace application has increased due to its superiority over other NDT techniques in weld inspection and in-service crack detection. Phased array technology uses multi-element probes in a single capsule that can steer the ultrasonic beams in desired directions which is refereed as sectorial scanning with movement of the probe. By this way, weldment inspection is carried out with multiple angles that increases high probability of detection of defects. This method also increases inspection speed to an extent of ten times over conventional UT. Simultaneous scanning with multiple angles is possible for inspection of larger areas and weld joints by single linear scan. The imaging setup of S-Scan is used for finding the defects at appropriate angles.

Conventional UT relies entirely on single-element transducer that uses one piezoelectric crystal. Because of that the beam is diverted and unidirectional for monocrystal probe, while it is focused and multiangled for phased array probe. Crack of most orientations can be detected by phased array probe shown in Fig. 3.

4.2 Limitations of RT, UT and PAUT

Limitations in RT

- Radiographic testing needs safety and permitted working environment. The safety parameters should maintained.

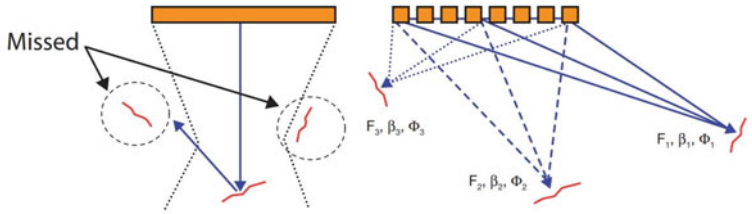

Fig. 3 Detection of flaws with convention UT (left) and PAUT (right)

- This testing needs trained operator with licensing certificate.
- Poor detection capability in finding of planar defects and depth of the defect.
- RT causes radiation hazards to the operator.
- RT requires films storage facility.
- It produces chemical waste which is hazards to the environment.

Limitations in UT

- Ultrasonic testing operates on the single-element transducer with one piezoelectric crystal
- Storage and recording facility is not available
- Multiple probes and multiple setups are require for inspection
- This technique completely depends on single imaging setup
- Detection probability and sizing of small stress corrosion defects are difficult
- It requires more time for inspection of larger areas
- Trained operator is required.

Limitations in PAUT

- Equipment is higher in cost
- Requires highly skilled operator for operation and data interpretation.

4.3 Experimental Arrangement

The experimental arrangement for inspection of thin pressure vessel is detailed with a block diagram in Fig. 4. Before testing on the real component, PAUT requires few setup steps. A reference plate of size 300 × 300-mm maraging steel weld plate with implanted F-notch as shown in Fig. 5. A probe of 16 element and frequency of 4 MHz is used. PAUT equipment of OLYMPUS make, MX model is used for the inspection. Various focal parameters are setup in the machine. Focal parameters such as material velocity, material thickness, range of scanning, sweep angle, gate settings, imaging setup, and probe settings. After completion of the parameter setting in machine then scanning is carried over reference plate to setup gain dB, range and sweep angle setup as shown in Fig. 5. Inspection is carried out on the pressure vessel and while

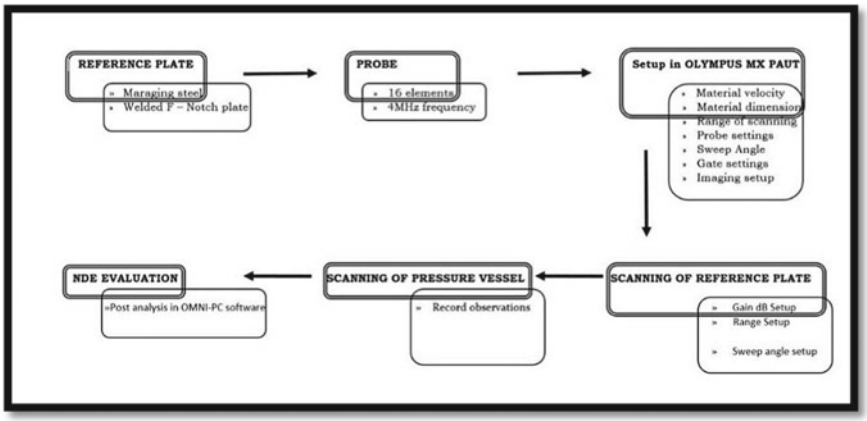

Fig. 4 Block diagram of evaluation methodology

scanning if any observation or defects are recorded in the machine for post-analysis. Recorded observations are evaluated in detailed by using OMNIPC software.

4.4 Reference Standard

A reference plate of size 300 × 300-mm maraging steel weld plate is used as a reference as shown in Fig. 5. The notches are prepared on the reference plate to a size of the 'F' notch. Notches are created in both longitudinal and transverse direction for parent metal, weldment and heat-affected zone (HAZ) as shown in Fig. 6. Scanning of this reference notch is carried out with phased array probe.

4.5 Acceptance Criteria

Ultrasonic test acceptance criteria for thin pressure vessel section are SAE AMS 2632. The acceptance level is selected from SAE AMS F-notch. The notch acceptance criterion is chosen to correspond to critical crack size arrived by fracture design. The dimensions of the notch are shown in Table 2. PAUT test performed using this evaluation criterion.

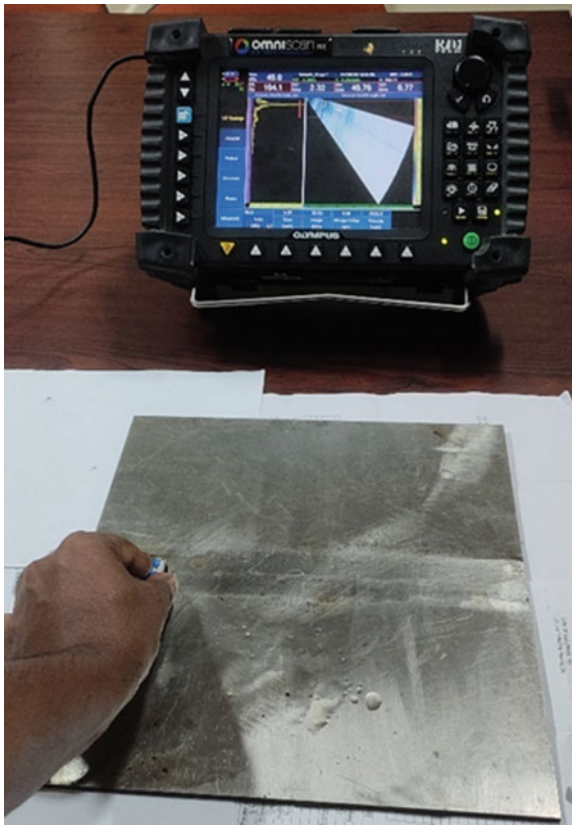

Fig. 5 Scanning of F-notch reference plate

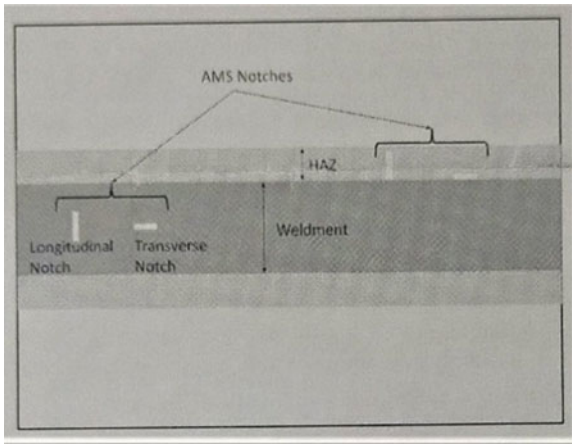

Fig. 6 Typical ultrasonic welded reference plate. *Source* IJDR [7]

Table 2 Dimensions of F-notch

SAE AMS notch	Length in mm	Depth in mm	Width in mm	Area in mm^2
F	1.27	0.76	0.25 maximum	0.97

5 Case Studies

An experimental study is carried out in the flaw detection capacities of RT and PAUT. 3.8-mm-thick and 630-mm-diameter shells of maraging steel pressure vessel are the inspected in this case study. Weld joint of single V 60º is made as shown in Fig. 1. In A-Scan imaging setup, range is calculated as per the skip distance calculation, i.e., skip distance $= 2t \times \tan\theta$, where t is the thickness of the pressure vessel and θ is the scanning angle of probe and gain of 42 dB is set as per reference standard. In S-Scan imaging setup, a sectorial view of 50º–80º ultrasonic beam spread angle is generated for the entire weld coverage. In the combination of A–S-Scan imaging scanning is carried on pressure vessel. In a particular weld joint, a lack of fusion, under-cuts, and porosities are noticed in radiographic film as shown in Figs. 7a, 8a, and 9a. Due to low sensitivity, poor detectability for planar defects in the film and evaluation through conventional UT is difficult to evaluate the observed defect. For demonstration of RT and conventional UT over PAUT, the defect noticed in radiographic film is scanned with phased array ultrasonic testing. PAUT equipment OLYMPUS make, MX model, and 4 MHz and 16 element probe is used for scanning.

5.1 Case Study 1

In radiographic film review a lack of fusion (LF) is noticed to a length of 10 mm from $D + 35$ to 45 mm shown in Fig. 7a. In radiographic review, it is difficult to identify the orientation, position, and the depth of the defect in the welding. To eliminate this problem case and to demonstrate the detection capability of PAUT, an experimental study is carried out. SAE AMS F-notch is taken as a reference, and Setup is made as per the reference standard shown in Fig. 5 and dB equivalent to 100% amplitude of full screen height (FSH) as per acceptance criteria. Imaging setup of A-Scan and S-Scan is used while scanning. Scan plan has to be configured in the phased array instrument as per weld configuration. The regions, which are identified as problem in radiographic review that is DE segment, are scanned and found the defects beyond the acceptable criteria. While scanning the weld segment, it is observed that a peak of amplitude 108% at a depth of 2.80 mm for a length of 10 mm is noticed as shown in Fig. 7b.

Inference of Case Study 1. PAUT analysis reveals the exact size, location and orientation of defect there by the weld joint is recommended for repair.

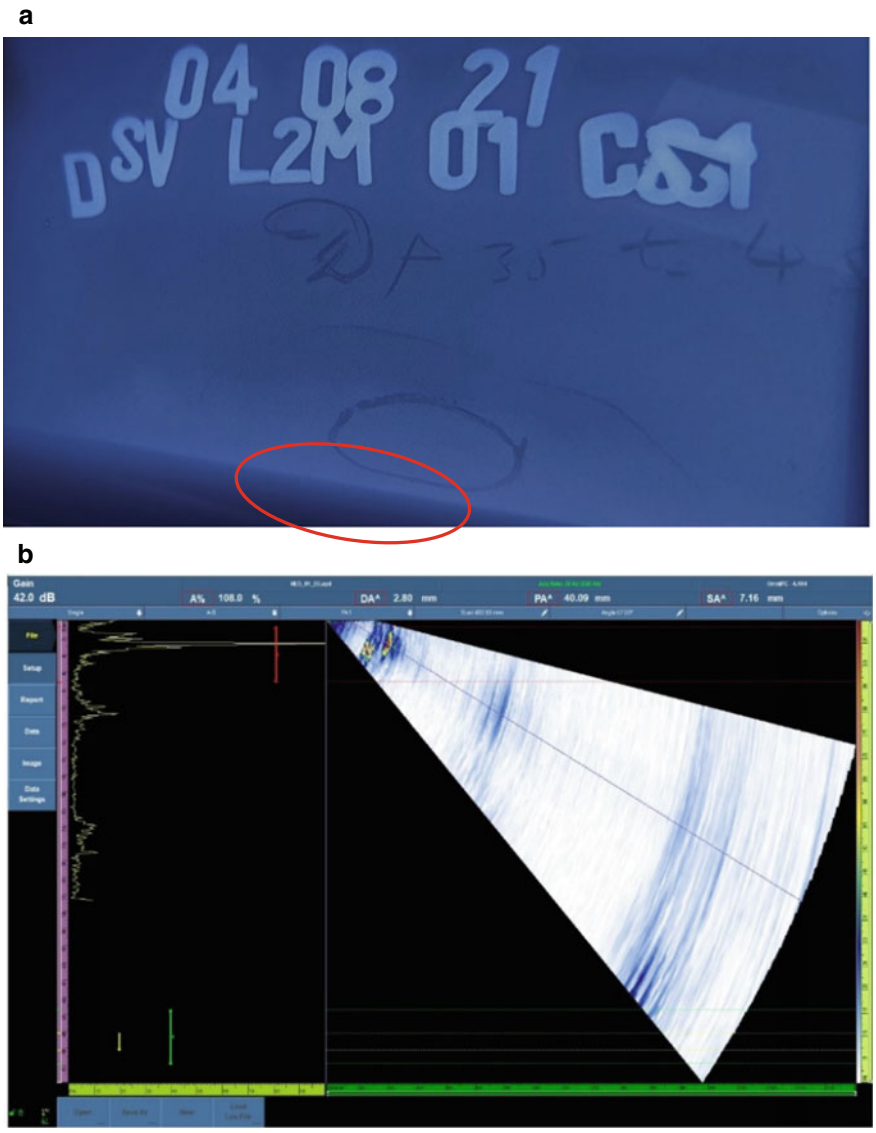

Fig. 7 **a** RT film of segment DE before repair-1 **b** PAUT image of segment DE before repair-1

5.2 Case Study 2

In radiographic film review, two porosities are noticed in the same segment after 1st weld repair in the vessel 3.8 mm thickness show in Fig. 8a. But, in RT review the depth and distance between the two porosities are not able to distinguish. To estimate

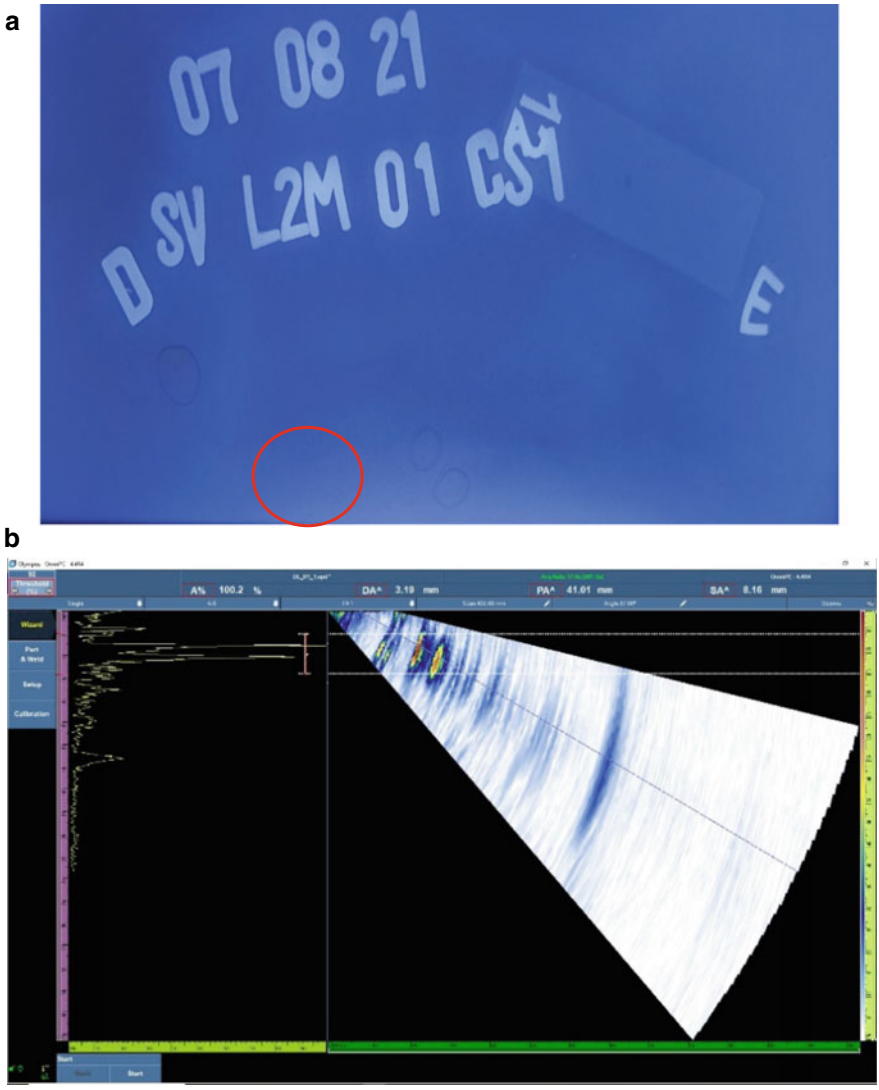

Fig. 8 **a** RT film of segment DE after repair-1 **b** PAUT image of segment DE after repair-1

the depth and the position of the defect, PAUT is carried out on the weld segment. The same setup used in case 1 is made for PAUT scanning. While scanning, it is observed two peaks with amplitude of 110% at a depth of 3.19 and 3.38 mm the distance between the two porosities is 0.5 mm which can also be seen as shown in Fig. 8b.

Inference of Case Study 2. This technique precisely distinguishes the adjacent porosities; thereby, it is proven the resolution precision is <0.5 mm.

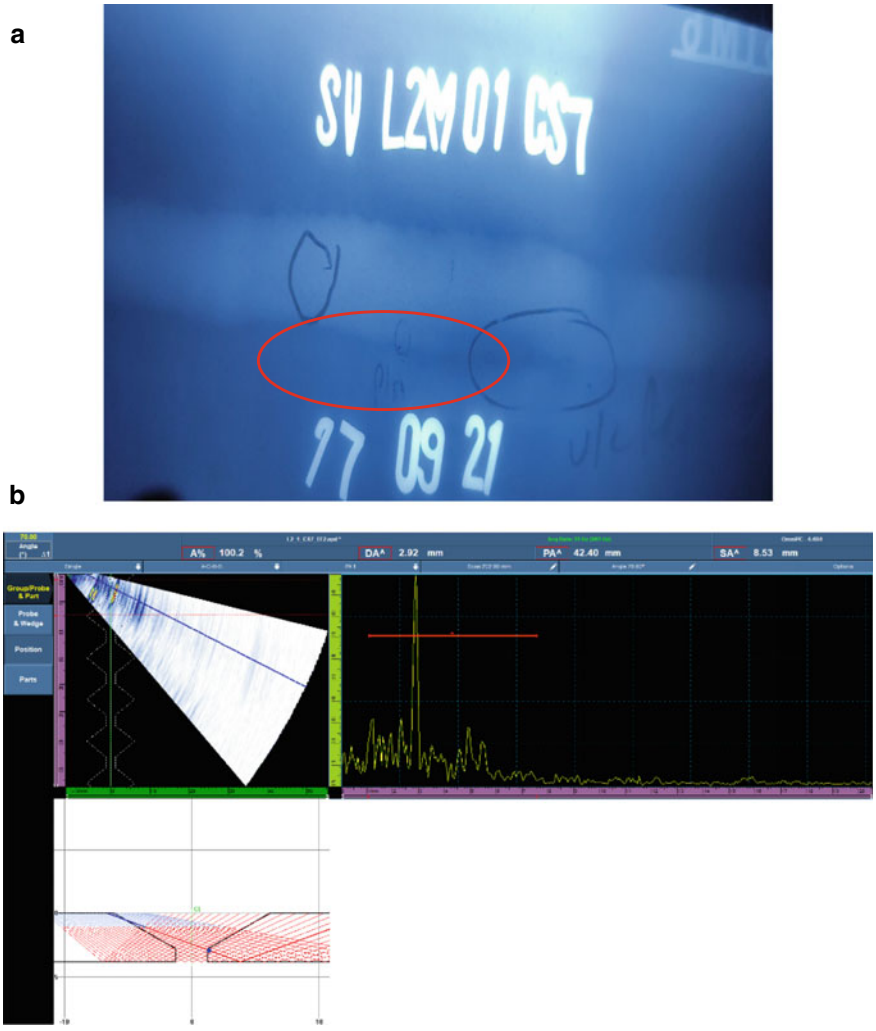

Fig. 9 **a** RT film of sidewall fusion **b** PAUT image of sidewall fusion

5.3 Case Study 3

In radiographic film review, side wall fusion is noticed in one of the weld joint in the same pressure vessel shown in Fig. 9a. By RT interpretation, finding the exact position and defect is the most challenging task. By scanning the weld joint with PAUT, it is easy to find out the location of side-wall fusion. While scanning, it is observed a peak with an amplitude of 100% at a depth of 2.92 mm. In this case, a detailed analysis is done by using OMNIPC analysis software. By using that analysis software, exact position of sidewall fusion is able to show in the weld joint in Fig. 9b.

Inference of Case Study 3. The bevel side where LF is present could be identified for weld repair preparation, require area is gouged for repair on one side exactly where the defect is identified.

6 Conclusion

PAUT is a superior technique compared with conventional techniques such as UT and RT. The case studies described above demonstrate the advantages of using PAUT such as:

- PAUT offers ease of setup, reduced inspection time through use of single probe as demonstrated in case study 1.
- PAUT gives precise sizing of defects. The PAUT has best resolution. The case study 2 demonstrated that PAUT has resolved the distance between two closely located isolated porosities.
- PAUT could precisely determines the orientation and exact location of the defect as demonstrated in case study 3.
- High-detection probability and sizing of small stress corrosion cracking in pressure vessels when compared with conventional UT and RT.
- By using PAUT technique it decreases the amount of radiation; the personnel is exposed to with RT technique. Defects detected in RT technique are unable to classify due to low sensitivity and poor capability in finding of planar defects.

PAUT is more sensitive technique in finding the variety of discontinuities in thin weld joints. The defects detected by RT technique are precisely detected by PAUT in a one scan with probe angle range 30º to 70º. In addition, PAUT analysis reveals the geometry, orientation, and exact location of the defect in thin weld joints. By using PAUT results, engineering decision can confidently take for acceptance/rejection/repair of the weld joints. This technique provides exact information needed to evaluate the severity of defects in components there by life assessment and structural integrity of products can be evaluated.

References

1. Erhard A, Khan MH, Rana LA (1993) Application of ultrasonic phased-array techniques for in-service inspection. J King Saud Univ Eng Sci 5(2):229–240
2. Parker D, Zimmermann DC (2002) Phased arrays-part 1: theory and architectures. IEEE Trans Microw Theory Tech 50(3):678–687
3. Moles M, Ginzel E (2012) Phased arrays for small diameter, thin-walled piping inspections. In: 18th World conference on nondestructive testing, Durban, South Africa
4. Xiao K, Wang Q, Dong H (2012) Post signal processing of ultrasonic phased array inspection data for non-destructive testing. Procedia Eng 43:419–424
5. Gowrishankar W et al (2015) Quality assessment of high strength metallic rocket motor casings-a non destructive testing approach

6. Thakur PP, Chapgaon AN (2016) A review on effects of GTAW process parameters on weld. IJRASET 4:136–140
7. Prema Kumar M, Malolan V, Gowri Shankar Wuriti, Srinivasa Gopal AS (2017) Phases array ultrasonic evaluation of ultra-high strength steel weldments for aerospace applications. IJDR 7(1):10951–10956
8. Dheeraj PR, Khaja SM, Mohsin I (2016) Advanced phased array technology application for single-sided access weld inspection. Insight-Non-Destructive Testing Cond Monit 58(11):585–595
9. Kutelu BJ et al (2018) Review of GTAW welding parameters. J Miner Mater Characterization Eng 6(5):541
10. Li W, Zhou Z, Li Y (2019) Inspection of butt welds for complex surface parts using ultrasonic phased array. Ultrasonics 96:75–82
11. Pei C et al (2020) Fully noncontact measurement of inner cracks in thick specimen with fiber-phased-array laser ultrasonic technique. NDT E Int 113(2020):102273
12. Kumar A (2020) Phased array ultrasonic imaging using angle beam virtual source full matrix capture-total focusing method. NDT E Int 116:102324
13. Olympus NDT (2004) Introduction to phased array ultrasonic technology applications. Olympus NDT, August 2004
14. Zhang H (2020) Application research on ultrasonic phased array technology in weld seam inspection. J Phys: Conf Ser 1601(4). IOP Publishing, 2020. SDJNN
15. Society for automotive engineers (SAE), Aerospace material standards-SAE AMS 2632B
16. Lei X, Wirdelius H, Rosell A (2020) Experimental validation of a phased array probe model in ultrasonic inspection. Ultrasonics 108:106217
17. Kumar S, Menaka M, Venkatraman B (2021) Performance comparison of phased array transducers for inspection of dissimilar welds on nuclear reactor components. Ann Nucl Energy 162:108482
18. Vithanage RKW et al (2020) A phased array ultrasound roller probe for automated in-process/interpass inspection of multipass welds. IEEE Trans Indus Electron 68(12):12781–12790
19. Liu XY et al (2021) Power plant small-diameter tube phased array inspection verification and inspection technology. J Phys: Conf Ser 2005(1). IOP Publishing
20. Šimeková B, Hodúlová E, Kovaříková I (2017) Phased array ultrasonic testing of thin DP steel electron beam weld joints. In: Materials science forum, vol 893. Trans Tech Publications Ltd

Artificial Cells as Programmable, Micro-/Nano-structured Bio-materials

Pasquale Stano

Abstract Artificial cells occupy a prominent place in the agenda of bottom-up synthetic biology, representing a genuine new technology that will lead to advanced bio-materials with programmable behavior. In this contribution, the potential role of artificial cells as smart drug delivery agent is introduced, with a focus on the general design principles. In particular, artificial cell dynamics is discussed with respect to their machine-like features, discussing those aspects that depend on the necessary interactions with the artificial cell environment. The latter, in particular, is far from being a neutral background. It co-determines, together with internal artificial cell organization, the artificial cell behavior. In this article, thanks to a preliminary high-level (conceptual) analysis of how artificial cells and environment are dynamically coupled, we conclude that adopting systems' dynamics approaches will help to progress the field. In particular, this contribution highlights the necessity of designing, modeling, and constructing artificial cells in a new engineering framework, currently missing among the most common approaches and suggests that it can guide experimental realizations toward novel engaging directions.

Keywords Synthetic biology · Artificial cells · Chemical robotics

1 Artificial Cells (ACs)

Synthetic Biology (SB) is a new scientific discipline, which aims to apply the engineering approach to biology [1, 2]. It consists in the design and construction of new biological parts, devices and systems, and in redesigning existing natural biological systems in order to make them useful for some purposes.

P. Stano (✉)
Department of Biological and Environmental Sciences and Technologies (DiSTeBA), University of Salento, Lecce, Italy
e-mail: pasquale.stano@unisalento.it

K. Geetha et al. (eds.), *Recent Trends in Materials*, Springer Proceedings in Materials 18, https://doi.org/10.1007/978-981-19-5395-8_4

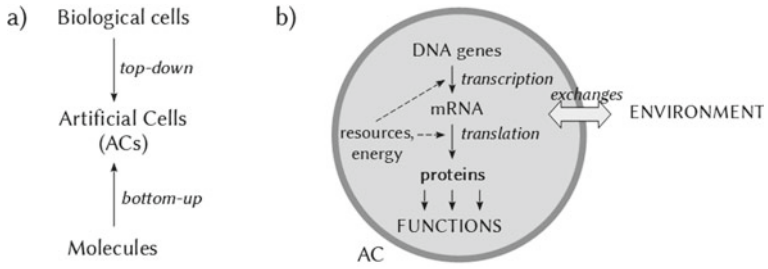

Fig. 1 Artificial cell technology. **a** Synthetic biology provides two different approaches for AC construction. In top-down approaches, extant biological cells are modified in various manners, for example, by substituting the natural genome with an artificial one [3]. Bottom-up approaches foresee the assembly of bio/chemical molecules in order to literally build a cell-like structure [4]. **b** ACs engaged in gene expression (DNA → mRNA → proteins). The produced proteins perform useful functions, such as pore formation, sensing, metabolic reactions, and transcription regulation. ACs can exchange matter and energy (and information) with the environment

An exciting and challenging SB frontier deals with the bottom-up construction of artificial cells (ACs)[1], achieved thanks to a combination of chemical, biophysical, and biochemical techniques [4] (Fig. 1a). Although most of the current ACs are not alive, the ultimate goal in this field is the achievement of living ACs, to demonstrate that life is an emerging property deriving from a special type of structural and dynamic organization of molecules, the so-called *autopoietic organization* (interested readers will find in-depth discussion about autopoiesis and emergence of life elsewhere [5, 6]).

Here, instead, we will focus on non-living ACs, which attracted attention because of their possible applications in biotechnology and nano-medicine. In this narrower context, ACs are typically designed and constructed as they were machines (wetware molecular machines [7]), i.e., programmable systems that behave as devised by the experimenter in order to accomplish pre-fixed tasks. A very interesting application refers to the biomedical field, for example, to fight tumors [8].

Under this bio-engineering lens, ACs can be treated as it is usually done with machines, i.e., in terms of structure, organization, information processing (input/output), and realization of a certain expected behavior. Importantly, as it happens with machines, current ACs have a well-defined scope, fixed by their designer/constructor.

[1] Here we refer to "bottom-up" approach only. The renowned "top-down" approach, which has led to living ACs via the transplantation of a synthetic genome into cells deprived of their own genome [3] will not be considered.

2 ACs: Structure and Construction

ACs host and realize only processes of interest. All activities, reactions, and interactions that are generally found in biological cells, but that are not useful in ACs, can be simply excluded from the AC plan. Therefore, ACs are quite different than biological living cells, being very much simpler. Whenever possible, ACs are built with the minimal complexity compatible with the successful accomplishment of the desired functions.

ACs technology derives from pioneer studies in the field of origins-of-life. In particular, the roots of the modern technology can be found in early attempts to create primitive forms of cells, including the Oparin coacervates [9], and especially in liposome systems developed by Pier Luigi Luisi in the 1990s [10–12]. Currently, we can recognize four pillars of AC technology: (*i*) micro-compartments—in general, (*ii*) cell-free systems, and in particular gene expression ones, (*iii*) microfluidics, and (*iv*) deterministic and stochastic numerical models.

Figure 1b schematically shows an AC engaged in gene expression. The latter is a very common design [13] and can be realized by co-encapsulating more than hundred different biochemicals (obtained by cell extracts or individually purified), each in hundreds/thousands of copies, inside a liposome whose size can range from a few tenths to tens of micrometers (Fig. 2). Gene expression is a key "module" in ACs because it allows the in situ production of proteins for developing additional functions, such as metabolic reactions, membrane pores, cytoskeleton elements, transcription factors for the regulation of gene expression, sensors, and sending and receiving signals to/from the environment.

By combining gene expression and direct protein incorporation, quite sophisticated ACs can be built. Actually, a good balance between pre-given and in situ produced components is a key combination for optimal AC functioning, programmability, and stimulus–response dynamics. The field has been reviewed by many Authors, who have described in detail several common operations made by ACs; interested readers can refer to recent excellent reviews [14–17]. For the sake of current discussion, emphasis should be given to those systems capable of exchanging signals with the environment, triggering an intra-AC response too [8, 18].

It results that in order to achieve complex behavior, the bio-materials required for the AC construction need to be complex too, i.e., already endowed with intrinsic stimulus–response capacity. Accordingly, the type of ACs here described is based on biomolecules such as DNA, ribosomes, and sets of biomolecules that can be extracted from living organisms (generally, but not exclusively, bacteria), sensor proteins, sugar, and phospholipids. Essentially, these ACs can be recognized as a class of "reconstituted" systems [17]. It should be noted that this is just an option. A classification of ACs based on which material has been employed for their realization is briefly reported in Table 1. ACs can be constructed by utilizing allegedly primitive compounds, to explore protocellular features and dynamics.

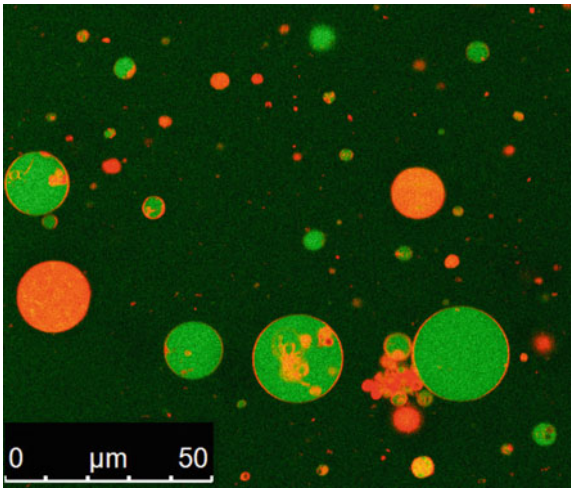

Fig. 2 Typical appearance of ACs. The circular objects in the image—realized by a confocal laser-scanning microscope—are lipid vesicles filled with bio-molecular systems that can lead to cell-like behavior. The red and the green colors refer to two different fluorescent dyes used to mark ACs. Note that when ACs are constructed by batch methods, as in this sample, a variety of size is obtained. Moreover, the concentration of inner chemicals can differ at a non-negligible extent. This leads to heterogeneity in structure and properties. On the contrary, the recent development of microfluidic devices is progressively allowing the generation of ACs with homogeneous size, homogeneous internal composition, and therefore homogeneous behavior. Size bar represents 50 μm

Table 1 (Bio)Chemical materials commonly used to construct artificial cells

Class of ACs	Typical materials
Primitive-like	Fatty acids, ribozymes, small- and oligo-peptides, …
Reconstructed	DNA, ribosomes, enzymes, phospholipids, sugars, …
Fully artificial	Block polymers, XNA, metal catalysts, redox factors, …
Hybrids (wetware)	Organellae (e.g., chromatophores) inside lipid vesicles
Hybrids (hardware/wetware)	Cell-free systems inside microfluidic channels/wells

When based on fully artificial materials, such as block polymers for their membranes, or on hybrid approaches (natural and artificial materials) ACs technology becomes an interesting platform for bio-chem-engineering, at three levels: molecular, supramolecular, and dynamically organized molecular systems. Sometimes, the hybrid approach is necessary to fully exploit features of pre-build particles, such as bio-organelle, to quickly become functionally complex. Finally, studies on

ACs obtained by a combination of hardware systems such as microfluidic channels or wells and molecular systems are also of interest [19].

To conclude this brief introduction to AC technology, the key aspect of energy requirements should be commented. In order to function, ACs require, for certain processes, high-energy compounds, such as adenosine triphosphate (ATP), or analogues.

We have emphasized in a previous review that the endogenous ATP production is one of the most important results to achieve, as it would correspond to the "emancipation from the current 'windup toy' approaches based on endowing SCs, at time zero, with all required chemical energy to run, and the consequent ceasing when such supply runs out" [20]. Indeed, the actual practice of loading ACs with an energy reservoir, letting its consumption during AC operations, is not rewarding on the medium-long term. Current strategies to overcome this limitation are based on transducing light into chemical energy. In turn, this requires three additional elements: (*i*) a first transducing element (a protein, or a set of proteins, that produces a chemical gradient upon irradiation), (*ii*) sub-compartments with limited permeability (to avoid the dissipation of the gradients), and (*iii*) a second transducing element (a protein that produces ATP, exploiting a chemical gradient). Although proven successful, this approach requires a sophisticated machinery, whereby molecular orientation and vectorial chemistry must combine in exact manner [21, 22]. In addition to these technical difficulties, providing light as primary energy source can be not a practical solution in certain contexts (e.g., imagine ACs operating inside a body).

Despite the impressive progress of AC technology, especially in the past few years, their real-world applications can be seen only in perspective, i.e., in the next decade. Today, ACs are intended as tools for basic understandings, while research is aiming at proof-of-principle investigations. No doubt, however, that one of the major areas of interest for future applications is nano-medicine, ACs being designed as "smart" drug delivery agents.

3 ACs as Smart Agents in Nano-medicine

Thanks to the capacity of encapsulating, producing, and releasing (bio)chemicals or other nanomaterials, ACs can play a crucial role in future nano-medicine, becoming a sort of smart drug delivery agents (Fig. 3a). Many scholars have imagined this scenario in the past decades [23, 24], but only recently, thanks to SB approaches, it seems within the experimental reach. Unlike liposomes and lipid nanoparticles—typical agents for drug delivery (and for anti-SARS-CoV-2 vaccination [25])—ACs are not limited to passive transport and diffusion, but can respond to microenvironments in complex way, can communicate with biological cells [18, 26, 27], and can synthesize and/or release therapeutic molecules in smart manner (at the right place, in the right moment). In other words, they are "programmable."

Recent studies show that genetic circuits can be implanted inside ACs [28, 29]. Properly designed circuits, for example, could guarantee a production of therapeutic

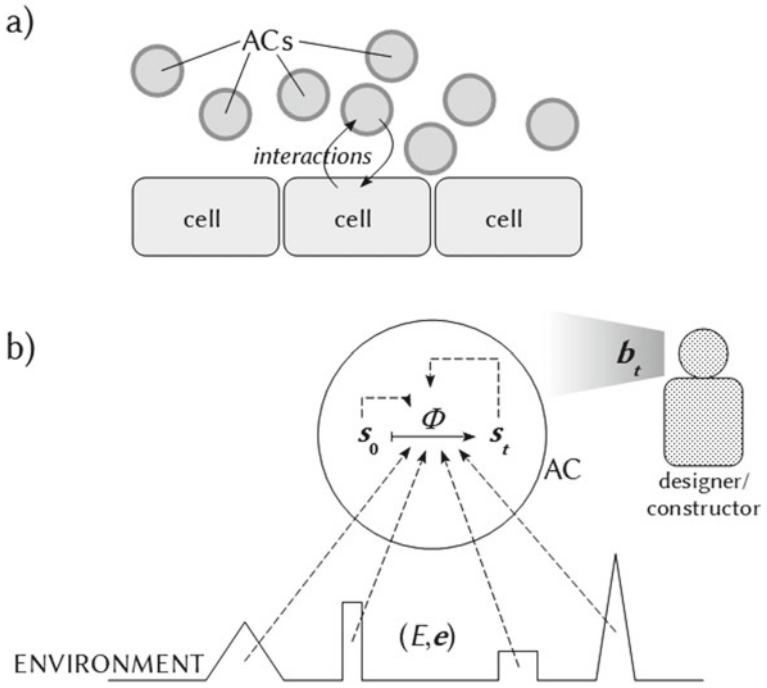

Fig. 3 Artificial cells engaged in interactions with their environment. **a** ACs as smart agents for nano-medicine. By exploiting to their intrinsic capacity of interacting with the environment (cells included), ACs can be designed in order to behave in controlled and programmable manner, according to predefined goals. **b** Schematic illustration of the general system dynamics modeling approach. Note that AC "behavior", "goal", and "purpose" (here represented by the behavior vector b_t), belong to the domain of the designer/constructor, while an AC has per se no scopes. See Sect. 4 for the explanation of symbols

molecules by an enzymatic assembly line, under control of external stimuli or specific chemical signaling waves. Moreover, it is possible to imagine that ACs can "feed" themselves by exploiting the presence of nutrients in the environment.

The Schroeder group reported ACs that synthesize cytotoxic proteins directly in the patient's body, in the tumor tissue (experiments were done on mice) [8]. Tan and colleagues have shown that ACs produce a bacteria-killing toxin once stimulated by a signal produced by bacteria themselves [18]. Another approach refers to "enzyme therapy," and it was proposed decades ago by T. M. S. Chang, who also coined the very term "artificial cells" to design enzyme-filled capsules performing on-demand metabolic transformation to compensate for the absence of the natural enzyme [23].

4 ACs as Chemical Machines Situated in a Wetware Environment

The realization of ACs for medical applications (and in general for any AC that should behave in a predefined manner) requires programmability and control. Non-living ACs are machines situated and operating in chem-bio-environments characterized by certain structures and patterns. Think, for example, to ACs traveling in a capillary of the circulatory system, directed toward a target cell. Our investigation aims at designing and realizing ACs whose internal mechanisms can be activated/deactivated by internal and external chemical signals in predictable manner.

What design principles must be followed? In this paper, we will not deal with specific control circuits such as those based on the regulation of gene expression, nor with detailed mechanisms of response to stimuli. Instead, we prefer a more general description, based on system dynamics and an abstract representation. In a sense, this is a preliminary report, that can inspire more realistic future models.

We—as observer—interpret the AC dynamics in terms of information processing and evaluate the AC behavior according to the fact that it matches (or not) a pre-fixed behavior. The latter has meaning (for us), in the sense of being useful or functional to a certain goal. AC input and output can be chemical concentrations, processes, fluxes, and relations between chemicals or between AC and other entities. The AC behavior, instead, can be described as a set of elementary events or variables, which can be specified in an operative manner within a spatio-temporal context where ACs exist and run. For instance, a programmed behavior can be defined in quali-quantitative fashion as the successful production of a therapeutic chemical (e.g., above a threshold concentration), when an AC is located near a target cell (within a certain distance), at the right moment (in a certain time window), and only after AC has received a certain stimulus (a controlled/predicted response).

Looking at ACs as machines, the crucial point for a successful design is that their behavior should be deduced from (and reduced to) an algorithm[2], which can be considered as the logical representation of a peculiar AC attribute, i.e., its "organization" Φ. In turn, Φ can be described by the set of interconnected relations (chemical transformations, recognition, binding, and especially the constraints) that are established when the AC chemical reaction network is "running." Φ acts as a causal factor in determining the AC behavior; it is the AC wiring scheme, embodied in the set of simultaneously occurring chemical reactions in ACs. However, Φ alone is not sufficient to determine the AC behavior. The other causal factors are the values of internal variables (the vector of concentrations at time zero, s_0, and at any time, s_t), the environmental spatio-temporal pattern (E), and the associated environmental variables (the vector e), see Fig. 3b. It should be noted that both Φ and E are essentially

[2] When, as specified above, the interest is focused on non-living ACs, many questions about how to best model ACs, and the "computability" of their behavior simplify at a great extent, because ACs can be simply considered special types of machines. Different is the case of living cells, for which several arguments warn against the organism/machine equivalence.

constraints, which decisively "shape" the AC internal mechanisms and the environmental effects, respectively. Their key role is best understood when a particular AC behavior is compared to the hypothetical set of all possible ACs organizations Φs situated in all possible environments *E*s.

The combined AC/environment system gives rise to a time- and location-dependent function $f(s_0, \Phi, s_t, E, e)$—representing the ongoing dynamics, which can be mapped into a behavior vector b_t. The latter indicates the success (or failure) of ACs in performing a predefined behavior thanks to the meaning we (the observers) assign to its components, as mentioned above. It also follows that optimal *b* is achieved when (Φ, s_0) somehow "matches" (E, e). Said differently, "successful" ACs must be designed according to (E, e) because it is not possible to cease the AC/environment interbred patterns. On the other hand, if we turn the argument upside down, given a certain (Φ, s_0)-AC, an optimal environment (E, e) will exist in order to achieve a best valued *b*, even if it can or cannot be the absolute maximum.

The environmental profile (E, e), however, is often not well known, or it can present so much variability that defining which is the best Φ is anything but trivial.

4.1 AC Diversity and Probabilistic Approaches

There is an additional non-negligible aspect of AC technology which needs to be taken into account for a correct AC design and modeling. It refers to the omnipresent heterogeneity of AC populations in terms of structure, resulting in a distribution of s_0 [30, 31] that can lead, in some cases[3], to a distribution of Φ. Given a known (E, e), AC behavior will spread among certain extremes, and this can be represented by a distribution of *b*. Additional diversity sources stem from the environment, as mentioned (including the targets cells to be healed/to be killed in the example of nano-medical application), and from the intrinsic stochastic dynamics of chemical systems [32, 33]—not commented here.

These considerations suggest that the best approach for modeling and analysis is *probabilistic*, as the noise sources collectively combine and contribute to diversify AC behaviors. It makes the AC design quite complex. Efforts should be carried out to design ACs with Φs which are robust enough against these internal and external variations, and at the same time favor methods for AC construction that lead to uniform structures and minimal Δs_0. But, intriguingly, a certain amount of AC diversity can even be profitable, because optimal *b*s could exist, given a set of (E, e), among the variety of the resulting behaviors.

[3] This can happen when chemical processes are concentration-dependent, in the sense that unintended functional relations between components can generate processes which are not explicit in a given design.

5 Concluding Remarks

The increasing interest in ACs is currently leading to a considerable number of new reports about the achievements of complex AC behavior. However, most investigation are restricted to dichotomical yes/no conclusions (e.g., can ACs perceive a signal from the environment? Are ACs able to produce toxins), without considering ACs as chemical machines submitted to systemic analysis. We envision that a new and more encompassing perspective should be considered—in the case of non-living Acs—in particular, designs based on systems dynamics [34], information theory, cybernetics, and cybersemiotics [35]. By analogy with "human-scale" design, typical of robotics, here we have emphasized the system/environment interbreeding, being actually a unity, a whole. In turn, this calls for more explicit and detailed models within the framework of the above-presented general scheme. In addition to the limitations of the present models, the most demanding efforts should be devoted in the experimental field, where finding applications of ACs in real-world situations is becoming crucial. As we have emphasized, their use as smart drug delivery agents seems obvious, but probably also quite challenging. Simpler targets might refer to in vitro biotechnological applications, such as sensors and micro- or nano-machineries for applications in well-defined problems, or to perform operations as micro- or nano-bioreactors.

Acknowledgements I am indebted with Luisa Damiano (IULM, Milan, Italy) and with Maurizio Magarini (Politecnico di Milano, Milan, Italy) for inspiring discussions.

References

1. Endy D (2005) Foundations for engineering biology. Nature 438:449–453
2. Andrianantoandro E, Basu S, Karig DK, Weiss R (2006) Synthetic biology: new engineering rules for an emerging discipline. Mol Syst Biol 2:2006.0028
3. Gibson DG, Glass JI, Lartigue C, Noskov VN, Chuang R-Y, Algire MA, Benders GA, Montague MG, Ma L, Moodie MM et al (2010) Creation of a bacterial cell controlled by a chemically synthesized genome. Science 329:52–56
4. Luisi PL, Ferri F, Stano P (2006) Approaches to semi-synthetic minimal cells: a review. Naturwissenschaften 93:1–13
5. Varela FG, Maturana HR, Uribe R (1974) Autopoiesis: the organization of living systems, its characterization and a model. BioSystems 5:187–196
6. Luisi PL (2003) Autopoiesis: a review and a reappraisal. Naturwissenschaften 90:49–59
7. Damiano L, Stano P (2021) A wetware embodied AI? Towards an autopoietic organizational approach grounded in synthetic biology. Front Bioeng Biotech 9:873
8. Krinsky N, Kaduri M, Zinger A, Shainsky-Roitman J, Goldfeder M, Benhar I, Hershkovitz D, Schroeder A (2018) Synthetic cells synthesize therapeutic proteins inside tumors. Adv Healthc Mater 7:e1701163
9. Hanczyc MM (2009) The early history of protocells—the search for the recipe of life. In: Rasmussen S, Bedau MA, Chen L, Deamer D, Krakauer DC, Packard NH, Stadler PF (eds) Protocells: bridging nonliving and living matter. MIT Press, Cambridge MA, pp 3–18
10. Oberholzer T, Wick R, Luisi PL, Biebricher C (1995) Enzymatic RNA replication in self-reproducing vesicles—an approach to a minimal cell. Biochem Biophys Res Comm 207:250–257

11. Oberholzer T, Albrizio M, Luisi PL (1995) Polymerase chain reaction in liposomes. Chem Biol 2:677–682
12. Oberholzer T, Nierhaus KH, Luisi PL (1999) Protein expression in liposomes. Biochem Biophys Res Commun 261:238–241
13. Stano P (2019) Gene expression inside liposomes: from early studies to current protocols. Chemistry 25:7798–7814
14. Cho E, Lu Y (2020) Compartmentalizing cell-free systems: toward creating life-like artificial cells and beyond. ACS Synth Biol 9:2881–2901
15. Ivanov I, López Castellanos L, Balasbas S, Otrin L, Marušič N, Vidaković-Koch T, Sundmacher K (2021) Bottom-up synthesis of artificial cells: recent highlights and future challenges. Annu Rev Chem Biomol Eng 12:287–308
16. Lussier F, Staufer O, Platzman I, Spatz JP (2021) Can bottom-up synthetic biology generate advanced drug-delivery systems? Trends Biotechnol 39:445–459
17. Gaut NJ, Adamala KP (2021) Reconstituting natural cell elements in synthetic cells. Adv Biol (Weinh) 5:e2000188
18. Ding Y, Contreras-Llano LE, Morris E, Mao M, Tan C (2018) Minimizing context dependency of gene networks using artificial cells. ACS Appl Mater Interfaces 10:30137–30146
19. Tayar AM, Karzbrun E, Noireaux V, Bar-Ziv RH (2017) Synchrony and pattern formation of coupled genetic oscillators on a chip of artificial cells. Proc Natl Acad Sci USA 114:11609–11614
20. Altamura E, Albanese P, Mavelli F, Stano P (2021) The rise of the nested multicompartment model in synthetic cell research. Front Molec Biosci 8:850
21. Berhanu S, Ueda T, Kuruma Y (2019) Artificial photosynthetic cell producing energy for protein synthesis. Nat Commun 10:1325
22. Altamura E, Albanese P, Marotta R, Milano F, Fiore M, Trotta M, Stano P, Mavelli F (2021) Chromatophores efficiently promote light-driven ATP synthesis and DNA transcription inside hybrid multicompartment artificial cells. Proc Natl Acad Sci USA 118:e2012170118
23. Chang TMS (1972) Artificial cells. Charles C. Thomas, Springfield IL
24. Leduc PR, Wong MS, Ferreira PM, Groff RE, Haslinger K, Koonce MP, Lee WY, Love JC, McCammon JA, Monteiro-Riviere NA et al (2007) Towards an in vivo biologically inspired nanofactory. Nat Nanotechnol 2:3–7
25. Walde P, Ichikawa S (2021) Lipid vesicles and other polymolecular aggregates—from basic studies of polar lipids to innovative applications. MDPI Appl Sci 11:10345
26. Lentini R, Martín NY, Forlin M, Belmonte L, Fontana J, Cornella M, Martini L, Tamburini S, Bentley WE, Jousson O et al (2017) Two-way chemical communication between artificial and natural cells. ACS Cent Sci 3:117–123
27. Rampioni G, D'Angelo F, Messina M, Zennaro A, Kuruma Y, Tofani D, Leoni L, Stano P (2018) Synthetic cells produce a quorum sensing chemical signal perceived by Pseudomonas aeruginosa. Chem Commun 54:2090–2093
28. Noireaux V, Bar-Ziv R, Libchaber A (2003) Principles of cell-free genetic circuit assembly. Proc Natl Acad Sci USA 100:12672–12677
29. Garamella J, Marshall R, Rustad M, Noireaux V (2016) The all E. Coli TX-TL toolbox 2.0: a platform for cell-free synthetic biology. ACS Synth Biol 5:344–355
30. Mavelli F, Stano P (2015) Experiments on and numerical modeling of the capture and concentration of transcription-translation machinery inside vesicles. Artif Life 21:445–463
31. Altamura E, Carrara P, D'Angelo F, Mavelli F, Stano P (2018) Extrinsic stochastic factors (solute partition) in gene expression inside lipid vesicles and lipid-stabilized water-in-oil droplets: a review. Synth Biol 3:ysy011
32. Mavelli F (2012) Stochastic simulations of minimal cells: the ribocell model. BMC Bioinform 13(S4):S10
33. Calviello L, Stano P, Mavelli F, Luisi PL, Marangoni R (2013) Quasi-cellular systems: stochastic simulation analysis at nanoscale range. BMC Bioinform 14:S7

34. Kolchinsky A, Wolpert DH (2018) Semantic information, autonomous agency and non-equilibrium statistical physics. Interface Focus 8:20180041
35. Nauta D (1972) The meaning of information. Mouton (De Grutyer), The Hague

Biosynthesis of PHBs by the Method of Full-Factorial Design for Obtaining PHB/Magnetite Composites

A. A. Dudun, V. A. Zhuikov, T. K. Makhina, E. A. Akoulina, V. V. Voinova, A. P. Bonartsev, and G. A. Bonartseva

Abstract Various variants of poly(3-hydroxybutyrate) (PHB) were synthesized by varying three factors (sucrose concentration, phosphate concentration, and aeration level) while growing the producer *Azotobacter vinelandii* 12 using full-factorial design. Bacteria grown at elevated sucrose concentration, low phosphate concentration, and high aeration level (C+/P−/O+) showed the maximum PHB yield (0.49 g/L). Molecular weights (MW) of PHB samples obtained under diverse conditions differed by more than 30 times (from 49 to 1698 kDa). Low molecular weight PHBs were observed at low sucrose levels and high aeration (C–/O+). All other PHB samples had MW over 1200 kDa. The crystallinity of all PHB samples was determined by differential scanning calorimetry and was within the range of 62–68%. These results show that, with optimization, it will be possible to synthesize PHBs with different physicochemical properties for a wide range of biomedical problems, including tissue engineering.

A. A. Dudun (✉) · V. A. Zhuikov · T. K. Makhina · G. A. Bonartseva
Research Center of Biotechnology of the Russian Academy of Sciences, Leninsky Ave, 33, Bld. 2, 119071 Moscow, Russia
e-mail: dudunandrey@mail.ru

V. A. Zhuikov
e-mail: vsevolod1905@yandex.ru

T. K. Makhina
e-mail: tat.makhina@gmail.com

G. A. Bonartseva
e-mail: bonar@inbi.ras.ru

E. A. Akoulina · V. V. Voinova · A. P. Bonartsev
Faculty of Biology, M.V. Lomonosov Moscow State University, Leninskie Gory 1-12, 119234 Moscow, Russia
e-mail: akoulinaliza@gmail.com

V. V. Voinova
e-mail: veravoinova@mail.ru

A. P. Bonartsev
e-mail: ant_bonar@mail.ru

K. Geetha et al. (eds.), *Recent Trends in Materials*, Springer Proceedings in Materials 18, https://doi.org/10.1007/978-981-19-5395-8_5

Keywords Polymers · Biosynthesis · Poly(3-hydroxybutyrate) · Full-factorial design · Magnetite

1 Introduction

Currently, the use of biopolymers for drug delivery systems (DDS) and materials as composites or scaffolds in tissue engineering has been widely used around the world [1, 2]. Polyhydroxyalkanoates (PHAs), like polyesters, are one of the most common biopolymers in regenerative medicine due to their biocompatibility and biodegradation properties [2]. Poly(3-hydroxybutyrate) (PHB) is one of the most common forms of PHA homopolymers [3]. PHB consists of D-3-hydroxybutyric acid monomers and is an isotactic polyester with regular units, which can be expressed by the degree of crystallinity of the polymer [4]. Due to the properties of biocompatibility and biodegradation, PHB can be used both alone and in combination with other polymers for biomedical applications as sutures, patches, and orthopedic pins, for the replacement or regeneration of various tissues (cartilaginous, bone, skin, nervous, etc.) [5–8]. PHB in addition to all this has piezoelectric properties, this ability allows the polymer to change its properties under the influence of an electric field, piezoelectric materials are attracting more and more attention from many researchers since they can electrically stimulate cells around their environment [9, 10].

One of the main advantages of PHB is its bacterial synthesis, unlike many other polymers. This feature makes it possible to avoid additional synthetic steps for polymerization, thereby making it one of the cost-effective materials for biomedicine [2, 11]. Soil bacteria of the genus *Azotobacter* sp. are producers of PHB, which plays the role of a storage material for bacteria and accumulates intracellularly in the form of granules [12]. Since the growth of bacteria can be regulated in the laboratory, it means that the synthesis and physicochemical properties of PHB can also be controlled, this advantage allows creating various variants of PHB for a wide range of biomedical problems [13]. First of all, it is possible to change the concentrations of substances, such as sucrose and phosphates in the growth medium, achieving different results in the growth of bacteria, and, as a result, in the synthesis of PHB [14, 15]. In addition to the influence of factors in the growth medium, it is also possible to change the conditions for cultivating bacteria; one of such influence factors for aerobic bacteria is oxygen limitation or aeration level [13]. All these factors make it possible to optimize the synthesis of PHBs with favorable physicochemical properties. However, the strength of each of the individual factors and their interaction with each other on the production and properties of PHB is currently still poorly understood.

This investigation aims to evaluate the influence of studied factors on the synthesis and physicochemical properties of PHB. To achieve this goal, the producer strain *A. vinelandii* 12 was chosen for the synthesis of PHB using the full-factorial design (FFD) method.

PHB has piezoelectric properties, and its piezo-response is depended on molecular weight of polymer. Piezoelectric properties of PHB can be improved significantly by

blending with magnetites. PHB/magnetite blend films are very promising magnetic biomaterials for tissue engineering applications [16].

2 Materials and Methods

The algorithm of the experiment is presented in the following diagram (Fig. 1).

2.1 Producer Strain

The bacterial strain *A. vinelandii* 12 was used to synthesize PHB. This microorganism is a typical representative of the soil habitat. The *A. vinelandii* 12 strain is stored at the Biotechnology Research Center of the Russian Academy of Sciences (Moscow, Russia) and is a laboratory object for the synthesis of alginate and PHB [17, 18]. The main phenotypic feature of the strain is that upon maturation, bacterial cells acquire a dark orange color, and the colonies themselves form a mucous film. In addition, bacteria are obligate aerobes and gram-negative pleomorphic cells [12]. They grow at moderate temperatures of 20–30 °C, as they are mesophilic microorganisms. Under laboratory conditions, all bacteria of the genus *Azotobacter* sp. are grown on nitrogen-free media (solid Ashby medium and liquid Burk's medium) because these microbes are able to fix molecular nitrogen from the air.

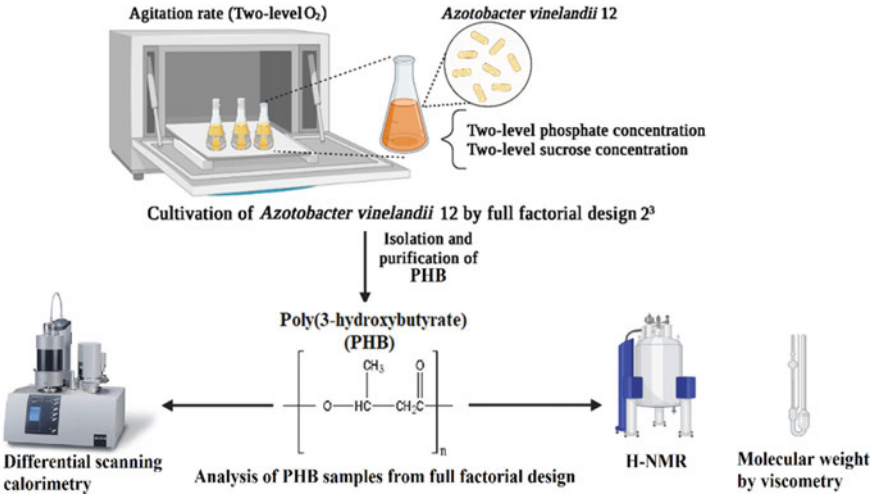

Fig. 1 The sequence of stages of the experiment

Table 1 Full-factorial design (FFD)

Variant	Sucrose (−)—15; (+)—35 g/l	Phosphates (−)—0.05; (+)—1.25 g/l	Oxygen (−)—150; (+)—210 rpm
No. 1	−	−	−
No. 2	+	−	−
No. 3	−	+	−
No. 4	+	+	−
No. 5	−	−	+
No. 6	+	−	+
No. 7	−	+	+
No. 8	+	+	+

2.2 Full-Factorial Design

The bacterial culture was maintained using Ashby solid nutrient medium [12]. The inoculum of *A. Vinelandii* 12 was grown on liquid Burk's medium in shaking flasks with a volume of 750 ml (200 ml of medium) at 250 rpm, the initial pH of the medium was 7.2; cultivation temperature is of 28 °C; seed age is 1 day; the volume of applied seed is 4%.

To establish a two-level FFD with three factors, various variants of Burk's liquid medium for growing bacteria were used. The liquid medium was varied in terms of sucrose and phosphates, and the level of aeration was also varied due to the speed of stirring the shaking flasks on an Innova 43 microbiological shaker (New Brunswick Scientific, USA) (Table 1).

Bacterial fermentation in FFD was performed under the same conditions as for inoculum growth, except that the cell growth time in all FFD experiments was not 24, but 72 h. The growth dynamics was traced by the optical density of the culture liquid at 520 nm. Cell morphology was recorded through a digital camera at 100 × magnification using a Biomed-1 microscope (Biomed, Russia).

2.3 Isolation of PHB

At the end of 72 h, bacteria grown on different variants in FFD were removed from fermentation, and PHB was isolated. Before direct isolation, the culture fluid was centrifuged at 11,000 g for 30 min to obtain cell biomass. After that, the cell biomass was extracted with chloroform for 12 h. The extract was filtered, and then, PHB was precipitated with isopropyl alcohol. This process was repeated at least 3 times. At the end of the isolation process, PHB was dried at 60 °C [12].

2.4 Molecular Weight Determination of PHB

All FFD PHB variants were measured for molecular weight (MW) by viscometry. MW was calculated using the Mark–Houwink equation:

$$[\eta] = K(M)^a \tag{1}$$

where M is the molecular weight, $[\eta]$ is the viscosity, K and a are constants, and the value of which depends on the nature of the polymer [19].

2.5 ^{1}H-NMR Analysis of PHB

To describe the molecular structure of the polymer, a PHB sample was prepared in a deuterated chloroform solution to record proton (H^1) NMR spectra on an MSL-300 spectrometer (Bruker, Germany) at an operating frequency of 400 MHz [20].

2.6 Differential Scanning Calorimetry (DSC) of Synthesized PHBs

The physico-thermal properties of various FFD PHBs, in particular, the degree of their crystallinity, were studied by differential scanning calorimetry (DSC) on a DSC 204 F1 Phoenix instrument (Netzsch, Germany). The samples were heated from 25 to 220 °C at a heating rate of 10 K/min in an argon atmosphere. The crystallinity of the PHB structure (Xc) was calculated using the formula:

$$\mathrm{Xc} = \frac{\Delta H_\mathrm{m}}{\Delta H_\mathrm{m}^0(\mathrm{PHB})} \times 100\% \tag{2}$$

where ΔH_m is the enthalpy changes caused by the melting of the test sample, respectively, $\Delta H_\mathrm{m}^0(\mathrm{PHB})$ is the theoretical value of the enthalpy of melting that would be obtained for 100% crystalline PHB samples (146.6 J/g). All calculations were carried out for the second heating cycle.

2.7 The Blend Films PHB/Magnetites Obtaining

To obtain a blend film, a sample of magnetites was placed in a glass bottle and trichloromethane was added at a ratio of 2.5 ml per 40 mg of magnetites (Iron (II, III) oxide nanopowder, 50–100 nm particle size, CAS Number: 1317-61-9; Merck,

Germany). The bottle was hermetically sealed with a ground-in lid and placed for 120 min in an ultrasonic bath Biosan (Latvia) equipped with an ultrasound transducer with an intensity of 37 kHz at room temperature. After sonication, such a volume of PHB solution in trichloromethane (with a concentration of 5 g/dL) was added to the contents of the bottle so that the mass of magnetites was 8% of the mass of PHB. The polymer solution was preliminarily filtered through a paper filter. The sealed box was then placed on the platform of a Thermomixer comfort Eppendorf shaker, and the contents were stirred overnight at 200 rpm. Thus, obtained suspension of magnetite particles in PHB solution was poured onto a Petri dish so that 10 mg of PHB per 1 sm^2 of surface and dried. In order to avoid film deformation, it is important that the trichloromethane evaporates slowly during drying. To slow down evaporation, the Petri dish was placed on the bottom of a desiccator with a ground-in lid equipped with a tap. The tap was opened, and a cotton filter was placed in the hole of the glass tube coming out of it.

2.8 Statistical Analysis

The results of the synthesis of PHB in FFD were statistically calculated by the nonparametric Kruskal–Wallis method. All calculations were made and visualized in the R environment using the rstatix, tidyverse, and ggpubr packages. The data obtained were presented as mean values with standard deviations (mean ± SD). The selection criterion for significant differences between groups was $p \leq 0.05$.

3 Results and Discussion

3.1 Bacterial Biomass and PHB Synthesis

The results of the synthesis of PHB by the bacterial strain *A. vinelandii* 12 showed that the growth of bacteria does not correlate with the accumulation of the biopolymer (Fig. 2).

As can be seen from Fig. 2a, all bacteria grown at high aeration (O+) showed stronger growth compared to bacteria grown at low aeration (O−). This result shows that *A. vinelandii* 12 is an obligate aerobe and a decrease in the concentration of molecular oxygen negatively affects many metabolic processes, which, in turn, negatively affects cell growth and division [21, 22]. It is also worth noting that, at high aeration, the (C−/P−) and (C−/P+) variants have less active growth and the biomass reaches less than 2 g/l by 72 h. Based on these results, it can be concluded that at a high agitation rate of shake flasks (O+), the consumption of sucrose by bacterial cells in the medium increases [23]. In one of their studies, Barrera et al. demonstrated that as the level of aeration increases, *A. vinelandii* begins to consume much more carbon

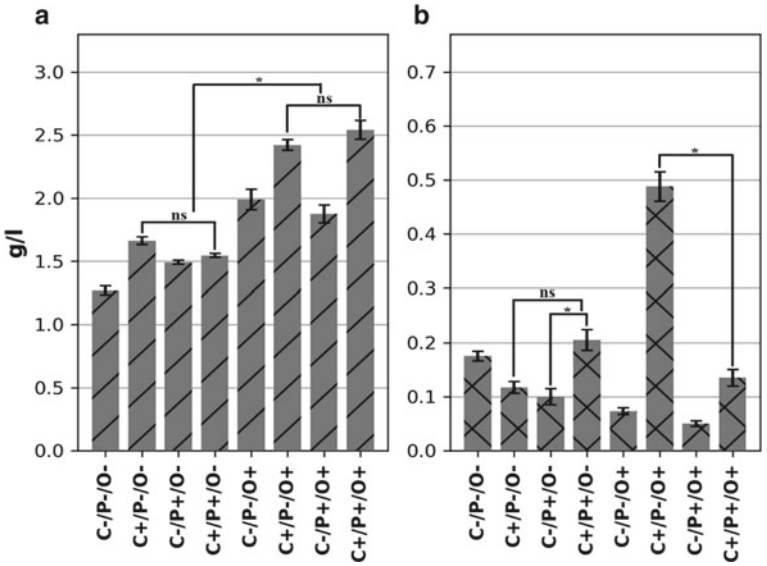

Fig. 2 **a** Cellular biomass and **b** PHB synthesis after 72 h of fermentation of bacteria *Azotobacter vinelandii* 12 in FFD

compared to the initial level of aeration [24]. Under the given fermentation conditions, the maximum growth of *A. vinelandii* 12 bacteria was facilitated by aeration and a high content of sucrose and phosphates in the medium (2.54 g/L). Minimal bacterial growth was noted at the minimum set fermentation parameters (1.27 g/l).

The results of the synthesis of PHB in FFD in Fig. 2b showed inhomogeneous results. Only a combination of a high content of sucrose in the medium and a high aeration (C+/P−/O+) leads to the efficient synthesis of the biopolymer (0.49 g/l). On the contrary, bacteria with a deficiency of sucrose with an increased concentration of phosphates in the medium and a high level of aeration produced the minimum amount of PHB (0.05 g/L). Such a strong scatter is primarily associated with the sucrose factor, since it is this component, as a carbon source, that is the main component for the synthesis of PHB in the bacteria *Azotobacter* sp. [25]. It can also be added that, in addition to PHB, bacteria of the genus *Azotobacter* sp. synthesize exopolymer alginate, which plays a role as a protective barrier against excessive concentration of molecular oxygen in the medium to protect nitrogenase complexes from their oxidation [26]. In addition, it has been shown that at a sufficient concentration of phosphates in the medium, bacteria begin to actively form cysts and synthesize capsular alginate [17]. Thus, it can be concluded that the synthesis of PHB depends on the level of sucrose in the medium and on which direction the synthesis will take, toward PHB or alginate by the bacteria *A. vinelandii* 12.

3.2 *Physicochemical Properties of PHB*

PHB after synthesis was determined for physicochemical properties. The chemical structure of PHB was confirmed by 1H-NMR (Fig. 3).

As can be seen from the figure, clear spectra are presented, which characterize that PHB is a homopolymer consisting of 3-hydroxybutyric acid residues. It is worth noting that no other spectra except those that describe the PHB structure were found. Thus, it can be argued that the PHB we isolated has a high degree of purity.

The molecular weights of all PHBs in the FFD determined by viscometry had a mass of over 1200 kDa, except for two variants, namely (C−/P−/O+) equal to 331 kDa and the variant (C−/P+/O+) whose mass was equal to 49 kDa (Fig. 4).

In this case, we obtained a large scatter of MW in the FFD (more than 30 times from 49 to 1698 kDa). Thus, it can be concluded that this approach will make it possible to obtain PHB in a wide range of MWs, which, in turn, can be suitable for a wide range of biomedical problems [27, 28]. The results of the (C−/P−/O+) and (C−/P+/O+) variants show that the combination of low sucrose concentrations and high aeration has a negative effect on the MW of the polymer. It is likely that, as with the synthesis of PHB in these FFD experiments, there is an increased production of alginate to protect bacterial cells from an excessive concentration of molecular oxygen and, as a result, the bacteria *A. vinelandii* 12 do not have enough energy resources due to the low concentration of carbon in the medium for the accumulation

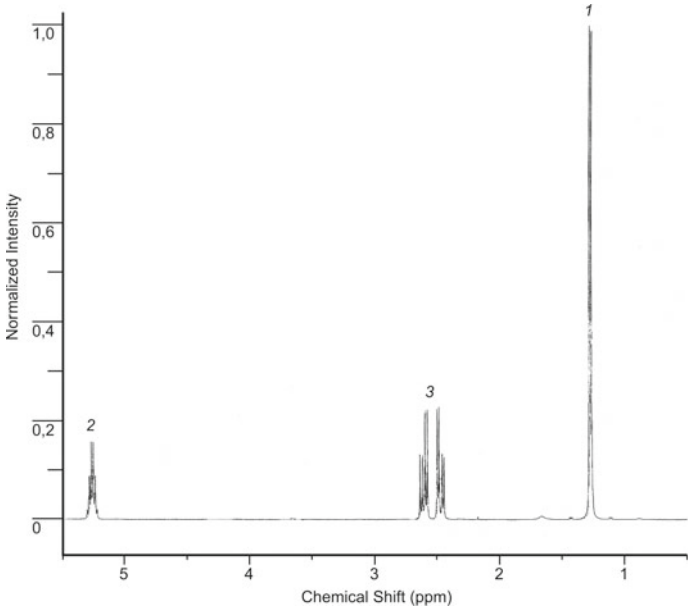

Fig. 3 Chemical structure of PHB homopolymer. 1—CH_3; 2—CH and 3—CH_2 groups represent the backbone of the polymer chain

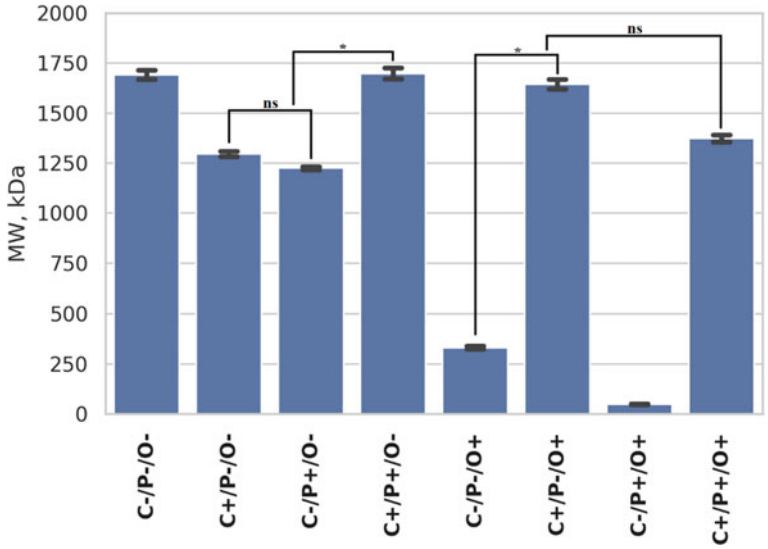

Fig. 4 Molecular weights (MW) of PHB in FFD

of PHB [26]. It can also be assumed that bacteria from the variants (C–/P–/O+) and (C–/P+/O+) enter the stationary growth phase during fermentation due to the lack of a carbon source in the medium. The work of Millan and his colleagues demonstrated that, at the time of exponential growth of *A. vinelandii* bacteria, the *phbC* gene, which encodes PHB synthase, is actively expressed, as a result of which the MW of PHB increases [29]. At the moment when the bacteria enter the stationary phase, the MW of PHB, on the contrary, begins to drop sharply due to the active expression of the *phbZ* gene encoding PHB depolymerase [29].

In addition to determining the MW, the thermophysical properties of the obtained samples were studied using the differential scanning calorimetry method.

Figure 5 shows typical heating and cooling curves for PHB. The first stage of heating corresponds to the red curve with a melting peak of 179.64 °C and the second to the purple curve with melting peaks of 169.18 and 174.87 °C. The melting enthalpies are 100.2 J/g and 97.74 J/g, respectively. The presence of two peaks is explained by the different degrees of perfection of the crystallites in the polymer [16]. On cooling, the polymer crystallizes. The peak of crystallization during the first cooling is 82.92 °C and during the second—78.57 °C. The degree of crystallinity of this polymer was 66%. The degree of crystallinity of the remaining polymers varied in the range of 62–68%.

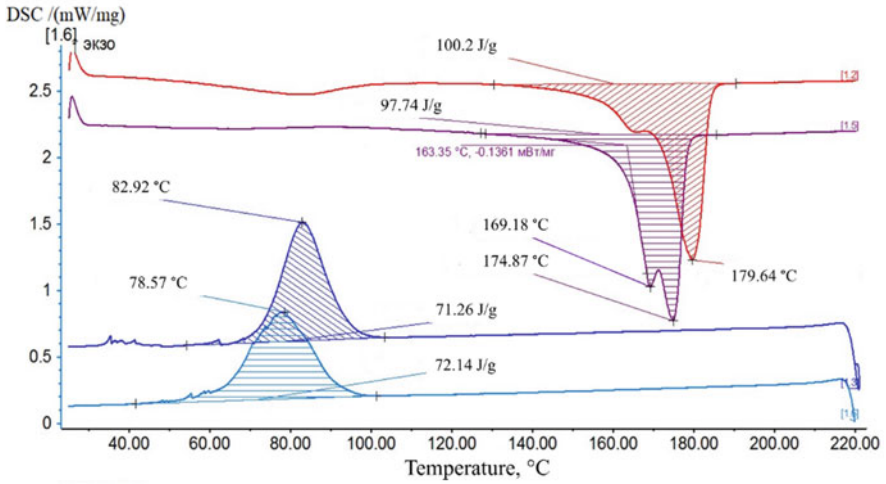

Fig. 5 The image of DSC curves of obtained PHB samples

3.3 The Blend PHB/Magnetites Films

We produced blend films from the obtained PHBs: 49, 331, and 1698 kDa with magnetite. (Fe_3O_4) nanoparticles M1 that were synthesized by a co-precipitation method [30]. The PHB/Magnetite composite films were produced by blending (see Methods section). The thickness of the produced blend films was 100 mkm, and the content of magnetites in the blend films was 6% (*w/w*).

4 Conclusion

In this study, an assessment of the influence of three factors on the synthesis and properties of PHB was shown. The sucrose factor in FFD had a more pronounced response to PHB synthesis in comparison with phosphates and the level of aeration. The MW of PHB begins to decrease during the stationary growth phase of *A. vinelandii* 12 bacteria due to the lack of sucrose as the main source of carbon and an increased level of aeration ((C−/P−/O+) = 331 kDa; (C−/P+/O+) = 49 kDa). An assessment of the crystallinity of the obtained PHB samples showed the predominance of the crystalline phase over the amorphous one and varied in the range of 62–68%. Thus, this work lays the foundation for understanding the regulation of bacterial PHB synthesis and will allow in the future to optimize the process of bacterial fermentation to obtain a biopolymer that will match a number of physicochemical properties in advance for various biomedical problems [31, 32], e.g., for development of PHB biomaterials with piezoelectric properties. PHB/magnetite blend films from

PHB of different molecular weight can be used for development of piezo-materials for tissue engineering applications [33].

Acknowledgements This work was supported by the Russian Science Foundation, project No 20-64-47008 and was carried out within the framework of government assignment of the Ministry of Science and Higher Education of the Russian Federation (the part of biosynthesis of bacterial PHB). The equipment used in this work was from the User Facilities Center of Research Center of Biotechnology of Russian Academy of Sciences.

References

1. Tan GA, Chen C, Li L, Ge L, Wang L, Razaad I, Li Y, Zhao L, Mo Y, Wang J (2014) Start a research on biopolymer polyhydroxyalkanoate (PHA): a review. Polymers 6(3):706–754
2. Elmowafy E, Abdal-Hay A, Skouras A, Tiboni M, Casettari L, Guarino V (2019) Polyhydroxyalkanoate (PHA): applications in drug delivery and tissue engineering. Expert Rev Med Dev 16(6):467–482
3. Zhuikov VA, Zhuikova YV, Makhina TK, Myshkina VL, Rusakov A, Useinov A, Voinova VV, Bonartseva GA, Berlin AA, Bonartsev AP, Iordanskii AL (2020) Comparative structure-property characterization of poly(3-hydroxybutyrate-Co-3-hydroxyvalerate)s films under hydrolytic and enzymatic degradation: finding a transition point in 3-hydroxyvalerate content. Polymers 12(3):728
4. Zhuikov VA, Bonartsev AP, Bagrov DV, Yakovlev SG, Myshkina VL, Makhina TK, Bessonov IV, Kopitsyna MN, Morozov AS, Rusakov AA, Useinov AS, Shaitan KV, Bonartseva GA (2017) Mechanics and surface ultrastructure changes of poly(3-hydroxybutyrate) films during enzymatic degradation in pancreatic lipase solution. Mol Cryst Liq Cryst 648(1):236–243
5. Chen Z, Song Y, Zhang J, Liu W, Cui J, Li H, Chen F (2017) Laminated electrospun nHA/PHB-composite scaffolds mimicking bone extracellular matrix for bone tissue engineering. Mater Sci Eng, C 72:341–351
6. Mohan A, Girdhar M, Kumar R, Chaturvedi HS, Vadhel A, Solanki PR, Kumar A, Kumar D, Mamidi N (2021) Polyhydroxybutyrate-based nanocomposites for bone tissue engineering. Pharmaceuticals 14(11):1163
7. Ferlic PW, Nogler M, Weinberg AM, Kühn KD, Liebensteiner M, Coraça-Huber DC (2021) Material modifications enhancing the antibacterial properties of two biodegradable poly(3-hydroxybutyrate) ımplants. Biomed Mater 16(1):015030
8. Rodriguez-Contreras A (2019) Recent advances in the use of polyhydroyalkanoates in biomedicine. Bioengineering 6(3):82
9. Surmenev RA, Orlova T, Chernozem RV, Ivanova AA, Bartasyte A, Mathur S, Surmeneva MA (2019) Hybrid lead-free polymer-based nanocomposites with improved piezoelectric response for biomedical energy-harvesting applications: a review. Nano Energy 62:475–506
10. Soleymani Eil Bakhtiari S, Karbasi S, Toloue EB (2021) Modified poly(3-hydroxybutyrate)-based scaffolds in tissue engineering applications: a review. Int J Biol Macromole 166:986–998
11. Butt FI, Muhammad N, Hamid A, Moniruzzaman M, Sharif F (2018) Recent progress in the utilization of biosynthesized polyhydroxyalkanoates for biomedical applications—review. Int J Biol Macromol 120:1294–1305
12. Dudun AA, Akoulina EA, Voinova VV, Makhina TK, Myshkina VL, Zhuikov VA, Bonartsev AP, Bonartseva GA (2019) Biosynthesis of alginate and poly(3-hydroxybutyrate) by the bacterial strain Azotobacter agile 12. Appl Biochem Microbiol 55(6):654–659
13. Díaz-Barrera A, Urtuvia V, Padilla-Córdova C, Peña C (2019) Poly(3-hydroxybutyrate) accumulation by Azotobacter Vinelandii under different oxygen transfer strategies. J Indus Microbiol Biotechnol 46(1):13–19

14. Wu F, Zhou Y, Pei W, Jiang Y, Yan X, Wu H (2022) Biosynthesis of poly-(3-hydroxybutyrate) under the control of an anaerobically induced promoter by recombinant Escherichia coli from sucrose. Molecules 27(1):294
15. Shang L, Jiang M, Chang HN (2003) Poly(3-hydroxybutyrate) synthesis in fed-batch culture of Ralstonia eutropha with phosphate limitation under different glucose concentrations. Biotech Lett 25(17):1415–1419
16. Iglesias-Montes ML, Soccio M, Luzi F, Puglia D, Gazzano M, Lotti N, Manfredi LB, Cyras VP (2021) Evaluation of the factors affecting the disintegration under a composting process of poly(lactic acid)/poly(3-hydroxybutyrate) (PLA/PHB) blends. Polymers 13(18):3171
17. Bonartsev AP, Bonartseva GA, Myshkina VL, Voinova VV, Mahina TK, Zharkova II, Yakovlev SG, Zernov AL, Ivanova EV, Akoulina EA, Kuznetsova ES, Zhuikov VA, Alekseeva SG, Podgorskii VV, Bessonov IV, Kopitsyna MN, Morozov AS, Milanovskiy EY, Tyugay ZN, Bykova GS, Kirpichnikov MP, Shaitan KV (2016) Biosynthesis of poly(3-hydroxybutyrateco-3-hydroxy-4-methylvalerate) by strain Azotobacter chroococcum 7B. Acta Naturae 8(3):77–87
18. Bonartseva GA, Akulina EA, Myshkina VL, Voinova VV, Makhina TK, Bonartsev AP (2017) Alginate biosynthesis by Azotobacter bacteria. Appl Biochem Microbiol 53(1):52–59
19. Akita S, Einaga Y, Miyaki Y, Fujita H (1976) Solution properties of poly(D-β-hydroxybutyrate). 1. Biosynthesis and characterization. Macromolecules 9(5):774–780
20. Bonartsev AP, Yakovlev SG, Zharkova II, Boskhomdzhiev AP, Bagrov DV, Myshkina VL, Makhina TK, Kharitonova EP, Samsonova OV, Feofanov AV, Voinova VV, Zernov AL, Efremov YM, Bonartseva GA, Shaitan KV, Kirpichnikov MP (2013) Cell attachment on poly(3-hydroxybutyrate)-poly(ethylene glycol) copolymer produced by Azotobacter chroococcum 7B. BMC Biochem 14(1):12
21. Noar JD, Bruno-Bárcena JM (2018) Azotobacter vinelandii: the source of 100 years of discoveries and many more to come. Microbiology 164(4):421–436
22. Nivens DE, Ohman DE, Williams J, Franklin MJ (2001) Role of alginate and its O acetylation in formation of Pseudomonas aeruginosa microcolonies and biofilms. J Bacteriol 183(3):1047–1057
23. Castillo T, López I, Flores C, Segura D, García A, Galindo E, Peña C (2018) Oxygen uptake rate in alginate producer (algU+) and nonproducer (algU−) strains of Azotobacter vinelandii under nitrogen-fixation conditions. J Appl Microbiol 125(1):181–189
24. Díaz-Barrera A, Martínez F, Guevara PF, Acevedo F (2014) Evaluation of gene expression and alginate production in response to oxygen transfer in continuous culture of Azotobacter vinelandii. PLoS ONE 9(8):e105993
25. Parshad J, Suneja S, Kukreja K, Lakshminarayana K (2001) Poly-3-hydroxybutyrate production by Azotobacter chroococcum. Folia Microbiol 46(4):315–320
26. Sabra W, Zeng A-P, Lünsdorf H, Deckwer W-D (2000) Effect of oxygen on formation and structure of Azotobacter vinelandii alginate and its role in protecting nitrogenase. Appl Environ Microbiol 66(9):4037–4044
27. Reusch RN (1995) Low molecular weight complexed poly(3-hydroxybutyrate): a dynamic and versatile molecule in vivo. Can J Microbiol 41(13):50–54
28. Adaya L, Millán M, Peña C, Jendrossek D, Espín G, Tinoco-Valencia R, Guzman J, Pfeiffer D, Segura D (2018) Inactivation of an intracellular poly-3-hydroxybutyrate depolymerase of Azotobacter vinelandii allows to obtain a polymer of uniform high molecular mass. Appl Microbiol Biotechnol 102(6):2693–2707
29. Millán M, Segura D, Galindo E, Peña C (2016) Molecular mass of poly-3-hydroxybutyrate (P3HB) produced by Azotobacter vinelandii is determined by the ratio of synthesis and degradation under fixed dissolved oxygen tension. Process Biochem 51(8):950–958
30. Mukhortova YR, Pryadko AS, Chernozem RV, Pariy IO, Akoulina EA, Demianova IV, Zharkova II, Ivanov YF, Wagner DV, Bonartsev AP, Surmenev RA, Surmeneva MA (2022) Fabrication and characterization of a magnetic biocomposite of magnetite nanoparticles and reduced graphene oxide for biomedical applications. Nano-Struct Nano-Objects 29:100843
31. Akoulina EA, Demianova IV, Zharkova II, Voinova VV, Zhuikov VA, Khaydapova DD, Chesnokova DV, Menshikh KA, Dudun AA, Makhina TK, Bonartseva GA, Volkov AV, Asfarov

TF, Ivanov SY, Shaitan KV, Bonartsev AP (2021) Growth of mesenchymal stem cells on poly(3-hydroxybutyrate) scaffolds loaded with simvastatin. Bull Exp Biol Med 171(1):172–177
32. Kang J, Hwang J-Y, Huh M, Yun SI (2020) Porous poly(3-hydroxybutyrate) scaffolds prepared by non-solvent-induced phase separation for tissue engineering. Macromol Res 1:1–9
33. Chernozem RV, Surmeneva MA, Abalymov AA, Parakhonskiy BV, Rigole P, Coenye T, Surmenev RA, Skirtach AG (2021) Piezoelectric hybrid scaffolds mineralized with calcium carbonate for tissue engineering: analysis of local enzyme and small-molecule drug delivery, cell response and antibacterial performance. Mater Sci Eng C Mater Biol Appl 122:111909

Validation of the Experimental Results of the Concrete with M-sand Using ABAQUS Software

Anup K. Chitkeshwar and P. L. Naktode

Abstract The experimental process is carried out in the present work related to the use of manufactured sand. The manufactures sand was used in the concrete as a partial replacement of natural sand. The present work is essential in the field of concrete technology, testing on the concrete cubes and beams. This work is important as a quality control techniques where experiments have got the proof as well. The experimental results for the case of the concrete with manufactured sand by zero to 100% replacement are carried out. The validation process is to be carried out in the ABAQUS software; the finite element analysis was used in the software. The modelling is carried out in the software, and the graphical representation was carried out. The comparison of the experimental results and the software results has been carried out. The comparison showed that the results are in good conjunction.

Keywords Validation · ABAQUS · Concrete · M-sand

1 Introduction

1.1 General

There are certain situations where the confinement related to the concrete is present, and in that case, the reinforcement placed in the transverse direction may be the reason for the failure, and in such situation, experimentally specimen have been tested. The circular openings for the transverse reinforcement with the connectors are shear in nature while the parameters related to the material as well as the geometry have been studied [1]. The finite element method for the method which is called as

A. K. Chitkeshwar (✉)
Department of Civil Engineering, P. R. Pote Patil College of Engineering and Management, Amravati, India
e-mail: anupkchitkeshwar@gmail.com

P. L. Naktode
Department of Civil Engineering, School of Engineering and Technology, Sandip University, Nashik, India

K. Geetha et al. (eds.), *Recent Trends in Materials*, Springer Proceedings in Materials 18, https://doi.org/10.1007/978-981-19-5395-8_6

indirect method is found to be having good result when the proper parameters are used. Variance is found in the concrete, and it is obtained higher as compared to the procedure adopted in the indirect method. Delhi searcher has found out certain discrepancy related to the indirect method using the finite element method for analysis [2]. Collapse is observed in structures made up of reinforce concrete, and this is considered to be the failure locally occurred, and the loads could be abnormal in nature. The losses as well as casualties are the result as well as the outcome of certain collapse situation. The finite element method with the help of ABAQUS software is used so that such collapse behaviour can be simulated properly. Numerical model is validated with finite element method-based software [3].

The research is carried out on the self-compacting concrete, and the mix design process has been experimentally investigated. It depends upon the mix design method which has been proposed by the researcher, and also the theory of packing has been used so that the target strength has been achieved; apart from these, the durability has been enhanced by minimum paste volume [4]. The validation of the model has been carried out for the case of self-healing concrete. The capsule slenderness ratio to the strength of the concrete capsule is considered to be the very important factor so that the process of the cell filling can be effectively carried out. It is considered that if the length of the capsule is smaller, then the process of the breaking will be longer [5].

The models are prepared using the software by the finite element method, and the different concrete beams have been tested experimentally. The validation process is carried out in terms of remote shape as well as using Eigen frequency. The author confirms that the verification process for the response related to spatial average is very important [6]. Numerical analysis is carried out where the coding of the finite element method is considered so that the propagation of the crack and capturing of it in the case of elements which are having interface are obtained. In addition to this validation is carried out for this code of finite element method as well as the results obtained from the experiment [7]. Additional part related to modelling have been carried out for the case of nonlinear response in particular to the concrete walls, and forces applied is also used in planar direction. The analytical model has been proposed by an author which has the method related to the share as well as pleasure and combined interaction [8].

The composite beams are experimentally tested but this procedure is time consuming while the complications are also involved in this as well as some of the advanced testing facilities are also needed [9]. The finite element procedure in terms of modelling such kind of beams is very helpful so that the proper behaviour of such specimen can be effectively studied and the results can be compared. The finite element method has been used for the cold formed steel tube section [10]. In nuclear power plant, the steel plates which have been used for the reinforcement to get the good quality of the concrete resulted into the good protection system so that the aircraft impact will not be there. The analysis of the simulation models related to these days as well as the test of the impact is carried out in the ANSYS software. The finite element method is used for the numerical analysis [11].

The products which have been recycled from the tyres are used in the concrete which is considered as green concrete, and this can be used very effectively in the pavement of the concrete. The experimental results which are obtained in this case have been tested and validated with the obtained results from the finite element-based method where the software is used [12]. The experimental procedure is carried out related to these panel which have to be used so that the resistance to the blast forces can also be investigated. While the field blast test was used, and apart from this, their simulation in terms of numerical has been investigated [13]. The models which have been proposed by researchers are considered to be the problems in the case of stability for the numerical analysis. For the case of models which are traditionally used and also in the research the equation in terms of finite element as well as the diffusion of the chloride is obtained. The accuracy in the method of computation as well as the method where the model is proposed considered to be good [14]. The experiment has been carried out on the high strength concrete with the help of steel fibre reinforcement, and it is a pain that there is certain displacement in the flexure as well as shear. The equations are also proposed by author while the validation process is carried out with the help of experimental analysis and the results obtained through experiment. Researcher found that equations and the variation are in good condition [15].

The present work deals with the validation process which is carried out using the ABAQUS software. This software is finite element-based software; the experimental results are obtained in the terms of the concrete having manufacturing sand in varying proportions. This work consists of the concrete having the manufactured sand as partial replacement of the natural sand in the replacement percentage of 0–100% and the use of silica fume to replace the cement in partial replacement to increase the strength of the concrete has been considered along with the validation in the ABAQUS software, the work which is different than that of the work in the past literatures.

1.2 The Process of Manufacturing M-sand

The M-sand is produced when the granite rocks have been crushed [16]. The deposits related to the hard rocks have to be crushed in machines of the crusher, the segregation process is carried out for the materials which are crushed, and the fractions need to have in the different parts [17]. The fine particles have been removed from this, while the impurities present can be removed through the process of washing as well as sieving [18]. Generally, the m-sand involve the process of the extraction, crushing of aggregate, screening, sorting, classifying of air, handling and storage [19]. The advantages of the m-sand involves that it is free from the different impurities like clay or dust [20]. The properties of the m-sand related to the physical as well as the chemical are considered to be very strong to resist different conditions of the climate [21].

Table 1 Physical properties of aggregates

Aggregate	Bulk density (kg/m^3)	Fines content (%)	Fineness modulus	Water absorption	Moisture content	Specific gravity
Natural sand	1600	4.08	2.79	7.14	3.74	2.79
M-sand	1650	10.97	3.72	11.13	0.57	2.77
Coarse aggregate	1625	–	–	0.57	0.09	2.85

2 Materials and Methods

2.1 Materials

The ordinary Portland cement was used for the experimental analysis of the concrete by replacing natural sand with the manufacturing sand; Indian standard code used is IS 1489-1991. The physical property of the cement includes fineness is 325 m^2 per kg, initial setting time of 47 min, final setting time of 378 min, standard consistency of 25.8 percentage, soundness is 1.2 mm, and specific gravity is 3.21. The silica fume was also used in the concrete, and it is obtained from the industry nearby to the city, and properties of the silica fume include the specific gravity of 2.31, surface area is 20500 m^2 per kg, size of silica fume is 0.1 micron, and bulk density is 581 kg per metre. The coarse aggregate used in this experimental analysis is confirmed to the Indian standard code IS 2386-1963. The river sand which is available in the local market has been used as a fine aggregate in this experiment. Manufacture sand was considered from the crusher available outside the city. The potable water has been considered for this experiment. This superplasticizer was also used for improving the property of workability in the concrete. The superplasticizer is in the form of sulphonated naphthalene polymer. The physical properties of m-sand and natural sand are shown in Table 1.

2.2 Mix Proportion

The experimental investigation is carried out for the case of concrete having natural sand and, manufacturing sand. The replacement of the natural sand is carried out by the manufacturing sand in the proportion of 0–100%. The mix proportion for the M-30 grade of the concrete having the replacement of natural sand by the manufacturing sand have been mentioned in Table 2. Coarse aggregate content is 1130 kg, water contained is 190 L, cement content is 394.975 kg, and silica fume content is 32.025 kg. Table 2 shows the mix proportion of the materials used in the concrete.

Table 2 Mix proportion for M-30 grade concrete

% Replacement	Cement (kg)	Silica fume (kg)	Natural sand (kg)	M-sand (kg)
0	427	0	730	0
10	394.975	32.025	657	73
20	394.975	32.025	584	146
30	394.975	32.025	511	219
40	394.975	32.025	438	292
50	394.975	32.025	365	365
60	394.975	32.025	292	438
70	394.975	32.025	219	511
80	394.975	32.025	146	584
90	394.975	32.025	73	657
100	394.975	32.025	0	730

3 Modelling in ABAQUS

3.1 Model Creation

Before creating the model, property related to the material has to be assigned to that particular file. This tape is also called as pre-processing where the model of the material as well as the property of the material which includes linear property, elastic property and isotropic property has to be assigned. The proper co-ordinate system is to be given so that the modelling is properly carried out. The following block diagram is to be followed for the software of ABAQUS (Figs. 1, 2, 3 and 4).

3.2 Process of Meshing

The command related to the meshing has been assigned to the model, and it is to be considered for the analysis of finite element method. The process of meshing is carried out in the support condition which is to be given to the model which has been carried out in the first process that is preprocessing. The load has to be assigned to the particular model.

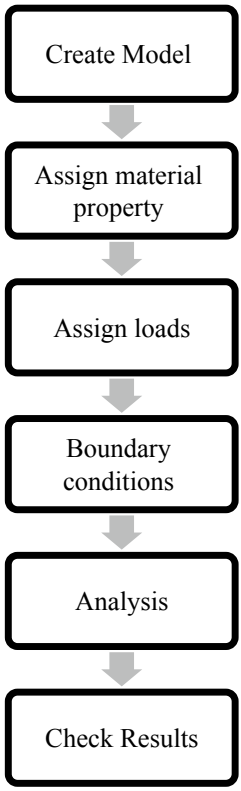

Fig. 1 Block diagram for the modelling in ABAQUS software

4 Result

The post-processing operation is to be carried out on the model so that the output is generated. The results have to be obtained in terms of graphical format as well as tabular format for the model (Figs. 5 and 6).

The analysis of the model was carried out using ABAQUS software and the results obtained have been shown as follows.

Figure 7 gives the details about the starting of the damage to the model of the beam as per ABAQUS software. This shows the damage in the centre portion with the green colour and at the bottom edge of the beam model.

Figure 8 the data related to the damage of beam model as the modelling is carried out using ABAQUS software. The damages as observed in the centre portion from top surface to the bottom surface. Some damages at the bottom edges can also be observed. In the figure 8, the top left corner gives the details for the values and the colour of the damages as observed in the post-processing of the software.

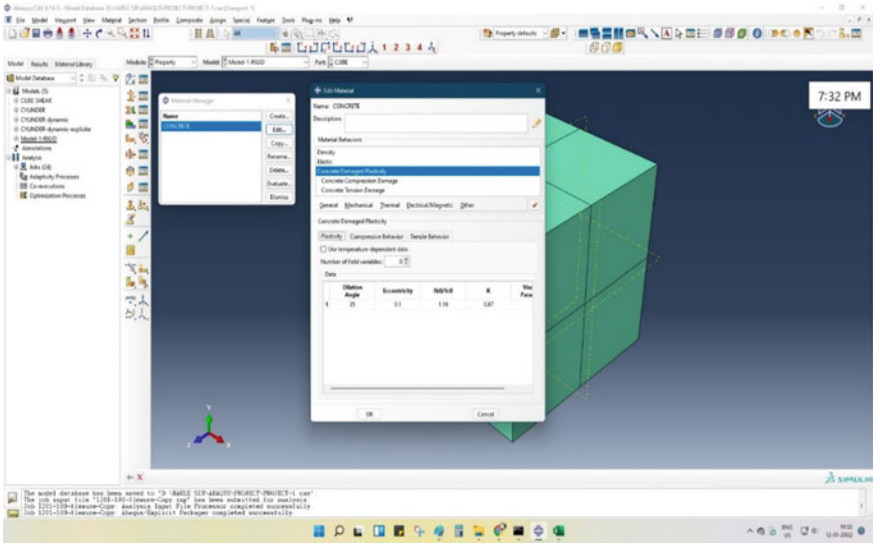

Fig. 2 Assigning material properties (concrete damaged plasticity) to model concrete cube (m-sand)

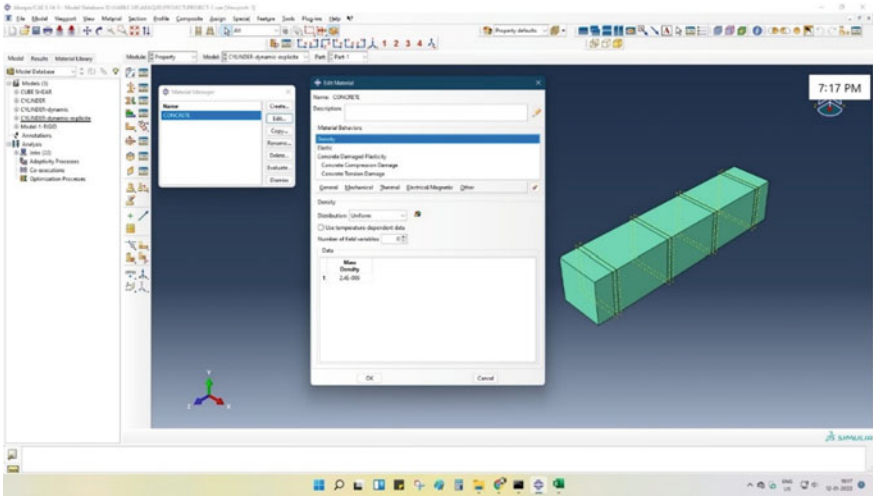

Fig. 3 Assigning material properties (density) to model- concrete beam (m-sand)

4.1 Results for Concrete with M-sand

The results obtained in the experimental investigation are as follows in Table 3.

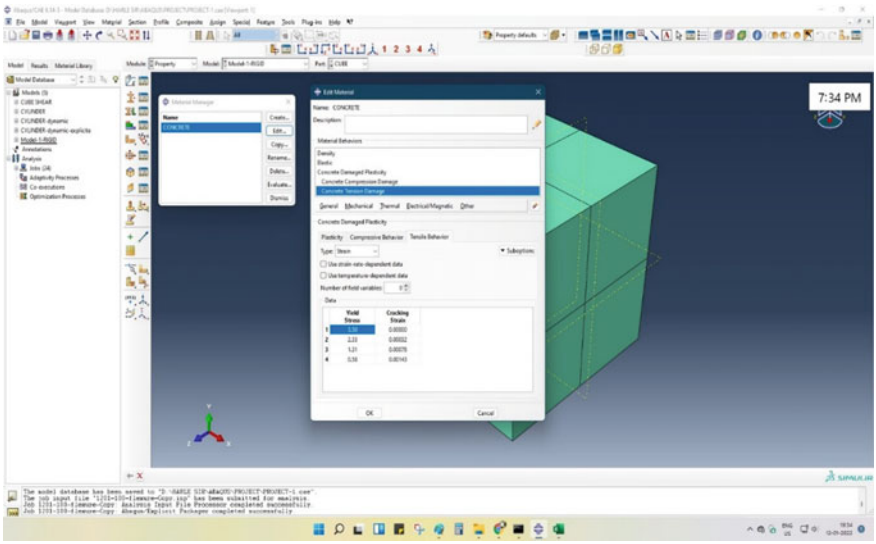

Fig. 4 Assigning material properties (concrete tension damage) to model concrete cube (m-sand)

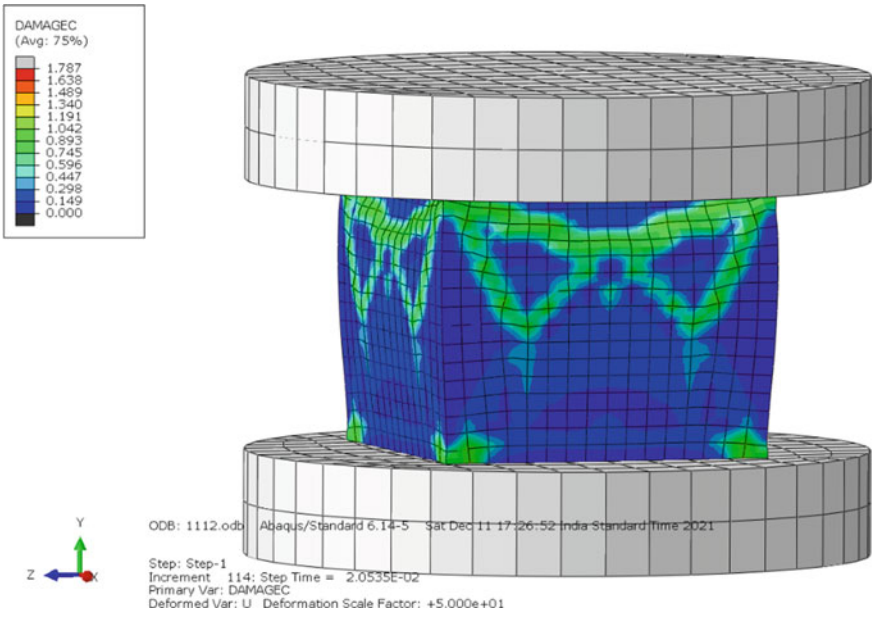

Fig. 5 Damage details of the cube model in the ABAQUS software

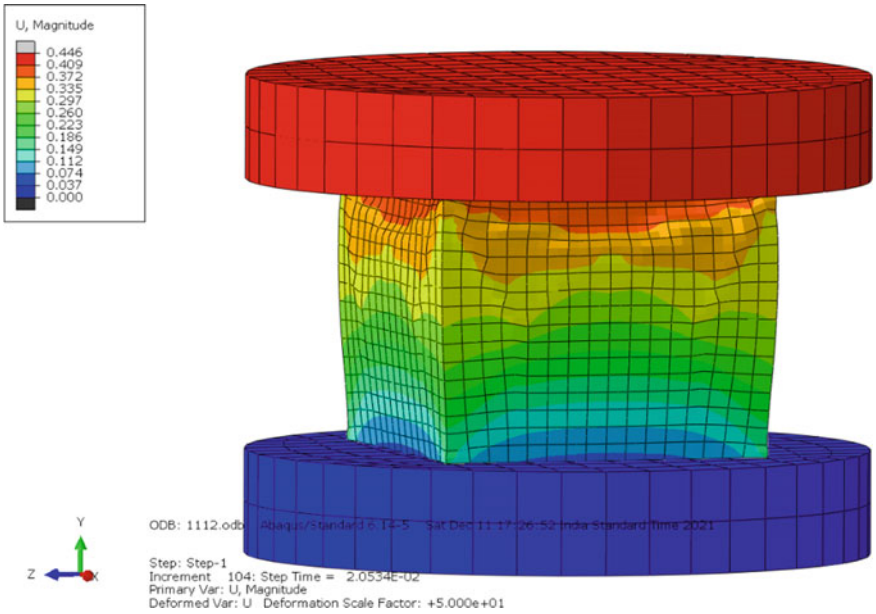

Fig. 6 Deformation details of the cube model in the ABAQUS software

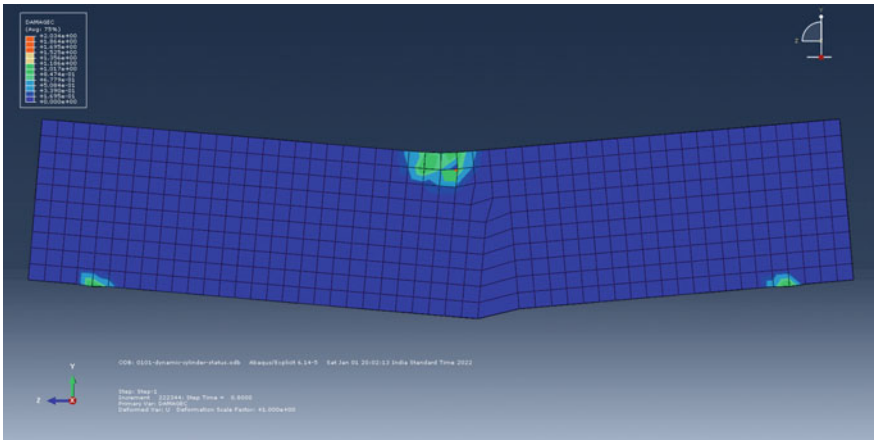

Fig. 7 Starting of the damage details of the beam model in the ABAQUS software

The above results are related to the experimental investigation on the concrete cubes for the case of compressive strength. From the results it is observed that the strength of concrete is maximum for the 100% replacement of the natural sand by the m-sand.

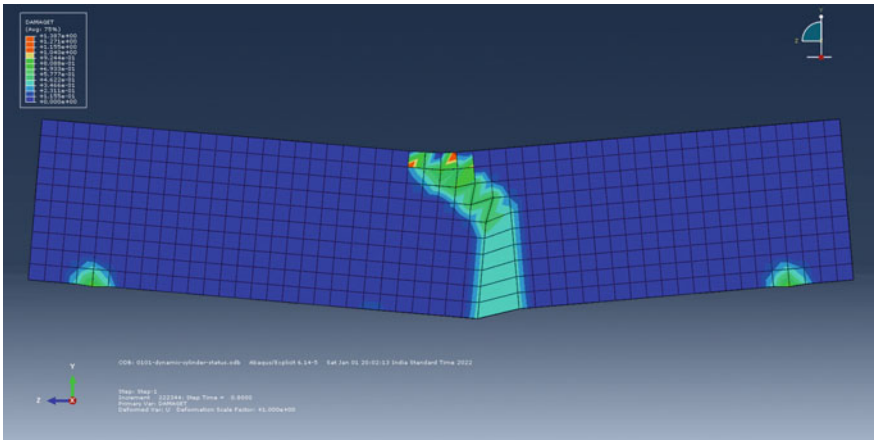

Fig. 8 Damage details of the beam model in the ABAQUS software

Table 3 Compressive strength-M30 concrete with MS

% Replacement	7 days	28 days	56 days
0	25	32	35
10	25.63	32.80	35.88
20	26.27	33.62	36.77
30	26.92	34.46	37.69
40	27.60	35.32	38.63
50	28.29	36.21	39.6
60	28.99	37.11	40.59
70	29.72	38.04	41.6
80	30.46	38.99	42.64
90	31.22	39.96	43.71
100	32.00	40.96	44.8

Figures 9, 10, 11 and 12 gives the details about the comparison of the analytical results and the experimental results for the case of the concrete with manufactured sand from zero to 100% replacement. From the Figs. 9, 10, 11 and 12 it can be observed that the variation of the stress and the displacement is in good co-relation.

The comparative analysis of the experimental data and the data obtained from the past literature has been mentioned in Table 4.

From Table 4, it is observed that various experiments have been performed on the concrete with m-sand, concrete with silica fume and the combined effect of the m-sand and the silica fume. Compressive strength obtained in the present work is having comparative results. The maximum percentage replacement is observed for the ranges from 0 to 50%, very few experiments have been performed on the percentage replacement above 50%, and the silica fume percentage was also varying

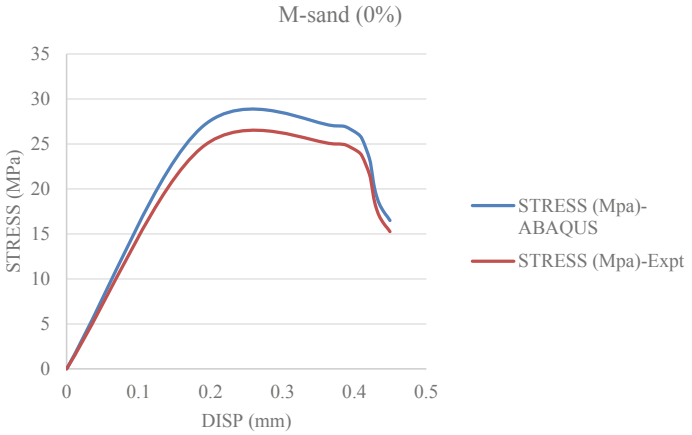

Fig. 9 Comparison between analytical and experimental results for M-sand (0%)

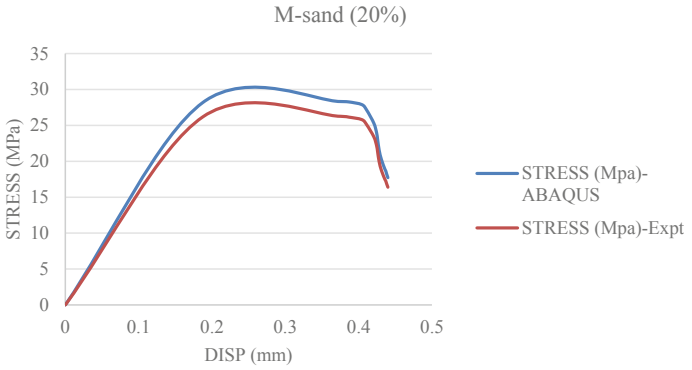

Fig. 10 Comparison between analytical and experimental results for M-sand (20%)

in the experiments from the past literature. The present work consisting of the M-Sand ranging from 0 to 100%, the maximum strength obtained for the 100% replacement, this concrete also contain few percentage of silica fume.

5 Conclusion

This section deals with the results obtained for the modelling as carried out in the ABAQUS software. The software processing has been mentioned in the paper. The results have been observed for the concrete with M-sand as partial replacement of natural sand using the software. The analytical results and the experimental results

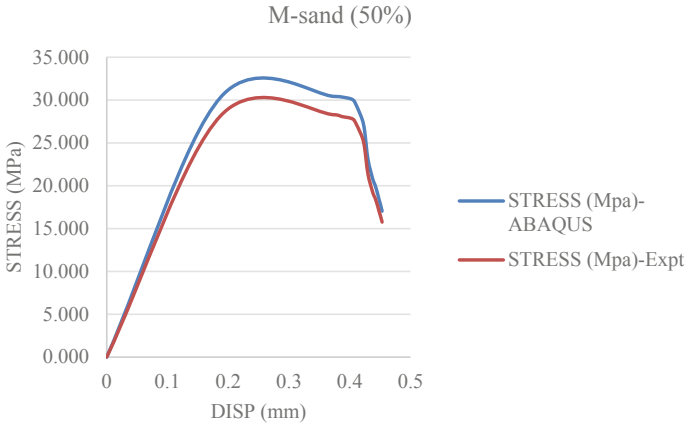

Fig. 11 Comparison between analytical and experimental results for M-sand (50%)

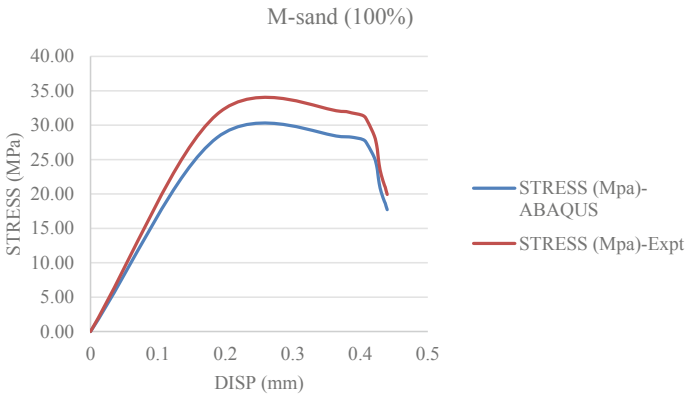

Fig. 12 Comparison between analytical and experimental results for M-sand (100%)

are compared using graphical format. The stress and the displacement variation has been found to be in good conjunction with each other.

Table 4 Comparative analysis of the compressive strength of the concrete

% Replacement	References used						
	(Present work)	[22, p. 8]	[23, p. 445]	[24, p. 1386]	[25, p. 645]	[26, p. 48]	[27, p. 102]
0	32	–	–		44	–	38
10	32.80	–	–	45	42	36	
20	33.62	–	–	43	38	–	39
30	34.46	34	–	44	37	–	
40	35.32	–	–	–	36	37	39.5
50	36.21	–	39.8	–	34	38	
60	37.11	–	–	–	–	37.5	41
70	38.04	–	–	–	–	–	
80	38.99	–	–	–	–	–	
90	39.96	–	–	–	–	–	
100	40.96	–	43.4	–	–	–	

References

1. Aguiar OP, Silvério PEC, Miranda LGJ, Caldas RB (2022) Circular openings with transverse rebar as steel-concrete shear connection (part 2/2): experimental investigation, model validation and parametric analysis. Eng Failure Anal 133:106004
2. Aloisio A, Pasca DP, Di Battista L, Rosso MM, Cucuzza R, Marano GC, Alaggio R (2022) Indirect assessment of concrete resistance from FE model updating and Young's modulus estimation of a multi-span PSC viaduct: experimental tests and validation. In: Structures, vol 37. Elsevier, pp 686–697
3. Alshaikh IMH, Bakar BHA, Alwesabi EAH, Zeyad AM, Magbool HM (2021) Finite element analysis and experimental validation of progressive collapse of reinforced rubberized concrete frame. In: Structures, vol 33. Elsevier, pp 2361–2373
4. Ashish DK, Verma SK (2019) Determination of optimum mixture design method for self-compacting concrete: Validation of method with experimental results. Constr Build Mater 217:664–678
5. Dai Z, Tsangouri E, Van Tittelboom K, Zhu X, Gilabert FA (2022) Understanding fracture mechanisms via validated virtual tests of encapsulation-based self-healing concrete beams. Mater Des 213:110299
6. Filippoupolitis M, Hopkins C (2021) Experimental validation of finite element models representing stacked concrete beams with unbonded surface contacts. Eng Struct 227:111421
7. Garcia-Llona A, Ortega-Lopez V, Piñero I, Santamaría A, Aguirre M (2022) Effects of fiber material in concrete manufactured with electric arc furnace slag: experimental and numerical study. Constr Build Mater 316:125553
8. López CN, Massone LM, Kolozvari K (2021) Validation of an efficient shear-flexure interaction model for planar reinforced concrete walls. Eng Struct:113590
9. Massone LM, López CN, Kolozvari K (2021) Formulation of an efficient shear-flexure interaction model for planar reinforced concrete walls. Eng Struct 243:112680
10. Saadi TH, Al-Zaidee SR (2021) Validation of FE modeling of cold-formed tube lightweight concrete composite system. Mater Today: Proc
11. Sadiq M, Yun ZX, Rong P (2014) Simulation analysis of impact tests of steel plate reinforced concrete and reinforced concrete slabs against aircraft impact and its validation with experimental results. Nucl Eng Des 273:653–667

12. Soleimani SM, Roudsari SS, Banthia N, Alaqqad AR, Mohammad N, Jumaah A (2021) Analytical and experimental study of using recycled tire products in pavement-grade concrete suited for hot weather climates. Constr Build Mater 312:125343
13. Wu J, Liu Z, Yu J, Xu S (2022) Experimental and numerical investigation of normal reinforced concrete panel strengthened with polyurea under near-field explosion. J Build Eng 46:103763
14. Yu B, Ling G-Z, Fan Z-H, Chen Z, Yang L-F (2021) Numerical modelling and experimental validation of two-dimensional chloride concentration distribution within concrete. Constr Build Mater 298:123804
15. Zhang Y, Zhang H, Lu X (2022) Seismic performance evaluation and experimental validation of steel-fiber-reinforced high-strength-concrete composite shear walls. In: Structures, vol 35. Elsevier, pp 765–779
16. Das SK, Mustakim SM, Adesina A, Mishra J, Alomayri TS, Assaedi HS, Kaze CR (2020) Fresh, strength and microstructure properties of geopolymer concrete incorporating lime and silica fume as replacement of fly ash. J Build Eng 32:101780
17. Manjunatha M, Seth D, Balaji KVGD, Chilukoti S (2021) Influence of PVC waste powder and silica fume on strength and microstructure properties of concrete: an experimental study. Case Stud Constr Mater 15:e00610
18. Brescia-Norambuena L, González M, Avudaiappan S, Saavedra Flores EI, Grasley Z (2021) Improving concrete underground mining pavements performance through the synergic effect of silica fume, nanosilica, and polypropylene fibers. Constr Build Mater 285:122895
19. Ibrahim KIM (2021) Recycled waste glass powder as a partial replacement of cement in concrete containing silica fume and fly ash. Case Stud Constr Mater 15:e00630
20. Patil S, Somasekharaiah HM, Rao HS, Ghorpade VG (2021) Durability and micro-structure studies on fly ash and silica fume based composite fiber reinforced high-performance concrete. Materials Today: Proc
21. Kansal CM, Goyal R (2021) Analysing mechanical properties of concrete with nano silica, silica fume and steel slag. Materials Today: Proc 45:4520–4525
22. Ali T, Buller AS, Ahmed Z, Shabbir S, Lashari AR, Hussain G (2022) Investigation on mechanical and durability properties of concrete mixed with silica fume as cementitious material and coal bottom ash as fine aggregate replacement material. Buildings 12(1):44
23. Babu DS, Anveshkumar M (2016) Manufactured sand with silicafume, an alternative to river sand and in concrete industry. Int J Appl Res 2(3):441–448
24. Kumar SV, Rajkumar R, Umamaheswari N (2019) Study on mechanical and microstructure properties of concrete prepared using metakaolin, silica fume and manufactured sand. Rasayan J Chem 12(3):1383–1389
25. Dash MK, Patro SK (2021) Performance assessment of ferrochrome slag as partial replacement of fine aggregate in concrete. Eur J Environ Civ Eng 25(4):635–654
26. Joe MA, Rajesh AM, Brightson P, Anand MP (2013) Experimental investigation on the effect of M-sand in high performance concrete. Am J Eng Res 2(12):46–51
27. Jadhav PA, Kulkarni DK (2012) An experimental investigation on the properties of concrete containing manufactured sand. Int J Adv Eng Technol 3(2):101–104

A Review on the Use of Industrial Waste and Agricultural Waste in the Production of Alkali-activated Concrete

Sonal Thakkar, Abhishek Chanda, and Shivanjali Rawat

Abstract Due to rapid growth and urbanization, the need for better infrastructure and population rehabilitation has increased to a huge extent. This has led to an increased demand for buildings and industrial infrastructure which imposes a huge demand for basic building material cement, which is one of the major contributors to global warming. The ever-increasing demand of the population has also led to cause a huge generation of waste in the environment. The waste generation has further polluted the environment and has disturbed the ecology. This paper mainly aims at using various agricultural and industrial wastes in alkali-activated concrete (AAC) which provides a solution to both the problems since this concrete replaces the cement material and reduced the production of carbon dioxide and also the utilization of waste material for the betterment of the society.

Keywords Alkali-activated concrete · Agricultural waste · Industrial waste · Mechanical properties

1 Introduction

The most important and commonly used building construction material that has been popular for the last two centuries among other mineral binders is the Ordinary Portland Cement (OPC). The OPC manufacturing process uses a large amount of natural resources and consumes a high amount of heat and energy. The building business is growing at a faster rate, and as per statistical data, nearly 260,000,000 tonnes of cement is required annually to meet the need for the current infrastructure development. Nearly, 1 tonne of carbon dioxide is produced in manufacturing 1 tonne

S. Thakkar (✉) · A. Chanda · S. Rawat
Civil Engineering Department, Nirma University, Ahmedabad, Gujarat, India
e-mail: sonal.thakkar@nirmauni.ac.in

A. Chanda
e-mail: 21ftphde64@nirmauni.ac.in

S. Rawat
e-mail: 21ftphde51@nirmauni.ac.in

K. Geetha et al. (eds.), *Recent Trends in Materials*, Springer Proceedings in Materials 18, https://doi.org/10.1007/978-981-19-5395-8_7

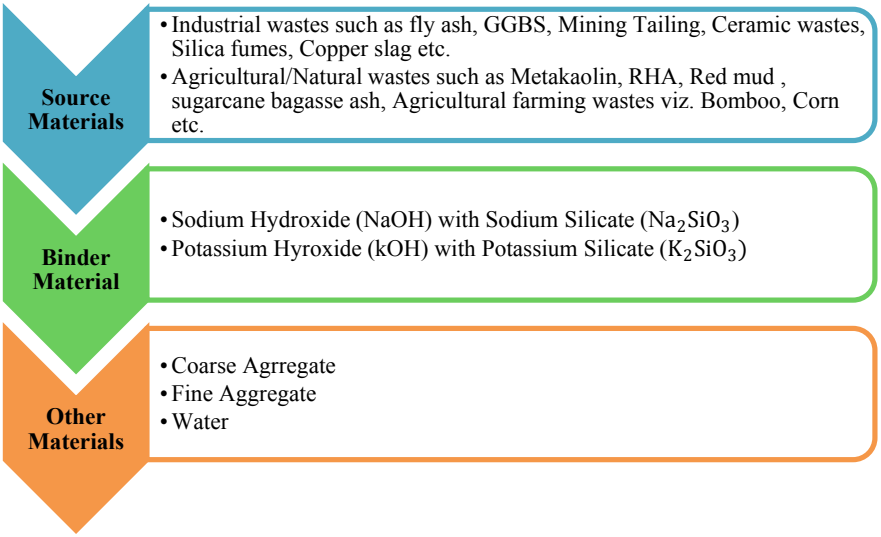

Fig. 1 Artefacts showing ingredients for alkali-activated concrete

of portland cement. Hence, the cement industry is responsible for higher pollution in the environment. The theme of cement production has shifted in multiple ways, viz. lowering the volume of waste produced from the manufacturing process, increasing the output of the portland cement mix with lower clinker and low carbon emission. According to a recent study, it has been proved that improving upon the cement technology will reduce carbon dioxide (CO_2) emission level to half as compared to that produced in 1990 [1]. Around 90–95% of the world's waste is dumped on open land causing significant harm and loss to the environment. As a result, the new binders formed can be utilized in both cases, viz. maintaining the demand of the concrete for manufacturing and development purposes and meeting the requirement of CO_2 reduction too at a larger amount. One such solution is the alkali-activated concrete (AAC). The AAC uses both industrial waste and agricultural waste as a source material which in turn results in the solution of waste disposal in landfills and also reduces the use of carbon dioxide emission into the atmosphere (Fig. 1).

2 Alkali-activated Concrete with Different Wastes

The source material and alkaline solution are the two basic components of the AAC. Aluminosilicate as the source material should have high silicon (Si) and Aluminium (Al) ions. Because geopolymerization includes a rather quick chemical reaction between the aluminosilicate material, it has a 2- to 3-dimensional network and is a time-consuming process (Figs. 2 and 3).

Fig. 2 Flow diagram representing types of waste as a source in AAC

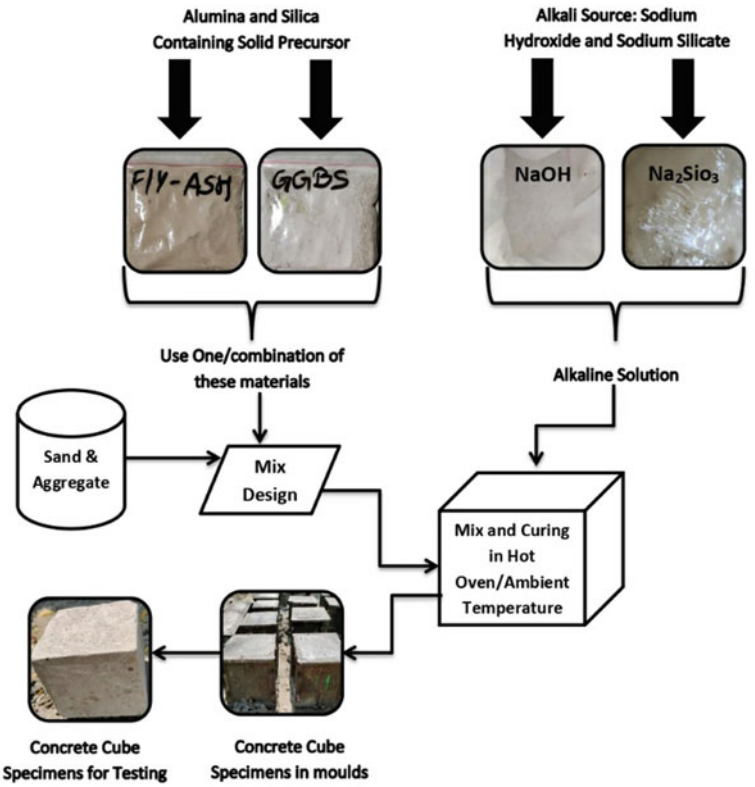

Fig. 3 Block diagram representing the formation of AAC

2.1 Industrial Waste

A large number of industrial wastes are either stored or deposited on the ground in landfills due to its high worldwide demand for services and products. In the Civil Engineering sector, most of the portion of the industrial waste generated is being used to enhance the property of the concrete qualities but the problem lies in capitalizing them. The use of a few of these wastes in AAC and their effect on various properties are described below.

Fly Ash. In an experimental investigation by Rao et al., it was observed that there was an increase in the strength of geopolymer concrete with the increase in the concentration of NaOH. Researchers also concluded that the geopolymer concrete can perform well under ambient conditions under sunlight, but the setting time of this concrete was higher as compared with the ordinary portland cement [2]. Davidovits in the year 1978 postulated that binders may be made up of geopolymeric reaction of alkaline liquids in geologically derived materials such as fly ash [3]. Williamas et al. studied the mechanical effect of fly ash on the characteristics of geopolymer at room temperature. There was a change in the particle size and morphology when the reactivity of the alkaline solution increased [4]. Sanjayan et al. based their study on the workability and strength of class F fly ash with two activators and different dosages of superplasticizer and concluded that as the superplasticizers dosage was increased, the workability and strength of the fly ash geopolymer also increased [5].

GGBS/Slag. Atkinson et al. studied that the glassy samples had relatively little crystalline material. On activation with 1.5 M solution, high strength was achieved. The setting period differed with different batches of slag [6]. Shi et al. in their study observed the physical and chemical features of the solidified steel slag which was influenced by molten cooling. Steel slag can be utilized for cementing purposes. The inclusion of activators can enhance the cementing potential of the steel slag as they are composed of oxides [7]. Pedraza et al. studied the performance of AAC with various slag ratios and compared it with the OPCC. At 28 days, they observed that increasing the binder concentration resulted in improved strength in both the AAC and PCC. However, at 90 days, the performance of the OPCC was better than AAC [8]. Brouwers et al. studied the normal response steps which included acceleration, induction and steady period of the activator in the fly ash/slag ratio. The initial dissolution time was unaffected but the reaction intensity was rising. It was found that raising the slag/fly ash ratio and reducing the activator modulus boosted the reaction intensity and shortened the primary reaction process in the AAC [9].

Construction & Demolition (C&D) Waste. The construction and Demolition Wastes (CDWs) are mostly made up of chemically unreactive substances such as cement concrete, building construction bricks, tiles and ceramics. The recycling of CDWs is critical since they are heavy and bulky, unsuitable for landfill disposals. Most C&D wastes are extremely useful for reuse and recovery purposes since they reduce energy and carbon dioxide emission and limit the use of natural resources,

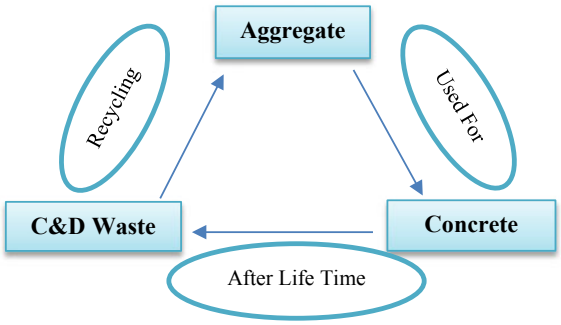

Fig. 4 Schematic representation of recycling technique in C&D wastes

they are significantly important from the environmental perspective [10]. Figure 4 shows a schematic diagram of the production of C&D waste.

The quality of adhering property of mortar, the absorption of water of the aggregates that are recycled and the amount of moisture that is freely available determine the role of the *w*/*c* ratio in the recycled aggregate [11]. Luhar et al. suggested the use of ceramic aggregate in place of natural sand and found a positive result in terms of compressive strength, flexural strength and split tensile strength. The increase in the waste ceramic powder improved the setting time and workability of the alkali-activated mortars [12]. The utilization of the porcelain tile polishing leftover as a raw material in the synthesis of geopolymers from trash promotes their usage as low energy and efficient construction materials. When porcelain polishing tiles were combined with metakaolin for the synthesis of geopolymer, the compressive strength increased up to 10%. The achieved compressive strength was greater than 70 Mpa [13].

Mining Tailing (MT). Mamani et al. activated mine tailing with a 9 M sodium hydroxide solution to evaluate creep response of geopolymeric concrete when subjected to a temperature of 500–600 °C. It was observed that diffusion occurred at grain boundaries and a temperature of 600 °C, and the mechanical response was ductile [14]. Capasso et al. in their study found that the compressive strength did not increase significantly on the addition of aggregate and when the mining waste content was added whose aggregate size was greater than 20%, the uniaxial strength remained low for the fly ash geopolymer mix this was attributed to the formation of an interface between the binder and the mining waste aggregate which indicated good quality geopolymer matrix[15].

Nano Silica and Fibre Waste. Nanosilica (NS) in geopolymer cement has remarkable growth in the property index, compressive strength and flexural strength. Rahmawati et al. in an observation noted that in 90 days there was an increase in compressive strength of the geopolymer when 2% of nano-silica was added with 10% micro silica, from 53.2 to 92.1 Mpa. Changes in the flexural strength were seen at the time of adding nanofibres at a concentration of 1–3% in geopolymers [16]. Silva et al. in an investigation suggested that geopolymer matrix reinforced with various natural fibres such as wool and cotton produced higher compressive,

flexural and tensile strengths and also improved ductility. Also, it was proven that fibre-reinforced geopolymer composites had a lot of promising characteristics for the production of structural and non-structural pre-fabricated parts in the construction industry [17].

Waste Foundry Sand and Miscellaneous Industrial Ash. Bharadwaj et al. observed that the compressive strength of the mixes showed incremental characteristics as the natural sand was replaced by waste foundry sand (WFS) up to 60%. At 28 days of curing process, 40% of the natural sand with 60% of waste foundry sand gave a compressive strength value around 60 MPa. The whole strength was nearly 47% greater when there was a full substitution of naturally available sand with the waste foundry sand. In a set of observations, it was seen that the addition of WFS reduced the workability of the geopolymer concrete when the dosage of superplasticizers was between 1 and 3%. This was attributed to the water-absorbing characteristics done by the finer particles present in the WFS [18]. It was also observed that WFS can work as a filler in filling pores which can enhance the durable property and gain the strength of the mix. But, the presence of finer WFS particles, substituting the naturally occurring coarse aggregate with 50% and 10% of the recycled coarse aggregate, can result in the reduction of compressive strength [19].

Mukri et al. used a combination of laterite soil and ash from the palm oil boiler and observed that by increasing the qualities of the laterite soil with an alkaline solution as a binder, there was an increase in compressive strength value. The curing was done at an ambient temperature in a carrier bag to match the conditions of the field, and the results showed the compressive strength of 76 kPa at 28 days [20]. Ban et al. used high calcium wood ash (HCWA) and pulverized fly ash (PFA) with sand and water, to understand the effect on the compressive strength and the binding property. Since the HCWA is obtained from the burning of rubberwood waste and mixed with PFA, it had a high content of calcium hydroxide and potassium oxide which are further high in the aluminosilicate compound and can produce a solid binder mix for the manufacturing or production of cementless paste. The bond strength and the variation of curing temperature were very less influenced [21]. Bhutta et al. observed that the blended waste fuel ash geopolymer concrete (BFAGC) did not have a change in mass as compared to the OPC whose mass reduced by 4%. Also, the chemical stability and the compressive strength got enhanced in BFAGC as compared to OPC [22]. Amin et al. used bagasse ash, china clay, sodium silicate and sodium hydroxide, and as binder materials with varying Si/Al ratios, it was concluded that the proportion of silicon to aluminium composites determines the compressive strength [23].

2.2 Agricultural Waste

Natural source raw materials and agricultural wastes such as metakaolin, sandy clay, red mud, pozzolanic volcanic rocks and others can be used to make alkali-activated

geopolymer materials. The biggest setback of using these materials is they are only available in selective geological locations and restricted amounts.

Sugarcane bagasse Ash. 13% of cultivated sugarcane nearly produces 231 kg of bagasse as a residue. Kathirvel et al. in their study investigated the replacement of GGBS with sugarcane bagasse ash (SCBA) for the production of geopolymer concrete. SCBA which has been pulverized to ash was used as a pozzolanic material and was also taken as source material in the supplementary cement replacement process. The consistency of the paste got improved as the amount of GGBS was replaced by SCBA. Since consistency also influences the setting time, it was observed that the setting time escalated with the addition of SCBA as a substitute for GGBS. When there was a 10% replacement level, the strength of compression was found to be high, and 20–30% replacement resulted in the comparison with the conventional mix. This change at 10% replacement was credited to the high demand for water of the material. The compressive strength increased up to 22% as compared to the replacement of 10% in the controlled mix but yet it gave higher compressive strength up to 20% replacement when there was a comparison with the controlled mix [24]. When the SCBA was used with Blast Furnace slag (BFS) and cured at 65 °C for 3–7 days, it gave good compressive strength because of the gel matrix formation [25].

Red Mud (RM). The disposal of RM was a tough choice for the environmentalist to make, and hence, the use of RM in the geopolymerization met the demand and hence reduced the adverse effect on the ecology and the ecosystem. The expensive cost of the alkali activator solution can be relieved as RM has a high NaOH content and can fulfil the demand of the chemicals present in the sodium hydroxide [26]. Liang et al. in their studies found that when RM was used with blast furnace slag for geopolymer mortar, 40% RM was replaced as a cementitious material in the geopolymer concrete, and the chloride ion permeability gave the desired result in the range of the requirement of the construction material. Again, the corrosion current of the steel bar in the geopolymer mortar was substantially less than that of the cement mortar with the same concentration of chloride salt. Steel bars were better protected from corrosion by the geopolymer mortar when compared with the cement mortar [27]. In an investigation carried out by Chen et al. with red mud and GGBS-activated geopolymer, it was observed that the strength and adsorption of metals with heavy ions were influenced by the RM concentration. As the RM concentration increased from 0 to 50% by weight, there was a reduction in strength and the adsorption of heavy metals ions increased. Also, the C–S–H gel with a low Ca/Si ratio made up the hardened geopolymer concrete because of the raw red mud particles in geopolymer concrete. This was because the Ca/Si ratio had a huge surface area and pore, and the inert RM adsorbed the ions of the heavy metals. In the study on compressive strength, the 28-day result showed that with the usage of 30% of RM, the strength got lowered by 5% only, but was hugely successful in eliminating the heavy metal ion from 33 to 120% which indicated that the pervious concrete could be used for light road pavement construction [28].

Miscellaneous Agricultural Farming Wastes. In a set of experiments carried out by Rajan et al. in the synthesis of geopolymer concrete with rice husk ash (RHA) as agricultural waste in producing sodium silicate, it was observed that RHA can be used to produce a low-cost alkaline activator at a temperature of 100 °C which results in low energy emission. The activators which are produced with the help of RHA showed better compressive strength, irrespective of the ratio of RHA to NaOH. The compressive strength was at its highest when the ratio of RHA to NaOH was 1:1 because of the production of dense microstructure formation due to C-A–S–H gel [29]. Cheng et al. used some of the agricultural farming wastes which included natural wastes such as bamboo, corn, barley, wheat, olive, sisal, date palm and various aquacultural farming waste such as oyster and mussel shell, for the partial substitution of binders or aggregates in green concrete. The experimental setup showed that Natural waste from agricultural farming (NWAGF) and Natural waste from Aquacultural farming (NWAQF) can be used to build several types of green concrete either by substituting a part of OPC or aggregate or by reinforced concrete fibre. When dosages are added in a controlled manner as additional material, an economic and sustainable range of green concrete can be achieved. Hence, the study stated that it will be helpful in carbon dioxide emission, preserving natural aggregates and solving the issue of landfilling too [30].

2.3 Bio-medical Waste

Incinerated Bio-Medical waste Ash (IBWA) is a hazardous waste product that has a high potential of damaging the health of humans as well as the environment. This trash is dumped in landfills containing groundwater, and the ecosystem is at high stake. Muthukannan et al. in a set of experiments used IBWA as a replacement for GGBS-activated geopolymer in the variation of 5% from 0 to 50% by weight. The study concluded that with better use of IBWA, there was an improvement in setting time and flow of the concrete while the density decreased but the mechanical properties of the concrete improved. These findings demonstrated that IBWA can be used as a raw material in introducing a source to the geopolymer concrete [31].

3 Mechanical Properties

The mechanical properties are being reviewed when various wastes either industrial or agricultural are added to the AAC as an activator or binder or as supplementary cementitious material for the enhancement of the properties. The compressive strength, flexural strength, split tensile strength and Modulus of Elasticity were conducted using various binders. Table 1 shows the chemical composition of source materials along with the country of origin discussed in the paper. Table 2 gives an idea about the range of compressive strength with different types of binders. Table

3 shows flexural strength of geopolymer concrete with varying source materials. Table 4 shows a range of split tensile strength and Table 5 shows These different characteristics show the optimum value of the Alkali-activated concrete with various chemical compositions, the raw materials used, the binder ratio and the brief idea of the range of materials that can provide us with the optimum result, thus solving the problem of using waste material and hence solving the problem of landfill disposal too.

4 Applications of AAC

The geopolymer has various applications in the real world when it comes to the field construction purpose In the case of reinforced concrete, AAC can be used in both precast and in situ applications. These include the precasting of retaining walls, bridge decks, floor beams and various structural floor elements [33]. Among various field applications, AAC is used in geotechnical engineering for the stabilization of soft and weak soil surfaces. Jet grouting technique with geopolymers is a favourable soil stabilization method whose strength gaining aspect is yet to be discovered. Moreover, the AACs have also found their applications in the airport construction design to build various segments such as taxiways and aircraft turning areas. Due to the dense microstructural characteristics of AAC, it has low permeability and high durability and hence can be used in marine construction purposes. Also, the geopolymers at harsh environmental conditions perform well from the durability point of view, and they can be applied as an alternative to conventional cement mortar for restoration of buildings [34]. Other applications of the AAC are they can be used as a repair material compared to the OPC as they exhibit excellent properties of durability in both acidic and salty environments. One use of the geopolymer incorporated with fly ash also proves to be a good fire resisting material and has resistive responses at the higher temperature. They are also used as an immobilized material for heavy metals due to their property of low permeability and dense network [35]. Due to its high mechanical strength, thermal and chemical resistance and good toughness, the AACs have found their commercial applications in the construction industry too [36]. It has been found that the AACs not only have application on the field but have also been a great retarder in damaging the environmental pollution process. The global warming potential can be reduced up to 64% by using AAC which in turn implies the reduction of carbon dioxide emission into the atmosphere due to the reduction of the cement production process.

Table 1 Chemical composition of source material on AAC

Type of waste	Country	Name	SiO_2	Al_2O_3	CaO	MgO	Fe_2O_3	LOI	Ref. No.
AW	Brazil	Blast furnace slag (BFS)	30.19	10.66	39.53	7.5	1.31	5.62	[25]
		Sugar cane bagasse ash (SCBA)	31.41	7.57	16.06	1.07	6.02	32.2	
IW	Malaysia	Pulverized fuel ash (PFA)	46.7	35.9	3.9	0.8	5	1	[22]
		Palm oil fuel ash (POFA)	53.5	1.9	8.3	4.1	1.1	18	
IW	Malaysia	High calcium wood ash (HCWA)	43.22	17.61	11.28	5.94%	13.73	1.80%	[21]
IW	Finland	Fluidized bed combustion fly ashes	42.4	9.4	16.2	3.7	14.8	0.1	[32]
			40.2	10.1	13.8	2.8	22.3	0.1	
		Mine tailings (MT)	49.8	10.7	11.7	6.7	9.1	0.2	
			25.3	7	10.9	6.6	25.7	1.6	
IW	Italy	MK	56.16	39.08	–	–	1.78	–	[10]
		SL	36.48	9.31	44.36	6.2	0.57	–	
AW	China	GBFS	34.58	15.01	37.51	9.02	0.27	1.1	[28]
		RM	21.43	22.72	16.49	0	9.98	13.41	
IW	Brazil	Porcelain tile polishing residue (PPR)	–	54	0.5	0.1	42	2	[13]
		Metakaolin	–	67.7	0.7	2.6	21	0.8	
IW	India	Fly ash (%)	59.87	23.96	5.06	0.48	3.7	2	[18]
IW	Malaysia	Laterite soil (LS-P)	56	30.3	0.381	-	9.54	–	[20]
		Palm oil boiler ash (POBA)	43.9	4.55	13.1	3.27	4.11	–	
IW	India	Fly ash (%)	59.87	23.96	5.06	0.48	3.7	2	[19]
		GGBS (%)	33.06	22.29	35.37	7.61	0.9	0.26	

(continued)

Table 1 (continued)

Type of waste	Country	Name	SiO_2	Al_2O_3	CaO	MgO	Fe_2O_3	LOI	Ref. No.
		WFS (%)	78.5	5.5	2.44	2.76	4.45	4.65	
AW	India	RHA	95.64	0.07	0.49	0.62	0.05	–	[29]
		GGBFS	32.4	15.7	43.1	6.62	0.48	–	

Table 2 Compressive strength by source material using wastes on AAC

Type of waste	Source material	Type of curing	Strength/Aged (Days)	Ref. No.
AW	Blast furnace slag (BFS) and sugar cane bagasse ash (SCBA)	Ambient	62 MPa at 65 °C (BFA/SCBA-100/0)/7	[25]
IW	High calcium wood ash (HCWA) and Pulverised fuel ash (PFA)	Oven dry	10.12 MPa (6500 psi, 100 °C)/7	[21]
IW	Pulverized fuel ash (PFA) and Palm oil fuel ash (POFA)	Ambient	20–25/28	[22]
			25–30/28	
IW	Lightweight expanded clay aggregates (LECA)	Ambient	15–20 (for concrete, C0a & C0b)/28	[32]
	Fluidized bed combustion (FBC) fly ashes		20–25(M1), 25–30(M2), 20–25(C1 & C2)/28	
	Mine tailings (MT)		15–20(M3), 20–25(M3), 15–20(C3 & C4)/28	
IW	Bottom ash of sugar industry, China clay	Ambient	18.85/7	[23]
IW	Porcelain tile polishing residue (PPR) and metakaolin	Ambient	72 (15%PPR)/28	[13]
IW	Waste foundry sand (WFS)	Ambient	(40% NA + 60% WFS) 48.5/28	[18]
AW	Red mud (RM)	Ambient	18.53 (the replacement rate of RM to GBFS is up to 30 wt.% and 0% PC)/28	[28]
IW	In-house grinding of concrete	Ambient	78–107/28	[10]
	Fired clay scraps		40–87 /28	
IW	Mining tailings dust (MT)	Oven dry	40 MPa (525 ºC) (Type 1)/28	[14]
			20 MPa (575 ºC) (Type 2)/28	
IW	Palm oil boiler ash	Ambient	0.076 MPa/28	[20]
AW	Red mud	Ambient	64.25 (RHA: NaOH 1:1.0)/28	[29]
BMW	Incinerated bio-medical waste ash (IBWA)	Ambient	43.3 (IBWA30-30% IBWA + 70%GGBS)/28	[31]

Table 3 Flexural strength by source material using wastes on AAC

Place of work	Waste	Flexural strength (MPa)	Ref. No.
		Aged at 28 days	
Finland	Lightweight expanded clay aggregates (LECAs)	5–10	[32]
	Fluidized bed combustion (FBC) fly ashes	5–10	
	Mine tailings (MT)	5–10 (M3), 5 (M4)	
India	Incinerated bio-medical waste ash (IBWA)	8.227 (IBWA30-30%IBWA + 70%GGBS)	[31]

Table 4 Split tensile strength by source material using wastes on AAC

Type of waste	Binder	Alkali activator	Split tensile strength (MPa)	Ref. No.
IW	Commercial MK	Potassium-silicate	5.4–7.9	[10]
	Commercial furnace slag		2.6–5.6	
IW	OPC and low calcium fly ash	NaOH and Na_2SiO_3	4.82	[18]
IW	Fly ash and GGBS	NaOH and Na_2SiO_3	4.50–5.00	[19]
BMW	GGBS and ıncinerated bio-medical waste ash (IBWA)	NaOH and Na_2SiO_3	43.3	[31]

Table 5 M.O.E by source material using waste on AAC

Type of waste	Source material	Alkali activator	MOE (GPa)	Ref. No.
IW	High calcium wood ash (HCWA) and pulverized fuel ash (PFA)	–	12.35–12.80	[21]
IW	Lightweight expanded clay aggregates (LECs)	NaOH and Na_2SiO_3	20–25	[32]
	Fluidized bed combustion (FBC) fly ashes, Mine tailings (MT)		20–25, 25–30	
IW	Porcelain tile polishing residue (PPR) and metakaolin	NaOH and Na_2SiO_3	8	[13]

5 Research Gap

Many studies have aimed at the mechanical, physical and chemical properties of the AACs, but the durability properties are not adequately tested. Following are the enlisted researchers for future work:

- An in-depth study of GPC in the application of 3-D printing has to be studied and the LCA with various proportions of aluminosilicate material and activators should be carried out.
- Study of brittle behaviour and stiffness gradation with different wastes should be carried out for a better understanding of the AAC.
- More investigations on the structural elements of the GPC at higher temperatures should be studied.
- Reinforced GPC incorporated with wastes should be further studied for various understanding of the properties such as shear strength and bond strength, corrosion resistance.
- The experimental investigations on the serviceability, i.e. the repairing of building with respect to crack propagation should be carried out.
- More studies with non-FA-based geopolymers need to be studied for a better understanding of the role of other wastes in strength development, durability, thermal resistance, etc.
- It has been observed that when the origin of the source material varies, there is a change in the set of results obtained. Hence, it becomes very essential for setting up of general code of practice for the Alkali-activated concrete.

6 Conclusion

Recycling garbages and lowering greenhouse gas emissions are the two most important goals for construction or any type of industry for achieving long-term growth, which can be possible by using these as a material for producing geopolymer concrete. This paper deals with the waste coming from the industry, agriculture and bio-medical waste which help in the reduction of cement requirement and in turn help with eliminating the environmental difficulties. Since these wastes generated from various sectors are having varied physical and chemical characteristics, when these are taken into use for the production of geopolymer compounds, the mineralogical composition should be taken care of.

With the growing research on geopolymer in applications such as geopolymer bricks, pavement blocks, or with heavy structures such as bridge decks and airport runways, it implicates a cause for replacing the OPC in the mere future. From the studies made, it can be further said that the mechanical activation of waste-based geopolymer can be seen as a viable method to achieve the required strength of the geopolymer concrete. Moreover, since the source materials are the wastes coming from either the industry or from agriculture, these types of AACs are best suitable

concerning the economical condition as well as the sustainability of the environment. Considering all the discussions made above, the wastes can be used to produce green geopolymer concrete intended for eco-friendly building materials. In the pursuit of sustainability, the manufacturing is also performed at an environmental temperature which will lead to low-cost production and hence will in turn raise the profit margins for the construction industry too.

References

1. Habert G, D'Espinose De Lacaillerie JB, Roussel N (2011) An environmental evaluation of geopolymer based concrete production: reviewing current research trends. J Clean Prod 19(11):1229–1238. https://doi.org/10.1016/j.jclepro.2011.03.012
2. Venkateswara Rao K (2015) Study on strength properties of low calcium based geopolymer concrete. Int J Civ Eng Technol 6(11):149–155
3. Patil AA, Chore HS, Dodeb PA (2014) Effect of curing condition on strength of geopolymer concrete. Adv Concr Constr 2(1):29–37. https://doi.org/10.12989/acc.2014.2.1.029
4. Temuujin J, Williams RP, van Riessen A (2009) Effect of mechanical activation of fly ash on the properties of geopolymer cured at ambient temperature. J Mater Process Technol 209(12–13):5276–5280. https://doi.org/10.1016/j.jmatprotec.2009.03.016
5. Nematollahi B, Sanjayan J (2014) Effect of different superplasticizers and activator combinations on workability and strength of fly ash based geopolymer. Mater Des 57:667–672. https://doi.org/10.1016/j.matdes.2014.01.064
6. Brough AR, Atkinson A (2002) Sodium silicate-based, alkali-activated slag mortars—part I. Strength, hydration and microstructure. Cem Concr Res 32(6):865–879. https://doi.org/10.1016/S0008-8846(02)00717-2
7. Shi C (2004) Steel slag—its production, processing, characteristics, and cementitious properties. J Mater Civ Eng 16(3):230–236. https://doi.org/10.1061/(asce)0899-1561(2004)16:3(230)
8. Bernal SA et al (2011) Cement and concrete research effect of binder content on the performance of alkali-activated slag concretes. Cem Concr Res 41(1):1–8. https://doi.org/10.1016/j.cemconres.2010.08.017
9. Gao X, Yu QL, Brouwers HJH (2015) Reaction kinetics, gel character and strength of ambient temperature cured alkali activated slag—fly ash blends. Constr Build Mater 80:105–115. https://doi.org/10.1016/j.conbuildmat.2015.01.065
10. Panizza M, Natali M, Garbin E, Tamburini S, Secco M (2018) Assessment of geopolymers with construction and demolition waste (CDW) aggregates as a building material. Constr Build Mater 181:119–133. https://doi.org/10.1016/j.conbuildmat.2018.06.018
11. Behera M, Bhattacharyya SK, Minocha AK, Deoliya R, Maiti S (2014) Recycled aggregate from C&D waste & its use in concrete—a breakthrough towards sustainability in construction sector: a review. Constr Build Mater 68:501–516. https://doi.org/10.1016/j.conbuildmat.2014.07.003
12. Luhar I et al (2021) Assessment of the suitability of ceramic waste in geopolymer composites: an appraisal. Materials (Basel) 14(12):1–30. https://doi.org/10.3390/ma14123279
13. Ramos GA, Pelisser F, Gleize PJP, Bernardin AM, Michel MD (2018) Effect of porcelain tile polishing residue on geopolymer cement. J Clean Prod 191:297–303. https://doi.org/10.1016/j.jclepro.2018.04.236
14. Huamán-Mamani FA, Gamarra-Delgado JF, Paredes-Paz JJ, Bringas-Rodríguez VC, Mayta-Ponce DL, Rodríguez-Guillén GP (2020) Creep of geopolymeric concrete obtained from mining tailings. In: Proceedings of the 3rd world congress on mechanical, chemical, and material engineering, pp 1–8. https://doi.org/10.11159/mmme20.132

15. Capasso I et al (2019) Reuse of mining waste as aggregates in fly ash-based geopolymers. J Clean Prod 220:65–73. https://doi.org/10.1016/j.jclepro.2019.02.164
16. Rahmawati C, Aprilia S, Saidi T, Aulia TB (2021) Current development of geopolymer cement with nanosilica and cellulose nanocrystals. J Phys Conf Ser 1783(1). https://doi.org/10.1088/1742-6596/1783/1/012056
17. Silva G, Kim S, Aguilar R, Nakamatsu J (2020) Natural fibers as reinforcement additives for geopolymers—a review of potential eco-friendly applications to the construction industry. Sustain Mater Technol 23:e00132. https://doi.org/10.1016/j.susmat.2019.e00132
18. Bhardwaj B, Kumar P (2018) Effect of waste foundry sand addition on strength, permeability and microstructure of ambient cured geopolymer concrete. IOP Conf Ser Mater Sci Eng 431(9). https://doi.org/10.1088/1757-899X/431/9/092009
19. Bhardwaj B, Kumar P (2021) Performance assessment of graphene oxide-reinforced sustainable geopolymer concrete. J Mater Civ Eng 33(11):04021322. https://doi.org/10.1061/(asce)mt.1943-5533.0003942
20. Zainuddin AN, Mukri M, Lat DC, Rosli R, Rani NHA (2021) Influence of different percentage boiler ash-based geopolymer in laterite soil. IIUM Eng J 22(2):67–82. https://doi.org/10.31436/iiumej.v22i2.1589
21. Ban CC, Nordin NSA, Ken PW, Ramli M, Hoe KW (2014) The high volume reuse of hybrid biomass ash as a primary binder in cementless mortar block. Am J Appl Sci 11(8):1369–1378. https://doi.org/10.3844/ajassp.2014.1369.1378
22. Bhutta MAR, Hussin WM, Azreen M, Tahir MM (2014) Sulphate resistance of geopolymer concrete prepared from blended waste fuel ash. J Mater Civ Eng 26(11):04014080. https://doi.org/10.1061/(asce)mt.1943-5533.0001030
23. Nawab NL, Ghani U (2017) Synthesis and characterization of chloride resistant cement from industrial waste through geopolymerization. J Clean Prod 156:577–580. https://doi.org/10.1016/j.jclepro.2017.04.079
24. Kathirvel P, Gunasekaran M, Sreekumaran S, Krishna A (2020) Effect of partial replacement of ground granulated blast furnace slag with sugarcane bagasse ash as source material in the production of geopolymer concrete. Medziagotyra 26(4):477–481. https://doi.org/10.5755/j01.ms.26.4.23602
25. Castaldelli VN et al (2013) Use of slag/sugar cane bagasse ash (SCBA) blends in the production of alkali-activated materials. Materials (Basel) 6(8):3108–3127. https://doi.org/10.3390/ma6083108
26. Kumar A, Saravanan TJ, Bisht K, Kabeer KISA (2021) A review on the utilization of red mud for the production of geopolymer and alkali activated concrete. Constr Build Mater 302(June):124170. https://doi.org/10.1016/j.conbuildmat.2021.124170
27. Liang X, Ji Y (2021) Experimental study on durability of red mud-blast furnace slag geopolymer mortar. Constr Build Mater 267:120942. https://doi.org/10.1016/j.conbuildmat.2020.120942
28. Chen X et al (2019) Utilization of red mud in geopolymer-based pervious concrete with function of adsorption of heavy metal ions. J Clean Prod 207:789–800. https://doi.org/10.1016/j.jclepro.2018.09.263
29. Rajan HS, Kathirvel P (2021) Sustainable development of geopolymer binder using sodium silicate synthesized from agricultural waste. J Clean Prod 286:124959. https://doi.org/10.1016/j.jclepro.2020.124959
30. Luhar S, Cheng TW, Luhar I (2019) Incorporation of natural waste from agricultural and aquacultural farming as supplementary materials with green concrete: a review. Compos Part B Eng 175(March):107076. https://doi.org/10.1016/j.compositesb.2019.107076
31. Suresh Kumar A, Muthukannan M, Kanniga Devi R, Arunkumar K, Chithambar Ganesh A (2021) Reduction of hazardous incinerated bio-medical waste ash and its environmental strain by utilizing in green concrete. Water Sci Technol 84(10–11):2780–2792. https://doi.org/10.2166/wst.2021.239
32. Yliniemi, Paiva, Ferreira, Tiainen, Illikainen (2017) Development and incorporation of lightweight waste-based geopolymer aggregates in mortar and concrete. Constr Build Mater 131:784–792.https://doi.org/10.1016/j.conbuildmat.2016.11.017

33. Mo KH, Alengaram UJ, Jumaat MZ (2016) Structural performance of reinforced geopolymer concrete members: a review. Constr Build Mater 120:251–264. https://doi.org/10.1016/j.conbuildmat.2016.05.088
34. Nawaz M, Heitor A, Sivakumar M (2020) Geopolymers in construction—recent developments. Constr Build Mater 260:120472. https://doi.org/10.1016/j.conbuildmat.2020.120472
35. Hassan A, Arif M, Shariq M (2020) A review of properties and behaviour of reinforced geopolymer concrete structural elements—a clean technology option for sustainable development. J Clean Prod 245:118762. https://doi.org/10.1016/j.jclepro.2019.118762
36. Farooq F et al (2021) Geopolymer concrete as sustainable material: a state of the art review. Constr Build Mater 306(Aug):124762. https://doi.org/10.1016/j.conbuildmat.2021.124762

Various Geometrical Parameters of the Topography Elements of the Honeycomb Films from PHB and Its Copolymer with 3-Hydroxyvalerate

Nikita Belishev, Elizaveta Akoulina, Vera Voinova, Irina Demianova, Garina Bonartseva, Tatiana Makhina, Viktoria Nikalaichuk, Viktoryia Kulikouskaya, and Anton Bonartsev

Abstract Polymer films are commonly used in different biotechnological applications. The effect of polymer film surface on its efficiency is of interest to study. In this article, porous polymer films (PHB and PHBHV) were obtained under different conditions using the honeycomb method—when water droplets concentrate on liquid polymer solution, while polymer dries thereby modifying the surface of polymer film into a regular structure. Pores on the surface of polymer films were characterized by mathematical processing—areas of pores, circularity, and aspect ratio were assessed. The data processing showed that by variation of the type of polymers and their concentration it is possible to influence the structure of the polymer film surface. This provides an opportunity to further study the effect of surface roughness in various applications.

Keywords Biopolymers · Honeycomb method

N. Belishev (✉) · E. Akoulina · V. Voinova · A. Bonartsev
Faculty of Biology, Moscow State University, Moscow, Russia
e-mail: nbelishev@gmail.com

I. Demianova
Moscow State University—Beijing Institute of Technology, Beijing, China
e-mail: irinydem@yandex.com

G. Bonartseva · T. Makhina
Federal Research Centre "Fundamentals of Biotechnology" of the Russian Academy of Sciences, Moscow, Russian Federation
e-mail: bonar@inbi.ras.ru

V. Nikalaichuk · V. Kulikouskaya
Institute of Chemistry of New Materials, National Academy of Sciences of Belarus, Minsk, Republic of Belarus

K. Geetha et al. (eds.), *Recent Trends in Materials*, Springer Proceedings in Materials 18, https://doi.org/10.1007/978-981-19-5395-8_8

1 Introduction

Biopolymer materials of microbiological origin are useful in tissue engineering. These polymers, such as poly-3-hydroxybutyrate (PHB), have the necessary properties such as biodegradability and biocompatibility. In tissue engineering, the structure of the substrate with which cells interact is important [1]. It acts as a matrix for cellular interactions and also provides structural support to newly formed tissue. The inclusion of polymer substrates with different surface microstructures in places of damage or defects creates new centers of tissue formation due to the properties of supporting the proliferation and differentiation of mesenchymal stem cells [2]. It is important that the substrate has a certain set of functions: mechanical strength, biocompatibility, and biodegradability [3]. Thus, poly-3-hydroxybutyrate (PHB) substrates can perform all these functions, as PHB products provide biocompatibility, biodegradability, and smaller amounts of cytotoxicity. Due to their high biocompatibility, PHB and its copolymers such as copolymer with 3-hydroxyvalerate (PHBHV) can be used in the production of films, for example, for experimental modeling of cell growth in vitro [4] and for controlled prolonged drug delivery [5], as well as wound dressings [6]. One of the strategies for improving the properties of biopolymers for their use in tissue engineering is to obtain products with different surface roughness. Different microstructures of the polymer surface can influence cell growth [7] and can infuse differentiation [8, 9], which can reinforce the impact of PHB itself [10] There are several methods to create polymer films with different surface structures, such as spin coating using an organized matrix, and different leaching methods, as well as many others [11]. But, not all of them can provide a controlled organized surface. Even using spin coating on a substrate with the pre-organized surface can give rise to some difficulties such as solvents' compatibility for polymers and substrate material, and difficulty in obtaining samples of different microstructure sizes.

In this study, we used the directed self-organization of microdroplets of an evaporating liquid to fabricate large-scale-ordered films with controlled microstructures. The manufacturing process of biopolymer films is variable and scalable, and when working with biopolymers of various densities and viscosities, it allows the production of functional films with controlled porosity [12]. This suggests an effective strategy for creating microstructures by combining directed self-assembly with manipulation of biopolymer properties specified for both design accuracy and diversity structures on a macroscopic scale [13]. Evaporation is a simple but effective pathway for the self-assembly of a surface of a biopolymer substrate, which, under changing conditions, allows the polymer solution to assemble into ordered structures on a macroscopic scale. Due to evaporation, the liquid polymer solution solidifies, and the evaporating microdroplets give different shapes to the pores in the matrix microstructure. Changes in the energy landscape caused by evaporation determine the rearrangement of microdroplet networks [14]. To obtain desirable various porous structures, it is important to carefully choose conditions, which can be difficult,

but after conditions are picked the result is stable [15]. The simplicity of the self-organization method makes it possible to use the method for the synthesis of artificial imitators of natural materials with periodic patterns.

2 Materials and Methods

2.1 Biosynthesis of Polymers

For the biosynthesis of the polymer, the *Azotobacter chroococcum* 7B strain was used. For the synthesis of PHB and PHBHV polymers (Table 1), the cell culture was grown in shake flasks (the volume of the medium in the flask was 100 mL) at 30 °C in Burke's medium (g/L): $MgSO_4$ $7H_2O$, 0.4; $FeSO_4$ $7H_2O$, 0.01; 0.006, Na citrate—0.5, $CaCl_2$—0.1, K_2HPO_4 $3H_2O$—1.05, KH_2PO_4—0.2, sucrose—30. Peptone was added at a concentration of 0.1%. As precursors of HV units in the PHB chain, valeric acid was added to the nutrient medium at a concentration of 20 mM in the form of sodium salt after 10 h of culture incubation. The polymer was isolated by the standard method after 48 h of incubation [16].

2.2 Obtaining Films via the Honeycomb Method

The self-organization method was used to obtain films from PHB and PHBHV. A promising approach to the creation of ordered microgrids with hexagonal cell symmetry is their production by "self-organization" of water microdroplets on a liquid polymer film [12, 13].

The basis of the method is the process of water vapor condensation on the surface of a polymer solution followed by solidification of the polymer, which makes it possible to form polymer structures with a controlled pore size and degree of their ordering. Silicon plates were used as a substrate, which was rapidly cooled due to the evaporation of chloroform, creating the temperature difference necessary for the deposition of water droplets on the polymer surface. The device is an isolated chamber into which moistened heated air is supplied with a small stream. The air is humidified by passing it through a saturated NaCl solution, creating a humidity of 70%. The air is heated immediately before it enters the chamber. Inside the chamber,

Table 1 Polymers properties

Polymer type	Content of copolymer, %	Molecular mass, kDa
PHB	–	365
PHBHV	9	740

Table 2 List of obtained polymer films obtained under different conditions

Number	Polymer type	Amount of polymer on the silicon substrate
1.1	PHB	150
1.2	PHB	300
2.1	PHBHV	150
2.2	PHBHV	300

conditions are varied by varying the distance between the sample and the air source, thus creating a variation of depressions of different widths and heights.

PHB (365 kDa) and PHBHV ((740 kDa) with valerate content 9%) at concentration 40 μg/mL in chloroform were chosen to obtain films. The films were obtained at a distance of 3 cm from the socket of the moist airflow source. The amount of polymer poured onto the silicon substrate was varied (150, 300 μl) (Table 2).

2.3 Imaging

The imaging was performed in order to investigate whether the change of polymer type and their respective concentrations will affect the films' pore surface shape, size, and depth. Images of the film's surface were obtained using scanning electron microscopy (JCM-6000PLUS, Jeol, Japan).

2.4 Mathematical Processing

To effectively assess the wells' size, shape, and depth, a number of parameters were chosen, such as area, circularity, solidity, and aspect ratio, where:

$$\text{Area} = \text{total area within the particle measured in } \mu\text{m}^2.$$

$$\text{Circularity} = 4\pi(\text{area}/[[\text{perimeter}]]^2) \tag{1}$$

The circularity (1) value ranges from 0 to 1, where a value of 1 signifies that the particle has a perfect circular shape and a value of 0 demonstrates that the particle approaches the shape of an elongated polygon. The bigger the pore area is, the more circular it is. However, an increase in the pore perimeter drastically reduces its circularity.

Aspect Ratio = is the object's width to length ratio and can be mathematically expressed as

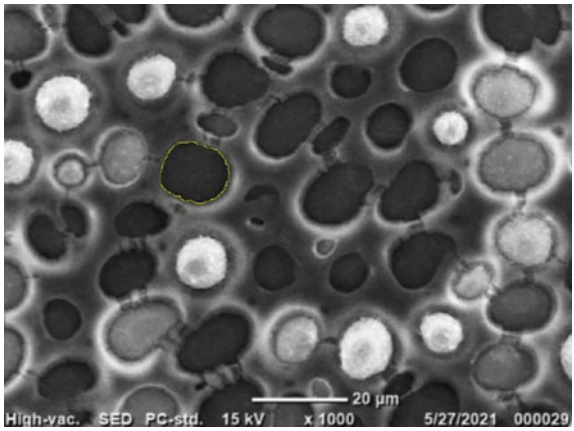

Fig. 1 Image demonstrating the application of the "Magic Wand" tool in Image J. The particle outlined in yellow gets recognized by the tool, which allows a deep sample analysis based on its size, shape, and depth

$$\text{Aspect Ratio} = (\text{Well Width})/(\text{Well Length}) \tag{2}$$

For instance, the aspect ratio of a circle will be equal to 1 [17].

The particles were identified using a "Magic Wand" tool in Image J software, which distinguished the outlines of each well in contrast to the background as can be seen in Fig. 1.

3 Results and Discussion

3.1 Obtained Films

A total of 4 different porous polymer films of 2 different concentrations (40 mg/mL, 150 uL and 40 mg/mL, 300 uL) and 2 different polymers (PHB 350 kDa and PHBHV 9% (740 kDa), respectively) were analyzed (Table 1). Depending on the composition of the polymer, its concentration, as well as the distance from the source of moist air and the volume applied to the substrate, films contained different microstructure patterns on the surface (Fig. 2). To evaluate the differences in the structures on the surface of the films, their SEM micrographs were subjected to mathematical processing.

3.2 Mathematical Processing

The purpose of mathematical processing was to evaluate differences between the polymers' pores by assessing a number of parameters that would provide the best numerical pore characterization. This way mathematically verified differences in

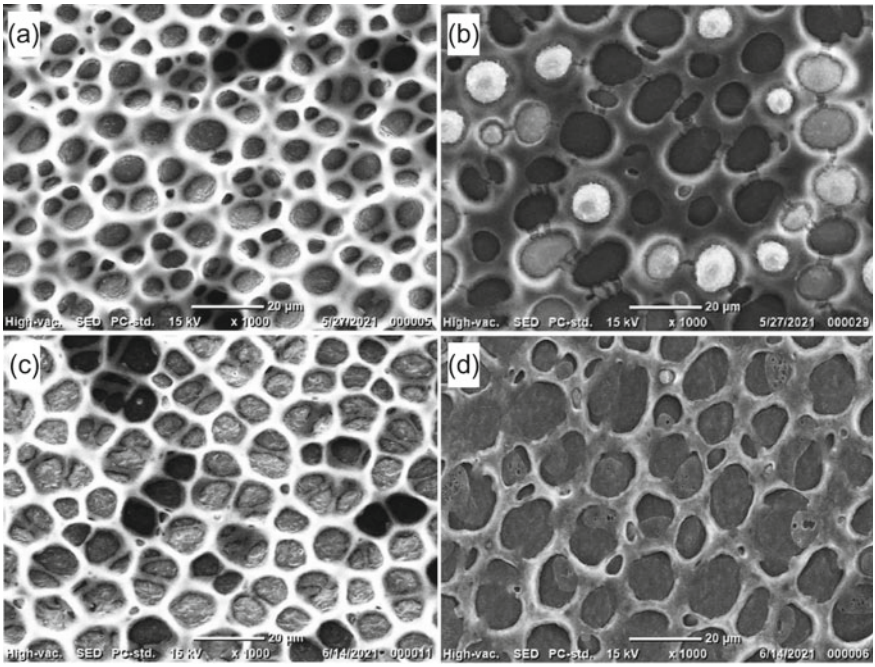

Fig. 2 SEM images of different polymer pores. **a** PHB/3/40/150, **b** PHB/3/40/300, **c** PHBHV 3/40/150, **d** PHBHV 3/40/300

polymer surface roughness can be achieved, which will be useful for further surface roughness research in biotechnological applications. The differences in pores areas, circularities, and aspect ratios were assessed. Implementing this kind of processing approach is a known method for complementing 2D SEM images [18, 19]. Prior to the image processing, differences between the different polymer types were visually apparent. Imaging revealed significant differences in pore sizes across the polymer types.

Upon analyzing differences in polymers' pore sizes, the wells with the largest areas were observed in polymer PHBHV 9% 3 cm 40 mg/mL, 300 µL (Fig. 3). The wells with the smallest areas were produced by the polymer PHB 350 kDa 3 cm 40 mg/mL, 150 µL with respect to all the other polymers in the study.

Polymer pores' aspect ratio and circularity analyses have demonstrated that all the wells tended to form shapes close to a perfect circle rather than an elongated structure. As previously mentioned in the methods section, particles with circularity values closer to 1 have a shape closer to a perfect circle, which in the case of this study was observed in all polymers with a minimum circularity value of 0.7.

Structures having an aspect ratio of 1 have a zero degree of structure elongation and therefore are circular in nature. With a maximum aspect ratio value of 1.45 ± 0.2 (which was only observed in a single polymer PHB 3/40/300) and the rest of the

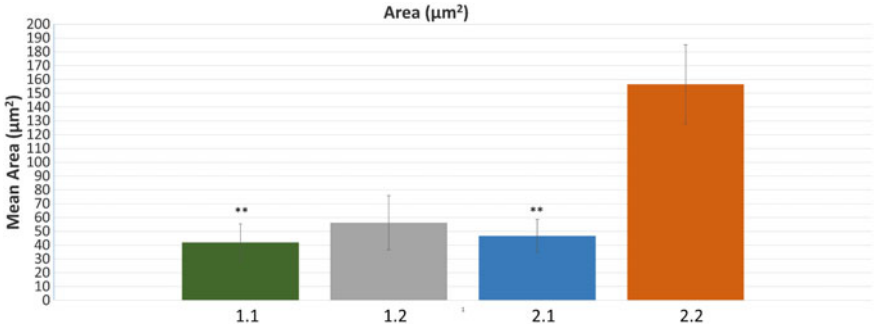

Fig. 3 Histogram representing polymer pores' mean area values (μm^2), where each polymer film is numbered respectively: 1.1—PHB 350 kDa 3 cm, 40 mg/mL, 150 µL, 1.2—PHB 350 kDa 3 cm, 40 mg/mL, 2.1—PHBHV 9% 3 cm, 40 mg/mL, 150 µL, 2.2—PHBHV 9% 3 cm, 40 mg/mL, 300 µL. Asterisks (*) show groups of different polymer types, which did not have statistical differences between each other ($p > 0.05$)

polymer films having an aspect ratio of approx. 1.2, it is to hypothesize that almost all of the polymers in the study had a small degree of structure elongation.

Figure 4 demonstrates a distinctive trend, where an increase in concentration of PHBHV leads to a larger pore area, when compared to PHB polymer pores (2.1 and 2.2). It can also be observed that with the PHBHV concentration change the mean pore area range increases drastically, as opposed to PHB concentration change. This suggests that elevation of PHB concentration forms pores with a more consistent size when compared to PHBHV concentration increase. Finally, it can be spotted that with an elevation of the PHB pore concentration, there is a slightly bigger change in circularity in contrast to PHBHV concentration change.

4 Conclusion

All the aforementioned analysis suggests that there is a way to control the size and regularity of the pores on the polymer film surface by changing the polymer type and concentration. It seems that altering the concentration of PHBHV polymer has a significant impact on the pore size, which can have various applications in the biomedical field, such as tissue engineering to regulate MSCs proliferation and differentiation by polymer surface topography.

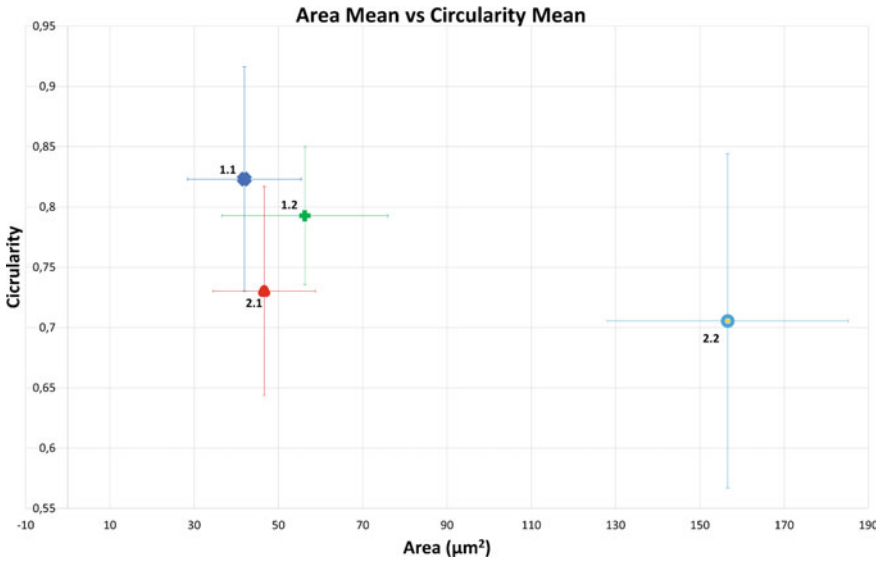

Fig. 4 Scatter diagram representing polymers pores' mean area (*x*-axis, μm^2) versus mean circularity (*y*-axis) values, where each polymer is numbered respectively: 1.1—PHB 350 kDa 3 cm, 40 mg/mL, 150 μL, 1.2—PHB 350 kDa 3 cm, 40 mg/mL, 2.1—PHBHV 9% 3 cm, 40 mg/mL, 150 μL, 2.2—PHBHV 9% 3 cm, 40 mg/mL, 300 μL

Acknowledgements This work was supported by the Russian Foundation for Basic Research, project No 20-54-00021 (biosynthesis of polymers and mathematical analysis of porous films morphology), and by Belarusian Republican Foundation for Fundamental Research, project No X20P-165 (polymer films manufacturing and study of film morphology).

Author Contributions Conceptualization, Bonartsev A., Kulikouskaya V.; methodology, Bonartsev A., Kulikouskaya V., Bonartseva G., Akoulina E.; validation, Bonartsev A.; investigation, Nikalaichuk V., Belishev N., Akoulina E., Demianova I.; resources, Makhina T, Bonartseva G.; data curation, Bonartsev A.; writing—original draft preparation, Belishev N., Akoulina E., Demianova I.; writing—review and editing, Bonartsev A., Bonartseva G.; supervision, Bonartsev A., Kulikouskaya V.; project administration, Bonartsev A., Kulikouskaya V. All authors have read and agreed to the published version of the manuscript.

References

1. Bonartsev AP, Bonartseva GA, Reshetov IV, Kirpichnikov MP, Shaitan KV (2019) Application of polyhydroxyalkanoates in medicine and the biological activity of natural poly(3-Hydroxybutyrate). Acta Naturae 11/2(41):4–16
2. Bonartsev AP et al (2018) Poly(3-Hydroxybutyrate)/Poly(Ethylene Glycol) scaffolds with different microstructure: the effect on growth of mesenchymal stem cells. 3 Biotech 8(8):328

3. Takahashi Y, Tabata Y (2004) Effect of the fiber diameter and porosity of non-woven PET fabrics on the osteogenic differentiation of mesenchymal stem cells. J Biomater Sci Polym Ed 15(1)
4. Muraev AA et al (2016) Development and preclinical studies of orthotopic bone ımplants based on a hybrid construction from poly(3-hydroxybutyrate) and sodium alginate. Sovrem Tehnol v Med 8(4):42–50
5. Kulikouskaya V, Chyshankou I, Pinchuk S, Vasilevich I, Volotovski I, Agabekov V (2020) Fabrication and characterization of ultrathin spin-coated poly(l-lactic acid) films suitable for cell attachment and curcumin loading. Biomed Mater 15
6. Savencu I, Iurian S, Porfire A, Bogdan C, Tomuță I (2021) Review of advances in polymeric wound dressing films. React Func Polym 168
7. Surmenev RA, Chernozem RV, Syromotina DS, Oehr C, Baumbach T, Krause B, Boyandin AN, Dvoinina LM, Volova TG, Surmeneva MA (2019) Low-temperature argon and ammonia plasma treatment of poly-3-hydroxybutyrate films: surface topography and chemistry changes affect fibroblast cells in vitro. Eur Polymer J 112:137–138
8. Faia-Torres AB, Charnley M, Goren T, Guimond-Lischer S, Rottmar M, Maniura-Weber K, Spencer ND, Reis RL, Textor M, Neves NM (2015) Osteogenic differentiation of human mesenchymal stem cells in the absence of osteogenic supplements: a surface-roughness gradient study. Acta Biomater 28:64–75
9. Lewallen EA, Trousdale WH, Thaler R, Yao JJ, Xu W, Denbeigh JM, Nair A, Kocher JP, Dudakovic A, Berry DJ, Cohen RC, Abdel MP, Lewallen DG, van Wijnen AJ (2021) Surface roughness of titanium orthopedic ımplants alters the biological phenotype of human mesenchymal stromal cells. Tissue Eng Part A 27:1503–1516
10. Gredes T, Gedrange T, Hinüber C, Gelinsky M, Kunert-Keil C (2015) Histological and molecular-biological analyses of poly(3-Hydroxybutyrate) (PHB) patches for enhancement of bone regeneration. Ann Anatomy—Anatomischer Anzeiger 199:36–42
11. Peng X, Dong K, Wu Z et al (2021) A review on emerging biodegradable polymers for environmentally benign transient electronic skins. J Mater Sci 56:16765–16768
12. Kulikouskaya VI, Chyshankou IG (2021) Fabrication of microstructured polylactide films by templating techniques. Theor Exp Chem 57(4)
13. Calejo MT, Ilmarinen T, Jongprasitkul H, Skottman H, Kellomäki M (2016) Honeycomb porous films as permeable scaffold materials for human embryonic stem cell-derived retinal pigment epithelium. J Biomed Mater Res Part A 104(7):1646–1656
14. Zhu P, Kong T, Zhou C, Lei L, Wang L (2018) Engineering microstructure with evaporation-ınduced self-assembly of microdroplets. Small Methods 2(6)
15. Shadrina VI, Bashmakov IA, Gracheva EA, Agabekov VE, Kaputskii FN (2010) Influence of the conditions of formation of nitrocellulose honeycomb-structure films on their morphology. Russian J Appl Chem 83
16. Bonartsev AP et al (2016) Biosynthesis of poly(3-Hydroxybutyrateco-3-Hydroxy-4-Methylvalerate) by strain Azotobacter chroococcum 7B. Acta Naturae 8(3)
17. Szmańda JB, Witkowski K (2021) Morphometric parameters of Krumbein grain shape charts—a critical approach in light of the automatic grain shape image analysis. Minerals 11(9):3–4
18. Sinkhonde D, Rimbarngaye A, Kone B, Herring TC (2022) Representativity of morphological measurements and 2-d shape descriptors on mineral admixtures. In: Results in engineering, vol 13
19. Matsumoto N, Ogawa M, Takayasu K et al (2015) Quantitative sonographic image analysis for hepatic nodules: a pilot study. J Med Ultrason 42:505–512

Effect on Structural Characteristics After Adding Gypsum Wall Waste and Polymer

Mukunda D. Bhor and Manendra P. Verma

Abstract Recycling or reusing waste materials in the building of civil constructions is a critical topic in the twenty-first century. Utilisation of waste materials in the building sector decreases per cubic metre of concrete volume used. OPC manufacturing consumes a lot of energy and emits a lot of pollution, which may be reduced by partly replacing waste materials for cement. Adding mineral admixtures to concrete and mortar improves the compressive strength and characteristics of both materials. The emphasis of researcher is to review the research works investigating the suitability of waste materials such as gypsum wall waste and polymer as construction materials with fibre reinforced plastic laminated steel bars.

Keywords Compressive strength · Mineral admixtures · Suitability

1 Introduction

In recent years, there has been an upsurge in the use of recycled concrete in the demolition and renovation of buildings. As a result of today's environmental concerns as well as the aim to keep building costs as low as possible whilst yet keeping excellent quality, recycling of leftover concrete has become a more appealing choice. Certain materials, referred to as Pozzolana, which have no cementation capabilities on their own, react with Ordinary Portland cement to generate cementation materials. The use of fractional replacement of Portland cement in concrete helps to reduce the amount of Portland cement needed in the final product. Building expenses, energy usage, and waste emissions like carbon-dioxide are all reduced as a result of this decrease in cement use (CO_2). As a bonus, this reduces the amount of energy used, which decreases global warming.

As an interior finish, gypsum composites have been overused. In the United States and Europe, gypsum-based materials are often utilised in the construction or interior

M. D. Bhor (✉) · M. P. Verma
Department of Civil Engineering, Madhyanchal Professional University, Bhopal, India
e-mail: mukundadbhor@gmail.com

K. Geetha et al. (eds.), *Recent Trends in Materials*, Springer Proceedings in Materials 18, https://doi.org/10.1007/978-981-19-5395-8_9

lining of residential buildings. Designers use them because of their great characteristics, which include affordable raw materials, volumetric stability, acoustic and thermal insulation, fire resistance, low toxicity, and the comparably low energy and temperature requirements for manufacturing [1]. There are many more uses for the mineral gypsum, such as the production of moulds for ceramic items [2], medicinal [3], and dentistry [4]. As a result, Portland cement sets more slowly due to the presence of this substance as the principal ingredient [6, 7]. Gypsum plaster has a wide range of uses because of its unique qualities [6, 7]. It has been proposed [8–15] that adding further additives to the gypsum material might improve its properties and broaden its application range.

For the most part, carbon fibres are used to strengthen composite materials [16], but they are also utilised in high-tech applications including aeronautics and nuclear engineering [17]. In terms of modulus and strength, carbon fibre reinforcement is the strongest of all fibre reinforcing materials. When subjected to normal temperatures, carbon fibres do not suffer from stress corrosion or stress rupture failure, in contrast to glass and organic polymer fibres. Strength and modulus are superior to those of other materials at higher temperatures [16]. For applications needing high stiffness, low weight, and excellent fatigue qualities, carbon fibre composites are an excellent choice. Additionally, they discovered that adequate damping, chemical inertness, and high temperature implementations are required. Additionally, strong electrical and thermal conductivity, a low linear coefficient of thermal expansion, and a low temperature coefficient all contribute to the material's benefits. The carbon structure used determines the properties of carbon fibre. Lightest and stiffest material is carbon fibre [19]. Concrete, cement mortar, and asphalt's response to various fibres has been studied in depth [20–25], and the results are noteworthy.

A. *Concrete composed of waste materials*

To begin, cement manufacturing is an energy-intensive operation that has a considerable influence on the environment. Cement manufacturing is also a source of pollution. In order to produce one tonne of conventional Portland cement, approximately one tonne of carbon-dioxide gas must be produced. As a result, approximately 1.6 billion tonnes of carbon-dioxide are released into the atmosphere each year, accounting for approximately 7% of global carbon-dioxide production. Environmental limits and regulations will continue to rise in the future, necessitating an increase in the usage of extra cementitious materials.

There are many significant reasons for the rising usage of additional ingredients in cement concrete:

1. To reduce the consumption of cement though replacing the cement with materials having cementations properties.
2. To enhance the qualities of newly placed and hardened concrete. Recently, several researchers produced high performance concrete by reducing water/cement ratio through the application of super-plasticizers and ultrafine mineral admixtures.

Concrete composed by partially replacing cement with industry wastes are termed are green cement. This developed green cement is put side by side with ordinary Portland cement by many investigators. This "green" material makes less use of natural resource, energy and releases less CO_2. Various concrete mixes are composed of using theses admixtures such as—lightweight concrete (LWC) and high performance concrete.

Light weight concrete: *Fly ash (FA) and furnace bottom ash (FBA) are two coal-fired thermal power plant waste products. They are, in comparison to typical coarse aggregate, OPC, and natural sand, lighter. The concrete mixtures created with these elements are lightweight.* The use of light weight concrete in place of concrete may greatly decrease the dead load on structural components, making it especially desirable in multi-story structures and allowing for more design freedom due to cost savings and reduced dead load.

High performance concrete: The American Concrete Institute describes HPC as a specifically engineered concrete with many unique properties increased by the selection of component ingredients and mix proportions. The use of chemical and mineral admixtures, as well as specialised production techniques, has resulted in improved mechanical and durability qualities in these materials, which are referred to as "twenty-first century concrete."

It is created from recovered materials such as fly ash, blast furnace slag, and silica fumes, amongst other things. HPC increases the strength and durability of pavements and structures, resulting in pavements and structures that persist for a longer period of time. Additionally, the capacity to create may be enhanced by correct mixture proportioning and testing.

Concrete aggregate collected from demolition sites is processed with the help of a crusher equipment …. Crushing facilities will only take clean concrete that is free of debris, wood, paper, and other pollutants, such as sand and gravel. Magnetic separators and other sorting equipment may be used to separate metals such as rebar, which can then be melted down and reused elsewhere. The remainder of the aggregate pieces are sorted according to their size. Larger pieces may be re-crushed. Following crushing, further particles are removed using a number of processes, including hand-picking and water flotation. When opposed to transporting material to and from a quarry, crushing on-site using portable crushers minimises construction costs and pollutants. Large road-portable units are capable of crushing up to 600 tonnes of concrete and asphalt debris per hour. For the most part, these systems include a rubble crusher, a side discharge conveyor, a screening plant, and a return conveyor that links the screening plant to the crusher intake for the processing of heavy materials, amongst other components. Aside from the regular mini-crushers with a capacity of 150 tonnes per hour, smaller, self-contained variants are also available. The trend towards on-site recycling of smaller quantities of garbage is quickening with the introduction of crusher attachments—those that can be attached to various kinds of construction equipment, such as excavators. At least 100 tonnes per hour is required for these attachments.

2 Literature Review

Several studies have been conducted to determine the advantages of pozzolanic materials in enhancing the characteristics of concrete. The transformation from a conservative consumption-based culture to a sustainable society is critical immediately globally because to environmental degradation, depletion of natural resources, and dwindling capacity of final product disposal facilities. According to the current situation, the construction industry accounts for 19% of overall industrial waste disposal, signalling the need of recycling to maintain the surrounding ecology. Reusing building debris, in particular, is a critical issue that must be promoted. Pozzolanic materials have been studied extensively to discover the benefits of employing them in concrete production and quality improvement.

Thomas and Shehata [1] Researchers investigated whether ternary cementitious mixes of Portland cement, fly ash, and silica fume give considerable benefits over binary cementitious mixtures and much bigger advantages over pure Portland cement.

Sandor [2] When Portland cement-fly ash-silica fume systems were evaluated in concrete, the addition of silica fume to the fly ash cement mortar increased the strength, workability, and ultrasonic velocity test results when compared to the control. With the improvement of concrete technology, it may be possible to minimise or eliminate the usage of traditional assets and energy sources, hence lowering or eliminating the environmental pollution burden. At the present, a significant amount of marble powder is being produced in conventional stone processing factories, posing a serious threat to the environment and human health [3].

Lam et al. [4] They stated in their study titled Effects of fly ash and silica fume on compressive and fracture behaviour of concrete that various amounts of fly ash and silica fume improved the strength qualities of concrete by a factor of two. The qualities of concrete progressively improve with the addition of the waste marble powder that has been acquired up to a particular point limit. The addition of Marble powder to concrete causes a significant boost in the strength of the concrete very quickly. It has been discovered that the optimal proportion for the replacement of marble powder with cement and the best binder for both casted cubes and cylinders is roughly 10% [6].

According to Khatri et al. [8], the lowest required mixing time was determined by the growth of the power provided to the tool during mixing. It was determined that high values of *w/c* resulted in rapid stabilising periods. Additionally, the amount of silica fume and quartz flour, as well as the kind of cement and superplasticizer used, had a significant effect on the stabilisation time.

For many years, concrete made from recycled aggregates has been utilised in numerous nations that pioneered this idea [9]. Numerous large-scale projects have been accomplished successfully in various nations. Its usage is so widespread around the globe that numerous nations have accepted it and are now drafting regulation guidelines governing its use. The use of fine recycled particles to concrete increases its characteristics. Reinforced or pre-stressed concrete's long-term endurance depends

on carbonation and chloride penetration. Various percentages of fine recycled aggregates made from crushed concrete were used in experiments. When the same mix proportions were tested without recycled aggregates, the results were compared to concrete.

Reuse of waste materials from construction industry is a creative step towards sustainable and green construction [10]. Usage of waste materials in construction has been considered as good thought; however, this thought has been not accepted widely between the researchers. It is possible to achieve required strength and a broad variety of construction applications using recycled aggregate concrete when the concrete mix is designed correctly. A thorough understanding of durability and the factors that affect durability is essential when using recycled aggregate in construction.

Pacheco-Torgal and Jalali [11] discussed the robustness and design technique for recycled aggregates. Compression, ultrasonic pulse velocities, shrinkage and water absorption are all examined in this study. The findings indicate that recycled aggregates concrete has a greater ultrasonic pulse velocity and a low inherent permeability to water absorption. It is possible to achieve the requisite crushing strength by substituting recycled aggregates for 80% of the total coarse aggregate and following the Department of the Environment's mix design technique.

Radlinski et al. [12] in an experiment titled "impact of mixture composition and early curing circumstances on the scaling resistance of ternary concrete," researchers looked at how changing amounts of materials in a ternary binder mix affected the scaling resistance of concrete at low temperatures. Adding hydrated lime and silica fume to fly ash concrete results in increased initial compressive strength, as well as increased long-term strength development and durability, according to the findings.

Aliabdo et al. [14] has published a study on the accumulation of waste marble dust in cement. It has been shown that the addition of marble dust to cement mortar and concrete improves the performance of these materials in this job. Concrete composed adding of marble dust as replacement of sand reveals improved act compared to replacement of cement. The chief idea of this investigation has been found to be examine the opportunity of utilising waste marble dust in cement and concrete making.

The usefulness of waste marble dust as preservative material combine together with cement is examined by Aruntaş et al. [15]. For this plan, waste marble dirt added cements were attained by inter blending with marble dust with Portland cement ashes at dissimilar combine ratios at different percentages by weight. Standard cube size of mortar prisms has been artificial with the obtained cements. On these mortar prisms, strength tests have been accepted sample on different days of curing.

Sancak et al. [16] explored the unique features of mixed cements created using construction stone powder in 2015. The performance of cements has been established via the use of compressive and tensile tests. Exclusively cements created by replacing waste have similar strength data to regular Portland cement when compared to the ages of various curing days in mixed binders when compared to ordinary Portland cement.

A study conducted by Shayan and Xu [17] looked at the presentation of glass powder in concrete in real-world circumstances, a field examination has been

performed by means of a 40 MPa concrete combination, including and considering a range of proportions of glass powder in and as cement replacement. Several blends were formed and most of the mixtures also involves sand-size meshed glass collective substance, were used to cast several concrete slabs. Concrete casted has been tested for the compressive and separating tensile strength, shrink and rise, ultrasonic pulse velocity, and permeability of chloride. Basic models had been cut from the slabs of various life spans for the same as well as for micros assessment. Mixtures with glass powder blend showed acceptably when compared in drying shrinkage and alkali reactivity. The findings demonstrated that GLP may be integrated into high strength concrete at significant quantities, such as 20–30% by weight, to replace for cement in high strength concrete applications. The use of glass powder results in a significant increase in the well-utilisation of waste glass in prepared mixes as well as significant reductions in the generation of toxic gases that pollute the environment.

Kirgiz [18] evaluated the effect of chemical additives on a small number of excellent strength improvements in mixed cement mortars in order to widen the scope of a more comprehensive examination for the improvement of hydration and strength of freshly mixed cements in the future. The blended mixes and conventional cement had also been combined to make pastes and mortars, which had been cured in water prior to being subjected to further testing. Experimentations including test of chemical compositions of mixtures and strengths after different curing periods have been performed according to standard codes.

On the basis of their research, Ma and Wang [19] have researched the effects of ground waste concrete powder resulting from close mixing on the water requirements for normal characteristics in concrete. According to the findings, the addition of 20% waste powder to the weight of mix cement has only a little impact on the typical evaluated qualities.

3 Experimental Works

3.1 Constituent Materials

Gypsum Plaster

The current project heavily relied on locally sourced gypsum plaster. $CaSO_{4.1}/2H_2O$, a calcium sulphate hemihydrate gypsum, was the principal raw material, and it was imported from Iraq.

Chopped Carbon Fibre

As seen in Fig. 1, the carbon fibres were cut from a manufacturing source to a length of 8 mm, and the properties of a typical carbon fibre are provided in Table 1 [26].

Mixing Water

All gypsum mixtures in this study were mixed with water that is safe to drink.

Fig. 1 Chopped carbon fibres

Table 1 Chopped carbon fibres properties

Properties	Results
Fibre type	Carbon
Elongation	1.5%
Unit weight	1.79 g/cm^3
Fabric diameter	166 μm
Tensile strength	(3450–3900) MPa
Tensile modulus of elasticity	230 GPa

Gypsum Mixes

To carry out this research, six gypsum mixes were created and divided into two groups according to the weight to grain (W/G) ratios (0.5 and 0.6), with each group being further divided into three subgroups based on the volume fraction of CCF (0.0, 0.2, and 0.4%), as depicted in Figs. 2 and 3.

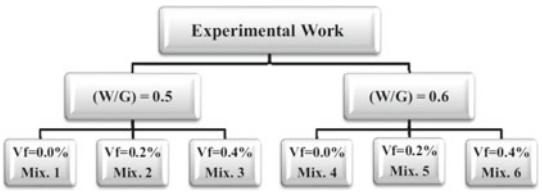

Fig. 2 Plan of experimental work

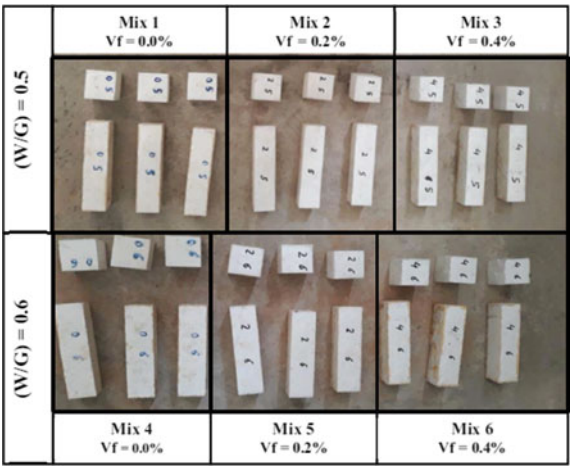

Fig. 3 Groups of tested specimens

Mixing Procedure

A weighted quantity of gypsum plaster was mixed with CCF first, and the mixture was dry-mixed carefully to ensure that the CCF was evenly distributed and dispersed throughout the dry mix. After the water was added to the mixture, it was manually stirred for approximately 15 min, in order to achieve the best results (30 s). For roughly a minute, the mould is vibrated with the slurry. When the moulds were taken out of the cubes and prisms after an hour or so, the samples were ready to be inspected. Finally, all samples were dried for about one week in direct sunlight at a temperature of around 30 °C.

Testing Program

At Mustansiriyah University, a lab known as "The structural materials laboratory," where numerous researchers have conducted tests for their investigations, we will use instruments and testing machines for this project's testing programme to demonstrate the impact of adding CCF on gypsum mix's compressive and flexural strengths.

Compression Strength

Compressive strengths of 50 mm cubic specimens at an age of around a week were measured in this study. Figure 4a depicts the testing apparatus utilised in this investigation, which was set up in line with ASTM: C472-99 [32].

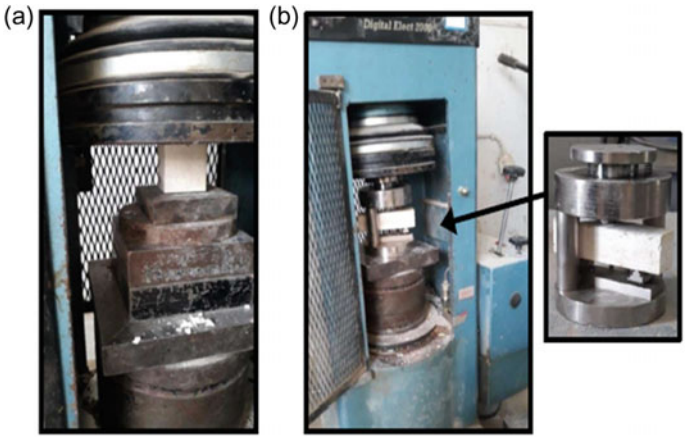

Fig. 4 **a** Strength test of compressive. **b** Rupture test of modulus

4 Discussion Based on Outcomes

4.1 The Effect of Chopped Carbon Fibre (CCF) Ratios on the Compressive Strength of Gypsum with Variable (WIG) Ratios

At two different (*W*/*G*) ratios, two different concentrations of CCF were added to gypsum plaster to test the compressive strength. This is shown in table of Fig. 5 (0.5 and 0.6). Compared to the mixes Mixl and Mix4, compressive strength improves as CCF content rises. This is true for both (*W*/*G*) ratios, and the effect is the same.

If you add CCF to your concrete mix in amounts of 0.2 or 0.4% (depending on how much W/G ratio changes), the percentage gain in compressive strength is more pronounced as the W/G ratio rises (from 0.5 to 0.6). This is shown in Fig. 5. (Mixl and Mix4). It gets stronger when CCF is added at (0.2 and 0.4%) (0.5 and 0.6). To understand why the compression strength of the cubic specimens failed, we looked

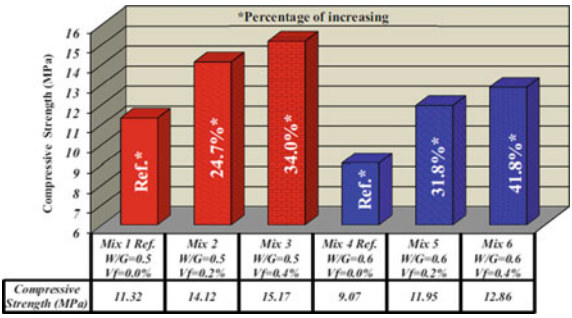

Fig. 5 CCF volume fraction effect (*Vf*) on compressive strength with various (*W*/*G*) ratios

at two different WIG ratios. The impact of CCF on compressive strength was very similar for both, and this might be the reason (0.5 and 0.6). Compressive strength is going to get stronger as the *W*/*G* ratio goes up. That's because the mix with (*W*/*G* = 0.6: Mix4) has less compressive strength than the mix with (*W*/*G* = 0.5: Mixl).

4.2 *Effect of Chopped Carbon Fibre (CCF) on Gypsum Modulus of Rupture with Variable (WIG) Ratios*

As shown in Fig. 7, the modulus of rupture of gypsum plaster was tested with two different concentrations of CCF (0.2 and 0.4%). The results are shown in the tables (0.5 and 0.6). For both (*W*/*G*) ratios, they found that increasing the concentration of CCF improves the rupture modulus, compared to the mixes that were used in the study (Mixl and Mix4). CCFs have a lot of tensile strength, which might be why they don't start new cracks in the tension zone and slow down the spread of existing fractures that are already there because of the way the load moves.

Additional evidence suggests that CCF may help alleviate the deleterious impact of voids in the gypsum mass on its capacity to withstand tension stresses in the tension zone, as indicated visually by the fact that CCF-containing samples did not separate, but reference specimens did separate (Fig. 6).

In addition, the modulus of rupture rises at two concentrations (0.2 and 0.4%) when CCF is added, as demonstrated in table of Fig. 7.

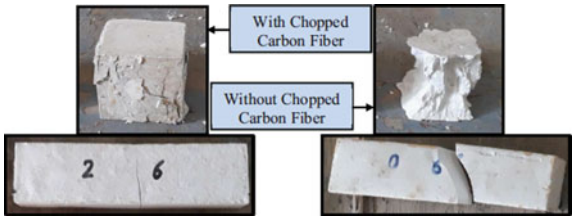

Fig. 6 Different failed specimens with CCF and without CCF of various shapes

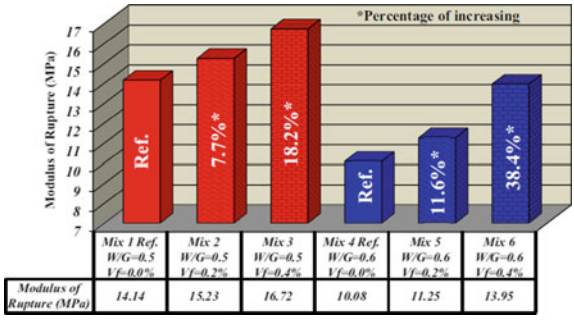

Fig. 7 Effect of CCF volume fraction (*Vf*) on modulus of rupture with various (*W*/*G*) ratios

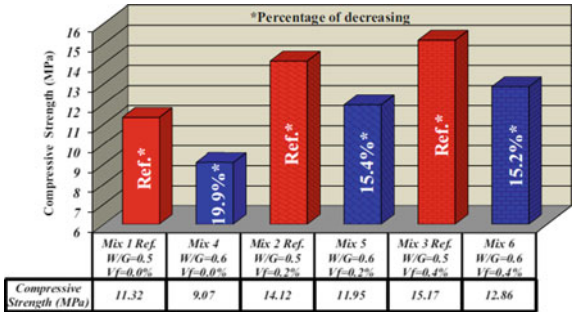

Fig. 8 Effect of (*W/G*) ratios on compressive strength with various CCF volume fractions

4.3 Strength with Variable Chopped Carbon Fibre (CCF) Volume Fractions (VJ)

Figure 5 show the compressive strength of gypsum plaster at three CCF concentrations when the *W/G* ratios are (0.5)–+(0.6) and the *W/G* ratios are (0.5)–+(0.6) (8). In this range, there are no percentages to be found. Increases in (W/G) ratios are associated with decreased compressive strength when compared to the reference mixes (Mixl, Mix2, and Mix3), and this effect is consistent over the range of CCF concentrations tested. Porosity in a hardened mixture is increased by evaporation, which occurs when water volume increases (due to the reaction—water). Thus, gypsum's internal structure is harmed and the mixture strength is reduced [11, 36]. Consequently.

Furthermore, as indicated in Fig. 8, the percentages of compressive strength loss are decreased in the presence of CCF. As a result, for all CCF concentrations, the amount of compressive strength loss caused by an increase in the (*W/G*) ratio is very close to zero (0.0, 0.2, and 0.4%). It is possible that the cubic specimens' failure mode (crushing) leads in a very close link between the impact of CCF on compressive strength growth for the two (*W/G*) ratios, resulting in this finding. One possible reason for the lower rate of compressive strength deterioration in CCF-containing mixes (Mixes 2 and 3) is that CCF-containing mixes have higher compressive strengths than non-CCF-containing mixes (Mixl).

4.4 Influence of (WIG) Ratios on Modulus of Rupture with Variable Chopped Carbon Fibre (CFF) Volume Fractions (VJ)

Figure 9 show the results of an investigation into the impact of increasing the (*W/G*) ratios from (0.5) to +(0.6) on the modulus of rupture of gypsum plaster with three different CCF concentrations (0.0, 0.2 and 0.4%). The modulus of rupture decreases when the (*W/G*) ratio is raised above the reference mixes (Mix1, Mix2, and Mix3).

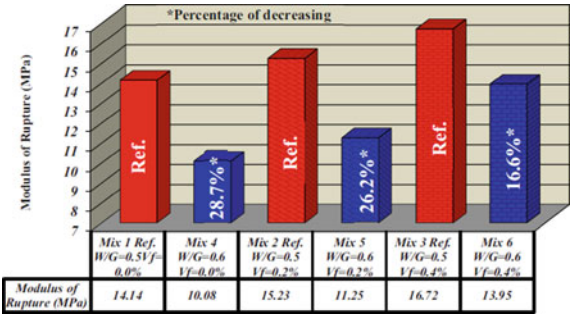

Fig. 9 Different CCF volume percentages and varying (*W/G*) ratios have different effects on rupture modulus

This holds true for each of the three CCF concentrations shown in the table and graphic. The first paragraph of this section explains why this is the case (4.3).

CCF reduces the proportion of rupture degradation modulus, as seen in table of Fig. 9. CCF's ability to enhance rupture modulus is magnified by an increase in the (*W/G*) ratio, as discussed in Sect. 4.2's second paragraph, which explains why the percentage of rupture modulus degradation is lower when CCF is present.

5 Conclusion

As a result of the widespread usage and manufacturing of Portland cement, which is the principal building material in concrete construction, a negative effect on the environment is created by the release of massive volumes of CO_2 gas into the atmosphere. Additionally, there is a direct correlation between cement usage and greenhouse gas emissions. Numerous research have attempted to decrease the usage of Portland cement in order to mitigate these issues without raising building costs. Partial substitution of Portland cement with supplemental cementitious materials is one of these methods, and when done properly, it has the advantage of increasing the characteristics of concrete, lowering costs, saving energy, and decreasing waste emission.

Experimental results are concluded below:

- When compared to reference mixes, both (W/G) ratios demonstrate a continuous improvement in compressive strength with increasing CCF concentration (i.e., CCF-free: Mix4 and Mixl).
- When ($W/G = 0.5$) and (Vf of CCF is raised from (0.2% to 0.4%), compressive strength rises by (24.7% and 34.0%, respectively) (Mixl and Mix4)
- In order to enhance the compressive strength of CCF, the value of Vf must be raised from (0.2% to –*0.4%) when (WIG = 0.6) to (31.8% and 41.8%, respectively).
- In comparison to reference mixes, a higher (WIG) ratio (from 0.5 to 0.6) enhances the percentage improvement in compressive strength when CCF is added at 0.2 and 0.4% concentrations, respectively (Mixl and Mix4).

- It has been shown that compressive strength decreases as the (WIG) ratio increases from (0.5 to 0.6), which is consistent with the behaviour of the three CCF (Vf)s with WIG = 0.5 (i.e., Mixl, Mix2, and Mix3).
- Compressive strength drops by 19.9%, 15.4%, and 15.2% when WIG is increased from 0.5 to 0.6 at each (*Vf*) of CCF (0.0, 0.2, and 0.4%) (Mixl, Mix2, and Mix3).
- As (WIG) ratio increases from (0.5 to −*0.6), the percentage of compressive strength degradation in the presence of CCF is reduced.

References

1. Thomas MDA, Shehata MH (1999) Use of ternary cementitious systems containing silica fume and fly ash in concrete. Cement Concr Res 29
2. Sandor P. Portland cement- fly ash- silica fume systems in concrete. Department of civil and Architectural Engineering, Drexel University, Philadelphia, Pennsylvania
3. Sakalkale AD (2014) Experimental study on use of waste marble dust in concrete. Int J Eng Res Appl 4(10, Part-6):44–50, October 2014
4. Lam, Wong, Poon (2012) Utilization of fly ash, rice husk ash, and palm oil fuel ash in glass fibre–reinforced concrete. J Mat Civ Eng:1281–1288, Sep 2012
5. Singh T, Nanda AK (2012) Influence of marble powder on mechanical properties of mortar and concrete mix. In: NMBCW, June 2012
6. Corinaldesi V, Moriconi G, Naik TR (2010) Characterization of marble powder for its use in mortar and concrete. Constr Build Mater 24(1):113–117, January 2010. ISSN 0950-0618
7. Hendriks ChF, Janssen GMT (2003) Use of recycled materials in constructions. Mater Struct 36(9):604–608
8. Khatri RP, Sirivivatnanon V, Gross W (1995) Effect of different supplementary cementitious materials on mechanical properties of high performance concrete. Cem Concr Res 25(1):209–220
9. Kwan WH, Ramli M, Kam KJ, Sulieman MZ (2012) Influence of the amount of recycled coarse aggregate in concrete design and durability properties. Constr Build Mater 26:565–573
10. Uygunoğlu T (2011) Use of hydrated mortar as partial replacement material in cement. Adv Cem Res 23(3):113–122
11. Pacheco-Torgal F, Jalali S (2011) Compressive strength and durability properties of ceramic wastes based concrete. Mater Struct 44:155–167
12. Radlinski, Olek, Nantung (2010) Durability performance of concrete made with fine recycled concrete aggregates. Cement Concr Compos 32:9–14
13. Barbhuiya SA, Gbagbo JK, Russell MI, Basheer PAM (2009) Properties of fly ash concrete modified with hydrated lime and silica fume. Constr Build Mater 23(10):3233–3239
14. Aliabdo AA, Abd Elmoaty M, Auda EM (2014) Re-use of waste marble dust in the production of cement and concrete. Constr Build Mater 50:28–41, 15 January 2014, ISSN 0950-0618
15. Aruntaş HY, Gürü M, Day M, Tekin I (2010) Utilization of waste marble dust as an additive in cement production. Mater Des 31(8):4039–4042
16. Sancak E, Özkan S (2015) Sodium sulphate effect on cement produced with building stone waste. J Mater 2015, Article ID 813515, 12 pages. https://doi.org/10.1155/2015/81351
17. Shayan, Xu (2006) Performance of glass powder as a pozzolanic material in concrete: a field trial on concrete slabs. Cement Concr Res 36:457–468
18. Kirgiz MS (2014) Effects of blended-cement paste chemical composition changes on some strength gains of blended-mortars. The Scien World J 2014, Article ID 625350, 11 pages. https://doi.org/10.1155/2014/625350

19. Ma X, Wang Z (2013) Effect of ground waste concrete powder on cement properties. Adv Mater Sci Eng 2013, Article ID 918294, 5 pages. https://doi.org/10.1155/2013/918294
20. Khalil AA, Gad GM (1972) Mineral and chemical constitutions of the UAR gypsum raw materials. Indian Ceramics 16:173–177
21. Combe EC, Smith DC (1964) Some properties of gypsum plaster. J Brit Dent 17:237–245
22. Bharathidasan S, Krushnadesikan TK (2015) Carbon fibre reinforced gypsum buildings. Int J Inno Sci Eng Technol 2(2), February 2015
23. AL-Ridha ASD, Ibrahim AK, AL-Taweel HM, Dheyab LS (2019) Effect of steel fibre on ultrasonic pulse velocity and mechanical properties of self-compact light weight concrete. IOP Conf Ser: Mater Sci Eng 518(2):022017. https://doi.org/10.1088/1757-899X/518/2/022017
24. AL-Ridha ASD (2014) The ınfluence of size of lightweight aggregate on the mechanical properties of self-compacting concrete with and without steel fibre. Int J Struct Civ Eng Res 3(1), February 2014
25. AL-Ridha ASD, Abbood AA, Al-Chalabi SF, Aziz AM, Dheyab LS (2020) A comparative study between the effect of steel fibre on ultrasonic pulse velocity (UPV) in light and normal weight self-compacting concretes. IOP Conf Ser: Mater Sci Eng 888(1):012081. https://doi.org/10.1088/1757-899X/888/1/012081
26. Elaiwi EH, Al-Chalabi SF, Al-Asadi LS, Abbood AA, AL-Ridha AS (2020) Evaluating the performance of fibrous cement mortar containing chopped carbon fibre (C.C.F.). IOP Conf Ser: Mater Sci Eng
27. Al-Ridha ASD, Hameed A, Ibrahim SK (2014) Effect of steel fibre on the performance of hot mix asphalt with different temperatures and compaction. Austr J Basic Appl Sci 8(6):123–132
28. AL-Ridha ASD, Ibrahim SK, Dheyab LS (2016) Steel fibre effect on the behavior of hot mixture asphalt with variable asphalt content. Int J Adv Technol Eng Sci 4(1), February 2016
29. AL-Ridha ASD, Abuzaid EKM, Abbood AAR (2018) Effect of addition of chopped carbon fibre on the behavior of reinforced concrete beams with variable (shear distance to effective depth) ratios. J Eng Sustain Dev 22(1):137–148
30. AL-Ridha ASD, Atshan AF, Hussein HH, Abbood AA, Dheyab LS, Faqri AMA (2019) Evaluation of tensile strength and durability of microbial cement mortar. In: International congress and exhibition sustainable civil ınfrastructures. Springer, Cham, pp 80–89. https://doi.org/10.1007/978-3-030-34249-4_8
31. Al-Ridha AS, Atshan AF, Mahmoud KS, Hameed QK (2019) Effect of strengthening of steel beams with variable length by using carbon fibre. J Eng.https://doi.org/10.1155/2019/1631692
32. Al-Ridha AS, Hameed QK, Atshan AF, Abbood AA, Dheyab LS (2020) Evaluation of strengthening steel beams using the technique of carbon fibre confinement by a steel plate (CFCSP). Adv Civ Eng Mater 9(1):53–66. https://doi.org/10.1520/ACEM20190164
33. AL-Ridha ASD, Abbood AA, Atshan AF (2020) Evaluating the efficiency of strengthening hot-rolled ı-sectioned steel beams by using additional plates and ınclined stiffeners with various widths. IOP Conf Ser: Mater Sci Eng 870(1):012102. https://doi.org/10.1088/1757-899X/870/1/012102
34. AL-Ridha ASD, AA Abbood, AF Atshan (2020) Assessment of the effect of replacing normal aggregate by porcelinite on the behaviour of layered steel fibrous self-compacting reinforced concrete slabs under uniform load. J Eng 2020. https://doi.org/10.1155/2020/3650363
35. ASTM C472-99 (2014), Standard test methods for physical testing of gypsum, gypsum plaster gypsum concrete. ASTM International, West Conshohocken, PA
36. ASTM C348-14 (1988) Standard test method for flexural strength of hydraulic-cement mortars, ASTM International, West Conshohocken, PA, 2014 “Iraqi standard specification for physical tests of gypsum for building purposes” No. 27. (In Arabic), Ministry of Planning
37. Lewry J, Williamson J (1994) The setting of gypsum plaster: part II the development of microstructu and strength. J Mater Sci 29:5524–5528
38. Pinheiro M, Camarini G (2015) Characteristics of gypsum recycling in different cycles. IACSIT Int J Eng Technol 7(3)
39. Yu QL, Brouwers HJH (2011) Microstructure and mechanical properties of bhemihydrate produced gypsum: an insight from its hydration process. Constr Build Mater 25:3149–3157. Cited by reference Sayonara M

FEA of Femur Bone Implant of Calcium, PEEK, Ti–6Al–4V Alloy and 316L Steel

Jihan Mehra, Kushank Khandelwal, Aditya Jain, Rushikesh Dandagwhal, and Rakesh Chaudhari

Abstract The regularly used materials in bone implants have certain drawbacks of not exactly matching with actual bone in terms of density and stiffness. Lighter biocompatible material and advance manufacturing methods can overcome this drawback. Femur bone is one of the sturdiest and lengthy bones in human body which carries majority of human body weight. Additive manufacturing is effectively used in forming these bones. In present work, CAD model of human femur bone is extracted from DICOM image keeping all intrinsic structure of the bone using 3D slider software. ANSYS analysis is done on this extracted bone formed by using different implant materials such as calcium, stainless steel, Ti–6Al–4V and Polyether ether ketone (PEEK). Analysis is carried out by applying 750 Pa load on the femur head. The results of FEM analysis have shown considerable load carrying capacity in bone fabricated by PEEK material. This material can be much easily used in additive manufacturing to fabricate actual implant.

Keywords Implants · Femur · PEEK · Ti–6Al–4V · ANSYS · 3D slicer

1 Introduction

Femur popularly called as thighbone is an upper bone of the leg in human body. At the acetabulum, the head and hip create a ball-and-socket joint. It is maintained in place within the socket by a ligament termed the ligamentum teres femoris, which is encircled by ligaments. In the human body, the neck of the femur links the shaft and head at a 125° angle, making it effective for walking [1]. Femur is considered as one of the sturdiest and lengthy bones in human body and carries most of the body

J. Mehra (✉) · K. Khandelwal · A. Jain
Department of Mechanical Engineering, MPSTME, SVKM'sNarseeMonjeeInstituteofManagementStudies(NMIMS), Mumbai Campus, Mumbai, Maharashtra 400056, India
e-mail: vrnmhr50@gmail.com

R. Dandagwhal · R. Chaudhari
Department of Mechanical Engineering, MPSTME, SVKM's Narsee Monjee Institute of Management Studies (NMIMS), Shirpur Campus, Shirpur, Maharashtra 425405, India

K. Geetha et al. (eds.), *Recent Trends in Materials*, Springer Proceedings in Materials 18, https://doi.org/10.1007/978-981-19-5395-8_10

weight. Human femur is found to be capable of resisting compression forces in the body [2].

Femur bone is made of isotropic and homogeneous material of calcium phosphate which is linear elastic in nature. A variety of material is used nowadays in medical application for fabricating artificial human implants. Biomaterial have been employed in the field of orthopedics for hip joint replacement from the early days of metals, polymers, and ceramics [3]. A biocompatible material is mostly used for this use especially for implantation into human tissue. Biomaterials are naturally available in nature or created in the laboratory using advance processes. These materials are significantly used in different medical and healthcare applications to enhance the body function [4]. The use of these materials has shown evolutionary improvement in functioning of number of active human body parts such as heart valve and hip implants [5]. Austenitic stainless steel (316L), titanium alloy (Ti–6Al–4V), cobalt chrome molybdenum (Co–28Cr–6Mo), polyethylene (UHMWPE), Polyether ether ketone (PEEK), Polyether-ketone-ketone (PEKK) and Polymethylmethacrylate (PMMA) are commonly used biocompatible materials in for forming prototypes in medical and healthcare fields [6].

The use of these biocompatible materials in medical prototyping strongly requires some desirable characteristics. It should be significantly compatible with the human tissues and should not generate any side effects on the human body after implantation. Moreover, it should have desirable mechanical and thermal properties such as tensile strength, toughness, permeability, thermal transition temperatures, corrosion and wear resistance for functioning of the artificial implants [7].

2 Literature Review

Physiological loading of bone or artificial implant becomes very important in investigations such as implant design, micro-motion, fracture healing or fixation, primary stability, etc. Implants fabricated by using most of biomaterials can effectively restore bones, tissues and other human body parts lost due to illness and accident. Titanium alloys such as Ti–6Al–4V and 316L stainless steel are very effective in restoring the functioning of these organs. Niobium-based fine coatings on stainless steel in dental implants helps to improve the strength and life [8]. However, these materials have also shown some concern in few applications such as probability of metal ion discharge and resultant allergenicity or osteolysis after their use. As these materials are not radiolucent, their implants produce scattered image during X-ray, MRI as well as CT scan. These constraints are prevented by developing substitute biomaterials to Ti–6Al–4V titanium alloys and 316L stainless steel to prevent unfavorable post-implant biological effects [9]. Porous titanium constructs have high and variable stiffness and strength, allowing them to be employed for bone defect treatment [10].

Biocompatible magnesium alloys have great potential as absorbable implant materials. It has proved effective healing characteristics until implants support fractured bones. In comparison with stainless steel and titanium implant materials, porous

nickel titanium alloys have superior biocompatibility [11]. Because titanium and its alloys have significantly higher elastic moduli and strength than human bones, stress shielding, and implant failure may occur [12]. Ti–6Al–4V alloy is made up of a graded lattice with a regulated property distribution that reduces bone repair and interface failure at the same time [13]. Polyether ether ketone (PEEK) is a thermoplastic natural polymer that is gaining in popularity owing to its use in the production of surgical instruments, gadgets, implants, etc., due to high-temperature stability [14, 15]. Polyether ether ketone (PEEK) is a suitable alternative material for bone tissue engineering [16]. Low-volume production of PEEK is practically achievable using innovative 3D printing technology. The minimization of scrap material during process enables its use for personalization. PEEK is exceptionally chemically resistant and has great thermal stability at extremely high temperatures. It will be found as key alternative for metallic components in medical treatments of orthopedics and trauma. PEEK possesses very low elastic modulus, a high degree of stability and a low density that makes it a suitable alternative to biomaterials [17]. PEEK offers several clinical benefits as a dental implant material as compared to titanium alloys. In addition, it is radiolucent that results in less magnetic resonance imaging artifacts [18]. PEEK is found very effective in providing metal-free restorations to dental patients those have allergies [19]. The research on human osteoblast responses to diverse PEEK samples investigated that implantable grade PEEK found to be almost similar in rough titanium's bone forming potential [20].

Finite element analysis is found to be very useful for structural analysis of femur bone. The analysis helps for healing the support provided to fractured bones [21]. This type of analysis is very useful for designing the implants in many applications. The structural analysis carried out on various material helps to determine strength to enhance the healing as well as loss of bone mineral density [22, 23]. The FEA analysis of femur bone made of different materials helps to select the suitable materials compatible with human body conditions [24].

The present paper carried out comparative analysis of femur bone of various materials used in prosthetics in order to maximize the power-to-weight ratio and to foster advancement via the use of high-performance materials. Finite element analysis of femur bone formed by different biocompatible materials such as Ti–6Al–4V, 316L stainless steel, calcium and PEEK. The results are used to compare the potential use of femur bone of these materials in human body.

It has been observed that calcium bone is prone to osteoporosis in humans having long time low calcium intake. It also decreases the bone density increasing chances of fracture making bones weak and brittle. Titanium alloys implant exhibits better fatigue resistance as compared to natural calcium bones whoever the implants surface easily allows osseointegration that results in weak bone to implants contacts in number of cases.

The material selection for artificial bone implants is based on literature review from number of case studies, research article and clinical reports. Moreover, human body biological condition, materials properties making them suitable for natural bone replacement cost and performance and implants reaction while inserting a foreign material to human body are additional factors consider for selecting these materials.

Table 1 Material assignment

Materials	ρ(kg/m^3)	E (GPa)	Υ
Calcium bone	2000	2.130	0.3
PEEK	1436	11	0.37
Stainless steel 316L	8000	193	0.27
Ti–6Al–4V	4512	119	0.31

3 Methods

3.1 Material

The type of material used for forming artificial femur bone depends on particular implant applications. The most commonly used biocompatible materials in femur bone application ranging from cardiovascular to otorhinolaryngology are 316L type of stainless steel and Ti–6Al–4V titanium alloys. Due to some issues reported by these materials in the form of radiolucency and resultant allergenicity, Polyether ether ketone (PEEK) is innovatively used nowadays in forming femur bone. It has shown closer performance to calcium bone. In present analysis, 316L stainless steel, Ti–6Al–4V and PEEK are used along with calcium for femur bone. The material assignment of the femur bone is done in engineering data of ANSYS 16.0. Table 1 gives the properties of materials that has significant role in forming femur bone.

3.2 3D Slicer

The 3D model of the femur bone of 30 years male patient was built utilizing the CT scan report which was in DICOM design from. 3D slicer is open-source programming useful for imagining the clinical pictures for investigating the CT scan output and MRI report of the patients. Select a DICOM image (.dcm extension) file in 3D slicer software as shown in Fig. 1. Then select the required part of the bone you need and then apply the 'Crop Volume' and 'Segment Editor' modules (Fig. 2). Now we can generate the 3D model of the selected island by clicking on 'Show 3D' command. As the femur bone is connected with the hip bone, we separated it by creating a new segment as shown in Fig. 3. Click on the segmentation from the left interface and save our selected segmentation in the format of .stl file as shown in Fig. 4.

For threshold selection as shown in Fig. 2, you need to find the perfect threshold value of your model by a hit and try method and by observing it at every step possible for this work, we have found out the threshold range to be 124.37 to 1521. And then apply the threshold.

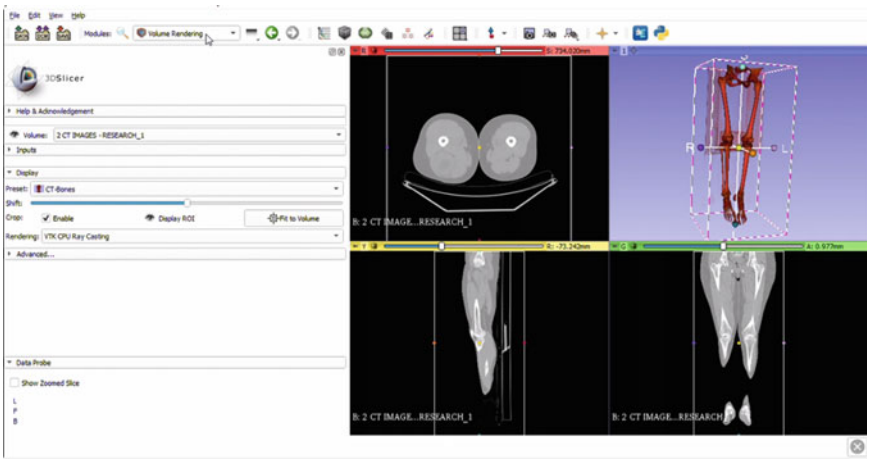

Fig. 1 Four up view of DICOM image

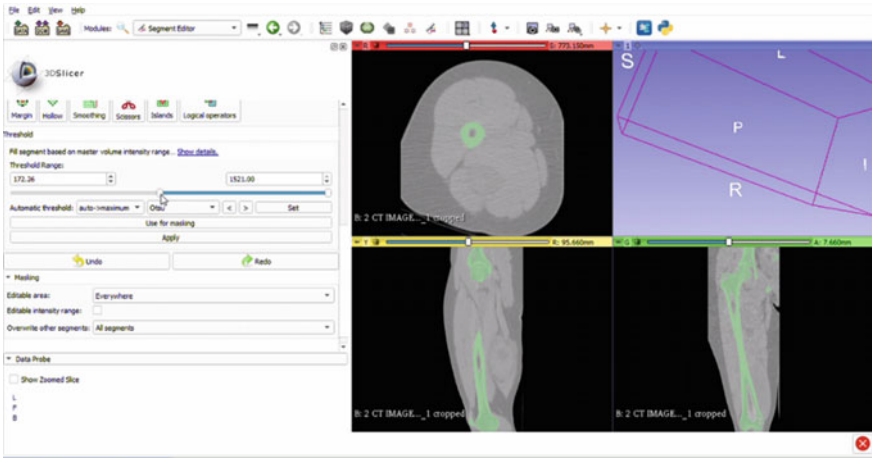

Fig. 2 Threshold selection

3.3 Finite Element Analysis (FEA)

Finite element analysis is useful tool for simulations of components with complex geometries and helps to meet the customer requirement prior to fabrication. The human femur bone has large chances to fracture due to bearing of most of the body weight. FEA of patient's femur bone made of different listed materials is carried out to investigate the stresses, deformation and fracture in the bone due to various types of loads acting on it during regular movement. ANSYS 16.0 is used to do the structural analysis in static conditions. There are 15,453 nodes and 8502 elements in

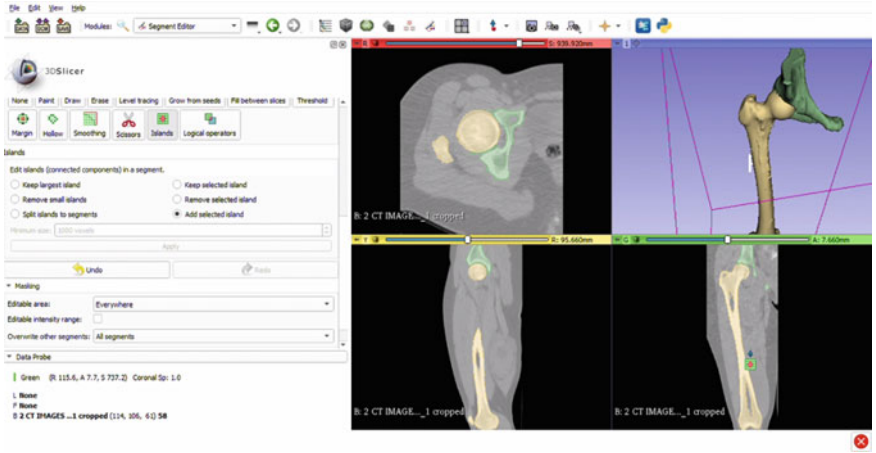

Fig. 3 Separating femur bone

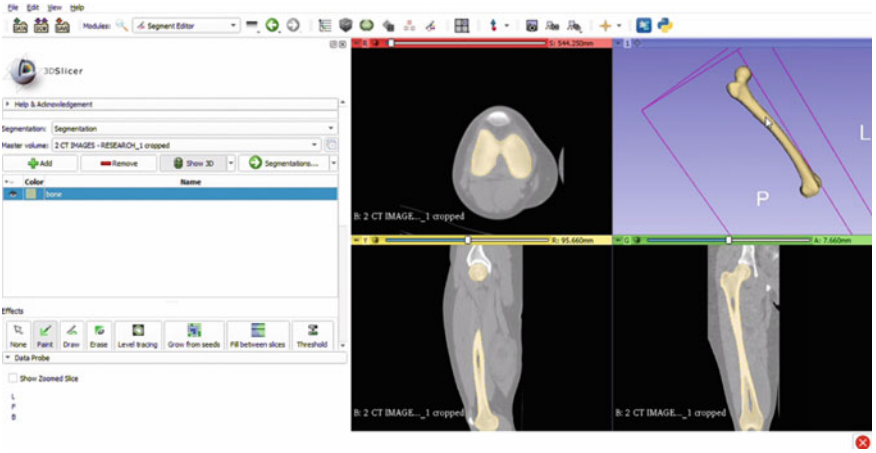

Fig. 4 Saving femur bone 3D model

the three-dimensional finite element model of the femur bone. The surface meshing of the bone is done with tetrahedron components as shown in Fig. 5. The test is performed by delivering a 750 Pa load on the head of the femur bone with fix support on the lateral, medial and patellar surfaces. As shown in Fig. 6, it depicts the boundary condition employed during the femur bone analysis. The findings of the analysis are contrasted for discussion on femur bone manufactured from four different materials (Table 2).

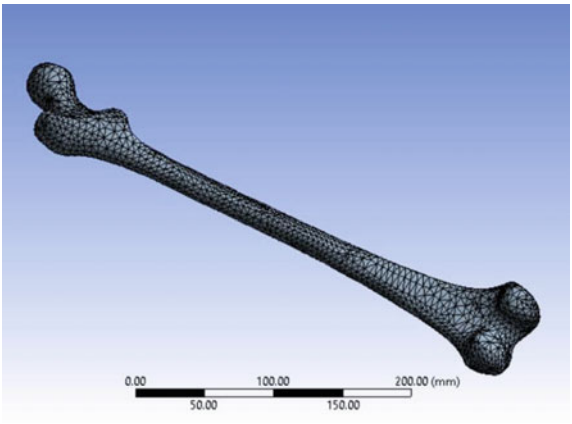

Fig. 5 Mesh generation on femur bone

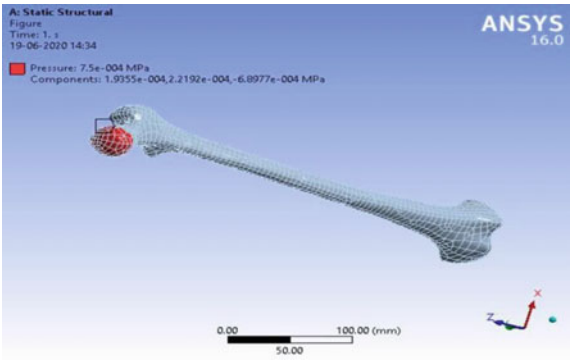

Fig. 6 Load at the head of the femur

Table 2 Femur dimension

Length *X*	86.324 mm
Length *Y*	89.161 mm
Length *Z*	413.26 mm

4 Results and Discussion

Finite element analysis is carried out on femur bone made with different materials for stress analysis. The stresses are calculated in standing condition when maximum weight of human body will be acting on the bone. The von Mises stresses and deformation obtained for same boundary conditions is useful for comparative analysis. The stability of a femur implant can now be better understood owing to these findings.

4.1 Stresses in Calcium Femur Bone

The equivalent von Mises stress in calcium femur bone varies from 0.25277 MPa to 4.004 * e^{-5} MPa as shown in Fig. 7a. The total deformation of 0.17817 mm is exhibited by femur bone as shown in Fig. 7c. The central region of the bone has the highest primary stress of 0.22224 MPa as shown in Fig. 7b

4.2 Stresses in PEEK Femur Bone

For the same load as applied in calcium bone, the maximum principal stress of 0.23933 MPa as shown in Fig. 8b, whereas equivalent von Mises stress of 0.24451 MPa as shown in Fig. 8a is measured in PEEK femur bone. The maximum principal stress is observed in the central section of the bone. The total deformation of 0.034625 mm is observed at the head of the femur bone as shown in Fig. 8c. The maximum deformation measured in PEEK femur bone is comparably less than calcium femur bone.

4.3 Stresses in Ti–6Al–4V Alloy Femur Bone

Titanium is effectively used in many biomedical implants due to its biocompatibility and ability of surface modifications. It exhibits good resistance to corrosion to bodily fluids. The equivalent von Mises stress of 0.24843 MPa as shown in Fig. 9a is measured in Ti–6Al–4V titanium alloy femur bone in standing condition. The maximum principal stress is measured about 0.227 MPa which is less than PEEK femur bone as shown in Fig. 9b. Comparatively, very less amount of total deformation of 0.003197 mm is measured in head of the in this femur bone as shown in Fig. 9c.

4.4 Stresses in 316L Stainless Steel Femur Bone

Because of its superior corrosion resistance to biological fluids, stainless steel 316L is employed in implants. In stainless steel bone, the corresponding von Mises of 0.25482 MPa is messaged as shown in Fig. 10a. In standing posture, the highest primary stress of 0.22107 MPa is produced at the central section of the bone as shown in Fig. 10b. The total deformation of 0.001963 mm is measured as shown in Fig. 10c. The deformation in stainless steel bone implant is very much less than actual calcium bone and other implants made using PEEK and titanium alloys. The measure amount of deformation in all cases is observed in head portion of the bone.

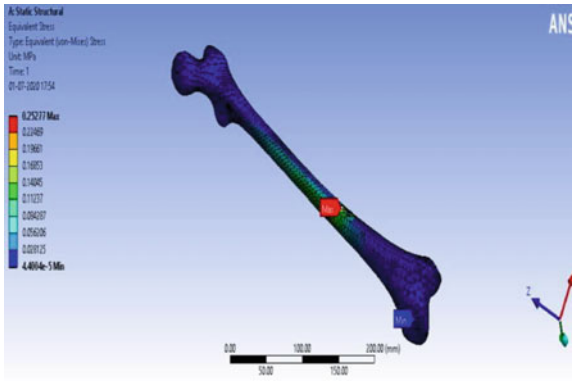

(a) Equivalent Von Mises Stress

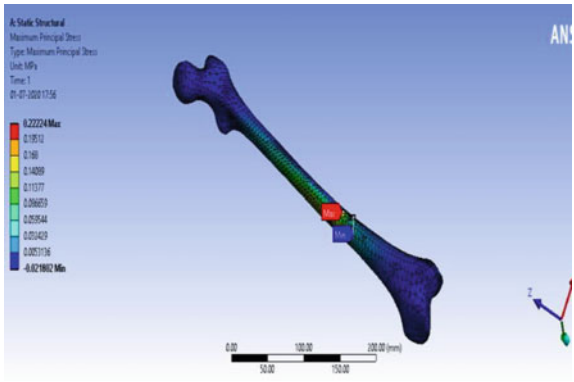

(b) Maximum Principal Stress

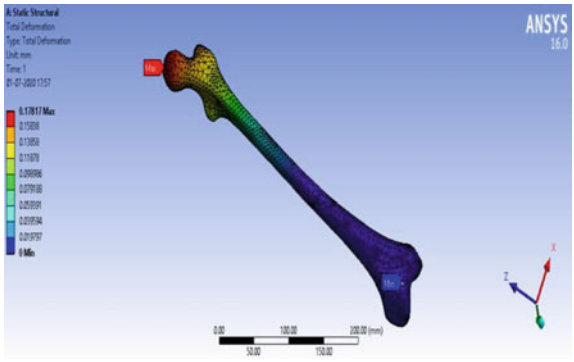

(c) Total Deformation

Fig. 7 Equivalent von Mises stress, maximum principal stress and deformation in calcium femur bone

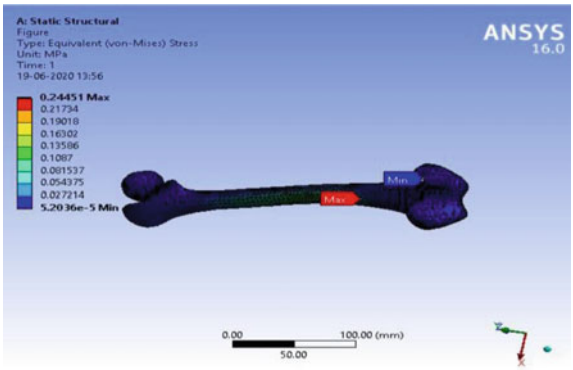

(a) *Equivalent Von Mises Stress*

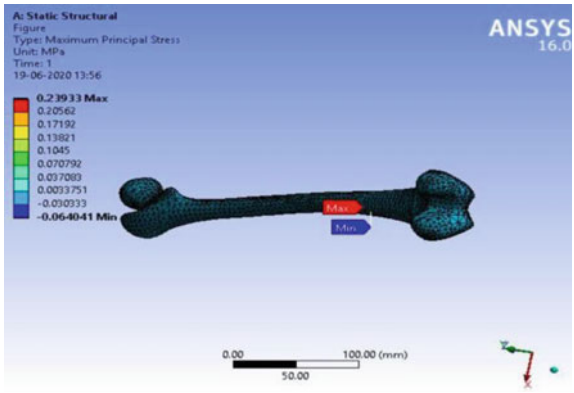

(b) *Maximum Principal Stress distribution*

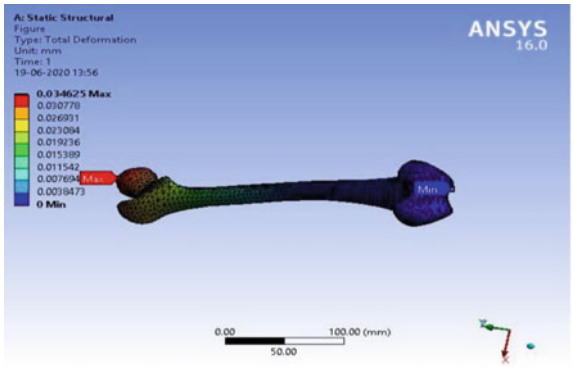

(c) Total Deformation

Fig. 8 Equivalent von Mises stress, maximum principal stress and deformation in PEEK femur bone

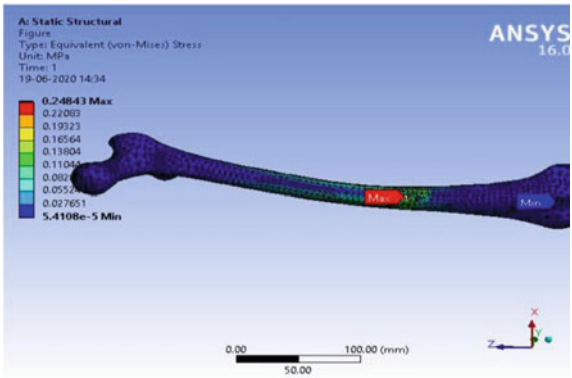

(a) *Equivalent Von Mises Stress*

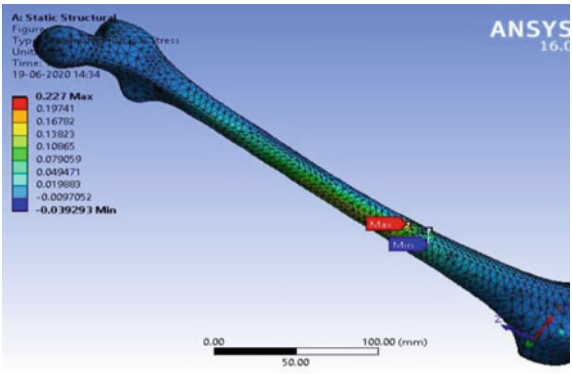

(b) Maximum Principal Stress distribution

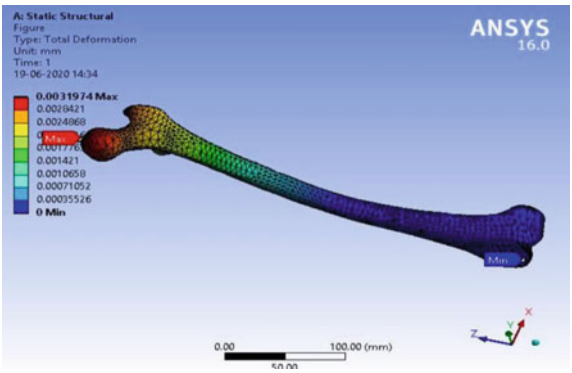

(c) Total Deformation in the femur bone

Fig. 9 Equivalent von Mises stress, maximum principal stress and deformation in Ti–6Al–4V femur bone

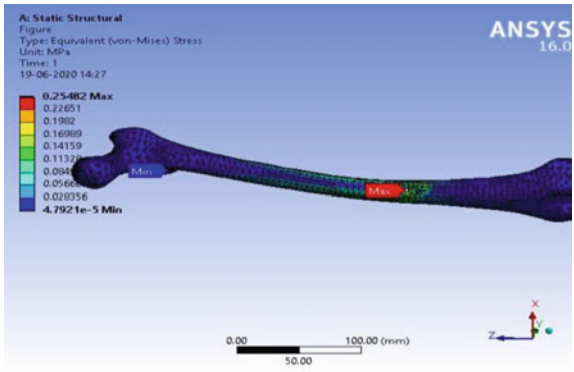

(a) Equivalent Von Mises Stress distribution

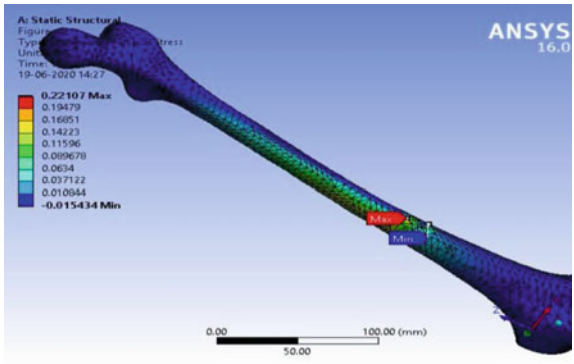

(b) Maximum Principal Stress distribution

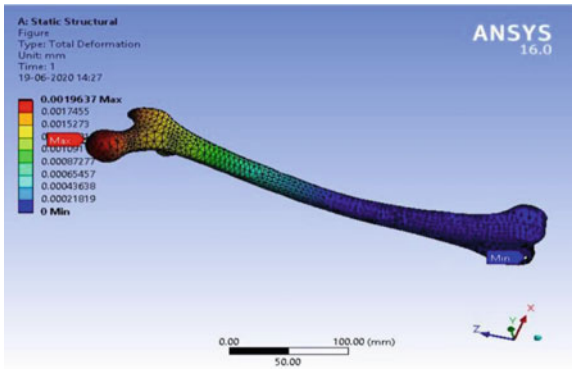

(c) Total Deformation in the femur bone

Fig. 10 Equivalent von Mises stress, maximum principal stress and deformation in 316L stainless steel femur bone

Table 3 Stress and deformation in bone implants

Material	Equivalent von Misses stress (N/mm^2)	Maximum principle stress (N/mm^2)	Deformation (mm)
Calcium	0.25277	0.22224	0.17817
PEEK	0.24451	0.23933	0.034625
Ti–6Al–4V titanium alloy	0.24843	0.227	0.003197
316L stainless steel	0.25482	0.22107	0.001963

The comparative analysis of femur bone implants is given in Table 3. The equivalent von Mises stress and maximum principal stress are nearly same in all bone implants. It is observed that PEEK material implant has exhibited extremely lesser deformation than actual calcium bone in same working condition. Titanium alloy and stainless steel bone implants have also exhibited least deformation than all other materials. But PEEK material implant is advisable to use as alternative to calcium bone due to very low cost and adaptability to human body compared to other materials. If used with all other medical guidelines, PEEK can be evolutionary alternative materials in bone implants surgery of human body.

5 Conclusion

Finite element analysis is performed on femur bone implant formed by using traditional calcium as wells as Ti–6Al–4V alloys, PEEK and 316L stainless steel. The analysis was done for static loading on femur head of 750 Pa. PEEK materials sustained the applied load with minimum deformation of 0.034625 mm. The femur bone implant weight of Ti–6Al–4V alloy is measured about 1.2828 kg, whereas it is about 0.4093 kg for PEEK implant. All the implants yielded almost same Equivalent von Misses stress for applied load. The PEEK and 316 stainless steels have shown very less deformation as compared to traditionally used calcium and as Ti–6Al–4V alloys. All the materials implants have shown same maximum principal stress for same applied loading. PEEK material implant is suggested as alternative to calcium bone due to very low deformation supported by very low cost. PEEK is also found very adaptable to human body compared to other materials due to non-toxicity, high strength and excellent corrosion resistance. However, PEEK implants have shown little concerns about thermal degradation at high temperature in few traditional fabrication processes. These concerns can be efficiently overcome by using proposed additive manufacturing process that involves comparatively low temperatures.

References

1. Gangwar AKS, Rao PS (2020) Biodynamic response of femur bone. Int J Innov Technol Explor Eng 9(5):1406–1412
2. Maharaj PS, Maheswaran R, Vasanthanathan A (2013) Numerical analysis of fractured femur bone with prosthetic bone plates. Procedia Eng 64:1242–1251
3. Yánez A, Cuadrado A, Martel O, Afonso H, Monopoli D (2018) Gyroid porous titanium structures: a versatile solution to be used as scaffolds in bone defect reconstruction. Maters Des 140:21–29
4. Bairagi D, Mandal S (2021) A comprehensive review on biocompatible Mg-based alloys as temporary orthopaedic implants: current status, challenges, and future prospects. J Magnesium Alloys
5. Mujahidin D, Puspitasari P, Kustono D (2018) Simulation of human bone implant duralium material with variation loading using Ansys software. In: MATEC web of conferences, vol 204. EDP Sciences, p 07020
6. Olivares-Navarrete R, Hyzy SL, Slosar PJ, Schneider JM, Schwartz Z, Boyan BD (2015) Implant materials generate different peri-implant inflammatory factors: poly-ether-ether-ketone promotes fibrosis and microtextured titanium promotes osteogenic factors. Spine 40(6):399–404
7. Toyohara R, Kurosawa D, Hammer N, Werner M, Honda K, Sekiguchi Y, Ohashi T (2020) Finite element analysis of load transition on sacroiliac joint during bipedal walking. Sci Rep 10(1):1–10
8. Ramírez G, Rodil SE, Arzate H, Muhl S, Olaya JJ (2011) Niobium based coatings for dental implants. Appl Surf Sci 257(7):2555–2559
9. Torstrick FB, Lin AS, Potter D, Safranski DL, Sulchek TA, Gall K, Guldberg RE (2018) Porous PEEK improves the bone-implant interface compared to plasma-sprayed titanium coating on PEEK. Biomaterials 185:106–116
10. Turnbull G, Clarke J, Picard F, Riches P, Jia L, Han F, Shu W (2018) 3D bioactive composite scaffolds for bone tissue engineering. Bioact Mater 3(3):278–314
11. Bahraminasab M, Jahan A (2011) Material selection for femoral component of total knee replacement using comprehensive VIKOR. Mater Des 32(8–9):4471–4477
12. Nhlapo N, Dzogbewu TC, De Smidt O (2020) A systematic review on improving the biocompatibility of titanium implants using nanoparticles. Manuf Rev 7:31
13. Khanoki SA, Pasini D (2013) Fatigue design of a mechanically biocompatible lattice for a proof-of-concept femoral stem. Mech Behav Biomed Mater 22:65–83
14. Panayotov IV, Orti V, Cuisinier F, Yachouh J (2016) Polyetheretherketone (PEEK) for medical applications. J Mater Sci Mater Med 27(7):1–11
15. Jia D, Li F, Zhang C, Liu K, Zhang Y (2021) Design and simulation analysis of lattice bone plate based on finite element method. Mech Mech Adv Mater Struct 28(13):1311–1321
16. Chaudhari R, Loharkar PK, Ingle A (2022) Medical applications of rapid prototyping technology. In: Recent advances in industrial production. Springer, Singapore, pp 241–250
17. Haleem A, Javaid M (2019) Polyether ether ketone (PEEK) and its manufacturing of customised 3D printed dentistry parts using additive manufacturing. Clin Epidemiology Glob Health 7(4):654–660
18. Deng L, Deng Y, Xie K (2017) AgNPs-decorated 3D printed PEEK implant for infection control and bone repair. Colloids Surf B 160:483–492
19. Schwitalla AD, Spintig T, Kallage I, Müller WD (2015) Flexural behavior of PEEK materials for dental application. Dent Mater 31(11):1377–1384
20. Sagomonyants KB, Jarman-Smith ML, Devine JN, Aronow MS, Gronowicz GA (2008) The in vitro response of human osteoblasts to polyetheretherketone (PEEK) substrates compared to commercially pure titanium. Biomaterials 29(11):1563–1572
21. Chaudhari R, Ingle A (2018) Finite element analysis of dissimilar metal weld of SA335 P11 and SA312 TP304 formed by transition grading technique. Mater Today 5(2):7972–7980

22. Kumar V, Bakhtari AR, Himanshu P, Akhtar W (2021) Comparative analysis of femur bone's compatible materials by finite element analysis (FEA) tool. In: Advances in engineering design. Springer, Singapore, pp 507–516
23. Kalaiyarasan A, Sankar K, Sundaram S (2020) Finite element analysis and modeling of fractured femur bone. Mater Today 22:649–653
24. Shrivastava A, Jain NK, Salhotra R (2021) Pre-stressed buckling analysis of human femur bone for predicting injury while load bearing at standing position. AIP Conf Proc 2341(1):020038

Literature Review in Artificial Neural Network for the Strength Calculation of Soil

Rahul Ramdas Wankhade and P. V. Durge

Abstract The soil properties are considered to be the important parameter related to the soil. There are different factors associated with it so that the proper results can be generated. Shear strength is considered to be the resistance internally present and applied for the forces which are external in nature. The other parameters are also involved for the calculation of the strength of soil. It is determined in laboratory using sophisticated equipment and is found to be associated with errors. Alternative such as the empirical correlations are considered to be valid for particular range. With the advent of computational technics, mathematical, numerical and artificial intelligence are explored for determination of shear strength. The artificial neural network is the technique where the prediction of the different soil properties is to be obtained. The properly collected data of different soil samples are then given as input to ANN Technique. It is very much necessary to predict the strength of the soil as there are numerous applications including construction, testing, sports, agriculture, military, etc. The different parameters are to be considered for the proper relationship to be obtained. The present paper is related to the review which has been carried out on the use of the artificial neural network in the strength calculation of the soil.

Keywords ANN · Strength · Soil and shear

1 Introduction

The prediction of the soil properties for the subsurface is possible in the case of exploration related to the site while the testing should be carried out for this. But this is considered to be a very complex as well as difficult because of the certain situations especially related to the uncertainties [1]. These uncertainties include variability in

R. R. Wankhade (✉)
Department of Civil Engineering, Prof Ram Meghe College of Engineering & Management, Badnera, Amravati, India
e-mail: rahul.wankhade@prmceam.ac.in

P. V. Durge
Department of Civil Engineering, Mauli College of Engineering, Shegaon, India

K. Geetha et al. (eds.), *Recent Trends in Materials*, Springer Proceedings in Materials 18, https://doi.org/10.1007/978-981-19-5395-8_11

spatial domain, noise in the process of measurement, bias in the process of model and measurement, and errors in the statistics because of the measurements which are limited in number [2]. The determination of the shear strength of the soil is most of the time needed. Shear strength is considered to be very important property related to the soil, and because of which, the determination in the exploration of the site is possible [3]. This property is related to the resistance to the process of sliding along the surfaces which are internal in nature and well within the mass so that it will be having the influence related to the loading which is external in nature [4]. Shear strength is very important parameter related to the stability of any kinds of structure especially related to the foundation as well as embankment of the road and apart from that retaining wall. There are certain structures where this parameter is required and that consists of footing with sinking property, wedge soil with the movement, and bearing capacity related to the method such as Vesic method and Hansen method [5]. The theory of Mohr–Coulomb as per the different researches with the shear strength parameters related to Geotechnical engineering is carried out.

The determination of the shear strength is possible in the case of laboratory as well as in the case of actual site with the help of different tests. Shear stress is also possibly determined in the case of specimen which is undisturbed and related to the soil sample with fine grain and also for the sample which is disturbed while the specimen which is remoulded and related to the soil having fine grained or coarse grained [6]. The test to be carried out in the laboratory includes triaxial shear test, direct shear box test and unconfined compression test. Latest are generally carried out at the site and include standard penetration test, Piezo-cone test, cone penetration test, pressure metre reading test and field vane shear test.

Thus, alternative techniques, such as judgmental values, correlation with index soil properties and computational modelling, are used and explored by many practising Engineers and researchers.

Empirical correlation is often thought to be a better alternative for the determination of undrained shear strength of the soil as a cross verification. Many researchers have done extensive work for the development of correlations between undrained shear strength of the soil and basic index properties of the soil. Comparative study of the empirical correlations and site-specific shear strength any studies many concludes that empirical correlations should not entirely replace carefully performed site-specific laboratory tests measuring residual strength, when reliable values are required.

In the quest for better accuracy, Computational Methods such as Regression analysis and artificial neural network (ANN) modelling are explored by many researchers. These methods are projected as reliable, realistic for prediction of shear strength over cumbersome and tedious laboratory work. Regression is one of the most popular statistical methods used for empirical deterministic modelling extensively used to develop correlation between dependent and independent variables. It comprises ordinary linear with one or several variables and non-linear such as polynomial, exponential and logistical. Artificial neural network (ANN) simulates structure and functionalities of human brain and nervous system by forming network of numbers of simple mathematical models called as neuron, arranged in layers. It is widely adopted

in the field of geotechnical engineering, water resources and coastal engineering. The geotechnical Engineering ANN's prediction models include Over consolidation Ratio (OCR), liquefaction potential, foundation settlement, piles bearing capacity and compaction control.

There are advantages and disadvantages related to every test which is to be carried out in the laboratory as well as at the actual site. The tests shall be carried out at specified loading rate, representative boundary conditions, at stress level corresponding to confining pressure and initial stress condition and with all other variables representing site specific conditions.

2 Artificial Neural Network Predictions

The author has carried out the literature survey related to the different applications which are based upon the artificial neural network in the prediction system of the capacity of pile, the behaviour of the soil and its modelling, characteristics of deciding condition, structures related to the earth retainment, settlement in the case of structural part, etc. [7].

There are certain factors relating to the applications where the artificial neural network can be used and that includes the ability of the slope consideration, soil classification, soil compaction, etc. Prediction of the piles which is to be driven and capacity which is to be calculated, prediction in the case of properties of the soil as well as process of liquefaction, and the behaviour of the soil are some of the applications where artificial neural network can be effectively used. This new technology can be used in other parts of the soil engineering but need to have proper precautions as well as the research is to be carried out in depth [8].

The researchers have developed a model which is related to the soil properties and includes parameters of the shear strength, permeability of the soil, index of the plasticity, liquid limit and dry density. The perception network has many layers, and also, this includes the backpropagation which is feedforward in nature, and the hidden layers were also present in different numbers. The test data was related to the soil specimen of up to 68 and out of that 47 specimen data has been used in the case of training purpose for the remaining specimen that is 27 numbers for the soil data have been used for the testing purpose. Disposes include the input and different numbers as well as the hidden layers in different numbers and architecture having the output also include [9]. From the result, it can be observed that the model studied by the researcher is very useful for the prediction purpose of the shear strength and need to be considered for the other prediction system which includes parameter of the strength as well as permeability of the soil with the help of system and model related to artificial neural network [10] (Fig. 1).

The researcher analyses artificial neural network models and application of fit so that it can be used properly in the field of soil technology [12]. The research was carried out for the models based on ANN, and it is observed that these models need

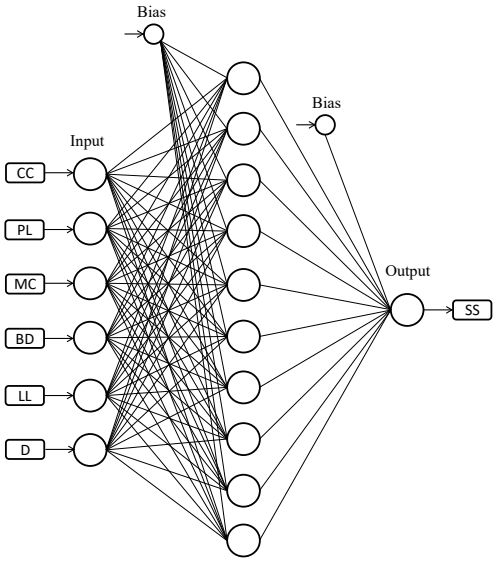

Fig. 1 The network with architecture having multi-layers in ANN [9, p. 55]

to have proper transparency in the process as well as the extraction of the knowledge (Fig. 2).

Network is considered to be good and new tool in the case of prediction for the different characteristics related to the soil and the past research which has been carried out in this field proves this. The combination of the logic of fuzzy, theory of chaos, algorithm of BAT and the algorithm of optimization related to the whale is very useful when the model is to be created so the estimation process can be obtained in the case of different parameters [13] (Fig. 3).

The system to check the quality can be predicted when the algorithm is related to the analysis of the component in the programme as well as the algorithm related to the stump with the decision [15]. There is the device called as disdrometers which is used for the case of estimation of drop size distribution, when the RF-based system is involved in it; then, the cost-effective solution is obtained, the same system when used with the radar having dual polarization for effective results [16].

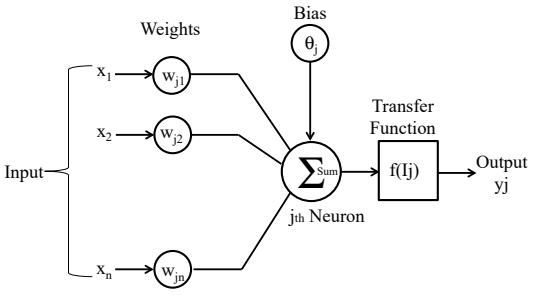

Fig. 2 Typical artificial neutron

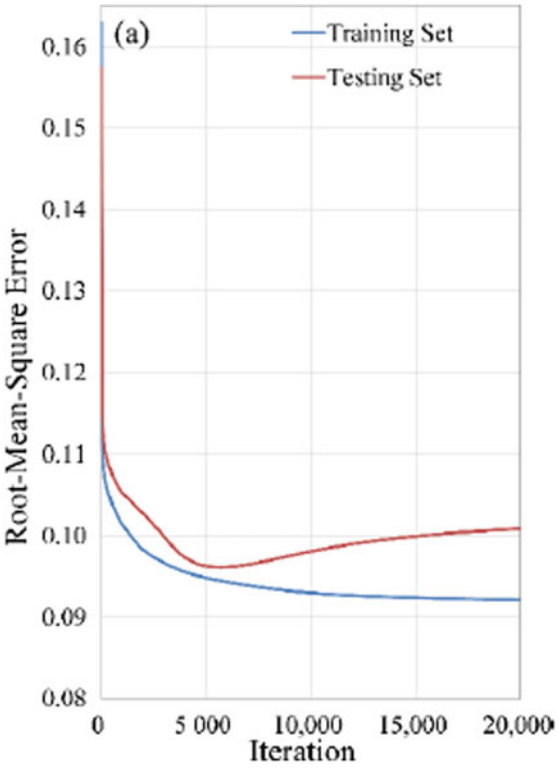

Fig. 3 The results for the case of hidden layers having 3 neurons [17, p. 5]

Table 1 gives the data related to the ANN, the data set used in the system and the performance obtained by various researchers. The architecture in the network used by the authors is also mentioned so that the hidden layers shall be obtained.

The assertion of the model development framework and the relevance of the chosen soil parameters is verified by dataset to variables ratio as per Frank and Todeschini (1994), and by relative importance of predictor variables using Garson's algorithm (Garson 1991) as shown in Fig. 4. With dataset to variable ratio of (121/6)

Table 1 Details for the models performed using ANN

Sr. No.	Data used in ANN	Architecture in network number of neurons in the hidden layers	Performance of the model	References
1	72	11	$R = 0.97$	[17]
2	129	10	$R^2 = 0.97$	[18]
3	48	12	$R = 0.99$	[19]
4	72	8	$R = 0.99$	[20]
5	69	9	$R = 0.99$	[21]

over 20, the model suggests strong acceptability. Garson's algorithm uses absolute values of connection weights to determine relative importance of each input variable in the network. Accordingly, the input-hidden and hidden-output weights of the trained MLP model were partitioned and the absolute values of the weights were taken to calculate the relative importance values. The relative importance values of the input parameters of the MLP model as presented in Fig. 5 suggest more dependency on plastic limit and bulk density in comparison with other parameters of the soil.

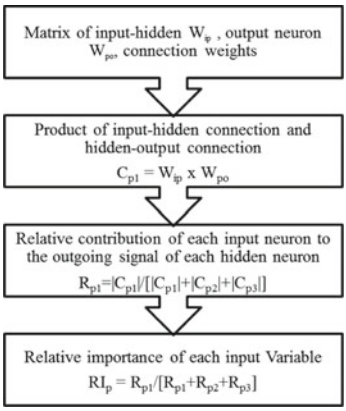

Fig. 4 Garson's algorithm (Garson's 1991) for determining the relative importance of each input variable

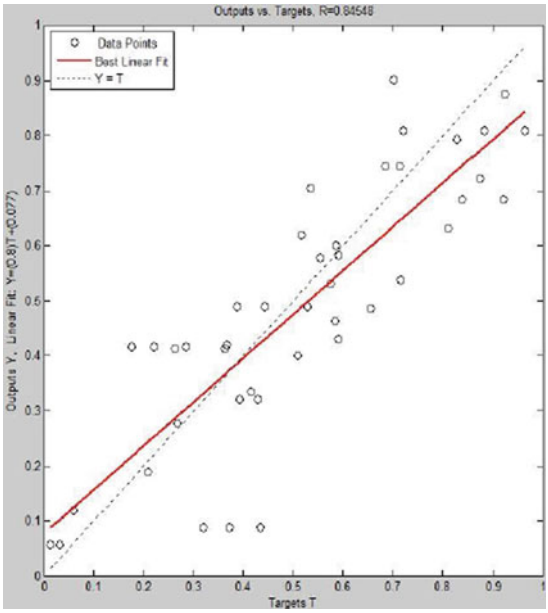

Fig. 5 Strength comparison for predicted and the experimental results [23, p. 8]

3 Parameters

3.1 Variability

There is certain variation in the properties related to the natural soil as the property at one point is different while at the other point is different since there is certain difference in the composition of the soil as well as variation in the consistency when the process of formation of the soil was carried out. Author has carried out research related to the problem related to variation, it was observed that when did properties which have been considered for the modelling purpose and it has to be considered as case of normal distribution or even it can be considered as Gaussian distributions [12].

3.2 Characteristic Value

The characteristic value is considered to be used for the representation in the case of properties of the soil just like the properties of the shear strength. The characteristic value is considered to be governed with process of problem in the design as well as it is governed with the property of the geometry. Characteristic value is also considered to be the value which is mean and for the application for the process where the fluctuations are possible locally in the property of the soil and need to have assumptions.

3.3 Best Estimates

Best estimates are related to the property of the soil and are considered to be unbiased and have the errors which are almost negligible. Best instruments are generally considered to be in the case of assessing the serviceability conditions in the limit States, and this means the prediction system to be carried out for the different problems is needed. Suppose the production system of the settlement was the consolidation is orchid and need to be expected in that case this best estimate value is very useful for the process where the parameters related to the formation of the soil are required and especially with the help of Oedometer test.

3.4 Variance

The uncertainties in the field of soil mechanics are categorized in terms of dissident model for epistemic models and aleatoric model. Inherent variability is a kind of

uncertainty over the physical system involved and where inheritance and intrinsic properties are involved. This is considered to be inherent as well as the reduction is not possible even when the investigation has been carried out at the site. Modelling is to be carried out in terms of the field which is random in nature and the description is possible very effectively with the coefficient of variation as well as the scale which is related to the fluctuation [22].

Epistemic uncertainty is a kind of uncertainty variation in the measurement aeroplane because of the uncertainties which are involved related to the measurement as well as the errors when the modelling process is carried out. So the errors involving this uncertainty can be possibly reduced when the data is bigger in number or the knowledge which is involved in the particular problem has been properly used.

3.5 Coefficient of Variance

Literature survey has been carried out related to the estimation of the inherent behaviour of the soil with the variability process where the error is involved in the measurement. From the literature, it can be observed that the coefficient of variance for the case of inherent variability particularly in the situation of the sand is considered to be higher in nature when the comparison is carried out for the case of clay. When the type is considered to be of the measurement in that case for efficient of variance for the case of inherent variability found to be almost negligible particularly where the situations related to the parameters of index. The maximum or the highest coefficient of variance in case of variability which is inherent in nature found to be even the measurement system is carried out for the direction horizontal in nature or the measurement where soil modulus is involved.

The parameter uncertainty is present in some of the cases while the uncertainty letter to the observation also is present in that case the process of estimation related to the uncertainty in the model becomes complex. Research for the uncertain behaviour has been studied properly with the help of different parameters as well as the uncertainties of the model studied. The model is related to the Bayesian concept where the definition of the different ranges is to be given for the case of model uncertainty where the judgement is involved in the engineering knowledge while the update for the knowledge is important [9].

4 Correlations

The correlation system for the case of shear strength as well as the different parameters is related to the soil behaviour where the proper empirical correlations are very important. The correlation in terms of empirical form has been founded in the many research areas related to Geotechnical engineering. The prediction of the

different properties related to geotechnical engineering has been studied by different researchers [2].

The relationship between the case of shear strength related to the soil and plasticity index has been studied by the researcher. This relationship is obtained as the plasticity index as well as the parametric shell strength is related to the composition of the soil and mainly for the clay. Is observed that when the clay content is to be increased, then the increase in the plasticity index has been found out but there is a decrease in the strength of the shear [8].

The research is carried out for the case of obtaining the relationship between content of fine and cohesion when the analysis is carried out in the laboratory for the sample specimen which is of laterite soil. To obtain the relationship, the procedure involves separating fine component from the course portion and preparing remoulded soil specimen of different ratio. Mehandi specimens have been tested for the unconsolidated undrained triaxial test from which the parameter of the shear strength has been determined [5].

The research has been carried out for the properties of the soil; the role of files has been studied. This research was the experiment of being carried out so that the experimental results are obtained and the relationship has been obtained for fine contents as well as internal friction angle particularly for the soil which is laterite. The empirical relationship has been obtained for this parameter where the specimen has been analysed in the laboratory for the state which is natural in nature as well as the property of the index has also been determined. To obtain this relationship, the content of the files has been separated from the components of the quotes related to the soil and then specimen has been removed late in the ratio which is kept wearing. Specimen of soil is then subjected to the triaxial test so that the determination of the parameter for social strength has been obtained [10].

5 Research Problems

The application of artificial neural network in different fields proved to be fruitful however its application in the field of soil mechanics is not up to the mark. There are certain issues related to the modelling in the artificial neural network and need to have the proper attention so that the different parameters involved for this model and that involves robustness transparencies as well as the extraction of the knowledge while uncertainties are also involved apart from extrapolation [24]. The proper approach has to be carried out so that the factors can be studied for the determination in the different parameters in the case of models where the input data as well as the preprocessing of such model while the network architecture is to be studied. Apart from that, the internal parameters have to be selected properly so that they can be controlled in the method where the optimisation can be obtained. The validation related to the model is very important.

5.1 Model Robustness

Model robustness is considered to be the ability related to the artificial neural network so that the generalization is obtained in the case of data where the similarity is also there for training of the model. Some of the researchers have found that the performance of this model where the data is to be used so that the calibration of the model is also carried out apart from that validation is not suitable for these models. Since the models can be performed very well, the range of the data is related to the model where the calibration process is used. The analysis of the sensitivity is important so that the investigation and the response of the model related to the artificial neural network for the output as well as the input have the proper relationship [22]. The robot nest related to the model needs to be determined properly what the predictions of the model are in correlation with the process of the problem whether the input has good range.

5.2 Model Transparency and Knowledge Extraction

Transparency in the model as well as the extraction procedure of the knowledge is possible so that the interpretation from the model of the artificial neural network will be very good and inputs related to the model may have effects on the output. The mathematical modelling with the involvement of the colour coding is obtained, and then, it can be classified into white model and black model apart from grey box model. White box model is a system where the first principle is involved related to the physical or where the variables of the models as well as the parameters of the model are the known parameters while relationship can be used.

5.3 Model Extrapolation

Extrapolation of the model is considered to be the ability of the model of the artificial neural network which can have the prediction even when the range of the data is not available for the case of calibrating the model [25]. Some of the results have carried out research related to the transformation model so that the artificial neural network is used for the prediction of the values when a river flows which is peak in nature. The methodology used is very good for the system of prediction when the data is transformed when compared with the untransformed data.

6 Conclusion

The literature has been studied related to the use of artificial neural network in the case of calculating the strength of the soil. There are numerous problems faced by the geotechnical engineer to calculate the strength accurately. It is found that there are many advantages in the use of ANN as compared to the traditional methods. It is found that this method is very suitable for the results in terms of shear strength, unconfined strength, swell index and characteristics of the compaction. The used ANN can lead to the reduction in the efforts as well as the time required to predict and calculate the strength.

References

1. Abu-Farsakh MY, Mojumder MAH (2020) Exploring artificial neural network to evaluate the undrained shear strength of soil from cone penetration test data. Transp Res Rec 2674(4):11–22
2. Dungca JR, Galupino JG (2017) Artificial neural network permeability modeling of soil blended with fly ash. Geomate J 12(31):77–82
3. Erzin Y, Rao BH, Patel A, Gumaste SD, Singh DN (2010) Artificial neural network models for predicting electrical resistivity of soils from their thermal resistivity. Int J Therm Sci 49(1):118–130
4. Erzin Y, Gumaste SD, Gupta AK, Singh DN (2009) Artificial neural network (ANN) models for determining hydraulic conductivity of compacted fine-grained soils. Can Geotech J 46(8):955–968
5. Ferreira EC, Milori DMBP, Ferreira EJ, Da Silva RM, Martin-Neto L (2008) Artificial neural network for Cu quantitative determination in soil using a portable laser induced breakdown spectroscopy system. Spectrochimica Acta Part B: Atomic Spectrosc 63(10):1216–1220
6. Hanandeh S, Ardah A, Abu-Farsakh M (2020) Using artificial neural network and genetics algorithm to estimate the resilient modulus for stabilized subgrade and propose new empirical formula. Transp Geotech 24:100358
7. Kalantary F, Kordnaeij A (2012) Prediction of compression index using artificial neural network. Scien Res Essays 7(31):2835–2848
8. Keshavarzi A, Sarmadian F, Omran ESE, Iqbal M (2015) A neural network model for estimating soil phosphorus using terrain analysis. The Egyptian J Rem Sens Space Sci 18(2):127–135
9. Kiran S, Lal B (2016) Modelling of soil shear strength using neural network approach. Electron J Geotech Eng 21(10):3751–3771
10. Mozumder RA, Laskar AI (2015) Prediction of unconfined compressive strength of geopolymer stabilized clayey soil using artificial neural network. Comp Geotech 69:291–300
11. Bunyamin SA, Ijimdiya TS, Eberemu AO, Kolawole JO (2018) Artificial neural networks prediction of compaction characteristics of black cotton soil stabilized with cement kiln dust. J Soft Comput Civ Eng 2(3):50–71
12. Ozturk M, Salman O, Koc M (2011) Artificial neural network model for estimating the soil temperature. Can J Soil Sci 91(4):551–562
13. Sungheetha A, Sharma R (2021) Fuzzy chaos whale optimization and BAT integrated algorithm for parameter estimation in sewage treatment. J Soft Comput Paradigm (JSCP) 3(01):10–18
14. Lin C-J, Nan-Jing W (2021) An ANN model for predicting the compressive strength of concrete. Appl Sci 11(9):3798
15. Karthigaikumar P (2021) Industrial quality prediction system through data mining algorithm. J Electron Inf 3(2):126–137

16. Pratibha C, Reddy KM, Bharathi L, Manasa M, Gandhiraj R (2019) Simulation of dual polarization radar for rainfall parameter and drop size distribution estimation. In: International conference on ıntelligent computing, ınformation and control systems. Springer, Cham, pp 424–433
17. Salahudeen AB, Sadeeq JA, Badamasi A, Onyelowe KC (2020) Prediction of unconfined compressive strength of treated expansive clay using back-propagation artificial neural networks. Nigerian J Eng 27(1)
18. Priyadarshee A, Chandra S, Gupta D, Kumar V (2020) Neural models for unconfined compressive strength of Kaolin clay mixed with pond ash, rice husk ash and cement. J Soft Comput Civ Eng 4(2):85–102
19. Ali B, Rahman MA, Rafizul IM (2016) Prediction of California bearing ratio of stabilized soil using artificial neural network. In: Proceedings of the 3rd ınternational conference on civil engineering for sustainable development (ICCESD 2016)
20. Salahudeen AB, Sadeeq JA (2019) California bearing ratio prediction of modified black clay using artificial neural networks. In: Book of proceedings, West Africa built environment research (WABER) conference, Accra, Ghana, pp 268–281
21. Vakili AH, Davoodi S, Arab A, Selamat MR (2015) Use of artificial neural network in predicting permeability of dispersive clay treated with lime and pozzolan. IJSRES 3(1):23–37
22. Pham BT, Nguyen MD, Bui KTT, Prakash I, Chapi K, Bui DT (2019) A novel artificial intelligence approach based on multi-layer perceptron neural network and biogeography-based optimization for predicting coefficient of consolidation of soil. Catena 173:302–311
23. Rao RMP, Rao HS (2012) Prediction of compressive strength of concrete with different aggregate binder ratio using ANN model. Int J Eng Res Technol 1(10):1–10
24. Park HI, Kim YT (2011) Prediction of strength of reinforced lightweight soil using an artificial neural network. Eng Comput
25. Shahin MA, Jaksa MB, Maier HR (2001) Artificial neural network applications in geotechnical engineering. Australian Geomech 36(1):49–62

Rheological and Tribological Characterization of Completely Biogenic Grease

Ravikiran, Srikara Kundargi, S. L. Aravind, V. M. Akhil, and R. Madhusudhana

Abstract Grease plays a major and a vital role in lubrication of bearings and also acts as an effective sealant. In the current situation, depletion of mineral oils and its adverse effects on environment demand a cleaner, cheaper, and a reliable source for grease. The biodegradable grease which is prepared from various biodegradable raw materials is being developed and tested for its usage in lubrication. Various bio-grease has been developed using bio-oils like castor and palm and many more oils and metallic soaps as thickeners. The research for completely bio-grease is going on. Sorbitan monostearate currently used extensively in cosmetic and food industry is used as thickener along with various base oils, to obtain an edible grease. The grease has been extensively used in bearings both as lubricant and a sealant, being a shear thinning fluid it is very much important to take a note of shear thinning rate of the grease. This work emphasizes on preparation of biogenic grease, rheological characterization of the prepared greases for shear thinning behavior.

Keywords Bio-grease · Rheological fluid · Shear thinning

1 Introduction

It has been ages we are using machines, and for the smooth working of it, we require a substance to reduce friction between surfaces in mutual contact. Friction is the factor which is responsible for the wear and tear of machine elements, heat generation, etc., which should be avoided for long and smooth running of machine, for which a lubricant is used. Lubricants can be solid, liquid, dry film, and coating [1]. Vegetable oils and animal fat were largely used as a lubricant for centuries until the discovery of mineral oils. The low price and better properties, the market for mineral oil-based grease started growing. This growth accelerated during the industrial revolution. The use of grease as a lubricant can be dated back to 2400 BC, where wet sand was used to move a large statue [2]. The wheel and axle of Hittite chariot which dates back to 1400

Ravikiran (✉) · S. Kundargi · S. L. Aravind · V. M. Akhil · R. Madhusudhana
The National Institute of Engineering, Mysuru, India
e-mail: nayak.ravikiran@gmail.com

K. Geetha et al. (eds.), *Recent Trends in Materials*, Springer Proceedings in Materials 18, https://doi.org/10.1007/978-981-19-5395-8_12

BC had been lubricated with a mixture of tallow and limestone, which can be stated as an early form of grease [3]. Vegetable oils, animal fat, and bio-based materials were used as lubricants for 4000 years, but in second half of nineteenth century these materials were replaced by mineral and synthetic oil-based grease [4]. The thermal stability and viscosity index of synthetic or mineral oil-based greases were high, and this promised a better performance than the bio-grease. But the developments in automotive and industrial sector have maximized the use of lubricants, and therefore, the synthetic and mineral oil-based grease have posed a threat to the environment.

Greases are used from 2400 BC, and it is extensively used till date for the lubrication purpose. Grease is a thickened oil which consists of thickener, base oil, and some additives that improves tribological properties and shelf life of grease. The base oil acts as a matrix in which the thickener is dispersed. The base oils are usually mineral oils, synthetic oils, or any other oil which provides lubricating properties. The use of biodegradable greases dates back to 2400 BC, where Egyptians used water and sand mixture to transport stones and gradually biodegradable greases had been taken over by mineral and synthetic oils. Some of the synthetic base oils used are poly-alpha-olefin, poly-iso-butene, poly-alkylene-glycol, perfluoropolyether, silicones, and some synthetic esters. The resistance to oxidation shown by these oils was very high and guaranteed a good life for grease. The thickeners which were used were calcium sulphonate, poly-urea, lithium complex, calcium complex, polyamides, and many more. The synthetic grease promised high thermal stability and high viscosity index. Though synthetic greases promised excellent properties, these appeared as a threat to the environment. The growth of industries and mobility increased dumping rate which posed a threat to soil and aquatic life. The move towards biodegradable and renewable resources has made the market for biodegradable grease.

Major portion of the lubricants consumed worldwide ends up polluting the environment as they are toxic, posing a threat to soil and aquatic life. The price and supply fluctuation in petroleum products caused due to the oil crisis in 1973 and oil crisis in 1979. These crises made the world to look for an alternative of crude oil [5]. The biodegradable lubricants have a very narrow market, but they find applications in food industry lubricants, marine oils and outboard engine lubricants, oil for underground pumps, tractor oils, agriculture, shock absorber lubricants, open gear oils, biodegradable grease, and hydraulic fluids. Yearly 5 million tons of hydraulic oils are used in the United States, and this huge amount calls for the use of biodegradable lubricants [6]. Though synthetic and mineral oil-based grease were with better advantages, government agencies and the researchers emphasized on using bio-based lubricants by only considering the environmental issues. At present, even the consumers are thinking about the negative impacts while buying the lubricants. Food and agricultural industry also demand a less toxic lubricant. Therefore, there is a move towards less toxic, biodegradable, and renewable lubricants [7]. Industries are trying to formulate a bio-based grease which have superior characteristic compared to the mineral oil-based grease. Nowadays, there are many works on biodegradable grease, and we are trying to move back to the older lubrication methods. Palm grease has been employed in many industries like agriculture, forestry, construction, and many other industries which demands for an ecofriendly lubricant [8]. The use of tri glyceride grease is

already found in Germany [9]. The palm-based greases have shown better tribological properties as they contain polar groups [8]. There are many works in which vegetable oils have been used as base oil and, lithium soaps and some biogenic materials as thickeners. In this work, grease is prepared using castor oil, jatropha oil, and blend of both oils as base oil, Sorbitan Monostearate as thickener, and Zinc Dialkyldithiophosphate as thickener which is a good antioxidant. The shear thinning property was studied using rheometer in rotary mode, and the discussion is carried out. The tribological characterization of the grease was carried out using fourball tester. The anti-wear properties induced by the additives were also tested.

2 Literature Review on Bio-grease

Present works on biodegradable grease focus on use of biodegradable base oils. These oils include vegetable oils such as palm oil, high oleic sunflower oil (HOSO), and castor oil. The palm greases are extensively used in industries like forestry, agriculture, construction, and other industries which deal directly with the environment. Many works have been done on palm oil and using lithium or calcium soaps as thickeners. These greases provide better lubricating properties than synthetic grease while using a smaller amount of thickener. This can be accounted to the presence of polar functional groups like hydroxides, oxirane ring, besides the ester functional group. The other edible oil which can be used for production of grease was black date seed oil. In one of the works, grease was prepared using black date seed oil as base oil and calcium hydroxide and steric acid as thickeners and it was also mentioned that the prepared grease showed better lubricating properties than the commercial grease [10]. Though the black date seed oil was renewable, but the production required high amount of effort and cost. In other works, grease was prepared using chemically modified vegetable oil as base oil. This modification was done by transesterification or epoxidation reaction. The thickener used here was lithium-12-hydroxysterate. Results show that the grease produced had higher load carrying capacity and good tribological properties under extreme pressure when compared to petroleum-based grease [11]. There are many works in which jojoba oil is used as base oil and metallic soaps as thickeners. There are few works where jatropha oil used as base oil with metallic soap thickeners. Ponnekanti Nagendramma and Prashant Kumar have used jatropha oil and jatropha residual oil as base oils and lithium-12-hydroxystearate and lithium oleate as thickeners and conveyed that residual jatropha oil with lithium oleate showed better tribological properties.

Biodegradable grease produced from metallic soaps was not completely biogenic; a grease is called completely biogenic when both base oil and thickener used are biodegradable. Sorbitan monostearate (SMS) is a biodegradable thickener, and SMS can be ingested by an animal in large amount which does not cause any health hazards. Completely biogenic grease was prepared using SMS and castor oil, optimum thermo-mechanical processing parameters of the grease were investigated, and it was mentioned that the prepared grease exhibited better tribological properties, though the

mechanical stability of grease was less [7]. In one of the works, grease was prepared using castor oil as base oil and epoxidized cellulose pulp as thickener. Various ethers were used for epoxidation. The grease formed showed excellent thermal stability and no appreciable change in viscoelastic functions. The thickener was also able to protect the metal surface from wear [12]. In another alternative of preparation of biodegradable grease, grease was prepared using organic thickeners like polypropylene, chitosan, and cellulose, and base oil used was castor oil. The grease produced had high consistency but poor thermal stability [13]. The other alternative which was exploited was a grease prepared using castor oil as base oil and ethylated cellulose as thickener. The thickener was formed by ethylation of Kraft bleached cellulose, and the stability and the rheological properties of the bio-grease prepared were satisfactory. In some works, ethylated cellulose and castor oil were combined to form a medium; then, at room temperature methylated cellulose was added and mixture was homogenized. But the mechanical stability shown by methylcellulose-based gel-like dispersion was reported to be poor [14]. Many works reported other biogenic thickeners. The base oils used were high oleic sunflower oil, castor oil, and a mixture of high oleic sunflower oil and castor oil. Thickeners like mixture of beeswax, glyceryl monostearate, and cetyl alcohol, mixture of glyceryl monostearate, cetyl alcohol, and sorbitol monostearate, mixture of cellulose ether and glycerin, isoprene derivatives, lignosulfonate, natural cellulose fibers 18 μm, corncob grits 80–120 μm, natural cellulose 20–40 μm, natural wood pulp from soft wood 70–150 μm, mixture of lignin and polyethylene glycol diglycidyl ether (PEGDGE), and a mixture of lignin and hexamethylene diisocyanate (HMDI) were used. It was reported by the works that these completely biogenic greases showed better tribological and rheological properties [15].

The decline in mineral oil supply and also the hazards caused by synthetic grease have opened a new avenue for biodegradable grease. The growth in food processing industries has added a necessity for providing an edible and completely biogenic grease. Therefore, this work focuses on synthesis of completely biogenic grease and evaluation of the grease using tribological and rheological characterizations [16, 17].

3 Material Preparation and Characterization

Grease is a thickened oil which consists of thickener, base oil, and some additives that improves tribological properties and shelf life of grease. The base oils used in the samples are castor oil, jatropha oil, and blend of both castor and jatropha oils. The oils were procured from the local market. The thickener used was Sorbitan Monostearate Span 60, and Zinc Dialkyldithiophosphate was used as thickener for antioxidant properties. Table 1 gives the composition of the samples.

All six samples were analyzed for their viscosity in Megapascal (MPa) using Anton Paar MCR 102 rheometer in rotational mode at room temperature. The shear rate was increased logarithmically from 0.997 to 1000, and corresponding shear stress and the viscosity were measured.

Table 1 Composition of the sample grease prepared

Heading level	Font size and style
Sample1	Jatropha + castor (1:1) (72%), SMS (25%), ZDDP (3%)
Sample 2	Castor (72%), SMS (25%), ZDDP (3%)
Sample 3	Jatropha (72%), SMS (25%), ZDDP (3%)
Sample 4	Castor + jatropha (1:1) (75%), SMS (25%)
Sample 5	Castor oil (25%), SMS (25%)
Sample 6	Jatropha oil (75%), SMS (25%)

The microstructure of prepared grease samples was analyzed under scanning electron microscope (SEM). The SEM images were obtained for samples using SEM–EDS analyzer (Make: TESCAN, Model: VEGA SBH).

The anti-wear properties and the coefficient of friction were evaluated using four-ball wear tests. The grease was tested at room temperature, under the load 40 ± 0.2 kgf, with ball rotating at speed of 1200 ± 60 rpm, and the time duration for the test was 60 min.

4 Results and Discussions

4.1 Morphological Analysis

Figure 1 shows the different microstructure of prepared grease samples. The microstructure of prepared grease samples was analyzed under scanning electron microscope (SEM). The sample 3 and sample 6 that is grease prepared with jatropha oil and SMS were a homogenous grease and its microstructure is shown in Fig. 1a, b, respectively. The sample 2 and sample 5 that is the grease prepared using castor oil do not have a homogenized structure due to the agglomeration. Due to the increased time of heating and speed of stirring, we could obtain better homogenous grease. The grease prepared from blend of oils has some agglomerates present, as shown in Fig. 1c and d respectively.

4.2 Tribological Analysis

Table 2 gives the results of four ball wear test. Castor oil with SMS and ZDDP sample gives the lowest wear rate. The blend of castor oil and jatropha oil gives highest wear rate as this can be related to the non-miscibility of the oils which leads to a less viscoelastic grease which is very weak both in consistency and gives a high rate of wear. The grease prepared from jatropha oil has intermediate wear.

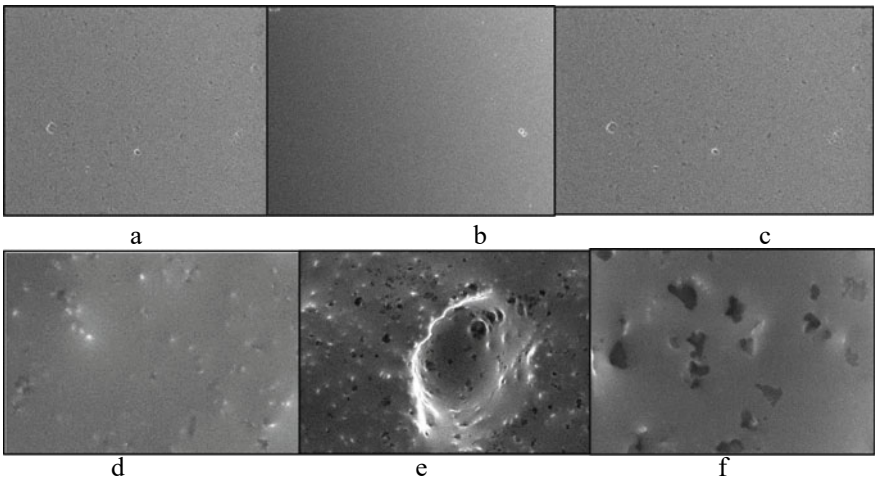

Fig. 1 SEM images of grease samples. **a** Sample 3, **b** sample 6, **c** sample 1, **d** sample 4, **e** sample 2, **f** sample 5

Table 2 Four ball wear test results

Sample	Wear scar diameter in micrometer	Coefficient of friction
Sample 1	615.8	0.095
Sample 2	511.8	0.08
Sample 3	581.8	0.09
Sample 4	630.9	0.095
Sample 5	534.7	0.089
Sample 6	594.5	0.090

4.3 Rheological Test

Figure 2 shows the characteristic shear thinning curve of all six samples. The sharp increase in the shear thinning rate of the samples depicts the instability of thickener to hold the base oil at that increased shear rate. The sample 3 showed an initial high viscosity at 0.997/s shear rate but gave a sharp decline further, which shows the instability of thickener to hold base oil. The viscosity changes at the initial shear rate for sample 3 and sample 6 are due to the additive ZDDP. The similar trend can be noticed in other samples too.

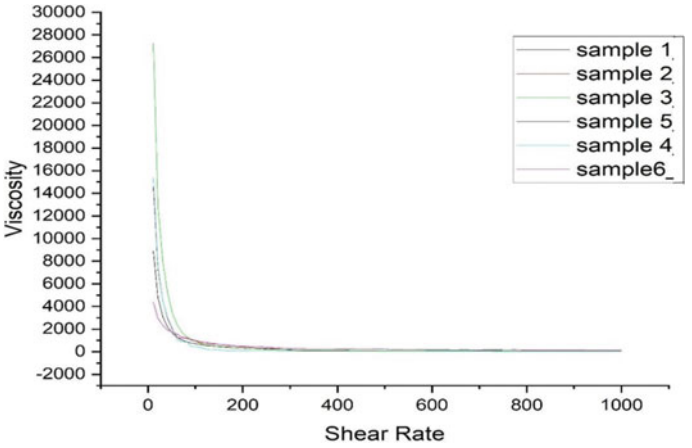

Fig. 2 Viscosity versus shear rate graph depicting shear thinning effect

5 Conclusion

The morphological analysis was done on the prepared grease samples, grease prepared from castor oil had agglomerates, and increasing heating time and stirring speed can increase homogeneity. The grease prepared from jatropha oil was more homogenous. The grease prepared from castor oil and SMS with additive ZDDP showed better anti-wear among other samples. The ZDDP was added as additive for better anti-wear and antioxidant properties. The grease samples with ZDDP showed better anti-wear properties. The prepared greases are highly unstable at higher shear rates which can be observed from the above curves. The sharp increase in shear thinning also affects the functionality of the grease to act as a sealant in the bearing. The effect of additive can also be noticed which gave high viscosity at initial shear rate, but there was no effect on shear thinning of the grease. Therefore, the prepared bio-grease can be used in the applications of lower amount shear rates.

References

1. Grease glossary. https://www.nlgi.org/grease-glossary
2. Hekkenberg A. Ancient Egyptians transported pyramid stones over wet sand. http://phys.org/news
3. History of grease. http://www.kyodoyushi.co.jp/english/grease
4. Kumar A, Mallory B (2013) How friendly are bio based grease with other grease. NLGI Spokesman 77(2):34–47
5. Sharma UC, Singh N. Biogreases for environment friendly lubrication
6. Padavich RA, Honary L (1995) A market research and analysis report on vegetable based industrial lubricants. Soc Automotive Eng Tech Pap 952077

7. Sánchez R, Franco JM, Delgado MA, Valencia C, Gallegos C. Effect of thermomechanical processing on the rheology of oleogels potentially applicable as biodegradable lubricating greases
8. Sukirno RF, Bismo S, Nasikin M. Bio grease based on palm oil and lithium soap thickener-evaluation of antiwear property
9. Abel WD. Rapidly biodegradable greases for switches. In: Proceedings of the 11th international colloquim tribology, Esslingen, Germany, 17–19 Jan 1998
10. Awoyale AA, Odubiyi OA, Eloka-Eboka AC. Production and testing of biodegradable grease from black-date (Canariumschweinfurthii) oil
11. Panchal TM, Patel A, Chauhan DD, Thomas M, Patel JV. A methodological review on bio-lubricants from vegetable oil-based resources
12. Cortés-Triviño E, Valencia C, Delgado MA, Franco JM. Thermo-rheological and tribological properties of novel bio-lubricating greases thickened with epoxidized lignocellulosic materials
13. Japar NS, Aziz MA, Razali MN, Zakaria NA, Rahman NW. Preparation of grease using organic thickener
14. Martín-Alfonso JE, Núñez N, Valencia C, Franco JM, Diaz MJ. Formulation of new biodegradable lubricating greases using ethylated cellulose pulp as thickener agent
15. Acar N, Kuhn E, Franco JM. Tribological and rheological characterization of new completely biogenic lubricating greases: a comparative experimental investigation
16. Pirro W (2001) Lubrication fundamentals. Marcel Dekker, New York
17. U.S. Army Corps of Engineers. Engineering and design—lubricants and hydraulic fluids. EM 1110-21424 CECW-ET, 1999

Piezoelectric Energy Harvesting from Automotive Wheels

Vaishak, Roopa Manjunatha, and G. L. Manjunath

Abstract The need for energy harvesting technology is steadily growing in the field of self-powered sensor systems for intelligent wheels. This paper has proposed a piezoelectric sensor-based energy harvester that can supply energy to low-powered sensors embedded in the intelligent vehicle wheels. The next generation of cars will be equipped with different kinds of integrated sensors for facilitating advanced driver assistance systems (ADAS) and autonomous driving (AD). The wheel spoke-mounted piezoelectric energy harvester proposed in this paper can convert rotating mechanical energy to electrical energy and can be used for charging the battery. Simulation experiments were carried out using MATLAB-Simulink for a speed range of 20–120 km/hr and the harvested energy is used to charge a lead–acid battery with an initial state of charge of 60% and 8 V. From the results, it is observed that from 60 km/hr onwards sufficient power is harvested, which can be used to charge a 12 V lead–acid battery. At a speed of 120 km/hr, the state of charge of the battery increases to 61.31% in just 10 s of charging time, and battery voltages increase to 9.263 V. This shows enough power required to charge a 12 V lead–acid battery is harvested by the wheel spoke-mounted piezoelectric energy harvester proposed in this paper. The results demonstrate that the proposed piezoelectric energy harvester can be used as an energy source to power the low-consumption sensors embedded on the intelligent wheels after making minor improvements.

Keywords Energy harvesting · Intelligent wheels · Piezoelectric sensor · State of charge · Wheel spokes

Vaishak · R. Manjunatha (✉) · G. L. Manjunath
Energy Institute Bengaluru (A Center of Rajiv Gandhi Institute of Petroleum Technology), Bengaluru, Karnataka 560064, India
e-mail: rmanjuntha@rgipt.ac.in

Vaishak
e-mail: 20eb1ev07@rgipt.ac.in

G. L. Manjunath
e-mail: glmanjunath@rgipt.ac.in

K. Geetha et al. (eds.), *Recent Trends in Materials*, Springer Proceedings in Materials 18, https://doi.org/10.1007/978-981-19-5395-8_13

1 Introduction

Autonomous vehicles and electric vehicles have received greater attention and development in recent years. These vehicles are equipped with more comprehensive sensing systems to sense the environment and to track the status of driving [1].

Wheels are the principal component determining the driving safety as they are in direct contact with the road surface [2]. Wheels of the autonomous vehicles will be equipped with some sensors which can obtain different parameters like tire pressure [3], deformation [4], torque [5], slip angle [6], etc., based on different principles like piezoelectric [6], magnetic [7], capacitive [8] and so on. These tires can provide important information to vehicle control systems and to driver. Attaining a perfect adjustment in the parameters is difficult [9]. At present, tires mounted with pressure sensors are only available [10]. This shows that the absence of an appropriate source for energy is hindering the development and applications of so-called intelligent wheels [3]. To address demand in energy needs, network expansion planning is an optimal method [11].

Proposed energy harvesting innovation makes it possible to overcome the challenges in the development of intelligent wheels. This proposed energy harvester converts the mechanical energy of wheels to electrical energy. Due to the advancements in technology, the necessity of energy harvesting gained importance [12]. Energy harvesting is a process that captures small amounts of energy that would otherwise be lost as vibrations, heat etc.

Recently, many piezoelectric polymers were launched. However, none of them demonstrated the piezoelectric properties as good as polyvinylidene fluoride (PVDF). PVDF is having a high tensile strength in the category of all processable hydrocarbons and thus found applications in the manufacturing of piezoelectric materials. Usage of PVDF in piezoelectric materials is having many advantages such as wide frequency response, high power to electricity conversion efficiency, and high mechanical strength. These materials are having a good yield strength of 50 MPa and Young's modulus of 4.18GPa [13].

A large number of literature on vibration and rotational energy harvesting are available. These studies are based on the principles of piezoelectric [14], magnetic [15], and on nano-generators [16]. The majority of these studies focused on the tire.

Eight units of compressible hexagonal structured triboelectric nanogenerators were used by Guo et al. [16] and obtained power of 1.9 mW. Lee et al. [17] embedded piezoelectric material onto the inner surface of the tire to obtain 1.37 $\mu W/mm^3$ power density. Energy harvester designed by Maurya et al. [18] generated maximum power of 580 μW using polyvinylidene fluoride (PVDF) material. Project reports by European APOLLO tires [19] advise not to use any sensors and equipment inside tires due to the increased rolling movements. The compatibility of the sensors and durability issues are also needed to be considered.

Apart from usual tire-mounted energy harvesters, researchers suggested energy harvesters mounted on the rim. Wang et al. [20] developed an electromagnetic energy harvester with frequency matching with the rotational frequency. But the usage of

magnets leads to certain drawbacks such as they may attract nails and other debris on roads, which may lead to punctures or accidents.

Collectively, these studies outline the necessity of some energy harvesters for intelligent/smart wheels. Previous Studies have focused more on extra structures between rim and tire, which will lead to balancing issues and is not convenient for easy maintenance. As the proposed wheel spoke-mounted energy harvester is of very lightweight, it can be easily implemented on the vehicles without disturbing the normal working and balancing of the wheels. Hence, the safety and practicability are very much improved as compared to the previous energy harvesters.

Apart from the previous studies, to build a more feasible energy harvester for intelligent wheels, this paper put forward a wheel spoke-mounted piezoelectric energy harvester. In contrast to long-established base exciting cantilever structures, here the base is fixed in wheel spokes. When the vehicle is moving, the cantilever beam is undergoing rotational motion and the free end where mass is attached will undergo upward and downward motion due to gravity. These upward and downward motions will provide excitations to the piezoelectric energy harvester. This proposed wheel spoke-mounted energy harvester will provide a technical basis that helps in the development of intelligent wheels.

2 Methods and Materials

Piezoelectric materials belong to the ferroelectrics category. In this type of material, their molecular structure is oriented in such a way that material exhibits charge separation which leads to the formation of randomly arranged electric dipoles. When this is heated up to a temperature called curie temperature and an electric field is applied, these dipoles will be aligned with respect to an applied electric field. This process is called polling. When the material is cooled, this dipole will maintain its orientation. It is said to be poled and the material will exhibit piezoelectric property, i.e., the ability to generate an electric potential in response to applied stress.

The block diagram of piezoelectric energy harvesting is shown in Fig. 1. The piezoelectric sensor remains in contact with wheel spokes, and these piezoelectric sensors undergo vibrations, and as a result, some alternating voltage will be induced across its terminals. A full-wave diode bridge rectifier circuit is used to convert this induced alternating voltage into pulsating DC waveform. A boost converter is used to improve the voltage value sufficient to charge a 12 V lead–acid battery.

Here, the piezoelectric energy harvesters are mounted on the wheel spokes which is long and thin, in such a way that the width direction is normal to the brake disk. The fixed end will be facing the center of the rim as shown in Fig. 2. As they are mounted on the wheel spokes, proper insulations are required to protect the harvester from dust and water on the road. Some lightweight plastic shielding can serve this purpose. When the vehicle is running, the wheel rotates in a 2D plane around the central axis. Thus, the energy harvester is equivalent to a rotational piezoelectric

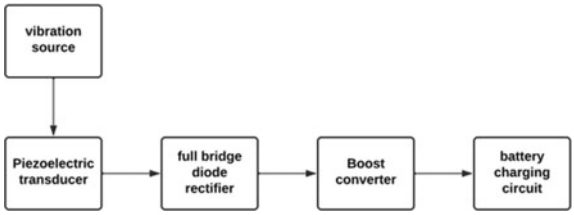

Fig. 1 Block diagram of piezoelectric energy harvesting

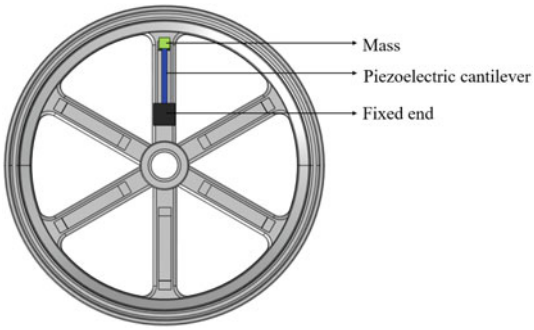

Fig. 2 Proposed wheel spoke-mounted energy harvester

coupling system. It will convert the rotational mechanical energy of the wheel to electrical energy.

3 Matlab Simulation Model

The model of piezoelectric energy harvester is drawn in MATLAB-Simulink as shown in Fig. 3. This model comprises of main five sections.

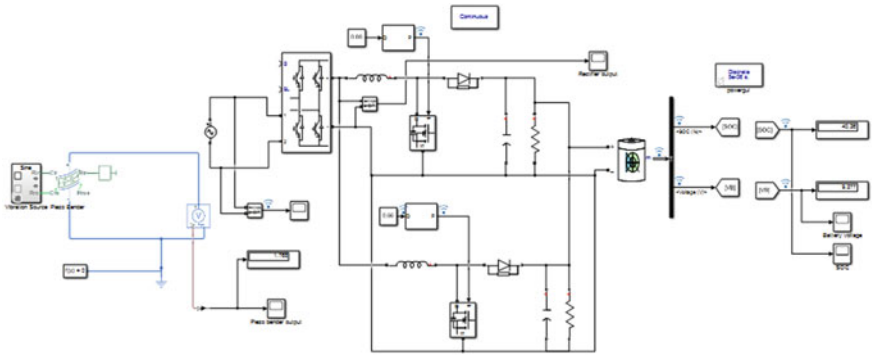

Fig. 3 MATLAB-Simulink model of piezoelectric energy harvesting

3.1 Vibration Source

This subsystem models the vibration from the wheels corresponding to different speeds. The vibration source modeled using MATLAB-Simscape is shown in Fig. 4.

Here, the mechanical rotational reference will act as a reference point for the rotating wheel. Sine wave reference is given for vibratory motion as sinusoidal vibration is the most simple form of vibratory motion.

In a displacement time graph, the gradient of the line is equal to the velocity of the object.

$$\text{Velocity} = \frac{\text{Displacement}}{\text{Time}} \tag{1}$$

$$\text{Displacement} = 2\pi r, \tag{2}$$

where r represents radius of the wheel in meter.

$$\text{Displacement} = \pi D, \tag{3}$$

where D is the wheel diameter in meter.

$$\text{Frequency} = \frac{1}{\text{Time}} \tag{4}$$

Substituting Eq. (1) in (4),

$$\text{Frequency} = \frac{\text{Velocity}}{\pi D} \tag{5}$$

Converting velocity to kmph Eq. (5) changes to,

$$\text{Frequency} = \frac{\text{Velocity}}{3.6\pi D} \tag{6}$$

where

Frequency is the wheel rotational frequency in Hertz

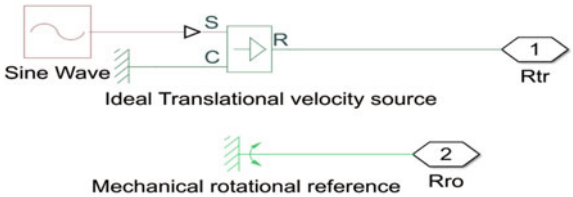

Fig. 4 Simulink model of vibration source

Table 1 Rotational frequencies corresponding to each vehicle speed

Speed in kmph	Rotational frequency in Hz
0	0
20	2.7374
40	5.4748
60	8.2123
80	10.94977
100	13.6872
120	16.42

Velocity is the speed of a vehicle in kmph

D is the wheel diameter in meter.

Considered a vehicle with a wheel diameter of 0.646 m, and the rotational frequencies for a speed range of 0–120 km/h are calculated. Therefore, at the speed of 0–120 km/h, the corresponding wheel rotational frequency range is 0–16.42 Hz. For the vehicle speed of 60 km/h, the corresponding rotational frequency is found to be 8.2123 Hz. The rotational frequencies corresponding to different speeds were shown in Table 1 and are plotted in Fig. 5.

From Fig. 5, it is observed that as the vehicle speed is increasing, the rotational frequency is also increasing, and the vehicle speed and rotational frequency is having a linear relation.

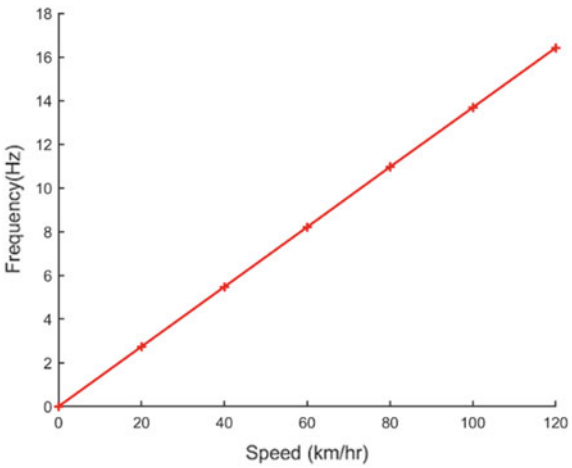

Fig. 5 Vehicle speed is plotted against rotational frequency

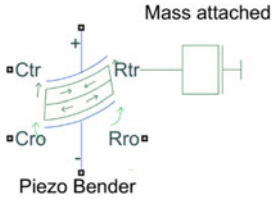

Fig. 6 MATLAB-Simscape model of piezobender with mass attached

Table 2 Specifications of the beam

Design parameter	Specifications
Length of beam (mm)	100
Width of beam (mm)	20
Thickness of beam (mm)	0.2

3.2 Piezobender

A piezoelectric beam of a rectangular cross-section is modeled using the piezobender block. This block is having both mechanical and electrical parts. The piezobender block consists of six ports out of which two are electric ports and the remaining four are mechanical ports.

When an electrical potential is applied to the electrical ports, the piezoelectric bender will bend. Similarly, when mechanical stress or vibrations is applied to the mechanical ports, the corresponding electrical potential will be developed across the electrical ports.

Different layers of piezoelectric materials in rectangular shapes comprise one piezobender, and the polarization direction will be perpendicular to the stack.

The left end of the piezobender is connected to a vibrating object which undergoes motion. The right end of the piezobender is connected to an extra mass as shown in Fig. 6.

Due to the elasticity and inertia of the piezobender, the motion of both ends will not be synchronized. The deformations produce a voltage across the electrical terminals of the piezobender that are harvested into power. While designing the piezobender, block length, breadth, and thickness of beam are taken as 100 mm, 20 mm, and 0.2 mm, respectively. Table 2 shows the specifications of the piezobender.

3.3 Rectifier Block

The output from the piezobender electrical terminals will be alternating in nature. So, a full-wave diode bridge rectifier block is used for converting these alternating signals to pulsating DC. The converter is modeled with IGBT pairs controlled by firing pulses produced by a pulse width modulated (PWM) generator. Snubber capacitance of 1 μF

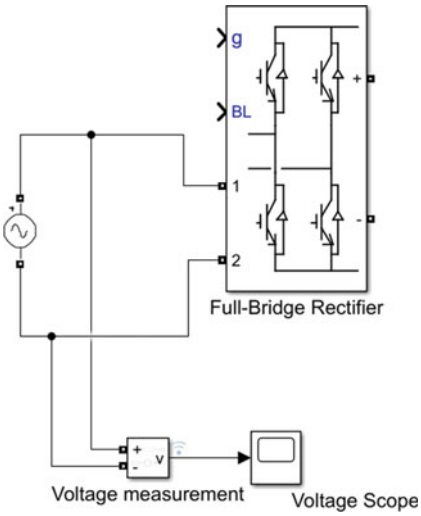

Fig. 7 Simulink model of rectifier block

is used as a filter to smooth the DC voltage. The Simulink model of the rectifier block is shown in Fig. 7.

3.4 Converter Block

The rectified DC output from the rectifier block will not be sufficient enough to charge the battery. So, a converter block is required to amplify the voltage from the rectifier block.

The proposed model uses a boost converter, and the output from the converter block is given to a battery charging circuit. The boost converter is a DC-to-DC converter that steps up the voltage from its input to its output. Here, the output of the rectifier will be the input to the boost converter, and output from the boost converter is given to the battery charging circuit.

DC voltage from the rectifier output terminals is connected to an inductor of 0.00165 H. The solid-state semiconductor MOSFET switch is connected across the source. The second switch used is a diode and is connected to a capacitor of 1.32 nF.

The controlled MOSFET switch is turned ON and OFF by using Pulse Width Modulation (PWM) technique. The duty ratio during designing is considered to be 0.66, and the boosted voltage output is given to the battery circuit and can be used to power the sensors. The Simulink model of the converter block is shown in Fig. 8.

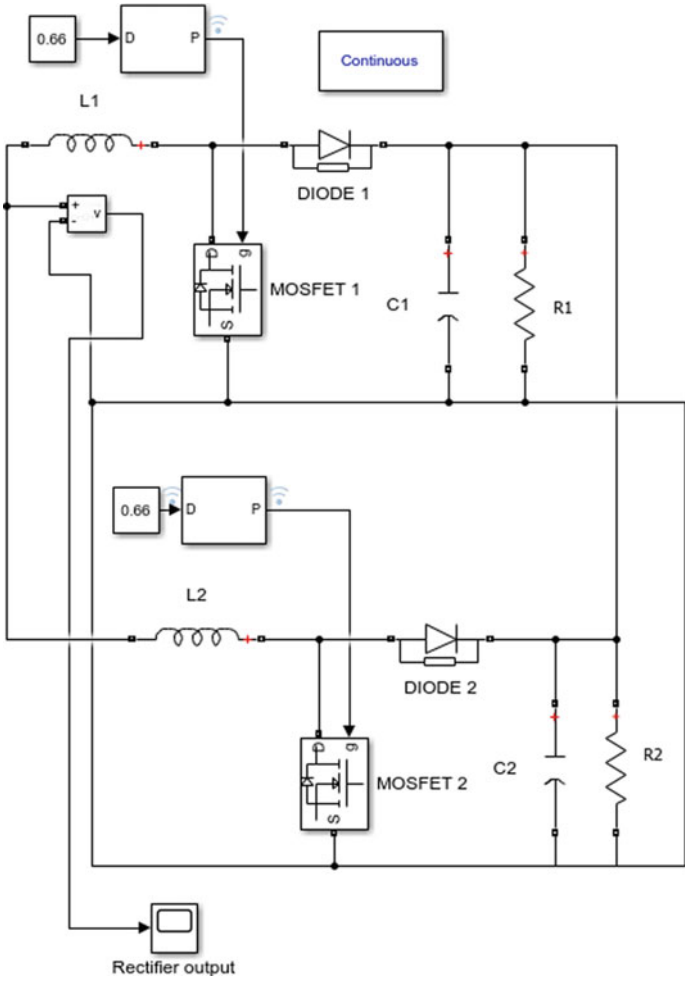

Fig. 8 Simulink model of converter

3.5 Battery Circuit

The energy harvested by the sensor can be used to power the sensors directly, and the unused power after powering these sensors can be stored in a battery or ultra-capacitor. Here, a 12 V lead–acid battery is considered with an initial state of charge (SOC) as 60% and 8 V. The State of charge is defined as the ratio of available capacity to the maximum possible charge that can be stored in a battery; i.e., it is the present capacity of the battery. The harvested energy is used for charging the 12 V lead–acid battery. It is observed that the SOC of the battery increases from 60 to 60.25% in 10 s of charging time. Figure 9 shows the Simulink model of the lead–acid battery

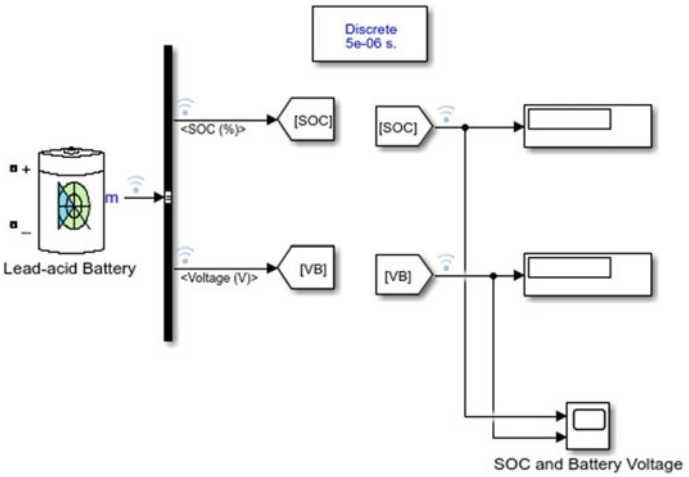

Fig. 9 Simulink model of battery circuit

used with scopes attached for viewing both voltage and SOC of the battery while charging condition.

4 Results and Discussions

The piezoelectric energy harvester is simulated using MATLAB-Simulink. Corresponding to each vehicle speed, the rotational frequency is obtained and is given to the vibration source. For each frequency of vibration given to the mechanical ports of the piezobender, AC voltage waveforms are obtained and are summarized in Table 3.

From Table 3, it is observed that amplitude of output voltage increased with increase in vibration frequency and an amplitude of 5.71 V is obtained for a frequency of 16.42 Hz.

Table 3 Amplitude of AC waveform generated from piezobender

Rotational frequency in Hz	Amplitude of AC waveform in V
0	0
2.7374	0.9405
5.4748	1.8825
8.2123	2.8287
10.94977	3.78
13.6872	4.74
16.42	5.71

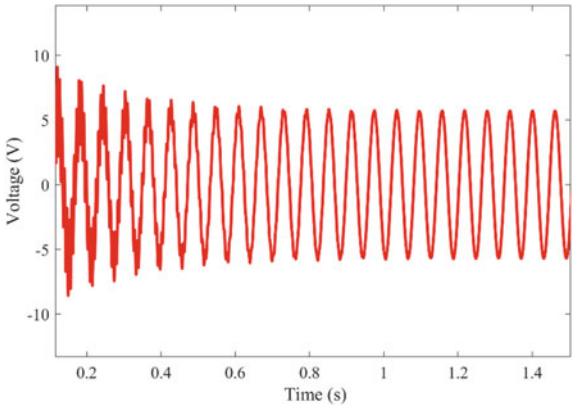

Fig. 10 AC waveform generated from piezobender

The AC waveform obtained from the piezobender for a speed of 100 kmph speed, and 13.6872 Hz frequency is shown in Fig. 10. From Fig. 10, it is observed that a pure sinusoidal waveform is obtained from the piezobender.

The output from the piezobender will be of AC in nature, so it uses a full-bridge rectifier block to convert this AC waveform to DC waveform. Pulsating DC waveform obtained after rectification using a full-bridge rectifier is shown in Fig. 11.

This rectified waveform is given to a DC–DC converter and is given to a 12 V lead–acid battery. The battery with a state of charge of 60% is considered with 8 V and is connected to the converter output. The output from the converter is used to charge the battery, and it is observed that the state of charge and the voltage across the battery is increasing from the initial conditions 8 V and 60% SOC to 8.636 V and 60.43% at a speed of 100 km/hr after 10 s of charging. The state of charge and voltage across the battery is plotted against time in Figs. 12 and 13, respectively. From Fig. 12, it is observed that, State of charge of the battery is rising from an initial SOC of 60% and crosses 60.25% and is still increasing which shows the battery is

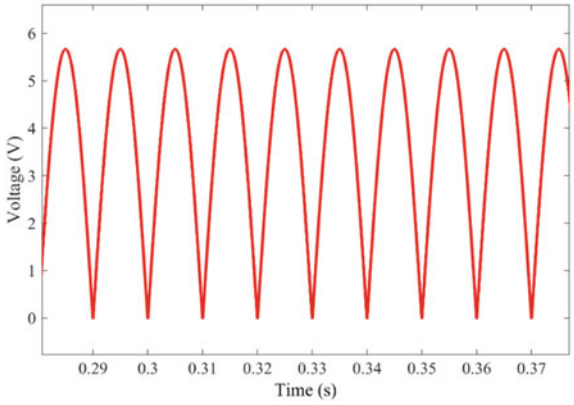

Fig. 11 Pulsating DC waveform after rectification

getting charged from the harvested energy. From the voltage waveform shown in Fig. 13, it is observed that voltage is increasing from the initial 8 V considered.

The voltage developed and the SoC of the battery for different vehicle speeds after 10 s of charging time is shown in Table 4.

The initial voltage reference is taken as 8 V, and the voltage of the battery during different vehicle speeds is shown in Fig. 14. Up to a speed of 60 km/hr, the generated voltage will not be sufficient enough to charge the 12 V lead–acid battery. It is observed that from 60kmph the battery is getting charged. And, the voltage rises to 9.263 V at a speed of 120 kmph and after 10 s of charging. From Fig. 15, it is observed

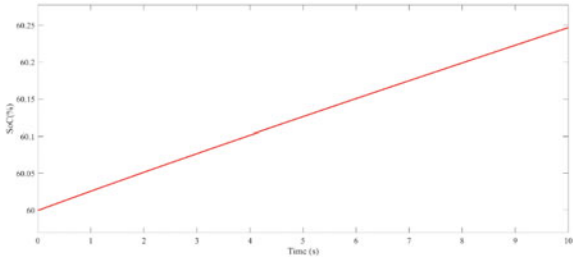

Fig. 12 SoC across battery while charging

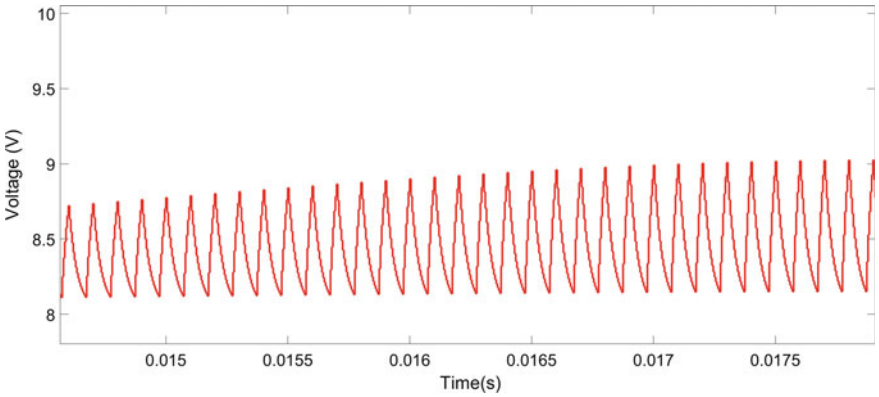

Fig. 13 Voltage across battery while charging

Table 4 Voltage and battery SoC corresponding to each vehicle speed after 10 s of charging time

Vehicle speed	Voltage	SoC in percentage
20	7.869	60
40	7.899	60
60	8.043	60.01
80	8.397	60.12
100	8.636	60.43
120	9.263	61.31

that from a speed of 60 km/hr onwards the SOC of the battery is increasing. That, is from 60 km/hr onwards the power generated will be sufficient enough to charge the 12 V lead–acid battery. The SOC reference is considered as 60%, and when the vehicle reaches a speed of 60 kmph and above, the SOC is increasing from initially considered 60%.

The effect of changing load resistance on the output power is investigated, and it is found that maximum power transfer occurs at a load resistance of 130 kΩ. The simulation part used to calculate the power output is shown in Fig. 16 and the power output corresponding to each vehicle's speed from 0 to 120kmph at an interval of 20 kmph is shown in Table 5 and is plotted in Fig. 17. From Fig. 17, it is observed that, as the vehicle speed is increasing, the power generated is also increasing and reaches 12.84 mW for a speed of 120kmph.

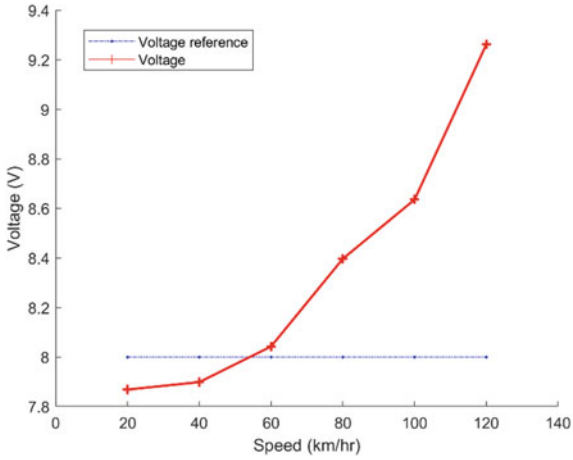

Fig. 14 Vehicle speed and the corresponding voltage developed

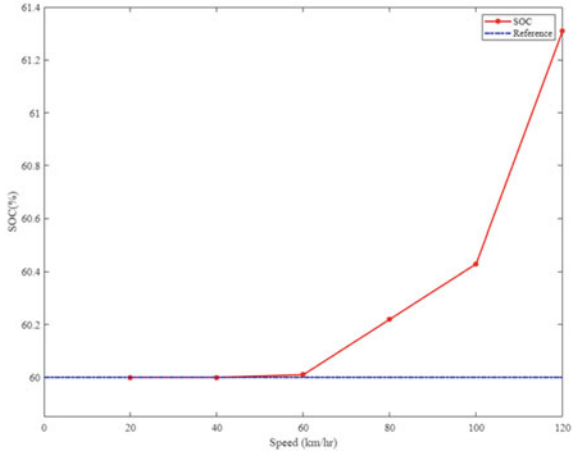

Fig. 15 Vehicle speed and the corresponding state of charge

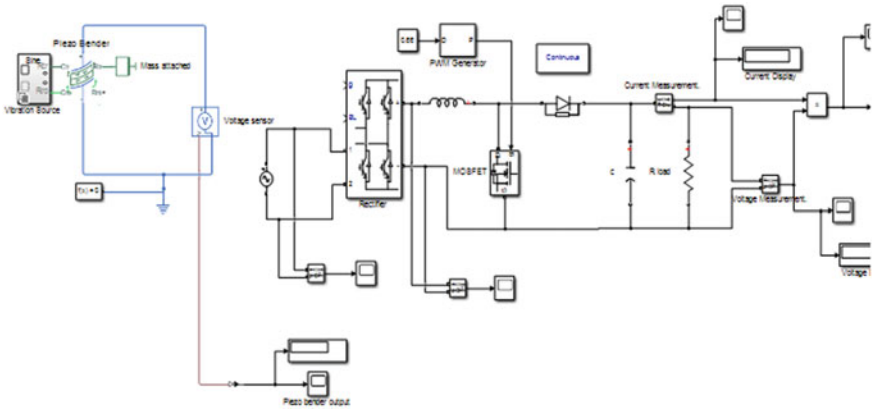

Fig. 16 Simulink model for power calculations

Table 5 Power output in mW corresponding to each vehicle speed

Vehicle speed in kmph	Power output in mW
0	0
20	0.299
40	1.316
60	3.06
80	5.545
100	8.795
120	12.84

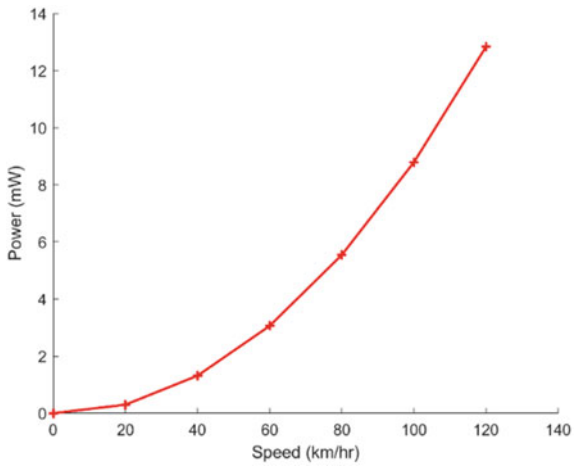

Fig. 17 Power output corresponding to each vehicle speed

The main limitation of this wheel spoke-mounted piezoelectric energy harvester is that the varying vehicle speed will reduce the energy conversion efficiency, and the other limitation is the decrease in energy conversion efficiency due to aging and wear and tear.

5 Conclusion

Energy harvesting is nowadays a substantial topic of research, and motion-driven devices represent a large fraction of this research activity.

This paper presents a wheel spoke-mounted piezoelectric energy harvester specifically targeted to power different sensors embedded on the intelligent vehicle wheels. This wheel spoke-mounted energy harvester is more feasible and compatible than the reported ones installed on tires.

The piezoelectric energy harvester is simulated using MATLAB-Simulink for a vehicle speed range of 0–120 km/hr. From the results, it is observed that when the vehicle is moving with a speed of 60 km/hr and above, sufficient power is generated to charge a 12 V lead–acid battery.

Simulation studies were carried out for a vehicle speed range of 0–120 kmph, the state of charge of the battery and the voltage developed corresponding to each vehicle speed are obtained. The load resistance for which the maximum power flow occurs is also simulated.

The simulation results conclude that the system can be used as an energy source for powering different sensors embedded on the vehicle wheels, after doing some minor modifications. The results from this study have several important hints for the future deployment of intelligent vehicle wheels.

References

1. Koopman P, Wagner M (2017) Autonomous vehicle safety: an interdisciplinary challenge. IEEE Intell Transp Syst Mag 9(1):90–96
2. Tang X, Zhang D, Liu T, Khajepour A, Yu H, Wang H (2019) Research on the energy control of a dual-motor hybrid vehicle during engine start-stop process. Energy 1(166):1181–1193
3. Mak KH, McWilliam S, Popov AA (2013) Piezoelectric energy harvesting for tyre pressure measurement applications. Proc Inst Mech Eng, Part D: J Autom Eng 227(6):842–852
4. Lundberg OE, Kari L, Arteaga IL (2017) A compact internal drum test rig for measurements of rolling contact forces between a single tread block and a substrate. Measurement 1(103):370–378
5. Matsuzaki R, Todoroki A (2009) Intelligent tires for improved tire safety based on strain measurements. In: Health monitoring of structural and biological systems, vol 7295, Apr 8, 2009. International Society for Optics and Photonics, p 72952E
6. Erdogan G, Alexander L, Rajamani R (2009) A novel wireless piezoelectric tire sensor for the estimation of slip angle. Meas Sci Technol 21(1):015201

7. Miyoshi A, Tsurita T, Kunii M, inventors; Sumitomo Rubber Industries Ltd, Sumitomo Electric Industries Ltd, assignee (2007) System and method for determining tire force. United States patent US 7,249,498. 31 July 2007
8. Matsuzaki R, Todoroki A (2007) Wireless flexible capacitive sensor based on ultra-flexible epoxy resin for strain measurement of automobile tires. Sens Actuators, A 140(1):32–42
9. Sathesh A (2020) Metaheuristics optimizations for speed regulation in self driving vehicles. J Inf Technol Digit World 2(1):43–52
10. Lee H, Taheri S (2017) Intelligent tires? A review of tire characterization literature. IEEE Intell Transp Syst Mag 9(2):114–135
11. Bindhu V, Ranganathan G (2021) Energy storage capacity expansion of microgrids for a long-term. J Electr Eng Autom 3(1):55–64
12. Ribhu NS, Ahamed Khan MKA, Ramasamy M, Ang CK, Hong LW, Tran DC (2021) Investigation of gait and biomechanical motion for developing energy harvesting system. In: Proceedings of ınternational conference on sustainable expert systems. Springer, Singapore, pp 151–167
13. Song J, Zhao G, Li B, Wang J (2017) Design optimization of PVDF-based piezoelectric energy harvesters. Heliyon 3(9):e00377
14. Bowen CR, Arafa MH (2015) Energy harvesting technologies for tire pressure monitoring systems. Adv Energy Mater 5(7):1401787
15. Tornincasa S, Repetto M, Bonisoli E, Di Monaco F (2012) Energy harvester for vehicle tires: nonlinear dynamics and experimental outcomes. J Intell Mater Syst Struct 23(1):3–13
16. Guo T, Liu G, Pang Y, Wu B, Xi F, Zhao J, Bu T, Fu X, Li X, Zhang C, Wang ZL (2018) Compressible hexagonal-structured triboelectric nanogenerators for harvesting tire rotation energy. Extreme Mech Lett 1(18):1–8
17. Lee J, Choi B (2014) Development of a piezoelectric energy harvesting system for implementing wireless sensors on the tires. Energy Convers Manage 1(78):32–38
18. Maurya D, Kumar P, Khaleghian S, Sriramdas R, Kang MG, Kishore RA, Kumar V, Song HC, Park JM, Taheri S, Priya S (2018) Energy harvesting and strain sensing in smart tire for next generation autonomous vehicles. Appl Energy 15(232):312–322
19. Makinen T, Wunderlich H (2002) Intelligent tyre promoting accident-free traffic. In: Proceedings of the IEEE 5th ınternational conference on ıntelligent transportation systems, Sept 6. IEEE, pp 606–609
20. Wang YJ, Chen CD, Sung CK (2010) Design of a frequency-adjusting device for harvesting energy from a rotating wheel. Sens Actuators, A 159(2):196–203

Modeling of Graphene Oxide Coated QCM Sensor for E-Nose Application

Alisha Das and Roopa Manjunatha

Abstract Volatile Organic Compounds (VOCs) concentration in breath is an important area of research for non-invasive diagnosis of different diseases. Its concentration in breath can directly be used for diagnosis of health condition. Quartz crystal microbalance (QCM) sensor is widely used for the detection of these compounds using a suitable sensing layer. This paper reports Modeling of graphene oxide coated Quartz crystal Microbalance (QCM) sensor. Finite Element Method in COMSOL Multiphysics is used to analyze change in resonant frequency at different concentration levels of two important VOCs, i.e., Benzene and Toluene. This study modeled graphene oxide as coating layer on QCM sensor and analysed the effect of adsorption of Benzene and Toluene on graphene oxide layer. Partition constant of graphene oxide with benzene and toluene molecules is used to determine concentration of these molecules after adsorption at standard temperature and pressure. The drop in the resonance frequency of 655.201 kHz on adsorption of 100 ppm toluene and 7189.199 kHz on adsorption of 100 ppm benzene molecules have been observed.

Keywords QCM · VOCs · Finite element method (FEM) · Graphene oxide · COMSOL multiphysics · E-Nose · Electronic nose

A. Das · R. Manjunatha (✉)
Energy Institute Bengaluru, Bengaluru, India
e-mail: rmanjuntha@rgipt.ac.in

A. Das
e-mail: 20eb0002@rgipt.ac.in

K. Geetha et al. (eds.), *Recent Trends in Materials*, Springer Proceedings in Materials 18, https://doi.org/10.1007/978-981-19-5395-8_14

1 Introduction

Detection of biomolecules such as Volatile organic compounds (VOCs) in exhaled breath samples are new area of research for non-invasive diagnosis of different diseases. Some of the VOCs are termed as biomarkers in breath for diagnosis of different diseases [1–4]. To identify these VOCs as biomarkers in breath, different techniques are used. Of these techniques- electronic nose (E-Nose) which mimics biological nose is used extensively to detect biomarkers in breath [5]. E-Nose works on the same mechanism as sensory system for smell in humans. Architectural view of E-Nose for medical diagnosis is represented in Fig. 1. Environment monitoring, quality assessment in food industry and bomb detection in defense industry are some other applications. In E-Nose, sensors react with VOCs present in the air by means of different interaction (physical or chemical). These interaction result in change in properties of these sensors.

Different sensors such as resistive, acoustic, optical, are used for E-Nose application. These sensors generate signals. The signal is processed through a computer program which extracts the most characteristic feature of each VOC present in breath or environment through different pattern classification algorithm. Electronic nose-based techniques include sensors such as electrochemical sensors, carbon nanotubes-based sensors, acoustic sensors, and optical sensors. The use of Quartz crystal microbalance (QCM) sensor which is a bulk acoustic wave sensor has increased because of its simplified operation and temperature stability. It detects nanogram concentration of compounds. Sensing layer of chemical is deposited on the electrode surface of AT-cut quartz crystal. This crystal is exposed to gases molecules, which on adsorption to the sensing layer result in corresponding change in resonance frequency. This paper presents a Finite Element Method (FEM) simulation-based QCM model to analyze the selectivity and sensitivity of graphene oxide (GrO) coated QCM sensor to identify benzene and toluene molecules. These molecules are carcinogenic and

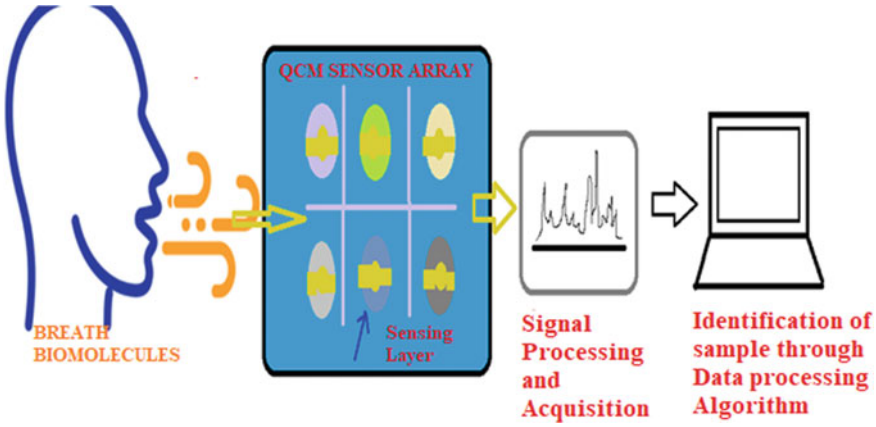

Fig. 1 Quartz crytal microbalance sensor-based electronic nose

present in ppm concentration in many oil and gas industries. Gas chromatography and Mass Spectroscopy is the gold standard method used in these industries but this require sample preconcentration. Simplified real time continuous analysis of these molecules using E-Nose will ensure health and safety of worker of these industries. 1 ppm of benzene and 200 ppm of toluene is the exposure limit defined by OSHA. The proposed model is simple and can be easily fabricated as compared to already discussed model in previous studies.

2 Literature Review

QCM sensors are used for microgram and nanogram level of mass changes. AT-cut Quartz sensor works efficiently at room temperature. All these properties make QCM a suitable choice for E-nose application. There is different sensing layer used to detect different volatile organic compounds in breath. Some of the work is tabulated in Table 1 in which QCM sensor is coated with different sensing layer. QCM sensors can also be used for the detection of odor molecules [10–15]. The effect of graphene oxide as sensing layer on QCM sensor to detect VOCs in not appropriately analyzed in previous research articles. This paper reports the use of graphene oxide as sensing layer to detect benzene and toluene molecules. Previous papers have reported different simulation model for QCM sensor with different coating layer [16–19].

Hu et al. analyzed the mass sensitivity of QCM sensor with modified electrode structure using FEM. This paper discusses the vibration displacement distribution in QCM sensor. The limitation with the proposed work is that its real time application is limited as to prepare a QCM sensor with modified electrode structure involves complex fabrication procedure. Hekiem et al. simulated polyisobutylene and chitosan sensing layer on QCM sensor to detect different compounds such as toluene. The model is well designed and simulated but the chemical layer used for analysis gives very less variation of frequency on adsorption which is not easy to measure in real

Table 1 Different sensitizers used with QCM sensors for detection of biomolecules

Methodology	Sensitizer	QCM frequency (MHz)	References
E-nose-based blood glucose level monitoring from exhaled breath	Phthalocyanine	10	[5]
Polymer coated QCM E-Nose	PAN, PVDF, PVP, PVA	21	[6]
Multiple channel QCM array	TiO_2-MWCNT, CoPc silica	10	[7]
Lung cancer diagnosis by exhaled breath	8 Metalloporphyrin	20	[8]
Tuberculosis diagnosis by exhaled breath	8 Metalloporphyrin	20	[9]

time application. Calculation for sensitivity of different molecule to chitosan and polyisobutylene is also analyzed. Hazadi et al. modeled the QCM sensor for exhaled breath analysis. Change in frequency is analyzed for different acetone concentrations. This work has not used any sensitizer layer over QCM sensor which can affect the sensitivity and accuracy of proposed work. Zainuddin et al. designed a MEMS-based QCM sensor array for biosensing application. The fabrication of this QCM sensor involves complex fabrication and has limited real time applications. In this paper, an array of four mass sensor was designed and the simulation results are presented.

3 Materials and Methodology

Quartz crystals are piezoelectric materials that oscillate at a resonance frequency on the application of AC voltage through metal electrodes. The crystal resonance frequency is changed on the deposition of the calculated amount of mass on the electrode surface. This change in frequency can be calibrated with respect to change in mass to determine the property of molecules deposited on the QCM surface. The relation between change in frequency and change in mass is expressed through the Sauerbrey equation.

$$\Delta f_{g\cdot} = -\frac{2 f_0^2 \Delta M}{\rho_q \mu_q A} \tag{1}$$

where Δf_g is the change of resonance frequency after deposition, f_0 is the fundamental resonance frequency of oscillation, ρ_q, μ_q is density and shear modulus of quartz crystal, ΔM represents change in mass and A represents active area for deposition of mass on electrode. Block diagram representation of the workflow to model QCM sensor is shown in Fig. 2. Different parameter used for Modeling of sensor is tabulated in Table 2. Sensing layer is deposited on the surface of QCM sensor for target analyte detection. This model is designed and simulated in COMSOL Multiphysics software.

The mesh model of the 20 MHz QCM sensor is illustrated in Fig. 3. The resonance frequency (the frequency of maximum displacement) is inversely proportional to the thickness of QCM sensor. Graphene/air partition constant for benzene and toluene molecule is specified. Partition constant is the ratio of the concentration of a substance in two media under equilibrium conditions is used to determine the adsorption of benzene molecules on the graphene oxide layer.

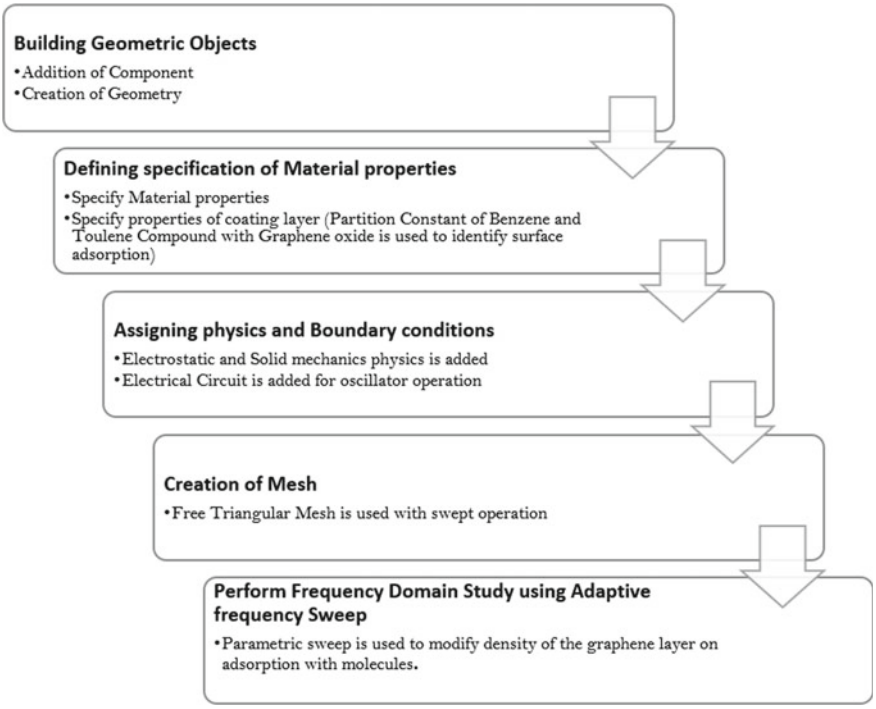

Fig. 2 Block diagram representation of the workflow for Modeling Graphene oxide coated QCM sensor in COMSOL multiphysics software

4 Simulation and Results

The paper discusses graphene oxide coated QCM sensor modeled using COMSOL MULTIPHYSICS software is used for FEM simulation. To analyze the effect, graphene/air partition constant for benzene and toluene is taken as 0.55 and 0.52, respectively [20]. The result of the simulation is tabulated in Table 3. QCM sensor of 10 MHz resonance frequency was designed with quartz crystal of 102 μm thickness and 20 MHz resonance frequency with 354 μm thickness. The detailed specification of quartz is explained in Table 2. A drop in frequency of 763.6 kHz was observed on coating a graphene oxide layer on 10 MHz quartz crystal. On addition of 1000 ppm of toluene molecule by increasing density of graphene oxide layer through parametric solver, an effective drop in frequency of 108.399 kHz was observed. A drop in frequency of 2765.599 was observed on coating graphene oxide layer on 20 MHz quartz crystal. On addition of 1000 ppm and 100 ppm of benzene change in frequency of 4425 kHz and 4423.6 kHz was observed, respectively. On addition of 1000 ppm and 100 ppm of toluene change in frequency of 4425.201 kHz and 4423.6 kHz was observed, respectively. This change in frequency was put in Sauerbrey equation to identify change in mass in micrograms.

Table 2 Material parameters for qcm sensor coated with graphene oxide as sensing layer

Variable	Expression	Value	Description
QR	3.5 [mm]	0.0035 m	Oscillator radius
H0	354 [nm]	3.54E-7 m	Oscillator thickness
GT	20 [nm]	2E-8 m	Layer thickness
R0	2.25 [mm]	0.00225 m	Electrode radius
p	101.325 [kPa]	1.0133E5 Pa	Air pressure
T	25 [°C]	298.15 K	Air temperature
c0	1000	1000	Concentration in ppm
c_air	10e-6*c0*p/(R_const*T)	4.0874E-4 mol/m^3	Concentration in air
M_B	78.11 [g/mol]	0.07811 kg/mol	Molar mass of Benzene
M_T	92.14 [g/mol]	0.09214 kg/mol	Molar mass of Toluene
K_b	0.55	0.55	Graphene/air partition coefficient of benzene
K_t	0.52	0.52	Graphene/air partition coefficient of toluene
rho_b	K_b*M_B*c_air	1.756E-5 kg/m^3	Mass concentration of benzene
rho_t	K_t*M_T*c_air	1.9584E-5 kg/m^3	Mass concentration of toluene
E_GO	380 [GPa]	3.8E11 Pa	Youngs modulus of graphene oxide
nu_GO	0.064	0.064	Poisson's ration of graphene oxide
eps_GO	915	915	Permittivity of graphene oxide
rho_GO	0.26 [g/cm^3]	260 kg/m^3	Density of graphene oxide

It can be observed that as the thickness of QCM sensor is increased, the change in frequency with the mass changes are more pronounced. For less thick crystal 600 to 700 kHz frequency change is observed. The quartz crystal microbalance sensor should be connected to an oscillator circuit so that it operates in its natural frequency of operation. A simple oscillator circuit with 2N2222 (CL100S) transistor to analyze the resonance frequency of operation and analysis of frequency changes with change in deposited mass is illustrated in Fig. 4. The change in resonance frequency with adsorption of toluene and benzene vapor is illustrated in Fig. 5. This circuit is designed and tested in Multisim software and then used in COMSOL to detect frequency changes with change in mass.

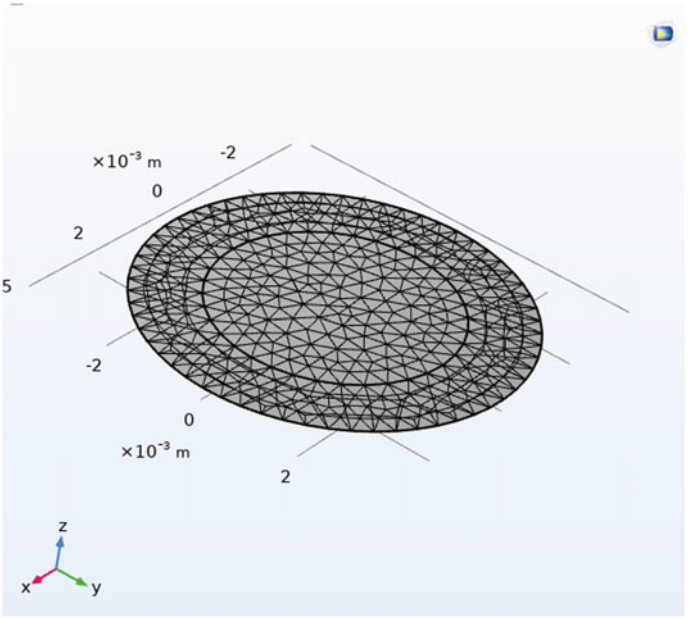

Fig. 3 20 MHz QCM sensor mesh model for finite element analysis

Table 3 Simulation results for different concentration of Benzene and Toluene vapors

Resonant frequency (MHz)	Thickness of quartz crystal (micrometers)	Sensor coating	Change in mass (Micrograms)	Change in frequency (MHz)
10.3546	102	GrO	10	0.7636
10.3546	102	GrO + 1000 ppm Toluene	10.0016533	0.655201
20.162399	354	GrO	10	7.765599
20.162399	354	GrO + 1000 ppm Benzene	10.0015754	7.190599
20.162399	354	GrO + 100 ppm Benzene	10.0009675	7.189199
20.162399	354	GrO + 1000 ppm Toluene	10.0016533	7.1908
20.162399	354	GrO + 100 ppm Toluene	10.0009753	7.189199

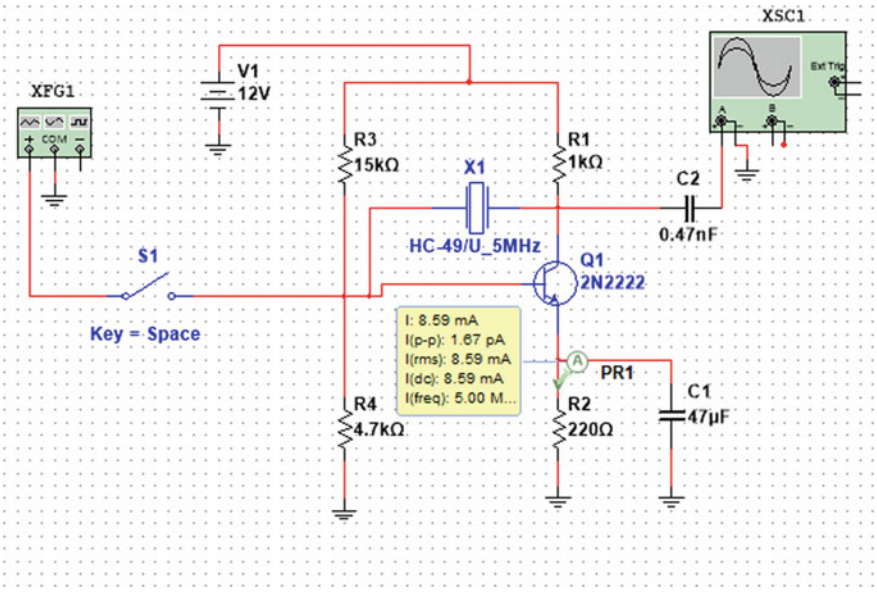

Fig. 4 Simplified oscillator circuit design in multisim software for mass sensitivity analysis of QCM sensor

5 Conclusion

Graphene oxide material has the properties such as high mechanical strength, flexibility and best heat conductivity. The proposed simplified model presents the preliminary results for the change in resonant frequency (in kHz) of QCM sensor on adsorption of ppm level of benzene and toluene molecules to graphene oxide layer. This methodology can be used as reference for the development of E-Nose using an array of QCM sensors for detection of these molecules in real time.

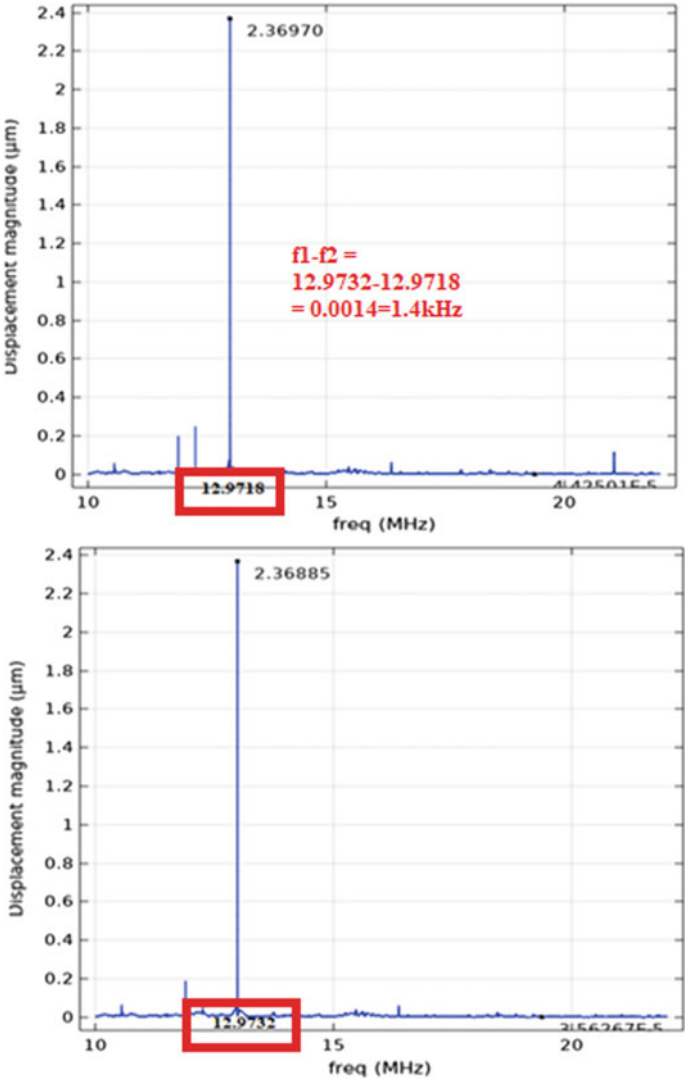

Fig. 5 Variation of resonant frequency of 1.6 kHz with adsorption of ppm level of toluene vapors

References

1. Sánchez C, Santos J, Lozano J (2019) Use of electronic noses for diagnosis of digestive and respiratory diseases through the breath. Biosensors 9(1):35
2. Zetola N et al (2017) Diagnosis of pulmonary tuberculosis and assessment of treatment response through analyses of volatile compound patterns in exhaled breath samples. J Infect 74(4):367–376
3. Buszewski B, Grzywinski D, Ligor T, Stacewicz T, Bielecki Z, Wojtas J (2013) Detection of

volatile organic compounds as biomarkers in breath analysis by different analytical techniques. Bioanalysis 5(18):2287–2306
4. Hashoul D, Haick H (2019) Sensors for detecting pulmonary diseases from exhaled breath. Eur Respir Rev 28(152):190011
5. Saraoğlu HM, Selvi AO, Ali Ebeoğlu M, Taşaltin C (2013) Electronic nose system based on quartz crystal microbalance sensor for blood glucose and HbA1c levels from exhaled breath odor. IEEE Sens J 13(11):4229–4235
6. Julian, T, Hidayat SN, Rianjanu A, Dharmawan AB, Wasisto HS, Triyana K (2020) Intelligent mobile electronic nose system comprising a hybrid polymer-functionalized quartz crystal microbalance sensor array. ACS Omega 5(45):29492–29503
7. Tao W, Lin P, Ai Y, Wang H, Ke S, Zeng X (2016) Multichannel quartz crystal microbalance array: fabrication, evaluation, application in biomarker detection. Anal Biochem 494:85–92
8. Di Natale C, Macagnano A, Martinelli E, Paolesse R, D'Arcangelo G, Roscioni C, Finazzi-Agro A, D'Amico A (2003) Lung cancer identification by the analysis of breath by means of an array of non-selective gas sensors. Biosens Bioelectron 18(10):1209–1218
9. Zetola NM, Modongo C, Matsiri O, Tamuhla T, Mbongwe B, Matlhagela K, Sepako E et al (2017) Diagnosis of pulmonary tuberculosis and assessment of treatment response through analyses of volatile compound patterns in exhaled breath samples. J Inf 74(4):367–376
10. Okur S, Qin P, Chandresh A, Li C, Zhang Z, Lemmer U, Heinke L (2021) An enantioselective e-nose: an array of nanoporous homochiral MOF films for stereospecific sensing of chiral odors. Angew Chem Int Ed 60(7):3566–3571
11. Okur S, Sarheed M, Huber R, Zhang Z, Heinke L, Kanbar A, Wöll C, Nick P, Lemmer U (2021) Identification of mint scents using a QCM based E-Nose. Chemosensors 9(2):31
12. Temel F, Ozaytekin I (2021) The monitoring of hydrocarbon vapor by electrospun PBINF modified QCM chemosensor. Sens Actuators, A 326:112688
13. Liu C, Miyauchi H, Hayashi K (2022) DeepSniffer: a meta-learning-based chemiresistive odor sensor for recognition and classification of aroma oils. Sens Actuators, B Chem 351:130960
14. Debabhuti N, Neogi S, Mukherjee S, Dhar A, Sharma P, Vekariya R, Sarkar M, Tudu B, Bhattacharyya N, Bandyopadhyay R, Muddassir M (2021) Development of QCM sensor to detect α-terpinyl acetate in cardamom. Sens Actuators, A 319:112521
15. Liu Y, Fan Y, Hou C, Du W, Zhang D, Liu Y, Xu J, Bai Y (2021) Highly selective chloromethanes detection based on quartz crystal microbalance gas sensors with Ba-MOFs. Inorg Chem 60(21):16370–16377
16. Hu J, Huang X (2018) QCM mass sensitivity analysis of modified electrode structures using finite element method. In: 2018 IEEE International conference on applied superconductivity and electromagnetic devices (ASEMD), pp 1–2. IEEE
17. Hekiem NLL, Ralib AAM, Hatta MAM, Ahmad FB, Ab Rahim R, Za'bah NF (2021) Performance analysis of VOCs detection using polyisobutylene and chitosan overlayed on QCM sensor. In: 2021 IEEE regional symposium on micro and nanoelectronics (RSM), pp 157–160. IEEE
18. Hazadi AHF, Ralib AAM, Saidin N (2018) Design and simulation of electroacoustic sensor for exhaled breath analysis. In: 2018 7th ınternational conference on computer and communication engineering (ICCCE), pp 388–391. IEEE
19. Zainuddin AA, Nordin AN, Ralib AAM, Ab Rahim R, Khan S, Guines C, ... Pothier A (2017) Design and optimization of a MEMS quartz mass sensor array for biosensing. In: 2017 IEEE 4th ınternational conference on smart ınstrumentation, measurement and application (ICSIMA), pp 1–5. IEEE
20. Kumar V, Lee YS, Shin JW, Kim KH, Kukkar D, Tsang YF (2020) Potential applications of graphene-based nanomaterials as adsorbent for removal of volatile organic compounds. Environ Int 135:105356

Low-Temperature Reduction Processing of Copper Slag

Sokhibjon Turdalievich Matkarimov, Bakhriddin Tilovkabulovich Berdiyarov, Zaynobiddin Turdalievich Matkarimov, Raimkul Rakhmonkulov, and Sevara Dusmuratovna Jumaeva

Abstract The iron-containing raw materials which can be extracted from copper slags are essential for Uzbeksteel JSC. In this regard, the relevance of this work is undeniable. The problem of processing slags of metallurgical plants is more acute in both ferrous metallurgy and non-ferrous metallurgy. This problem has not been practically solved in any country around the world. Slags, accumulating around metallurgical plants, create substantial environmental issues for enterprises. The tightening of environmental legislation and the consequent payment of significant fines force enterprises to seek alternative solutions.

Keywords Raw materials · Reduction · Slag · Recovery · Slag · Granulometric characteristics · Coal of angren field · Coke · Low temperature

1 Introduction

The need of iron for humankind is well known. The high-industry level in the Republic of Uzbekistan has led to a significant increase in metal consumption. Thus, the total demand for the rolling of ferrous metals is about 1.8 million tons per year. Of these, 600 thousand tons are provided due to the processing of scrap and waste of ferrous metals at the JSC Uzbeksteel in Bekabad; the rest 1.2 million tons is imported.

S. T. Matkarimov (✉) · B. T. Berdiyarov
Tashkent State Technical University, 2, University Street, Almazar District, Tashkent, Uzbekistan
e-mail: sohibtm@gmail.com

Z. T. Matkarimov
Tashkent Chemical-Technological Institute, Navoiy Street, 32, Tashkent, Uzbekistan

R. Rakhmonkulov
Tashkent State Technical University Almalyk Branch, 45, Mirzo Ulugbek Street, Almalyk city, Uzbekistan
e-mail: rrakhmonkulov@tdtu.uz

S. D. Jumaeva
National Institute of Art and Design Named After Kamoliddin Behzod, 123, Mironshoh Street, Mirabad district, Tashkent, Uzbekistan

K. Geetha et al. (eds.), *Recent Trends in Materials*, Springer Proceedings in Materials 18, https://doi.org/10.1007/978-981-19-5395-8_15

After some reconstruction, the plant can recycle iron ore concentrates (metalized pellets) up to 1 million tons per year. However, the supply of scrap and ferrous metal waste is continuously decreasing. Therefore, the creation of its raw material base for the steel industry, the development of which can become competitive for the import of ferrous metals, is a priority [1].

The problem of processing has not been practically solved. Slags, accumulating around metallurgical plants, create substantial environmental issues for enterprises. The most developed countries bring this production to third states and work according to the tolling system. Several countries, such as Finland, have adopted legislation under which smelting slags containing no more than 0.60–0.65% of Cu can be sold to an external organization and thereby organize wasteless production. Such a way of solving the problem of slags is entirely unacceptable for Uzbekistan. The country has its own economic and social development path based on a careful attitude to natural wealth and almost exclusive use of all its valuable components. Natural minerals are irreparable and require close attention. Already today, it is a requisite to think about what will remain for our children and grandchildren, on what basis they will build their happy future.

Slags are an inevitable component of all types of pyrometallurgical methods of metal production. In terms of their volumes, they are several times higher than the production scale of primary metals. Slags are inherently a waste of production, associated with a decrease in the coefficient of integrated use of raw materials and environmental problems. But at the same time, slags are valuable raw materials from which copper, iron, and noble metals can be extracted. For example, the slags of the Almalyk Mining and Metallurgical Plant's copper-smelting plant (AMMC) contain 0.45–3.5% copper, 30–55% iron, a large amount of noble metals, and other valuable components. Of course, it is more expensive to extract these metals from slags than by processing raw ores and concentrates. However, two circumstances need to be considered: Natural mineral inputs are not inexhaustible and have limited reserves; prices of non-metals such as copper, gold, iron, and some others have recently increased significantly. This trend has continued to this day. Because of these circumstances, while simultaneously solving environmental problems, extracting these components from slags can be profitable.

The relevance of this work lies in the fact that, for the first time, the task of processing the slag of copper smelters after their dehumidification is set to extract iron and its compounds from them. Uzbekistan has several iron ore deposits. However, they are not currently involved in industrial production. The main reasons are the relatively low content of the main component, relatively small reserves, the lack of acceptable processing technology, and problems with engineering communications. For these reasons, the involvement of these fields in industrial production is not expected shortly. At the same time, iron-containing raw materials are essential for the JSC Uzbeksteel, and this material can be extracted from copper slags. In this regard, the relevance of this work is undeniable.

2 Material and Methods

Deal with issues of processing of slags of copper-smelting production practically in all countries and continents having the relevant branch of the industry. Numerous technologies and recommendations about specific conditions of production are developed. It is explained by various structures, properties, and the mechanism of formation of slag, demanding for the processing of individual technological decision.

All known ways of the impoverishment of slags of copper-smelting production can be classified in the form of the following main directions [2]:

- Hydrometallurgical
- Flotation
- Pyrometallurgical
- Combined.

The specific merits and demerits are inherent in each direction. Their applicability is defined by the composition of initial raw materials and gumboils and particular conditions of the enterprises. Technological schemes of production of draft copper practically at all plants occur in two-stage and include melting on matte and converting the last. General–theoretical provisions on the processing of slags allow approaching reasonably the choice of the technological modes of melting to minimize losses of metals. At the same time, the metallurgist can change the slag mode directionally; regulate the composition of matte, temperature, and structure of the gas atmosphere in the metallurgical unit.

Slag has to be rather fusible, free flowing, and have low density. The solubility of non-ferrous metals in slag has to be minimum, and an interphase tension on border matte-slag, on the contrary, whenever possible may be higher. And, an exit of slag has to be minimized. Slags with high concentrations of oxides of iron dissolved in a large amount of non-ferrous metals. The interphase tension on the matte border with such fusions is not enough.

At the plants using traditional technologies of melting on matte (reflective, mine, and electric melting), slags of the central melting unit are formed substantially due to the return and completion of converter slags and are dumped. When using melting on matte of autogenous technology in suspension slags of the central melting unit that are not dumped, processing converter slags is almost impossible. This circumstance leads to the fact that practically all plants using autogenous melting have independent repartitions of the impoverishment of slags.

Industrial development of the process of impoverishment of melting and converter slags at the copper plants, despite a considerable number of results, generally comes down to electro–thermal and floatation ways. Dissolution is carried out through slag processing by a solvent after crushing and crushing with a possibility of chemical treatment for the additional transfer of copper to soluble forms or without that. A transfer of copper insoluble forms can be made by sulfurization, chlorination, biotechnological methods, and other ways.

The advantage of a hydrometallurgical way is the possibility of high extraction of copper in the high-concentrated deposit in the absence of technological gases, excepting thereby pollution of the air basin. However, this way has also essential shortcomings:

- Low performance
- Low selectivity of solvents
- Formation of solutions of complex structure because of the interaction of solvent with slag components
- Significant losses of reagents owing to the interaction with components of slag and formation of insoluble connections
- Practical impossibility of extracting precious metals.

The complexity of the above-stated reasons leads to the fact that the hydrometallurgy of slags did not find practical application; technological developments are generally limited to a framework of laboratory and semi-industrial research [3].

The impoverishment of cupriferous slags flotation found quite a broad application. Flotation is subjected to quickly and slowly cooled slags. In addition, one of the contents in them is up to 18–20% of silicon dioxide, and the technical and economic indicators practically coincide. At higher silicon content, it is preferable to cool slags in bars or ladles slowly. In addition, receiving when melting and converting the high-basic ferrite-calcium slags having properties of a self-molder is of considerable interest. Works in this direction were carried out at the metallurgy ASC of Russia, the Ural scientific center, etc. The essential possibility of receiving well the FSF float slags possessing a self-molder was confirmed during trial tests on Gintsvetmet OEMZ.

Flotation of slags of the primary melting has found application at the following plants using the technology of "Outokumpu," "Haryavalta" (Finland), Mount-Morgan, "Teppan Krik" (Australia), Samsun (Turkey), Khetri (India), Garfield (USA). In addition, these plants also float converter slags. Flotation of converter slags is carried out almost at all plants using electrothermal impoverishment of slags weighed melting. Electrothermal impoverishment of converter slags is applied at the Onson plants (Korea) and "Nordoyche Arfineri" (Germany). Slags of processes of Norand perform "TVRS" overwork flotation [4].

The technology of flotation of slags is similar at all enterprises. For example, at the Haryavalta plant (Finland) process includes separate three-phasic crushing to fineness, 4 mm; Two-stage joint crushing to a class exit, and 0.053 mm (90–91%). The general flotation time is 40 min when receiving a concentrate with the maintenance of 20% of copper at an exit of 15% of the slag mass. Copper content in flotation tails at the level of 0.4–0.5%, and extraction of copper from slags up to 60–70% is provided [4].

V. N. Sigedin, V. L. Aranovich, V. M. Piletsky, etc., in the research, showed a possibility of joint processing of cupriferous slags with sulphidic ores. Extraction of copper in a concentrate simultaneously reached 80–85%, at residual contents in tails of 0.08–0.1%.

However, several essential shortcomings are inherent in the flotation processing of slags:

- Warmly melted slag is not used
- Hardness of slags considerably surpasses the indicator of initial ore that creates great difficulties when crushing
- Flotation of slags does not allow to resolve an issue of extraction of other components, such as nickel, cobalt, zinc, etc., that excludes their application for processing of slags from melting of polymetallic raw materials
- The use of an iron-silicate part of slags for any purpose is complicated and does not give the chance to implement waste-free technology.

All these shortcomings significantly limit the possibilities of the use of technology of flotation of slags, and they are used only where other technologies for any reason are not effective.

Most of the plants use melting in suspension, impoverishing slags of the central melting unit in electric furnaces. Asano, Kosaka, Saganoseki, Toyo, Tamano (all Japan), Gatsila (India), Gloguv-P (Poland), "Nordoyche Affineri" (Germany), Uelov (Spain), Hidalgo (USA), Onsa (Korea), Passar (Philippines), NGMK (CIS), etc., are a few. At different plants, the electric power expense on the impoverishment of slags makes from 50 to 200 kWh/t of slag, the content of copper decreases to 0.4–0.6%, as reducers use coal or coke, as a sulfide–pyrite, a concentrate, or other sulfur-containing materials. The impoverishment of slags is carried out, as a rule, in one stage in the separate round or rectangular electric furnace. In the combined process of Mitsubishi (Japan), the three-electrode oval electric furnace is used. The Tamano plants (Japan) and Passar (Philippines) have the intra-oven electro-settlers combined with a lame zone. Such design allows cutting electric power consumption for 25%, to liquidate difficulties with the transport of matte of impoverishment, and to lower on 14% volume of flue gases [8].

The copper content in slags after electrothermal impoverishment at the level of 0.5–0.6% is an economic minimum. Its further decrease is possible at the increase in the extent of restoration and sulphidation or an increase in the number of stages a process impoverishes. At the same time, there is inevitably a significant increase in energy consumption, the expense of gumboils, reagents, and technology complications.

Low-temperature restoration of slag with completion of the restored product enrichment and electric melting is the main direction on the creation of complex technology of processing slags of the reflective furnace and furnace after thermo-gravitational impoverishment of liquid slags with the subsequent granulation offered. The justification for this way is given in the previous sections. The choice of the main direction taking into account these factors can be carried out after carrying out trial tests. However, it is necessary to carry out additional data on critical parameters of iron restoration from slags. It is essential to determine the following parameters:

- Dependence of depth of restoration of iron on the consumption of reducer, temporary and temperature condition

- Dependence of the amount of the received metal on parameters of the slag-recovery process
- Interdependence of depth of restoration and quality of metal at various options of the process of restoration of slags
- Dependence of parameters of the slag-recovery process on a way of preparation of slags.

Proceeding from the aforesaid conducting laboratory trials on two types of the slags prepared in three ways is necessary. The Flash Smelting Furnace (FSF) and Reverberating Furnace (RF) common slags containing 32–36% silicon dioxide are used as initial materials.

Results of laboratory trials are used for primary analysis of technological features of restoration of slags, comparison of laboratory data to theoretical, and development of the recommendation for carrying out trial tests.

For laboratory and in minor detail, laboratory trials, (three tests) of slag of the reflective furnace and the FS furnace are selected. Each test is about 20 kg. The first test represents, from itself, quickly cooled slag without special preparation. The second test represents slag in the coarse way of filling by a squirt in water. The third test represents slag in the rough form of filling by a fountain in limy milk (10% of $Ca(OH)_2$). The fineness of the initial granules is from 8 to 25 mm.

The granulometric characteristics of copper-smelting plant slags are in a detailed study. All slags are crushed to a fineness less than 1 mm; they average the structure from each test. As limy gumboil, it uses the burned lime received at the limy plant Almalyk MMC. Limy gumboil is also crushed to a fineness less than 1 mm, averaged, and stored in tight ware for protection from absorption of moisture from the air. For each experience, hinge plates with a total weight of 1 kg, which are carefully averaged, are prepared. The lump of a hinge plate of 800 g arrived for conducting laboratory trials; the others (200 g) went to the control chemical analysis on the main components: Cu, CaO, Fe_{total}, SiO_2, Al_2O_3, S_{total} for prevention of possible mistakes by drawing up furnace charge [3, 5–7].

The research of low-temperature restoration of iron from slags of copper production is conducted on a complex of the laboratory installations including:

- The rotating tubular electric furnace
- System of supply of purified gas (nitrogen)
- System for the regulation of temperature
- The RF magnetic separator of the received magnetic fraction.

The rotating laboratory furnace is supplied with the system of stabilization of speed of rotation and temperature. In detail, this system has also discussed the application. The indicators vary initial material, blending of initial material, hold time, and temperature.

The received restored chilled material is crushed and divided into three parts directed to the chemical analysis after quartation of the research on the magnetometer for the definition of iron metal. Other materials are destroyed and are exposed to magnetic separation for allocation of the metal fraction. The magnetometer is tarred

Table 1 Variable parameters and their values during execution in the first stage of laboratory experiments

Parameter name	Unit of measure	Value parameter during experiments		
Temperature	°C	800	900	1000
The ratio of reducing agent to slag	%	15	22.5	30
Isotherm exposure time	min	90	150	240

on the definition of iron on a mix of iron powder and the crushed quartz gumboil. The use of slag for calibrating is excluded because of the collateral influence of magnetite.

At the first stage, laboratory trials on establishing optimum parameters of the restoration process of slags are made. As reducers, crushed coke and Angren coal are used. The varied parameters and their sizes when conducting laboratory trials are specified in Table 1. On the laboratory furnace at restoration in crucibles, only check experiments showing a bare chances of a low-temperature minimization of iron from slags coke or Angren was made by coal [8]. The maximum slag reduction is obtained at a temperature of 1000 °C, a reducing agent flow rate of 30%, and an isothermal holding time of 240 min for slags of RF lime granulation. The smallest value of the degree of minimization is obtained for quickly cooled FSF slags, with a reducing agent flow rate of 15%, the temperature of 800 °C, and an isothermal holding time of 90 min [9–14].

Six reconstituted material samples with minimal, intermediate, and maximum reduction are selected for further investigation. These samples undergo additional grinding in a laboratory mill and three-fold magnetic separation with intermediate grinding. The optimal consumption reduction to be 20%, 25%, and 27% forms the mass of slag, and it was determined by using slag granulated in lime milk under the temperature of 1000 °C and the holding time of isothermal as 240 min. This results obtain that the reducing agent to slag over of 25% increased but not the degree of reduction.

As a result, the influence of isothermal holding time on degrees is recovered for RF slags and FSF of lime granulation in laboratory trials at the following parameters: Temperature 1000 °C, agent consumption 25% of slag mass, isothermal holding time 120, 150, 180, 240 min. As the findings in this table show, increasing the isothermal holding period beyond 180 min has little effect on the degree of reduction [15–20]. Laboratory studies are carried out to evaluate the influence of lime on slag recovery at the determined optimal mode, temperature 1000 °C, reducing agent flow rate 25%, isothermal holding period 180 min. The slag-coke combination is supplemented with 5, 10, or 15% calcined lime. FSF slags and RF lime granulation slags are utilized in scientific studies. According to the results of laboratory research, the inclusion of lime has little effect on the results of low-temperature reduction. Control studies demonstrate that partial melting of slag happens in this instance; hence, laboratory tests at temperatures exceeding 1000 °C are not performed. Experiments

have demonstrated that when the amount of active carbon is equal, Angren coal is equivalent to coke.

Graphs of the main dependencies are created based on the results. Figure 1 depicts the relationship between the reduction degree of iron oxide in slag and the time of isothermal holding at a 25% drop in agent flow rate. Figure 2 depicts the relationship of metalized iron yield (percentage of the starting one) on the length of isothermal holding at $T = 900$ °C and 1000 °C (Fig. 3).

The dependence of an exit of magnetic fraction (percentage of initial) at $T = 1000$ °C and consumption of reducer (Angren coal) from isothermal endurance is given in graphics, in Fig. 4 (Fig. 5).

The dependence of extent of restoration of iron in slag from consumption of reducer (coke) (percentage of the mass of slag) at $T = 1000$ °C is given in schedule.

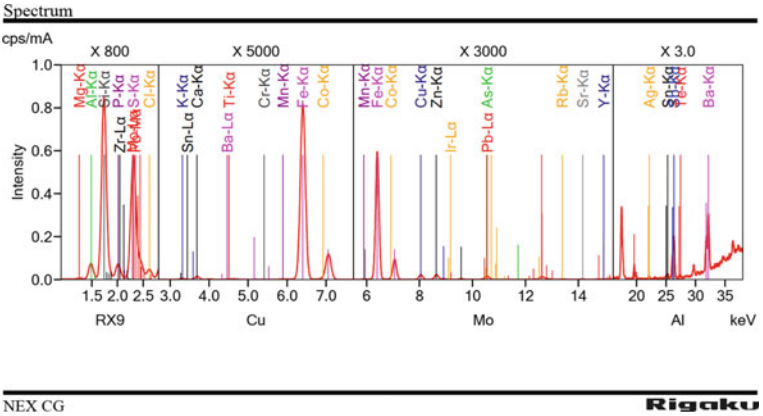

Fig. 1 X-ray fluorescence spectro copper slag

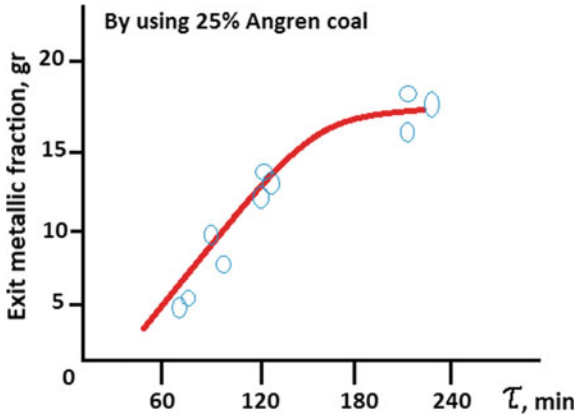

Fig. 2 Dependence of reduction degree of iron oxide in slag on the duration of isothermal holding at $T = 1000$ °C

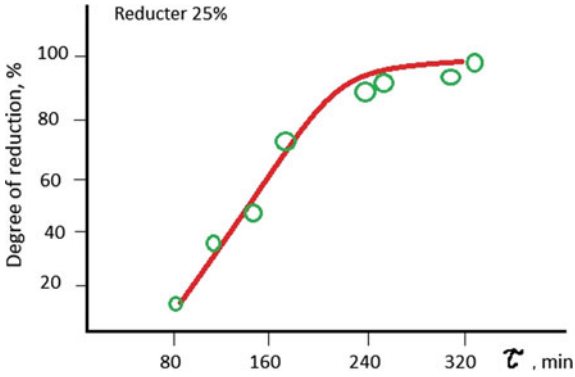

Fig. 3 Dependence of metalized iron yield on the duration of isothermal holding at different temperatures (percentage of initial slag)

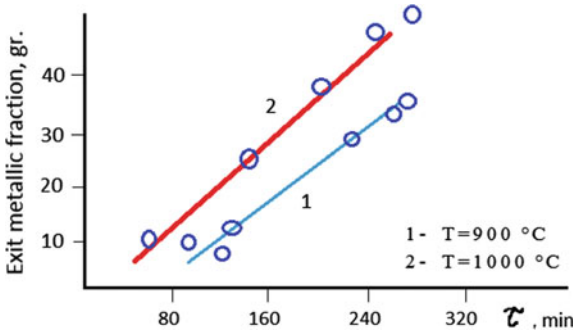

Fig. 4 Dependence of change of iron reduction degree in slag (a, %) on the consumption of reducing agent (coke) (percentage of slag weight) at $T = 1000$ °C

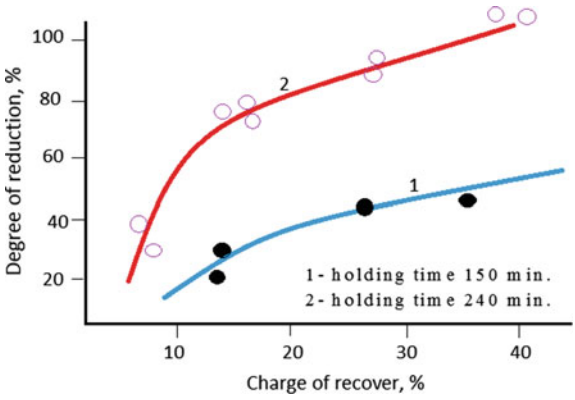

Fig. 5 Dependence of iron reduction degree from slag (a, %) on reducing agent consumption (percentage of slag weight)

The graph shows the dependence of iron reduction degree (percentage of initial slag on reducing agent consumption (Fig. 6).

As a result of the assessment of the obtained patterns, the following conclusions can be drawn:

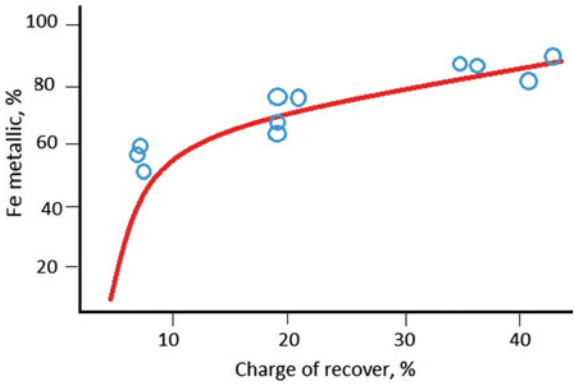

Fig. 6 Degree of reduction of iron oxide in metal slag depends on the duration of isothermal holding and temperature

- Optimum temperature of the process 900–1000 °C
- Optimum consumption of reducing agent 25–35%
- Optimum holding time of 180–240 min.

In principle, the results obtained are consistent with data on reducing iron and iron-silicate materials in ferronickel production. To ensure thermal balance, increasing the consumption of reducing agents by 10–15% for industrial furnaces.

3 Results

After briquette, the iron-containing fraction can be remelted to make an iron alloy or cast iron. The silicate residue can be utilized to make slag and recover copper using well-known procedures. Work on the Angren coal is distinguished by the specifics. Low-temperature reduction is typically carried out with coke fines, anthracite, or coal. To eliminate the inevitable breach of the temperature profile in this situation, replacing coke with Angren coal in an industrial furnace will necessitate numerous extra precautions.

This issue is addressed through the following activities:

- Natural gas flooding
- Separation of carbon from the obtained material and its return to the head of the process
- Selection of fractional raw material of reducing agent.

In general, the issues of appropriate coke substitution (full or partial) with Angren coal are beyond the scope of this paper (Table 2).

Table 2 Results of magnetic separation to obtain magnetic fraction

Notes, reducer	Receiving				
	Output max., gr	Magnet. part		Nemagnite part	
		gr	%	gr	%
Angren coal	59	6	10.16	52.3	88.64
	54	7.5	13.88	46	85.18
	56	18	32.14	38	67.86
	68	13	9.09	55	80.88
	55	5.0	9.09	50	90.9

4 Conclusion

Previously grown poor slags have to be exposed to complex processing with the extraction of the iron and the silicate rest, suitable for different construction materials. At the same time, the extent of restoration of iron and capacity of correction of the structure of the slag silicate rest are greater. The cost of the received materials is higher.

There are two options of restoration of reverse slags:

- Direct high-temperature restoration in a liquid or firm look
- Low-temperature restoration in tubular furnaces with the subsequent division and divisions of processing of products of repair.

The laboratory testing method of low-temperature restoration of slags in laboratory furnaces is developed and established that the optimum temperature of restoration of 1000 °C, and the slag which is previously granulated in limy milk is restored quicker more intensely than not granulated slag or the slag granulated in water. Check is carried out for a fraction of slag of identical fineness. It is connected with the fact that slag after granulation in limy milk has considerable porosity and cracks that provide carbon protoxide penetration more deeply into grains.

References

1. Ore fields of Uzbekistan. Group of authors. Tashkent: GIDROIN GEO. The 2001–611th
2. Malysheva TY, Dolitskaya OA (2016) Petrography, and mineralogy of iron ore raw materials. M: MISIS, p 424
3. Corby G, Robert AC (2014) Mineral progressing and extractive metallurgy: 100 years of innovation, p 386
4. Percy J (2012) Metallurgy: the art of extracting metals from their ores, and adapting them to various purpose of manufacture
5. Vegman EF, Pokhvisnev AN, Yusfin YS (2004) Metallurgy of cast iron. AkademBook 774
6. Yusfin YS, Danshin VV (1982) Theory of metallization of iron ore raw materials. Metallurgy 256

7. Kozin VZ (1985) Approbation and control of technological processes of enrichment. Subsoil 295
8. Yusupkhodjayev AA, Hudoyarov SR, Muminov SA (2014) Technology of preparation of titanium magnetite ores for metallurgical conversion. In: Articles of the international scientific and practical conference "innovation-2014". TashSTU, Tashkent, pp 178–180
9. Yusfin YS, Danshin VV, Pashkov NF (2000) Theory of metallization of iron ore raw materials. Metallurgy 256
10. Linchevsky BV (1998) Tekhnika of a metallurgical experiment. Metallurgy 344
11. Matkarimov ST (2020) Heat treatment processes of steel-smelting slags in the recovery environment. In: Paper presented at the METAL 2020—29th international conference on metallurgy and materials, conference proceedings, pp 105–112. https://doi.org/10.37904/metal.2020.3439, Retrieved from www.scopus.com
12. Matkarimov ST, Yavkochiva DO, Berdiyarov BT, Nosirov FD (2020) Hydrometallurgical processing of copper-smelting dust. Int J Emerg Trends Eng Res 8(7):3088–3094. https://doi.org/10.30534/ijeter/2020/35872020
13. Matkarimov ST, Berdiyarov BT (2020) Development of the wasteless technology of processing of steel-smelting slags. https://doi.org/10.1007/978-3-030-46817-0_35, Retrieved from www.scopus.com
14. Kholikulov DB, Abdurahmonov S, Boltaev ON, Matkarimov ST (2020) Separation of metals from technological solutions copper production. Int J Emerg Trends Eng Res 8(7):3557–3561. https://doi.org/10.30534/ijeter/2020/110872020
15. Vanyukov AV, Zaytsev VY (2003) Theory of pyrometallurgical processes. Metallurgy 504
16. Pyrikov AN, Jacques AR, Borisov AVK (1986) To a question of carbon heat thermal restoration of super magnetite concentrate//Izv of higher education institutions. Ferrous Metall 1:14–17
17. Arkhipov VS, Smolyaninov SI, Strakhov VM (1986) Theory and practice of direct receiving iron. Science 131–135
18. Arkhipov VS, Smolyaninov SI (1989) Influence of reactionary ability of carbon on hematite restoration speed//Izv. Higher education institutions. Ferrous Metall 1:10–13
19. Matkarimov ST, Yusupkhodjaev AA, Khojiev ST, Berdiyarov BT, Matkarimov ZT (2020) Technology for the complex recycling slags of copper production. J Critical Rev 7(05). https://doi.org/10.31838/jcr.07.05.38
20. Matkarimov ST, Berdiyarov BT, Yusupkhodjaev AA (2019) Technological parameters of the process of producing metallized iron concentrates from poor raw material. Int J Innov Technol Expl Eng 8(11):600–603. https://doi.org/10.35940/ijitee.k1586.0881119

Dimensionless Bending Rigidity Ratio and Material Dependency of Microbeams with Size Effects

R. Resmi, V. Suresh Babu, and M. R. Baiju

Abstract Microbeams are extensively used for many applications in the MEMS/NEMS industry. The structural material properties modulate the performance of the beam-based resonators in microscale. In the current analysis, the flexural behaviour of microbeams subjected to various structural materials is analysed and the bending rigidity, the most significant flexural parameter associated with it, is investigated. As the device dimensions are scaled down, nonclassical continuum theories are applicable in structural domain to represent its dynamic characteristics. The current analysis incorporates modified couple stress theory as the chosen nonclassical elasticity theory to accurately model the vibrating microbeams with five different structural materials: Si, polySi, GaAs, diamond and SiC. In the analysis, the impacts of scaling effect on bending rigidity ratio of microbeams are investigated. Quality factor limited by thermoelastic damping (Q_{TED}) is an important performance parameter of resonating microstructures and found to be depending on the flexural characteristics. The variation of bending rigidity ratio with Poisson's ratio is also investigated. The material order in which bending rigidity varies with dimensionless length parameter is explored for the five structural materials. The size effect parameter (l/h) increases the bending rigidity ratio and eigenfrequencies according to our study. The simulations have been conducted numerically using MATLAB 2015a. The structural materials with high bending rigidity ratio can be chosen for developing low energy dissipation MEMS/NEMS-based resonators in today's leading edge technologies like IoT and 5G networks.

Keywords Microbeam resonators · Size effects · Dimensionless length scale parameter · Dimensionless bending rigidity ratio · Poisson's ratio

R. Resmi (✉)
University of Kerala, LBS Institute of Technology for Women, Poojappura, India
e-mail: resmilbs@gmail.com; resmi@lbsitw.ac.in

V. S. Babu
APJ Abdul Kalam Technological University, College of Engineering Trivandrum, Trivandrum, Kerala, India

M. R. Baiju
University of Kerala, Kerala Public Service Commission, Trivandrum, Kerala 695004, India

K. Geetha et al. (eds.), *Recent Trends in Materials*, Springer Proceedings in Materials 18, https://doi.org/10.1007/978-981-19-5395-8_16

1 Introduction

Microbeam-based structures are widely used for many applications mainly because of its enhanced adaptability and flexibility by varying the structural material properties. The dynamic and thermal functionality of the microbeams relies on the coupled stress and strain of the structural materials used for making the devices [1]. Microbeams are simple two-dimensional structural units with superior vibrational and mechanical characteristics such as high quality factor, very low mass, high bearing capacity and exceptional stiffness properties [2].

The application and quality of the beam structure are determined by its tensile property which can be considered as one of the significant fundamental structural mechanical properties [3]. The study of flexure mechanisms associated with its deformation in micro/nanobeams leads to the development of systems having superior performance, low cost, reduction of friction, etc. Micro/nanobeams with proper complaint mechanisms are extensively used for applications like high precision actuators and sensors [4].

To accurately represent the theoretical tensile model, the elemental properties which are bending rigidity, Poisson's ratio (υ), Young's modulus (E) and the geometric parameters of the structure are needed. The bending rigidity of the resonator is the most significant factor affecting the elongation and compression of elastic structures [5, 6]. The resistance to deformation during bending of the microstructure represents bending rigidity (BR) or bending stiffness [7, 8]. Bending rigidity depends on Young's modulus, moment of inertia and geometric parameters of the microbeam. Poisson's ratio of a material is the ratio of lateral strain and axial strain developed along the microplate. The theoretical limits of the values of Poisson's ratio are in between -1 and 0.5 where 0.5 corresponds to the value of a completely incompressible material like rubber. Usually, negative values for Poisson's ratio are not preferred. The values of Poisson's ratio for almost all materials lie between 0 and 0.5. The values of υ for most of the metals lie between 0.25 and 0.35. Young's modulus is the modulus of elasticity in tension and defined as the ratio of stress to strain along the axial direction along which it elongates. Young's modulus is required to be non-negative for all materials, i.e. $E > 0$ [9, 10].

Flexural stiffness is different from torsional stiffness by incorporating shear modulus instead of Young's modulus. Stiffness of a material is the rigidity of an object to resist deformations and can be defined as rigidity per unit length. The product of Young's modulus (E) and second moment of inertia (I) is flexural rigidity while the product of shear modulus (G) and polar second moment of inertia (J) is the torsional rigidity [11, 12].

In modern times, all the technology-related works and researches need to solve the issue of selecting the appropriate material which can satisfy the technological requirements cost-effectively. Thermoelastic damping is a decisive issue in resonators and much affected by the material properties as reported in literature [13, 14]. The biggest challenge for the researchers today is to develop different theories in continuum mechanics to analyse the material properties when the size of the devices

is scaled down [15]. Consequently, several nonclassical elasticity theories are evolved to include size effects like nonlocal theory [16] and strain gradient theories [17]. The nonlocal theories predict larger deflection, smaller natural frequency and softening effect, while strain gradient theories are inconsistent with this by providing stiffening effect. According to strain gradient theories, higher natural frequency and smaller deflections are obtained. The experimental results exhibit softening effect and so nonlocal theory is inconsistent with it. Hence, modified couple stress theory (MCST) which is a simplified version of strain gradient theory is selected in the current analysis. MCST is first developed by Yang et al. with a single material length scale parameter to incorporate downsizing of structures [18]. The main advantages of MCST are its computational efficiency and accuracy. The importance of size scaling and application of MCST is very much helpful in accurate prediction of TED also. There are several works associated with thermoelastic damping in microplates and microbeams with nonclassical theories [19, 20].

Park et al. experimentally proved the size dependence effects in microstructures, and hence, the scaling effect should be included in the flexural analysis also for accurate modelling [21]. The importance of the length scale parameter in rectangular microplates based on MCST is analysed by Razavilar et al. [22] Rezazadeh et al. studied the plane stress/plane strain conditions and bending of microbeams applying MCST [23]. Resmi et al. explored the influence of dimensionless length scale parameter (l/h) on thermoelastic attenuation of microplate resonators with different structural materials [24]. The impact of material length scale parameters on the normal and shear deformation of 2D-FG microbeams is studied by Karamanlı et al. [25]. The bending rigidity of a liquid membrane is analysed by Liu P et al. who performed molecular dynamics simulations and found that the bending rigidity of graphene decreases with increasing temperature [26]. Sun Fengxin et al. studied handle evaluation system for fabrics and yarn, and the significance of surface friction of fabrics, the effect of bending rigidity and Poisson's ratio [27] on stretching are explored.

In the literature, dimensionless bending rigidity ratio of microbeams based on different structural materials is not available. Flexural mechanical behaviour of microbeams from previous research works is illustrated in the introduction section. In this paper, the basic analytic equations of bending rigidity ratio of a rectangular microplate applying size effect are given in Sect. 2. To include size effect, MCST is used in the analysis. The results and discussions are presented in Sect. 3 which analyses the impact of size effects and Poisson's ratio on bending rigidity ratio. The plots of the bending rigidity ratio for varying dimensionless length parameter for different materials are illustrated in Sect. 3. In Sect. 3.1, dimensionless bending rigidity ratio is investigated with three different values of dimensionless length scale parameter. Section 3.2 elaborates the relation between Poisson's ratio and dimensionless bending rigidity ratio of the microbeams. In Sect. 3.3, the assessment of impact of l/h with dimensionless bending rigidity ratio with diverse structural materials having different Poisson's ratio is given. The conclusions of the work are given in Sect. 4.

2 Expression for Dimensionless Bending Rigidity Ratio of a Microbeam

A nonclassical theory, Modified couple stress theory, is applied to incorporate size scaling effects. In MCST, the strain energy density is a function of both strain and curvature tensors. The impact of scaling effect on thermoelastic damping limited quality factor (Q_{TED}) is very remarkable, and Q_{TED} is very much enhanced. The reason behind this noteworthy effect is explained as follows: the size effect parameter (l/h) increases the bending rigidity of the microplate which enhances the size-dependent frequencies and quality factor of the resonators. This tendency shows a large amount of trimming in energy dissipation due to thermoelastic damping.

Bending rigidity or bending stiffness of the beam,

$$D = \frac{EI}{(1-\upsilon^2)} = \frac{Eh^3}{12(1-\upsilon^2)} \tag{1}$$

where E is Young's modulus, I is the moment of inertia per unit length of the plate, υ is Poisson's ratio of the material, and h is the thickness of the plate.

Poisson's ratio,

$$\upsilon = \frac{-\varepsilon_{yy}}{\varepsilon_{xx}} \tag{2}$$

Dimensionless bending rigidity ratio denoted by R is defined as the ratio of bending rigidity with size effect to that of without size scaling.

The dimensionless bending rigidity ratio (BRR),

$$R = \frac{D + \mu l^2 h}{D} = 1 + 6(1-\upsilon)\left(\frac{l}{h}^2\right) \tag{3}$$

where l/h is the dimensionless length scale parameter.

Due to the presence of dimensionless length scale parameter when applying MCST, stiffness will increase leading to smaller deflections and higher natural frequency. If mode numbers (m, n) for the thermoelastic plate are considered, the thermoelastic frequency dispersion relation between ω_i and l/h can be obtained as [24]

$$\omega_i = \pi^2 \sqrt{\frac{M'}{\rho h}}\left(\frac{m^2}{L^2} + \frac{n^2}{W^2}\right) = \omega_0 \sqrt{1 + \frac{M_1}{M_0} + \frac{\Delta_E}{2}[1 + f(\omega)]} \tag{4}$$

where ω_0 is the isothermal value of the eigenfrequency of the microplate, and

$$\omega_0 = \pi^2 \sqrt{\frac{M_0}{\rho h}} \left(\frac{m^2}{L^2} + \frac{n^2}{W^2} \right) \tag{5}$$

$$\omega_0 = \pi^2 \sqrt{\frac{D + \mu l^2 h}{\rho h}} \left(\frac{1}{a^2} + \frac{1}{b^2} \right) \tag{6}$$

The influence of size effect is significant in determining the eigenfrequency of the microplate as in Eq. (6). The real and imaginary parts are represented by Re(ω) and Im(ω), respectively. While considering thermoelastic coupling, Re(ω) gives the eigen frequencies and Im(ω) accounts for the attenuation of the vibration amplitude of the microbeam resonators.

The quantity of thermoelastic energy is expressed in terms of the inverse of the quality factor,

$$Q^{-1} = 2 \left| \frac{|\mathrm{Im}(\omega)|}{\mathrm{Re}(\omega)} \right| \tag{7}$$

3 Results and Discussions

The numerical results are generated using MATLAB 2015 for a microbeam resonator with five different structural materials—diamond, SiC, Si, polySi and GaAs. The structural material properties of the microbeams are taken from [19]. In the current analysis, the material length scale parameter is taken to be equal to the thickness of the plate; i.e. instead of material length scale parameter (l), dimensionless length scale parameter (l/h) is taken. The numerical results are presented for different values of dimensionless length scale parameters to study the flexural dynamics of simply supported microbeams by investigating the bending rigidity ratio. In Sect. 3.1, dimensionless bending rigidity ratio is investigated with three different values of dimensionless length scale parameters. Section 3.2. elaborates the relation between Poisson's ratio and dimensionless bending rigidity ratio of the microbeams. In Sect. 3.3., the impact of size effect on bending rigidity ratio is clearly demonstrated.

3.1 Dimensionless Bending Rigidity Ratio (BRR) Analysis

The numerically simulated values of the dimensionless bending rigidity ratio of a microbeam for three different dimensionless length scale values, i.e. $l/h = 0$, 0.5, 1, are shown in Table 1. The values are generated for all the five chosen structural materials such as polySi, diamond, Si, GaAs and SiC.

Table 1 Dimensionless bending rigidity ratio

l/h	0	0.5	1
PolySi	1	2.161	5.664
Diamond	1	2.3965	6.586
Si	1	2.08	5.32
GaAs	1	2.035	5.14
SiC	1	2.212	5.848

When $l/h = 0$, the values of dimensionless BRR corresponding to classical theory, i.e. with no size effects, are obtained. While analysing the results, it is verified that as the value of *l/h* increases, dimensionless bending ratio also increases which leads to enhanced quality factors.

Figure 1 clearly illustrates the values of dimensionless bending rigidity ratio of the microbeams applying both classical and nonclassical theories. The classical theory is realized by taking $l/h = 0$, and then, the dimensionless bending ratio becomes 1 since it indicates the ratio of bending rigidity with and without size effect.

Microbeams with size effects are perceived with a nonclassical higher order theory like modified couple stress theory (MCST). The nonclassical theory is implied with nonzero values of *l/h*, and the selected values are 0.5 and 1.

From Fig. 1, while analysing the bending rigidity ratio (BRR) of beams with size effects, the maximum value (6.586) is found to be for diamond with $l/h = 1$ and the minimum value (2.035) is obtained for GaAs with $l/h = 0.5$. For classical theory, the value of dimensionless BRR is 1 for all the chosen structural materials.

The dimensionless bending rigidity with different values of *l/h* is plotted in Fig. 2 for investigating the variation in an explicit manner. The change in dimensionless bending rigidity ratio is high when *l/h* is switched from 0 to 1 rather than from 0

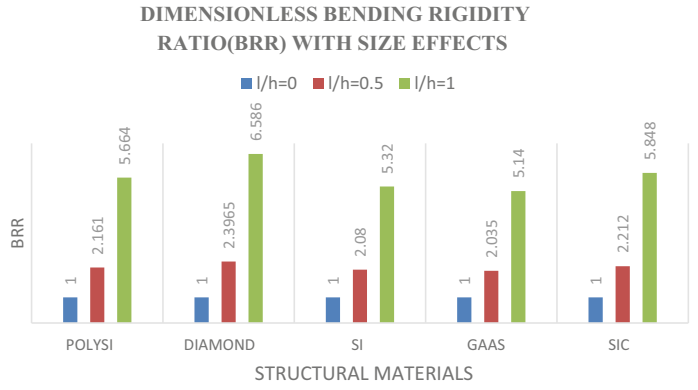

Fig. 1 Variation of dimensionless bending rigidity ratio for five structural materials with size scaling *(l/h* = 0, 0.5, 1)

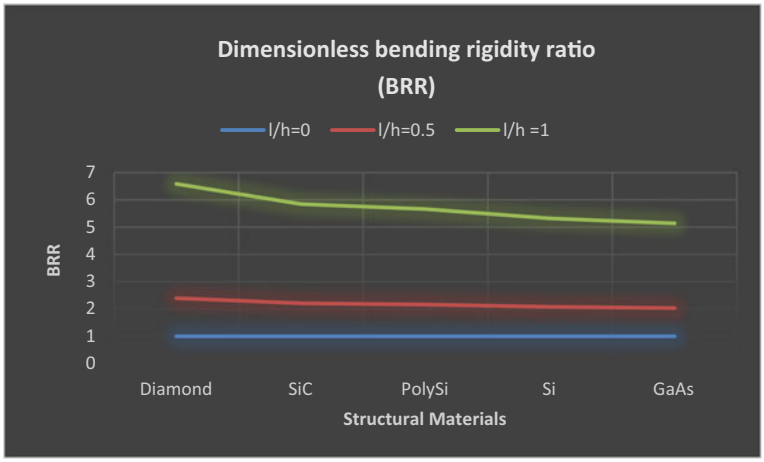

Fig. 2 Variation of dimensionless bending rigidity ratio for different values of *l/h* (*l/h* = 0, 0.5, 1)

to 0.5. It is noted that the dimensionless bending rigidity ratio change is more for dimensionless length parameter switching from 0.5 to 1 rather than from 0 to 0.5.

The percentage difference (%) in BRR is also highest for diamond and lowest for GaAs when size effect is included. As the dimensionless length scale parameter (*l/h*) increases, the change in dimensionless bending ratio is in the same material order for all transitions of *l/h* and the order in which its magnitude varies is 0 to 1 > 0.5 to 1 > 0 to 0.5. As a result, dimensionless frequency changes also prevail in the same order which causes the stiffness to increase in the same pattern. The elevated stiffness causes the maximum normalized amplitude of microbeam oscillations of the beam to reduce, and as a consequence, natural frequency increases. The reduction in energy dissipation and enhanced quality factor limited by thermoelastic damping (Q_{TED}) with size effect is mainly due to the large frequency and augmented dynamic stability threshold. Figure 3 depicts the disparity between bending rigidity ratio of microbeams with five structural materials with continuously varying *l/h* values.

Even though the largest change in BRR and frequency change is achieved with diamond, the overall percentage change in Q_{TED} is obtained for PolySi due to the impact of its thermal properties.

The material order in which dimensionless bending rigidity ratio diminishes is diamond > SiC > polySi > Si > GaAs as shown in Fig. 3. BRR depends on Poisson's ratio of each material as discussed in the following section.

3.2 Effect of Poisson's Ratio

Section 3.2 is dedicated to analyse the correlation of Poisson's ratio with dimensionless bending rigidity ratio and found to be interrelated. Poisson's ratio of five

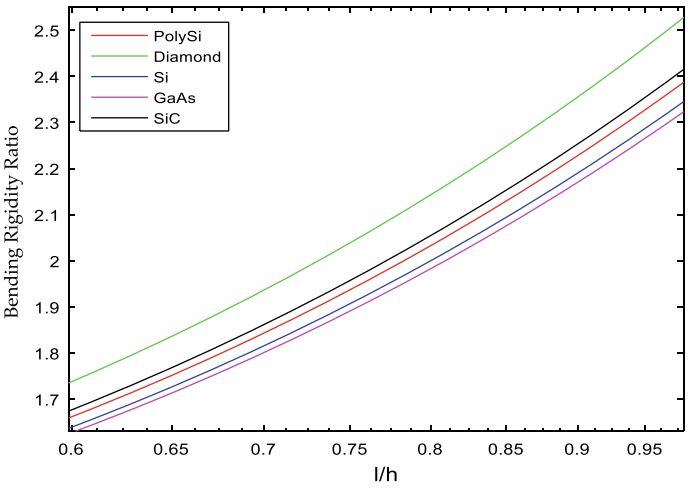

Fig. 3 Variation of bending rigidity ratio with continuously varying dimensionless length scale parameter *l*/*h* for a simply supported microbeam

structural materials chosen for analysis is plotted as a graph as shown in Fig. 3. The increasing order of the same is diamond (0.069), SiC (0.192), polySi (0.226), Si (0.28) and GaAs (0.31) taken from [19]. Figure 4 plots Poisson's ratio of each structural material, to indicate the material order in which it increases.

Table 2 shows the values of Poisson's ratio and corresponding values of dimensionless bending rigidity ratio with size effects. From Table 2, it is substantiated that the numerically simulated values of dimensionless bending rigidity ratio are reciprocally related to Poisson's ratio. Figure 5 also shows the variation of BRR values

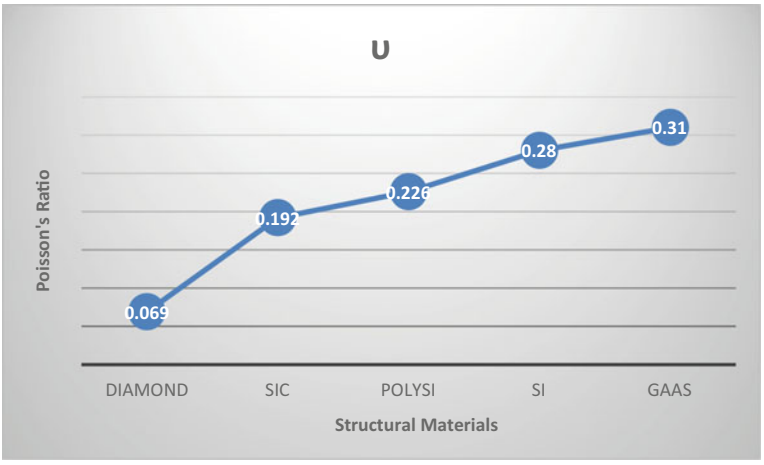

Fig. 4 Poisson's ratio (υ) of different structural materials

Table 2 Numerically simulated values of dimensionless bending rigidity ratio with size effects and Poisson's ratio values

Parameters	υ	$l/h = 0$	$l/h = 0.5$	$l/h = 1$
PolySi	0.226	1	2.161	5.664
Diamond	0.069	1	2.3965	6.586
Si	0.28	1	2.08	5.32
GaAs	0.31	1	2.035	5.14
SiC	0.192	1	2.212	5.848

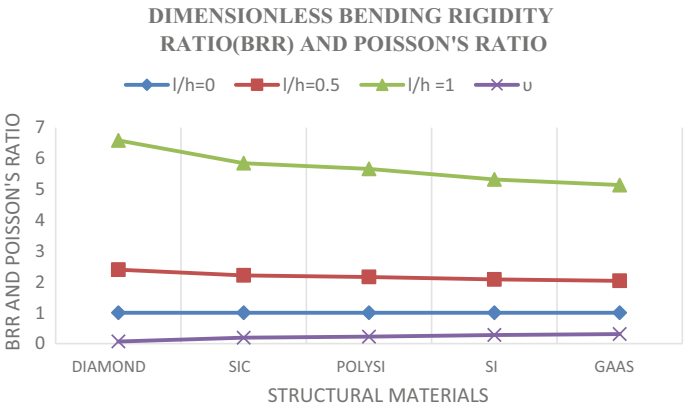

Fig. 5 Variation of bending rigidity ratio (BRR) values and Poisson's ratio (υ) of different structural materials

along with Poisson's ratio of each material to exhibit the inverse relation between the two in a vivid manner.

Another important finding regarding the dimensionless BRR is, as the value of dimensionless length scale increases, it enhances much. The dependence of dimensionless BRR on dimensionless length scale is obvious from the Table 2. The bending rigidity ratio variation with Poisson's ratio of structural materials is inversely proportional as verified from our results.

3.3 Impact of Dimensionless Length Scale Parameter on Bending Rigidity Ratio

The impact of size effect on bending rigidity of microbeams for various structural materials is presented in this section. The size effect impact is involved in the investigation by varying the dimensionless length scale (l/h) values. It is verified that the

current analysis shows the influence of size effect on bending rigidity ratio apparently. The influence on bending rigidity ratio with larger *l/h* values is higher than that compared to lower values. Figures 6 and 7 illustrate the divergence of bending rigidity and Poisson's ratio with size effects, i.e. for $l/h = 0.5$ and $l/h = 1$, respectively.

It should be noted that results of microbeams given in Fig. 6 show larger bending rigidity ratios with $l/h = 1$ as already discussed. The maximum (6.586) and minimum (5.14) values of BRR are obtained for diamond and GaAs, respectively. From Fig. 7, the relation between BRR and Poisson's ratio with $l/h = 0.5$ is shown. The maximum (2.3965) and minimum (2.035) values of BRR are obtained for diamond and GaAs as in the previous case. The major difference between the former and the latter ones

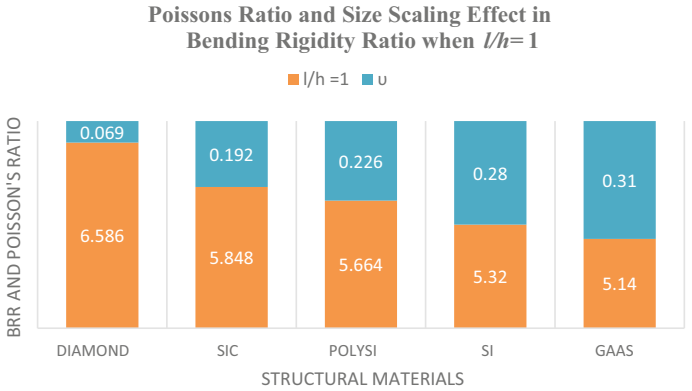

Fig. 6 Relation between Poisson's ratio (υ) and bending rigidity ratio for the chosen structural materials with $l/h = 1$

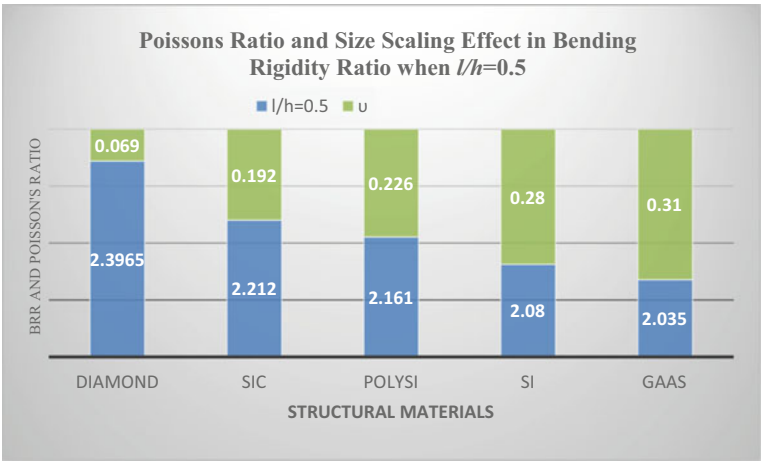

Fig. 7 Relation between Poisson's ratio (υ) and bending rigidity ratio for the chosen structural materials with $l/h = 0.5$

is, in the second case, the difference between maximum and minimum values is not high. For all the five selected materials, only a slight variation in BRR is attained as shown in Fig. 7.

The aim of the current analysis is to find out the variation of dimensionless bending rigidity ratio of various structural materials—Si, polySi, GaAs, diamond and SiC used for making the micro/nanobeams by applying a nonclassical elasticity theory.

4 Conclusion

The variation of dimensionless bending rigidity ratio of microbeams for different structural materials (Si, polySi, GaAs, SiC and diamond) with dimensionless length scale parameter is analysed in the work. The relation of Poisson's ratio of structural materials with dimensionless bending rigidity ratio is also revealed in our work. The modified couple stress theory is employed for incorporating the size effects caused by reduction of the device size to micron scales. The flexural behaviour analysis of the vibrating beams with scaling effect can be investigated by knowing its dimensionless bending rigidity ratio. The numerical results verify the variation of dimensionless bending rigidity ratio with dimensionless length scale parameter for different materials and found to be in the order of diamond > SiC > polySi > Si > GaAs. The material sequential order in which bending rigidity ratio changes is the same for all the three values of dimensionless length scale parameters, even though its quantification is different. Another important observation regarding the bending rigidity is Poisson's ratio and dimensionless bending rigidity ratio are inversely related to each other. The larger values of dimensionless bending rigidity ratio are obtained for higher *l*/*h* values. The results obtained assist designers to select suitable materials for microbeam resonating structures with proper bending rigidity to improve the flexural characteristics.

References

1. Arathy US, Resmi R (2015) Analysis of pull-in voltage of MEMS switches based on material properties and structural parameters. In: 2015 international conference on control, instrumentation, communication and computational technologies (ICCICCT), pp 57–61. https://doi.org/10.1109/ICCICCT.2015.7475249
2. Fu Y, Li L, Hu Y (2018) Enlarging quality factor in microbeam resonators by topology optimization. J Therm Stresses 42:1–20. https://doi.org/10.1080/01495739.2018.1489744
3. Schmid S, Hierold C (2008) Damping mechanisms of single-clamped and prestressed double-clamped resonant polymer microbeams. J Appl Phys 104:093516. https://doi.org/10.1063/1.3008032, https://doi.org/10.1063/1.3008032
4. Toledo J, Ruiz-Díez V, Diaz-Molina A, Ruiz D, Donoso A, Bellido JC, Wistrela E, Kucera M, Schmid U, Hernando-García J, Sánchez-Rojas JL (2017) Design and characterization of in-plane piezoelectric microactuators. Actuators 6(2):19. https://doi.org/10.3390/act6020019

5. Lesnic D (2006) Determination of the flexural rigidity of a beam from limited boundary measurements. J Appl Math Comput 20:17–34. https://doi.org/10.1007/BF02831922
6. Šubic B, Fajdiga G, Lopatič J (2018) Bending stiffness, load-bearing capacity and flexural rigidity of slender hybrid wood-based beams. Forests 9:703. https://doi.org/10.3390/f9110703
7. Peng Y-C, Ding W-Q, Yan Z, Huang X-C, Xiao B-F (2013) Analysis and calculation method of effective bending rigidity ratio in modified routine method. Yantu Gongcheng Xuebao/Chinese J Geotech Eng 35:495–500
8. Ghane M, Sheikhzadeh M, Khaburi S, Ghaeli I (2009) Investigation on the ratio of bending rigidity of fabric to yarn for low twist filament yarn. Fibres Text Eastern Europe 74:51–53
9. Wolff-Vorbeck S, Langer M, Speck O et al (2019) Twist-to-bend ratio: an important selective factor for many rod-shaped biological structures. Sci Rep 9:17182. https://doi.org/10.1038/s41598-019-52878-z
10. Wang S, Li X (2010) The effect of bending rigidity on measuring the adhesion work of membrane. Adv Mater Res 97–101:3272–3275. https://doi.org/10.4028/www.scientific.net/AMR.97-101.3272
11. Wang T, Zhou Y, Zhang J (2020) Calculation on bending stiffness of RC short beam strengthened by CFRP. Adv Civil Eng 2020(8836284):13. https://doi.org/10.1155/2020/8836284
12. Pan D, Feng Z, Lu P, Zheng Z, Zhao B (2021) Resonance-based approach for section flexural rigidity identification of simply supported beams. Eng Struct 236:112070. https://doi.org/10.1016/j.engstruct.2021.112070
13. Resmi R, Suresh Babu V, Baiju MR (2021) Numerical study of thermoelastic damping effects on diamond based beams with plane stress and plane strain conditions applying nonclassical elasticity theory. Adv Dynam Syst Appl 16(2):1371–1379, ISSN 0973-5321
14. Resmi R, Suresh Babu V, Baiju MR (2021) Analysis of thermoelastic damping limited quality factor and critical dimensions of circular plate resonators based on axisymmetric and non-axisymmetric vibrations. AIP Adv 11:035108. https://doi.org/10.1063/5.0033087
15. Li Z, He Y, Lei J, Han S, Guo S, Liu D (2019) Experimental investigation on size-dependent higher-mode vibration of cantilever microbeams. Microsyst Technol 25. https://doi.org/10.1007/s00542-018-4244
16. Yang Z, Cheng D, Cong G, Jin D, Borjalilou V (2021) Dual-phase-lag thermoelastic damping in nonlocal rectangular nanoplates. Waves Random Complex Media. https://doi.org/10.1080/17455030.2021.1903117
17. Li X, Li L, Hu Y, Ding Z, Deng W (2017) Bending, buckling and vibration of axially functionally graded beams based on nonlocal strain gradient theory. Compos Struct 165:250–265
18. Yang F, Chong A, Lam DCC, Tong P (2002) Couple stress based strain gradient theory for elasticity. Int J Solids Struct 39(10):2731–2743
19. Resmi R, Baiju MR, Suresh Babu V (2019) Thermoelastic damping dependent quality factor analysis of rectangular plates applying modified coupled stress theory. In: AIP conference proceedings 2166:020029. https://doi.org/10.1063/1.5131616
20. Vahdat AS, Rezazadeh G, Ahmadi G (2012) Thermoelastic damping in a micro-beam resonator tunable with piezoelectric layers. Acta Mech Solida Sin 25:73–81
21. Park SK, Gao X-L (2006) Bernoulli-Euler beam model based on a modified couple stress theory. J Micromech Microeng 16:2355–2359
22. Razavilar R, Alashti RA, Fathi A (2016) Investigation of thermoelastic damping in rectangular microplate resonator using modified couple stress theory. Int J Mech Mater Des 12(1):39–51
23. Rezazadeh G, Vahdat AS, Tayefeh-rezaei S et al (2012) Thermoelastic damping in a micro-beam resonator using modified couple stress theory. Acta Mech 223:1137–1152. https://doi.org/10.1007/s00707-012-0622-3
24. Resmi R, Suresh Babu V, Baiju MR (2021) Impact of dimensionless length scale parameter on material dependent thermoelastic attenuation and study of frequency shifts of rectangular microplate resonators. 2021 IOP Conf Ser Mater Sci Eng 1091:012067
25. Karamanlı A, Vo TP (2018) Size dependent bending analysis of two directional functionally graded microbeams via a quasi-3D theory and finite element method. Composites Part B: Eng 144:171–183, S1359836817342142. https://doi.org/10.1016/j.compositesb.2018.02.030

26. Liu P, Zhang YW (2009) Temperature-dependent bending rigidity of graphene. Appl Phys Lett 94(23):231912. https://doi.org/10.1063/1.3155197
27. Sun F, Du Z, Yu W, Feng G, Chen N (2016) Effect of bending rigidity, Poisson's ratio and surface friction of fabrics on the stretching step of the comprehensive handle evaluation system for fabrics and yarns. Text Res J 86:1–15. https://doi.org/10.1177/0040517515617428

Characterization and Slurry Erosion Performance of Plasma Sprayed Ni–Al_2O_3 and Ni–TiO_2–Al_2O_3 Coatings on Turbine Steel

Vishal Kumar Rana, Vibhu Sharma, and Sushma Singh

Abstract In the Himalayan region, hydro turbine parts are prone to significant erosion, particularly during the rainy season. In the present work, the performance of plasma spray Ni–Al_2O_3, and Ni–Al_2O_3–TiO_2 composite coatings were studied, in order to protect the CA6NM hydro turbine steel from slurry erosion. The microstructural characterization of the as-sprayed coatings was studied using the SEM, EDS, and XRD techniques, whereas, for mechanical characterization, various tests were performed for evaluating the micro-hardness, porosity, fracture toughness, surface roughness, and coating density in the as-sprayed coatings. The test was conducted by using the slurry jet erosion test rig. Impact of different parameters which influence the erosion process namely Inflight velocity, Concentration of slurry particles, and average size of erodent's was also evaluated. The as-sprayed Ni–TiO_2–Al_2O_3 coating outperformed the Ni–TiO_2–Al_2O_3 coating and uncoated steel specimens in terms of slurry erosion resistance for all the experimental conditions.

Keywords Plasma spray · Ni–Al_2O_3 · Ni–TiO_2–Al_2O_3 · Slurry erosion · SEM · EDS and XRD

1 Introduction

The deteriorate of the turbine steel used specifically for the hydro turbine steel due to the slurry erosion is the challenging task for its mitigation. The slurry erosion is commonly seen in the turbine blades, propellers, fluid transfer pipelines, spheres, and other part of the machineries. It is the crucial problem in the exiting power generation systems in order to the meet the power demand and supply. Slurry erosion is undesirable in hydro power systems that is primarily connected with the erosion of exposed parts of the turbine to particles laden fluids [1]. The turbine industry faces huge

V. K. Rana (✉) · V. Sharma · S. Singh
Baddi University of Emerging Sciences and Technology, Baddi, India
e-mail: ranavishal413@gmail.com

V. Sharma
e-mail: vibhu.sharma@baddiuniv.ac.in

K. Geetha et al. (eds.), *Recent Trends in Materials*, Springer Proceedings in Materials 18, https://doi.org/10.1007/978-981-19-5395-8_18

economic loss approximately US $120–150 million dollars [2, 3]. Though steel used in the hydro turbine power plants have good erosion resistance properties, it faces severe erosion problem when exposed to the incoming slurry specially in the rainy season. There is always a need of engineering materials which act as barrier between the exposed part of the turbine and slurry. In a severe monsoon season situation, plants must shut down for maintenance when the water-silt concentration exceeds the permitted limit of 5000 ppm. Particle velocity, impingement angle, concentration, hardness, and erodent shape are some of the elements that have caused the turbine components to deteriorate, affecting performance [4]. A variety of approaches have been devised to reduce the impact of sedimentation erosion on the targeted surface. As a result, wear-resistant alloys or wear-resistant coatings are recommended to counteract the erosion problem. Various processes, such as weld overlay, diffusion coatings, and thermal spray coatings, can be used to develop these coatings. Weld overlays and diffusion coatings have some downsides, such as inappropriate coating thickness, altered microstructure of base metal, and numerous overlay passes leading to embrittlement of existing overlays. All of these issues make it difficult to apply weld overlay and diffusion coatings. On the other hand, thermal spray coatings are commonly used to develop slurry erosion resistance in steel due to their low cost and outstanding mechanical quality [5–7]. Each thermal spray coating technique has its own set of characteristics, making it difficult to pick one that is best suited to all coating requirements. Plasma spraying is a well-known and commonly used process for surface coating engineering, with high deposition rates, fast application speeds, and low costs. In the plasma spray process, feed stock powder material is fed into a high-temperature plasma jet, where it is rapidly heated and accelerated at high flow velocity. The molten particles collide and solidify quickly on the substrate surface, forming a coating [8–11]. Ni-based coatings have been investigated as a base material in combination with Ti, Al, SiO_2, Co, and Cr as reinforcement materials in previous literature surveys of the tungsten carbide (WC) potential [12, 13]. Micron-size base material and micron-size reinforcement material were combined to make these composites. In comparison with the untreated surface, the results showed that the coated surface had a higher hardness, lower porosity, and stronger erosion resistance. The major components used to make hard coatings are ceramics such as Al_2O_3, TiO_2, and WC [14]. Compare the Ni–Al_2O_3 and Ni–Al_2O_3–TiO_2 ceramic coating compositions placed on the CA6NM turbine steel. The addition of TiO_2 to coatings improved binding strength and surface roughness. The Ni–Al_2O_3 coatings on CA6NM turbine steel were investigated. According to the author, the addition of alumina to nickel improved the coating's mechanical qualities and boosted erosion resistance [15]. Several researchers have looked into the field of tungsten carbide-based coatings because of their exceptional mechanical properties. Slurry erosion reduction is best achieved with WC-10 Co-4Cr coatings [16, 17]. Carbide coating powders are expensive, which limits their usefulness for hydro turbine applications [3, 18]. Furthermore, the researchers highlighted the advantages of Ni–TiO_2 coatings in terms of mechanical qualities for large-scale industrial applications which includes high-pressure valves, automotive components, maritime applications, etc. [19, 20]. In their literature review, found that adding TiO_2 ceramic material to

the Al_2O_3–$13TiO_2$ coating composition improved fracture propagation resistance for wear applications when compared to conventional coatings [21]. Because of the greater toughness property produced during applying the coating, it displayed outstanding wear performance. Despite their remarkable qualities such as high hardness and wear resistance, coating deposition employing multi-dimensional Al_2O_3 and TiO_2 metal-ceramic particles has received relatively little attention. There has been an observation that various thermal spraying methods are used for developing variety of coating materials as shown in Table 1. Many researchers in their studies reported the effect of the erosion on the developed coating by HVFS, HVOF, Cold spray, and D-Gun methods. Due to high velocity of in-flight coating particles, low flame temperature range in HVFS and HVOF has shown various defects such as presence of unmelted particles, non-uniform coating structure, and high porosity. Moreover, the coating developed by such methods is more expensive than the plasma spray method. In spite of high degree of particle melting, and flame temperature in plasma spray method that enable it most suitable for all materials to be sprayed giving high density coatings with low heat input, the studies of erosion effects on $NiAl_2O_3$–TiO_2 coatings developed by plasma-sprayed method are limited [22–26]. Hence, in the present work, Ni–Al_2O_3 and Ni–TiO_2–Al_2O_3 coatings were developed using the plasma thermal spray method and the performance of the developed coatings was studied under slurry erosion conditions. The effects of erosion parameters were also studied on the developed coating. The current coating formulations are designed to have superior erosion resistance to uncoated steel while maintaining outstanding mechanical qualities. The study's findings were an attempt to gain a better understanding of the Ni–Al_2O_3, and Ni–TiO_2–Al_2O_3 coatings slurry erosion performance.

2 Experimental Details

2.1 Substrate Material

The selected steel as substrate which is known as 13Cr4Ni steel (ASTM A-743) was provided by the Hindustan Industrial Steels Limited, Ludhiana, Punjab, India. The coating substrate samples were prepared initially by cutting into number of specimens with 20 mm × 20 mm × 5 mm size.

Before the initiation of coating process, the specimen top surface was made rough by sand blasting process using alumina abrasive particles with an average particle size of 80 grit. Surface roughness was measured with a surface roughness tester (Make: Mitutoyo, Model No, SJ-210) and observed between 5 μm and 8 μm. The values of the parameters set in the grit blasting machine in order to generate the rough surface on the substrate are listed in Table 2. This pre-treatment is required so that coating can properly stick to the substrate surface.

Table 1 Present the betterment of the proposed approach over the traditional method

References	Coating composition	Coating method	Remarks	Application
[22]	NiCrBSi–Al_2O_3	HVOF	Improper metal deposition, presence of unmelted particles	Slurry erosion
[23]	Ni–20Cr_2O_3	HVOF	Presence of unmelted particles, low melting temperature, Improper metal deposition	Slurry erosion
[24]	Ni–20Cr_2O_3, Ni–30Al_2O_3, and Al_2O_3–13TiO_2	HVOF	Low melting temperature, presence of unmelted particles	Slurry erosion
[25]	Ni–Wc	Cold spray	Low pressure. When particles strike the surface, they do not stick properly	Slurry erosion
[26]	Ni–20Cr_2O_3, Ni–20Al_2O_3, Ni–15Cr_2O_3–5TiO_2 and Ni–15Al_2O_3–5TiO_2	HVOF	Presence of unmelted particles, improper metal deposition	Slurry erosion

Table 2 List of parameters used for generating rough surface on substrate by blasting machine

Parameters	Value
Type of abrasive particles	Brown Al
Avg. size of abrasive particles (μm)	20
Impinging Pr. (kPa)	411–539
Impinging angle	90°
Working distance (mm)	152–177
Value of surface roughness (μm)	6–10

2.2 Formulation of Feedstock Powder and Coating Deposition

Present study employed commercially available pure Nickel (Ni) powder, titanium oxide (TiO_2) powder, and alumina (Al_2O_3) powders for the development of the coating on substrate. The composition of Ni–50Al_2O_3 powder was prepared in a 50:50 weight ratio, and Ni–25Al_2O_3–25TiO_2 powder composition was prepared in a 50:25:25 weight ratio. The composition of the coating powders was prepared by

Table 3 Coating elements designation and percentage proportion

Designation	Elements		
	Nickel (%)	Titanium (%)	Alumina (%)
Ni–Al_2O_3	50	–	50
Ni–TiO_2–Al_2O_3	50	25	25

Table 4 Plasma spray parameters used for deposition of coatings

Spray parameters	Value
Spray distance	3–4 inch
Powder feed rate	35 gm/min
Carrier/Primary gas	Argon (38 nlpm)
Arc current	550–600 A
Arc voltage	69 V
Secondary gas	Hydrogen (5 nlpm)

simply mixing them in a blender machine. Table 3 shows the coating compositions and designations in greater detail. At MECPL (Metallizing Equipment Company Pvt. Ltd.) in Jodhpur, Rajasthan, India, the facility of Plasma Spray process was used to deposit the coating particles on given substrate material. Table 4 shows the parameters used during the plasma spray process in order to deposit the coating.

2.3 Microstructural Characterization and Mechanical Analysis

The distinct elements and phases present in the coating powders and as-sprayed specimens were identified using XRD (Model: Expert Pro, make: PAN analytical) analysis. In the XRD analysis test, CuKα radiation was used in the 2θ range from 0° to 90°. X'pert HighScore Pro software and scanning electron microscope (SEM) were used to analyze the different phases present and surface morphology of the composite powders and as-sprayed specimens (Model: JSM IT500), respectively. The components present in the coating powders and as-sprayed coatings were determined using Energy-Dispersive Spectroscopy (EDS). A low-speed diamond cutter was used to cut the as-sprayed specimens in order to estimate micro-hardness at cross section. Using hot mounted hydraulic mounting press, the cut specimens were mounted in transoptic epoxy resins (Model: ECOPRESS 52). Afterward, the mounted specimens were mirror polished with 600, 800, 1200, 1500, and 2000 grit sizes of emery papers and finally polished with 1-μm levigated alumina by using disk polishing machine. Subsequently, the specimens were thoroughly cleaned with water and dried before being examined. The fracture toughness and coating density of the as-sprayed specimens were analyzed using Eqs. (1) and (2), respectively.

$$K_c = 0.079\left(\frac{p}{a}\right)^{\frac{3}{2}} \log\left(4.5\frac{a}{c}\right) \quad (1)$$

where:

p = Indented Load (mN)
c = Half-diagonal Indentation (μm)
a = Crack Length from the Center of the Indentation (μm)

$$\text{Coating density}(\rho)\text{gm/cm}^3 = \rho_1\left(\frac{m_1}{m_a - m_1}\right) \quad (2)$$

where:

ρ_1 = water density at room temperature (g/cm^3)
m_a = the coating weight in the air (g)
m_1 = the coating weight in water (g).

The Archimedes technique was used to determine the coating density. In a beaker of water, the weight m_1 of the as-sprayed specimens was first measured. The specimen coating was then carefully scraped away with emery paper, and the weight of an identical sample was calculated in a beaker of water. The mass of the coting in water was calculated using the differences between these two values. In the same way, m_a was estimated by weighing coated and uncoated samples in the air. The mass of the coating in the air was determined by the difference between the two numbers. A Mitutoyo SJ-210 surface roughness tester was used to examine the surface roughness values for the as-sprayed samples. Surface roughness was measured using an average of three observations, and the results are shown in Table 5. A micro-hardness tester machine (Model: DM-1000ZDT) with digital display was used to measure the micro-hardness of the substrate steel, on the top coated surface. The diamond indenter was used for indentation and was given a 500 gm indenting load for surface penetration with a dwell time of 20 s. The micro-hardness value of the coating was calculated as the average of three readings.

Table 5 Observed values in as-sprayed coatings for Mechanical Characterization

Samples	Coating thickness (μm)	Avg. micro-hardness (HV)	Avg. surface roughness Ra (μm)	Avg. coating density (Kg/m^3)	Porosity (%)	Fracture toughness (MPa m$^{\frac{1}{2}}$)
Ni–TiO_2–Al_2O_3	586 ± 10	821 ± 21	6.034 ± 0.3	5910 ± 80	1.85–4.56	1.62 ± 0.10
Ni–Al_2O_3	289 ± 10	746 ± 46	7.11 ± 0.4	5800 ± 50	0.67–1.12	1.59 ± 0.09
Steel	–	310 ± 10	1.37 ± 0.3	–	–	–

2.4 Slurry Erosion Test Setup

The experiment of erosion study tests was performed using an erosion jet machine. This high speed machine creates the non-recirculated high velocity jet, on exposed specimen under erosion study. The set-up constructed with some main components namely (1) fresh tank, (2) waste tank, (3) main pump, (4) slurry discharged pump, (5) an erosion room, feeder used for inserting slurry, and flow control valves were all incorporated in the test rig, as shown in Fig. 1. The erosion room, which was placed above the water tank, impinged on the test specimens with a stream of slurry particles. The nozzle used to create the high velocity jet of slurry was of tungsten carbide material with an outer diameter of 2 mm. The use of such material ensures the harder surface than slurry particles and ensures that the nozzle surface wears as little as possible while the slurry passes through it [27]. As a result, a uniform flow rate was achieved at the nozzle's outlet. There are two storage tanks on the rig: one for fresh water and one for wastewater. A hopper-shaped slurry feeder was used to make a mixture of fixed amount of sand in the water. The slurry feeder had an agitator to ensure that the sand particles were suspended uniformly in the water [27]. From an experimental view, it is crucial to estimate the slurry concentration at the nozzle's exit. The slurry concentration was obtained by loading the specified weight of sand into the water and subsequently charge this mixture into the feeder with a specified amount of sand particles and water. The slurry concentration at a particular time was calculated using the weight of residual sand by method of evaporation as per ASTM D-3977 standards. An ultrasonic flow meter (mounted on the main line) was used to measure the amount of slurry flow rate passes at the inlet of the nozzle. This flow rate of the slurry was measured in order to determine the velocity of jet at the exit of nozzle. Afterward, the continuity equation was used to compute the jet's velocity. Flow control valves were used to modulate the flow rate in order to achieve the desired velocity. The test on each specimen was carried out for 12 min in order to evaluate the performance of as-sprayed coatings. The mass loss from the coated and uncoated specimens was measured after a 2-min gap with 6 cycles. The same process is repeated thrice to ensure the reproducibility of experiments. A Micro-Balancing Machine (Model No. ABT100-5 M, Kern and Sohn GmbH) was used to measure the mass change of the exposed specimens with the least count of 1 mg. The samples of as-sprayed and uncoated steel were cleaned with acetone; subsequently, the moisture was dried using the blower in order to obtain the accurate measurement. To assess the impact of erosion conditions, sand was acquired from the Rampur Hydroelectric Substation in Himachal Pradesh for slurry preparation. For size testing, the collected sand was sieved into various grain sizes [15]. A systematic technique was employed to prepare sand samples. The sand preparation technique for various sizes of sand samples is detailed in Table 6. The Average Fineness Number (AFN) (3) was computed by dividing the total mass of the sand sample by the sum of the obtained values.

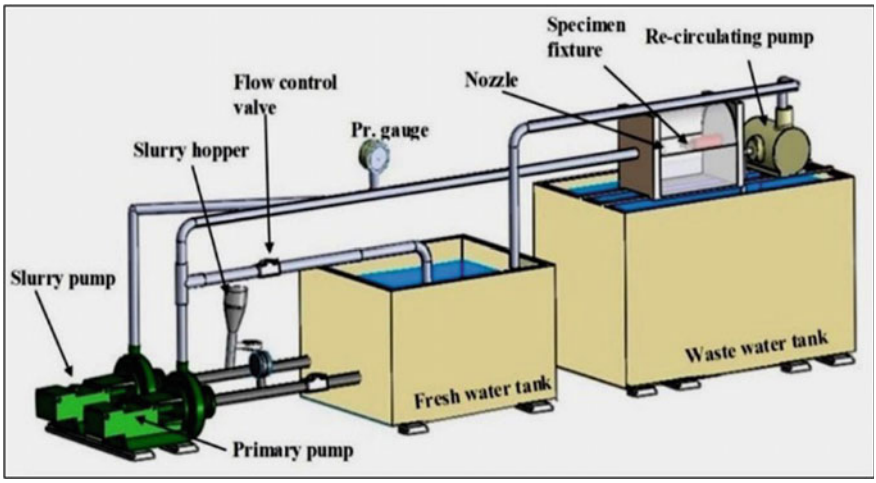

Fig. 1 Setup used in the experiment [15]

Table 6 Sieve analysis for the preparation of slurry

B.S.S. No	Mesh size (μm)	Multiplier (Mi)	Wt used (gm)	Mi × Wt. used	Wt. used (gm)	Mi × Wt. used	Wt. used (gm)	Mi × Wt. used
25	600	22	400	8800	600	13,200	800	17,600
36	425	25	400	10,000	600	15,000	800	20,000
52	300	36	400	14,400	600	21,600	800	28,800
72	212	52	400	20,800	2500	130,000	3000	156,000
100	150	72	400	28,800	1000	72,000	1000	72,000
150	106	100	1000	100,000	1000	100,000	1000	100,000
200	75	150	1000	150,000	–	–	–	–
		Total Wt. = 4000 gm		Total = 532,800	Total Wt. = 6300 gm	Total = 351,800	Total Wt. = 7400 gm	Total = 394,400
		AFN = 532,800/4000			AFN = 351,800/6300		AFN = 394,400/7400	
		AFN = 133.2			AFN = 55.84		AFN = 53.29	
		B.S.S. No. = 10.56 ≈ 150 μm			B.S.S. No. = 55.84 ≈ 300 μm		B.S.S. No. = 53.29 ≈ 450 μm	

$$\text{AFN} = \frac{\sum M_1 W_1}{\sum W_1} \tag{3}$$

This formula has been used by other researcher for the preparation and analyzing the grain size of abrasive particles [1] and [4].

2.5 Experimental Design with Testing Conditions

Several studies have been carried out to assess the possible impacts of sand concentration, impact velocity, and erodent particle size on material erosion, and these factors have been proven to have a significant influence [7] and [4]. Grewal et al. [28] discovered that the highest erosion of coatings occurs at a 90° impact angle for brittle materials. As a result, in the current study, a fixed 90° impact angle was used. Furthermore, based on the literature review, three operating parameters for the tests were chosen: slurry concentration (PPM), average particle size (μm), and impact velocity (m/s). The effect of various parameters under various test settings was calculated in order to predict coating performance. Taguchi's L9 array technique was used to obtain the optimal number of tests run. In comparison with other statistical techniques, the Taguchi method reduces the number of experiments that must be performed. This technique also aids in the creation of various combinations of parameters and their level involved in the erosion for optimized testing. Tables 7 and 8 show the experiment design of erosion parameters as well as their levels that were used during the experiment. These parameters were chosen based on conditions seen in actual hydropower facilities. Fig. 2 shows the steps followed for the complete experimentation in each cycle run. The experiments results were recorded as a cumulative volume mass (g/m^2) (4) versus exposure time and a cumulative erosion rate (g/m^2–min) (5) versus exposure time, which were calculated using the following formula [24]:

$$\text{Cumulative mass loss } (g/m^2) = \frac{\text{Mass loss(g)}}{\text{Area}\left(mm^2\right)} \tag{4}$$

$$\text{Cumulative erosion rate} = \frac{\text{cumulative mass loss } (g/m^{2)}}{\text{time(min .)}} \tag{5}$$

The results were also documented in order to have a better knowledge of the effect of slurry exposure over time.

3 Result and Discussion

3.1 Microstructure and Mechanical Characterization

Figure 3 illustrates the surface morphology of the as-sprayed Ni–Al_2O_3–TiO_2 coating along with XRD and EDS analyses. The SEM and EDS test of the coating revealed various thermal spray method characteristics such as coating elements, splats, pores, and molten and unmolten portions. All the coating elements are observed as uniformly distributed on the entire surfaces. Some way at different locations,

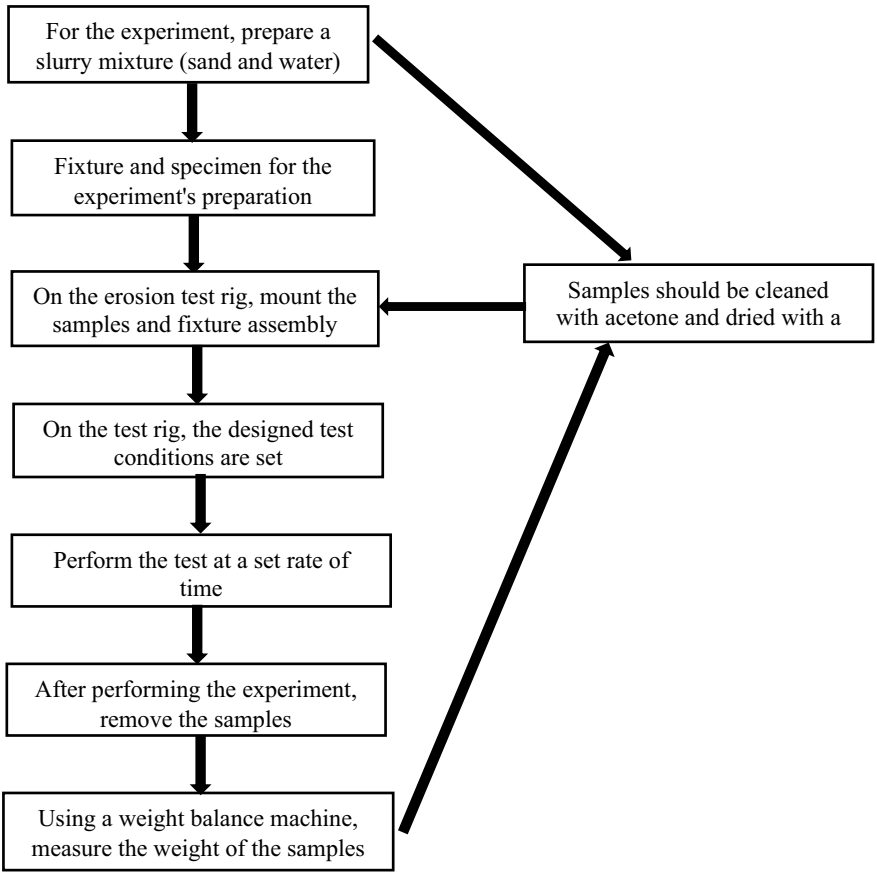

Fig. 2 Represents the sequential steps followed for the conduct of the experiment

Table 7 List of experimental parameters used for study

Parameters	PPM	Size (μm)	Velocity (m/s)
Level 1	5000	150	5
Level 2	10,000	300	10
Level 3	15,000	450	15

unmelted particles of Al and Ti can be seen. It is due to fact that the higher melting temperature and in-flight velocity may be attributed to such characteristics. The XRD test of coating indicated that there is no intermetallic bonding between the coating elements Ni and TiO_2 phases observed as main phase present in the coating. Similar results were observed [15].

Figure 4 shows the SEM, EDS, and XRD analyses of Ni–Al_2O_3 coating. The SEM and EDS analyses reveal the presence of Ni splats along with Al_2O_3 unmelted

Table 8 L9 experimental design

Experiment No	Parameters and their levels		
	Concentration (PPM)	Size (μm)	Velocity (m/s)
Exp. Condition 1	Level I	Level I	Level I
Exp. Condition 2	Level I	Level II	Level II
Exp. Condition 3	Level II	Level III	Level III
Exp. Condition 4	Level II	Level I	Level II
Exp. Condition 5	Level II	Level II	Level III
Exp. Condition 6	Level II	Level III	Level I
Exp. Condition 7	Level III	Level I	Level III
Exp. Condition 8	Level III	Level II	Level I
Exp. Condition 9	Level III	Level III	Level II

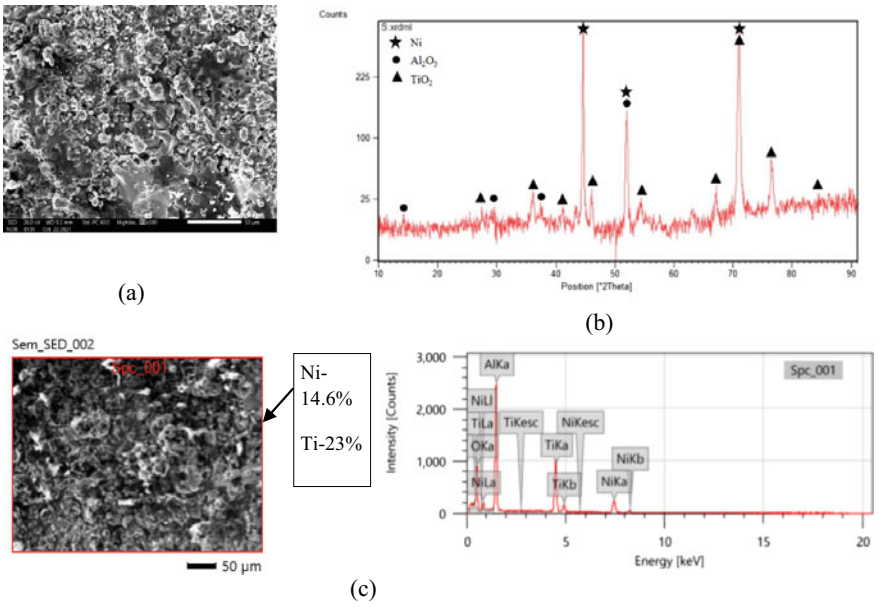

Fig. 3 **a** SEM, **b** EDS, and **c** XRD analysis of deposited Ni–Al_2O_3–TiO_2 coating

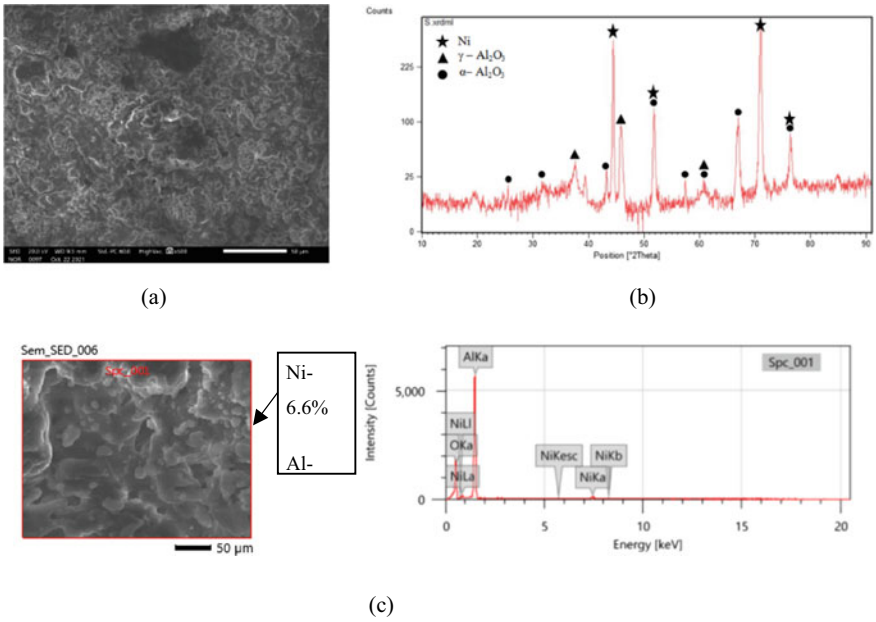

Fig. 4 **a** SEM, **b** EDS, and **c** XRD analysis of deposited Ni–Al_2O_3 coating

particles and few pores over entire surface. The overall surface of the coating is observed as dense and having a lamellae structure. The XRD diffractogram test showed the Ni and α Al_2O_3 as the main phase present in the coating. Figure 5 shows the SEM images of Ni–Al_2O_3 and Ni–Al_2O_3–TiO_2 coating. Both the coatings showed uniform bonding at coating substrate interface. The average micro thickness of Ni–Al_2O_3 and Ni–Al_2O_3–TiO_2 coatings are observed as 289 ± 10 µm and 340 ± 10 µm, respectively, as revealed from SEM image.

3.2 Mechanical Properties Analysis

Table 5 shows the results of density, average micro-hardness, and porosity estimated on the Ni–Al_2O_3 and Ni–Al_2O_3–TiO_2 coatings. The coating porosity in Ni–Al_2O_3 coating was found in the range of 0.67–1.12%, while in the Ni–Al_2O_3–TiO_2 coating porosity was found between 1.85 and 4.56%. The presence of micro cracks and weak intermetallic bonding between coating elements might be contributed for such behavior of the coatings. The Ni–Al_2O_3 coating showed average micro-hardness value (HV = 821) with a standard deviation (SD) of 46 HV where the Ni–Al_2O_3–TiO_2 coating showed average micro-hardness value (HV = 746) with a standard deviation (SD) of 21 HV measured on the surface. Further, at the cross section the average micro-hardness is observed as 1029 ± 50 HV and 1211 ± 50 HV for Ni–Al_2O_3 and

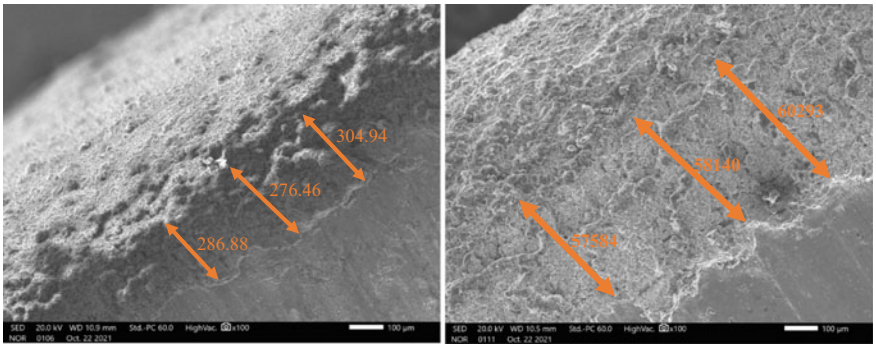

(a) (b)

Fig. 5 SEM micrograph of as-sprayed coating on cross section **a** Ni–Al_2O_3, **b** Ni–Al_2O_3–TiO_2

Ni–Al_2O_3–TiO_2 coating, respectively. The existence of unmelted particles, different grain sizes of coating, and variation in the phases generated might all contribute to difference in hardness levels. Sharma et al. [15] found the same thing in their research.

3.3 Results of Slurry Erosion

Slurry erosion tests were performed on plasma-sprayed Ni–Al_2O_3, Ni–Al_2O_3–TiO_2, and uncoated steel specimens to explore the slurry erosion response. These tests were carried out under the different experimental settings, as shown in Tables 7 and 8. When the specimens were exposed to different slurry erosion conditions, the cumulative mass loss was observed from the surface and estimated erosion rate in terms of g/m^2-min. The results revealed that for all the experimental conditions the Ni–Al_2O_3–TiO_2 exhibit higher erosion resistance in comparison with other counters parts (Fig. 6.). The higher value of fracture toughness and micro-hardness might be attributed for such behavior [15].

3.4 Synergy Effect of Erosion Parameters

The impact of increasing the slurry concentration on the mass of the specimens is seen in Fig. 7a. The mass loss for all specimens increased when the slurry concentration was raised from 5000 PPM to 10,000 PPM. The mass loss for the specimens increased when the slurry concentration was raised from 10,000 to 15,000 PPM. The mass loss for all specimens increased as the impact velocity increased from 5 m/s to 15 m/s (Fig. 7b). As the impact velocity of the sand particles increased, the kinetic energy

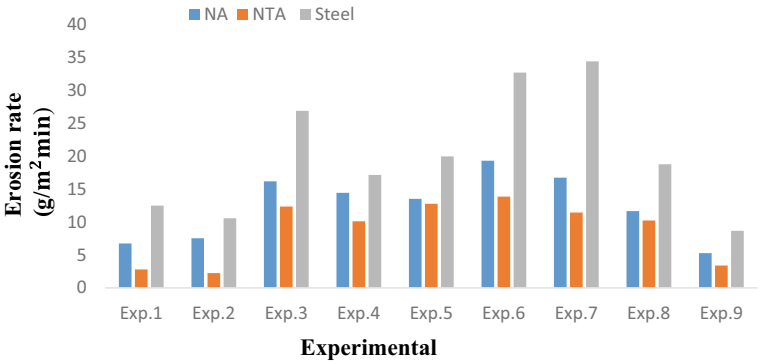

Fig. 6 Overall specific mass loss results of test coatings under different experimental runs

of the particles increased as well. As a result of the increased impact energy of the particles impinging on the exposed surface, more material was removed. Based on the results of their experiments, many publications [29, 30] have confirmed this finding. The behavior of the specimens might be related to the difference in hardness between sand particles and uncoated steel. Figure 7c shows the influence of particle size on the mass loss of uncoated steel, Ni–Al_2O_3, and Ni–Al_2O_3–TiO_2 coatings. The mass loss of all the specimens was observed to increase as the particle size was increased from 150 μm to 450 μm. The uncoated steel observed the stronger particle size effect in comparison with all other specimens. Reason behind this may be that momentum of particles moved through water increases with increase in particle size. As a result, particles with higher impinging on the exposed surface removed more material from the specimen's surfaces. The Ni–Al_2O_3–TiO_2-coated steel had the lowest mass loss of all the tested samples.

4 Conclusion

Under different slurry erosion conditions, the performances of Ni–Al_2O_3, Ni–Al_2O_3–TiO_2, and uncoated steel specimens were evaluated in this study. The following are the findings:

- Using a plasma spraying method, both coatings, Ni–Al_2O_3 and Ni–Al_2O_3–TiO_2, were successfully formed onto the substrate material.
- In comparison with Ni–Al_2O_3–TiO_2 and Ni–Al_2O_3 coatings, Ni–Al_2O_3–TiO_2 coating showed higher value of micro-hardness, facture toughness, and lower surface roughness.
- The Ni–Al_2O_3–TiO_2 coating performed better than Ni–Al_2O_3 coating and uncoated steel in terms of erosion resistance.

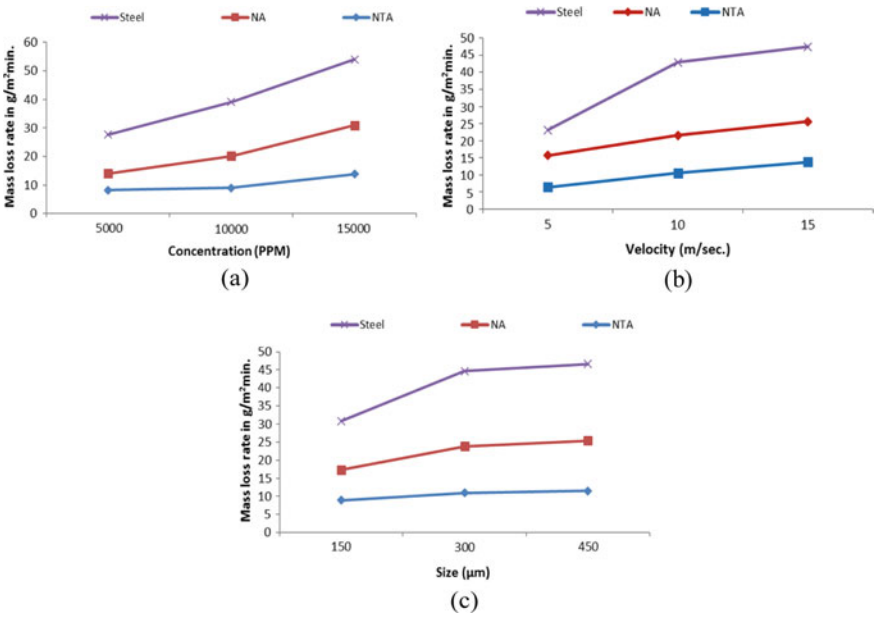

Fig. 7 Presenting the effect of **a** slurry concentration, **b** impact velocity, **c** average particle size on given specimens

- For uncoated and coated specimens, mass loss was observed proportional relation to the erosion parameters.

References

1. Kumar R, Bhandari S, Goyal A (2018) Synergistic effect of c/TiO_2 reinforcements on slurry erosion performance of nickel-based composite coatings. Proc Inst Mech Engin Part J: J Eng Tribol 232(8):974–986
2. Mann BS, Arya V (2001) Abrasive and erosive wear characteristics of plasma nitriding and HVOF coatings: their application in hydro turbines. Wear 249(5–6):354–360
3. Grewal HS, Bhandari S, Singh H (2012) Parametric study of slurry-erosion of hydroturbine steels with and without detonation gun spray coatings using taguchi technique. Metall Mater Trans A 43(9):3387–3401
4. Sharma V, Kaur M, Bhandari S (2019) Slurry jet erosion performance of high-velocity flame-sprayed nano mixed Ni–40 Al_2O_3 coating in aggressive environment. Proc Inst Mech Engin, Part J: J Eng Tribol 233(7):1090–1106
5. Thakur L, Arora N (2013) A comparative study on slurry and dry erosion behaviour of HVOF sprayed WC–CoCr coatings. Wear 303(1–2):405–411
6. Thakur L, Arora N, Jayaganthan R, Sood R (2011) An investigation on erosion behavior of HVOF sprayed WC–CoCr coatings. Appl Surf Sci 258(3):1225–1234
7. Grewal HS, Agrawal A, Singh H (2013) Slurry erosion performance of Ni–Al_2O_3 based composite coatings. Tribol Int 66:296–306

8. Ramesh CS, Devaraj DS, Keshavamurthy R, Sridhar BR (2011) Slurry erosive wear behaviour of thermally sprayed Inconel-718 coatings by APS process. Wear 271(9–10):1365–1371
9. Kaushal S, Singh S (2018) Slurry erosion behavior of plasma sprayed coating on turbine steel. Indust Lubricat Tribol
10. Sharma V et al (2022) Influence of velocity, concentration, and size of silt particles on erosion of thermal sprayed Ni/TiO_2/Al_2O_3 coatings. Surf Rev Lett. https://doi.org/doi.org/10.1142/S0218625X22400017
11. Zhao HX, Goto H, Matsumura M, Takahashi T, Yamamoto M (1999) Slurry erosion of plasma-sprayed ceramic coatings. Surf Coat Technol 115(2–3):123–131
12. Cui SY, Miao Q, Liang WP, Huang BZ, Ding Z, Chen BW (2017) Slurry erosion behavior of F6NM stainless steel and high-velocity oxygen fuel-sprayed WC-10Co-4Cr coating. J Therm Spray Technol 26(3):473–482
13. Liu SL, Zheng XP, Geng GQ (2010) Influence of nano-WC–12Co powder addition in WC–10Co–4Cr AC-HVAF sprayed coatings on wear and erosion behaviour. Wear 269(5–6):362–367
14. Kumar R, Bhandari S, Goyal A (2017) Slurry erosion performance of high-velocity flame-sprayed Ni–20Al 2O3 and Ni–10 Al_2O_3–10 TiO_2 coatings under accelerated conditions. J Therm Spray Technol 26(6):1279–1291
15. Sharma V, Kaur M, Bhandari S (2020) Performance investigation of high velocity flame sprayed multi-dimensional Ni–TiO_2 and Ni–TiO_2–Al_2O_3 coated hydro turbine steel under slurry erosion. Wear 462:203498
16. Ding X, Cheng XD, Li C, Yu X, Ding ZX, Yuan CQ (2018) Microstructure and performance of multi-dimensional WC-CoCr coating sprayed by HVOF. Int J Adv Manuf Technol 96(5):1625–1633
17. Vashishtha N, Khatirkar RK, Sapate SG (2017) Tribologicalbehaviour of HVOF sprayed WC-12Co, WC-10Co-4Cr and Cr3C2−25NiCr coatings. Tribol Int 105:55–68
18. Wood RJK, Mellor BG, Binfield ML (1997) Sand erosion performance of detonation gun applied tungsten carbide/cobalt-chromium coatings. Wear 211(1):70–83
19. Chen W, He Y, Gao W (2010) Electrodeposition of sol-enhanced nanostructured Ni–TiO_2 composite coatings. Surf Coat Technol 204(15):2487–2492
20. Li Q, Yang X, Zhang L, Wang J, Chen B (2009) Corrosion resistance and mechanical properties of pulse electrodeposited Ni–TiO_2 composite coating for sintered NdFeB magnet. J Alloy Compd 482(1–2):339–344
21. Lima RS, Moreau C, Marple BR (2007) HVOF-sprayed coatings engineered from mixtures of nanostructured and submicron Al_2O_3–TiO_2 powders: an enhanced wear performance. J Therm Spray Technol 16(5–6):866–872
22. Senapati P, Sutar H (2020) Surface erosion behaviour over NiCrBSi–Al_2O_3 composite coatings. Mater Res Express 7(7):076512
23. Bansal A, Goyal DK, Singh P, Singla AK, Gupta MK, Bala N, ... Setia G (2020) Erosive wear behaviour of HVOF-sprayed Ni–20Cr_2O_3 coating on pipeline materials. Int J Refract Metals Hard Mater 92:105332
24. Singh J (2021) Wear performance analysis and characterization of HVOF deposited Ni–20Cr_2O_3, Ni–30Al_2O_3, and Al_2O_3–13TiO_2 coatings. Appl Surf Sci Adv 6:100161
25. Kazasidis M, Verna E, Yin S, Lupoi R (2021) The effect of heat treatment and impact angle on the erosion behavior of nickel-tungsten carbide cold spray coating using response surface methodology. Emerg Mater 4(6):1605–1618
26. Singh A, Kumar H, Kumar S (2021) Comparison of slurry erosion performance of thermally sprayed coatings with the addition of TiO_2 feedstock powder. Mater Today: Proc 45:5202–5206
27. Grewal HS, Agrawal A, Singh H (2013) Design and development of high-velocity slurry erosion test rig using CFD. J Mater Eng Perform 22(1):152–161
28. Grewal HS, Agrawal A, Singh H, Shollock BA (2014) Slurry erosion performance of Ni–Al_2O_3 based thermal-sprayed coatings: effect of angle of impingement. J Therm Spray Technol 23(3):389–401
29. Bhandari S, Singh H, Kumar H, Rastogi V (2012) Slurry erosion performance study of detonation gun-sprayed WC-10Co-4Cr coatings on CF8M steel under hydro-accelerated conditions. J Therm Spray Technol 21(5):1054–1064

30. Gandhi BK, Singh SN, Seshadri V (1999) Study of the parametric dependence of erosion wear for the parallel flow of solid–liquid mixtures. Tribol Int 32(5):275–282

On Complex Loading of Shell of Revolution

R. A. Abirov

Abstract Problem of loading of shell or revolution under complex loading is presented in this issue. Shells can be affected under multiparametric loading at technological processes, etc. In this paper, the calculation was provided by taking into account of experimental approximation for plasticity functional and by traditional incremental plasticity. Complex loading is the reason for divergence between experiment and theory. Here, significance on stress–strain states the fact of loading path and sequence of application of external forces is shown.

Keywords Plasticity · Complex loading · Shell · Stress · Strain

1 Introduction

Complex loading processes are widely investigated in various problems [1–8]. Influence of complex loading conditions has great importance for failure, fatigue, fracture and metal processing problems. Taking into account of complex loading can be done by improving of existing constitutive relations or new conception for theory of plasticity.

Scalar functions included in the tensor-nonlinear constitutive relations need their specification for various types of complex loading processes. It is possible to concretize these functions on the basis of the experiments under complex loading on typical specimens. Let us define dominant properties for the plasticity functionals that characterize the process of two-parameter loading in the form of two-link polylines without a partial unloading part (Fig. 1). It means they are considered an active loading, and it corresponds to the break angles in the range of values $\theta \leq \pi/2$.

Here, the following relation is accepted:

$$\overline{\sigma} = A_0 \overline{p}_0 + A_1 \overline{p}_1, \tag{1}$$

R. A. Abirov (✉)
Institute of Mechanics and Earthquake Engineering, Tashkent, Uzbekistan 100125
e-mail: rustam.abirov@gmail.com

K. Geetha et al. (eds.), *Recent Trends in Materials*, Springer Proceedings in Materials 18, https://doi.org/10.1007/978-981-19-5395-8_19

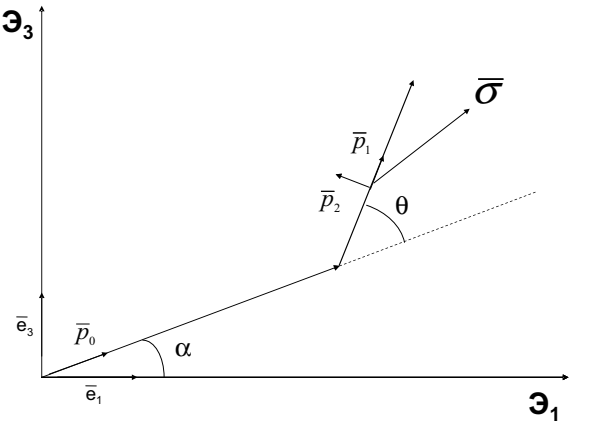

Fig. 1 Loading process

Here, $\overline{p}_0 = \overline{\mathfrak{Э}}_0/|\overline{\mathfrak{Э}}_0| = \overline{\sigma}_0/|\overline{\sigma}_0|$, $\overline{p}_1 = d\overline{\mathfrak{Э}}/ds$, A_0 and A_1 generally are unknown and depend from parameters like Δs, s_0, θ. Let us differentiate (1) by the length of deformation trajectory arc chosen as the process tracking parameter and take into account that $d\overline{p}_1/ds \equiv 0$. Let us obtain a differential relation between stresses and strains in view [9]:

$$d\overline{\sigma} = Nd\overline{\mathfrak{Э}} - (N - P)d\overline{\mathfrak{Э}}\,\overline{p}_0\overline{p}_0, \tag{2}$$

where $N = \dot{A}_1$, $P = \dot{A}_1 - \dot{A}_0/\cos\theta$.

On the base of the Isotropy postulate by Il'yushin, without limiting generality for considered processes, the vector $\overline{p}_0$ can be taken in the following form: $\overline{p}_0 = \overline{p}_0(1; 0)$. Let's decompose expression (2) by components and can itemied follow form:

$$N = d\sigma_3/d\ \mathfrak{Э}_3,\ \ P = d\sigma_1/d\ \mathfrak{Э}_1 \tag{3}$$

Hence, as can be seen, the value of N apparently depends just from the torque moment and torsional strain, while the value of P relies for the tensile force and tensile strain.

The diagram $\sigma_3 \sim \mathfrak{Э}_3$ for a two-link loading process can be represented as [10]: $\sigma_3 = \mathrm{A}\mathrm{arctg}B\ \mathfrak{Э}_3\ /\sin^2\theta$, $\mathfrak{Э}_3 \sin\theta = \Delta s$ and from here find:

$$N = \frac{\mathrm{AB}}{1 + B^2\ \mathfrak{Э}^2} = \mathrm{AB}\cos^2\left(\frac{\sigma_3}{A}\right) \tag{4}$$

here $A\ B = 2G$, $B^2 = \left[\frac{2G}{G_t} - 1\right]/\left(\overline{\lambda}^2 \sin^2\theta\right)$.

For the angle of alteration ϑ, the following approximation can be proposed [10], where the dependence on the trace of delay $\overline{\lambda}(s_0)$ is taken into account:

$$\vartheta = \tilde{A}/\exp\left(\tilde{k}\left(1/\overline{\lambda}+1\right)\Delta s\right) \tag{5}$$

Here, $\tilde{k} = \ln 16/\left(\overline{\lambda}+1\right)$, $\tilde{A} = \theta$.

The adoption of coefficients has subjected to the following conditions:

$$\text{at } \Delta s = 0 \Rightarrow \vartheta = \theta;\ \text{at } \Delta s = \overline{\lambda} \Rightarrow \vartheta \approx 0 \text{ and at } \Delta s \to \infty \Rightarrow \vartheta \to 0.$$

The exponential form of the curve $\vartheta \sim s$ was proposed by other investigators also. It should be underlined that, so types of curves are average ones and lead to few errors from the real situation in practice. However, they are enough to reflect the qualitative and quantitative behaviour of these functionals at numerical calculations.

Relations (2) with term for the N (4) and ϑ (5) can be accepted like constitutive relations that may be used at solving of boundary problems where processes occur in the form of two-link broken lines or to determine the reliability area for plasticity, where instead of an experiment by test facility machine, one can use given ratio expression. Experimental data for multi-link processes was investigated [11–13] and results of so processes cannot be described by classic plasticity theories.

2 Main Part

The majority of plasticity theories are widely used in calculations which often gives different results [12, 13] at solving of boundary problems and from experiments also. This difference is largely the result of complex loading. At experiments for solving of boundary problems is largely difficult and impossible in some cases. The constructed experimental approximations make it possible to solve boundary problems more reliably.

Let us consider a complex loading of a shell of revolution, with taking into account of proposed experimental data for plasticity functionals. Most of solutions of technical problems are calculated according to the momentless theory, where the problems of hardening, shell pressing, moulding, etc., are considered. These problems do not take into account the influence of bending and torsional moments arising in shells on their stress state due to their insignificance.

For comparing the calculations of continua by using the above constitutive relations and classical theories under complex loading, at the first stage, it is expedient to consider the momentless state of shells under axisymmetric loading. It should also be taken into account that particular questions of the momentless theory are of practical importance. Under axisymmetric and momentless loading are:

$$\left.\begin{aligned} \frac{\partial}{\partial \ell}(rT_1) - \cos\hat{\theta}\, T_2 + rq_1 = 0 \\ -\frac{r}{R_1}T_1 - \sin\hat{\theta}\, T_2 + rq_n = 0 \end{aligned}\right\} \tag{6}$$

here T_1 and T_2,—are the tensile and shear forces in the normal section of the shell, $\hat{\theta}$ is the angle between the normal to the surface and the direction of +OY axis when moving counter clockwise from the normal to the axis. R_i are radius of curvature, l is the coordinate axis, q_i are external loads.

The first equilibrium equation in (6) can be replaced by an equilibrium equation in integral form (the sum of projections onto the axis of symmetry of the forces applied to the end section of the shell):

$$\left(T_1 \sin\hat{\theta} - Q\cos\hat{\theta}\right) \cdot 2\pi r = F(s) \tag{7}$$

Under internal pressure, surface force to the base and tensile force in the direction of the top (Fig. 2), the total axial load on the selected part of the shell will have the form:

$$F(s) = P_0 + \int_{s_0}^{s} \left(q_n \cos\hat{\theta} - q_1 \sin\hat{\theta}\right) 2\pi r ds$$

In this case, for the axisymmetric deformation of shells of revolution is:

$$-\frac{T_1}{R_1} - \frac{T_2}{R_2} + q_n = 0, \;\; T_1 = \frac{F}{2\pi r \sin\theta}$$

It is more convenient for us further to use the vector formulation. Stress vectors are defined as: $\sigma_{ll} = T_1/h$; $\sigma_{\varphi\varphi} = T_2/h$; $\sigma_1 = \sqrt{2/3}\left(\sigma_{ll} - 0,5\sigma_{\varphi\varphi}\right)$; $\sigma_2 = \sigma_{\varphi\varphi}/\sqrt{2}$. The displacements are found from the following formulas:

$$\xi = r\varepsilon_{\varphi\varphi}; \varphi = \Delta\hat{\theta};$$

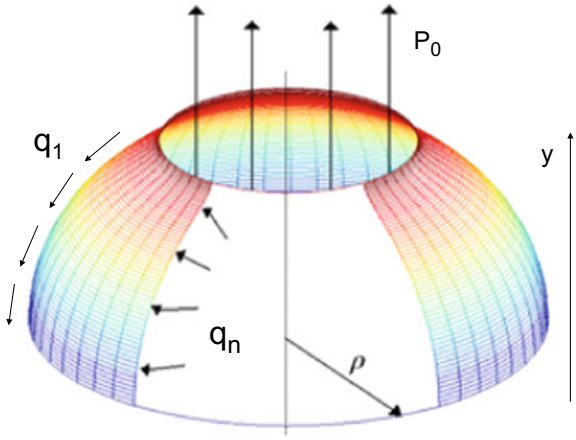

Fig. 2 Shell of revolution under the action of external forces

$$\left.\begin{aligned}\frac{d\xi}{dl} &= (\varepsilon_{rr}+1)\cos\left(\hat{\theta}+\Delta\hat{\theta}\right)-\cos\hat{\theta}\approx\varepsilon_{rr}\cos\hat{\theta}-\varphi\sin\hat{\theta}\\ -\frac{d\zeta}{dl} &= (\varepsilon_{rr}+1)\sin\left(\hat{\theta}+\Delta\hat{\theta}\right)-\sin\hat{\theta}\approx\varepsilon_{rr}\sin\hat{\theta}+\vartheta\cos\hat{\theta}\end{aligned}\right\}$$

For considered shells of revolution: $\sin\hat{\theta}=-\frac{dy}{dl}$; $\cos\hat{\theta}=\frac{dx}{dl}$; $\frac{d\hat{\theta}}{dl}=\left|\frac{1}{R_1}\right|$.

If the angle between the positive directions $\overline{R}_1$ and OY is acute, then $R_1>0$.

The shell (Fig. 2) is formed by rotating a parabola around the OY axis. For a paraboloid of revolution is:

$$R_1=-\frac{\left(4a^2x^2+1\right)^{3/2}}{2a};\ dl=\sqrt{1+4a^2x^2}dx;$$

$$l=\frac{x\sqrt{1+4a^2x^2}}{2}+\ln\left(\frac{2ax+\sqrt{1+4a^2x^2}}{4a}\right);$$

$$\frac{d\hat{\theta}}{dl}=-\frac{1}{R_1}=\frac{2a}{\left(1+4a^2x^2\right)^{3/2}};\ \hat{\theta}=\operatorname{arctg}2ax;\ R_2=-\frac{\sqrt{4a^2x^2+1}}{2a}$$

$$\cos\hat{\theta}=\frac{dx}{dl}=\frac{1}{\sqrt{1+4a^2x^2}};\ \sin\hat{\theta}=-\frac{dy}{dl}=\frac{2ax}{\sqrt{1+4a^2x^2}};$$

$$F(x)=P_0+\pi\left[q_n\left(x^2-x_0^2\right)-\frac{4a}{3}q_1\left(x^3-x_0^3\right)\right]$$

Under multiparameter loading in the form (8), in each section of the shell, complex loading processes arise in the form of two-link zigzag polyline (Fig. 3). As can be seen, the magnitude of the load trajectory kink increases closer to the shell's base. Plastic deformations do not occur in all sections (Fig. 4). Let us consider the solution of this problem according to various theories of plasticity (Prager and I'lyushin's theories) and on the basis of the results proposed for the angle of alteration ϑ.

Material is steel-3: $C=48$, $a=0.12$, $h_0=0.1$, $h_n=0.4$, $x_0=2$, $x_n=20$.

$$\begin{cases} q_n=60t\ \text{kg/cm}^2\ P_0=0, \quad q_1=0 & 0\le t\le 1\\ q_n=60\ \text{kg/cm}^2,\ P_0=-100(t-1)\ \text{kg/cm}^2,\ q_1=10(t-1)\ \text{kg/cm}^2 & 1\le t\le 2\end{cases} \tag{8}$$

Since two-link loading processes are realized in each section of the shell, it is more convenient to use relations (2), (4) and (5) for solving the problem. These relations can be considered as a special case of the theory of mean curvatures.

Since the relations for the angle of alteration ϑ are proposed for processes in the strain space, and two-link processes are realized in the stresses space, the solution of the problem, taking into account the above-given constitutive relations, follows an iterative path. As first approximation, let us take the solution according to the Ilyushin's theory. In this case, the convergence of the iterative process is then achieved at the second step.

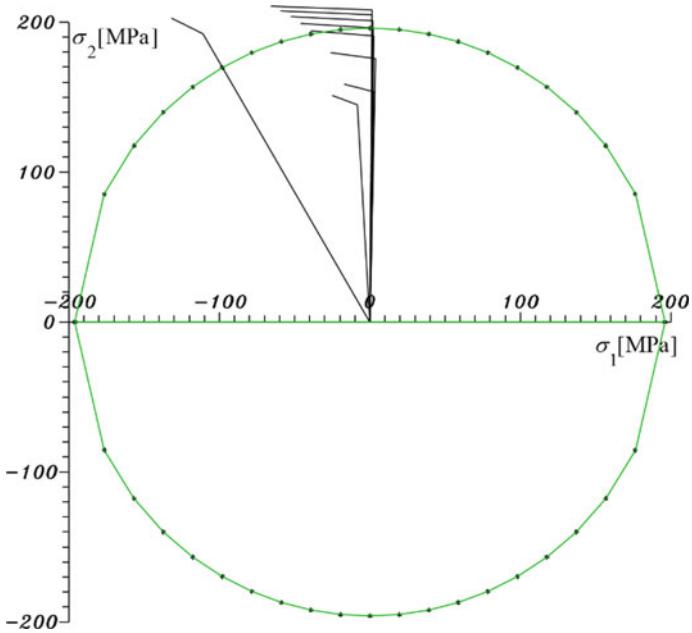

Fig. 3 Loading trajectories in different sections of the shell

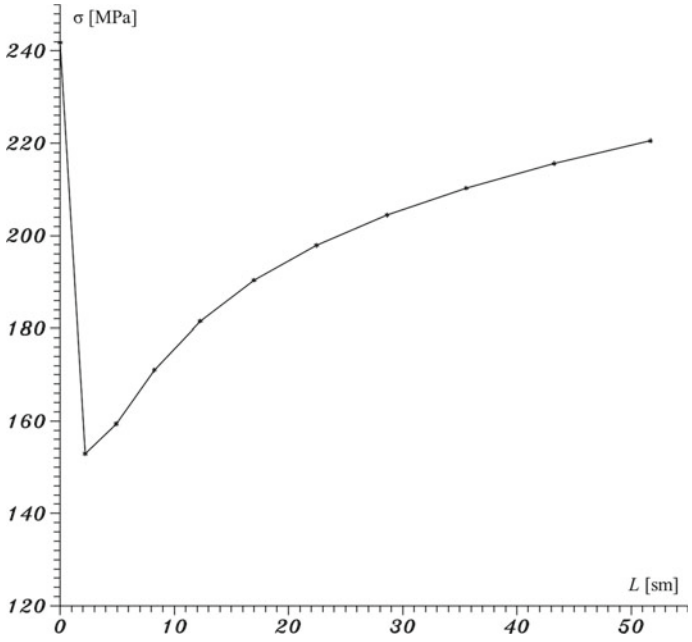

Fig. 4 Distribution of the stress modulus along the length of the generating line of shell

Theories of Ilyushin and Prager give overestimated values for strains (Figs. 5 and 6) and deviations increase with the development of the loading process.

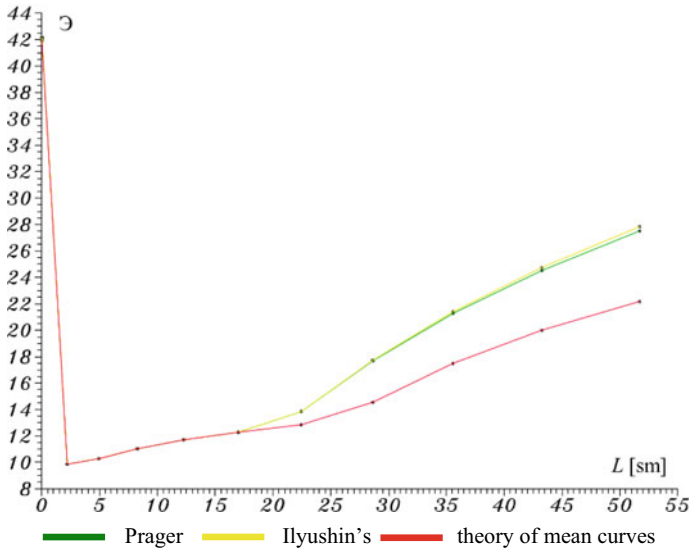

Fig. 5 Distribution of the strain modulus along the length of the generating line of shell

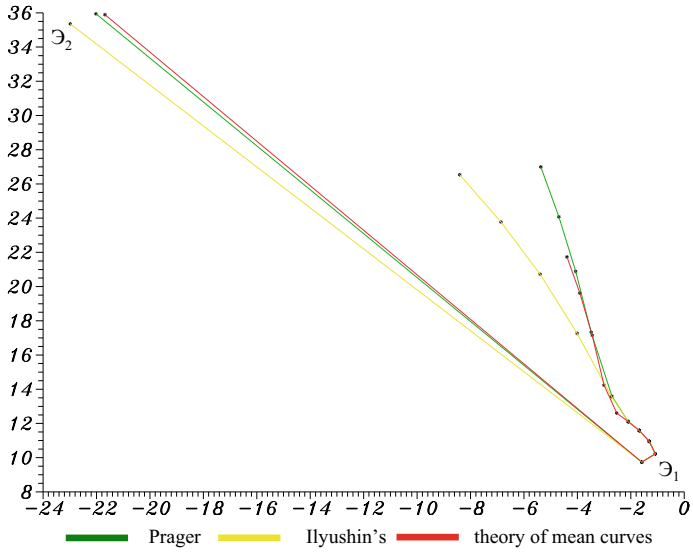

Fig. 6 Strain path along the length of the generating line of shell

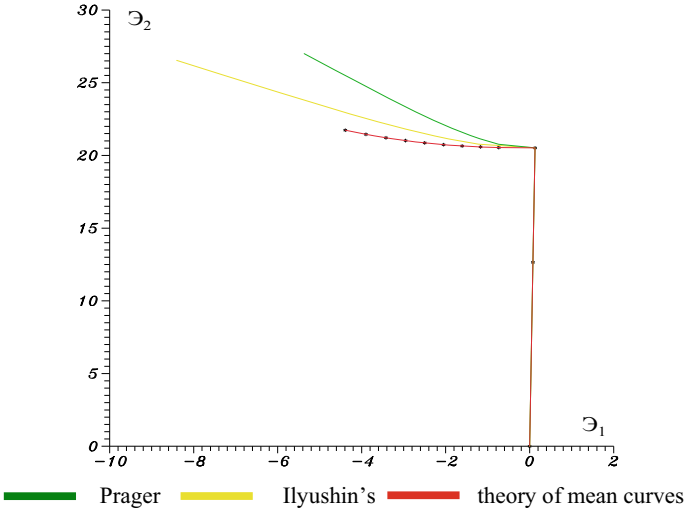

Fig. 7 Trajectory of at base of the shell

3 Result and Discussion

Analysis of the calculation results shows that strain trajectories (Fig. 7) at base of shell and stress ones (Fig. 8) along the length of the generating line realize complex loading processes. In each site of shell where arise plasticity situation the same. At calculation of radial and tangential displacements (Figs. 9 and 10) along contour of body shows divergences of calculation results. It can lead to significant errors and design of constructions and in some cases to detect of bearing capability of materials [14–16]. The above results show the nature of stress–strain state at multiparametric complex loading.

4 Conclusion

The problems of loading of shells of revolution are considered on the base of proposed approximation for the angle of alteration ϑ, and these results are compared with calculations by Prager's theories and deformation theory of Ilyushin. Calculations showed that for two-link loading processes (external forces were applied sequentially), differences in calculations by deformation theory and incremental one give solutions that differ from the solution by taking into account of complex loading. These divergences can reach significant values. In considered case, up to 20%. This indicates that the fact of ignoring the form in what way and in what sequence external

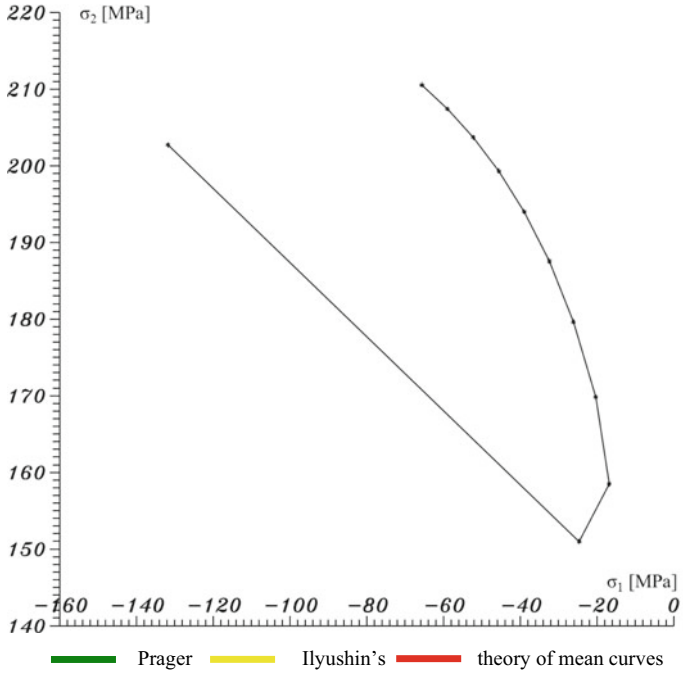

Fig. 8 Stress distribution along the length of the generating line of shell

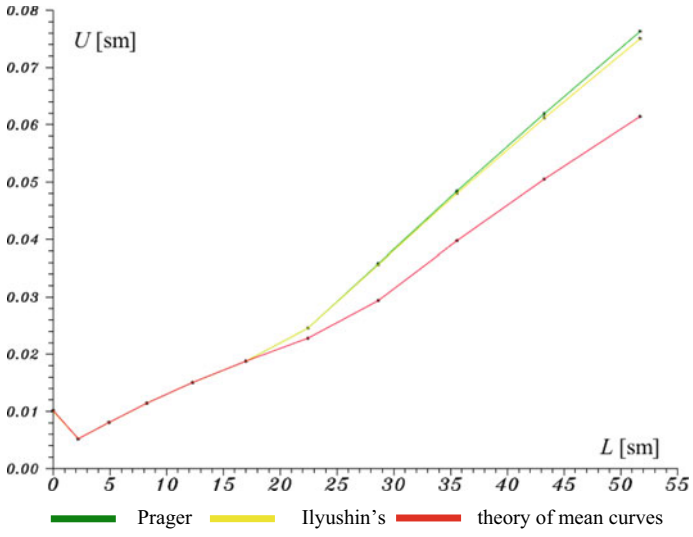

Fig. 9 Radial displacements

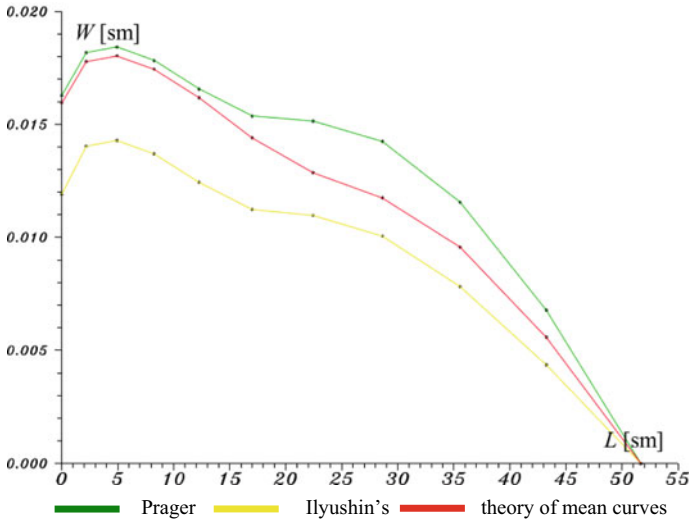

Fig. 10 Tangential displacements

forces are applied can significantly affect the stress–strain state of the body. Consideration of complex loading allows detection of material strength reserves and can be used in metalworking processes.

References

1. Berger-Roscher N, Casaroli G, Rasche V, Villa T, Galbusera F, Joachim Wilke H (2017) Influence of complex loading conditions on intervertebral disc failure. Spine 42(2):E78–E85
2. Carranza I, Crocombe AD, Mohagheghian I, Smith PA, Sordon A, Meeks G, Santoni C (2019) Characterising and modelling the mechanical behaviour of polymeric foams under complex loading. J Mater Sci 54:11328–11344
3. Wang Z, Qiu J, Shu X, Jin T (2020) Experimental study on the fracture behavior of AZ91D magnesium alloy under complex loading. Results Phys 16:102917
4. Chen H, Zarkevich NA, Levitas VI, Johnson DD, Zhang X (2020) Fifth-Degree elastic energy for predictive continuum stress–strain relations and elastic instabilities under large strain and complex loading in silicon. NPJ Comput Mater 6:115
5. Gérard C, Bacroix B, Bornert M, Cailletaud G, Crépin J, Leclerq S (2009) Hardening description for FCC materials under complex loading paths. Comput Mater Sci 45(3):751–755
6. Abirov RA (2021) Deformation of metals under complex loading. In: Minerals, metals and materials series. https://doi.org/10.1007/978-3-030-75381-8_169
7. Xiao Y (2021) Development of structural testing equipment for impact and complex loading. J Struct Integ Maintenan 6(1):1–15
8. Petre MT, Erdemir A, Cavanagh PR (2006) Determination of elastomeric foam parameters for simulations of complex loading. Comput Methods Biomech Biomed Engin 9(4):231–242
9. Shevchenko YuN, Babeshko ME, Terekhov RG (1992) Thermo-viscous-plastic processes of complex deformation of structural elements. Naukova Dumka, Kiev

10. Abirov R (2020) On behaviour of plasticity functionals at complex loading Mater. Today Proc. 38:1480–1483
11. Zubchaninov VG, Alekseev AA, Gultyaev VI, Alekseeva EG (2019) The processes of a complex loading of structural steel in a five-link piecewise polygonal strain path. Vestn Tomsk Gos Univ Mat Mekhanika 81:32–44
12. Babamuratov KS, Abirov RA (2001) On physical reliability in the theory of plasticity. Strength Mater 33:1–7
13. Abirov RA (2008) On the physical reliability and taking complex loading into account in plasticity. Mater Sci 44:512–516
14. Rustam A (2020) On work of external forces at complex loading. In: AIP conference proceedings of in 3rd international conference on inventive material science application, pp 268–271
15. Wang B (2021) Material strength: a rational nonequilibrium energy model for complex loadings. J. Appl. Mech. Trans. ASME 88:021008
16. Gitman MB, Stolbov VY, Nadymov AN (2013) Strengthening of pump rods with regard for the stochastic distribution of plastic properties of the material. Strength Mater 45:242–247

Analysis of Effect of Pitch Error on Transmission Error and Mesh Stiffness in Spur Gear Using SciLab and Ansys Software

Vijay Kumar Karma and Govind Maheshwari

Abstract Any impurity or defects in gears due to various factors affect power or torque transmission resulting in unwanted noise and vibrations. These impurity/defects generate deformations such as crack, spalls and transmission error. This necessitates to study the effects arising due to these causes on power transmission. Numerous methods including analytical, numerical, experimental and/or computer simulations are used now a days to analyse the results or predictions of the effects and their minimization processes. This paper deals with the analysis of the effects of one such factor, pitch error on transmission error (TE) and time-varying mesh stiffness (TVMS) in spur gear using SciLab and Ansys software. The TVMS for gear without pitch error is calculated analytically using computer programme in SciLab and FEA in Ansys software. These results were then compared, and afterwards, the TE and TVMS are determined by considering pitch error of 1% and 2% variation using FEA in Ansys. These variations in pitch are sufficient to analyse the effects. Various graphs are plotted representing TE and TVMS for pinion rotation angle. It is observed that the pitch error affects TE and TVMS of a gear pair in a significant way. The presented work will help in the early prediction/detection and reduction of malfunctioning in gear box, which will result in increasing transmission power in gear box section which are used in wind turbines, automobiles, helicopter, etc.

Keywords Spur gear · Ansys · SciLab · Pitch error · Transmission error · Time-varying mesh stiffness

V. K. Karma (✉) · G. Maheshwari
Department of Mechanical Engineering, Institute of Engineering and Technology, Devi Ahilya University, Khandwa Road, Indore, Madhya Pradesh 452001, India
e-mail: vkarma@ietdavv.edu.in

G. Maheshwari
e-mail: gmaheshwari@ietdavv.edu.in

K. Geetha et al. (eds.), *Recent Trends in Materials*, Springer Proceedings in Materials 18, https://doi.org/10.1007/978-981-19-5395-8_20

1 Introduction

Gears are subjected to very wide and varied range of loads during the transmission and therefore subjected to different deformations leading towards failures of the gear. Any variation in torque or power transmission due to the geometrical imperfections or deformations due to the load results in TE. These causes unwanted noise and vibrations in the drives which leads to the variation in TVMS. TE is the deviation in the position of the output gear in a drive from its ideal or actual position to the working position during operation of drive. It is represented either in angular deformation or in linear deformation form. Pitch error is the deviation in pitch of the gear due to the geometrical imperfections, and TVMS is the mesh stiffness of gear pair during transmission of power.

Kohler et al. [1] in their experiments found that pitch error has significant effect on overall TE in gear transmission. Jianfeng et al. [2] in their work on cylindrical gears made a 3D model. The model when tested gives very accurate results using FEA. Thus, in this way required, mesh stiffness is obtained. Sainsot et al. [3] were successful in generating an analytically bi-dimensional formulae that give accurate reading of tooth deflection obtained due to gear body. Tian [4] in his work derived an analytical equation to find mesh stiffness using potential energy and involute gear teeth characteristics method. Noise in gear power transmission is due to acoustic signals of very high amplitude. Thermakulasingam [5] in his work find out the effects of tooth profile modifications on TE and in its noise generated. Here, an optimization procedure is also developed to change or design tooth modifications. Spur gears are more often characterised by its torsional mesh stiffness. Kiekbusch et al. [6] in their work created 2D and 3D FEA model by using Ansys software. From these models, a formula is generated to find torsional mesh stiffness. Results obtained from the above two models were obtained and compared. Saxena et al. [7] in their works use computer simulations to find and analyse the effect of TVMS for spur gears having different spalling shapes. In addition, Zhan et al. [8] also estimated TVMS by using CAD-FEA-QSA integration technique to determine vibration and noise in gear vibrations. Sanchez et al. [9] find meshing stiffness of spur gear by taking into consideration of global and local tooth deflection. Model created is highly accurate and can also be used in case of dynamic system. Parameters such as meshing stiffness, load-sharing ratio and quasi-static transmission error (QSTE) are intermingled with each other. A model is developed by Sanchez et al. [10] by taking into consideration of load-sharing ratio and QSTE for spur gears. Chang et al. [11] devised a novel procedure to forecast accurate spur gear pair TE varying parameters such as manufacturing errors (MEs), assembly errors (AEs), tooth deflections (TDs) and profile modifications (PMs) are taken into consideration. A large amount of stress is being made to reduce noise levels or vibrate, especially in automotive industry. Czako et al. [12] determine static transmission error (STE) by using FEA method for helical gears. Bruzzone et al. [13] created a 2D nonlinear and non-hertzian gear tooth model to determine STE. Mesh stiffness plays a significant role in determining transmission performance. Chin et al. [14] determine gear transmission error from a new angle. TE detailed

diagnostic has been done by the researchers. A more accurate spur gear dynamic model is proposed by Chen et al. [15] which considered tooth profile deviations. Flek et al. [16] work proposes a TVMS for spur gear pair, which is an important parameter in calculation of TE. Simulation is done using computer-aided engineering (CAE) software. Gear box is an important tool for power transmission. To reduce its malfunction rate, dynamic modelling and simulation of spur gear by considering flank pitch error is done by Tian et al. [17]. TVMS, noise and vibration amplitude are unavoidable in gear transmission. Backlash increases transmission error drastically. Analysis of having backlash on TE and TVMS is done by Ambaye et al. [18]. A lot of changes in gear transmission has been evolved with the invention of new technology. A detailed revision of modelling of mesh stiffness for cylindrical gears has been done by Marafona et al. [19]. Sun et al. [20] in their work developed an improved comprehensive modification model for TVMS for spur gears. Kumar et al. [21] proposed an analytical model to calculate TVMS for a carburized spur gear pair in which teeth are having cracks. TE in gear box generally occurs due to gear box vibration. Duan et al. [22] calculate TE by considering housing flexibility, shaft flexibility both theoretically and experimentally. Lee et al. [23] propose an efficient algorithm to calculate TE in spur gear by considering a very large number of uncertainties results obtained were statistically analysed.

As gone through plethora of past researches, some lacking or insufficiency were found such as effect of friction, deformations and negligible experimental validation of the results obtained analytically. Thus, accuracy claimed by many researchers has been in a questionable form. From the literature, it is learnt that a lot of work is underway to study the causes, prediction and minimization of the effects of these variations using different techniques, computer simulation tools, experimentations, etc. It is therefore in this study work an open-source software SciLab is used along with the CAD analysis software Ansys to study the effects of one of the gear geometry imperfections, i.e. pitch error on TE and TVMS in spur gear of standard proportions.

2 Determination of TE and TVMS

2.1 Transmission Error

Any geometrical imperfections in the gear during manufacturing result in the development of TE. Pitch error (PE) or pitch deviation is one of the geometric imperfections. It is the difference between the actual teeth spacing and the theoretically correct teeth spacing in a gear. In other words, it is considered a deviation or angular malposition of the circumference in the gear tooth which causes TE and ultimately leads to the developments of noise, vibrations or failure of the gear. PE causes to affect the position occupied by the output gear shaft from its correct position. TE is defined as the difference in the theoretically correct position of the output gear shaft with respect to the predicted/occupied position of the gear shaft in an unmodified or

correct drive system. It is represented in angular as well as in linear forms. Equations (1) and (2) represent TE in angular and linear form when measured at the base circle [19].

$$\mathrm{TE} = \theta_g - \left(R_{bp}/R_{bg}\right)\theta_p \tag{1}$$

$$\mathrm{TE} = R_{bg}\theta_g - R_{bp}\theta_p \tag{2}$$

where θ_g is rotational angle of gear and R_{bg} is base radius of gear, θ_p is rotational angle of pinion, and R_{bp} is base radius of pinion.

In this paper, TE is calculated using the angular displacements obtained from the analysis of gear pair in Ansys workbench using quasi-static algorithm (QSA) procedure as described in [8]. The analysis is done for healthy gears and faulty gears having pitch error of 1% and 2% in circular pitch consisting of involute profile. The healthy and faulty gears are modelled and assembled/meshed in SOLIDWORKS software. The pitch error is created intentionally by varying the tooth thickness to 1% and 2% of theoretically correct pitch so that its effect on TE and TVMS can be predicted, respectively. This is already discussed and shown in results presented in the work. The specifications of the gear pair used for the analysis are represented in Table 1. First, the healthy gear pair (i.e. both gears pinion and gear) is imported into Ansys workbench, and then, they are meshed. The elements used in meshing are SOLID185 and CONTA170. The computation time is reduced by fine meshing of five number of teeth of both the gears. Figure 1 shows the meshed gear pair in Ansys workbench. The total number of nodes and elements is 586533 and 407,728, respectively. All degrees of freedom of gear pair except rotation about z axis (axis of rotation of gears in Ansys workbench, refer Fig. 2) are fixed. The pinion is given a constant rotational velocity of 1.02 rad/sec, whilst a resistive torque of 100,000 N-mm is applied to gear. To obtain the relative angular positions, flexible rotation probes are attached to both the pinion and gear, respectively. The angular rotational positions of pinion and gear after analysis are put into Eqs. (1) and (2) to obtained TE. After this, the analysis is done for gear pair consisting of healthy pinion and faulty (1% pitch error and 2% pitch error) gear, respectively, using the same procedure as for healthy gear pair. Figure 2 shows the TE obtain from the simulation of healthy gear pair, healthy and faulty gear pairs of 1% and 2% pitch error for two mesh cycles, respectively.

2.2 Time-Varying Mesh Stiffness

There are various methods available in the literature to determine the TVMS that includes analytical methods based on ISO standard approach, potential energy approach, numerical approach and finite element approach. The ISO standard approach for mesh stiffness uses empirical relations that are derived based on testing

Table 1 Specifications of the gear pairs used for the analysis

Parameters	Gear pair 1 Healthy/Healthy gear	Gear pair 2 Healthy/Faulty gear (1% Pitch Error)	Gear pair 3 Healthy/Faulty gear (2% pitch error)
Module, m (mm)	4	4	4
No. of teeth, Zp, Zg	20	20	20
Pressure angle, Φ (°)	18	18	18
Pitch, p (mm)	12.5664/12.5664	12.5664/12.6920	12.5664/12.8177
Tooth thickness, t (mm)	6.2832/6.2832	6.2832/6.3460	6.2832/6.4088
Face width, L (mm)	10	10	10
Modulus of elasticity, Ep, Eg (N/mm^2)	210,000	210,000	210,000
Poisson's ratio, ν	0.3	0.3	0.3
Bore radius, r_{int} (mm)	10	10	10

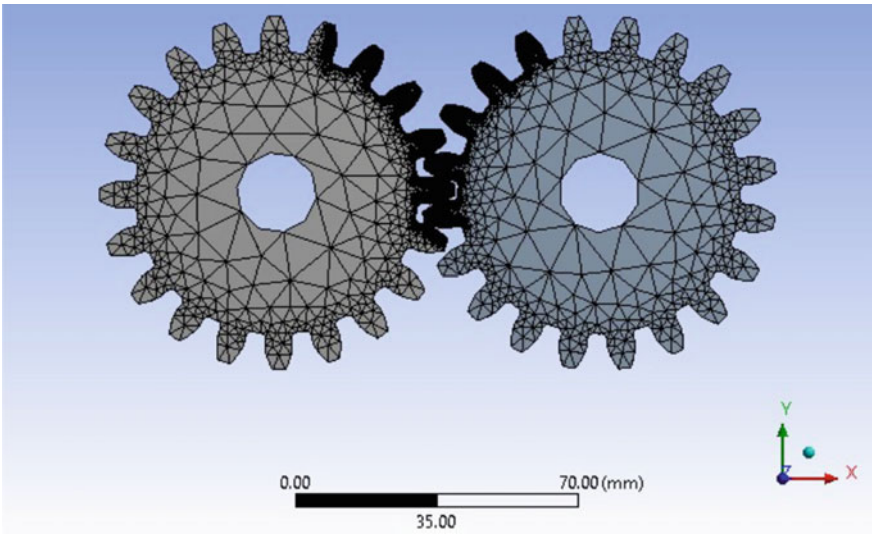

Fig. 1 Meshed gear pair (healthy gear pair, $m = 4$ mm, $Zp = Zg = 20$, $\Phi = 18°$)

of many gear samples and is not usable in cases where exact/accurate value is required. It is used in case when it is required only to find approximate values of single and double-pair mesh stiffness values. The potential energy approach (PEA) is also named as deformation energy method based on theory of elasticity. Past research works by well-known researchers as discussed in literature review section has considered PEA to be an ideal analytical procedure used popularly in modelling stiffness of gears and hence is used for analysis work. Here, the tooth is assumed as a cantilever beam fixed in the root circle with changing cross-section and force turns along the line

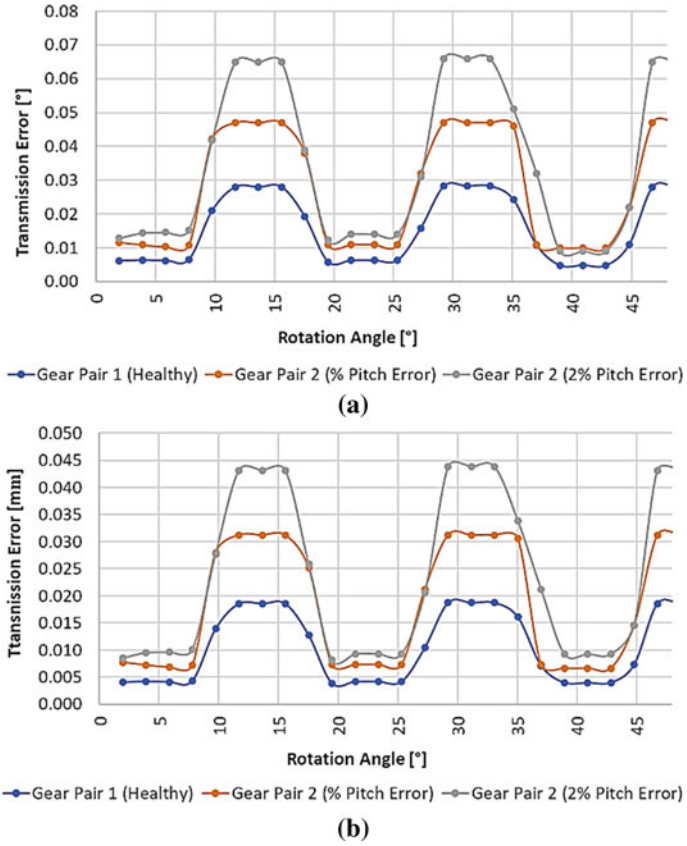

Fig. 2 (**a**) TE in angular form (°), and (**b**) TE in linear form (mm)

of action of gear pair. It provides a very good flexibility in finding parameter properties at different angular displacement of gears (pinion/gear). TVMS is determined using potential energy approach for healthy gear pair and finite element approach for both healthy and faulty gear pair. The potential energy method includes axial compressive energy, bending energy, shearing energy, hertzian contact energy and fillet foundation deflection to calculate the stiffness of the spur gear tooth by considering angular variables in place of linear variables. The following are the expressions (Eqs. (3) to (7)) for hertzian, shearing, bending, axial and fillet foundation deflection stiffnesses used by the various researchers and authors [3, 4, 6, 7, 15, 16, 18].

$$k_h = \frac{\pi \mathrm{EL}}{4\left(1-\nu^2\right)} \tag{3}$$

$$\frac{1}{k_s} = \int_{-\alpha_1}^{\alpha_2} \frac{1.2(1+\nu)\cos\alpha(\alpha_2-\alpha)\cos^2\alpha_1}{\mathrm{EL}[\sin\alpha+\cos\alpha(\alpha_2-\alpha)]}\mathrm{d}\alpha \tag{4}$$

$$\frac{1}{k_b} = \int_{-\alpha_1}^{\alpha_2} \frac{3\{1+\cos\alpha_1[(\alpha_2-\alpha)\sin\alpha-\cos\alpha]\}^2\cos\alpha(\alpha_2-\alpha)}{2\mathrm{EL}[\sin\alpha+\cos\alpha(\alpha_2-\alpha)]^3}\mathrm{d}\alpha \tag{5}$$

$$\frac{1}{k_a} = \int_{-\alpha_1}^{\alpha_2} \frac{\cos\alpha(\alpha_2-\alpha)\sin^2\alpha_1}{2\mathrm{EL}[\sin\alpha+\cos\alpha(\alpha_2-\alpha)]}\mathrm{d}\alpha \tag{6}$$

$$\frac{1}{k_f} = \frac{\cos^2\alpha_1}{\mathrm{EL}}\left\{L^*\left(\frac{u_f}{S_f}\right)^2 + M^*\left(\frac{u_f}{S_f}\right) + P^*\left(1+Q^*\tan^2\alpha_1\right)\right\} \tag{7}$$

where L, E, ν, α_1 represent tooth width, Young's modulus of elasticity, poison's ratio and working pressure angle, respectively, α_2 and α are represented in Fig. 3. The definition of other gear parameters u_f and S_f is represented in Fig. 4. L^*, M^*, P^* and Q^* are the coefficients and can be calculated using polynomial function given by Sainsot et al. [3] from Eq. (8).

$$X_i^*\left(h_{fi},\theta_f\right) = \frac{A_i}{\theta_f^2} + B_i h_{fi}^2 + C_i\frac{h_{fi}}{\theta_f} + \frac{D_i}{\theta_f} + E_i h_{fi} + F_i \tag{8}$$

where $X_i{}^*$ represents the coefficients L^*, M^*, P^* and Q^*; $h_{fi} = r_f/r_{\mathrm{int}}$; Fig. 3 defines the r_f and r_{int}, whilst Table 2 shows the values of A_i, B_i, C_i, D_i, E_i and F_i.

The single-tooth pair meshing stiffness and double-tooth pair meshing stiffness are represented by Eqs. (9)–(10) below.

$$k_{\mathrm{single}} = \frac{1}{\frac{1}{k_h}+\frac{1}{k_{sp}}+\frac{1}{k_{bp}}+\frac{1}{k_{ap}}+\frac{1}{k_{fp}}+\frac{1}{k_{sg}}+\frac{1}{k_{bg}}+\frac{1}{k_{ag}}+\frac{1}{k_{fg}}} \tag{9}$$

$$k_{\mathrm{double}} = \sum_{i=1}^{2}\frac{1}{\frac{1}{k_h}+\frac{1}{k_{sp,i}}+\frac{1}{k_{bp,i}}+\frac{1}{k_{ap,i}}+\frac{1}{k_{fp,i}}+\frac{1}{k_{sg,i}}+\frac{1}{k_{bg,i}}+\frac{1}{k_{ag,i}}+\frac{1}{k_{fg,i}}} \tag{10}$$

where the subscript p, g, $i = 1, 2$ denotes the pinion, gear, first and second tooth pair, respectively.

In this work, TVMS for healthy gear pair is calculated using Eqs. (3)–(10) and from Tian's work [4] by computer programme developed in SciLab [24] an open-source alternative of MATLAB software. The input parameters to the computer programme are listed in Table 1. The TVMS for healthy gear pair calculated from SciLab program and plotted against pinion rotation angle is represented in Fig. 5a–c. It also shows the single-pair mesh stiffness and double-pair mesh stiffness. The TVMS for healthy and faulty gear pairs is calculated from quasi-static finite element analysis using Ansys

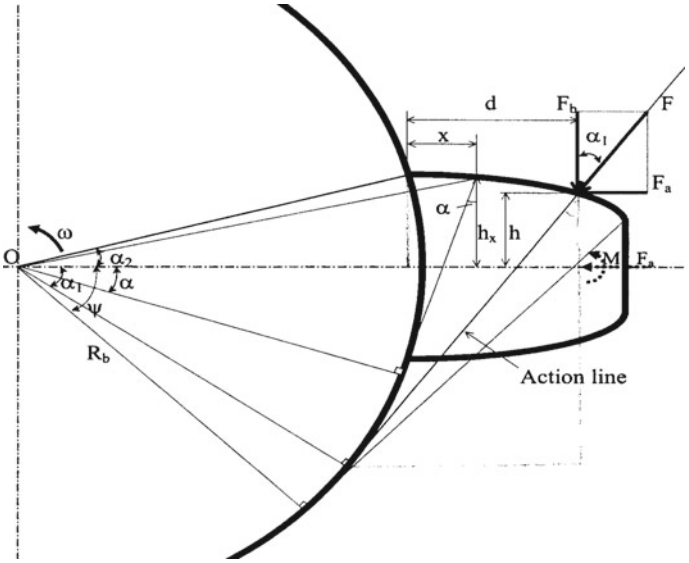

Fig. 3 Forces on healthy gear tooth model [4]

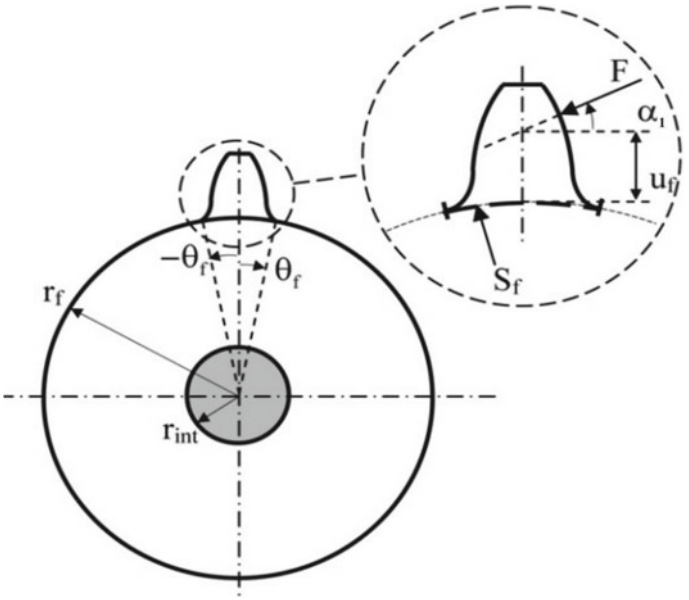

Fig. 4 Fillet Foundation deflection parameters. [3]

Table 2 Values of A_i, B_i, C_i, D_i, E_i and F_i [3]

	A_i ($\times 10^{-5}$)	B_i ($\times 10^{-3}$)	C_i ($\times 10^{-4}$)	D_i ($\times 10^{-3}$)	E_i	F_i
$L^*(h_{fi}, \theta_f)$	−5.574	−1.9986	−2.3015	4.7702	0.0271	6.8045
$M^*(h_{fi}, \theta_f)$	60.111	28.100	−83.431	−9.9256	0.1624	0.9086
$P^*(h_{fi}, \theta_f)$	−50.952	185.50	0.0538	53.3	0.2895	0.9236
$Q^*(h_{fi}, \theta_f)$	−6.2042	9.0889	−4.0964	7.8297	−0.1472	0.6904

software. In Sect. 2.1, the angular deflections obtained from Ansys software are put into Eqs. (1) or (2) to get TE in angular form or in linear form. The TE is then put into Eqs. (11–12) using QSA as described by Zhan et al. [8] to obtain the TVMS of healthy and faulty gear pair in torsional and linear form, respectively. Figure 6 represents the graph of TVMS obtained from Eqs. (11–12) for healthy and faulty gear pair cases.

$$k_{\text{Torsional}} = \frac{T}{|\text{TE}|} \tag{11}$$

$$k_{\text{Linear}} = \frac{k_{\text{Torsional}}}{R_{bp}^2} = \frac{k_{\text{Torsional}}}{R_{bg}^2} \tag{12}$$

3 Result and Discussions

3.1 Transmission Error

For analysis of TE, the healthy gear pair and faulty gear pairs are meshed in Ansys workbench as per the procedure describe in Sect. 2.1. The simulation results, i.e. deformations obtained from the Ansys workbench are feed into Eqs. (1) and (2) and are noted for 2 mesh cycles of the gear pair for both healthy and faulty gear pair. Using the values obtained from these equations, graph is plotted between TE and angle of rotation of gear. Figure 2a represents the plot of TE in angular form, and Fig. 2b represents TE in linear form.

From the graph, it is observed that the transmission error fluctuates when gear pair is rotated for one mesh cycle and repeats for another mesh cycle.

The maximum value of TE in angular form is 0.0282°, 0.0470° and 0.0650° for healthy gear pair, faulty gear pair of 1% pitch error and faulty gear pair of 2% pitch error, respectively, between pinion rotation angle 11° to 16°, and in linear form, it is 0.0188 mm for healthy gear pair, 0.0312 mm for faulty gear pair of 1% pitch error and 0.0432 mm for faulty gear of 2% pitch error, respectively, between 11° and 16° pinion rotation angle.

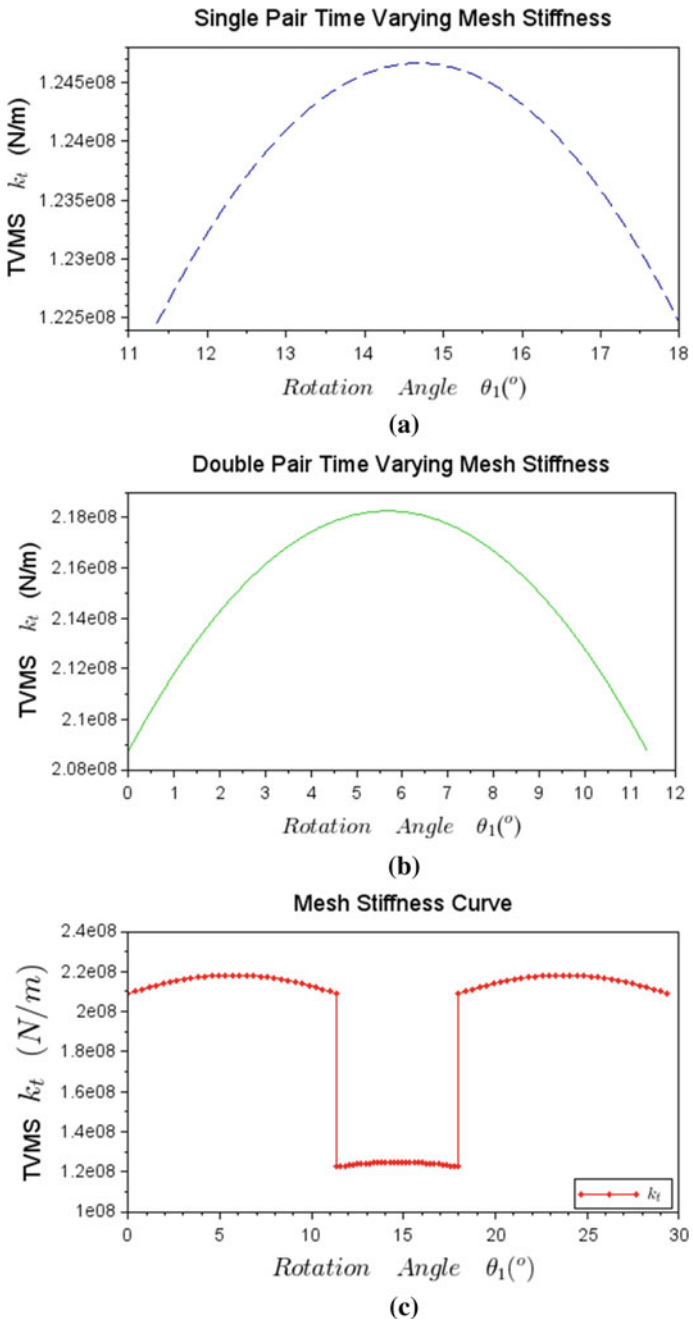

Fig. 5 **a** Single-pair TVMS curve of healthy gear pair calculated using SciLab, **b** double-pair TVMS curve of healthy gear pair calculated using SciLab, **c** total TVMS curve of healthy gear pair calculated using SciLab

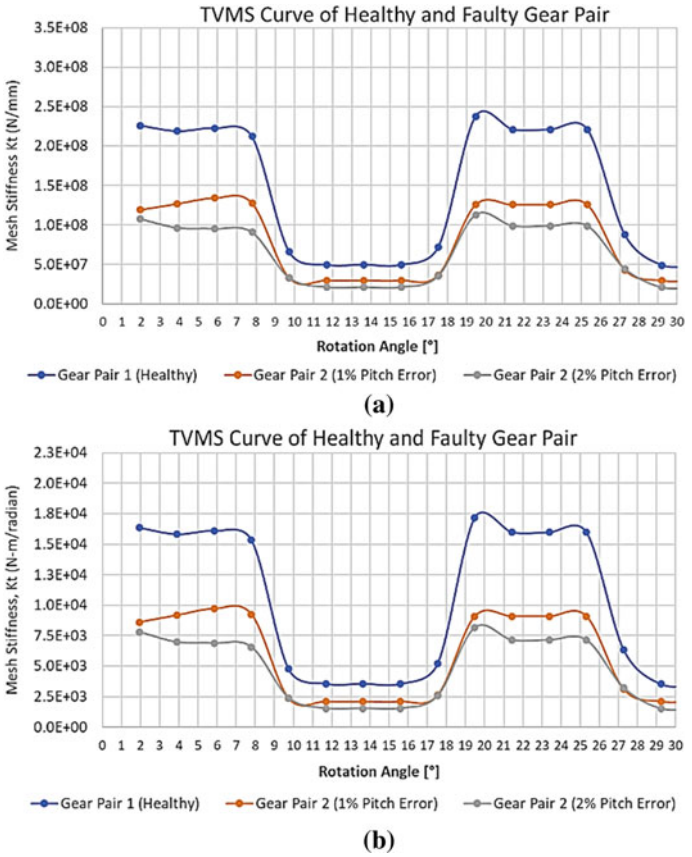

Fig. 6 **a** TVMS curve of healthy and faulty gear pairs calculated by using QSA in FEA software in linear form, **b** TVMS curve of healthy and faulty gear pairs calculated by using QSA in FEA software (torsional stiffness)

The minimum value of TE in angular form is 0.0061° at 1.9481° of pinion rotation, 0.0103° at pinion rotation angle of 5.8442° pinion rotation and 0.0128° at pinion rotation angle 1.9481° for healthy gear pair, faulty gear pair of 1% pitch error and faulty gear pair of 2% pitch error, and in linear form, it is 0.0041 mm for healthy gear pair at 1.9481° pinion rotation, 0.0068 mm for faulty gear pair of 1% pitch error at pinion rotation angle 5.8442° and 0.0128 mm for faulty gear of 2% pitch error at 1.9481° rotation of pinion, respectively.

3.2 Time-Varying Mesh Stiffness

The TVMS for healthy gear pair is calculated from analytical method and FEA method as mentioned in Sect. 2.2. The TVMS for faulty gear pairs is determined by FEA using Ansys software. The TVMS for healthy gear pair is determined using SciLab programme code, which takes gear input parameters listed in Table 1. Figure 7 represents the SciLab code for input parameters and other parameter calculations, and Fig. 8 shows partial code for TVMS calculations. The mesh stiffness of single-tooth pair and double-tooth pair calculated by analytical method using SciLab code and finite element analysis using Ansys for healthy gear pair is represented in Fig. 5a, b and Fig. 6a, respectively. Table 3 depicts the maximum difference in mean values of mesh stiffness calculated by SciLab code and FEA software Ansys for healthy gear pair and faulty gear pairs. It also represents the mesh stiffness for healthy and faulty gear pairs in torsional form. The linear form representation using analytical method for TVMS calculation of healthy gear pair is widely adapted by most of the researchers to verify the correctness of procedure as is clear from the literature review part; hence, here also, the analytical calculations are performed only for healthy gear pair only, and for faulty gear pairs, TVMS is conveniently calculated from the FEA work. Figure 6a, b shows the mesh stiffness curve obtained for healthy and faulty gear pairs having pitch error of 1% and 2% in linear as well as in torsional form, respectively.

4 Conclusions

In this paper, the work is done for analysis of effect of pitch error on TE and TVMS in spur gear using analytical method in SciLAb software and Ansys software.

The TE is determined in linear as well as in angular form from Ansys software as per the procedure discussed in Sect. 2.1. The simulation results from the Ansys software are then plotted between angle of rotation along horizontal axis and TE along vertical axis as shown in Fig. 2. From the graph, it is observed that there is variation in TE due to pitch error as the gear rotates for one mesh cycle, and same is repeated for next mesh cycle. The TE fluctuates during rotation, i.e. it is not constant for mesh cycle. The TE increases when pitch error increases from 0 to 2%, and the behaviour of curve is similar for a mesh cycle.

TVMS is calculated using SciLab programme based on the analytical equations as mentioned in Sect. 2.2 and using finite element software Ansys for healthy gear pair. The mean TVMS for healthy gear pair calculated from SciLab programme is 2.183×10^8 and from Ansys is 2.2163×10^8, the difference is 3.46% which is in the acceptable limit. Hence, the procedure is verified. The TVMS for faulty gear pair 1 and gear pair 2 is determined from using PEA by SciLab and Ansys software by using QSA approach as mentioned in Sect. 2.2. Table 3 represents the values of single pair, double pair and mean mesh stiffness of healthy and faulty gear pairs

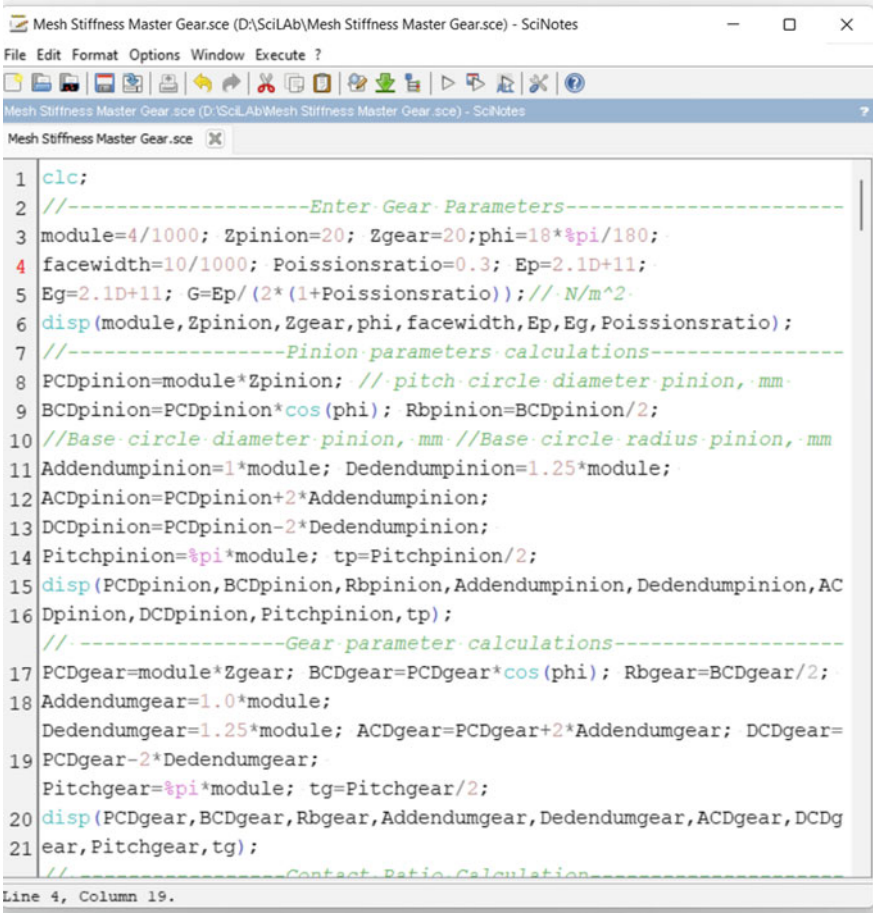

Fig. 7 SciLab window showing input and other parameter calculation part

calculated from Ansys simulation in linear and torsional form. It is observed that as the pitch error increases mean time-varying mesh stiffness is affected considerably as also reported by many researchers in the literature.

The work presented in this paper is of the area of gear research mainly TE and TVMS, i.e. reducing the vibration and noise which occurs due to gears meshing or interaction. Results are obtained using finite element analysis in Ansys software and analytical method using SciLab software.

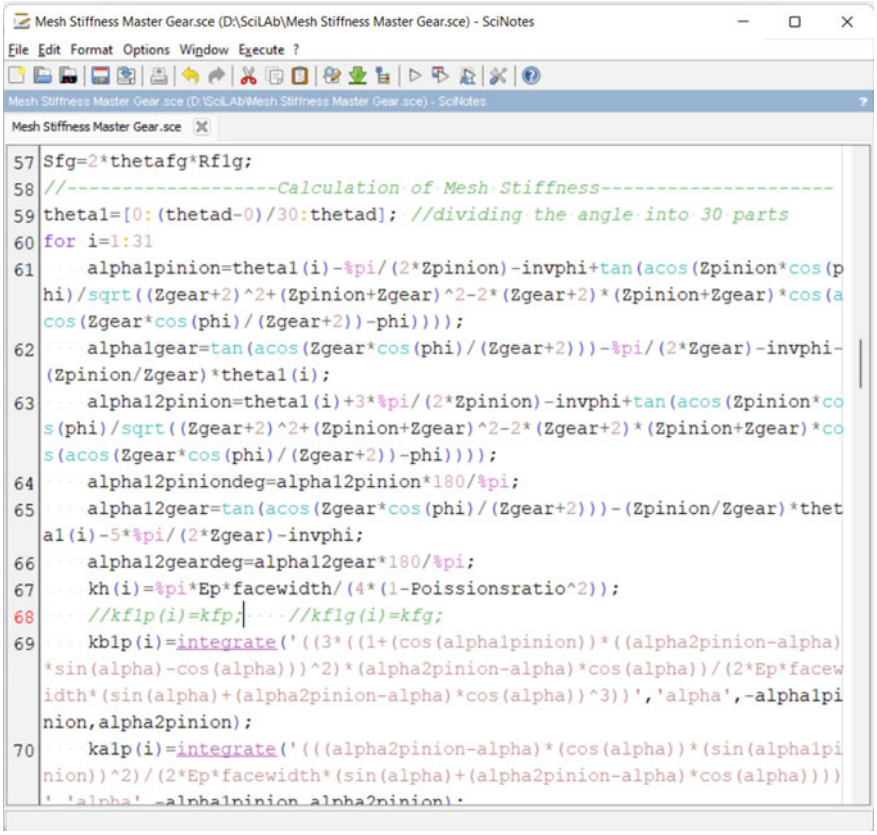

Fig. 8 Portion of TVMS calculation code in SciLab

Table 3 Mean values of TVMS (N/m) obtained by SciLab and Ansys software

Gear pair	Single-pair mesh stiffness (N/m)			Double-pair mesh stiffness (N/m)		
	Analytical method (SciLab code)	FEA (Ansys software)	Difference	Analytical method (SciLab code)	FEA (Ansys software)	Difference
Gear pair 1	1.247×10^8	0.8774×10^8	42.03%	2.183×10^8	2.261×10^8	3.46%
Gear pair 2	–	0.6281×10^8	–	–	1.382×10^8	–
Gear pair 3	–	0.4458×10^8	–	–	1.128×10^8	–
Torsional mesh stiffness						
Gear pair 1	–	5194.81	–	–	16,363.26	–
Gear pair 2	–	2127.66	–	–	9708.74	–
Gear pair 3	–	2564.10	–	–	8163.27	–

Acknowledgements The authors are thankful to the Director Dr. Sanjiv Tokekar of the institute and Dr. Ashesh Tiwari Head of the Mechanical Engineering Department for providing the necessary infrastructure and conducive environment to do the research work and colleague Dr. Vivek Kapoor for helping in writing the literature review part of the paper as per the journal guidelines and Dr. Ankur Saxena for providing the help in formulating the computer code.

References

1. Kohler H, Regan R (1985) The derivation of gear transmission error from pitch error records. Proc Inst Mech Engin part C J Mech Eng Sci 199:195–201
2. Jianfeng L, Mintian X, Shouyou W (1999) Finite element analysis of instantanous mesh stiffness of cylindrical gears (with and without felxible gear body). Commun Numer Methods Eng 15:579–587
3. Sainsot P, Velex P (2004) Contributions of gear body to tooth deflections—a new bidimensional analytical formula. Trans ASME 126:748–752
4. Tian X (2004) Dynamic simulation for system response of gearbox ıncluding localized gear faults. MS Thesis, Department of Mechanical Engineering, University of Alberta, Edmonton
5. Tharmakulasingam R (209) Transmission error in spur gears-static and dynamic finite-element modeling and design optimization. PhD Thesis, School of Engineering and Design, Brunel University, United Kingdom
6. Kiekbusch T, Sappok D, Sauer B, Howard I (2011) Calculation of the combined torsional mesh stiffness of spur gears with two and three dimensional parametrical FE models. Strojniški vestnik J Mech Eng 57(11):810–818
7. Saxena A, Parey A, Chouksey M (2016) Time varying mesh stiffness calculation of spur gear pair considering sliding friction and spalling defects. Eng Failure Analy 70:200–211
8. Zhan J, Fard M, Jazar R (2017) A CAD-FEM-QSA integration technique for determining the time-varying meshing stiffness of gear pairs. Measurement 100:139–149

9. Sánchez MB, Pleguezuelos M, Pedrero JI (2017) Approximate equations for the meshing stiffness and the load sharing ratio of spur gears including hertzian effects. Mech Mach Theory 109:231–249
10. Sánchez MB, Pleguezuelos M, Pedrero JI (2019) Influence of profile modifications on meshing stiffness, load sharing ratio and transmission error of involute spur gears. Mech Mach Theory 139:506–525
11. Chang L, Wan-kai S, Cura FM, Mura A (2020) A novel method to predict static transmission error for spur gear pair based on accuracy grade. J Cent South Univ 27:3334–3349
12. Czakó A, Řehák K, Prokop A, Ranjan V (2020) Determination of static transmission error of helical gears using finite element analysis. J Measur Eng 8(4):167–181
13. Bruzzone F, Maggi T, Marcellini C, Rosso C (2021) 2D nonlinear and non-Hertzian gear teeth deflection model for static transmission error calculation. Mech Mach Theory 166:104471
14. Chin YZ, Smith WA, Borghesani P, Randall RB, Peng Z (2021) Absolute transmission error: a simple new tool for assessing gear wear. Mech Mach Theory 146:107070
15. Chen Z, Ning J, Wang K, Zhai W (2021) An improved dynamic model of spur gear transmission considering coupling effect between gear neighbouring teeth. Nonlinear Dyn 106:339–357
16. Flek J, Dub M, Kolář J, Lopot F, Petr K (2021) Determination of mesh stiffness of gear-analytical approach vs FEM analysis. Appl Sci 11:4960
17. Tao L, Tian D, Tang S, Wu X, Li B. Dynamical modelling and simulation of spur gears with flank pitch error. https://doi.org/10.21203/rs.3.rs-534359/v1
18. Ambaye GA, Lemu HG (2021) Effect of backlash on transmission error and time varying mesh stiffness. IWAMA 2020 LNEE 737:18–28
19. Marafona DMJ, Marues MTP, Martins CR (2021) Mesh stiffness models for cylindrical gears: A detailed review. Mech Mach Theory 166:104472
20. Sun Z, Chen S, Hu Z, Tao X (2022) Improved mesh stiffness calculation model of comprehensive modification gears considering actual manufacturing. Mech Mach Theory 167:104470
21. Kumar V, Kumar A, Kumar S, Sarangi S (2022) TVMS calculation and dynamic analysis of carburaized spur gear pair. Mech Syst Signal Process 166:108436
22. Duan T, Wei J, Zhang A, Xu Z, Lim TC (2021) Transmission error investigation of gearbox using rigid-flexible coupling dynamic model: Theoritical analysis and experiments. Mech Mach Theory 157:104213
23. Lee J-H, Choi H-S, Sohn J-H, Lee G-H, Park D-I, Kim J-G (2021) Statistical analysis for transmission error of gear system with mechanical and thermal deformation uncertainties. Appl Sci 11:6582
24. SciLab—Open Source Software, https://www.scilab.org

On a Method of Calculating of Continua with an Initial Crack

F. F. Adilov

Abstract A method for calculating of continua with an initial crack of various orientations is presented in the article. The problem is solved under conditions of a plane stress state by the displacement discontinuity method. The solution method is based on the fundamental Papkovich–Neuber solution. In the numerical implementation, the values of the sought-for functions in each section of the boundary element were assumed constant. The influence of the crack orientation on the stress state of the body is determined based on the plotted graphs.

Keywords Stress · Strain · Displacement discontinuity · Fracture

1 Introduction

Rigid body response to a load manifests itself in the form of its strain and (or) destruction. The phenomenon of destruction is partly related to the study of the micro-mechanisms of the destruction process and partly to the substantiation of the damage criteria and other predictions at the macro-level. In the latter case, the greatest interest arises in such a parameter as the breaking load. A complete analysis considering the bearing capacity includes studies of the possibility of failure without large strains and with them. In the latter case, the critical load may be a limiting one (according to the theory of plasticity) or be a load that causes loss of stability, determined by the study of the deformed state of an undestroyed body.

In many building elements and parts of aggregates, there are stress concentrators, the presence of which is caused by technological necessity or they appear during operation. The main point in the strength analysis of structural elements with such weakening is the correct choice of the method for estimating their limit state based on the available strength criteria. The choice of the strength criterion in relation to the calculation of a particular structural element depends on many factors, the most important of which are the properties of the material of this element, the loading

F. F. Adilov (✉)
Institute of Mechanics and Seismic Stability of Structures, Tashkent, Uzbekistan
e-mail: mahzun86@gmail.com

K. Geetha et al. (eds.), *Recent Trends in Materials*, Springer Proceedings in Materials 18, https://doi.org/10.1007/978-981-19-5395-8_21

method, the shape and dimensions of the concentrator, and other factors. In each specific case, any factor or their combination may be dominant. Anyway, numerical and experimental investigation of crack propagation or stress–strain state around crack has to be solved by using of fracture mechanics positions. In [1–12], different approaches are proposed in this regard.

For instance, the mixed boundary value problem was solved for a piecewise homogeneous elastic body with a rectilinear semi-infinite crack on the line where the materials are joined [6]. There is the numerical method for solving of 3D problems of fracture mechanics by method of discontinuous displacements was proposed [8] and applied for solving of boundary problems. The displacement discontinuity method for modeling axisymmetric cracks in an elastic half-space or full space described in [9]. Here, the formulation was based on hypersingular integral equations that relate displacement jumps and tractions along the crack.

It is believed that when determining the limit state of structural elements, the leading idea for choosing the strength criterion is the presence or absence of a pointed defect (a crack). Then, if there is a crack in the body, strength criteria are used in strength calculations based on the simulation of the fracture mechanism in accordance with the theory of fracture mechanics; in the absence of a pointed defect in the structural element, classical and new criteria for the strength of solid materials are used. In the latter case, the mechanism of initiation and development of cracks is not taken into account. There are various strength criteria. As a rule, the deformation criterion is not considered preferable. However, in the presence of initial cracks, it is possible to trace its development by experimental monitoring. The solution to the problem in displacements is considered below.

We can consider the concept of brittle fracture in the presence of a crack in the body of the structure as a first approximation. In the presented article, the stress–strain state of the continuum in the presence of an initial crack (a cut) is considered based on the concept of brittle fracture (a linear problem). A plane stress state is assumed, and shears of types 1 and 2 cracks are considered, i.e., normal fracture and transverse shear.

2 Solution Method

The type of destruction is a geometric characteristic of damage. According to Irwin, type 1 crack characterizes symmetrical opening, in which the relative movements of the opposite edges are perpendicular to the fracture surface, while types 2 and 3 cracks characterize antisymmetric separation (of a body into parts) by relative shear displacements, perpendicular and parallel to the crack front, respectively. Note that crack growth often occurs according to type 1 or close to it. Probably, this type of destruction is most consistent with intuitive ideas.

Consideration of cracks, rock fracturing, layering is mostly necessary when solving the problems of rock mechanics. It makes it possible to assess the occurrence of dangerous stresses and the development of methods for strengthening these structures.

When solving problems numerically, cracks are modeled as cuts with a small opening. Such an approach, generally speaking, does not give a complete picture of the stress–strain state, since cohesion forces are not taken into account. That is, the problem with only types 1 and 2 cracks is considered.

In the most general case, stresses and displacements in a small neighborhood of a linear crack can be expressed in a polar coordinate system as follows:

$$\sigma_{ij}(r,\theta) = \frac{1}{\sqrt{2\pi r}} \sum_{\alpha} K_\alpha f_{ij}^{(\alpha)}(\theta) + 0(1)$$

$$u_i(r,\theta) = \frac{\sqrt{r}}{\nu\sqrt{2\pi}} \sum_{\alpha} K_\alpha \varphi_i^{(\alpha)}(\theta) + 0\left(r^{3/2}\right),$$

$$i,\ j = 1,2,3;\ \ a = I, II, III$$

Stress intensity factors depend on the magnitude of the external load applied, the size and geometry of the body, and the length and shape of the crack. These solutions are obtained for a crack in an infinite body with forces applied to the edges (fundamental solutions):

$$K_\alpha = \frac{1}{\sqrt{\pi l}} \int_{-l}^{l} p(\xi) \sqrt{\frac{1+\xi}{1-\xi}} d\xi$$

In the case of applying constant stresses, the stress intensity factors take the following form:

$$K_I = \sigma\sqrt{\pi l},\ \ K_{II} = \tau\sqrt{\pi l},\ \ K_{III} = \tau\sqrt{\pi l}$$

This approach to solving the problem in stresses is applicable in determining the critical stress when there is a possibility of crack initiation. The solution in displacements cannot be obtained in this way. In practical problems, it is possible to determine the value of the critical crack opening experimentally (using displacement sensors installed). In this case, it is more appropriate to obtain the solution to the problem in displacements.

One of the approaches to consider this type of problem with one or several narrow slit-like cuts and slits is to use the method of boundary elements in the form of displacement discontinuity [13]. The displacement discontinuity method is appropriate when considering problems with cracks since it uses a fundamental solution obtained on the basis of a single discontinuity in space.

The advantage of this approach is the representation of the solution in the form of finite series of expansion in terms of the found analytically presented functions. The

expansion coefficients can be determined from boundary conditions in the geometric centers of gravity of the boundary elements.

In a plane formulation, it can be used to consider type 1 and type 2 cracks; i.e., cracks of normal fracture and shear are considered. This method is based on the analytical solution to the problem of an infinite plane, displacements in which suffer a constant discontinuity. Physically, the displacement discontinuity is a crack, the opposite edges of which are displaced relative to each other. The displacement discontinuity method is based on the idea that displacement discontinuities distributed continuously along the fracture can be replaced by a discrete approximation. Like these problems can rise in other plasticity ones like soil, etc., regarding dynamic case. Finite different methods in so cases can be applied also [14–17]; however, for fracture problems, boundary element method are preferable. At finite element calculation technology, it is necessary to discretize the study inside your geometry boundary. By using the boundary element method, the system of equations is built in such a way that you only need discretization at the boundaries of the model geometry (this only works for linear ones within the computational domain). This approach usually results in fewer elements; however, the equations must connect all boundary elements (i.e., each with each), in contrast to the finite elements in the volume, which are connected at the level of equations only with their "neighbors." Both methods have both advantages and disadvantages.

However, displacement discontinuity method can conveniently solve fracture mechanics problems because the discontinuous displacement field across the fracture surfaces can be explicitly captured by the displacement discontinuity elements [13]. The potential of these approaches for solving crack propagation problems for quasi-brittle materials can covered also. In [13], the results of calculation by displacement discontinuity method were compared by experimental and finite element results simulations. In boundary element method in displacement discontinuity form as initial position is taking into numerical scheme fundamental solution of fracture mechanics. Finite element method has not so option.

The problem of constant displacement of cracks in a finite section of the x-, y-plane in the plane of infinite elastic constraints is determined by the condition of displacement continuity everywhere except for the considered section. A segment can be chosen so that it forms a certain part of the x-axis, for example, $|x| \leq a, \ \ y = 0.$. If we consider this section as a rectilinear crack, then we can define two surfaces that do not differ much from each other (Fig. 1). One of these surfaces is located on the positive $(y = 0_+)$ side of the $(y = 0)$ axis, and the other is on the negative $(y = 0_-)$ side. When moving from one side of the section to the other, the displacement area changes by the specified value of $D_i = \left(D_x, D_y\right)$.

Without dwelling on the derivation of formulas for constant elements along the boundary, the method of displacement discontinuity has the following form:

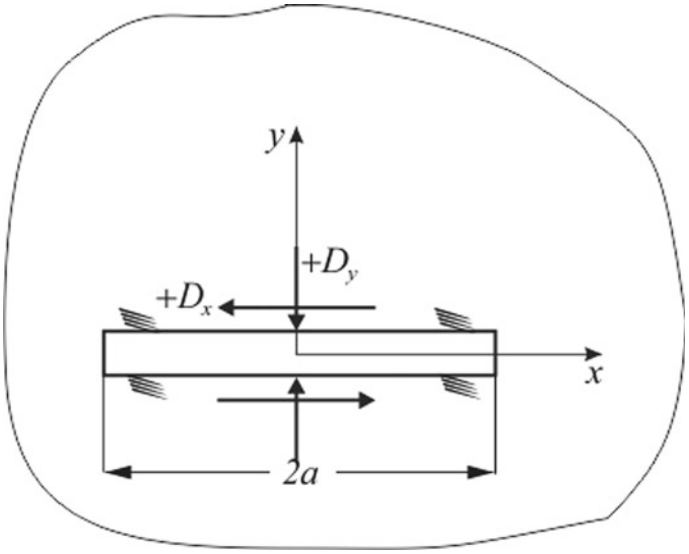

Fig. 1 Components of a constant displacement discontinuity

$$
\begin{aligned}
u_x &= D_x\left[2(1-\nu)f_{,y} - yf_{,xx}\right] + D_y\left[-(1-2\nu)f_{,x} - yf_{,xy}\right],\\
u_y &= D_x\left[(1-2\nu)f_{,x} - yf_{,xy}\right] + D_y\left[2(1-\nu)f_{,y} - yf_{,yy}\right].\\
\sigma_{xx} &= 2\mathrm{GD}_x\left[2f_{,xy} + yf_{,xyy}\right] + 2\mathrm{GD}_y\left[f_{,yy} + yf_{,yyy}\right],\\
\sigma_{yy} &= 2\mathrm{GD}_x\left[-yf_{,xyy}\right] + 2\mathrm{GD}_y\left[f_{,yy} - yf_{,yyy}\right],\\
\sigma_{xy} &= 2\mathrm{GD}_x\left[f_{,yy} + yf_{,yyy}\right] + 2\mathrm{GD}_y\left[-yf_{,xyy}\right].
\end{aligned}
$$

Here, D_i is the displacement discontinuity defined as the difference in displacements on both edges of fracture

$$D_i = u_i(x_1, 0_-) - u_i(x_1, 0+)$$

$$
\begin{aligned}
f(x,y) = -\frac{1}{4\pi(1-\nu)}\Bigg[& y\left(\operatorname{arctg}\frac{y}{x-a} - \operatorname{arctg}\frac{y}{x+a}\right)\\
& - (x-a)\ln\sqrt{(x-a)^2} + (x+a)\ln\sqrt{(x+a)^2+y^2}\Bigg]
\end{aligned}
\tag{1}
$$

where $f_{,x}$, $f_{,y}$, $f_{,xx}$, $f_{,xy}$, ... are the derivatives of function (1) with respect to x and (or) y.

Derivatives of functions are found by simple differentiation, and, for example, for third derivatives have the following form:

$$f_{,xyy} = -f_{,xxx} = \frac{1}{4\pi(1-\nu)}\left[\frac{(x-a)^2 - y^2}{\left[(x-a)^2+y^2\right]^2} - \frac{(x+a)^2 - y^2}{\left[(x+a)^2+y^2\right]^2}\right],$$

$$f_{,yyy} = -f_{,xxy} = \frac{2y}{4\pi(1-\nu)}\left[\frac{x-a}{\left[(x-a)^2+y^2\right]^2} - \frac{x+a}{\left[(x+a)^2+y^2\right]^2}\right].$$

3 Statement of the Problem

Consider the problem of loading a plate with a crack of length *2a* located at an angle α to the horizon (Fig. 2). The plate is 10 cm long and 5 cm high.

The following boundary conditions are set:

$$u_y\big|_{y=0} = u_y\big|_{y=h} = 0; \quad P_x|_{y=0} = P_x|_{y=h} = 0;$$
$$P_y\big|_{x=0} = P_y\big|_{x=l} = 0; \quad P_x|_{x=0} = P_x|_{x=l} = P.$$

The kinematic conditions correspond to hinged fastening, the side surfaces are loaded with a tensile force *P*. The following physical data of the problem are given $\nu = 0.3$, $E = 200\,\text{GPa}$, $P_x = 1000\,\text{N}$. The problem was solved under conditions of a plane stress state (Table 1).

This problem is solved in the local coordinate system, introduced for each boundary element. It can be taken as a natural coordinate system along a plane curve (in this case, a polyline with right angles). The stresses and strains at the boundary

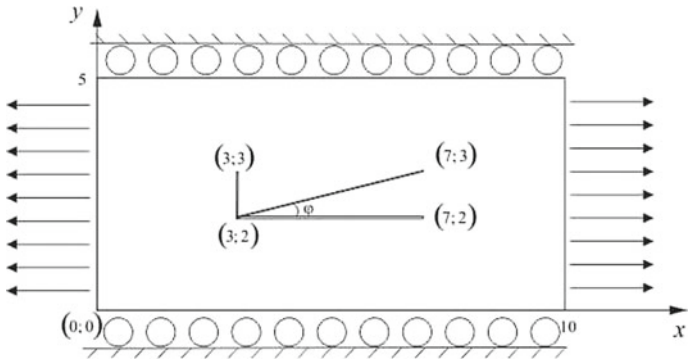

Fig. 2 Loaded sample with a crack

Table 1 Geometric dimensions and physical parameters of the material

Plate dimensions				Crack coordinates											
				$\varphi = 0$				$\varphi = 90°$				$\varphi = 14°$			
x_1	y_1	x_2	y_2	x_1	y_1	x_2	y_2	x_1	y_1	x_2	y_2	x_1	y_1	x_2	y_2
0	0	10	5	3	2	7	2	3	2	3	3	3	2	7	3

are expressed in the form of these local coordinates:

$$\begin{aligned}\sigma_s^i &= \sum_{j=1}^{N} A_{ss}^{ij} D_s^j + \sum_{j=1}^{N} A_{sn}^{ij} D_n^j \\ \sigma_n^i &= \sum_{j=1}^{N} A_{ns}^{ij} D_s^j + \sum_{j=1}^{N} A_{nn}^{ij} D_n^j\end{aligned} \quad i = \text{from } 1 \; to \; N \tag{2}$$

$$\begin{aligned}u_s^i &= \sum_{j=1}^{N} B_{ss}^{ij} D_s^j + \sum_{j=1}^{N} B_{sn}^{ij} D_n^j \\ u_n^i &= \sum_{j=1}^{N} B_{ns}^{ij} D_s^j + \sum_{j=1}^{N} B_{nn}^{ij} D_n^j\end{aligned} \quad i = \text{from } 1 \; to \; N \tag{3}$$

where A_{ss}^{ij}, ..., B_{ss}^{ij}, ... is the boundary coefficients of influence for stress and displacement, respectively.

In the general case, if the stress values of σ_s^i and σ_n^i are given for each element of the crack and outer boundary, then from expression (2), we obtain a system of $2\ N$ unknown linear equations for D_s^i and D_n^i ($i = 1,\ldots, N$) elementary displacement discontinuities. Solving this system of equations numerically by the Gauss method, we determine the unknowns D_s^i and D_n^i [13]. It should be understood that the displacement discontinuity values are fictitious values for the outer boundary.

The solutions obtained in the form of graphs of isoline are shown in Figs. 3, 4, 5 and 6. The crack opening is largely influenced by the values of normal and shear stresses.

The presence of cracks, cuts, and stress concentrators requires their consideration in the calculations and the development of methods for their strengthening to prevent

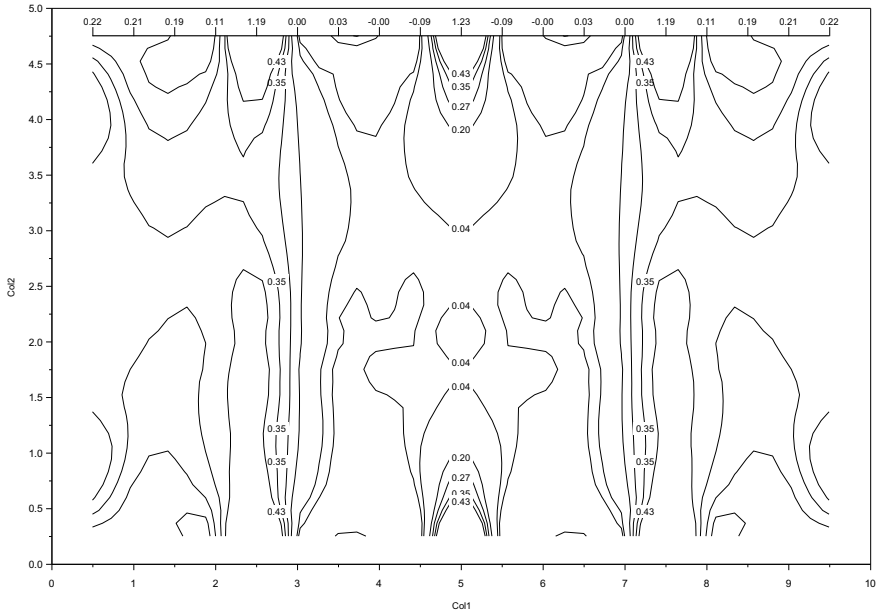

Fig. 3 Stress components σ_{yy} (kPa) (normal stresses for crack edges—a horizontal crack)

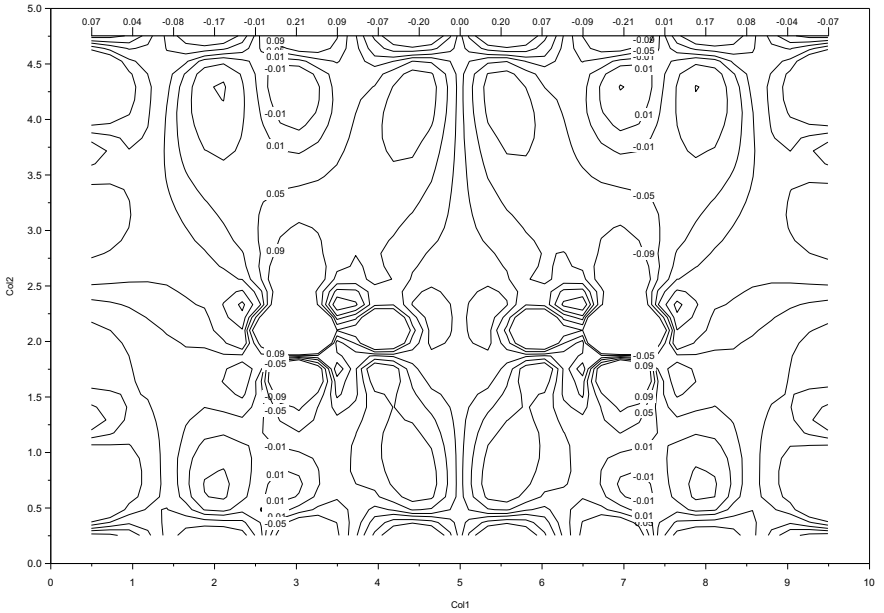

Fig. 4 Stress components σ_{xy} (kPa) (shear—a horizontal crack)

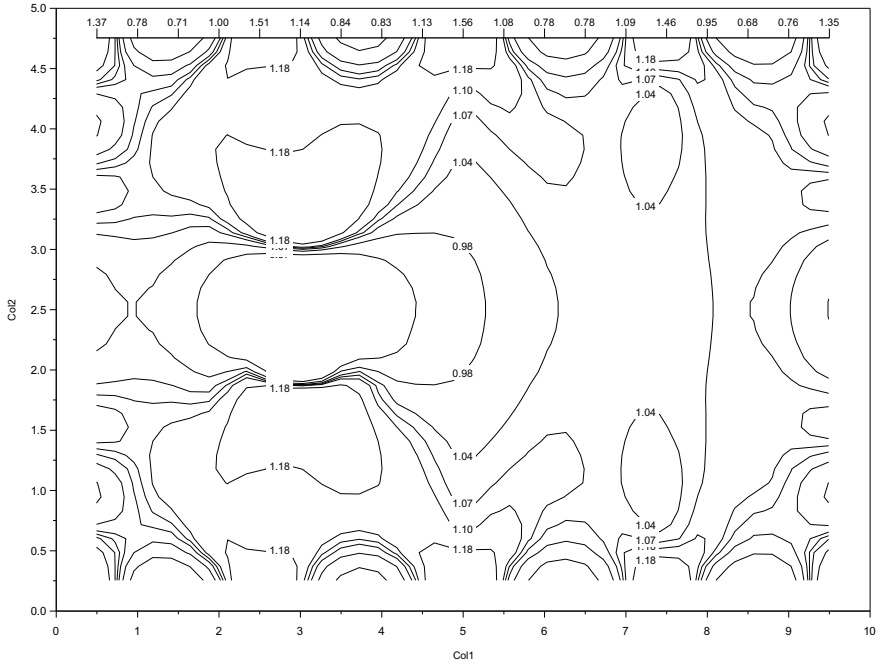

Fig. 5 Stress components σ_{xx} (kPa) (normal stresses for crack edges—a vertical crack)

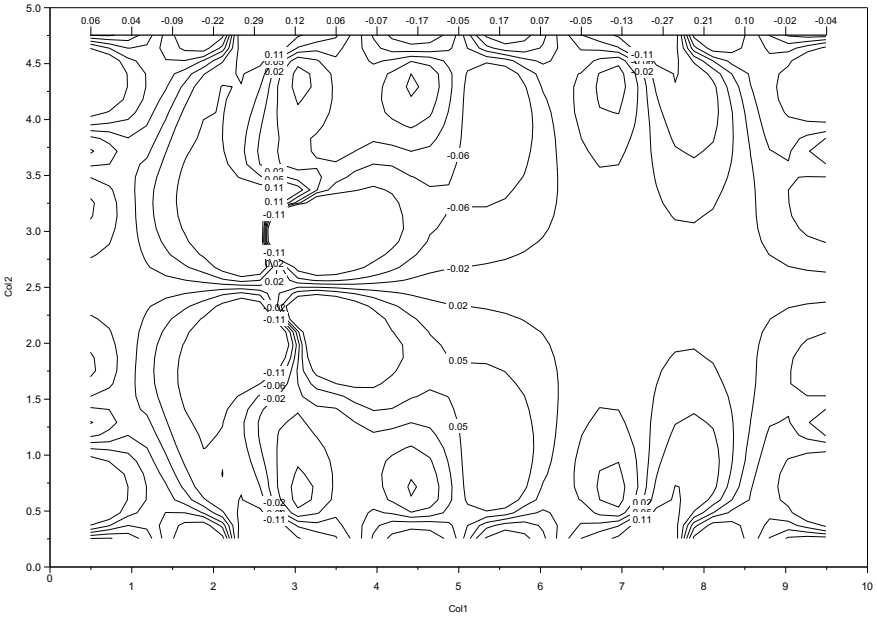

Fig. 6 Stress components σ_{xy} (kPa) (shear—a vertical crack)

their development leading to the collapse of the structure. The technologies developed imply the installation of devices in various sections of a body weakened by stress concentrators. Below are the changes in the stress intensity along the horizontal plane in the areas below and above the crack (Figs. 7 and 8). These data provide the necessary information about possible methods of structure strengthening.

4 Conclusion

According to the results of the calculation, it is possible to determine the degree of dependence of type 1 and type 2 crack development depending on the crack orientation. With a horizontal position of a cut, the development of type 2 crack prevails, while with a vertical position, the situation is reversed. With an inclined position of a crack in the selected range, the probability of crack initiation is equally probable.

When choosing a crack reinforcement, the changes in the stress intensity on two horizontal sections of the plate are given. According to the graphs, the magnitude of the stress intensity at the angular position of the cut (under given boundary conditions) is greater than at the horizontal and vertical positions. This indicates that in the energy assessment of the possibility of crack initiation; it is precisely at such a position that

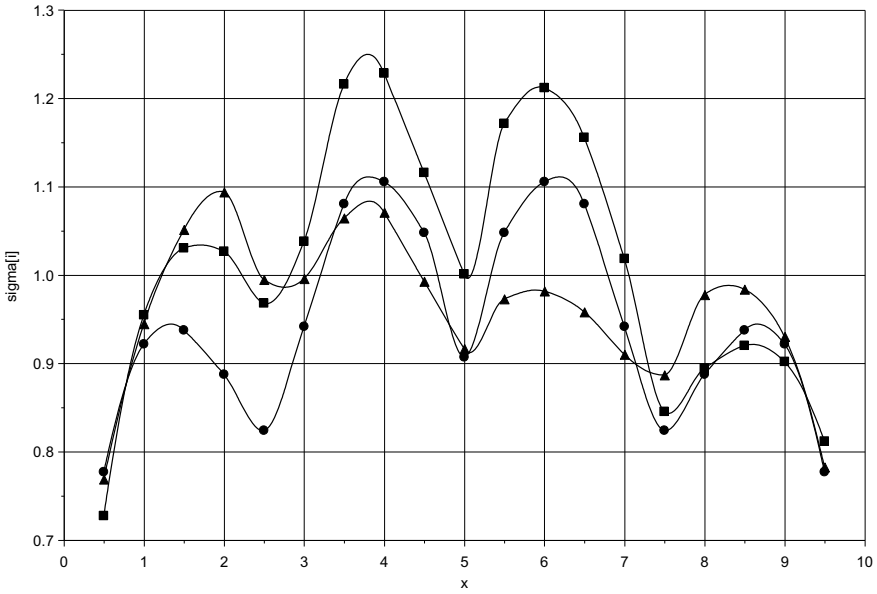

Fig. 7 Stress intensity for $y = 1$ (●- $= \varphi 0°$, ▲- $= \varphi 90°$, ■- $= \varphi 14°$)

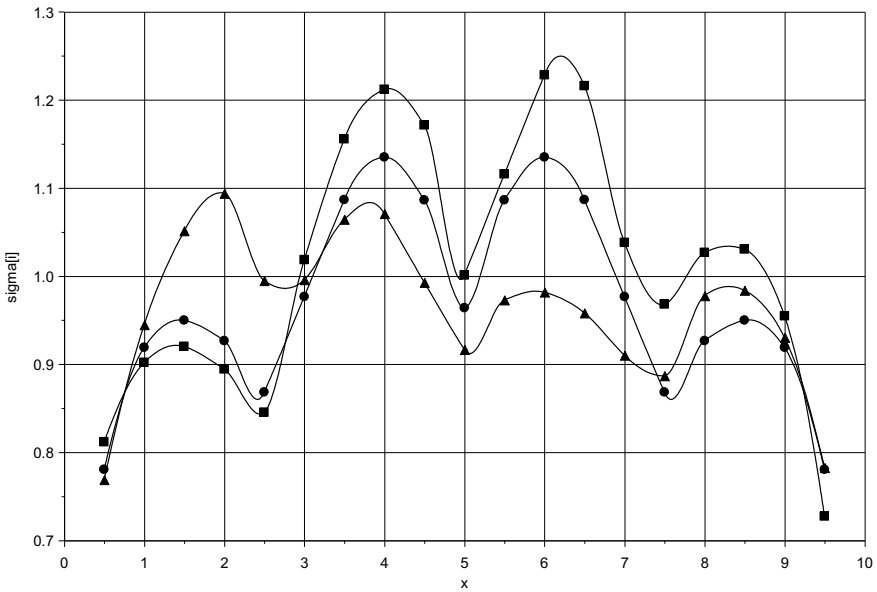

Fig. 8 Stress intensity for $y = 4$ (●- $= \varphi 0°$, ▲- $= \varphi 90°$, ■- $= \varphi 14°$)

fracture may occur (under the conditions of a linear model). With such a position of the crack, it is paramount to strengthen the structure.

References

1. Matvienko YG, Pisarev VS, Eleonsky SI, Chernov AV (2014) Determination of fracture mechanics parameters by measurements of local displacements due to crack length increment. Fatigue Fract Eng Mater Struct 37:1306–1318
2. Murakami S, Hirano T, Liu Y (2000) Asymptotic fields of stress and damage of a mode I creep crack in steady-state growth. Int J Solids Struct 37:6203–6220
3. Vasil'eva YO, Sil'vestrov VV (2011) The problem of an interface crack with a rigid patch plate on part of its edge. J Appl Math Mech 75:716–730
4. Abirov RA (2008) On the physical reliability and taking complex loading into account in plasticity. Mater Sci 44:512–516
5. Astaf'ev VI, Grigor'eva TV, Pastukhov VA (1992) Influence of material damage conditions on stress-strain state near the crack tip under creep. Fiz Mekhanika Mater
6. Vasileva I, Gürlebeck K, Silvestrov V (2016) Mixed antiplane boundary-value problem for a piecewise-homogeneous elastic body with a semi-infinite interfacial crack. Math Methods Appl Sci 39:4419–4427
7. Zhao J, Zhang X (2001) On the process zone of a quasi-static growing tensile crack with power-law elastic-plastic damage. Int J Fract
8. Zvyagin AV, Luzhin AA, Panfilov DI, Shamina AA (2021) Numerical method of discontinuous displacements in spatial problems of fracture mechanics. Mech Solids 56:119–130
9. Gordeliy E, Emmanuel D (2011) Displacement discontinuity method for modeling axisymmetric cracks in an elastic half-space. Int J Solids Struct 48(19):2614–2629
10. Liu Y (2016) On the displacement discontinuity method and the boundary element method for solving 3-D crack problems. Eng Fract Mech 164:35–45
11. Cong Z, Li Y, Liu Y, Xiao Y (2021) A new method for calculating the direction of fracture propagation by stress numerical search based on the displacement discontinuity method. Comput Geotech 140:104482
12. Wu K, Olson JE (2015) A simplified three-dimensional displacement discontinuity method for multiple fracture simulations. Int J Fract 193(2)
13. Crouch S, Starfield A (1983) Boundary element methods in solid mechanics London. George Allen & Unwin, p 328
14. Abirov RA, Khusanov BE, Sagdullaeva DA (2020) Numerical modeling of the problem of indentation of elastic and elastic-plastic massive bodies. In: IOP conference series: materials science and engineering
15. Rikhsieva BB, Khusanov BE (2021) Numerical analysis of shear interaction of an underground structure with soil. J Phys Conf Series 2131(3):032093
16. Khusanov B, Rikhsieva B (2019) Thickness dimensions of the contact layer of soil-rigid body interaction. E3S Web Conf 97:04040
17. Chen E, Leung CKY, Tang S, Lu C (2018) Displacement discontinuity method for cohesive crack propagation. Eng Fract Mech 190(1):319–330

Ultra-Broadband Absorber Based on Metasurfaces in the Infrared Regime

Vijay Laxmi, Abida Parveen, Deepika Tyagi, and Zhengbiao Oyuang

Abstract An ultra-broadband metasurface absorber is proposed that falls in the terahertz regime cover a wide spectrum. Here we theoretically demonstrate the novel design of angular and polarization-insensitive ultra-broadband multi-metasurfaces-based absorber (MMBA) on a metallic substrate in the infrared spectrum of wavelength 1.5–6 μm. The proposed device is composed of germanium and gold slabs arranged periodically to work as a metasurface on a metallic substrate. A metal–dielectric interface has been repeated to enhance the absorption. A circular top layer is used to reduce the dips in absorption peak and for broadband spectrum consequently, absorption improved up to 95% covering broadband from 2.5 μm to 6 μm. A systematic theoretical investigation about this model revealed that this absorber is insensitive to the incident angles and polarization of light with excellent performance for an s-polarized and p-polarized plane wave. The metamaterial (MM)-based absorber received significant attention due to their promising properties and have the potential for many applications such as thermal emitters, high-speed communication, imaging, optoelectronic devices.

Keywords Metamaterials · Absorber · Ultra-broadband · Metasurfaces · Angle insensitivity

1 Introduction

Recently, metamaterial (MM) absorbers have gained considerable attraction due to their outstanding properties in the field of nanoelectronics and nanophotonics [1–4].

V. Laxmi · A. Parveen · D. Tyagi · Z. Oyuang (✉)
THz Technical Research Center of Shenzhen University, Shenzhen Key Laboratory of Micro-Nano Photonic Information Technology, Key Laboratory of Optoelectronic Devices and Systems of Ministry of Education and Guangdong Province, College of Physics and Optoelectronic Engineering, Shenzhen University, Shenzhen 518060, China
e-mail: zbouyang@szu.edu.cn

V. Laxmi
International Collaborative Laboratory of 2D, Materials for Optoelectronics Science and Technology, Shenzhen University, Shenzhen 518060, P. R. China

K. Geetha et al. (eds.), *Recent Trends in Materials*, Springer Proceedings in Materials 18, https://doi.org/10.1007/978-981-19-5395-8_22

MM-based absorbers cover a very broad range including a few GHz to 10 THz and have auspicious applications in various fields from medical to communication. MMs can be defined as artificial material, composed of periodically arranged subwavelength microstructure. Their properties strongly depend on their designed nano-structure instead of the composition of materials. MMs exhibit many unusual phenomena such as cloaking, double negative index, anomalous light bending, superlens [5, 6] and MMs also display perfect electromagnetic absorption. The first metamaterial absorber was fabricated in 2008, with the help of two resonators [7]. After this discovery, many theoretical investigations have been published over metamaterials perfect absorber [8–12]. And their simplest structure makes them an excellent candidate to fabricate and commercialize in many daily life applications such as superlens, thermal emitters, wireless communications, sensing, light manipulation, and imaging [13–17]. Their macroscopic electromagnetic properties arise at a subwavelength scale due to the collective response of the individual structure. For future electronics, MM-based absorber plays a significant role in further improving the performance of the optoelectronics devices such as thermal emitters, thermal radiators, solar cells, and detection [4, 18]. To obtain a near-unity absorption is still a bottleneck for a perfect MM absorber (MMA). Nevertheless, with the help of MMs, it is somehow possible to reach the boundary of maximum absorption. Near-unity absorption with ultra-broadband is still an issue to resolve. Moreover, MMA falls in the THz regime leads to many attractive branches of terahertz devices because of their scalable features. Many multi-layer structures have been realized and experimentally demonstrated to gain the maximum absorption and expand the bandwidth, including five-layered [19] and three-layered [2] terahertz metamaterials. This multi-layer structure can be the composition of periodically arranged dielectric layers, metallic patterns, and a metal/dielectric, metal/dielectric/metal, and metal/insulator/metal (MIM). As it is previously mentioned that their properties are defined according to their structure therefore MMAs are typically designed of a tri-layer structure in the infrared or visible region [1, 20]. In recent years, MMAs have been effectively utilized to clarify and anticipate the resonances in metallic grating film structure [21, 22], narrow slit array [23, 24], double-layer nanoslit array [25], and deep grating [25, 26]. Usually, extreme absorptance reaches its limit when the effective impedance of the proposed structure matches with the impedance of the free space. Numerous efforts have been made to enlarge the absorption bandwidth of MMAs, such as, by joining two different resonators into one-unit, dual-band absorption [10, 27]. However, the average absorptivity efficiency is still not very high because those absorption spectra are composed of discrete peaks. While the single band MMA is not appropriate in certain zones, for example, phase imaging, spectroscopic detection where distinct absorption peaks are required, most MMAs generally require unit cells with complex geometries, including complex structure and cost of manufacture. Moreover, previous designs are incident angle and polarization-sensitive which may unblock numerous practical applications [28].

Here, we have theoretically designed and simulated this MMA which is incident angle and polarization insensitive (s-polarization and p-polarization). This broadband multi-layer metasurface-based absorber (MMBA) operates in a broad spectrum

ranging from 1.5 to 6 μm. The MMBA is designed by five layers in which semiconductor and metals layers are arranged alternatively in a periodic manner with perfect electric conductor (PEC, or metallic substrate) on the ground plane. Three benchmarks are studied to reveal the novelty of our work which includes usage of a resonator multi-structure, a dual-layered multi resonator for better absorption, and a metallic substrate. In this paper, an ultra-broadband absorber based on a metasurface is presented for the infrared spectrum in the terahertz (THz) region. The absorption bandwidth increased much significantly in our proposed absorber. The simulated total absorption increased more than 90% by using a multi-layered single structure. Besides, the results show that the absorption bandwidth is significantly enlarged by using multi-layers of the metasurface, also known as a dual-layered absorber. The top layer is used circularly to reduce the dips in absorption peak and expand the bandwidth of absorption by using multi-mode resonance absorption in the circular ring resonator. In addition, an angle-dependent study has been done which accomplishes that MMBA is angle insensitive and polarization-insensitive. This MMBA is an excellent contender for many applications such as spectroscopic imaging, thermal emitters, as well as thermal detectors due to its exceptional properties. For further improvement in the device, the unit cell keeps on repeating up to 12 square patches to design a dual-layered MIM structure within a subwavelength period, and consequently, the absorption exceeds up to 95% for a broad range spectrum. The dual-layered absorber has improved the bandwidth more than two times in contrast with the single resonator.

The absorptivity $A(\omega)$ is calculated from the Eq. (1):

$$A = 1 - R(\omega) - T(\omega), \tag{1}$$

where $R(\omega)$ and $T(\omega)$ are reflectivity and transmissivity as functions of frequency ω, respectively.

2 Device Design and Simulation

Generally, the geometric configuration and the geometrical parameters are considered the special factor in determining the resonance frequency. Multiple resonators of the same size and shapes are designed and fabricated to achieve unity absorption with maximized bandwidth. Typically, they are arranged periodically in a two-dimensional plane to form a metasurface. Here, a multi-metasurface broadband absorber (MMBBA) is theoretically demonstrated and simulated. This MMBBA is made of twelve metallic square patches of different geometric parameters, as shown in Fig. 1a. Previously reported absorbers are generally designed along the side with arranging of different sized subunits into one-unit cells or vertically stacking multi-layer structures, to get numerous absorption peaks [3].

Multi-layers and other parameters such as thickness, materials, and stacking, help to occur many resonant peaks during excitation and survived due to resonance

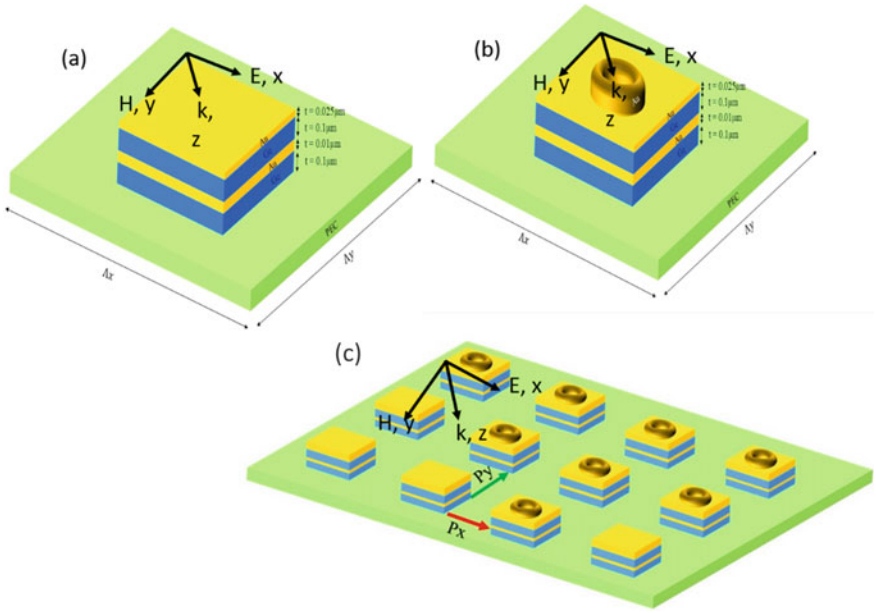

Fig. 1 Proposed devices; **a** perspective view of the single resonator (square patch) multi-structure metasurfaces arranged periodically, **b** a circular ring has been placed as the top layer, **c** the repeated unit cell of MMBBA with a complete structure made of twelve metallic square patches of different geometric parameters

independence. Initially, a single unit cell of a multi-layered resonator is examined to understand the concept of multi-band absorption as mentioned in Fig. 1a. A multi-surface absorber is designed with three different materials, the ground plane is made of the perfect electric conductor (PEC) and then a square slab has chosen over it, of a little smaller size. The conductivity of gold is 4.10×10^7 S/m. The next layer is an insulator made of germanium (Ge) with a refractive index of 4. An s-polarized and p-polarized plane wave enlightened the proposed device structure. The metal and dielectric are arranged periodically in the same manner with identical widths and height over the surface of PEC with a period of $\Lambda_X = 3.6$ μm with equal widths $\Lambda_y = 1$ μm. The thickness of Ge is 0.1 μm throughout the whole structure. The top metallic layer of gold has thickness $t_{\mathrm{Au}} = 0.025$ μm and the bottom layer of gold has thickness $t_{\mathrm{Au}} = 0.01$ μm. The refractive index of Ge becomes 0.0000000005 inside the measured frequency range. The substrate has a thickness of $t_{\mathrm{PEC}} = 0.1$ μm. For further improvement in absorption peak over broadband, A ring resonator of gold metal is designed on the top which has an outer radius of $R_1 = 0.2$ μm and an inner radius of $R_2 = 0.1$ μm shown in Fig. 1b. Figure 1c shows the perspective view of wide-band multi-sized resonators at normal incidence with identical spacing distance to neighbor resonators $P_x = 0.05$ μm, and $P_y = 0.05$ μm.

To examine the performance of the design in Fig. 1a, a full-wave simulation was completed using the finite-difference time-domain (FDTD) method. In the simulation arrangement, the PML boundary condition was set along the z-direction, and the periodical boundary conditions were set alongside the x- and y-directions. The presented Cartesian coordinate system shows that the propagation vector is along the z-direction while electric field (**E**) is in x-direction with normal to magnetic field (**H**) displayed with each structure. As it is mentioned in Fig. 1, a multi-layered single band absorber is investigated theoretically and the proposed structure is elucidated with all parameters. Figure 1b shows a similar structure with placing a gold ring resonator as a top layer of the device. The presented MMBBA has a high absorption peak of about 95% with covering 1.5–6 μm. Further information is revealed in Fig. 2. Figures 2a, b show the reflection and absorption spectra of the multi-layer single absorber with inset showing the corresponding structure. Using Eq. (1), it is seen that reflection works opposite of absorption and which concludes that the absorption peak is maximum at few wavelengths. Figure 2c depicted the reflection spectra of similar multi-metasurfaces with a gold ring as a top layer.

As it is apparent in Fig. 2d the number of absorption peaks enhanced after placing the top layer as a circular ring because the ring serves as a resonator and there is

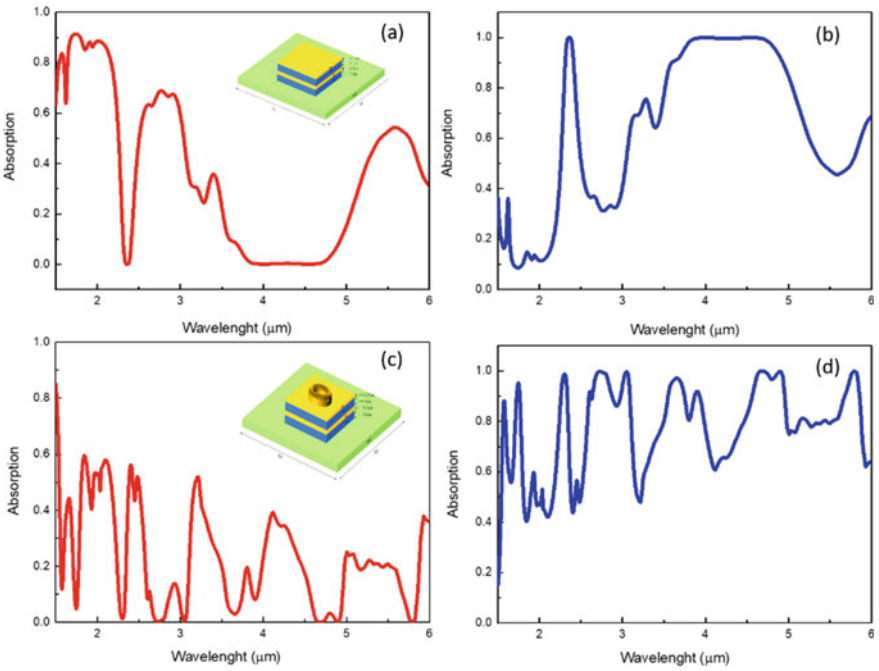

Fig. 2 Simulated reflection and absorption characteristics of the proposed device with inset of their proposed structures; **a** reflection spectra for multi-meta surfaces (single resonator), **b** absorption spectra for multi-meta surfaces (single resonator), **c** reflection spectra with a top layer as circular, **d** absorption spectra with top layer as circular

multi-mode resonance absorption in the resonator and this multi-mode resonance absorption greatly enhanced the absorption. While in Fig. 2a, from 1 μm to 4 μm there is no proper absorption peak. After placing the top layer circular, various absorption peaks are observed in a single resonator at wavelengths = 1.6 μm, 2.5 μm, 3.5 μm, etc., as shown in Fig. 2c. Moreover, an absorption spectrum is calculated with the gold ring resonator to clarify the above information. Figure 2d displays the absorption spectra ranging from 1.5 μm to 6 μm. A significant improvement is there. Nevertheless, these peaks occur due to distinct resonant peaks in a narrow band at their resonant frequencies.

To clear the concepts, a complete display of reflection spectra concerning the electric field and magnetic field as a function of wavelength is specified in Fig. 3. The four sub figures give the information about electric and magnetic field corresponding complete structure and across the circular top layer. This accomplishes that the electric field is focused on both sides of the metallic patch. The strong intensity of the electric field is high because of large charge accumulation over the metallic patches and this concludes the excitation of electric dipole resonance. For s-polarization mode, most energy is consumed by the metallic resonator. Figure 3 represents E and H for s-polarization mode, and p-polarization mode is not presented for brevity. Therefore, the required power stays in between the dielectric layers typically the upper layer. Electromagnetic waves start moving back and forth between dielectric and so metallic slab. Consequently, resonant absorption of Fabry–Perot induced mode occurred. It is reasonable that at corresponding resonance wavelength, the structure can efficiently confine the incident electromagnetic waves.

This MMA is theoretically designed and simulated to accomplish high absorption bandwidth and ultra-broadband. The multi-metasurface single band resonator with a circular top layer is repeated as a unit cell. As it was mentioned in Fig. 2d, the broadband resonance consists of several distinct resonances. Ultimately, a multi-layered dual-broadband absorber is designed by repeating the initial structure depicted in Fig. 4a and corresponding absorption spectra are demonstrated in Fig. 4b. Maximum absorption has been grasped at wavelength 2.25 μm and beyond this point, and it gradually decreases with a minimum value at 2.4 μm with very small dips [3]. Figure 4b also clarifies that individual resonant peaks are combined and a maximum absorption peak covers a broad spectrum range from 50 to 200 THz.

3 The Absorption Characteristics

Recently, many efforts have been made to design polarization-insensitive absorption or wide-angle absorption (only in the incident plane with a fixed azimuthal angle). They have many potential applications such as thermal detectors, thermal emitters, and solar cells. To make our device superior, the absorption spectra at different incident angle 10°, 20°, 30°, and 40°, 50° is calculated. While the azimuthal angle remains fixed, i.e., $\varphi = 0°$ shown in Fig. 5. The absorption spectra as a function of incident angle are also inspected at a fixed azimuthal angle ($\varphi = 0°$) and then incident angles

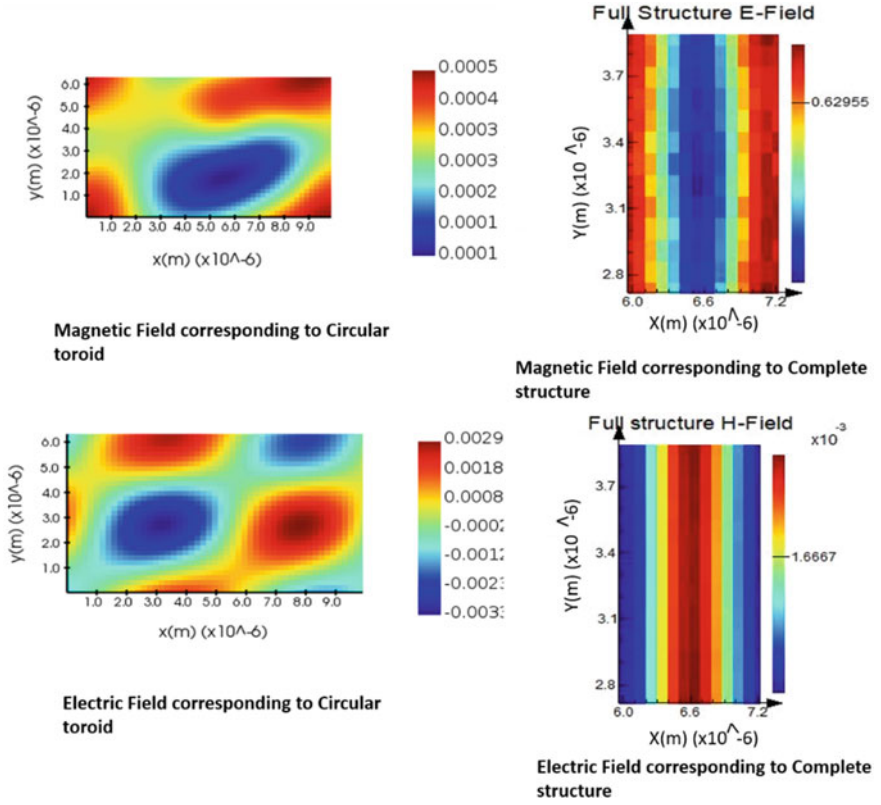

Fig. 3 Distribution map of electric filed and magnetic field intensity for the reflection spectra. The four sub figures include electric and magnetic field across the complete structure and across the top circular ring

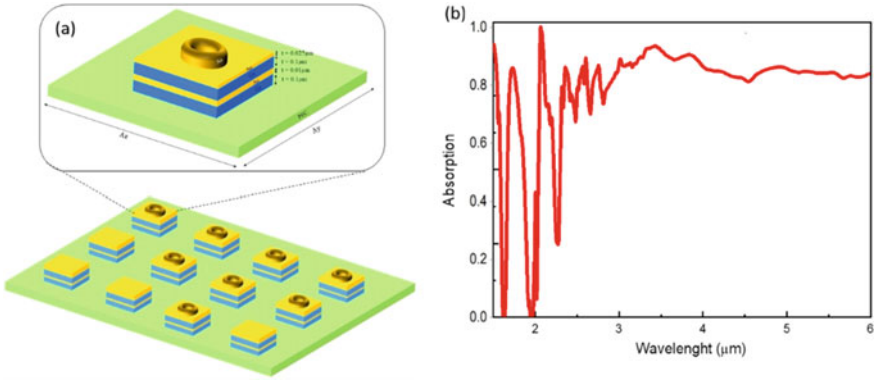

Fig. 4 Schematic diagram of the proposed dual-layered MMBBA-based absorber with same parameters; **a** unit cell of MMBBA with a complete structure, **b** the corresponding absorption spectrum

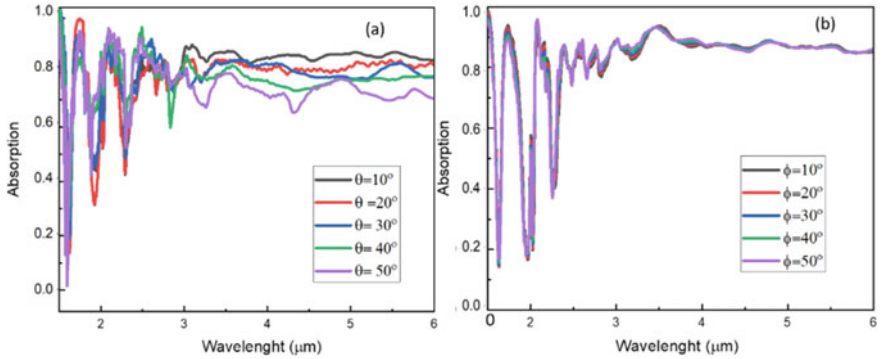

Fig. 5 Absorption spectra of MMBBA for p-polarized radiation; **a** absorption spectra of multi-structure at different incident angles, **b** at different azimuthal angles

keeps constant at 0° and azimuthal angle φ is changed and different absorption peak is calculated for p-polarization at angle ($\Phi = 0°$) as depicted in Fig. 5. Different incident angles make very slight difference in the absorption spectrum. The small peaks happened in between the broad spectrum are due to the surface plasmon polariton resonance was not able to excite the peaks. Therefore, absorption dips arise due to a limited number of resonance modes and the condition of destructive interference is less satisfied. Consequently, the complete absorption spectrum remains unchanged at a different incident angle. This means, the proposed absorber is incident angle insensitive.

Additionally, the absorption spectra are investigated as a function of azimuthal angle (φ) at a fixed incident angle ($\theta = 0°$) and vice versa with polarization angle ($\Phi = 90°$) also known as s-polarization revealed in Figs. 6a, b), where the angle "θ" is the angle of propagation, in degrees, with respect to the injection axis of the source and angle φ (azimuthal angle of propagation), rotated about the injection axis of the source in a right-hand context. The angle Φ defines different polarization angle includes orientation of the injected electric field, and is measured with respect to the plane formed by the direction of propagation and the normal to the injection plane. A polarization angle of zero degrees defines p-polarized radiation, regardless of the direction of propagation while a polarization angle of 90 degrees defines s-polarized radiation. Figure 6a represented the absorption spectra at $\varphi = 10°, 20°, 30°, 40°, 50°$ and vice versa for incident angels for the p-polarization ($\Phi = 90°$). The absorption spectra remain almost unchanged at these angles mentioned in Fig. 6a. Thus, the explored absorber shows a similar absorption mechanism as that for $\Phi = 0°$ and 90°, i.e., it is an omnidirectional and s- and p-polarization-insensitive perfect absorber. For metamaterials, (s and p) polarization-insensitivity is an essential factor for their practical application. Investigation of a polarization-independent absorber for the polarization angle and absorption spectra are plotted at different polarization angles as shown in Figs. 5 and 6, respected to the proposed light absorber. The absorber

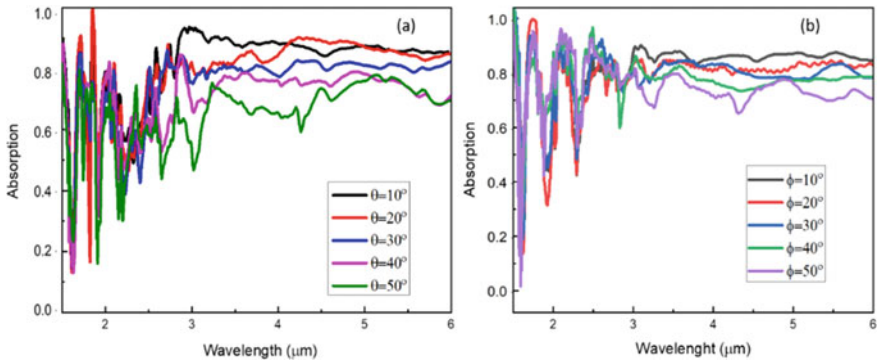

Fig. 6 Absorption spectra of MMBBA for S-polarized radiation for **a** at different θ of the incident angles and **b** at different azimuthal angle φ of the incident angle

shows similar bandwidth from 2.5 μm to 6.0 μm for S- and P-polarized light. This signifies the polarization-insensitivity of the proposed absorber.

The MMBBA is not showing any changes at angles because the surface is not even and because there is a metallic substrate, so the incident light of any polarization or any propagation angle looks basically the same for the metasurface and localization is enhanced between the metasurface and metallic substrate, and therefore the incident wave can interact with the metasurface effectively regardless of the directions of polarization and propagation. That is, the incident light wave can be converted to a plasmonic wave along the metasurface effectively and finally absorbed by the metasurface through plasmonic resonance absorption insensitive to the directions of polarization and propagation. Another reason is that the plasmonic resonance greatly enhanced the absorption so that any polarized or incident wave of any propagation can be effectively absorbed by the metasurface.

From the fabrication point of view, the top layer is replaced with a circle of radius $R = 0.1$ μm and thickness $t = 0.2$ μm displayed in Fig. 7a. And corresponding absorption spectra have been simulated and presented in Fig. 7b. This shows there is no change in absorption in comparison to previous structure. This helps to make it practical and the final proposed structure of the device, is easy to fabricate without compromising its properties. When the multi resonators are combined into a one-unit cell with a subwavelength period, the total absorption exceeds 90% from 2 μm to 6 μm. The absorption is high from 1.5 μm to 2.25 μm comes with peaks not continuous due to some metal loss which affects the device performance. But increased more than 95% from 1.5 μm to 2.25 μm because of germanium. Germanium has excellent optical properties and creates a great impact on the device. Recently, numerous devices have been proposed using Ge. And a paper based on absorber application using Tu/Ge is published in 2017 [29, 30]. Again, declining at 2 μm and starting cumulative up to 2.25 μm after that it remains constant till 6 μm, these falls are coming due to the superimposition of several peaks over the

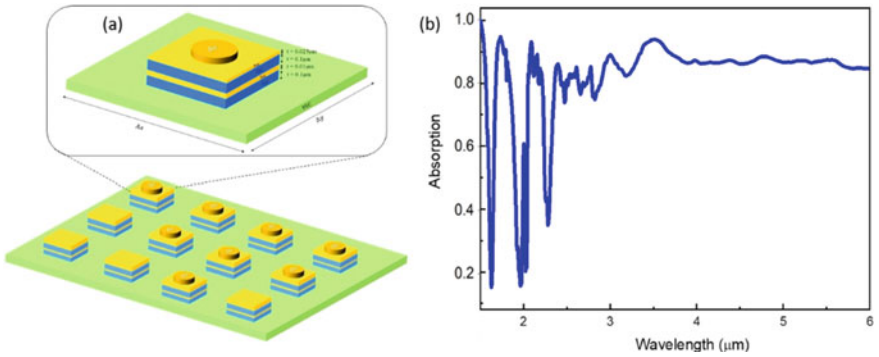

Fig. 7 **a** Perspective view of multi-metasurfaces absorber with gold disc on top having thickness $t = 0.2\ \mu m$ and radius $r = 0.1\ \mu m$, all the patches are of same parameters, **b** corresponding absorption spectra of MMBBA

absorption's phenomena [3]. For dual-layered structure, 95% absorptance is realized approximately near-unity in 1.5 μm to 6 μm spectral range.

4 Conclusion

This simplest and thinnest model of MMA has been realized in all aspects. An infrared broadband absorber with multi-metasurface has been designed and simulated using FDTD simulation. At first, a multi-structure single resonator with the same dielectric spacing layer is used, and then a dual-band multi-layer structure of the same thickness and dielectric spacing layer is used for further enhancement. The absorption is increased meaningfully and reaches a near-unity value by using a dual-band multi-layer structure, i.e., the absorption FWHM of single-layered is 50% and 95% (from 1.5 μm to 6 μm) for multi-layered structure, i.e., the absorption FWHM of single-layered is 50% and 95% (from 1.5 μm to 6 μm) for multi-layered structure. This MMA accomplishes outstanding results with previously reported MMAs [31, 32]. This absorption is very robust to the incident angle, azimuthal angle, and polarization angle.

Acknowledgements This research was funded by the National Natural Science Foundation of China, grant numbers: 61275043, 61307048, 60877034, and 61605128. Moreover, it was partially funded by the Natural Science Foundation of Guangdong Province, grant number: 2020A1515011154, and the Natural Science Foundation of Shenzhen City, grant numbers: JCYJ20190808151017218, JCYJ20190808161801637, JCYJ20180305124247521, and 20180123.

References

1. Hao J, Wang J, Liu X, Padilla WJ, Zhou L, Qiu M (2010) High performance optical absorber based on a plasmonic metamaterial. Appl Phys Lett 96(25):251104
2. Liu S, Chen H, Cui TJ (2015) A broadband terahertz absorber using multi-layer stacked bars. Appl Phys Lett 106(15):151601
3. Søndergaard T et al (2012) Plasmonic black gold by adiabatic nanofocusing and absorption of light in ultra-sharp convex grooves. Nat Commun 3(1):1–6
4. Park S et al (2018) Self-powered ultra-flexible electronics via nano-grating-patterned organic photovoltaics. Nature 561(7724):516–521
5. Smith DR, Pendry JB, Wiltshire MC (2004) Metamaterials and negative refractive index. Science 305(5685):788–792
6. Schurig D et al (2006) Metamaterial electromagnetic cloak at microwave frequencies. Science 314(5801):977–980
7. Landy NI, Sajuyigbe S, Mock JJ, Smith DR, Padilla WJ (2008) Perfect metamaterial absorber. Phys Rev Lett 100(20):207402
8. Pan H, Zhang H, Tian X, Zhang D (2021) Design, simulation, and analysis of an ultra-broadband polarization-insensitive terahertz metamaterial absorber. JOSA B 38(1):95–103
9. Barzegar-Parizi S, Ebrahimi A, Ghorbani K (2021) Dual-broadband and single ultrawideband absorbers from the terahertz to infrared regime. J Opt Soc Am B 38(9):2628–2637. https://doi.org/10.1364/JOSAB.432329
10. Liu Y, Huang R, Ouyang Z (2021) Terahertz absorber with dynamically switchable dual-broadband based on a hybrid metamaterial with vanadium dioxide and graphene. Opt Express 29(13):20839–20850
11. Li Z, Li J, Zhang Y, Zhai Y, Chu X, Zhang Y (2022) Mid-infrared dual-band absorber based on nested metamaterial structure. J Appl Spectro 88(6):1324–1330. https://doi.org/10.1007/s10812-022-01314-8
12. Xu X, Xu R, Lin Y-S (2022) A voltage-controllable VO_2 based metamaterial perfect absorber for CO_2 gas sensing application. Nanoscale 14(7):2722–2728. https://doi.org/10.1039/D1NR07746E
13. Chen X et al (2018) Light extraction enhancement and directional control of scintillator by using microlens arrays. Opt Express 26(18):23132–23141
14. Xuan Z, Li J, Liu Q, Yi F, Wang S, Lu W (2021) Artificial structural colors and applications. The Innovation 2(1):100081
15. Zhou J et al (2020) Ultra-broadband solar absorbers for high-efficiency thermophotovoltaics. Opt Express 28(24):36476–36486
16. Presutti F, Monticone F (2020) Focusing on bandwidth: achromatic metalens limits. Optica 7(6):624–631
17. Asano T et al (2016) Near-infrared–to–visible highly selective thermal emitters based on an intrinsic semiconductor. Sci Adv 2(12):e1600499
18. Suen JY et al (2017) Multifunctional metamaterial pyroelectric infrared detectors. Optica 4(2):276–279
19. Zhu J et al (2014) Ultra-broadband terahertz metamaterial absorber. Appl Phys Lett 105(2):021102
20. Cui Y et al (2011) A thin film broadband absorber based on multi-sized nanoantennas. Appl Phys Lett 99(25):253101
21. Lee BJ, Wang L, Zhang Z (2008) Coherent thermal emission by excitation of magnetic polaritons between periodic strips and a metallic film. Opt Express 16(15):11328–11336
22. Sakurai A, Zhao B, Zhang ZM (2014) Resonant frequency and bandwidth of metamaterial emitters and absorbers predicted by an RLC circuit model. J Quant Spectrosc Radiat Transfer 149:33–40
23. Chen C-J, Chen J-S, Chen Y-B (2011) Optical responses from lossy metallic slit arrays under the excitation of a magnetic polariton. JOSA B 28(8):1798–1806

24. Wang L, Zhang Z (2009) Resonance transmission or absorption in deep gratings explained by magnetic polaritons. Appl Phys Lett 95(11):111904
25. Wang L, Zhang ZM (2010) Effect of magnetic polaritons on the radiative properties of double-layer nanoslit arrays. JOSA B 27(12):2595–2604
26. Wang L, Zhang Z (2011) Phonon-mediated magnetic polaritons in the infrared region. Opt Express 19(102):A126–A135
27. Koechlin C et al (2011) Total routing and absorption of photons in dual color plasmonic antennas. Appl Phys Lett 99(24):241104
28. Lu Y, Li J, Zhang S, Sun J, Yao JQ (2018) Polarization-insensitive broadband terahertz metamaterial absorber based on hybrid structures. Appl Opt 57(21):6269–6275
29. Li H (1980) Refractive index of silicon and germanium and its wavelength and temperature derivatives. J Phys Chem Ref Data 9(3):561–658
30. Krishnamoorthy HN, Gholipour B, Zheludev NI, Soci C (2018) A Non-Volatile Chalcogenide Switchable Hyperbolic Metamaterial. Adv Opt Mater 6(19):1800332
31. Zhao YT, Wu B, Huang BJ, Cheng Q (2017) Switchable broadband terahertz absorber/reflector enabled by hybrid graphene-gold metasurface. Opt Express 25(7):7161–7169
32. Ye YQ, Jin Y, He S (2010) Omnidirectional, polarization-insensitive and broadband thin absorber in the terahertz regime. JOSA B 27(3):498–504

Analysis with Platinum for Optimized Performance of Perforated RF MEMS Switch

P. Chandini Begum, S. C. H. Kantha Rao, and K. Sravani

Abstract An RF switch has been designed using MEMS technology and a cantilever construction to provide excellent responsiveness. The materials with a low spring constant have been selected and examined in COMSOL by determining the relationship between Eigen recurrence and displacement. The proposed structure is tested using a variety of materials and thicknesses. The platinum material with an assessed bar thickness for which the most elevated dislodging occurs is used to determine the largest displacement and base uprooting for an Eigen recurrence. The beam design is also tested with and without holes and has a $6.75 * 10^{-4}$ awareness level for the intended 2 μm thickness. The Eigen recurrence and relocation charts have been drawn, and the characteristics have been confirmed.

Keywords RF switch · Eigen recurrence · Relocation · Thickness

1 Introduction

1.1 RF Switch

It is additionally named as microwave switch. This gadget passes high recurrence signals through transmission ways and is utilized for signal directing. This steering is in the middle of instruments and gadgets [1].

P. C. Begum (✉) · S. C. H. K. Rao · K. Sravani
Department of ECE, PACE Institute of Technology and Sciences, Ongole, Andhra Pradesh, India
e-mail: chandinibegump@gmail.com

K. Sravani
e-mail: sravani_sk@pace.ac.in

K. Geetha et al. (eds.), *Recent Trends in Materials*, Springer Proceedings in Materials 18, https://doi.org/10.1007/978-981-19-5395-8_23

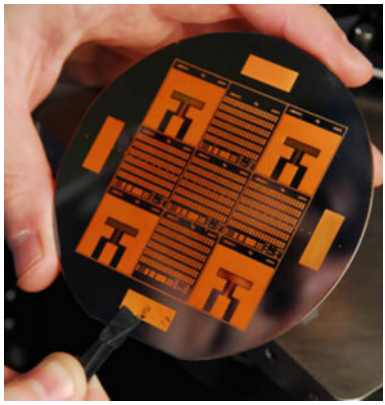

Fig. 1 MEMS device

1.2 MEMS

The microelectromechanical system is a device advancement with a limited scaled meter scale. MEMS is a combination of actuators, sensors, mechanical components, and physical sciences in a standard substrate [2]. CI process successions and these estimations are utilized in various applications, for example, show innovations, finder frameworks, for example, sensor frameworks and systems. Optical MEMS are awfully engaged for various applications in view of their gauge and weight. These MEMS measurements shift from micrometres to millimetres [3] (Fig. 1).

MEMS may be found in a variety of contexts, ranging from automobiles to integrated frameworks, physical science, communication, and restorative applications [4]. Projection screen chips, blood pressure sensors, accelerometers for airbag sensors, adaptable plate drive inspecting and composing heads, optical switches, and microvalves are all popular MEMS devices. Every one of these goods is manufactured in massive mechanical quantities on a production line. These MEMS frameworks can regulate and identify when anything is turned down a notch, causing macroscale effects. The RF MEMS switch has recently received as one of the rapid breakthroughs. This breakthrough provides incredible benefits and advantages over silicon exchanging gadgets and gas [5].

1.3 RF-MEMS Switches

RF MEMS switches are micromechanical switches. These switches are intended to work in radio recurrence at mm wave recurrence, which implies at 0.1–100 GHz [6] (Fig. 2).

RF MEMS switches are often employed in microwaves and other repeating devices, such as transmitters and beneficiaries, radio wire switches, and so on. These are unambiguous microswitches that should operate at RF to millimetre wave

Fig. 2 MEMS switch

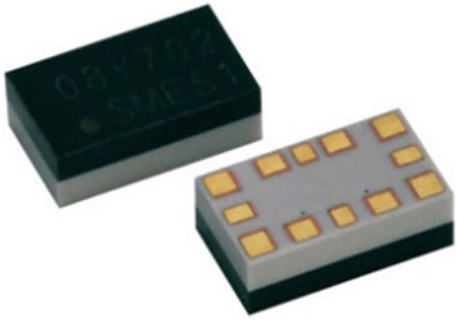

frequencies or 0.1–100 GHz [7]. In comparison with electrical switches, RF MEMS has a few optimal conditions. They consume less energy and possess characteristics such as low incorporation disaster, linearity, moderateness, impact handling, and high separation rates [8]. MEMS features combine reduced weight, small size, and expansion incident, but they soon require difficulties, such as high operating voltage, limited speed, and so on [9–12].

RF MEMS switches are little machined devices that use a mechanical social event inside a recurrent transmission line to achieve a short out or open electrical circuit. The incitation process is used to represent these transitions. The development of RF MEMS switches requires two types of abilities: appealing interest and electrostatic powers. In any event, the static power covers a high operating voltage and has no current usage. The enticing interest power, of course, combines a high current usage and a low operating voltage. The most common switches are static switches, which come in two types: course of action and avoid. In the millimetre and microwave wave ranges, appealing interest switches are employed [13].

1.4 RF Switch Circuit

See Figs. 3 and 4.

1.5 Resistive Contact Switches

These switches utilize metal-to-metal contact for the obstruction unit contact between the sign line and the contact shaft [14]. The assembling strategy utilized for such switches is a technique for mass small-scale machining or surface miniaturized scale machining. The polarization DC is applied between the ground and furthermore the cantilever pillar. The electrostatic power pushes the cantilever shaft to move along the side and contact the sign line [15]. This sort of switch is utilized for associate

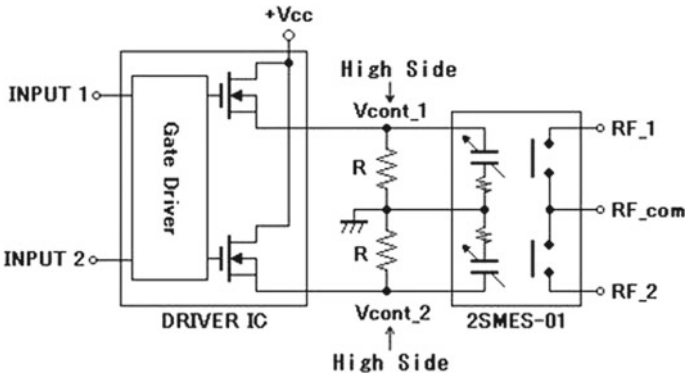

Fig. 3 RF MEMS switch circuit

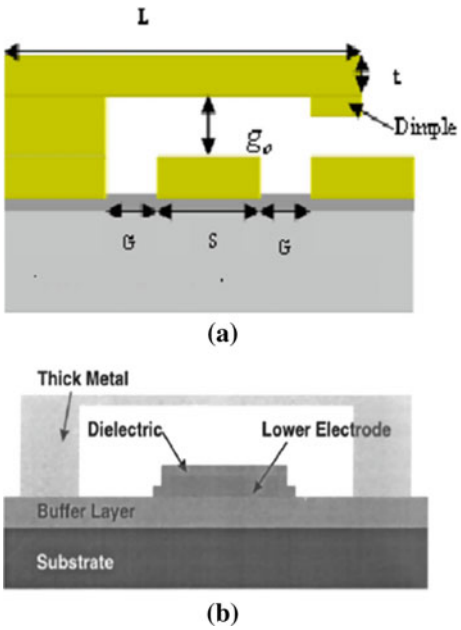

Fig. 4 **a** cantilever MEMS switch, **b** air bridge MEMS switch

in the advancement of the X-band reconfigurable resistivity tuner [3]. The resistive MEMS switch is as in Fig. 6 (Fig. 5).

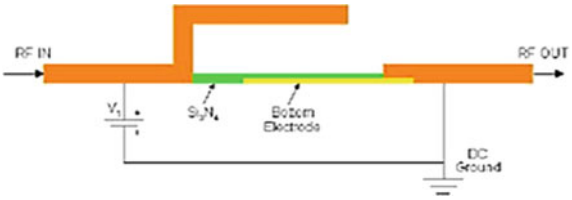

Fig. 5 Switch cross section cantilever beam capacitive MEMS switch

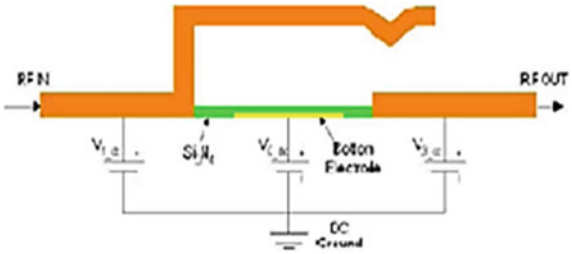

Fig. 6 Cross section of resistive MEMS

2 Types of RF MEMS Switches

There are two sorts of RF MEMS switches:

One is the arrangement MEMS switch, and the other is the shunt MEMS switch.

2.1 Shunt Switch

The MEMS sidestep switch (Fig. 7) is demonstrated by two short segments of cloned clr and a transmission line model as in Fig. 8a. The capacitance esteem changes all over with the condition of the scaffold since Cu is the rising state capacitance and Cd is the sliding state capacitance [16–18]. The segments of the transmission line are of length (w/2) + l, where 'l' is the good way from the reference plane to the edge of the MEMS connect (Fig. 8b).

The switch shunt impedance is

$$Z_s = R_s + j\omega L + \frac{1}{j\omega C} \tag{1}$$

With C = Cd or Cu relying upon the situation of the switch. The reverberation recurrence of the LC arrangement of the detour switch:

$$f_r = \frac{1}{2\pi\sqrt{\mathrm{LC}}} \tag{2}$$

The impedance of the detour switch can be determined by

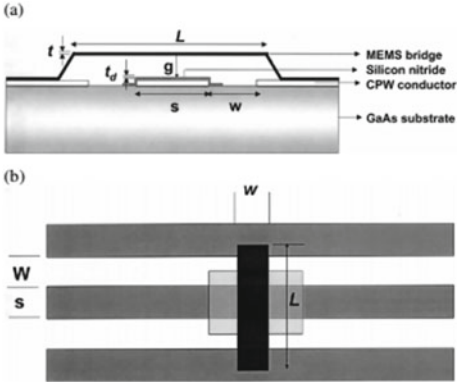

Fig. 7 Diagram of the MEMS sidestep switch in the upward express **a** cross segment and **b** top view

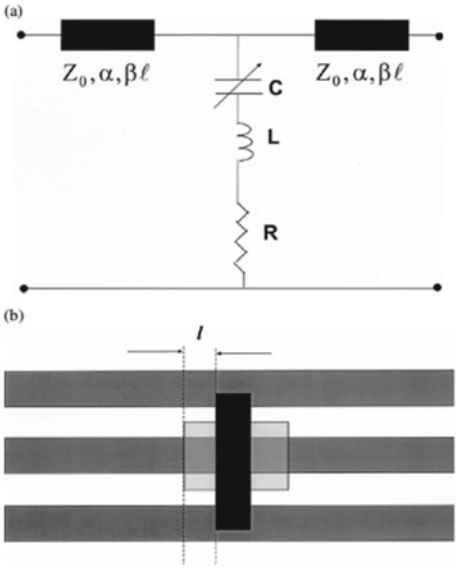

Fig. 8 **a** Equivalent circuit model and **b** schematic defining 'l'

$$Z_s = \begin{cases} 1/j\omega Cf = f_0 \\ R_s f = f_0 \\ j\omega Lf = f_0 \end{cases} \tag{3}$$

Government conditions during the ON state capacitance and inductance in the upper state position of the switch, the reflection coefficient are given by

$$S_{11} = \frac{-j\omega C_u Z_0}{2 + j\omega C_u Z_0} \tag{4}$$

$$S_{11}^2 = \frac{\omega^2 C_u^2 Z_0^2}{4} \tag{5}$$

and for |S11|<-10 dB or ωCuZu << 2.

Cu is the climbing state capacitance that incorporates parallel plate capacitance and strip capacitance 1. Typical up-state capacitance for shunt switches operating at microwave and millimetre-wave frequencies is ~35–160 fF, whereas inductance is of the order of few nH. The LC-series resonance frequency is

$$f_0 = \frac{1}{2\pi\sqrt{\mathrm{LC}_u}} \tag{6}$$

It very well may be seen that in the rising state position, the thunderous recurrence is basically chosen by the climbing state capacitance. The down-state capacitance of the switch is determined as $\mathrm{Cd} = \varepsilon_0 \varepsilon_r A/td$. The resounding recurrence in the latent state is given as the condition (2) utilizing Cd rather than Cu.

2.2 Series Switch

The course of action smart microwave switch is shown schematically in Fig. 9. The state off is at the zenith point, besides the state on at the base point. To change the microwaves, it should be possible to communicate microwave sign to and from the switch; thusly, it is related with the information and yield by transmission lines or waveguides. Exactly when shut, the switch can be a transmission device with some reflection. Inside the open express, the switch is totally astute with a little bothersome transmission.

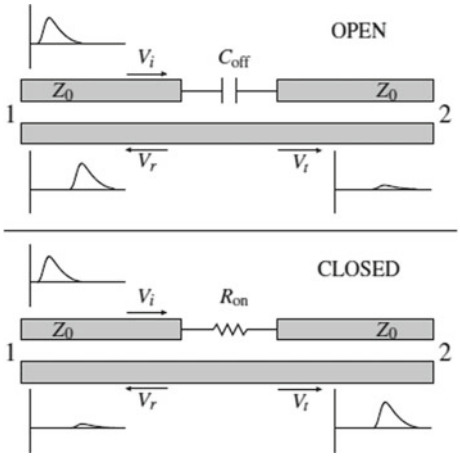

Fig. 9 Ideal series switch

On account of off express, a sign lands at port 1 of the open switch which is reflected with a voltage reflection consistent of +1 as indicated schematically inside the upper piece of Fig. 9. A little piece of the wave transmits through the change to port 2. The figures show the electrical sign as a short heartbeat, which accentuates the indication of the reflection coefficient that for the arrangement switch it is +1 and for the detour switch it is −1. In general, a heartbeat is selected to underline the appallingly broadband nature of the switch that can be utilized in MEMS. Considering microwave scattering parameters in the recurrence space, the reflected sign is S11, furthermore the transmitted sign is S21, and the immediate transmission is given by the accompanying conditions:

$$S_{11} = \frac{1}{1 + j\omega C_{\text{off}} 2Z_0}, \tag{7}$$

$$S_{21} = \frac{j\omega C_{\text{off}} 2Z_0}{1 + j\omega C_{\text{off}} 2Z_0}. \tag{8}$$

The perfect interest is $C_{\text{off}} = 0$, aside from touchy conditions. If $j\omega * C_{\text{off}} << 1$, the denominators of every condition are around 1. This offers unitary reflection, while in the transmission, the circuit is fundamentally a differentiator. Generally speaking, forward transmission under the off state conditions is called switch partition. In the impelled express, the most negligible piece of Fig. 1, and a picture is generally sent through the switch with a little reflection and some digestion. Incorporation hardship is the association between sent impact and the capability among event and reflected impact. If the reflected influence is low, then S21 is the consideration disaster. The power reflected under these circumstances is that the deficiency of return and inside the case portrayed is identical to S11. The state dissipating boundaries are assessments given by

$$S_{11} = \frac{R_{\text{on}}}{R_{\text{on}} + 2Z_0}, \tag{9}$$

$$S_{21} = \frac{2Z_0}{R_{\text{on}} + 2Z_0}. \tag{10}$$

The perfect condition is $R_{\text{on}} = 0$, however, obviously on the off chance that $R_{\text{on}} << 2Z_0$, at that point S11 ≈ 0 and S21 ≈ 1 (Fig. 10 and Table 1).

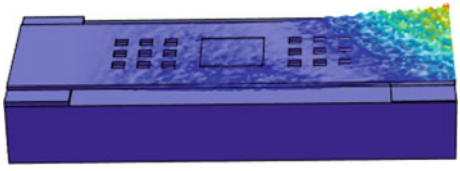

Fig. 10 Cantilever beam switch structure designed in COMSOL

Table 1 Values for different thickness of beam with different metals

(a) Different thickness of beam with Titanium

Material	Eigen Frequency	Total Displacement (μm)					
Titanium		2 μm	2.2 μm	2.4 μm	2.6 μm	2.8 μm	3 μm
	1666.6	$8.08 * 10^{-12}$	$1.76 * 10^{-12}$	$1.22 * 10^{-12}$	$1.06 * 10^{-12}$	$7 * 10^{-14}$	$7.4 * 10^{-13}$
	1775.6	$4.17 * 10^{-4}$	$1.11 * 10^{-5}$	$2.48 * 10^{-5}$	$1.77 * 10^{-6}$	$2.98 * 10^{-6}$	$3.13 * 10^{-6}$
	1777	$2.25 * 10^{-4}$	$1.85 * 10^{-5}$	$1.48 * 10^{-5}$	$3.99 * 10^{-6}$	$2.83 * 10^{-5}$	$2.28 * 10^{-6}$
	1791.9	$7.35 * 10^{-4}$	$5.13 * 10^{-6}$	$6.36 * 10^{-6}$	$3.25 * 10^{-6}$	$1.98 * 10^{-5}$	$2.99 * 10^{-5}$
	1838.3	$1.62 * 10^{-4}$	$2.06 * 10^{-5}$	$5.02 * 10^{-5}$	$2.65 * 10^{-4}$	$1.74 * 10^{-4}$	$4.05 * 10^{-5}$
	1888.7	0.06	$0.01 * 10^{-2}$	0.06	$7.79 * 10^{-3}$	$6.48 * 10^{-3}$	$0.03 * 10^{-2}$

(b) Different thickness of beam with Platinum

Material	Eigen Frequency	Total Displacement (μm)					
Platinum		2 μm	2.2 μm	2.4 μm	2.6 μm	2.8 μm	3 μm
	1666.6	$5.91 * 10^{-11}$	$1.17 * 10^{-11}$	$1.79 * 10^{-11}$	$3.43 * 10^{-12}$	$4.59 * 10^{-13}$	$8.94 * 10^{-13}$
	1775.6	$1.07 * 10^{-3}$	$3 * 10^{-5}$	$6.21 * 10^{-5}$	$3.61 * 10^{-6}$	$9.59 * 10^{-6}$	$8.76 * 10^{-6}$
	1777	$5.78 * 10^{-4}$	$5.01 * 10^{-5}$	$3.7 * 10^{-5}$	$8.12 * 10^{-6}$	$9.12 * 10^{-5}$	$6.4 * 10^{-6}$
	1791.9	$1.89 * 10^{-3}$	$1.44 * 10^{-5}$	$1.6 * 10^{-5}$	$6.62 * 10^{-6}$	$6.39 * 10^{-5}$	$8.39 * 10^{-5}$
	1838.3	$4.16 * 10^{-4}$	$5.58 * 10^{-5}$	$1.26 * 10^{-4}$	$5.4 * 10^{-4}$	$5.62 * 10^{-4}$	$1.13 * 10^{-4}$
	1888.7	0.15	$0.04 * 10^{-2}$	0.14	$0.02 * 10^{-2}$	$0.02 * 10^{-2}$	0.07

(c) Different thickness of beam with Tungsten

Material	Eigen Frequency	Total Displacement (μm)					
Tungsten		2 μm	2.2 μm	2.4 μm	2.6 μm	2.8 μm	3 μm
	1666.6	$6.3 * 10^{-12}$	$2.8 * 10^{-12}$	$3.92 * 10^{-12}$	$1.57 * 10^{-12}$	$3.76 * 10^{-13}$	$5.81 * 10^{-13}$

(continued)

Table 1 (continued)

(c) Different thickness of beam with Tungsten

Material	Eigen Frequency	Total Displacement (μm)					
	1775.6	$5.24 * 10^{-4}$	$1.37 * 10^{-5}$	$2.93 * 10^{-5}$	$1.75 * 10^{-6}$	$3.93 * 10^{-6}$	$3.75 * 10^{-6}$
	1777	$2.83 * 10^{-4}$	$2.29 * 10^{-5}$	$1.74 * 10^{-5}$	$3.93 * 10^{-6}$	$3.74 * 10^{-5}$	$2.74 * 10^{-6}$
	1791.9	$9.23 * 10^{-4}$	$6.58 * 10^{-6}$	$7.53 * 10^{-6}$	$3.2 * 10^{-6}$	$2.62 * 10^{-5}$	$3.6 * 10^{-5}$
	1838.3	$2.03 * 10^{-4}$	$2.55 * 10^{-5}$	$5.94 * 10^{-5}$	$2.62 * 10^{-4}$	$2.3 * 10^{-4}$	$4.86 * 10^{-5}$
	1888.7	0.07	$0.02 * 10^{-2}$	0.07	$7.68 * 10^{-3}$	$8.55 * 10^{-3}$	$0.03 * 10^{-2}$

(d) Different thickness of beam with Silver

Material	Eigen Frequency	Total Displacement (μm)					
Silver		2 μm	2.2 μm	2.4 μm	2.6 μm	2.8 μm	3 μm
	1666.6	$9.15 * 10^{-11}$	$8.27 * 10^{-12}$	$1.78 * 10^{-11}$	$3.79 * 10^{-12}$	$8.91 * 10^{-13}$	$1.81 * 10^{-12}$
	1775.6	$1.03 * 10^{-3}$	$2.88 * 10^{-5}$	$5.82 * 10^{-5}$	$3.62 * 10^{-6}$	$9.04 * 10^{-6}$	$8.44 * 10^{-6}$
	1777	$5.56 * 10^{-4}$	$4.81 * 10^{-5}$	$3.47 * 10^{-5}$	$8.16 * 10^{-6}$	$8.6 * 10^{-5}$	$6.17 * 10^{-6}$
	1791.9	$1.81 * 10^{-3}$	$1.38 * 10^{-5}$	$1.5 * 10^{-5}$	$6.65 * 10^{-6}$	$6.02 * 10^{-5}$	$8.08 * 10^{-5}$
	1838.3	$4 * 10^{-4}$	$5.35 * 10^{-5}$	$1.18 * 10^{-4}$	$5.43 * 10^{-4}$	$5.3 * 10^{-4}$	$1.09 * 10^{-4}$
	1888.7	0.14	$0.04 * 10^{-2}$	0.13	$0.02 * 10^{-2}$	$0.02 * 10^{-2}$	0.07

(e) Different thickness of beam with Aluminium

Material	Eigen Frequency	Total Displacement (μm)					
Aluminum		2 μm	2.2 μm	2.4 μm	2.6 μm	2.8 μm	3 μm
	1666.6	$1.6 * 10^{-11}$	$2.69 * 10^{-12}$	$1.57 * 10^{-11}$	$2.32 * 10^{-12}$	$2.77 * 10^{-13}$	$3.99 * 10^{-13}$
	1775.6	$3.97 * 10^{-4}$	$1.06 * 10^{-5}$	$2.13 * 10^{-5}$	$1.76 * 10^{-6}$	$2.71 * 10^{-6}$	$2.99 * 10^{-6}$

(continued)

Table 1 (continued)

(e) Different thickness of beam with Aluminium							
Material	Eigen Frequency	Total Displacement (μm)					
	1777	$2.14 * 10^{-4}$	$1.77 * 10^{-5}$	$1.27 * 10^{-5}$	$3.96 * 10^{-6}$	$2.58 * 10^{-5}$	$2.19 * 10^{-6}$
	1791.9	$6.99 * 10^{-4}$	$5.09 * 10^{-6}$	$5.47 * 10^{-6}$	$3.22 * 10^{-6}$	$1.81 * 10^{-5}$	$2.87 * 10^{-5}$
	1838.3	$1.54 * 10^{-4}$	$1.98 * 10^{-5}$	$4.32 * 10^{-5}$	$2.63 * 10^{-4}$	$1.59 * 10^{-4}$	$3.87 * 10^{-5}$
	1888.7	$0.05 * 10^{-2}$	$0.01 * 10^{-2}$	$0.05 * 10^{-2}$	$7.73 * 10^{-3}$	$5.91 * 10^{-3}$	$0.03 * 10^{-2}$

The following graphs show the plots for different metals with various thicknesses (Figs. 11, 12, 13, 14, 15, 16, 17, 18, 19, 20 and 21).

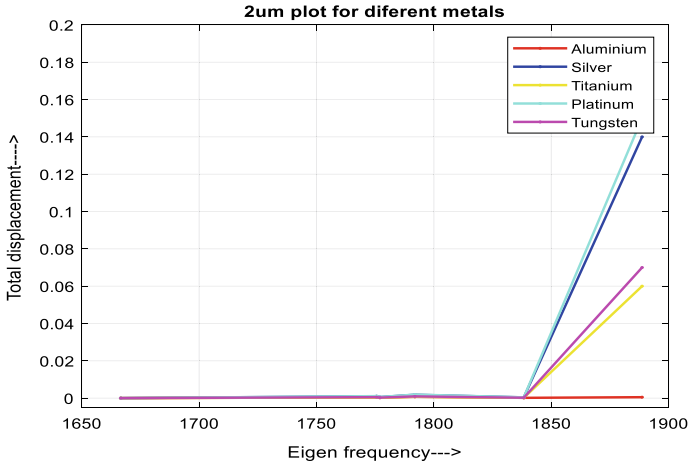

Fig. 11 2 μm plot for different metals

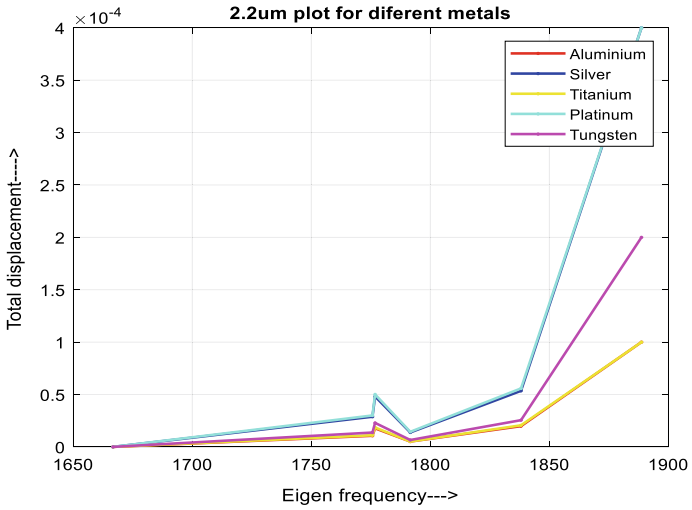

Fig. 12 2.2 μm plot for different metals

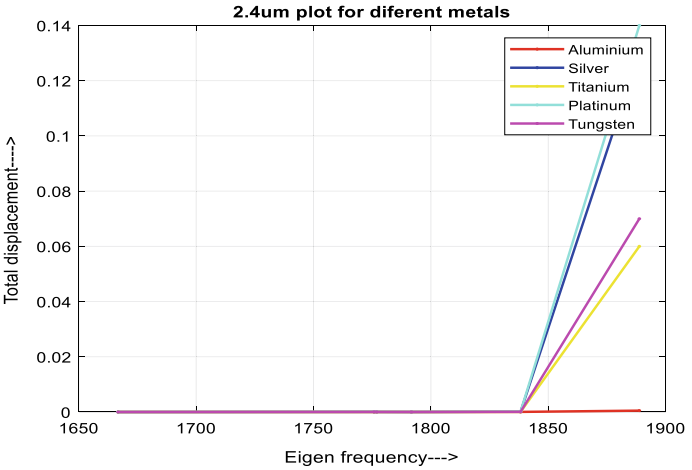

Fig. 13 2.4 μm plot for different metals

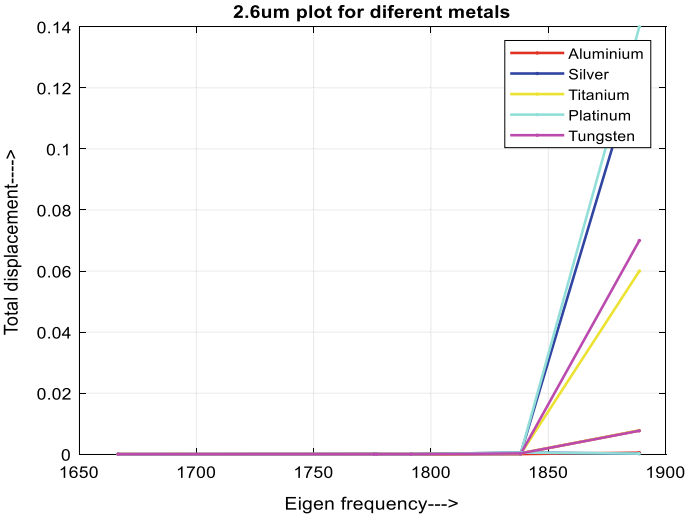

Fig. 14 2.6 μm plot for different metals

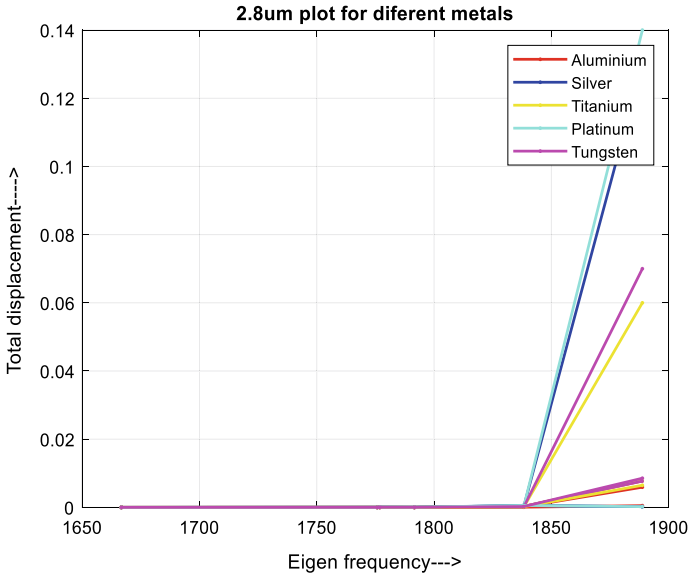

Fig. 15 2.8 μm plot for different metals

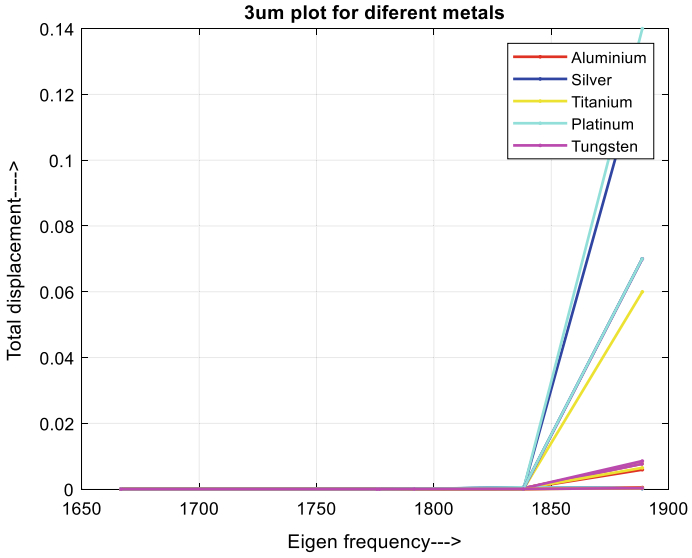

Fig. 16 3 μm plot for different metals

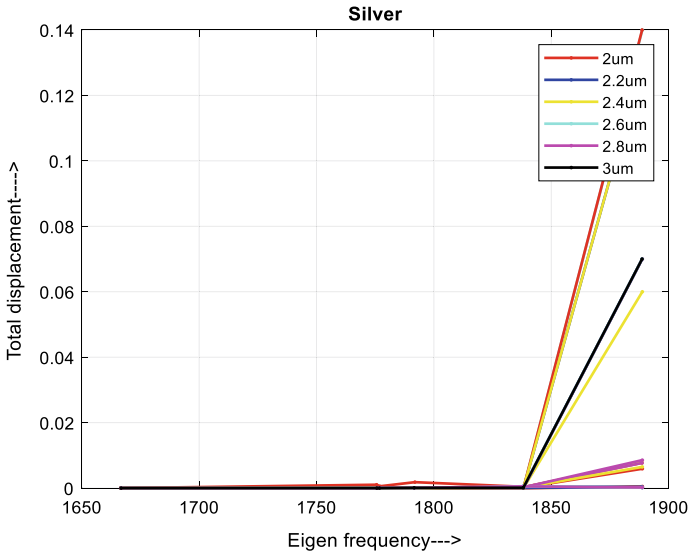

Fig. 17 Displacement of silver for various thicknesses

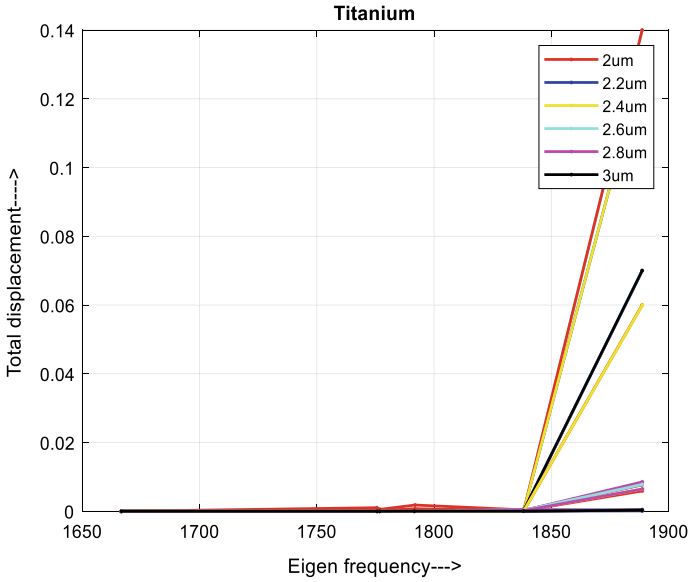

Fig. 18 Displacement of titanium for various thicknesses

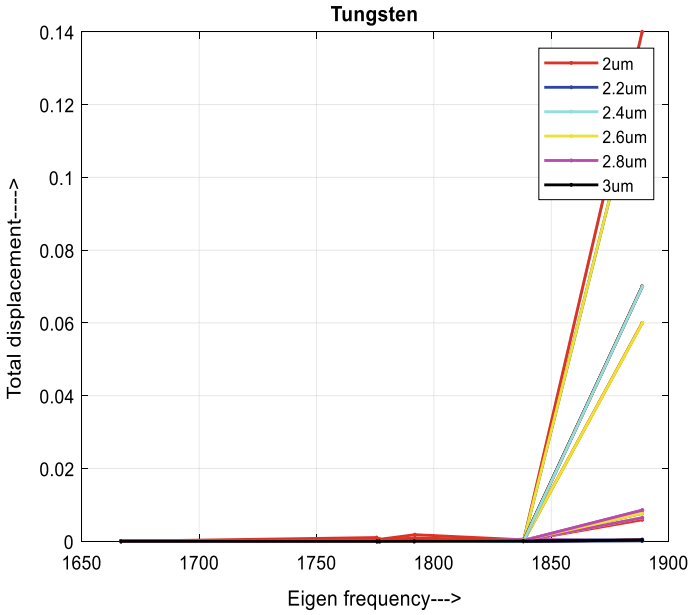

Fig. 19 Displacement of tungsten for various thicknesses

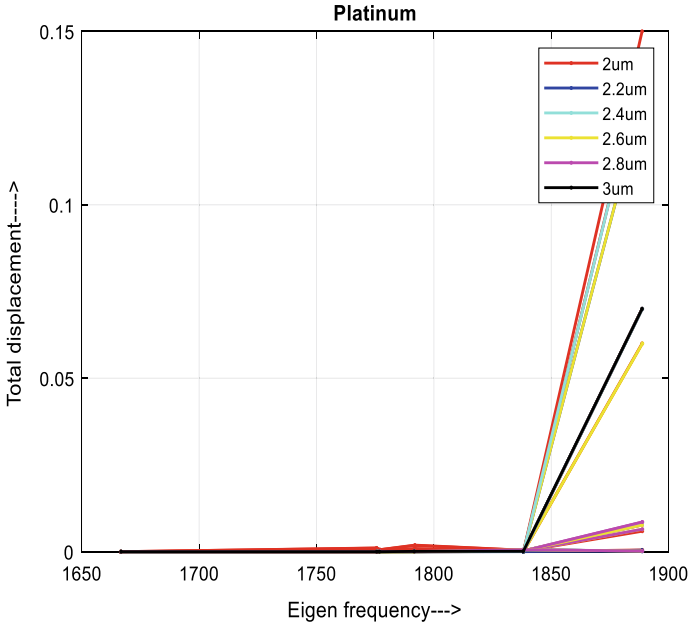

Fig.20 Displacement of platinum for various thicknesses

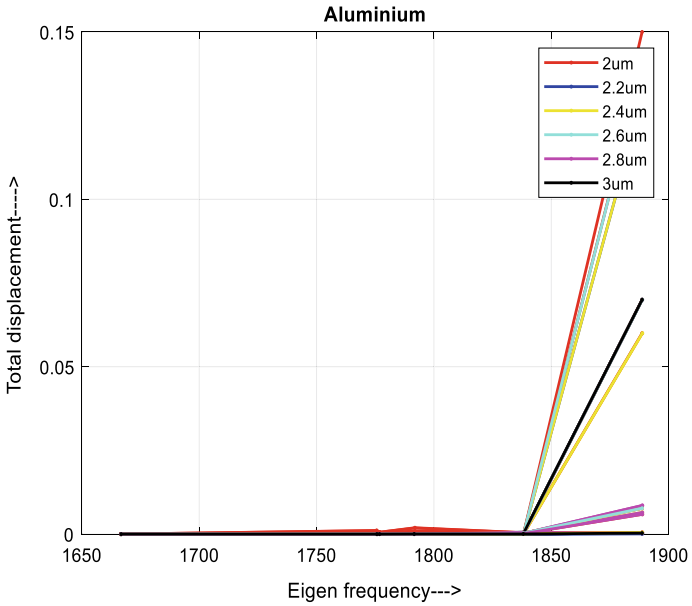

Fig. 21 Displacement of aluminum for various thicknesses

3 Conclusion

A model of RF switch has been designed utilizing MEMS innovation with a cantilever structure which produced high responsiveness. The materials having low spring consistent have been taken and inspected in Comsol by recognizing the connection between Eigen recurrence and relocation. The proposed structure is examined with different materials in different thicknesses (2 μm, 2.2 μm, 2.4 μm, 2.6 μm, 2.8 μm, and 3 μm). The corresponding Eigen frequencies and displacements have been shown. The maximum displacement is 0.15 μm for an Eigen frequency of 1888.7, and the minimum displacement is $5.91 * 10^{-11}$ μm for a Eigen frequency of 1666.6, for a material of platinum with a thickness of 2 μm beam thickness. The shaft structure is tried with holes and without holes which show high sensitivity of $6.75 * 10^{-4}$. The graphs for Eigen frequency and displacement have been plotted, and the values have been verified.

References

1. Patil GD, Kolhare NR (2003) A review paper on RF MEMS switch for wireless communication. Int J Eng Trends Technol 4(2):195–198. ISSN: 2231–5381
2. Sharma P, Koul SK, Chandra S (2007) Study on RF MEMS shunt switch. Indian J Pure Appl Phys 45:387–394

3. Grant PD, Denhoff MW (2004) A comparison between RF MEMS switch and semiconductor switch. In: Proceedings of the 2004 international conference on MEMS, NANO and smart systems (ICMENS'04) 0–7695–2189–4/04 © 2004 IEEE
4. George R, Kumar CRS, Gangal SA (2018) Design and simulation of low actuation voltage cantilever RF MEMS switches suitable for reconfigurable antenna applications. 3, ISSN: 2367–8879
5. Elliott RB (2015) RF switches for reconfigurable integrated circuits. IEEE Trans Microwave Theory Techn 46(11)
6. Cetiner BA (2016) Monolithic integration of RF MEMS switches with a diversity antenna on PCB substrate. IEEE Trans Microwave Theory Techn 51(1)
7. Pustan M (2017) Design, fabrication and characterisation of RF MEMS switches with robust contact. IEEE
8. Srinivasarao K (2017) Design and analysis of CPW based shunt capacitive RF MEMS switch. The Author(s), This open access article is distributed under a creative commons attribution
9. Peroulis D, Pacheco SP, Sarabandi K, Katehi LPB (2003) Electromechanical considerations in developing low-voltage RF MEMS switches. IEEE Trans Microwave Theory Techn 51(1):259
10. Rizk JB, Chaiban E, Rebeiz GM (2002) Steady state thermal analysis and high-power reliability considerations of RF MEMS capacitive switches. 0–7803–7239–5/02/$10.00 0 2002 IEEE
11. Liu X, Katehi LPB, Chappell WJ, Peroulis D (2010) High-Q tunable microwave cavity resonators and filters using SOI-based RF MEMS tuners. J Microelectromech Syst 10(23)
12. Stegner J, Fischer M, Gropp S, Podoskin D, Stehr U, Müller J, Hoffmann M, Hein MA (2016) Compact low phase-noise MEMS-BasedRF oscillator on a dedicated silicon-ceramic composite substrate. 978–2–87487–043–9 © 2016 EuMA, 4–6 Oct 2016, London, UK
13. Stefanini R, Martinez JD, Chatras M, Pothier A, Boria VE, Blondy P (2011) Ku band high-Q tunable surface-mounted cavity resonator using RF MEMS varactors. IEEE Microwave Wireless Compon Lett 21(5):237
14. Entesari K, Rebeiz GM, Brown AR (2007) A 25–75-MHz RF MEMS Tunable Filter. IEEE Trans Microwave Theory Tech 55(11):2399
15. Entesari K (2005) A 12–18-GHz Three-Pole RF MEMS Tunable Filter. IEEE Trans Microwave Theory Tech 53(8)
16. Zuo C (2010) 1.05-GHz CMOS oscillator based on lateral-field-excited piezoelectric AlN contour-mode MEMS resonators. IEEE Trans Ultrasonics, Ferroelectr Freq Control 57(1)
17. Otis BP, Chee YH, Lu R, Pletcher NM, Rabaey JM (2004) An ultra-low power MEMS-based two-channel transceiverfor wireless sensor networks. 0–7803–8287–01041 $20 00 0 2004 IEEE 2004 Symposium On VLSlClrcullsDigest of Technical Papers
18. Mardivirin D, Pothier A, Crunteanu A, Vialle B, Blondy P (2009) Charging in dielectric less capacitive RF-MEMS switches. IEEE Trans Microwave Theory Techn 57(1)

Analysis of Micro RF Switches Role in Reconfigurable Antenna Design

N. Gopi Chand, N. Durga Parameswara Rao, and Ch. Manasa

Abstract This paper presents reconfigurable antenna where both frequency and pattern are reconfigured. The antenna comprises T shaped stepped rectangular patch, where it is joined by two latitudinal slits. The antenna is designed and analyzed using ANSYS HFSS 18 with dimensions of 70 mm × 70 mm substrate. In this work, FR4 substrate is used as material which has the dielectric constant of 4.4. The frequency reconfigurations can be seen at 4.5, 5.8, 11.4, and 13.6 GHz which are used for the WLAN communications. The reconfiguration of pattern of about −15°, 15°, and 30° angles are seen in the radiation patterns at the same band. The design of the proposed antenna is simulated using HFSS 18.

Keywords Frequency-reconfigurable · Multiband antennas · Pattern-reconfigurable

1 Introduction

Wireless communication technology has been increasing day by day, and wireless devices are supporting a greater number of applications [1]. An antenna transports the signal from one end to another producing EM field consisting of electric field and magnetic field [2]. The reconfigurable antenna is used in high data speed and communication applications, which reduces the number of components and the complexity of hardware [3]. The reconfigurable antenna can change the frequency, pattern or polarization depending on the application used [4–7]. There are different techniques of reconfigurability used with different sizes and shapes of radiating elements. Electrical reconfigurable antennas use electrical switches such as RF MEMS, PIN Diodes, and varactor diodes [8]. However, PIN diode offers high speed switching compared

N. Gopi Chand (✉) · N. Durga Parameswara Rao (✉) · Ch. Manasa
Department of ECE, PACE Institute of Technology and Sciences, Ongole, Andhra Pradesh, India
e-mail: n.chandu4a3@gmail.com

Ch. Manasa
e-mail: Manasa_ch@pace.ac.in

K. Geetha et al. (eds.), *Recent Trends in Materials*, Springer Proceedings in Materials 18, https://doi.org/10.1007/978-981-19-5395-8_24

Table 1 Challenges of parameters

Parameter	Research challenges
PIN	Design of proper bias lines
Antenna	Frequency selectivity, gain, directivity

to other RF switches. This design uses the FR4 as the material and BAR64 PIN Diode and is designed using HFSS 18 [9].

2 Problem Statement

The capacitance of PIN diode is independent of bias level and diode possesses very low reverse recovery time [10]. The diode does not accept standard formula for all low frequency signals. The diodes are used in Radio Frequency (RF) switches, and these are mostly used for RF protection circuits as a RF switch [11–13]. There are some challenges involved in designing antenna for WLAN applications, such as antenna size, performance characteristics like bandwidth, gain, efficiency, etc. [14–19] (Table 1).

3 Design Methodology

The design represents the novel reconfigurable antenna, for which the antenna in HFSS 18 (High Frequency Structure Simulator) is designed which are shown in Fig. 1. Different antennas [20–23] are designed using patch and the design is simulated. The frequency of different antennas designed are obtained which is shown in Fig. 2.

The width and length of rectangular patch antenna is given by,

$$\text{Width} = \frac{c}{2f_o\sqrt{\frac{\varepsilon_R+1}{2}}};\ \varepsilon_{\text{eff}} = \frac{\varepsilon_R+1}{2} + \frac{\varepsilon_R-1}{2}\left[\frac{1}{\sqrt{1+12\left(\frac{h}{W}\right)}}\right]$$

$$\text{Length} = \frac{c}{2f_o\sqrt{\varepsilon_{\text{eff}}}} - 0.824\,\text{h}\left(\frac{(\varepsilon_{\text{eff}}+0.3)\left(\frac{W}{h}+0.264\right)}{(\varepsilon_{\text{eff}}-0.258)\left(\frac{W}{h}+0.8\right)}\right)$$

Length of the feed and width of the feed is given by,

$$L_f = \lambda/4\sqrt{\varepsilon_T}$$
$$W_f = 377(h+2)/z\sqrt{\varepsilon_T}$$

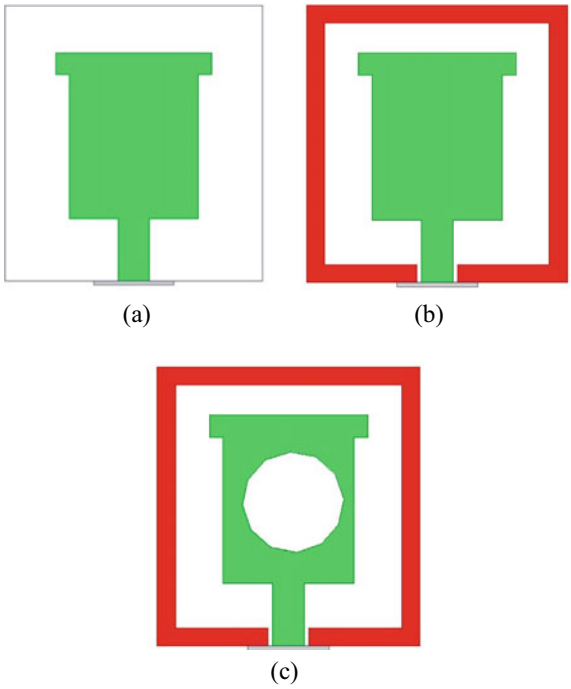

Fig. 1 Iterative design analysis, **a** antenna 1, **b** antenna 2, **c** antenna 3

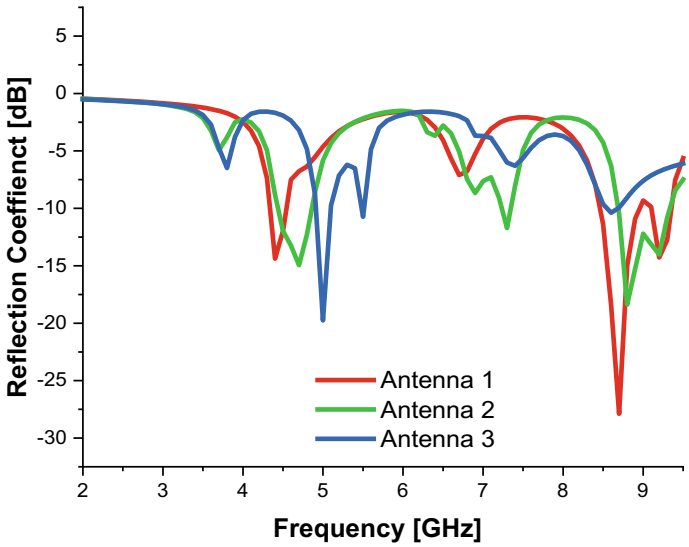

Fig. 2 Frequency of different antenna designs

4 Proposed Reconfigurable Antenna

The design of the proposed reconfigurable antenna can be seen in Fig. 3. The dimensions of the antenna are in mm. The antenna is designed using HFSS 18 and FR4 as a material with the dimension of 70 * 70 and using the four BAR64 PIN Diodes. The antenna is in T shaped rectangular patch that are joined by two latitudinal slits. The execution of PIN diode on the operation of antenna is due to the resistance given by the diode in both ON and OFF state. The PIN diodes are simulated at different ON and OFF conditions. The simulation is done in the High Frequency Structure Simulator (Figs. 4, 5, 6 and Tables 2, 3, 4, 5).

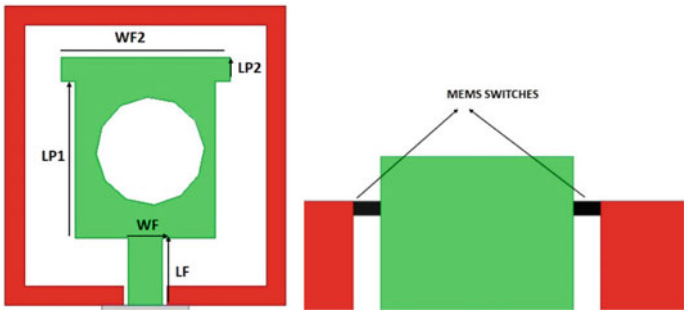

Fig. 3 Proposed antenna with reconfigurability

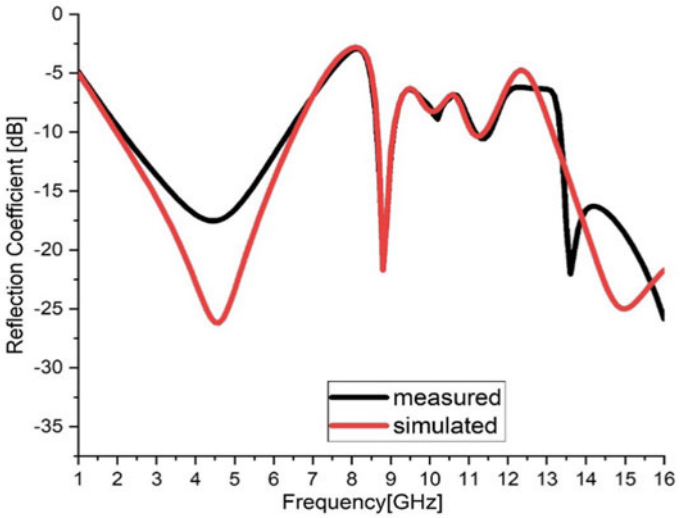

Fig. 4 Simulated and measured results

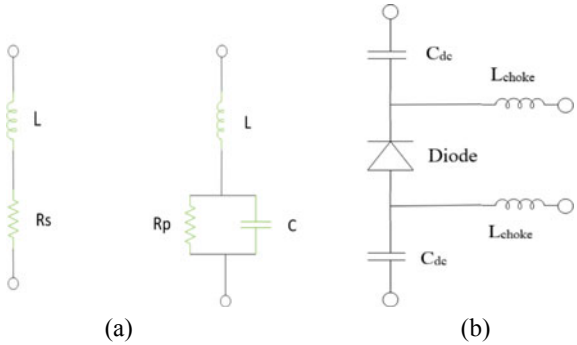

Fig. 5 **a** Diode ON and OFF conditions representation, **b** DC blocking circuit

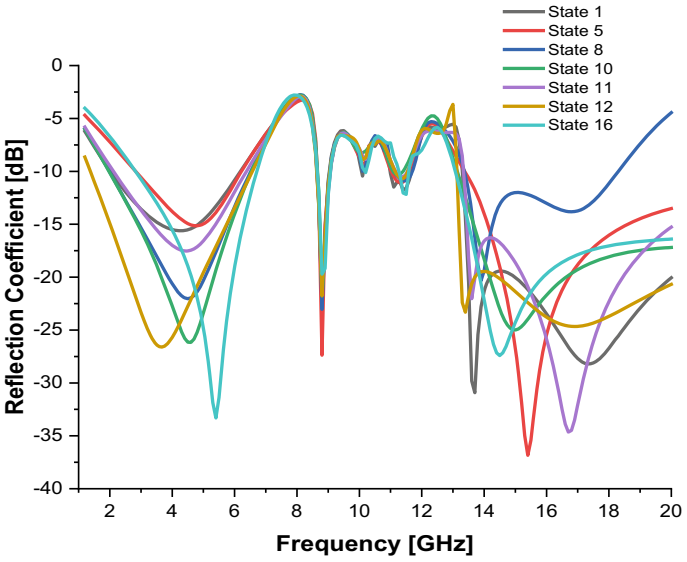

Fig. 6 Frequency at different states of proposed antenna

Table 2 Dimensions of the proposed antenna

Variable	Dimension (mm)	Variable	Dimension (mm)
Ws	70	WF2	30
Ls	70	S1	10
Lf	13	S2	6
WF	12	G	5
Lp1	11	H	1
Lp2	6	I	9

Table 3 Diode components and their values

Component	Value
Rs	2.1 Ω
Rp	300 k Ω
L	1.8 nH
C	0.2 pF
Cdc	20 pF
Lchoke	33 nH

5 Pattern Reconfiguration

The reconfiguration of pattern by altering the current sources by altering the patch and ground [24]. In normal scenario the current sources help the pattern to tilt the radiation pattern. In any method, for this situation, the excitation source is kept steady and the way that the current ventures will be changed. The current travel extra separation prompting way distinction, which further delivers a stage contrast with reconfigurable patterns [25–27]. The pattern reconfiguration is inferred by the subclass of State I and State V. In State I, D1, D2, D3, and D4 will be in OFF state. If anybody of these diodes is turned ON, the receiving wire radiation pattern can be tilted up to 15° (Table 6).

6 Radiation Patterns

The graphical view of radiation patterns of the antenna can be seen in Fig. 7 for the E-plane and H-plane at the different states. Radiation patterns have the power flux density, radiation intensity, field strength, directivity phase or polarization. The pattern of radiation is seen in two or three-dimensional spatial distribution of radiating energy. The radiation pattern is seen at the different conditions for ON and OFF stages. The radiation pattern is observed at the −15°, 15°, 30° angles (Table 7).

7 Conclusion

In this paper, a reconfigurable antenna has been designed using PIN diodes by reconfiguring both frequency and pattern. The shape of the antenna is T, attached by two longitudinal slits. The antenna is designed using HFSS 18 and FR4 substrate. The frequency reconfiguration is between 4.5, 5.8, 11.4, and 13.6 GHz which are used for WLAN communications. The radiation pattern is observed at the angle of 15°, 15°, and 300°. The simulation results are seen in HFSS.

Table 4 Diode switching conditions

Diode switching conditions				First resonant band	Second resonant band	Third resonant band	Fourth resonant band
D1	D2	D3	D4				
OFF	OFF	OFF	OFF	4.5 (2.09–6.36)	8.8 (8.65–9.06)	11.3 (11.11–11.48)	17 (13.31–20)
OFF	OFF	OFF	ON	8.8 (8.65–9.04)	10.1 (10.05–10.16)	11.20 (11.06–11.29)	13.7 (13.39–20)
OFF	OFF	ON	OFF	5.7 (4.43–5.81)	7.0 (6.70–7.51)	8.9 (8.68–9.08)	10.2 (10.09–10.23) 11.2 (11.04–11.50) 13.5 (12.97–20)
OFF	OFF	ON	ON	8.8 (8.67–9.07)	11.2 (11.03–11.62)	13.5 (13.27–20)	–
OFF	ON	OFF	OFF	4.8 (2.85–6.21)	8.8 (8.65–9.06)	11.4 (11.03–11.60)	15.4 (13.39–20)
OFF	ON	OFF	ON	8.8 (8.62–9.05)	11.4 (11.10–11.61)	14.3 (13.25–20)	–
OFF	ON	ON	OFF	5.6 (3.41–6.49)	8.9(8.65–9.08)	10.1 (10.07–10.20)	11.4 (11.06–11.63)
OFF	ON	ON	ON	4.5 (1.99–6.51)	8.8 (8.64–9.05)	11.5 (11.12–11.69)	13.9 (13.37–18.29)
ON	OFF	OFF	OFF	8.9 (8.70–9.08)	14.6 (13.03–20)	–	–
ON	OFF	OFF	ON	4.6 (1.99–6.53)	8.8 (8.66–9.06)	11.3 (11.09–11.38)	15.0 (13.15–20)
ON	OFF	ON	OFF	4.6 (2.75–5.82)	8.9 (8.64–9.09)	11.5 (11.35–11.58)	11.2 (13.10–20)
ON	OFF	ON	ON	3.7 (1.36–6.46)	8.9 (8.66–9.09)	11.4 (11.16–11.55)	13.9 (13.14–20)
ON	ON	OFF	OFF	6 (5.87–6.58)	9 (8.81–9.12)	10.2 (10.18–10.29)	11.5 (11.22–11.64) 17.5 (13.00–20)
ON	ON	OFF	ON	5.8 (4.52–6.30)	8.9 (8.62–9.08)	10.2 (10.11–10.23)	11.5 (11.19–11.60) 14.5 (13.11–20)
ON	ON	ON	OFF	5.5 (3.77–6.28)	8.9 (8.70–9.09)	11.4 (11.20–11.64)	14.5 (13.16–20)
ON	ON	ON	ON	5.4 (2.83–6.71)	8.8 (8.65–9.07)	10.2 (10.18–10.21)	11.5 (11.27–11.58) 14.5 (3.08–20)

Table 5 BandWidth and gain at the particular bands for the specified diode conditions

Diode switching conditions				B.W at 1st band	Gain at 1st band	B.W at 2nd band	Gain at 2nd band	B.W at 3rd band	Gain at 3rd band	B.W at 4th band	Gain at 4th band
D1	D2	D3	D4								
OFF	OFF	OFF	OFF	4.27	3.4135	0.41	4.9355	0.37	3.0835	6.69	7.4842
OFF	ON	OFF	OFF	3.36	−0.19	0.41	4.475	0.57	3.5726	6.61	6.9893
OFF	ON	ON	ON	4.52	3.4490	0.41	5.0313	0.57	4.2745	4.92	4.1304
ON	OFF	OFF	ON	4.54	0.8909	0.4	4.5360	0.29	3.9424	6.85	4.5536
ON	OFF	ON	OFF	3.07	0.7696	0.45	4.8084	0.23	2.7508	6.9	4.3675
ON	OFF	ON	ON	5.1	2.6672	0.43	4.8225	0.39	2.7334	6.86	4.2362
ON	ON	ON	ON	3.88	0.6367	0.42	4.5568	0.03	3.1775	0.31 16.92	1.5115 4.3317

Table 6 Efficiency of the antenna in different stages

State	Diode switching conditions				Efficiency (%) At resonant bands			
	D1	D2	D3	D4	1	2	3	4
1	OFF	OFF	OFF	OFF	44.75	48.27	33.52	42.39
5	OFF	ON	OFF	OFF	23.07	47.49	37.28	44.02
8	OFF	ON	ON	ON	41.38	49.53	37.33	42.53
10	ON	OFF	OFF	ON	28.37	46.93	33.52	45.17
11	ON	OFF	ON	OFF	28.19	48.80	33.71	39.05
12	ON	OFF	ON	ON	26.78	48.71	34.16	42.01
16	ON	ON	ON	ON	25.63	46.29	35.67	30.97/38.92

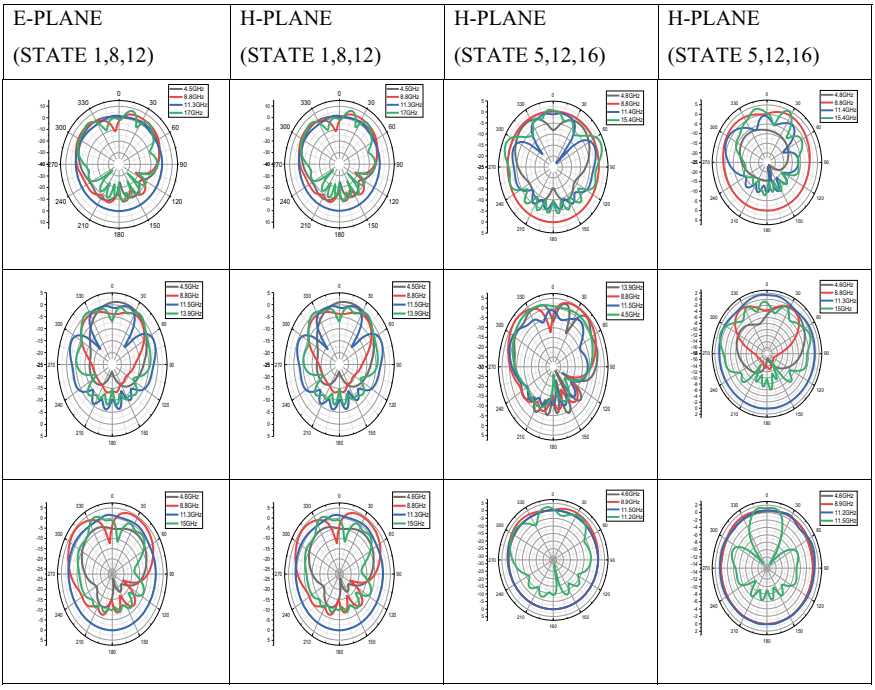

Fig. 7 Radiation patterns of the proposed antenna

Table 7 Work related to the proposed antenna

Work	Dimensions of the antenna (mm^2)	Reconfiguration seen	Elements used	Features		
				B.W (MHz)	Gain (dBi)	η (%)
[22]	46 × 20	Frequency	4 MEMS	90/125/100	−0.15/3.14/2.57	55/90/75
[23]	58 × 30	Pattern	2 PIN Diodes and 1 FSS	150	9.1	NR
[23]	130 × 160	Frequency and pattern	11 switches	200/150/150	5.6/4.6/3.3	88.7/87.7/89.5
[24]	80 × 45.8	Frequency and pattern	5 PIN Diodes	580/290	1.9/2.1	71/51
[25]	120 × 120	Frequency and pattern	12 PIN Diodes	63.4/88.3	9.15/10.52	94.9/94.8
[26]	34 × 36	Frequency and pattern	2 Switches	100/70	4/5.6	NR
[27]	50 × 50	Frequency and pattern	2 PIN diodes	120/100/100	NR	NR
This work	70 × 70	Frequency and pattern	4 PIN diodes	240/70/50/240		71/83/87/89

References

1. Palsokar AA, Lahudkar SL (2020) Frequency and pattern reconfigurable rectangular patch antenna using single PIN diode. Int J Electron Commun (AEU) 125:153370
2. Alieldin A, Huang Y, Boyes SJ, Stanley M (2018) A Reconfigurable broadband dual-mode dual-polarized antenna for sectorial/omnidirectional mobile base stations. Progress Electromagn Res 163(3):1–13
3. Chaouche B, Youcef FB, Nedil M, Messaoudene I, Benmabrouk I (2018) A frequency reconfigurable U-shaped antenna for dual-band WIMAX/WLAN systems. Progress Electromagn Res 87:63–71
4. AbouElEz AE, ElDiwany E, El Mashade MB, Konber HA (2018) Modelling and simulation of P-I-N quantum dot semiconductor Saturable absorber mirrors. Progress Electromagn Res 82:39–53
5. Liu Y, You P, Zhu C, Tan X, Liu QH (2016) Synthesis of sparse or thinned linear and planar arrays generating reconfigurable multiple real patterns by iterative linear programming. Progress Electromagn Res 155:27–38
6. Baruah R, Bhattacharyya NS (2017) A frequency reconfigurable meandered slot cut rectangular patch antenna using PIN diodes. Progress Electromagn Res 77:81–89
7. Boutayeb H (2017) Electrically reconfigurable radial waveguides and their potential applications in communications and radars systems. Progress Electromagn Res 75:147–153
8. Madhav BTP, Manikanta Prasanth A, Prasanth S, Krishna BMS, Manikantha D, NagaSai US (2015) Analysis of defected ground structure notched monopole antenna. ARPN J Eng Appl Sci 10(2):747–752
9. Madhav BTP, Sanikommu M, Pranoop MS, Bose KSNMC, Kumar BS (2015) Cpw fed antenna for wideband applications based on tapered step ground and EBG structure. Indian J Sci Technol 8:119–127

10. Ramkiran DS, Madhav BTP, Prasanth AM, Harsha NS, Vardhan V, Avinash K, Chaitanya MN, Nagasai US (2015) Novel compact asymmetrical fractal aperture Notch band antenna. Leonardo Electron J Pract Technol 14(27):1–12
11. Mohan Reddy SS, Mallikarjuna Rao P, Madhav BTP (2015) Asymmetric defected ground structured monopole antenna for wideband communication systems. Int J Commun Antenna Propag 5(5):256–262
12. Madhav BTP, Kaza H, Kartheek T, Kaza VL, Prasanth S, Chandra Sikakollu KSS, Thammishetti M, Srinivas A, Bhavani KVL (2015) Novel printed monopole trapezoidal notch antenna with S-band rejection. J Theor Appl Inf Technol 76(1):42–49
13. Lago H, Jamlos MF, Soh PJ, Vandenbosch GAE (2016) AMC-integrated reconfigurable beamforming folded dipole antenna with parasitic and RF MEMS. Progress Electromagn Res 69:159–167
14. Hany AA, Abdel-Rahman AB, Yoshitomi K, Pokharel RK (2016) Reconfigurable band-notched slot antenna using short circuited quarter wavelength microstrip resonators. Progress Electromagn Res 68:119–127
15. Nazir I, Rana IE, Ul Ain Mir N, Afreen K (2016) Design and analysis of a frequency reconfigurable microstrip patch antenna switching between four frequency bands. Progress Electromagn Res 68:179–191
16. Sharma S, Tripathi CC (2016) A wide spectrum sensing and frequency reconfigurable antenna for cognitive radio. Progress Electromagn Res 67:11–20
17. Koley S, Murmu L, Pal B (2016) A pattern reconfigurable antenna for WLAN and WiMAX systems. Progress Electromagn Res 66:183–190
18. Hussain R, Khan MU, Abu-Al-Saud W, Muqaibel AH, Sharawi MS (2016) Characterization of reconfigurable MIMO antennas for channel capacity in an indoor environment. Progress Electromagn Res 65:67–77
19. Wang F-W, Guo L, Gong S-X (2016) Reconfigurable radar absorbing structure applied to the antenna radar cross section reduction. Progress Electromagn Res 64:179–185
20. Yang L, Zhu Y, Yoshitomi K (2015) CPW-fed reconfigurable clover-shaped antenna with switchable circular polarization. Progress Electromagn Res 60:147–156
21. Lim S-L, Lim EH, Lo F-L (2015) Reconfigurable stepped-impedance slotline power dividers. Progress Electromagn Res 57:109–116
22. Soltani S, Lotfi P, Murch RD (2016) A port and frequency reconfigurable MIMO slot antenna for WLAN applications. IEEE Trans Antennas Propag 64(4):1209–1217
23. Bouslama M, Traii M, Denidni TA, Gharsallah A (2016) Beam switching antenna with a new reconfigurable frequency selective surface. IEEE Antennas Wireless Propag Lett 15:1159–1162
24. Majid HA, Rahim MKA, Hamid MR, Ismail MF (2014) Frequency and pattern reconfigurable slot antenna. IEEE Trans Antennas Propag 62(10):5339–5343
25. Li PK, Shao ZH, Wang Q, Cheng YJ (2015) Frequency- and patternreconfigurableantennaformultistandardwirelessapplications. IEEE Antennas Wireless Propag Lett 14:333–336
26. Ramli N, Ali MT, Islam MT, Yusof AL, MuhamudKayat S (2015) Aperture-coupled frequency and patterns reconfigurable microstrip stacked array antenna. IEEE Trans Antennas Propag 63(3):1067–1074
27. Huff GH, Feng J, Zhang S, Bernhard JT (2003) A novel radiation pattern and frequency reconfigurable single turn square spiral microstrip antenna. IEEE Microw Wireless Compon Lett 13(2):57–59

Analysis of Elevated Water Tank by Considering Slab, Wall, and Capacity in Seismic Zones

Dasari Tirupathi and Kota Srinivasu

Abstract Elevated water tanks are subjected to dynamic loads with varying capacity and located in different seismic zones. The history of the earthquake demonstrates that it has inflicted numerous losses to the life of people and has imposed damages caused to the public utility services such as water tanks. These buildings are particularly sensitive to horizontal wind pressures because of the considerable mass concentrated at the top of the narrow supporting structure. The structural parts of the elevated water tank have been subjected to rigorous computational testing in order to establish how well they function when subjected to wind loads. Four raised water tanks are modelled using finite element analysis and examined in the cloud. An axial load variation investigation of the columns with various staging heights is conducted after the completion of analysis. Results from this research will help better understand raised water tanks and how to construct them so that they can withstand wind loads.

1 Introduction

For liquid storage, there are a variety of tanks that can be found in practice, such as those that are either elevated or submerged in water. Among the various types of tanks, elevated tanks are the most important because of their high tank capacity and their ability to meet the demand of the public or industry. Patel [1] studied that water tanks play an important part in public utility and industrial structures, as they are essential for providing a steady flow of water over an extended distance with appropriate static head. Shakib and Omidinasab [2] said that reservoirs that hold water and other liquids are located on the ground and in the air. Reservoirs and tanks have a similar force analysis regardless of the chemical composition of the product. To prevent leaks, all tanks are constructed with no cracks or crevices. If

D. Tirupathi (✉)
Acharya Nagarjuna University, Guntur, India
e-mail: srimahabodhitejeswie@gmail.com

K. Srinivasu
NRI Engineering College, Guntur, India

K. Geetha et al. (eds.), *Recent Trends in Materials*, Springer Proceedings in Materials 18, https://doi.org/10.1007/978-981-19-5395-8_25

the reinforcement is well maintained, reinforced concrete can be used to build walls and slabs for the storage of water or petroleum products. Vyankatesh and Varsha [3] proposed that a additional treatment is needed on the concrete surface since water and petroleum react with it. Upadhyay and Chirag [4, 5] suggested that overhead distribution systems are often lower in size because they rely on gravity to distribute products.

1.1 Types of Bracing Systems Used

Different models are used for calculating base shear and nodal displacements for staging with cross bracing, staging with chevron bracing, staging with diagonal bracing, staging with k-type bracing, and staging with v-type bracing.

1.2 Response Spectrum Analysıs

In order to perform the seismic analysis and design of a structure to be built at a particular location, the actual time history record is required. Nemade [6] suggested that, however, it is not possible to have such records at each and every location. Further, the seismic analysis of structures cannot be carried out simply based on the maximum values of the ground acceleration as the response of the structure depends upon the frequency content of ground motion and its own dynamic properties. Mhetre [7] proposed that to resolve these difficulties, earthquake response spectrum is the most popular tool in the seismic analysis of structures. Yogeshwarana [8] mentioned that there are many advantages in using the response spectrum method of seismic analysis for prediction of displacements and member forces in structural systems. The method of analysis involves calculation of only the maximum values of the displacements and member forces in each mode of vibration using smooth design spectra that are the average of several earthquake motions. Gandhi [9] illustrated that the response spectral values depend upon energy release mechanism, epicentral distance, focal depth, soil condition, Richter magnitude, damping in the system, and time period of the system.

2 Lıterature Revıew

Upadhyay and Chirag [5] proposed that when an elevated water tank is subjected to away earthquakes, the response of the elevated water tank is examined and an evaluation of seismological response to the same. For earthquake-prone areas, tanks should be designed so that their tops are large enough to develop the seismic-weakness

constructions. Haroun MA and Ellaithy [10] studied the soil and foundation structure interactions during earthquakes which were examined by Reheat and Sunna for an elevated rectangular tank. Sloshing effects on the raised tanks' seismic behaviour and the soil's radiation dampening impact were ignored. The dynamic interaction between the tower and the supporting soil-foundation system was studied by Haroun and Temraz using two-dimensional X-braced elevated tank models supported on isolated footings. However, the sloshing effects were completely neglected [11]. Marashi and Shakib carried out an ambient vibration test to evaluate the dynamic characteristics of elevated tanks. Dutta et al. [12] examined the structural stability of elevated tanks as a part of their research. A set of estimated empirical equations for the stiffness of different frame supporting systems was proposed by the researchers. It was also studied how the tank system with unintentional eccentricity alters in torsional behaviour as the number of panels grows. Soil-structure interaction (SSI) has been shown to enhance base shear, particularly for tanks with high structures and short structural periods (Dutta et al. 2012). Additionally, the study found that disregarding the effect of SSI could result in high tensile strains in some of the staging columns due to seismic loads. For fluid-elevated tank-foundation-soil systems, they proposed a straightforward analytical approach and employed this approximation in selected tanks. Marashi and Shakib [13].

In this review work, Bansode [14] titled seismic investigation of raised water tank with variable staging design. Using staad-pro v8i 2007, he investigated the behaviour of several staging systems under various tank conditions. Response Spectrum Analysis was performed on three different types of bracing systems of elevated water tanks for various types of zones. He compared the base shear and nodal displacement of an elevated water tank while it was empty and full. Rajesh [15] published a review study on the behaviour of elevated water tanks at various staging heights. They concentrated on the behaviour of raised tanks under varied loads and the safer design of structures in their research. In his review paper titled "Seismic Analysis of RC Elevated Water Tank Using Different Staging Pattern", Quandri [16] considered different parameters such as water storage capacity, water tower height as consistent and variation in number of segment h/d ratio, and staging arrangement such as normal staging, hexagonal staging, cross staging, and radial staging with central column. Dhage [17] labelled her research "dynamic analysis of RCC elevated water tank". In her study, she considered two situations with the same tank capacity and found that changes in geometric features of the container can cause changes in the response of the elevated water tank. Gujar [18] laboured to secure a direct source of water from the rain for the water tank. Using water from a tank for irrigation is cost effective in areas where building a well is prohibitively expensive. The water obtained from the high water tank was suitable for home usage, for example, drinking, cooking, and washing. Using water from a tank for irrigation is cost effective in areas where building a well is prohibitively expensive. The water obtained from the high water tank was suitable for home usage, for example, drinking, cooking, and washing.

3 Methodology

The process comprises the simulation of a 100 mm^3-litre water tank. These overhead water tanks are analysed at staging heights of 15 m, 18 m, 21 m, and 25 m, accordingly. It is observed at a wind speed of 44 m/s. Wind load dynamic analysis is done using the Staad.Pro software. The design of the water tank must be able to endure earthquake loads, which increases as the seismic zones increase.

Methods of seismic analysis

Main two different types of design analysis are as follows.

Equivalent static analysis

Water tanks with an elevated water level can be effectively appealed statistically. When the seismic load is represented in the form of identical static loads, it is necessary, to get an accurate estimate, and it only needs one degree of freedom in the estimation in relation to the tank.

$$K = P/\Delta$$

where

K = Lateral stiffness of staging
P = Applied lateral force
Δ = Deflection in mm

Dynamic analysis

Water tanks with an elevated water level can be effectively applied numerically. When the seismic load is represented in the form of identical static loads, it is necessary to get an accurate estimate. It only needs one degree of freedom in the estimation in relation to the tank.

Seısmıc Analysıs of Elevated Water Tank

Equivalent static analysis of raised water tanks is used to convert seismic loads into equivalent static loads, which is the most common method of analysing tanks. The method for analysing an elevated water tank for seismic loading has been provided by IS: 1893–2002. Seismic loads have historically been measured in terms of equivalent static accelerations, which were affected by a variety of factors, including the location's seismicity, soil qualities, the natural frequency of the building, and its proposed usage. When a water tank is elevated, it can be analysed in both the full and empty states. A single-mass tank can be ideal for both conditions. Although both water and structure are assumed to be adhered to the container, the water-structure interaction indicates that both water and structure acquire picks at the same time for an identical static analysis.

General specifications

The dimensions of the circular and rectangular water tanks are regarded the same for all the different stage heights. The foundation, columns, and bracing all have a role in supporting the weight of the tanks above. Structural elements used to construct the water tank's staging must be strong enough to withstand axial loads, moments, and shear forces.

Foundation

Bottom of foundation 2 m

Centre of plinth beam 0 006D

Width of plinth beam 0.25 m

Depth of plinth beam 0.5 m

Columns

Diameter of the column 0.55 m

Bracing

Width of bracing beam 0.25 m

Depth of bracing beam 0.5 m

- **Floor beam**

Width of floor beam 0.3 m

Depth of floor beam 0.7 m

- **Floor slab**

Thickness of floor slab 0.2 m

- **Walking gallery**

Thickness of gallery 0.2 m

- Cylindrical wall or rectangular wall

Top width of wall 0.2 m

Bottom width of wall 0.2 m

Height of wall 4.2 m

- **Roof Slab**

Table 1 Weight of various components in kN of elevated service reservoir having Circular tank-1 of capacity 100m^3 l for different walls and floor slabs

Various components	15 m	25 m
Roof slab	2503	2503
Wall	1665	1665
Floor slab	2503	2503
Floor beam	1106	1106
Gallery	401	410
Water	19,640	19,640
Columns	2123	3459
Braces	2789	4463
Staging	4912	7922
Empty tank	8772	8772
Total weight	33,324	36,334

Thickness of roof slab 0.2 m

Weight of components

The weight of the components is determined by calculating the volume of the elements by the density weight of the concrete. Imperviousness is a condition for any water tank design. Wider fractures in the water tanks should be avoided, if possible, to make them impenetrable. M30 grade concrete which has a density of 25kN/m^3 is considered. Empty tank weight plus one-third of staging weight is included in the structural calculation procedure. A water load is considered a dead load. Furthermore, the freeboard is not considered in the depth of water while conducting dynamic analysis (Tables 1, 2, 3 and 4).

Table 2 Weight of various components in kN of elevated service reservoir having Circular tank-2 of capacity 100m^3 l for different walls and floor slabs

Various components	15 m	25 m
Roof slab	2503	2503
Wall	1890	1890
Floor slab	2500	2500
Floor beam	1106	1106
Gallery	401	410
Water	19,640	19,640
Columns	2123	3459
Braces	2789	4463
Staging	4912	7922
Empty tank	8772	8772
Total weight	33,324	36,334

Table 3 Weight of various components in kN of elevated service reservoir having rectangular tank of capacity 1 lakh litres for different walls and floor slab

Various components	15 m	25 m
Roof slab	2500	2500
Wall	1665	1665
Floor slab	2503	2503
Floor beam	919	919
Gallery	460	460
Water	19,620	19,620
Columns	2547	4150
Braces	3828	6125
Staging	6375	10,275
Empty tank	8982	8982
Total weight	34,977	38,877

Table 4 Weight of various components in kN of elevated service reservoir having rectangular tank of capacity 100 mm^3 l for different walls and floor slabs

Various components	15 m	25 m
Roof slab	2500	2500
Wall	1890	1890
Floor slab	2500	2500
Floor beam	919	919
Gallery	460	460
Water	19,620	19,620
Columns	2547	4150
Braces	3828	6125
Staging	6375	10,275
Empty tank	8982	8982
Total weight	34,977	38,877

Centre of gravity

The stability of objects is affected by their centre of gravity. Centre of gravity greatly simplifies calculations involving gravity and dynamics, allowing us to regard an object's mass as though it is concentrated at one location. Product of distance from top of floor beam to components of empty tank and component weights divided by total empty tank weight yields centre of gravity of empty tank.

Wind Force

According to a building's or structure's effective frontal area Ae and design wind pressure P_d, total wind load on that particular building or structure can be calculated using force coefficients (Figs. 1, 2 and Table 5).

Fig. 1 Circular tanks of capacity 100 m^3 l on staging heights 15 m and 25 m, respectively

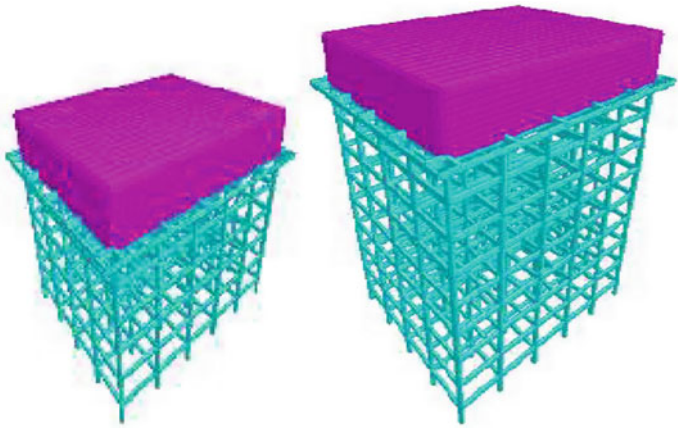

Fig. 2 Rectangular water tanks of capacity 100 m^3 l on staging heights 15 m and 25 m, respectively

Table 5 Calculation of centre of gravity from top of the floor beam for circular tank

Components	Distance	Weight	Distance × Weight
Roof slab	4.3	2503	10,762.9
Cylindrical wall	2.1	1665	3496.5
Floor slab	0.1	2503	250.3
Floor beam	0.35	1106	387.1
Gallery	0.05	401	20.05

4 Results and Discussions

The 100 mm^3 tank models are created and analysed in the software for the staging heights of 15 and 25 m, respectively. The x- and z-direction moments for the circular and rectangular tanks are compared to see how they are different. Circular and rectangular raised service reservoirs on different staging heights are studied in the maximum axial stress acting on the column RC 100 mm^3 capacity circular and rectangular water container. For all seismic zones, the tank is situated on a medium-soil base. Staging concrete is graded M30, and steel is graded Fe415, correspondingly. Concreting is 25 kN/m^3 in density, and the tanks are analysed for vibrations (Fig. 3 and Tables 6, 7).

Inferences

1. Displacement of Circular tank-1 > Circular tank-2 > Rectangular tank-1 > Rectangular tank-2.
2. In all the cases, displacement in full condition is more and in empty condition is less.
3. For staging height 15 m < staging height 25 m, i.e. 13 mm and 17 mm (Fig. 4 and Table 8).

Inferences

1. Base shear is more for Circular tank-2 and Rectangular tank-2 due to more wall thickness of 1890 mm.

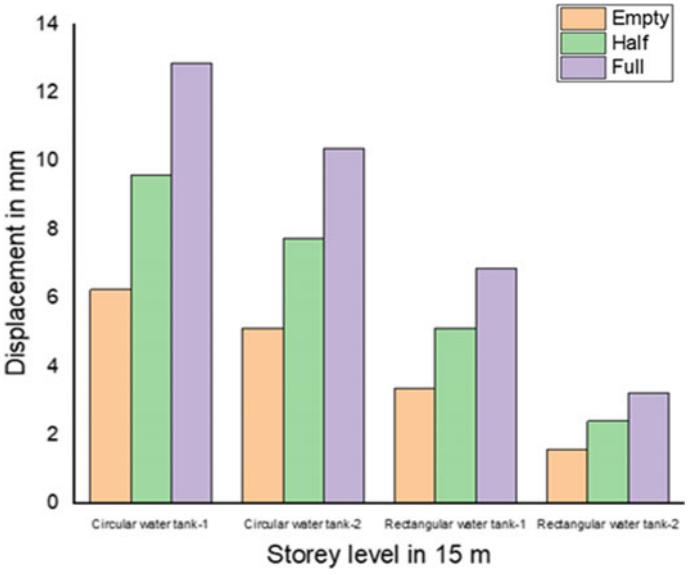

Fig. 3 Displacement (mm) versus storey level

Table 6 Zone II different storey levels in m

Storey level in m	Condition	Displacement (mm)		Base shear (kN)		Shear force (kN)	
		Stage-15 m	Stage-25 m	Stage-15 m	Stage-25 m	Stage-15 m	Stage-25 m
Circular water tank-1	Empty	6.26	6.32	275	278	285	289
	Half	9.58	11.59	210	212	225	233
	Full	12.85	16.93	220	222	239	242
Circular water tank-2	Empty	5.13	5.16	326	323	338	342
	Half	7.76	9.42	273	374	281	395
	Full	10.36	13.74	286	275	292	305
Rectangular water tank-1	Empty	3.37	3.41	270	272	284	295
	Half	5.13	6.37	205	208	258	285
	Full	6.86	9.30	208	210	252	279
Rectangular water tank-2	Empty	1.59	2.61	215	220	245	263
	Half	2.42	2.92	260	264	292	308
	Full	3.23	4.25	360	362	315	321

Table 7 Displacement (mm) Zone II in 15 m

Storey level in 15 m	Empty	Half	Full
Circular water tank-1	6.26	9.58	12.85
Circular water tank-2	5.13	7.76	10.36
Rectangular water tank-1	3.37	5.13	6.86
Rectangular water tank-2	1.59	2.42	3.23

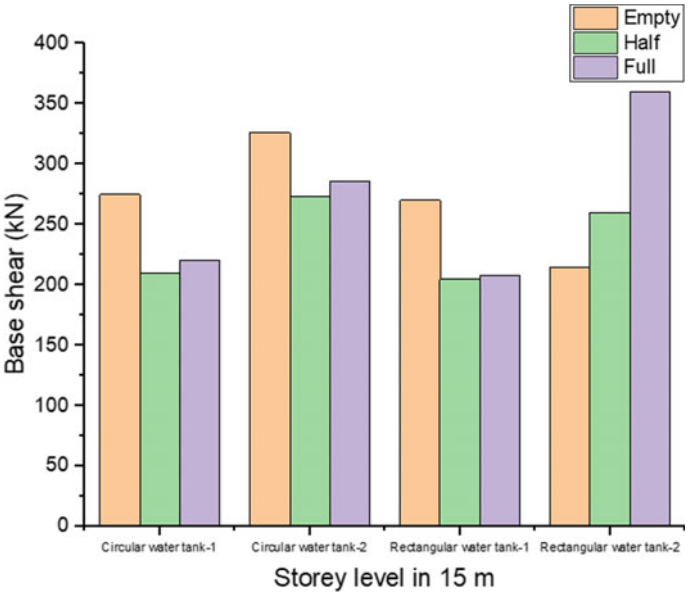

Fig. 4 Base shear (kN) versus storey level

Table 8 Base shear (kN) Zone II in 15 m

Storey level in 15 m	Empty	Half	Full
Circular water tank-1	275	210	220
Circular water tank-2	326	273	286
Rectangular water tank-1	270	205	208
Rectangular water tank-2	215	260	360

2. Circular tank-1 and Rectangular tank-1 show less base shear value due to less wall thickness of 1665 mm.
3. Base shear of staging height 15 m is almost equal to staging height 25 m (Fig. 5 and Table 9).

Inferences: Regarding Base Shear

1. Circular tank-2 and Rectangular tank-2 show more shear force values.
2. Empty condition for Circular tank-2 has the largest shear force value.

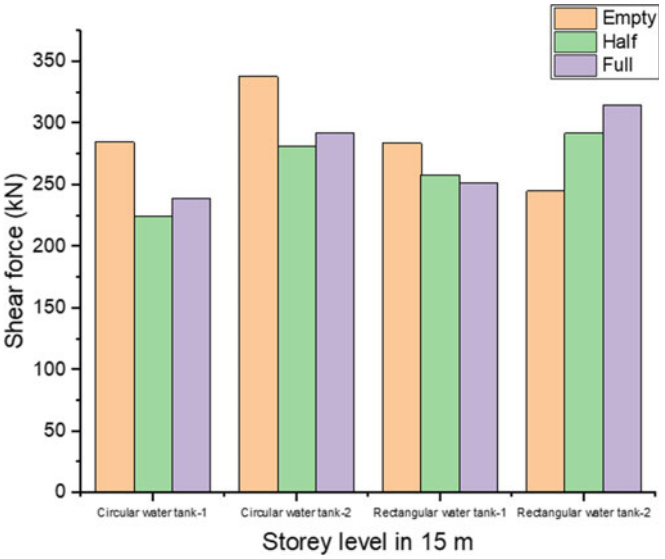

Fig. 5 Shear force (kN) versus storey level

Table 9 Shear force (kN) Zone II in 15 m

Storey level in 15 m	Empty	Half	Full
Circular water tank-1	285	225	239
Circular water tank-2	338	281	292
Rectangular water tank-1	284	258	252
Rectangular water tank-2	245	292	315

3. Full condition for the Rectangular tank-2 has the next largest shear force value.
4. Half condition for Circular tank-1 has the lowest shear force value (Fig. 6 and Table 10).

Inferences

1. In all the cases, full condition shows more displacement and empty condition shows less displacement.
2. Circular tank > rectangular tank.
3. Circular tank-1 > Circular tank-2 > Rectangular tank-1 > Rectangular tank-2 (Fig. 7 and Table 11).

Inferences

1. In all the cases, empty condition shows more base shear but in Rectangular tank-2, full condition shows more value, and in Circular tank-2, half fill tank condition shows more value.
2. Circular tank > rectangular tank.

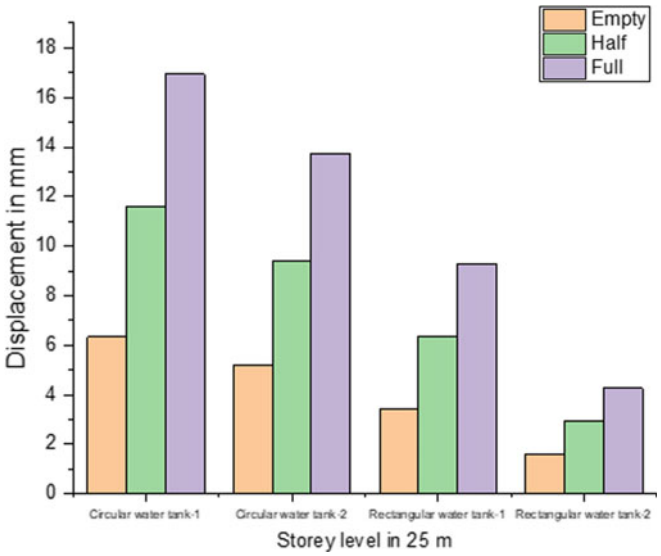

Fig. 6 Displacement (mm) versus storey level

Table 10 Displacement (mm) Zone II in 25 m

Storey level in 25 m	Empty	Half	Full
Circular water tank-1	6.32	11.59	16.93
Circular water tank-2	5.16	9.42	13.74
Rectangular water tank-1	3.41	6.37	9.30
Rectangular water tank-2	1.61	2.92	4.25

3. Circular tank-2 and Rectangular tank-2 show more values since the wall thickness is more (Fig. 8 and Table 12).

Inferences

1. In general, empty condition is more, but in Circular tank-2 half fill condition and in Rectangular tank-2 full fill condition effect is more.
2. Circular tank is more effective than rectangular tank.
3. Rectangular tank-2 has more effect than Rectangular tank-1 since the wall thickness is more. Therefore, capacity > demand.

Zone III Different Storey level with 15 m staging

Inferences: Regarding Displacement

1. Circular tank-1 > Circular tank-2 > Rectangular tank-1 > Rectangular tank-2.
2. Full condition > half fill condition > empty condition for all the shapes.
3. 15 m Staging > 25 m staging.

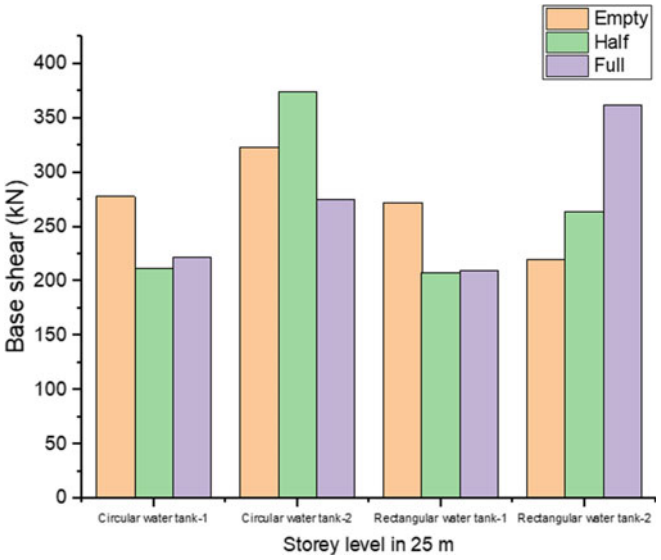

Fig. 7 Base shear (kN) versus storey level

Table 11 Base shear (kN) Zone II in 25 m

Storey level in 25 m	Empty	Half	Full
Circular water tank-1	278	212	222
Circular water tank-2	323	374	275
Rectangular water tank-1	272	208	210
Rectangular water tank-2	220	264	362

Inferences: Regarding Base Shear

1. In general, empty is more than other cases, except in Rectangular tank-2 full condition since for Rectangular tank-2, wall thickness is 1890 mm which is greater than Rectangular tank-1 of 1665 mm.
2. Rectangular tank-2 and Circular tank-2 show more base shear since wall thickness is more.
3. 15 m staging > 25 m staging.

Inferences: **Regarding Shear Force**

1. All most all the cases are equal; however, a slight more in Rectangular tank-2 and a slight less in Circular tank-1 are observed.
2. In general, empty conditions show more value except Rectangular tank-2 full fill condition.
3. 25 m staging < 25 m staging.

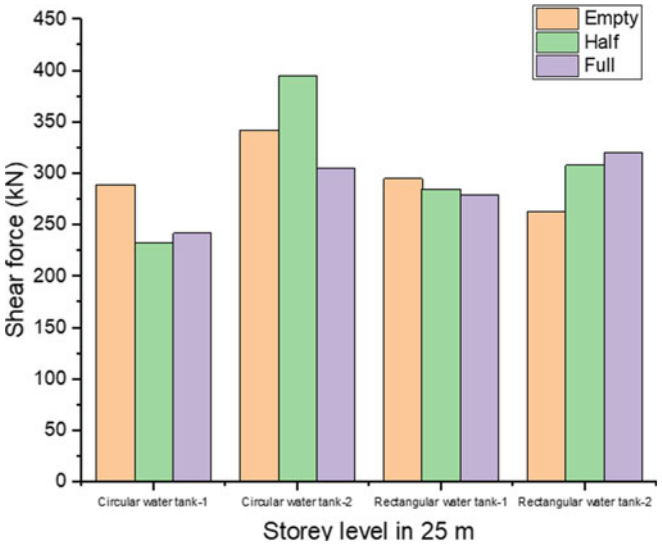

Fig. 8 Shear force (kN) versus storey level

Table 12 Shear force (kN) Zone II in 25 m

Storey level in 25 m	Empty	Half	Full
Circular water tank-1	289	233	242
Circular water tank-2	342	395	305
Rectangular water tank-1	295	285	279
Rectangular water tank-2	263	308	321

Zone III with 25 m staging

Inferences: Regarding Displacement

1. Circular tank-1 > Circular tank-2 > Rectangular tank-1 > Rectangular tank-2.
2. Circular tank > rectangular tank.
3. 15 m staging > 25 m staging.

Inferences: Regarding Base Shear

- Base shear is larger in Circular tank-2 half fill condition, and Rectangular tank-2 full fill condition is maximum since the wall thickness is more, i.e. 1890 mm.
- Circular tank-1, half fill condition and Rectangular tank-1, full fill condition have same values since they have same wall thickness 1665 mm which are less than Circular tank-2 and Rectangular tank-2.
- 25 m staging > 15 m staging.

Inferences: Regarding Shear Force

1. Circular tank-2 with half fill condition and Rectangular tank-2 with full condition show more values.
2. Circular tank-1 shows less value than all other cases.
3. 25 m staging > 15 m staging since distribution of base shear is more.

Zone IV Different Storey levels in m for 15 m staging

Inferences: Regarding Displacement

1. Circular tank-1 > Circular tank-2 > Rectangular tank-1 > Rectangular tank-2.
2. Full condition > half fill condition > empty condition.
3. Maximum 30 mm, minimum 3 mm.
4. 15 m staging < 2 m staging, i.e. 30 mm < 40 mm.

Inferences: Regarding Base Shear

1. Circular tank-2 and Rectangular tank-2 show more values, i.e. 320 KN and 350 KN, respectively.
2. Circular tank-2 with empty condition and Rectangular tank-2 with full condition shape influence more since thickness of wall is more, i.e. 1890 mm.
3. 15 m staging is almost equal to 25 m staging.
4. Maximum is 370 KN and minimum is 220 KN.

Inferences: Regarding Shear Force

1. Shear force is more in case of Rectangular tank-1 and Rectangular tank-2, which is about 325 KN to 330 KN even though maximum value exists in Circular tank-2 empty condition, i.e. 370 KN.
2. Circular tank-1 and Circular tank-2 show less values except empty condition of Circular tank-2, i.e. about 350 KN.
3. 25 m staging > 15 m staging since distribution of base shear is along the height.

Zone IV For 25 m staging

Inferences: Regarding Displacement

1. Circular tank-1 > Circular tank-2 > Rectangular tank-1 > Rectangular tank-2.
2. Full condition > half condition > empty condition 40 mm > 26 mm > 15 mm for circular tank.
3. 25 m staging displacement > 15 m staging displacement, i.e. 40 mm > 30 mm due to less stiffness.

Inferences: Regarding Base Shear

1. Circular tank-2 with half fill condition and Rectangular tank-2 with full condition show more base shear 350 KN and 400 KN, respectively.
2. Circular tank-1 and Rectangular tank-1 have almost same value, i.e. 275 KN in empty condition.

3. 25 m staging base shear is almost equal to 15 m staging base shear, i.e. 370 KN and 380 KN, respectively.

Inferences: Regarding Shear Force

1. Rectangular tank-2 and Rectangular tank-1 have about 340 KN to 350 KN, which are more than Circular tank-1 and Circular tank-2 except half fill condition in Circular tank-1 with 375 KN and empty condition in Circular tank-2 with 380 KN.
2. 25 m staging > 15 m staging, i.e. 380 KN > 370 KN.

Zone V Different Storey level for 15 m staging

Inferences: Regarding Displacement

1. Circular tank-1 > Circular tank-2 > Rectangular tank-1 > Rectangular tank-2.
2. Full condition > half fill condition > empty condition in each case.
3. Displacement of 25 m staging > 15 m staging, i.e. 60 mm > 45 mm.

Inferences: Regarding Base Shear

1. Circular tank-2 and Rectangular tank-2 show more values, i.e. 332 KN and 370 KN.
2. Circular tank-2 with empty condition and Rectangular tank-2 with full condition show more values because wall thickness is more, i.e. 1890 mm > 1665 mm.
3. Base shear for 25 m staging > 15 m staging, i.e. about 380 KN and 370 KN.

Inferences: Regarding Shear Force

1. Almost all are the same except Circular tank-1 with half fill condition having 375 KN and Circular tank-2 having 380 KN.
2. Rectangular tank has slightly more than that of the circular tank.
3. 25 m staging > 15 m staging, i.e. about 390 KN > 380 KN.

Zone V Different Storey level for 25 m staging

Inferences: Regarding Displacement

1. Circular tank-1 > Circular tank-2 > Rectangular tank-1 > Rectangular tank-2, i.e. 15 mm > 50 mm 32 mm > 18 mm.
2. Full Condition > half fill condition > empty condition.
3. 25 m staging > 15 m staging because of less stiffness.

Inferences: Regarding Base Shear

1. Circular tank-2 and Rectangular tank-2 are having maximum values. 375 KN and 360 KN values for Circular tank-2 in half fill condition and Rectangular tank-2 in full condition, respectively. Circular tank-1 and Rectangular tank-1 are less than Circular tank-2 and Rectangular tank-2.
2. Circular tank-2 dominates in empty condition.
3. Circular tank-1 and Rectangular tank-1 < Circular tank-2 and Rectangular tank-2.
4. 25 m staging > 15 m staging, i.e. 400 KN > 370 KN since the distribution of base shear is along the height.

Inferences: Regarding Shear Force

1. All are almost the same, except Circular tank-1 in half fill condition and Circular tank-2 in empty condition.
2. Rectangular tank-1 and Rectangular tank-2 are uniform. Circular tank-1 and Circular tank-2 are slightly more than rectangular tanks.
3. All the water fill conditions are almost the same.
4. 25 m staging is almost equal to 15 m staging, i.e. 375 K.

The maximum moments for circular tanks are lower than those for rectangular tanks. Increasing the height of the tanks' staging area for the same tank capacity increases the value of the moments. Due to the smaller effective area of a circular tank, it is less subjected to wind effects than a rectangular tank is. Due to the circular tank's lack of columns, this is more readily apparent than the rectangular tank.

5 Conclusion

Many good innovations and developments have been produced in various designs and forms for water tanks, which are highly significant for open utility and modern structure. The following are the results of the seismic analysis of the elevated water tank:

1. Because of the zone factor, response reduction factor, etc., the base shear of a full water tank and an empty water tank is both increased in seismic zones II–V.
2. Base shear in perfect working orders for the full tank is slightly higher than an empty tank because of the pressure difference or the absence of water.
3. Because of the zone factor, response reduction factor, etc., the displacement of a full water tank and an empty water tank is enhanced in seismic zones II–V.
4. When the tank is full, the wall of the tank has the maximum and smallest nodal deformations.
5. Comprehensive and empty water tanks are subjected to higher shear and bending moments due to the zone factor, response reduction factor, etc., in seismic analysis.
6. In a full tank, the shear force and bending moment are slightly larger than in an empty tank because of the lack of water or hydrostatic pressure.

References

1. Patel CN, Patel HS (2012) Supporting systems for reinforced concrete elevated water. Int J Adv Eng Tanks 2(1):68–71
2. Shakib H, Omidinasab F, Ahmadi MT (2010) Seismic demand evaluation of elevated reinforced concrete water tanks. Int J Civil Eng 8(3):204–220

3. Vyankatesh K, Varsha T (2017) Comparative study on dynamic analysis of elevated water tank frame staging and concrete shaft supported. IOSR J Mech Civil Eng (IOSR-JMCE) 14(1):38–46
4. Upadhyay S, Chirag N (2016) Seismic behavior of elevated storage reservoir by finite element method. Int Conf Recent Innov Eng Manage 4(3):1188–1197
5. Upadhyay S, Chirag N (2015) Seismic behavior of elevated storage reservoir by finite element method. Int Conf Recent Innov Eng Manage 4(3):1990–998
6. Nemade PS (2016) Parametric studies in design of staging configuration for elevated service reservoir for seismic consideration: a review. IJSTE Int J Sci Technol Eng 2(09). ISSN (online): 2349-784X
7. Mhetre MS, Patil GR. Analysis of elevated water storage structure using different staging system. IOSR J Mech Civil Eng (IOSR-JMCE) e-ISSN: 2278–1684, p-ISSN: 2320–334X, pp 21–32
8. Yogeshwarana J, Pavithra C (2015) Behaviour of an elevated RC tank subjected to various earthquake responses. Int J Eng Trends Technol (IJETT) 21(9)
9. Gandhi MN, Rajan A (2014) Necessity of dynamic analysis of elevated water storage structure using different bracing in staging. Int J Res Adv Technol 2(2). E-ISSN: 2321–9637
10. Haroun MA, Ellaithy MH (1985) Seismically induced fluid forces on elevated tanks. J Tech Top Civil Eng 111(1):1–15
11. Haroun MA, Termaz MK (1992) Effects of soil-structure interaction effects on seismic response of elevated tanks. Soil Dynam Earthq Eng 11(2):37–86
12. Dutta S, Mandal A, Dutta SC (2004) Soil-structure interaction in dynamic behavior of elevated tanks with alternate frame staging configurations. J Sound Vib 227(4–5):825–853
13. Marashi ES, Shakib H (1997) Evaluations of dynamic characteristics of elevated water tanks by ambient vibration tests. In: Proceedings of the 4th international conference on civil engineering, Tehran, Iran, I, pp 367–73
14. Bansode PA, Datye VP. Seismic analysis of elevated water tank with different staging configuration. MAT J Geotechn Stud 3(1)
15. Rajesh C, Jha S, Shrilakshmi P. Seismic behavior of an elevated water tank for different staging height. Int J Magaz Eng Technol Manage Res
16. Quadri SS, Sawant RM. Seismic analysis of RC elevated water tank using different staging pattern. Int J Struct Eng Analy
17. Dhage PN, Joshi MM. Review study an dynamic analysis of RCC elevated water tank. Int J Emerg Technol Innov Res
18. Gujar V, Sayyed S (2011) Review on seismic analysis of elevated water tank with different staging configuration. Int J Eng Res Technol (IJERT) 8(12). ISSN: 2278–0181
19. Lakhankiya J, Shah HJ (2015) A parametric study of an Intze tank supported on different staging. Int J Sci Res Eng Dev 3(9):1108–1112
20. Livaoglu R, Dogangün A (2007) Effect of foundation embedment on seismic behavior of elevated tanks considering fluid- structure-soil interaction. First Int Conf Seismol Earthq Eng (SEE) 27(1):855–863

Analysis of Machining Parameters of Wire Electric Discharge Machining Process on Polysilicon Material

Raminder Singh and Anish Kumar

Abstract The experimental investigation deals with wire electrical discharge machining (WEDM) of polycrystalline silicon ingot using zinc-coated brass wire as electrode, to analyze major technological response characteristics concerning cutting speed and kerf width. The experimental analysis is performed for cutting silicon ingots into wafers with the goal of minimizing kerf loss, facilitating the manufacture of thin wafers, and increasing productivity. The major goal of this article is to comprehend the impact of processing factors on the cutting process in order to obtain parametric circumstances that give high slicing rate, high productivity, and minimum kerf loss. Cutting silicon ingots in traditional machining to assist the manufacturing of solar cells are extremely tough for the semiconductor and solar industries. In this study, the WEDM non-conventional tool is used to cut polycrystalline silicon. Based on box Behnken's design of experiments (BBDOEs), sixty-two sets of experimental trials are done to assess the effect of various input parameters such as Ton, Toff, IP, SGV, WF, Wt, and WP. In addition, for experimental inquiry, predictive modeling, and multi response optimization, response surface methodology (RSM), analysis of variance (ANOVA), and statistical techniques (desirability) are used. To study the surface properties, the machined surface morphology is examined using SEM and EDX.

Keywords WEDM · Polycrystalline silicon ingot · OFTA · SEM · Surface morphology · Desirability function · T_{on} · T_{off} · IP · SGV · WF · WT and CS

1 Introduction

The silicon products have a wide range of applications in industry, including computers, electronics, textiles, vehicles, and architecture. In recent decades, semiconductors have been widely used in the electronics and microelectronics sectors

R. Singh · A. Kumar (✉)
Mechanical Engineering Department, Mullana Engineering College, Maharishi Markandeshwar (Demmed to Be University), Mullana, Ambala, Haryana, India
e-mail: anish_kaushik@rediffmail.com

K. Geetha et al. (eds.), *Recent Trends in Materials*, Springer Proceedings in Materials 18, https://doi.org/10.1007/978-981-19-5395-8_26

for computer systems and photovoltaic (PV) industry. Hence, the slicing of silicon ingots by increasing cutting speed and minimizing kerf loss is of much significance.

Luque and Hegendus [1] illustrated that wire saws have a kerf size of 200–250 m per wafer, which is extremely significant when compared to the industry typical wafer thickness of 250–350 m. Muthuraman and Ramakrishan [2] performed wire electrical discharge machining (WEDM) cutting operation on WC–Co composite using machining parameters. This process was used to study the effect of machining parameters on surface roughness (Ra) and material removal rate for the composite. Because wafers are so simple to break by hand, the yield was low in this situation. The silicon ingots were sliced in two ways: with an inner diameter (ID) saw and with an abrasive wire saw. WEDM was well known for its ability to create complicated forms fast and easily on metal and electrically conductive work materials such as copper. WEDM has recently been proposed as a good method for cutting silicon ingots. Uno et al. [3] utilized it for the first time to cut silicon ingots in 1992. People nickel-plated the silicon ingot and reversed its polarity to make it more electrically conductive. The silicon ingot was sliced into bits by slicing it with a wire moving at high speeds.

Sreejith et al. [4] investigated a new method of slicing monocrystalline silicon ingots using wire electric discharge machining with a low resistivity of 0.01 Ωcm, concluding that the new method of slicing silicon ingots reduced contamination caused by wire electrode material adhesion and diffusion to the machined surface, as well as producing a lower value of surface roughness. As per Peng and Liao et al. [5], research was done on various machining methods available for silicon processing and concluded that processing of silicon wafers from silicon ingots was done as required by industrial applications using wire electric discharge machining. Peng and Liao [5] studied WEDM slicing technology for slicing heavily doped silicon ingots. They were able to do this with no complications by cutting silicon wafers that were 1 mm thick without breaking the wires and using kerosene as the dielectric fluid. Takion et al. [6, 7] investigated the contouring of polished single crystal silicon plates using WEDM and carried out experiments on polished single crystal using WEDM. The purpose of this work is to use WEDM to slice PV grade silicon ingots. According to Shah et al. [8], the influence of varied machining parameters and material thicknesses on material removal rate and surface roughness was investigated for WEDM process optimization. Because of the modeling technique utilized, it was discovered that work material thickness had a significant impact on material removal rate and surface roughness. Yu et al. [9] studied the effects of various WEDM parameters on machining polycrystalline silicon with a resistivity of 2–3 using the wire electric discharge machining method, and it was discovered that open voltage was a critical parameter for breaking insulation of polycrystalline silicon, while pulse on affected cutting speed and groove width was improved due to wire strengthening, reducing electrode vibrations.

Singh et al. [10] investigated the use of AISI D2 steel as workpiece to study the effect of parameters such as pulse on time, pulse off time, peak current, servo voltage, and wire feed that affected the WEDM machining process. Luo et al. [11] determined the current carrying capacity and material removal rate for n type single crystal ingot

and observed that surface potential barrier of semiconductor had significant effect on the cutting speed and machining parameters. Rakhwal and Bamberg [12] investigated the slicing of germanium wafers from single crystal gallium doped ingots using WEDM. The wafers produced were analyzed using surface profiler and scanning electron microscopy. As per Satyanaryana and Rajkiran [13], the wire cut electro discharge machining was selected to achieve dimensional accuracy, surface roughness, and material removal rate with reduction in scrap of material during machining process. Dongre and Singh [14] proposed that WEDM is the potential process for slicing polycrystalline silicon to achieve maximum cutting speed with minimum kerf loss and surface roughness. According to Joshi and Sharma [15], WEDM is best method for Si ingot slicing with minimum kerf loss and to achieve crack free surface. Punturat and Tangwarodomnukun [16] studied the effect of process parameters on cut surface characteristics and damage in WEDM slicing of silicon. As per Mai and Chuang [17], the machining of 156 mm square ingots of polycrystalline silicon was performed, and higher machining rates (343 mm^3/min) were achieved. According to Murugan and Kumar [18], the effects of WEDM parameters were studied on ceramic composites using input factors like pulse current, pulse on time, and pulse off time. It was observed that experimental results were combined with parameters to study the range of different input parameters. As per Verma and Singh [19], the slicing of monocrystalline silicon was studied for response on material removal rate, surface roughness, and slicing speed with machining parameters like open voltage, pulse on time, servo voltage, pulse off time, and wire tension.

As per Tosun and Cogun [20], the effect of machining parameters on wire wear, size of erosion craters, and surface roughness were investigated using WEDM process, and regression analysis model was used to study relation between various machining parameters like pulse duration, wire speed, open circuit voltage, and dielectric flushing pressure. The machining of silicon ingots by wire EDM was discussed, and the cutting qualities were examined. Through experiment design, the paper demonstrated that WEDM can cut wafers from silicon ingots.

Wire cut electric discharge machining is a technique that employs electricity to cut through material. WEDM process deals with removal of material by generating a series of tiny sparks between the workpiece and the electrode wire. Dielectric fluid is directed to the working region through a series of miniature pipes, filling the space between the workpiece and the wire. As a result, process modeling and optimization has become one of the most important topics of research. This is due to the importance of producing high-quality parameters at a reasonable cost. The WEDM process was used for slicing of polycrystalline silicon and to study the influence of machining parameters like pulse on time, pulse off time, peak current, spark gap voltage, wire feed, wire tension, and water pressure on cutting speed during machining process. To determine the best values for machining the materials, an orthogonal array is used. WEDM parameters such as open circuit voltage, pulse duration, wire speed, and dielectric fluid pressure are investigated to see how they affect the surface roughness and overcut of polycrystalline silicon, as well as the thickness of the cut.

According to literature review, slicing is done traditionally using inner diameter blades and wire saws. Furthermore, past research has not delved deeply into the

WEDM method of cutting and various machining parameters. Moreover, parametric optimization is required for better results. According to the literature, not much work has been done on cutting polycrystalline silicon using WEDM for parameter tuning. Table 1 provides an overview of all prior research on cutting silicon ingots with the wire electric discharge machining technique.

2 Gap in the Literature

- The literature review identifies that some work was conducted on machining of different types of silicon materials using WEDM process, but the machining parameters (T_{on}, T_{off}, PC, SGV, WT, WF, and ~~WP)~~ were not selected to achieve desired results.
- Predictive processing has not been applied to the surface in order to reduce and eliminate cracks.
- The lack of information on how to produce affordable silicon slices in polycrystalline silicon manufacturing, which is due to the limited information on high temperature machining [27].
- There is no information to study the influence of machining parameters to minimize the kerf loss.
- Many scholars have used classic approaches like Taguchi, max–min, etc., to optimize their objectives. RSM was the kind of optimization strategy used to multi-target optimize process parameters such as polycrystalline silicon semiconductor slicing.
- Several studies have been conducted on the machining of polycrystalline semiconductor materials and the damage produced by surface contact forces. However, the current study uses composite wire technology and response surface methodology (RSM) to analyze the surface characteristics of polycrystalline silicon semiconductor materials.
- There has been no new literature on study of formation of microcracks during machining of polycrystalline silicon.
- Further the method of slicing using WEDM method using various machining parameters has not been investigated much in previous research work

2.1 Objectives of the Present Work

1. The cutting speed, kerf width, surface roughness, and overcut are the most significant performance measures in WEDM process during slicing of silicon ingots.
2. A study is conducted, and the parameters that affect cutting speed, surface roughness, and overcut when cutting polycrystalline silicon with the WEDM process are altered. The following input parameters are being investigated: pulse on time,

Table 1 Summary of previous research work on slicing of silicon ingot

Authors and date	Work material and tool material	Process parameters and machining characteristics	Key findings
Uno et al. [3]	P type monocrystalline silicon ingot Molybdenum wire with Φ0.18 mm	"Pulse interval. Pulse duration, discharge current, cutting rate, surface roughness"	WEDM machining possible to narrow kerf and large size of wafer. With reverse polarity and nickel plating, surface roughness was improved, and cutting speed was increased by increasing wire traveling speed
Tosun et al. [20]	"AISI 4140 steel (DIN $42CrMo_4$) of 50 mm diameter and 10 mm thickness used as workpiece material with brass wire 0.25 mm diameter 900 N/mm^2 tensile strength"	"Pulse duration, open circuit voltage, wire speed and dielectric flushing pressure"	The higher values of pulse duration and open circuit voltage have significant effect on WWR, whereas higher values of wire speed and dielectric fluid pressure decreased the WWR
Peng and Liao [5]	P type 3″ CZ (111)-oriented silicon ingot with 30 Ω resistivity was used, 0.25 mm Cu wire was used as electrode, and 0.2 mm Molybdenum wire was used	Pulse on time, servo voltage, and gap voltage	Wire breakage and slicing efficiency can be improved with higher gap voltage along when material characteristics were comparable with discharge parameters of material
Takion et al. [6]	Single crystal silicon plates with 0.02 Ωcm resistivity with 150 mm in diameter and 10 mm in thickness. Brass electrode wire of 200 μm was used	"Discharge current, pulse duration, Discharge frequency open voltage and removed speed"	For cutting in water, the polished surfaces have chips and cracks and are extremely rough, but cutting in oil gave better results than water for polished surface single crystal silicon
Joshi and Das [21]	Monocrystalline silicon ingot with brass-coated thin wire used as electrode	Voltage, current, wire diameter, and pulse on time	With increase in voltage, current, and pulse on time, there was an increase in plasma temperature, interface temperature, and erosion rate increased

(continued)

Table 1 (continued)

Authors and date	Work material and tool material	Process parameters and machining characteristics	Key findings
Rakhwal and Bamberg [12]	Single crystal gallium doped ingot was used with 75 and 100 μm Molybdenum electrode wire	The wafer characteristics such as surface profile and texture were analyzed using surface profilometer and scanning electron microscopy	Minimum wastage of material was observed using thin electrode wire during WEDM machining. The recast layer thickness was measured using Raman spectroscopy
Shah et al. [8]	Tungsten carbide plates were used for WEDM machining. A 250 μm diameter brass wire is used as tool electrode	"Open voltage, pulse on time, pulse off time, servo voltage, wire feed, wire tension, and dielectric pressure"	The material removal rate and surface roughness were largely affected by workpiece thickness
Shah et al. [8]	Tungsten carbide (88%WC, 12%Co) plates were used with 250 μm brass wire was used as tool electrode	Pulse on time, Pulse off time, servo voltage, material thickness, wire feed, wire tension and dielectric pressure	The material thickness had little effect on material removal rate and kerf width but is significant factor in surface roughness
Lee et al. (2011)	Polycrystalline silicon ingot with resistivity of 2-3Ωcm Brass wire Ø 0.2 mm	Open circuit voltage, pulse on time, flushing rate, and wire tension	Cutting speed was affected by open circuit voltage and pulse on time; flushing rate has no influence on cutting speed but improved machining groove width and surface roughness
Kumar et al. [23]	A metal matrix composite (MMC) of Al alloy and silicon carbide is used with negatively polarized brass wire 0.25 mm diameter as electrode	Pulse on time, Pulse off time, gap voltage, and wire feed are used as process parameters	MRR decreased with increase in percentage volume fraction of SiC particles while surface roughness increases with percentage volume fraction of SiC particles

(continued)

pulse off time, peak current, spark gap voltage, wire feed, wire tension, and water pressure. The best values for machining the materials are then determined using an orthogonal array.

3. WEDM factors such as open circuit voltage, pulse duration, wire speed, and dielectric fluid pressure are studied for their effects on polycrystalline silicon surface roughness and overcut.
4. The experimental study of optimization of machining parameters during the slicing of Polycrystalline silicon using WEDM process is given in Table 9.

Table 1 (continued)

Authors and date	Work material and tool material	Process parameters and machining characteristics	Key findings
Dongre et al. [14]	Polycrystalline silicon ingot Zn-coated brass wire with Ø 100 µm	"Pulse on time, pulse off time, voltage, water pressure slicing speed, kerf loss, and surface finish"	"Optimization was done using response surface methodology, and it was found that most significant parameter was pulse on time, pulse off time, and voltage: 30–40% higher MRR during slicing attained using WEDM process. The slicing speed largely influenced by current, voltage, and pulse on time. Width decrease in current, voltage, and pulse on time better surface finish was obtained"
Yu et al. [9]	P type polycrystalline silicon ingot, brass wire Ø 0.2 mm	Open circuit voltage, wire erosion, flushing rate, and pulse on time	Open circuit voltage and pulse on time affect cutting speed. Flushing rate has effect on cutting speed but with effective removal of debris, strengthening of wire improves groove width during machining
Punturat et al. [16]	n Type monocrystalline silicon with 250 µm brass wire with wafer thickness 508 µm and resistivity 0.001 to 0.005 Ωcm	Open voltage, wire speed, dielectric flushing rate, wire tension and electrode polarity, cutting mode (strong, moderate, and fine)	With increase in open voltage, the gap voltage and cutting speed increased, and fine cutting mode showed relation between spark energy density and open voltage
Dongre et al. [14]	"Monocrystalline silicon ingot, Molybdenum wire of Φ 40,60,80,100,120 mm"	"Current. duty cycle wire diameter, workpiece height, kerf width, cutting speed, and surface roughness"	Slicing rate is 1.26 mm/min, surface roughness is 3.1 m, and kerf width is 60.87 m in the optimized solution. Molybdenum is a vibration that reduces vibrations

(continued)

Table 1 (continued)

Authors and date	Work material and tool material	Process parameters and machining characteristics	Key findings
Cheng et al. (2015)	p Type polycrystalline square ingot with round and flat electrode wires and transistor type generator, workpiece (156 × 156 mm)	Wire tension. wire speed, open voltage, discharge current, feed rate, pulse off time, dielectric fluid	Kerf loss decreased with increase in wire tension, but increased value of flushing rate has no effect on kerf loss
Bisaria et al. (2020)	Shaped memory alloy $NI_{55.95}Ti_{44.05}$ in the form of square plate with thickness of 6 mm and length and width as 165 mm. Brass wire with 250 μm as diameter, and with negative polarity was used	Pulse off time, wire tension, spark gap voltage, wire feed rate, and pulse on time	Micro-hardness of material was directly proportional to spark gap voltage, pulse on time, and pulse off time, while surface crack density depends upon pulse on time
Shandilya and Bisaria [26]	Inconel-825 material with dimensions of 160mm × 160mm × 10mm was used with Molybdenum wire of 180 μm diameter as tool electrode	"Wire tension, spark gap voltage, dielectric conductivity, dielectric flushing pressure, and working temperature"	Minimum SR and maximum CR observed through response surface modeling. The GRA and GA techniques were used to predict optimum values of WEDM parameters for cutting Inconel-825
Lel and Liao [22]	A8 tool steel with size10 × 10 × 120 mm was used as workpiece and 0.18 mm diameter Molybdenum wire used as electrode	Processing current, pulse width, pulse interval, voltage, and size of electrode wire are used as process parameters	With increase in processing current, the cutting speed increased, and material removal per unit increased; so surface roughness and surface hardness increased, but the surface roughness and hardness also increased with increase in pulse width
Verma and Singh [19]	Monocrystalline silicon ingot with brass wire having diameter 250 μm as electrode	Open voltage, servo voltage, wire tension, pulse on time, and pulse off time	Pulse on time, wire tension, and open voltage were significant factors for slicing of monocrystalline silicon

(continued)

Table 1 (continued)

Authors and date	Work material and tool material	Process parameters and machining characteristics	Key findings
Chakraborty et al. (2021)	Deionized water was used as a dielectric fluid with Ti6Al4V as the workpiece material. As an input variable, different concentration levels of Al_2O_3 abrasive powder (size 10 m) have been taken Separately, a mixing chamber with a capacity of 20 L was built to supply dielectric. During the machining process, a stirring attachment was employed in the dielectric chamber to ensure that the powder is properly mixed	The pulse off time (T_{off}), pulse on time (T_{on}), peak current (I_p), and powder concentration (PC) are taken as process parameters	The suspended Al_2O_3 powder concentrations of 4 g/L with dielectric in WEDM showed higher value of MRR and surface roughness. With increase in T_{off} and I_p, the MRR value increases

5. The proposed mathematical model to study the output during machining of Polycrystalline silicon with cutting speed as parameter is given in Table 8.
6. To study the elemental composition of Polycrystalline silicon material and the presence of elements in electrode wire the Energy Dispersive X ray (EDX) method and Scanning Electron Microscope (SEM) are used. These methods are recommended to study the composition of material and the transfer of elements during the process. The composition of polycrystalline silicon material and electrode wire is given as per Table 10 and 11 and the procedure for SEM analysis.

Scanning Electron Microscope (SEM)

Wire spark parameters and the effect of different wires on the surface formed during processing can be seen in the SEM images. To examine the extent of mechanical surface recovery, samples were briefly cleaned with acetone using EMBRI paper (grades 100, 1200, 1500, 2000, 3000) to remove unwanted impurities such as dust particles, rust, etc. Did. The samples are then immersed in nitric acid (3mL HNO3, 47mL alcohol), which is used as an accent for the D2 samples to reveal the microstructure, for the purpose of polishing the samples. His SEM images of rearranged slices are acquired for two samples. Comparison of the difference in the composition of the rearranged layer obtained with a normal brass wire and a galvanized Wire.

3 Materials and Methods

A four-axis computer numeric control-type WEDM (Electronica India Sprintcut, 734 Model) has been used (Fig. 1). Table 1 displays the factors and their levels (coded and real) at each of the two levels. Tianjin Yucai Photoelectric Technology Co. Ltd. in China supplied the polycrystalline silicon ingot that is used for the studies. The machining parameters like pulse on time (T_{on}), the pulse off time (T_{off}), peak current (PC), spark gap voltage (SGV), wire feed (WF), wire tension (WT), and water pressure (WP) are used to study the cutting speed during slicing process. The design matrix for the major experimentation and its outputs have been shown in Table 2. The electrode (Zn-coated brass wire with a diameter of 0.25 mm) is used for the WEDM process. For analysis, the sample is sliced into a square form with dimensions of (105 mm 105 mm × 15 mm). Mitutoyo's SURFTEST is used to determine the SR of the machined surface (Model: SJ-301).

3.1 Poly Silicon Material

Glass substrates are often manufactured using a four-layered saw, which divides silicon ingots to generate wafers with a depth of 250–350 m and kerf losses of 200–250 m. The bulk of raw materials is wasted during processing (Pramanik et al. 2018). To reduce low yield rates of silicon wafer production, it is required to reduce the thickness of the wafer, and the secondary goal is to minimize kerf loss. Nonetheless, all of them regularly use machined materials having a high conductivity [9]. Recently, wire

Fig. 1 WEDM machine

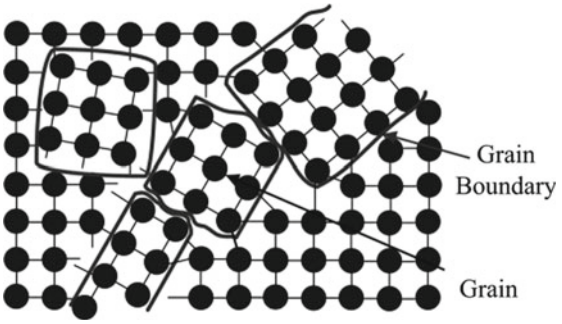

Fig. 2 Schematic grain structure of polycrystalline silicon

electric discharge machining (WEDM) has been used to machine semiconducting silicon. WEDM uses heat produced by electrodes consisting of conducting material strands to remove impurities. Because the machined device receives no cutting stress, the procedure includes non-contact manufacture and may therefore cut substances without stress distribution. WEDM is also the most acceptable option for machining operations and turning ultra-hard and complicated work components (Fig. 2).

3.2 Polysilicon Material Properties

See Table 2

Table 2 Attributes of polycrystalline silicon

Molecular weight	28.0080
Appearance	Silvery
Melting point	1414 °C
Boiling point	2900 °C
Density	2330.00 kg/m^3
Electrical resistivity	3–4 microhm-cm @ 0 °C
Electronegativity	1.8 Paulings
Poisson's ratio	0.0640–0.28
Specific heat	0.1680. Cal/g/K @ 25 °C
Thermal conductivity	1.49 W/cm/K @ 298.2 K
Thermal expansion	(25 °C) 2.6 μm m^{-1} K^{-1}
Young's modulus	51–80 GPa

3.3 Machining Method

A polycrystalline silicon ingot with dimensions of 125 × 125 × 10 mm as shown in Fig. 3a, b is cut using a thin single-strand zinc-coated 0.25 wire. As shown in Fig. 4, the cutting is done using a WEDM model-Sprintcut by Make Electronic Machine Tools Ltd. Silicon with a resistance of 0.5 cm is immersed in a tank of non-ionized dielectric fluid. This experiment examines seven WEDM parameters, each of which has five levels. Each of the seven parameters has five levels: T_{on}, T_{off}, IP, SGV, WF, Wt, and WP. For the experiment, one factor at a time method has been adopted. Table 3 displays the fixed and variable machining parameters that can be adjusted. Cutting speed (CS) and kerf width (KW) have been analyzed in this investigation. Machinists measure the cutting speed and kerf width with a Mitutoyo profilometer. Figure 2 depicts the grain structure of polycrystalline silicon.

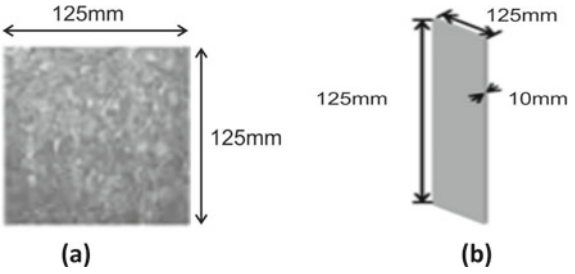

Fig. 3 **a**, **b** Schematics of specimen of silicon ingot

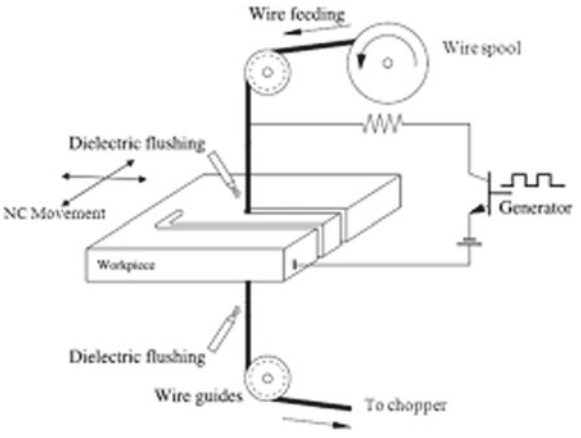

Fig. 4 Schematic of experimental setup

Table 3 Input parameters and their levels

Name	Units	Std. Dev.	Low	High
T_{on}	μs	0	110	125
T_{off}	μs	0	40	55
PC	A	0	25	45
SGV	V	0	35	55
WF	mm/min	0	2	6
WT	kg	0	2	6
WP	kg/cm^2	0	6	10
CS	mm/min	0.0234999	0.43	0.85

4 Experimentation

4.1 Objectives of the Study

1. The experimental inquiry examines wire electrical discharges manufacturing (WEDM) of fractured silicon ingots utilizing a Zn-coated brass wire as an electrode to determine significant technical response speed and depth of cut and kerf width.
2. To study the influence of processing factors on the slicing process to produce parametric circumstances that result in a high cutting rate, high productivity, and minimal kerf loss during machining by WEDM various process parameters are selected with the range of these parameters specified (PTON,PTOFF,PC,SGV,WF,WT and WP)

   PTON—pulse on time
   PTOFF—pulse off time
   PC—peak current
   SGV—spark gap voltage
   WF—wire feed
   WT—wire tension
   WP—water pressure

3. Using box Behnken's design of experiments (BBDOE), series are done to determine the influence of different model parameters such as T_{on}, T_{off}, IP, SGV, WF, WT, and WP.

4.2 Applications of Thin Wafers in Industry

The silicon wafers are widely used in semiconductor and electronics fabrication as integrated circuits (IC) and photovoltaic solar cells. The electronics industry uses

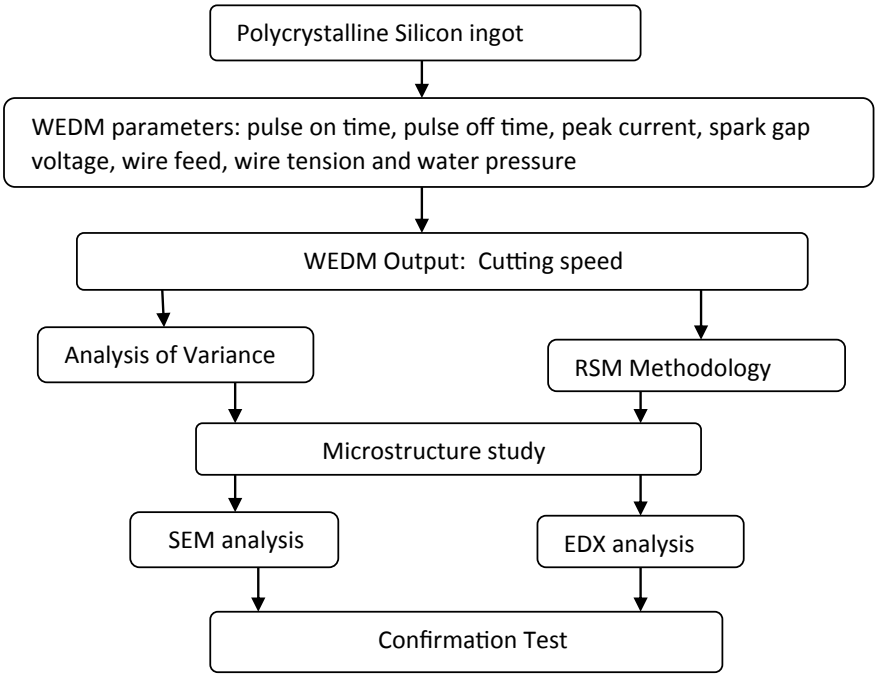

Fig. 5 Methodology of the present work

thin wafers of silicon in manufacture of IC and solar cells. These can also be used to manufacture electronic component, while it also serves as substrate for the production of semiconductors, transistors chips, and chipset. Silicon wafers are used in a variety of semiconductor applications, including air conditioners, rice cookers, CPUs, and many digital products such as mobile phones/smart phones and digital cameras.

4.3 Methodology Process

See Fig. 5

4.4 Model Adequacy and Analysis of Variance (ANOVA)

Three special assessments (SS, LOF, and models summation statistics) have been done for CS to determine the models' competence. The sum of squares (SS) shows a contrast here between sections' average prices and the mean percentage values. This test returns the biggest structured polynomials without encroached terms. The LOF

measures the data volatility across the estimated model. It is critical if the concept does not match the material accurately. The model description for the responses is shown in Table 1. The answer has been condensed to a quadratic system of equations. As demonstrated in Table 1, the RSM efficiently generates a box Behnken's design (BBD) matrix for both the experimental procedure and measured cutting terms of data. This investigation's design plan has chosen a set of three stages in format file (A to F), as seen in column 1. The encrypted form begins at 0 (the fundamental valuation) and extends to +1 (the upper value) and −1 (the lower value). After using the stepwise procedure, the statistical significance = 0.05 at the 95% confidence interval (CT) and the ANOVA for the simplified backwards quadratic models are calculated.

The LOF demonstrates that it is trivial compared to pure error (PE). Suitability is also determined by PR^2, AR^2, or adequate precision. It is relatively constant but has a larger than four-to-one ratio. ANOVA analysis is carried out with the assistance of the expert 12 applications. The following is a computation of CS's second-order quadratic regress extrapolation. The RSM model could efficiently be utilized to create the BBD vectors for a design of experiments and the measure process values of both CS and KW as shown in Table 3.2. The considerable value = 0.05 at the 95 CI and the ANOVA for the modified model equation are conducted using the consistent sampling approach. *P*-values of around 0.0500 are required to identify the existence of good organizational terms. In this instance, essential model variables are A, B, C, A^2, and B^2. The *F*-value of 64.21 suggests that the model fits the data. Lack with fit has an F-value of 2.63, showing that the lack without fit is insignificant compared to the standard error. There is also a 14.13% chance that a large *F*-value for lack of fit happens due to noise (Table 4).

$$\begin{aligned} \mathrm{CS} &= 26.1978 + 2.02786 * T_{\mathrm{on}} + -0.998251 * T_{\mathrm{off}} + -0.0924926 * I_{\mathrm{P}} \\ &\quad + -0.0782917 * \mathrm{SV} + -0.435903 * W_{\mathrm{S}} + -0.11125 * T_{\mathrm{on}} * \mathrm{SV} \\ &\quad + 0.00126488 * T_{\mathrm{off}} * I_{\mathrm{P}} + 0.00425 * T_{\mathrm{off}} * \mathrm{SV} + 7.65234 * T_{\mathrm{on}}^2 \\ &\quad + 0.00833617 * T_{\mathrm{off}}^2 + 0.000241309 * I_{\mathrm{P}}^2 + 0.0293403 * W_{\mathrm{S}}^2 \end{aligned}$$

4.5 Analysis for ANOVA for Cutting Speed (CS)

The ANOVA approach is used to estimate the relevance of all variables associated with answers at a 95% confidence interval. The importance of the variables on CS has already been quantified using *F* and *p* values. The *F* and *p* numbers are directly proportionate. In these other words, larger *F*-values and lower *p* values of 0.05 suggest that the individual factors are significantly associated with the answer characteristics at the 95% confidence interval. According to the ANOVA, the essential variables for CS are Ton, Toff, PC, and related relationships (Ton × Computer). The significance level of the CS for such LOF is 0.1413, indicating that this fits the data well.

Table 4 Experimental run order

		Factor 1	Factor 2	Factor 3	Factor 4	Factor 5	Factor 6	Factor 7	Response 1
Std	Run	A:PONT	B:POFFT	C:PC	D:SGV	E:WF	F:WT	G:WP	CS
		µs	µs	A	V	mm/min	kg	kg/cm^2	mm/min
38	1	118	48	45	35	4	4	10	0.51
4	2	118	48	35	55	6	2	8	0.54
41	3	110	48	25	45	2	4	8	0.49
58	4	118	48	35	45	4	4	8	0.51
25	5	110	40	35	35	4	4	8	0.65
28	6	125	55	35	35	4	4	8	0.75
53	7	118	40	25	45	4	6	8	0.59
20	8	118	55	35	45	6	4	6	0.47
21	9	118	40	35	45	2	4	10	0.62
42	10	125	48	25	45	2	4	8	0.72
60	11	118	48	35	45	4	4	8	0.54
33	12	118	48	25	35	4	4	6	0.54
5	13	118	48	35	35	2	6	8	0.51
8	14	118	48	35	55	6	6	8	0.49
18	15	118	55	35	45	2	4	6	0.51
17	16	118	40	35	45	2	4	6	0.67
11	17	110	48	35	45	4	6	6	0.52
61	18	118	48	35	45	4	4	8	0.52
52	19	118	55	45	45	4	2	8	0.57
43	20	110	48	45	45	2	4	8	0.49
27	21	110	55	35	35	4	4	8	0.48
39	22	118	48	25	55	4	4	10	0.46
7	23	118	48	35	35	6	6	8	0.52
24	*24*	*118*	*55*	*35*	*45*	*6*	*4*	*10*	*0.49*
29	25	110	40	35	55	4	4	8	0.52
51	26	118	40	45	45	4	2	8	0.68
14	27	125	48	35	45	4	2	10	0.75
40	28	118	48	45	55	4	4	10	0.49
30	29	125	40	35	55	4	4	8	0.78
56	30	118	55	45	45	4	6	8	0.57
22	31	118	55	35	45	2	4	10	0.54
36	32	118	48	45	55	4	4	6	0.56
47	33	110	48	45	45	6	4	8	0.49

(continued)

Table 4 (continued)

		Factor 1	Factor 2	Factor 3	Factor 4	Factor 5	Factor 6	Factor 7	Response 1
6	34	118	48	35	55	2	6	8	0.54
31	35	110	55	35	55	4	4	8	0.48
44	36	125	48	45	45	2	4	8	0.79
3	37	118	48	35	35	6	2	8	0.66
57	38	118	48	35	45	4	4	8	0.55
54	39	118	55	25	45	4	6	8	0.51
23	40	118	40	35	45	6	4	10	0.55
26	41	125	40	35	35	4	4	8	0.85
10	42	125	48	35	45	4	2	6	0.83
45	43	110	48	25	45	6	4	8	0.46
35	44	118	48	25	55	4	4	6	0.43
50	45	118	55	25	45	4	2	8	0.57
34	46	118	48	45	35	4	4	6	0.58
62	47	118	48	35	45	4	4	8	0.54
46	48	125	48	25	45	6	4	8	0.71
32	49	125	55	35	55	4	4	8	0.71
16	50	125	48	35	45	4	6	10	0.72
13	51	110	48	35	45	4	2	10	0.54
55	52	118	40	45	45	4	6	8	0.71
9	53	110	48	35	45	4	2	6	0.51
15	54	110	48	35	45	4	6	10	0.58
49	55	118	40	25	45	4	2	8	0.61
2	56	118	48	35	55	2	2	8	0.55
1	57	118	48	35	35	2	2	8	0.64
59	58	118	48	35	45	4	4	8	0.54
37	59	118	48	25	35	4	4	10	0.62
19	60	118	40	35	45	6	4	6	0.66
48	61	125	48	45	45	6	4	8	0.72
12	62	125	48	35	45	4	6	6	0.79

PONT—pulse on time;POFFT—pulse off time;PC—peak current;SGV—spark gap voltage;WF—wire feed,WT—wire tension,WP—water pressure

Additionally, the PR^2 value 0.9218 is consistent with AR^2 of 0.9491. As a result, the LOF is insignificant. The "PR^2" value of 0.9978 appears to be by the modified R^2 value of 0.9826, i.e., the discrepancy is less than 0.2, indicating extremely close compliance between measured and simulated values. The AP performs a signal-to-noise ratio calculation. A ratio more than four is necessary, and the proportion with

Table 5 ANOVA for CS (reduced quadratic after backward elimination)

Source	Sum of Squares	df	Mean square	*F*-value	*p*-value	
Model	0.6382	18	0.0355	64.21	<0.0001	Significant
A-T_{ON}	0.3528	1	0.3528	638.92	<0.0001	
B-T_{OFF}	0.0641	1	0.0641	116.01	<0.0001	
C-PC	0.0084	1	0.0084	15.28	0.0003	
D-SGV	0.0241	1	0.0241	43.58	<0.0001	
E-WF	0.0040	1	0.0040	7.25	0.0101	
F-WT	0.0067	1	0.0067	12.07	0.0012	
G-WP	0.0017	1	0.0017	3.02	0.0895	
AF	0.0018	1	0.0018	3.26	0.0780	
AG	0.0072	1	0.0072	13.04	0.0008	
BC	0.0021	1	0.0021	3.83	0.0570	
BD	0.0032	1	0.0032	5.79	0.0204	
BG	0.0055	1	0.0055	9.98	0.0029	
CD	0.0066	1	0.0066	11.97	0.0012	
CG	0.0078	1	0.0078	14.15	0.0005	
DF	0.0055	1	0.0055	9.98	0.0029	
A^2	0.1134	1	0.1134	205.40	<0.0001	
B^2	0.0222	1	0.0222	40.22	<0.0001	
F^2	0.0195	1	0.0195	35.25	<0.0001	
Residual	0.0237	43	0.0006			
Lack of fit	0.0226	38	0.0006	2.63	0.1413	Not significant
Pure error	0.0011	5	0.0002			
Cor Total	0.6620	61				

CS, which must be more greater than four, is seen to be 34.91, indicating a sufficient signal. As a result, this model may specify the system design (Table 5).

4.6 Main Factors and Their Interaction Effects on Cutting Speed (CS)

The primary impact graphs for CS are shown in Fig. 6. It is revealed that when the Ton rises from 110 to 125 μs, the CS grows by 43%. Additionally, when the Toff value is decreased between 55 and 40 s, the CS increases by 17%. When the Ton value increases, the spark strength causes both melting and vacuum distillation of the polycrystalline silicon substrate workpiece surface, resulting in craters occurring on the surface texture. However, a drop in the Toff value increases the CS value. Reduced Toff values result in an increase in the number of discharges throughout a

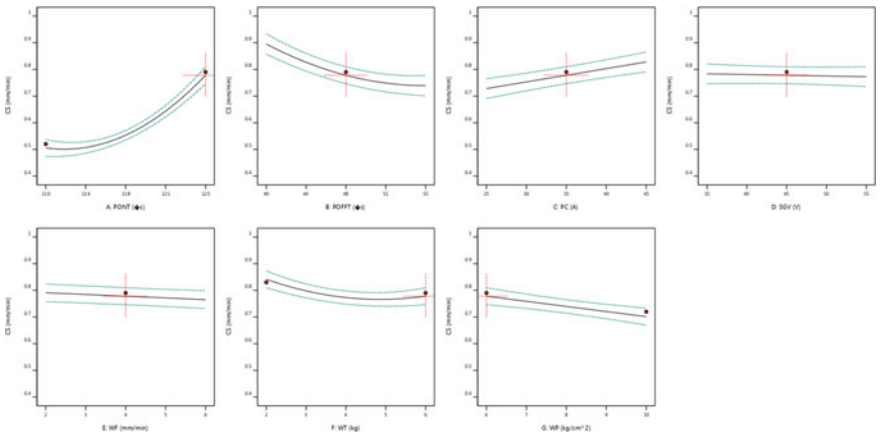

Fig. 6 Interaction effect for machining parameters

specific period which means that more expelled debris from the surface roughness will not be flushed down the drain effectively and will accumulate on the surface, resulting in higher CS rates. The dielectric fluid stream will not be fully deionized, resulting in dangerous sparks. While raising the PC value between 25 and 50 A, increases the CS by 25%, over 45A which results in electrode wire breaking. The graphs exhibit a continuous pattern.

The simultaneous interactions of numerous components begin with constructing a suitable response surfaces graph with each response, followed by the evaluation of a set of organizational circumstances. In the instance of CS, the study result reveals that by raising the elements till the value hits the center value, the CS value is improved. CS rises from 0.43 to 0.85 mm/min as reported. The relationships between Ton and PC rise from 0.43 to 0.85 mm/min, indicate that the CS value rises similarly. As a result, it is seen that increasing the T_{on} and PC values leads to a significant increase in CS. At greater Ton levels, an increase in CS is observed. Combining these interactions results in increased sparks duration, dissolving, and dielectric breakdown of the material, all of which contribute to a rise in the CS value. The perturbations plot visually describe the elements' influence at a given reference point. The response sheet can be seen and charted by varying just one element over the ranges and maintaining all other variables constant. These components exhibit a high slope or a unique curve for the response discussed before.

4.7 Mathematical Model and ANOVA for CS

Using the optimum signal-to-noise ratio approach, this article uses an independent *t*-test (ANOVA) to determine the ideal solution for machining polycrystalline silicon materials. The "*F*-value" of 64.21 indicates that somehow this is significant of the

Table 6 ANOVA analysis for cutting speed

Std. Dev.	0.0235	R^2	0.9641
Mean	0.5885	Adjusted R^2	0.9491
C.V. %	3.99	Predicted R^2	0.9218
		Model precision	34.9310

model. Model terms are considered "substantial" when $P > F$ and is less than 0.0500. Except for AB and AC, each variable is a vital model element. The "lack of fit F-value" of 2.63 is insignificant compared to "pure error," indicating that the model fits well. The "Pred R^2" value 0.9218 is consistent with the "Adj R^2" value 0.9491. R^2 is 0.9218, which is excellent since it approaches 1, whereas PRESS is 0.0518, which is acceptable for a strong signal. Model quality is 34.931, suggesting an adequate signal-to-noise proportion for signals measurement. Sufficient precision exceeds four. As a result, this model travels around the design process. Table 6 illustrates an ANOVA on CS during milling monocrystalline silicon billets substrate, demonstrating that the model matches the observations satisfactorily. The disturbance graph on CS for amorphous silicon ingot composition in Figs. 7 and 8 indicates that all input procedure factors significantly affect the responses CS. This package figure for power transformations on CS using crystalline semiconductor materials suggests that the optimal lambda equals 1.46, the current lambda is 1.0, and the confidence interval is (0.5200, 2.27) (Figs. 9, 10).

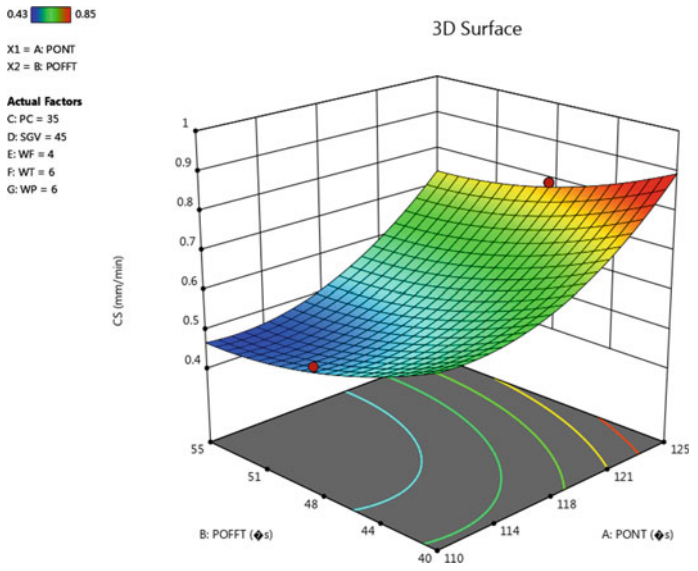

Fig. 7 3D response surface interaction 3D graph of T_{on} and T_{OFF} with CS

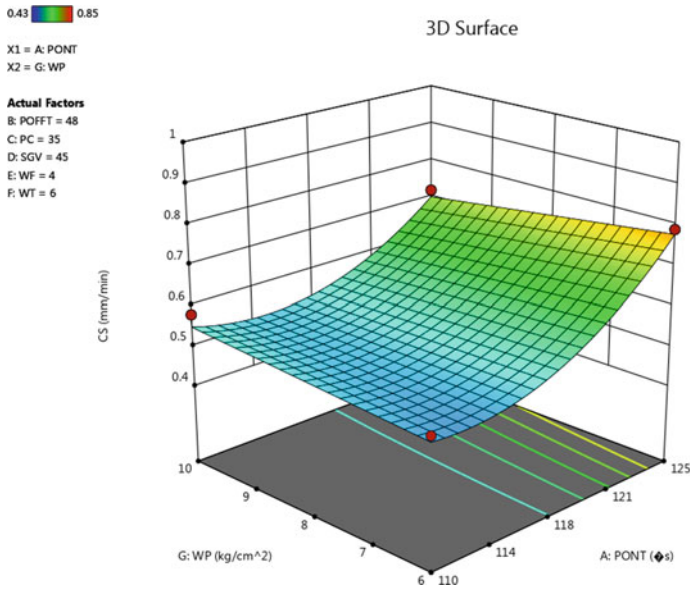

Fig. 8 3D response surface interaction 3D graph of Ton and WP with CS

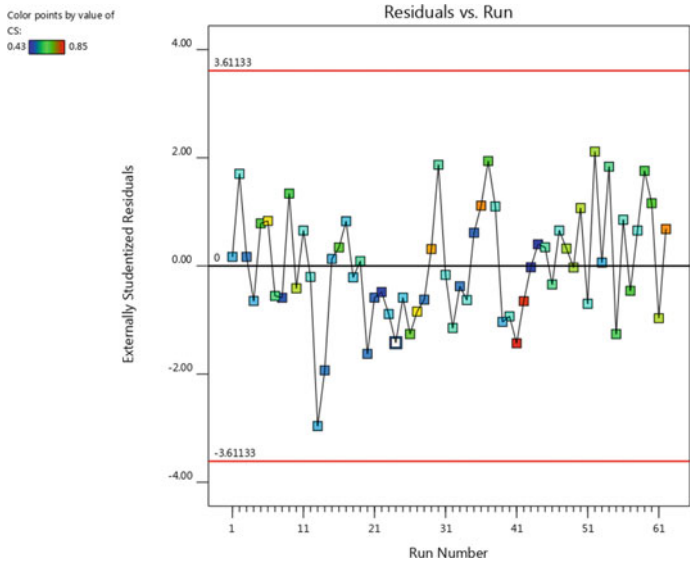

Fig. 9 Predicted versus run plot for CS

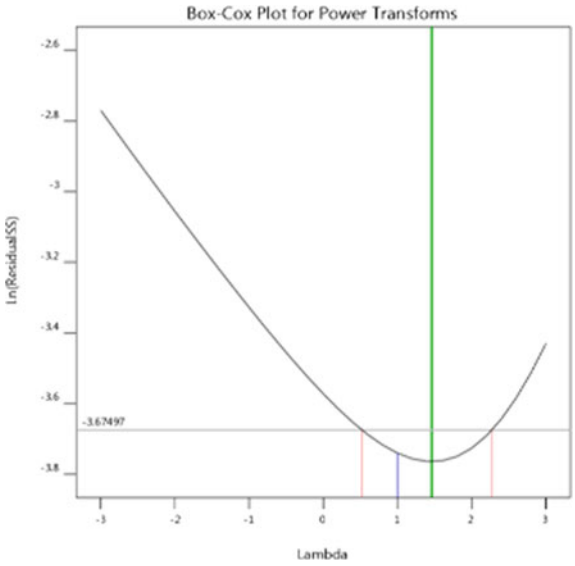

Fig.10 Box cox plot for CS

5 Analysis of EDX and SEM Testing

The The Energy Dispersive X-ray technique generates the elements transfer (in percent) between the instrument and the WEDM surfaces. A sample of five EDX spectra from random experiments are obtained in this investigation. C, O, Si, Fe, Na, and K are the most abundant elements on the WEDM ground using the EDX power spectrum. The presence of element C (46.26–56.83) enhances the toughness of the polycrystalline semiconductor materials, reducing the object's fracture toughness and weldability. And from the other extreme, this oxygen content on the WEDM interface is primarily due to the degradation of the insulators utilized in operation and the combustion and mixture of debris at elevated temperatures. More spark velocity results in increased metal melting from the electrodes that are not entirely washed away by the dielectric fluid. The O concentration ranges between (21.74–22.31%), and indeed the concentration of O is related to the increased plasma channels temperature caused by the longer T_{off} value.

Additionally, the data conducted (30.89–40.35%) contributes to the increased T_{on} value, which improves the surface characteristics of the crystalline semiconductor materials. During the processing of the WEDM surfaces with Zn-covered brass wire, the accumulation of Zn (0.02–2.12%) and Si (0.12–0.52%) components is discovered. The data points and the frequencies histograms are examined for all replies. The findings indicate a clear association between the practical and calculated values, which is near 0.788 (Figs. 11 and 12).

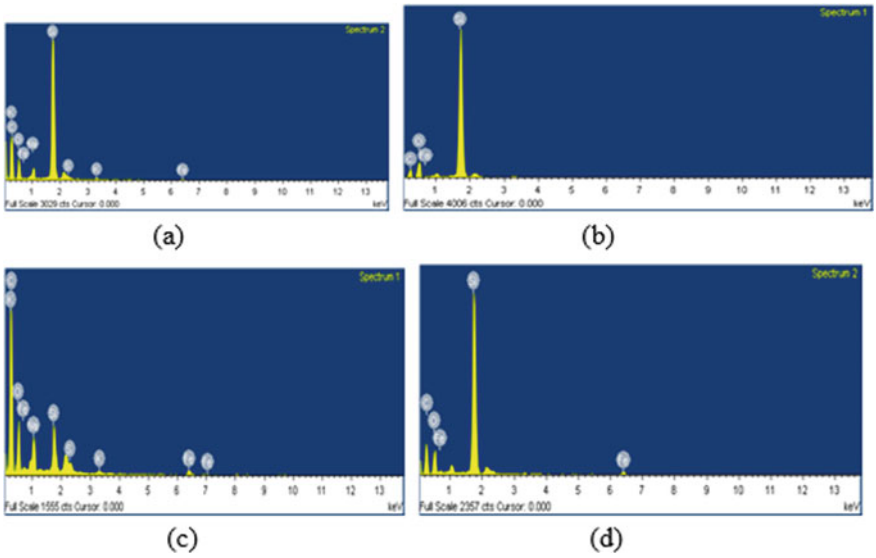

Fig. 11 Energy dispersive X-ray (EDX) analysis of machined samples

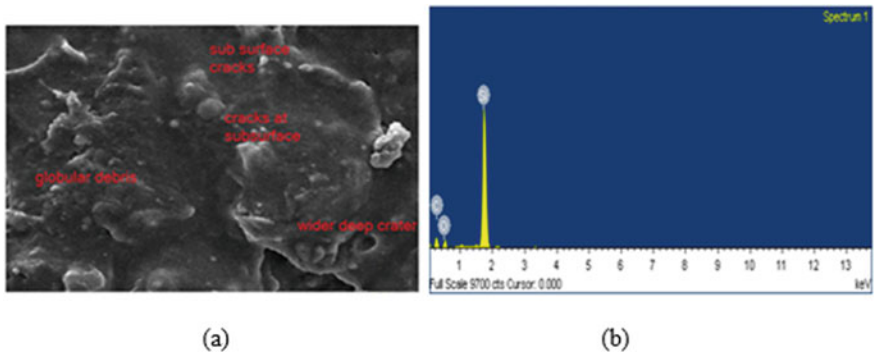

Fig. 12 SEM micrograph of polycrystalline silicon specimen (before machining)

5.1 Numerical Optimization

The quantitative optimization technique uses models to explore the factor space to accomplish numerous goals. The performance goals are to maximize, reduce, target, and stay within the band. Weight values have been allocated or emphasized to highlight the upper/lower boundaries or the desired importance. In this study, a goal of achieving a minimum CS of 0.85 is established, and weights for CS are obtained (lower weight = 0.2, higher weight = 0.8). Additionally, it can be shown that the priority of each objective may be adjusted from (+++) to five locations (+++++). A

Table 7 Goals and importance of numerical optimization

Name	Goal	Lower limit	Upper limit	Lower weight	Upper weight	Importance
A:T_{on}	Is in range	110	125	1	1	3
B:T_{off}	Is in range	40	55	1	1	3
C:PC	Is in range	25	45	1	1	3
D:SGV	Is in range	35	55	1	1	3
E:WF	Is in range	2	6	1	1	3
F:WT	Is in range	2	6	1	1	3
G:WP	Is in range	6	10	1	1	3
CS	Is target = 0.78	0.43	0.85	0.2	0.8	5

multi-objective optimization function called the incremental model is used to find the ideal approach. After using the optimum parameters, the twenty most optimum solutions are produced. The overall acceptability is between 0.953 and 1, and close to 1 (Table 7).

6 Results and Discussion

This study uses a BBD-based RSM to optimize the CS of silicon solar ingot material during the WEDM process. The input variables T_{on}, T_{off}, SGV, WT, WF, PC, and WP play a vital role in determining the ideal response setting. The ANOVA approach is used to estimate the importance of variables associated with all answers at a 95% confidence interval. As a result, a reduced quadratic (multiplication) formula has been produced for each answer. Therefore, a value of 1 is used to optimize all model parameters concurrently. The following findings have been reached from this study:

1. It is observed that, as the value of T_{on} increases the value of KW increases by 33% and during the decrease of T_{off} the value of KW value increases by 36%. With increase in PC, the value of KW decreases by 25%. With the increase in value of SGV, the value of KW reduces by 7%. With the effect of increase in value of WT, the kerf width (KW) reduces by 11%. With the increase in WP from 4 to 10 kg/cm^2, there is marginal effect on KW.
2. With the increase in value of SGV, the width of spark decreases, and electric field strength also decreases. Decreasing SGV that develops the narrow down the spark gap leads to a greater number of sparks per unit time. It increases the cutting speed from 0.452 to 0.485 mm.
3. It is observed that the increase of WF from 2 to 6 m/min increases the cutting speed from 0.28 to 0.56 mm/min whereas kerf width also increases from 0.359 to 0.384 mm. WF is the rate at which wire is fed continuously for sparking. Higher

Table 8 Adequacy checking model of cutting speed (CS)

Sequential model sum of squares						
Source	Sum of Squares	d*f*	Mean Square	*F*-value	*p*-value	
Mean versus total	21.48	1	21.48			
Linear versus mean	0.4617	7	0.0660	17.79	< 0.0001	
2FI versus linear	0.0453	21	0.0022	0.4600	0.9675	
Quadratic versus 2FI	**0.1377**	**7**	**0.0197**	**29.85**	**< 0.0001**	**Suggested**
Cubic versus quadratic	0.0160	21	0.0008	3.36	0.0911	Aliased
Residual	0.0011	5	0.0002			
Total	22.14	62	0.3571			
Lack of FIT tests						
Linear	0.1991	49	0.0041	17.93	0.0021	
2FI	0.1538	28	0.0055	24.23	0.0011	
Quadratic	**0.0160**	**21**	**0.0008**	**3.36**	**0.0911**	**Suggested**
Cubic	0.0000	0				Aliased
Pure error	0.0011	5	0.0002			
Model summary statistics						
Source	Std. Dev	R^2	Adjusted R^2	Predicted R^2	Press	
Linear	0.0609	0.6975	0.6583	0.5994	0.2652	
2FI	0.0685	0.7660	0.5675	0.0957	0.5986	
Quadratic	**0.0257**	**0.9741**	**0.9393**	**0.8256**	**0.1154**	**Suggested**
Cubic	0.0151	0.9983	0.9791		*	Aliased

Bold significance provides a Quadratic model is selected based upon Design Software 12 and the Modelling is done using this software (ANOVA analysis). The significance is that it provides a way to model a relationship between two set of variables. The result is regression equation that can be used to make predictions about data. This statistical technique is used to find the equation of the parabola that best fits a set of data

Table 9 Process parameters and their range

S. No.	Name of parameter	Symbol	Range
1	Pulse on time	T_{ON}	110–130 µs
2	Pulse off time	T_{OFF}	45–55 µs
3	Peak current	*I*p	20–60 A
4	Spark gap voltage	SV	35–60 V
5	Wire feed	WF	2–15 m/min
6	Wire tension	WT	2–6 kg
7	Flushing pressure	*W*p	5–20 kg/mm^2

the wire feed rate, there are more number of sparking that elevates the cutting speed and kerf width.

4. As the WT grows (2–6 kg), the cutting speed and kerf width slow down. The reason for this is that increasing WT reduces wire deflection due by dielectric and discharge pressure. This will reduce the kerf width even further. As previously said, cutting speed indicates how quickly it will take to maintain a tiny gap between the wire and the work material. A narrow gap would make it difficult for dielectric fluid to pass through and flush machining debris away. In this scenario, when WT is low, the wire bends more, causing the gap to widen. The larger gap allows more dielectric fluid to enter, removing dirt and increasing cutting speed.
5. With an increase in water pressure (from 4 to 15 kg/cm^2), the cutting speed improves (from 0.37 to 0.59). Higher water pressure quickly cools the wire and workpiece, removing any debris in the process. With increased water pressure, the kerf width (0.332 to 0.361 mm) is similarly influenced. As a result of faster debris removal between gaps, a wider kerf width and more stable machining are achieved.
6. It is discovered that as Ip increases from 25 to 45 A, the cutting speed increases from 0.44 to 0.72 mm/min. Higher peak currents are known to cause greater discharge energy across the wire, which causes more melting and evaporation of material, resulting in quicker cutting speeds. When the value of IP exceeds 49 A, the wire breaks, halting the machining process. The greater the amount of IP, the greater the material damage between the wire and the cutting of the silicon ingot. As the IP has increased, so has the cut. The width increases as the kerf is increased.

7 Conclusions

1. The highest cutting speed (0.77 mm/min) is obtained at 124 μs (T_{on}) and at 25 μs (T_{off}). Due to the increase of T_{on}, the discharge energy between cathode and anode increases which expedites the melting and evaporating of materials for a longer period of time
2. Highest kerf width (0.485 mm) is obtained with 25 VSGV.
3. The SEM appearance of polycrystalline silicon castings composition reveals wavy patterns, tiny fissures, broad and deep fractures, and gelatinous mass of debris with higher T_{on} and PC values. The experiment results indicate that increasing the T_{on} and PC values increases the kerf width of machined samples. In addition, groundwater fractures and entrance cracks have been incorporated into irregular circular debris, including craters.
4. This work determines that the WEDM can be used to process highly conductive material with a conductivity of 2–3 and discovers an excellent link between the stated process variables and the required WEDM characteristics which supports the use of RSM.

5. When the wire supply is low, the surface finish is more excellent, and the surface quality reduces when the wire feed increases. Therefore, conjunction of a longer pulse on time (110 s) and a shorter pulse out time (40 s) in conjunction with a wire flow rate of 6 mm/min is found to give better results.
6. The cutting parameters rise as the pulse on time changes. With an increase in pulse duration, the energy provided rises, causing more particles to impact the workpiece. Due to the increased power, the projectiles penetrate deeper into the workpiece, resulting in thick corrosion.
7. The SEM microstructure of crystalline silicon substrate ingots with increased T_{on} and IP values exhibit a wavy shape with many microcracks, craters, and debris agglomerates. At more excellent T_{on}, IP, and WF values, it is discovered that the surface finish of manufactured samples decreases significantly. The appearance of fissures under the surface shows that the majority of penetration fissures have been incorporated into irregular round debris, including craters. This is primarily due to the rapid subsequent heat treatment of the spark and deionized waters in sequence.

Appendix

Factor	Name	Level	Low Level	High Level	Std. Dev	Coding
A	PONT	113.72	110.00	125.00	0.0000	Actual
B	POFFT	40.00	40.00	55.00	0.0000	Actual
C	PC	45.00	25.00	45.00	0.0000	Actual
D	SGV	47.26	35.00	55.00	0.0000	Actual
E	WF	2.83	2.00	6.00	0.0000	Actual
F	WT	5.58	2.00	6.00	0.0000	Actual
G	WP	7.01	6.00	10.00	0.0000	Actual

Table 10 Optimal solution for cutting speed (desirability function)

Number	PONT	POFFT	PC	SGV	WF	WT	WP	CS	Desirability	
1	113.740	40.005	45.000	47.372	2.736	5.518	7.001	0.659	0.952	Selected
2	113.731	40.002	45.000	47.117	2.734	5.475	7.010	0.658	0.952	
3	113.695	40.000	44.999	47.152	2.794	5.485	7.051	0.657	0.952	
4	113.649	40.005	44.998	46.358	3.026	5.336	6.823	0.657	0.952	
5	113.654	40.001	45.000	46.345	2.915	5.139	7.131	0.646	0.952	
6	113.771	40.011	44.999	47.234	2.544	5.392	7.069	0.656	0.952	
7	113.611	40.000	44.997	46.119	3.094	5.049	6.995	0.647	0.952	
8	113.686	40.414	44.046	46.877	2.702	5.999	7.161	0.656	0.951	
9	113.681	40.000	44.999	46.075	2.726	5.102	6.623	0.660	0.951	
10	113.928	40.516	44.359	47.528	2.000	5.999	7.119	0.663	0.950	
11	113.513	40.001	42.720	46.013	2.693	6.000	6.869	0.664	0.950	
12	113.713	40.087	45.000	46.828	2.687	4.887	6.775	0.651	0.950	
13	113.474	40.001	44.733	44.529	3.482	4.643	7.144	0.636	0.949	
14	113.490	40.000	45.000	46.145	3.840	4.352	6.895	0.637	0.949	
15	113.540	40.003	44.999	47.438	3.727	4.519	6.661	0.643	0.949	
16	113.945	42.625	44.999	49.400	2.928	6.000	6.838	0.630	0.949	
17	113.676	40.000	45.000	49.502	3.196	4.831	7.121	0.637	0.949	
18	113.446	40.448	42.011	45.976	2.834	6.000	7.445	0.638	0.949	
19	113.682	40.290	44.997	44.286	3.002	5.997	7.153	0.661	0.949	
20	113.376	40.000	44.304	45.167	3.654	4.094	7.158	0.630	0.948	

Table 11 Properties of workpiece material

Material	Chemical composition	Hardness (HRC)	Thickness (mm)
Polycrystalline silicon	C-1.0%, Si-1.31% P-0.31%, S-0.042%	58	10

Table 12 Properties of brass wire electrode

Material	Chemical composition	Hardness (VH)	Tensile strength	Conductivity (% IACS)
Brass	Cu 63% Zn 37%	255	905 N/mm^2	22%

References

1. Luque A, Hegendus S (2003) Hanbook of photovoltaic science and engineering, vol 176, 1st edn. Wiley, New York, pp 223–225
2. Muthuraman V, Ramakrishan R (2011) Soft modelling of wire electrical discharge machining of WC-Co composite. Advanced Materials Research 335–336:535–540
3. Uno Y, Okada A, Okamoto Y, Hirano T (2002) High performance slicing method of monocrystalline silicon ingot by wire EDM. In: Proceedings of the 10th international conference on precision engineering (ICPE), pp 219–223

4. Sreejith PS, Udupa G (2001) Recent advances in machining of silicon wafers for semi conductor applications. Int J Advan Manuf Technol 17:157–162
5. Peng WY, Liao YS (2003) Study of electrical discharge machining technology for slicing silicon ingots. J Mater Process Technol 140:274–279
6. Takion H, Ichinohe T, Tanimoto K, Yamaguchi S, Nomura K, Kunieda M (2003) Cutting of polished single-crystal silicon by wire electrical discharge machining. Precis Eng 28(3):314–319
7. Takion H, Ichinohe T, Tanimoto K, Yamaguchi S, Nomura K, Kunieda M (2005) High-quality cutting of polished single-crystal silicon by wire electrical discharge machining. Precis Eng 29(4):423–430
8. Shah A, Mufti N, Rakwal D (2009) Material removal rate, Kerf, and surface roughness of tungsten carbide machined with wire electrical discharge machining. J Mater Eng Perform. https://doi.org/10.1007/S11665-010-9644-y
9. Yu PH, Lin YX, Lee HK, Mai CC, Yan BH (2014) Improvement of wire electrical discharge machining efficiency in machining polycrystalline silicon with auxiliary pulse voltage supply. Int J Adv Manuf Technol 57(9–12):991–1001
10. Singh N, Kumar P, Goyal K (2014) Experimental investigation of WEDM variables on surface roughness of AISI D3 die steel by using two cryogenically treated different wires. Manuf Sci Technol 2:20–25
11. Luo YF, Chen CG, Tong ZF (1992) Investigation of silicon wafering by wire EDM. J Mater Sci 27(21):5805–5810
12. Rakhwal D, Bamberg B (2009) Slicing cleaning and kerf analysis of germanium wafers machined by wire electrical discharge machining. Journal of Material Processing Technology 209:3740–3751
13. Satyanaryana K, Rajkiran K (2020) Role of cryogenic in wire cut EDM process, E3S Web of conferences, ICEMD 2020, vol 184, p 01067
14. Dongre G, Singh R (2015) Response surface analysis of slicing of silicon ingots with focus on photovoltaic application. Material Science and Technology, 16: 624–652. ISSN: 1091–0344 print/1532–2483 online, https://doi.org/10.1080/10910344.2012.731952
15. Joshi K, Sharma G (2014) Modeling of wire EDM slicing process for silicon. In: 5th International and 26th all India manufacturing technology, design and research conference (AIMTDR 2014). 12–14 Dec 2014, IIT Guwahati, Assam, India
16. Punturat J, Tangwarodomnukun V (2014) Surface characteristics and damage of monocrystalline silicon induced by wire-EDM. Appl Surf Sci 320:83–92
17. Mai C, Chang M (2015) High efficiency slicing of silicon ingots by flat wire-EDM. In: The 14th IFToMM World Congress, Taipei, Taiwan, 25–30 Oct 2015
18. Murugan C, Kumar S (2020) Investigations on electric discharge machining behaviour of Si_3N_4-TiN ceramic composite, silicon, 24 Nov 2020. https://doi.org/10.1007/s12633-020-00848-w
19. Verma A, Singh S (2020) Parametric optimization of silicon slicing using wire electro discharge machining. Materials Today Proceedings, 2214–7853/2020, Elsevier Ltd
20. Tosun N, Cogun C (2002) Analysis of wire erosion and workpiece surface roughness in wire electrical discharge machining. Proc Inst Mech Eng Part B: J Eng Manuf 217:633–642
21. Joshi SS, Das S (2004) Modeling of spark erosion rate in micro- wire EDM. Int J Adv Manuf Technol 48:581–596
22. LeI WM, Liao YS (2020) Adaptive control of the WEDM process using a self-tuning fuzzy logic algorithm with grey prediction. Int J Adv Manuf Technol 34:527–537
23. Kumar S, Singh S, Singh A (2011) Some investigations into machining of AISI D2 tool steel using wire electro discharge machining (WEDM) process. Mater Today Proc 5(11):24347–24357. https://doi.org/10.1016/j.matpr.2018.10.230
24. Mukherjee R, Chakarboraty S, Samanta S (2012) Selection of wire electric discharge machining process parameters using nontraditional optimization algorithms. Appl Soft Comput 12:2506–2516

25. Roy A, Narendranath N, Pramanik A (2020) Effect of peak current and peak voltage on machined surface morphology during WEDM of TiNiCu shape memory alloys. J Mech Sci Technol 34:3957–3961
26. Shandilya P, Bisaria H (2019) Processing of curved profiles on ni-rich nickel–titanium shape memory alloy by WEDM. J Mater Manuf Proc 34(12)
27. Kearns JK (2019) Silicon single crystals. In: Single crystals of electronic materials, pp 5–56

Gold/ZnO Interface-Based D-Shaped PCF Surface Plasmon Resonance Sensor with Micro-Openings, Analytic Designing, and Some Applications

Vinod Singh, Deepak Kumar, and Mukta Sharma

Abstract This paper proposed the D-shaped photonic crystal fiber-based surface plasmon resonance sensor with high sensitivity used for sensing in medical and biochemical fields. The plasmonic material taken for this work is gold which is known for its stable configuration and the photocatalyst taken is ZnO. The confinement losses have been calculated for different refractive indices and different gold and ZnO layers. The refractive index for the analyte was varied from 1.31 to 1.36, and the wavelength was varied from 1.5 to 1.7 μm. The thickness of the gold layer is taken near about 60 nm, and the thickness of ZnO is taken around 15 nm. The wavelength sensitivity of the sensor is 1325 nm RIU^{-1}, and the maximum amplitude sensitivity of the sensor is 240.2 RIU^{-1}. With the thorough study of literature, it is deduced that both the sensitivities are the highest for this range of refractive indices among the existing PCF-SPR-based sensors. The designed sensors can further be used for sensing applications in the medical field for the detection of diseases, as immunosensors, and for the detection of harmful compounds.

Keywords Biosensors · Thin films · Material surfaces · Surface plasmon resonance · Photonic crystal fibers

1 Introduction

In recent years, many advancements have been made in sensing technologies. The sensing industries have switched toward the more flexible, highly sensitive, and cost-efficient types of sensors. The surface plasmon resonance-based sensors are evolving as the best types of photonics sensors nowadays with a wide range of applications

V. Singh (✉) · D. Kumar · M. Sharma
Department of Applied Physics, Delhi Technological University, New Delhi 110042, India
e-mail: vinodsingh@dtu.ac.in

D. Kumar
e-mail: karndeepak11@gmail.com

M. Sharma
e-mail: muktasharma2912@gmail.com

K. Geetha et al. (eds.), *Recent Trends in Materials*, Springer Proceedings in Materials 18, https://doi.org/10.1007/978-981-19-5395-8_27

such as food safety [1], medical diagnostics [2], liquid detection [3, 4], and biochemical sensing [5]. Surface plasmon resonance can be defined as the phenomenon of collection of electrons at the surface of the dielectric medium, whenever a polarized light falls on it [6]. To achieve the resonance condition, it is important that the momentum of the incident light is high. This can be achieved by passing the light through an optical fiber, a plasmonic crystal fiber, or a prism [6]. Owing to the traditional methods, prisms were used to achieve SPR, and these methods were used to achieve high absorption loss curves. However, there are some limitations to these types of sensors which include low flexibility, complex design structures, bulky designs, and limited spectral response.

The photonic crystal fibers are used to deal with the above limitations. This is because the PCF is more robust, cost-effective, and compact which makes it a more suitable option to be used as the base material. The PCF when decorated with the plasmonic material layer helps the sensor to achieve the surface plasmon resonance and hence, the sensing properties are observed more efficiently. There are various types of photonic crystal fibers, such as D-shaped, internal metal coating, external metal coating, microfluid channel [7]. In the SPR-based PCF sensors, it is extremely difficult to coat the air holes internally which is resolved by the use of an external type of coating-based sensors. However, in practical applications, both types of sensors are difficult to achieve. These disadvantages are overcome by the use of the D-shaped SPR-based PCF sensors which have a thin layer deposited at the top of a silica-filled multiple air holes structure with analyte present at the external layer. The D-shaped sensors are known for their high sensitivities [8]. The thin layer is basically made up of gold or silver. Gold is chemically stable and is known for high resonance peaks as compared to the other plasmonic materials. Silver on the other hand shows a sharp resonance peak but can be oxidized easily [9]. Silver, on its use with a layer of graphene or aluminum, does not get oxidized and gives good results. The range for size of the layer of these plasmonic materials, abbreviated as d, should be of the order less than the wavelength of the incident light. Usually, the relation $d \ll \lambda$ is followed during the designing of the geometry of the D-shaped SPR sensors [10]. In order to catalyze the SPR phenomenon, some metal oxides such as ZnO, TiO_2, CdS, and SrO_2 are used as photocatalysts. ZnO, with a wide energy gap, i.e., of 3.37 eV and its chemical stability on interaction with the liquid analyte, high optical gain, and large binding kinetic energy, ZnO is the best metal oxide to act as the photocatalyst for SPR-based sensing [7]. ZnO has a wide energy gap of electrons, i.e., 3.37 eV, and it shows high stability when interacting with the analyte. Thus, analyzing the refractive index of ZnO and the behavior of the sensor at different refractive indices values becomes even more important. In biosensing, there is a requirement for the detection of many harmful gases and also for the detection of various diseases. It senses the phenol-based compounds and also detects the antibodies or antigen thus acting as immunosensors [11].

In this paper, a D-shaped SPR-based PCF sensor has been designed with a dual-core structure. As a part of the core, a thin layer of gold has been taken above which, a layer of ZnO has been taken which is acting as the photocatalyst. For the cladding, an analyte of refractive index 1.39 has been taken. There are 14 air holes

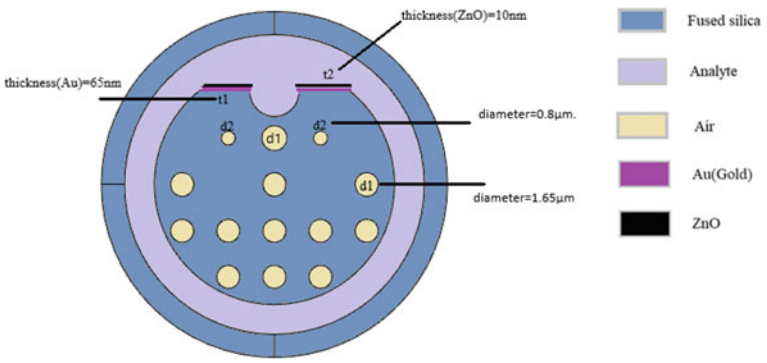

Fig. 1 Schematic diagram for the D-shaped SPR sensor

with varying diameters present with fused silica in order to ensure better coupling between the core and the surface plasmon polaritons mode. The structure has been designed and studied in COMSOL Multiphysics and the operating wavelength has been varied for different refractive indices. The confinement loss curves have been plotted with a variation with wavelength. The wavelength sensitivity of the sensor is 1325 nm RIU^{-1}, and the maximum amplitude sensitivity of the sensor is 240.2 RIU^{-1}.

2 Designing and Modeling

2.1 Theoretical Modeling

The design for the model has been represented in Fig. 1.

In the figure, the different materials have been represented which have been taken for each part of the sensor.

For designing the sensor, the COMSOL Multiphysics simulation has been used. The diameter of the air holes is 1.65 μm. The array has been built for air holes so as to construct 12 air holes of equal diameter and two air holes with a smaller diameter of 0.8 μm. The principle behind the presence of the air holes in this structure is that the air holes lead to a significant improvement in the coupling between the surface plasmon polaritons and core modes. The thickness of the gold layer is 65 nm, and the thickness of the ZnO layer is 10 nm.

2.2 Numerical Modeling

The fused silica has been filled all around the air holes and is acting as the background material. In order to calculate the refractive index of silica, the Sellmeier equation is

Table 1 Values of Sellmeier's constants for silica

b_1	b_2	b_3	c_1 (μm^2)	c_2 (μm^2)	c_3 (μm^2)
0.6961663	0.4079426	0.8974794	4.6791482×10^{-3}	1.351206×10^{-2}	97.934

Table 2 Values of Sellmeier's constants for ZnO

A	B	C (nm)	D	E (nm)
2.0065	1.5748×10^6	10^7	1.5868	260.63

used [5], which is given by

$$n(\lambda) = \sqrt{1 + \frac{{b_1}^2}{\lambda^2 - c_1} + \frac{{b_2}^2}{\lambda^2 - c_2} + \frac{{b_3}^2}{\lambda^2 - c_2}} \tag{1}$$

where λ is the operating wavelength and $b_1, b_2, b_3, c_1, c_2, c_3$ are the Sellmeier's constants. The values of the Sellmeier's constants for silica can be tabulated as (Table 1):

A layer of ZnO has been taken as photocatalyst, and for determining the refractive index of ZnO, the following form of the Sellmeier equation has been used,

$$n(\lambda) = \sqrt{A + \frac{B\lambda^2}{\lambda^2 - C^2} + \frac{D\lambda^2}{\lambda^2 - E^2}} \tag{2}$$

where λ is the operating wavelength and A, B, C, D, E are the Sellmeier's constants. The values of the Sellmeier's constants for ZnO can be tabulated as (Table 2):

The minimum operating wavelength for the model has been taken as λ =1.5 μm; maximum operating wavelength for the model has been taken as λ =1.72 μm. This range of operating wavelength has been opted to keep it comparable to the dimensions of the air holes and to observe the maximum sensitivity.

The confinement loss for the sensor can be calculated from the equation [13],

$$\propto_{\text{loss}} = 8.686 \times (2\pi\lambda) \times \text{Im}(n_{\text{eff}}) \times 10^4 \text{dB/cm} \tag{3}$$

where λ is the operating wavelength and n_{eff} is the net effective refractive index.

The wavelength and the amplitude sensitivities can be calculated from the confinement loss curve.

For calculating the wavelength sensitivity, the following equation is used [14],

$$S_\lambda = \frac{\Delta\lambda_p}{\Delta n_a} \tag{4}$$

where $\Delta\lambda_p$ is the change in the peak resonant wavelength corresponding to change in refractive index of analyte.

For calculating the amplitude sensitivity, the following equation is used [15–17],

$$S_\lambda = -\frac{1}{\alpha(\lambda_{n,a})}\frac{\partial\alpha(\lambda_{n,a})}{\partial n_a}\text{RIU}^{-1} \tag{5}$$

where $\alpha(\lambda_{n,a})$ is the confinement loss and $\partial\alpha(\lambda_{n,a})$ is difference of two consecutive loss spectra and ∂n_a is the corresponding change in refractive index.

3 Simulation and Results

3.1 Model Results

The concentration of the electric field in the various modes can be represented by Fig. 2. Figure 2a and b represent the core and the SPP modes of the sensor. Figure 2b and c represent the *x*-polarized and *y*-polarized electric field modes and Fig. 2d represents the *y*-polarized coupling mode.

3.2 Phase Matching

When the light is incident on the surface of ZnO, most of the free electrons get excited, and this excitation makes the evanescent field to be guided from the *x*-polarized to the *y*-polarized modes. The resonance is then achieved at maximum power. The peak for the curves is achieved, and this condition is termed as phase matching. The SPP modes can be represented by plotting the confinement loss Eq. (3), the net effective mode index for core and SPP modes. The following graph (Fig. 3) is showing the dispersion relation curve for the core and SPP modes.

3.3 Calculation of Wavelength and Amplitude Sensitivities

The confinement losses as calculated from Eq. (3) for different refractive indices of analyte are varied with respect to the wavelength. The confinement loss curves thus plotted are shown in Fig. 4 which can further be used for the measurement of the wavelength sensitivity.

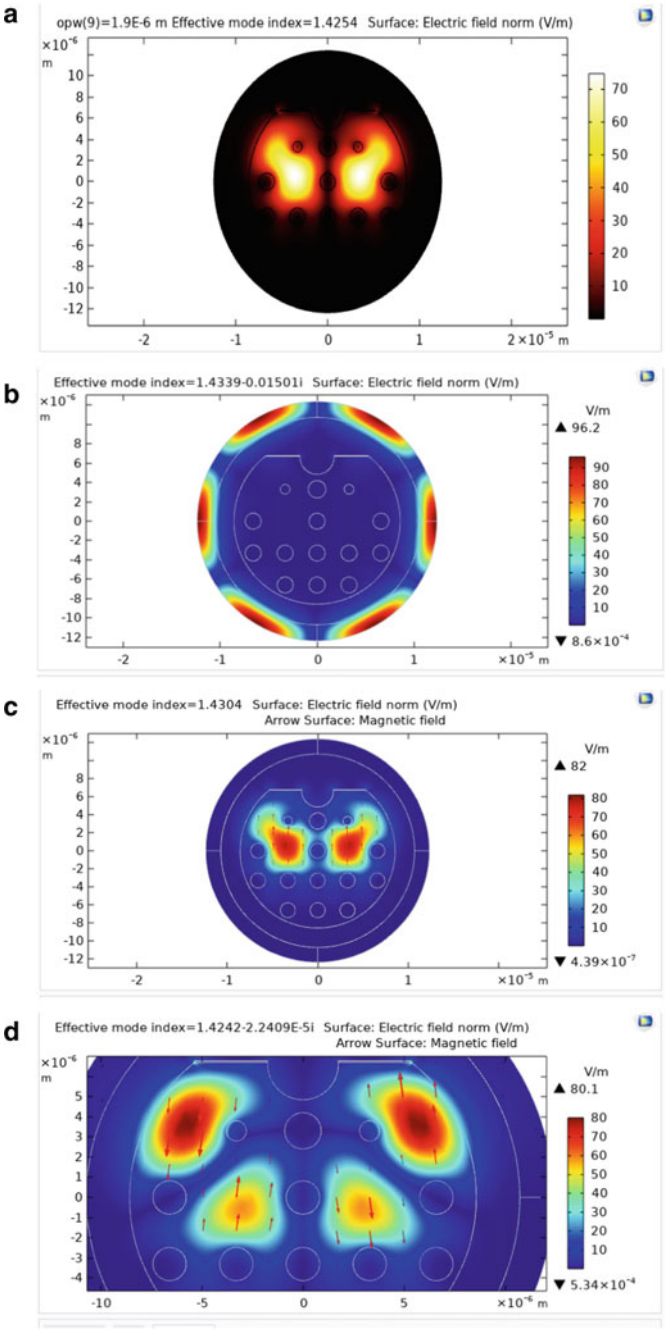

Fig. 2 **a** Thermal view of the core mode of sensor for effective mode index = 1.4254 and operating wavelength = 1.9 μm. **b** Unpolarized SPP mode for effective mode index = 1.4339–0.01501i. **c** *y*-polarized core mode for effective mode index = 1.4304. **d** *y*-polarized core mode for effective mode index = 1.4242–2.24E − 5

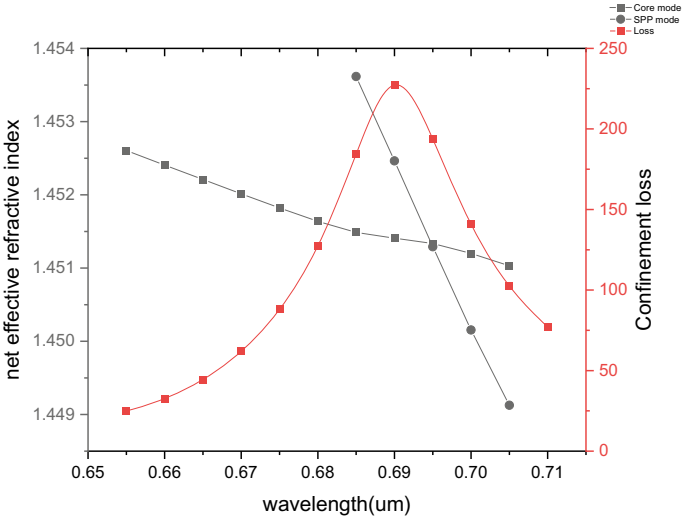

Fig. 3 Fundamental dispersion relation curves for core and SPP modes of the sensor

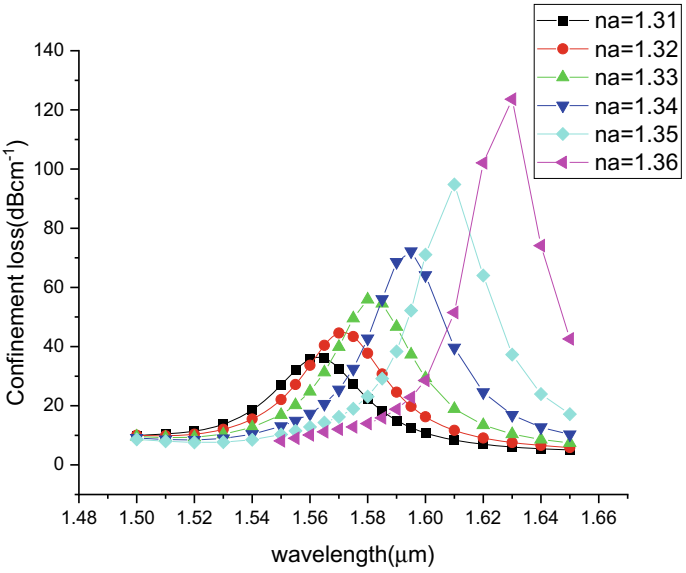

Fig. 4 Confinement loss curves for na = 1.31 to na = 1.36

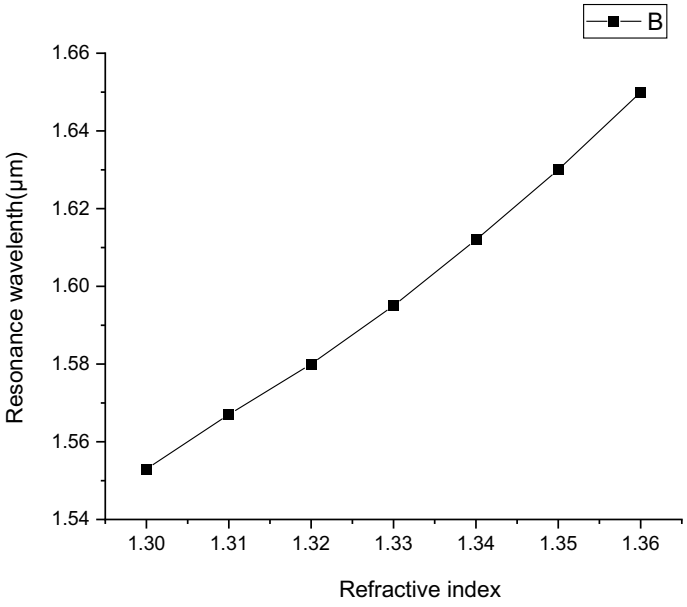

Fig. 5 Resonance wavelength versus refractive index

In the curve, it can be observed that the maximum resonance wavelength is obtained at na = 1.36. In fact, in order to follow the trend of the resonance wavelengths versus the refractive indices of the analyte, the following plot (Fig. 5) can be seen.

It is observed that on increasing the refractive index of the analyte, the sensor has to be targeted with a greater wavelength.

For calculating the wavelength sensitivity, the variation in the resonance wavelength corresponding to the change in the refractive index is noted down as given in Eq. 4.

Now, for the graph given in Fig. 5, slope = 1.325 μm RIU^{-1}

Hence, the wavelength sensitivity for the sensor is 1325 nm RIU^{-1}.

Now, calculating the amplitude sensitivity from Eq. 5, for different refractive indices of the analyte and varying it for different wavelengths, the following curve (Fig. 6) is obtained.

From the above curve, it can be deduced that the maximum amplitude sensitivity is 231.57 RIU^{-1} for na = 1.31, and the minimum peak amplitude sensitivity has been observed for na = 1.31, which is equal to 75.21 RIU^{-1}.

Another parameter that leads to the change in the amplitude sensitivity is the thickness of the gold layer and the thickness of the ZnO layer. In the following figures (Fig. 7a and b), the confinement loss—wavelength curves for different values of thickness of gold layer and that for different values of thickness for ZnO layer have been represented.

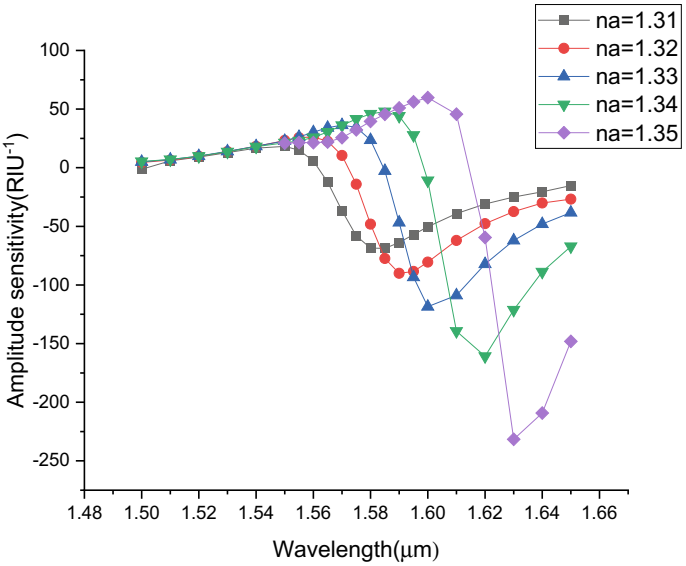

Fig. 6 Amplitude sensitivities for na = 1.31 to na = 1.36 at different wavelengths

From the above curves, the amplitude sensitivities for the different thickness values of the gold and ZnO layer provide a way of increasing the amplitude sensitivity to the maximum extent.

For the thickness of gold = 65 nm,
Maximum amplitude sensitivity = − 240.2 RIU^{-1}
For the thickness of gold = 60 nm,
Maximum amplitude sensitivity = − 160.84 RIU^{-1}
For the thickness of gold = 55 nm,
Maximum amplitude sensitivity = −118.5 RIU^{-1}
For the thickness of ZnO = 5 nm,
Maximum amplitude sensitivity = −350.52 RIU^{-1}
For the thickness of ZnO = 10 nm,
Maximum amplitude sensitivity = −240.76 RIU^{-1}
For the thickness of ZnO = 15 nm,
Maximum Amplitude sensitivity = −138.4 RIU^{-1}

Therefore, the more the thickness of the gold layer, the more is the maximum amplitude sensitivity for refractive index na = 1.35, and the more the thickness of the ZnO layer, the more is the value of the maximum amplitude sensitivity.

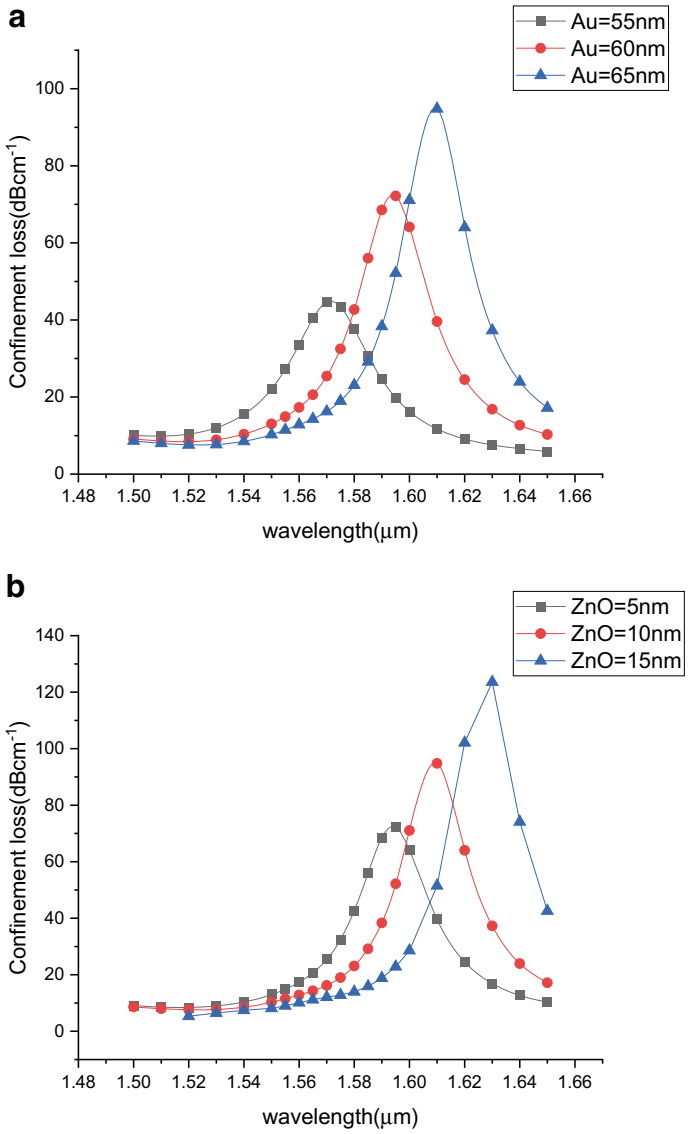

Fig. 7 **a** Confinement loss curves for thickness (Au) = 55,60 and 65 nm. **b** Confinement loss curves for thickness (ZnO) = 5, 10, and 15 nm

4 Applications of D-Shaped Plasmonic Sensor in Medical Field

The D-shaped SPR-based sensors have high recognition in the medical field. From biosensors to the detection of diseases as well as immunosensors, our D-shaped SPR-based sensors have a wide range of applications. The D-shaped biosensors can be used to detect the diseases like leukemia, hand-foot-mouth disease, and pneumonia [15]. In addition to this, these D-shaped SPR sensors also act as immunosensors. As immunosensors, the sensor is used to detect the antigen and the antibody. The antibodies get absorbed at the layer of ZnO and thus interact with the gold layer. The binding of the antibody and gold particles leads to a deflection in the refractive index and that particular antigen or antibody is tested [11]. Another application of SPR sensors is the detection of the harmful compound 1,4 dioxane. 1,4 dioxane has a wide range of applications in our daily products. The bath foam and many cosmetic products contain this as it acts as a stabilizing agent. However, 1,4 dioxane, if inhaled makes the heart rate drop or rise sharply and also causes kidney and liver problems. On the other hand, if it is taken along with food, this may cause the RBC counts to decline to such as level as to cause deaths [12]. So, it becomes essential to detect this compound and many other such gases or compounds. In the D-shaped SPR based sensor, when 1,4 dioxane is taken as the analyte and the sensitivity of the sensor can be recorded so as to detect the level of this gas present [18–20].

5 Conclusions

The D-shaped SPR sensors are quite well known for their high sensitivities, flexibility, low cost, and low-resolution properties. A D-shaped SPR sensor has been designed with gold as a plasmonic material and ZnO as a photocatalyst. The analyte is unknown, and the different refractive indices of the analytes are used to observe the confinement loss and sensitivities of the sensor. The wavelength sensitivity of the sensor is 1325 nm RIU^{-1}, and the maximum amplitude sensitivity is $-240.2\ RIU^{-1}$. The designed SPR sensor has various applications in the biochemical and medical field.

Acknowledgements We would like to thank Dr. Vinod Singh for their support.

References

1. Lee B, Roh S, Park J (2009) Current status of micro-and nano-structured optical fiber sensors. Opt Fiber Technol 15:209–221
2. Ashwell GJ, Roberts MPS (1996) Highly selective surface plasmon resonance sensor for NO/sub 2. Electro Lett 32:2089–2091

3. Mouvet C, Harris RD, Maciag C, Luff BJ, Wilkinson JS, Piehler J, Brecht A, Gauglitz G, Abuknesha R, Ismail G (1997) Determination of simazine in water samples by waveguide surface plasmon resonance. Analyti Chimic Acta 338:109–117
4. Nooke A, Beck U, Hertwig A, Krause A, Krüger H, Lohse V, Negendank D, Steinbach J (2010) On the application of gold based SPR sensors for the detection of hazardous gases. Sens and Actua B: Chemi 149:194–198
5. Kumar D, Sharma M, Singh V (2022) Surface Plasmon resonance implemented silver thin film PCF sensor with multiple-Hole microstructure for wide ranged refractive index detection, Materials Today Proceedings, Elsevier 62(12):6590–6595.
6. Rifat AA, Mahdiraji GA, Chow DM, Shee YG, Ahmed R et al (2015) Photonic crystal fiber-based surface plasmon resonance sensor with selective analyte channels and graphene-silver deposited core. Sensors 15:11499–11510. ISSN 1424–8220
7. Kaur V, Singh S (2020) Design of D-shaped PCF-SPR sensor with dual coating of ITO and ZnO conducting metal oxide. Optik 220:165135
8. Dash JN, Jha R (2016) Highly sensitive D shaped PCF sensor based on SPR for near IR. Opt Quant Electron 48:137
9. Zhang S et al (2017) Surface plasmon resonance sensor based on D-shaped photonic crystal fiber with two micro-openings. J Phys D: Appl Phys 51:305104
10. An G, Hao X, Yan X, Zhang X (2017) D-shaped photonic crystal fiber refractive index sensor based on surface plasmon resonance. Appl Opt 56(24):6988–6992
11. Akowuah EK, Gorman T, Ademgil H, Haxha S (2012) A highly sensitive photo crystal fiber (PCF) surface plasmon resonance sensor based on a bimetallic structure of gold and silver, IEEE
12. Thenmozhi H, Rajan MSM, Ahmed K (2018) D-shaped PCF sensor based on SPR for the detection of carcinogenic agents in food and cosmetics. Optik 180:264–270
13. Singh S, Prajapati YK (2020) TiO_2/gold-graphene hybrid solid core SPR based PCF RI sensor for sensitivity enhancement. Optik 224:165525
14. KadhimRA YL, Xu H, Wu J (2020) Highly sensitive D-shaped optical fibre surface plasmon resonance refractive index sensor based on Ag-α-Fe_2O_3 grating. IEEE Sens J 20(17):9816–9824
15. Delfino I, Diano N, Lepore M (2021) Advanced optical sensing of phenolic compounds of environmental applications. Sensors 21(22):7563
16. Mbarek H, Saadoun M, Bessais B (2006) Screen-printed Tin-doped indium oxide (ITO) films for NH_3 gas sensing. Mater Sci Eng, C 26:500–504
17. Choi SH, Kim YL, Byun KM (2011) Graphene-on-silver substrates for sensitive surface plasmon resonance imaging biosensors. Opt Express 19:458–466
18. Hassani A, Gauvreau B, Fehri MF, Kabashin A, Skorobogatiy M (2008) Photonic crystal fiber and waveguide-based surface plasmon resonance sensors for application in the visible and near-IR. Electromagnetics 28:198–213
19. Amouzad Mahdiraji G, Chow DM, Sandoghchi S, Amirkhan F, Dermosesian E, Yeo KS, Kakaei Z, Ghomeishi M, Poh SY, Gang SY et al (2014) Challenges and solutions in fabrication of silica-based photonic crystal fibers: an experimental study. Fiber Integr Opt 33:85–104
20. Fan ZK, Li SG, Liu Q, An GW, Chen HL, Li JS, Dou C, Li H, Zi JC, Tian WL (2015) High sensitivity of refractive index sensor based on analyte-filled photonic crystal fiber with surface plasmon resonance. IEEE Photonics J 7(3):1–9

Investigation of Micro-Cracks of Pure Titanium Using Wire Electric Discharge Machining (WEDM) Through Response Surface Methodology

Vinod Kumar, Renu Sharma, Jatinder Kumar, Ravinder Pal Singh, and Anish Kumar

Abstract In this study, micro-cracks analysis has been carried out on pure bio-implant titanium material in terms of length and number of micro-cracks after wire electric discharge machining (WEDM). The effect of WEDM parameters on micro-cracks propagation was subjected to metallurgical characterization through a scanning electron microscope and EDX. The experimental results show that the quantitative analysis of micro-cracks plays a significant role to deteriorate the morphology of machined surfaces, resulting in deeper, bigger globules of debris and micro-cracks. X-ray diffraction was used to study the phase transformations that occurred in the formation of substances like titanium dioxide (rutile), Ilmenite, titanium carbides (TiC), and copper titanium dioxide. To reduce the micro-cracks, an optimal parametric setting was obtained through the desirability function. A BBD approach was used to develop the experimental design. The effect of WEDM parameters: POT, PC, and SGV for micro-cracks were predominantly affected.

Keywords WEDM · Micro-cracks · Bio-implant · ANOVA · XRD · EDX

V. Kumar
Department of Mechanical Engineering, Thapar Institute of Engineering and Technology (Deemed to Be University), Patiala, Punjab 147004, India
e-mail: vsingla@thapar.edu

R. Sharma
Department of Physics, Maharishi Markendeshwar Deemed to Be University Mullana, Ambala, Haryana 133207, India

J. Kumar
Department of Mechanical Engineering, National Institute of Technology, Kurukshetra, Haryana 136119, India

R. P. Singh · A. Kumar (✉)
Department of Mechanical Engineering, Maharishi Markendeshwar Deemed to Be University, Mullana, Ambala, Haryana 133207, India
e-mail: anish_kaushik@rediffmail.com

K. Geetha et al. (eds.), *Recent Trends in Materials*, Springer Proceedings in Materials 18, https://doi.org/10.1007/978-981-19-5395-8_28

Abbreviations

DWP	Dielectric water pressure
DOF	Degree of freedom
F-Value	Fisher value
MS	Mean square
POT	Pulse on time
POFT	Pulse off time
PC	Peak current
SS	Sum of square
WEDM	Wire electric discharge machining
WS	Wire speed
WT	Wire tension

1 Introduction

In a manufacturing society, titanium is an important material that is widely utilized in the aviation, automotive, chemical, and biomedical sectors with its excellent features, such as high strength–weight ratio, high thermal stability, and outstanding corrosion resistance. As a result, titanium's surface characteristics are inappropriate for excessive loads that lead to severe wear, particularly when applied to rotating machinery parts. To improve titanium's mechanical properties and broaden its applications, researchers must develop a method of strengthening and modifying traditional mechanical cutting techniques with low machinability contributes to significant tooling costs. To machine, this alloy, advanced machining methods such as wire electric discharge machining (WEDM) have been investigated. WEDM is a non-contact machining technique that uses thermal energy to machine hard, high-strength, and temperature-resistant materials. An erosion spark between the wire and the workpiece melts and evaporates the material [1]. The material is removed by the liquid dielectric medium is continuously delivered to sweep the eroded particles and give the cooling effect in this operation. The tool electrode is a 0.25-mm wire with a smaller diameter. The wire is fed continuously from the supply spool through the workpiece, which is held in place by the wire traction rollers on the table [2–4]. Several researchers have attempted to improve the WEDM performance characteristics, but due to its complicated and stochastic nature, as well as a large number of variables remains unsolved [5, 6]. Çydas et al. [7] developed the model that can predict white-layer thickness and average surface roughness as a function of process parameters using an adaptive neuro-fuzzy inference system. Speeding and Wang [8] investigate the capability of removing the recast layer after the EDM process. The L9 orthogonal array regulates the analyzing the amount of recast layer removal of Ni-based superalloys was examined. Govindan and Joshi [9] investigated the micro-cracks analysis

after WEDM process. Lin et al. [10] used a tungsten carbide as the work material for WEDM process. Gray-fuzzy analysis was used with an orthogonal array to investigate the performance characteristics of the WEDM machining process. The main limitations of above past work were the researchers restricted to few number of process variables on the WEDM performance of alloys and composites. So far, only, limited machining performances have been investigated on WEDM, namely MRR and surface roughness. There has been no research done on the complex machining of pure titanium using WEDM, which focuses on multi-machining properties in applications such as die manufacture. The present investigation was interesting in that it used the response surface approach and Box–Behnken design to explore the effect of process parameters on the number of cracks and crack length. The validity of the models was tested using ANOVA. EDX, SEM, and XRD diffraction techniques were used to examine the surface morphology of performance metrics.

2 Material and Methods

The experimental plan was carried out on a 4-axis CNC-type WEDM in this research work, and the steps (1–9) have been followed as shown in Fig. 1. Table 1 shows the list of factors and their levels. The levels for the factors have been decided based on a pilot study and past work [11–16]. The accompanying is the chemical composition of the selected material: C has a concentration of 0.10%; N has a concentration of 0.03%; O has a concentration of 0.25%; H has a concentration of 0.015%; Fe has a concentration of 0.30%, and Ti has a concentration of 99.03%. Six input parameters, namely POT, POFT, PC, SGV, WS, and WT, have been adapted based on pilot and previous survey results. The experimental design matrix was developed through Design–Expert software 8.0 version using response surface methodology-based BBD approach, and its outputs are shown in Table 2. Electrode (brass wire with 0.25 mmØ), t: 26 mm, and DWP: 7 kg/cm^2 were the constant parameters. An SEM with an integrated EDX setup was used to study surface morphology. Acetone $(CH_3)2CO$ was used to clean the 54 work samples. In further, EDX was used to assess material migration from a brass wire, de-ionized water, and work sample. A scanning electron microscope was used to examine micrographs of samples at various magnification levels (ranging from 500X to 3000X). Performance measures were calculated using Carl Zeiss Axio-vision Rel.4.8 software. Micrographs of four sides were taken at different magnifications ranging from 500X to 3000X to observe the quantitative analysis of micro-cracks. The overall length of the micro-crack was also determined using the following formulae:

$$\text{Total length of crack } (\mu\text{m}) = \text{Average length of a crack } (\mu\text{m})/\text{Average number of cracks} \quad (1)$$

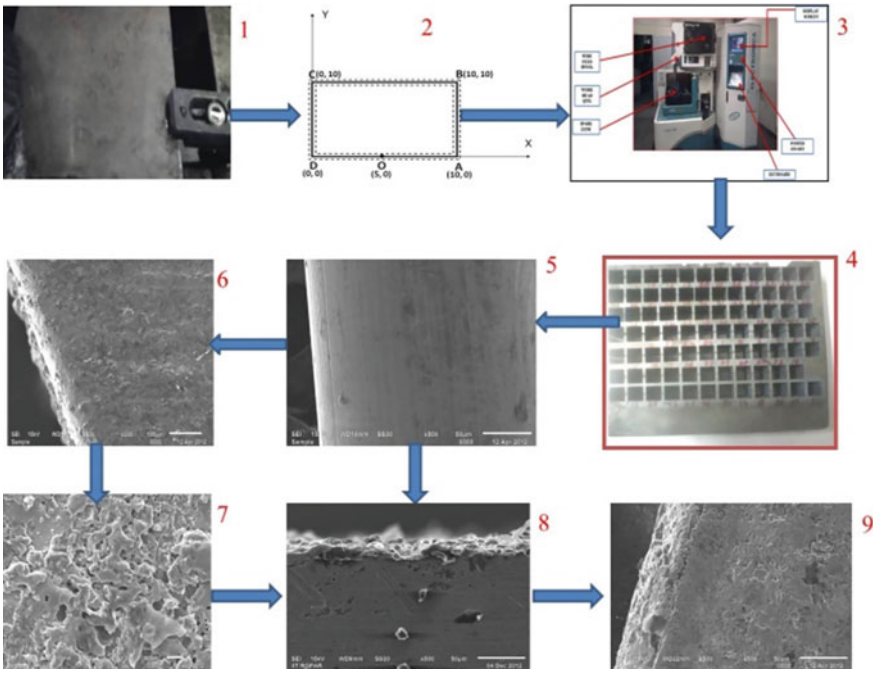

Fig. 1 Schematic diagram showing the various operations of processing the pure titanium using WEDM process (1) Holding workpiece on table, (2) Job profile, (3) Machine setup, (4) Job profile after WEDM, (5) Brass wire, (6) Workpiece micrograph without WEDM, (7) Micrograph after WEDM, (8) Recast layer micrograph, (9) Wire wear out after WEDM

Table 1 Selected parameters and their levels

Factor	Name	Units	Lower range	Upper range
A	POT	μs	0.7	1.1
B	POFT	μs	17	38
C	PC	A	120	200
D	SGV	V	40	60
E	WS	m/min	4	10
F	WT	g	500	1400

As illustrated in Fig. 2, the micrograph represents the measurement of the length of the crack and the number of cracks. The observed unit area for all micrographs was 12,400 $\mu m/\mu m^2$.

Table 2 Experimental runs as per design of experiment

Run no	POT (μs)	POFT (μs)	PC (A)	SGV (V)	WS (m/min)	WT (g)	No. of Cracks	Length of crack (μm)
1	1.1	28	200	50	7	500	20	210.44
2	0.9	38	160	50	4	500	13	169.95
3	0.7	28	160	60	4	950	12	152.45
4	0.9	17	120	50	10	950	20	187.70
5	0.9	28	120	60	7	500	15	165.03
6	1.1	28	160	40	4	950	23	194.64
7	0.9	38	160	50	10	1400	15	164.52
8	0.9	28	160	50	7	950	12	172.45
9	0.9	17	160	50	4	500	18	185.72
10	1.1	28	160	40	10	950	19	210.84
11	1.1	38	160	40	7	950	18	180.36
12	1.1	28	160	60	4	950	19	172.23
13	0.9	17	160	50	10	500	20	188.18
14	0.9	28	160	50	7	950	14	171.23
15	0.7	28	120	50	7	500	10	151.36
16	0.9	28	160	50	7	950	13	173.56
17	0.9	28	120	60	7	1400	13	166.68
18	0.7	38	160	40	7	950	15	154.60
19	0.9	38	120	50	10	950	12	172.62
20	0.9	28	200	40	7	1400	21	226.81
21	0.9	28	200	60	7	500	20	196.24
22	0.9	38	200	50	10	950	16	200.23
23	0.9	28	120	40	7	1400	18	189.64
24	0.7	28	120	50	7	1400	11	142.23
25	0.9	38	200	50	4	950	18	185.69
26	1.1	28	160	60	10	950	17	188.02
27	1.1	28	120	50	7	500	15	180.22
28	0.7	28	160	40	10	950	19	150.30
29	0.7	28	200	50	7	500	18	157.57
30	0.7	17	160	40	7	950	19	172.95
31	0.7	28	200	50	7	1400	18	165.65
32	0.9	28	160	50	7	950	17	179.67
33	0.9	17	200	50	4	950	25	218.25
34	0.9	28	160	50	7	950	18	184.62
35	1.1	17	160	40	7	950	26	221.95

(continued)

Table 2 (continued)

Run no	POT (μs)	POFT (μs)	PC (A)	SGV (V)	WS (m/min)	WT (g)	No. of Cracks	Length of crack (μm)
36	0.9	17	200	50	10	950	19	228.78
37	0.9	28	200	40	7	500	23	221.56
38	0.7	28	160	40	4	950	16	167.97
39	0.9	38	160	50	10	500	12	177.57
40	0.9	28	160	50	7	950	15	169.27
41	1.1	38	160	60	7	950	18	164.25
42	0.7	17	160	60	7	950	14	149.68
43	0.9	28	200	60	7	1400	21	181.72
44	0.9	17	120	50	4	950	15	184.33
45	0.7	28	160	60	10	950	14	143.72
46	1.1	28	120	50	7	1400	15	172.07
47	0.7	38	160	60	7	950	13	139.69
48	0.9	17	160	50	4	1400	17	174.57
49	0.9	28	120	40	7	500	19	158.84
50	1.1	17	160	60	7	950	20	207.87
51	0.9	38	120	50	4	950	12	169.15
52	1.1	28	200	50	7	1400	18	196.36
53	0.9	17	160	50	10	1400	18	189.57
54	0.9	38	160	50	4	1400	13	162.65

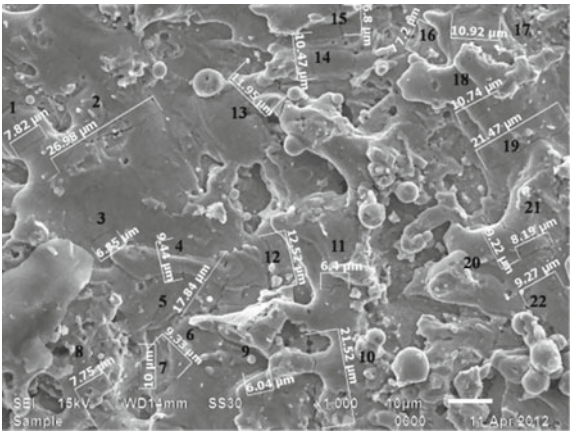

Fig. 2 Representation of micro-cracks on micrograph after WEDM

3 Results and Discussion

3.1 Experimental Design

Based on the response surface methodology, Box–Behnken design (BBD) is a statistical and mathematical strategy that was used to develop, optimize, and simulate the process parameters that affect responses using Design–Expert version 8 software. BBD identified the relationship between process parameters and experimental response in terms of linear, interaction, and quadratic effects. If the model could be rotated, it would have a very constant distribution of scaled prediction variance throughout the experimental design zone. The BBD also eliminates combinations in which all components are at their highest or lowest values at the same moment. As a result, these designs are successful in avoiding trials that are undertaken under harsh conditions, which can lead to unsatisfactory outcomes [17, 20]. The established models based on the RSM methodology are represented by Eqs. (2) and (3), which employ the backward elimination method to eliminate the model's non-significant variables.

Number of cracks

$$\begin{aligned} &69.51994 + 43.75000 \times \text{POT} - 1.21523 \times \text{POFT} - 0.000520833 \times \text{PC} \\ &- 3.00298 \times \text{SGV} + 4.22917 \times \text{WF} + 0.00831444 \times \text{POFT}^2 \\ &+ 0.000807292 \times \text{PC}^2 + 0.025417 \times \text{SGV}^2 - 0.10937 \times \text{POT} \times \text{PC} \\ &- 2.29167 \times \text{POT} \times \text{WF} + 0.010714 \times \text{POFT} \times \text{SGV} \\ &- 0.013542 \times \text{PC} \times \text{WF} \end{aligned} \tag{2}$$

Length of crack

$$\begin{aligned} &8.22256 + 595.87173 \times \text{POT} - 0.21876 \times \text{POFT} - 1.15577 \times \text{PC} \\ &- 2.30638 \times \text{SGV} - 10.05299 \times \text{WF} + 0.11171 \times \text{WT} \\ &- 274.42113 \times \text{POT}^2 + 0.040015 \times \text{POFT}^2 + 0.00736838 \times \text{PC}^2 \\ &+ 0.053507\text{SGV}^2 - 0.0000245091 \times \text{WT}^2 \\ &- 3.38512 \times \text{POT} \times \text{POFT} + 12.16458 \times \text{POT} \times \text{WF} \\ &- 0.016763 \times \text{PC} \times \text{SGV} - 0.00135889 \times \text{SGV} \times \text{WT} \end{aligned} \tag{3}$$

3.2 Assessment of Predictive Model Fitting

The process characteristics were evaluated and analyzed using the experimental results. The significance and contribution of parameters in the created model were

checked using the analysis of variance (ANOVA) test. Tables 3 and 4 show the results of the ANOVA test for the length of crack and number of cracks, respectively. The "*p*-value" (<0.0500) for both models statistically verified the importance of model terms with a 95% confidence level, as seen in the results of the ANOVA test shown in Tables 3 and 4. Furthermore, the lack of fit for the current model was determined to be "not significant" in terms of computation and interpretation. The "*p*-value" found for both models is 0.99 (for number of cracks model) and 0.388 (for a length of the crack model), respectively, indicating that "lack of fit" is an inconsequential term. This further showed that the model is accurate in all aspects of the design. The values of "Prob > F" less than 0.05 indicate that the model terms are significant [18–22]. The model's F values of 25.30 and 34.82 implied that all models are significant. There is <0.01% probability that a model *F*-value of this magnitude could be due to noise.

Table 3 ANOVA for number of cracks

Source	SS	DOF	MS	*F*-Value	Prob > F	At 95%CI
Model	593.38	12	49.45	25.30	< 0.0001	Significant
POT	100.04	1	100.04	51.19	< 0.0001	
POFT	130.67	1	130.67	66.86	< 0.0001	
PC	160.17	1	160.17	81.96	< 0.0001	
SGV	66.67	1	66.67	34.11	< 0.0001	
WS	0.000	1	0.000	0.000	1.0000	
POFT ^{2}	10.08	1	10.08	5.16	0.0284	
PC^2	20.02	1	20.02	10.24	0.0026	
SGV^2	77.52	1	77.52	39.67	< 0.0001	
POT × PC	6.13	1	6.13	3.13	0.0841	
POT × WS	15.13	1	15.13	7.74	0.0081	
POFT × SGV	10.13	1	10.13	5.18	0.0281	
PC t × WS	21.13	1	21.13	10.81	0.0021	
Residual	80.12	41	1.95			
Lack of fit	53.29	36	1.48	0.28	0.9907	Not significant
Pure error	26.83	5	5.37			
Total	673.50	53				
$R^2 = 0.8810$						
R^2 Adjusted = 0.8462						
Predicted $R^2 = 0.8045$						

Table 4 ANOVA for the length of cracks

Source	SS	DOF	MS	F-Value	Prob > F	At 95%CI
Model	23,689.85	15	1579.32	34.82	< 0.0001	Significant
POT	8478.05	1	8478.05	186.93	< 0.0001	
POFT	2998.70	1	2998.70	66.12	< 0.0001	
PC	5087.56	1	5087.56	112.17	< 0.0001	
SGV	2069.81	1	2069.81	45.64	< 0.0001	
WS	173.08	1	173.08	3.82	0.0582	
WT	38.03	1	38.03	0.84	0.3656	Not significant
POT^2	1265.16	1	1265.16	27.89	< 0.0001	
$POFT^2$	217.98	1	217.98	4.81	0.0346	
PC^2	1459.40	1	1459.40	32.18	< 0.0001	
SGV^2	300.61	1	300.61	6.63	0.0141	
POT × POFT	404.27	1	404.27	8.91	0.0049	
POT × WS	426.17	1	426.17	9.40	0.0040	
PC × SGV	359.66	1	359.66	7.93	0.0077	
SGV × WT	299.15	1	299.15	6.60	0.0143	
Residual	1723.47	38	45.35			
Lack of fit	1553.61	33	47.08	1.39	0.3881	Not significant
Pure error	169.87	5	33.97			
Total	25,413.33	53				
$R^2 = 0.9322$						
R^2 Adjusted = 0.9054						
Predicted $R^2 = 0.8353$						

3.3 Effect of Process Parameters on the Number of Cracks

The main effects graphs in Fig. 3 reveal that the number of cracks increases linearly as the POT increases from 0.7 to 1.1 μs. When the POFT was decreased, the number of discharges per unit of time increased, potentially resulting in more cracks. When PC was increased from 120 to 200 A with 14–19, the number of cracks and its width increased dramatically. İt was observed that to raise of PC and decrease of POFT, the rate of discharge energy increases this may results, rapid melting and vaporization of molten material which is suspended in the electrical discharge to raise the number of cracks. In Fig. 4, the 3D interactions between two parameters are shown. The number of cracks increased from 14 to 22 on the interaction between POFT and SGV. This is because when the SGV was decreased, the mean gap narrows, increasing the number of cracks [23–25]. Figure 5a–d shows the density of surface cracks at varied PC and POT. Micro-crack development was influenced not only by machining parameters but also by material properties. Machined samples with sub-surface cracks revealed

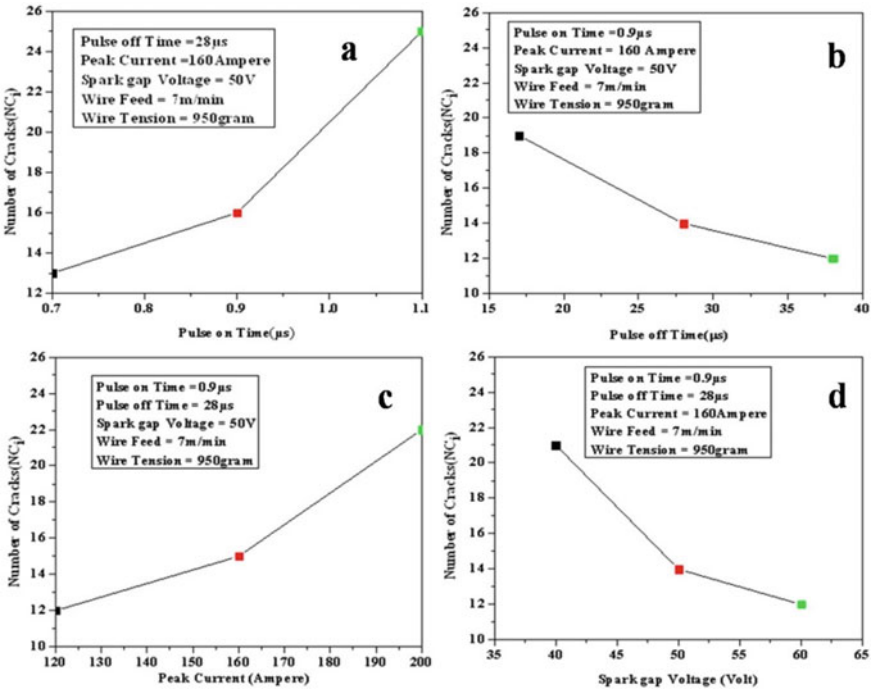

Fig. 3 Single parametric variation on number of cracks

that the material was amorphous. The cracks at different settings of PC and POT were observed on the sub-surface like penetrating sub-surface micro-cracks, crater rims, and abnormalities also seen in Fig. 6. Surface cracks were not observed when machining is done at optimal settings (POT = 0.7 μs, POFT = 50 μs, PC = 160 A, and SGV = 60 V), as illustrated in Fig. 7.

3.4 Effect of Process Parameters on Length of Crack

It can be observed from Fig. 8, the length of the crack increased dramatically from 146.701 to 191.991 μm concerning to WEDM parameters. The interaction effects of crack length are shown in Fig. 9. Four different interactions (POT × POFT, POT × WF, PC × SGV, and SGV × WT) have been observed. The crack length was most significantly affected by PC because cracks length is relative to spark width and frequency [26–29]. Energy-dispersive X-ray analysis (EDX) was the elemental composition (wt%) after the WEDM machining. The purpose of the EDX to analyze the surface and predict the elements was migrated from the brass wire and work material. Some carbon elements were also observed due dielectric medium. As demonstrated in Fig. 10, Cu and Zn elements moved from the brass wire electrode to the

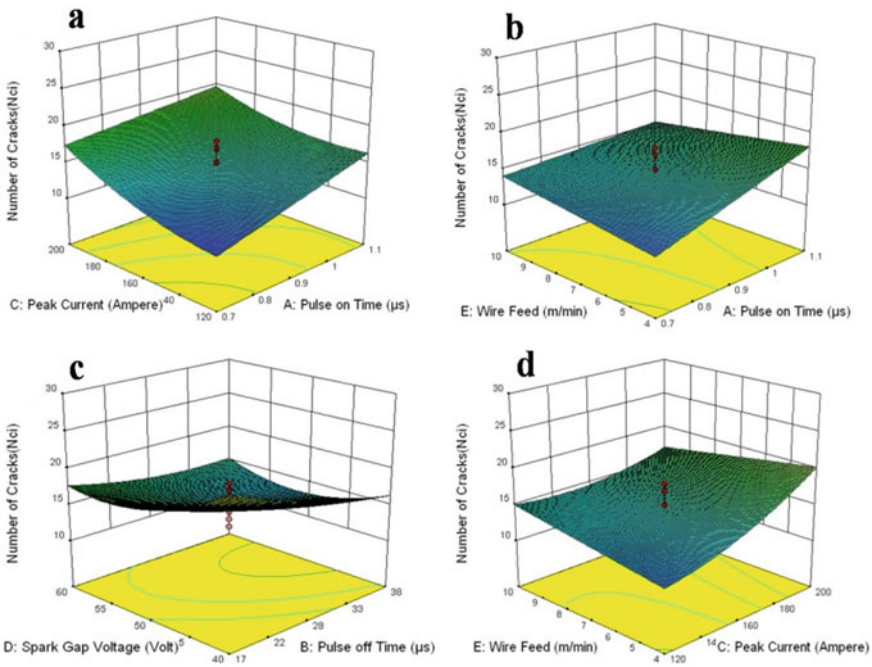

Fig. 4 Surface plots showing the interaction for number of cracks

work samples during WEDM process. X-ray diffraction (XRD) was utilized to further examine the chemical compound deposited as TiC and TiO_2. X'Pert High Score plus 2.0 is used to examine the phases (Fig. 11).

4 Conclusions

1. Deep and wide overlapping craters, pockmarks, globules of debris, and micro-cracks have been observed at high POT and PC.
2. Through XRD analysis, the chemical compounds and phases of titanium dioxide, ilmenite, copper titanium tetra-dioxide titanium, carbide (TiC) have been observed.
3. Due to high PC (200A) and short POFT (17 µs), the number of cracks increased from 19 to 26.
4. The length of the crack varies between 150 and 200 µm as the POT increases from 0.7 to 1.1 µs, and the POFT decreases from 38 to 17 µs.
5. Cu, C, O_2, Ti, and Zn elemental composition was observed with an EDX technique.

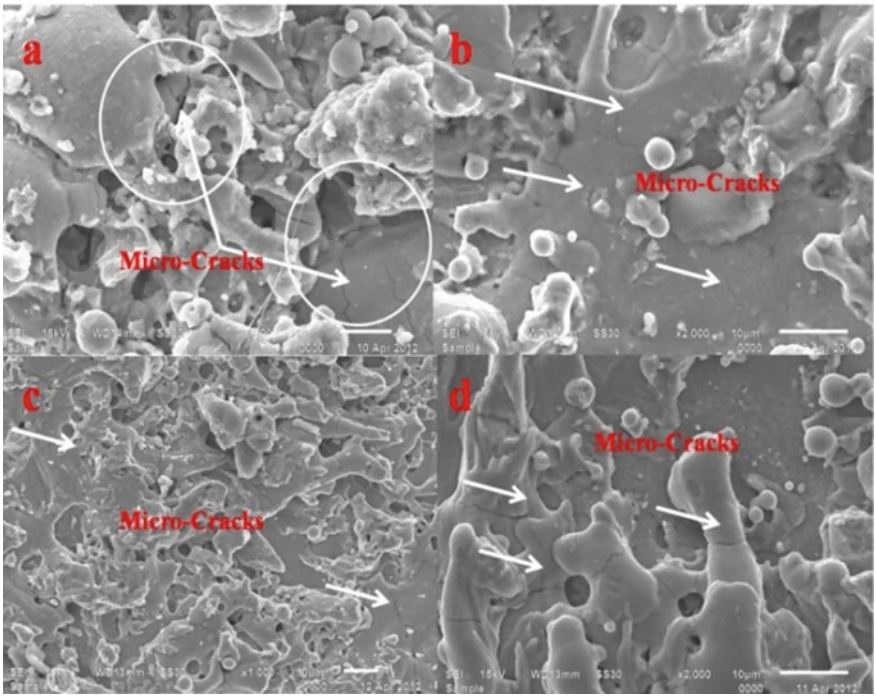

Fig. 5 SEM micrographs of cracks observed at run no. 4, 15, 25, 44

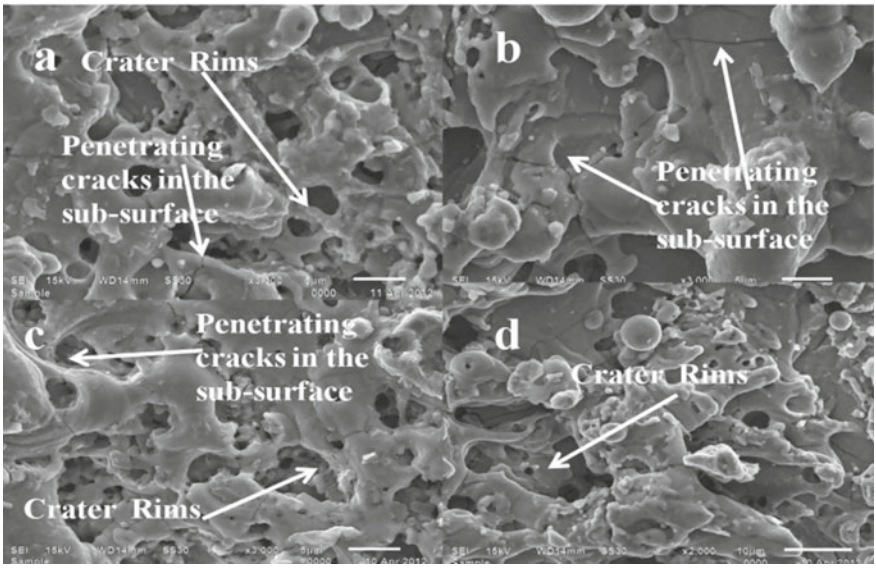

Fig. 6 SEM micrographs of different micro-cracks orientations

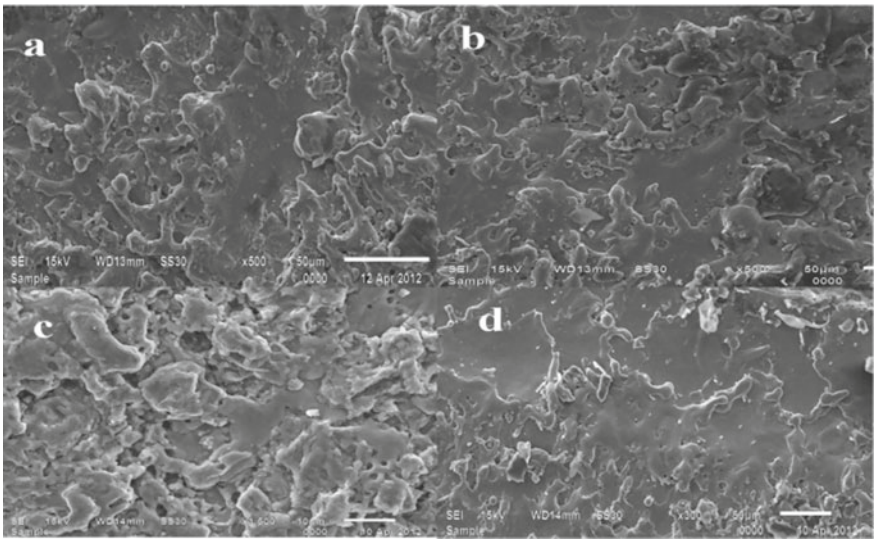

Fig. 7 SEM micrographs very few number of craters and cracks

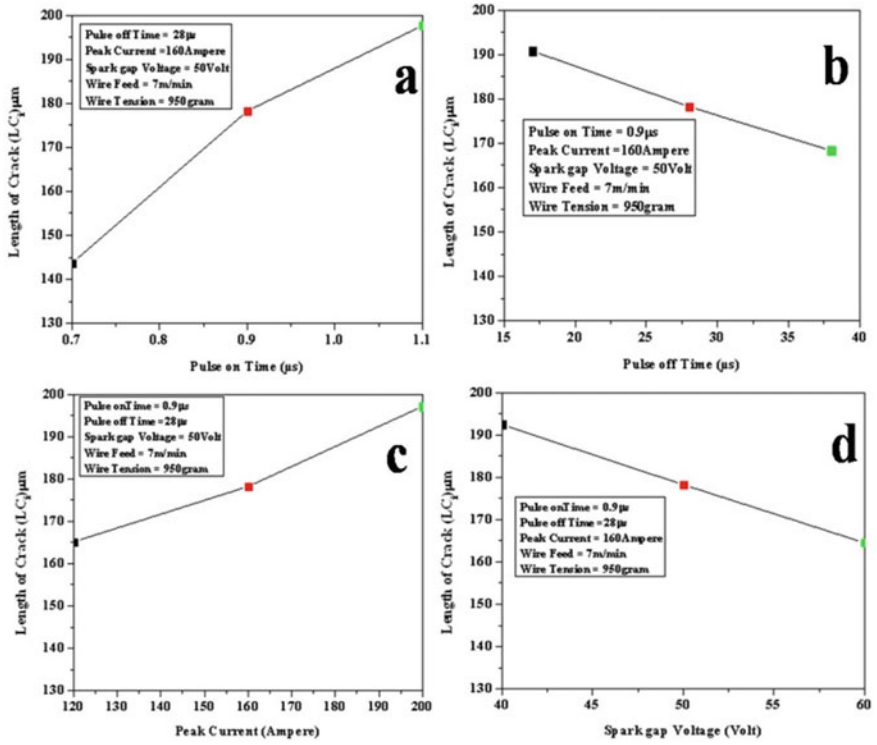

Fig. 8 Single parametric variation of length of the crack

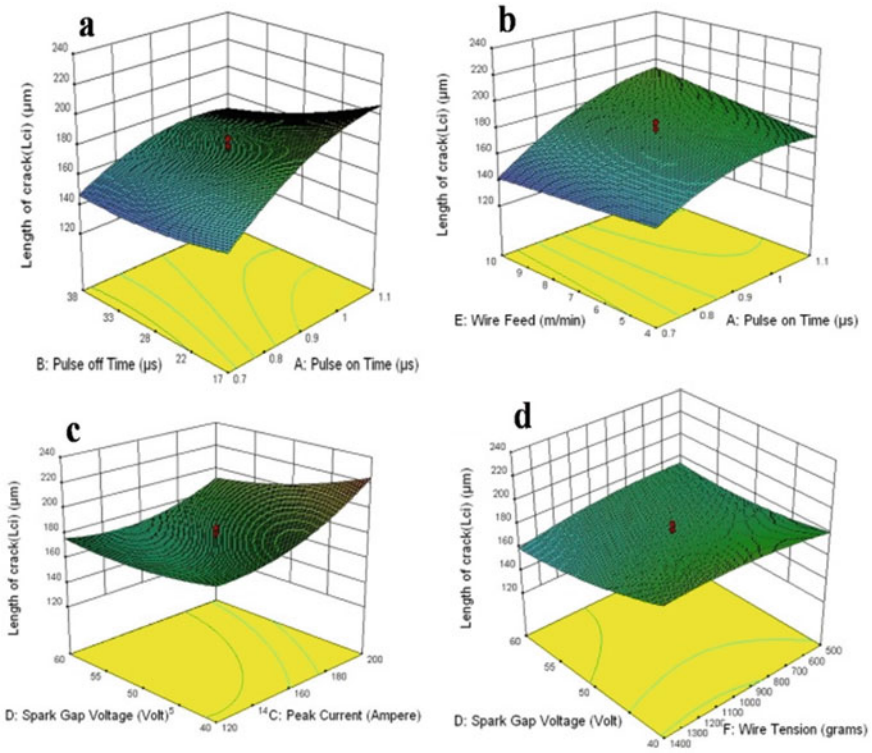

Fig. 9 Surface plots showing the interaction for length of crack

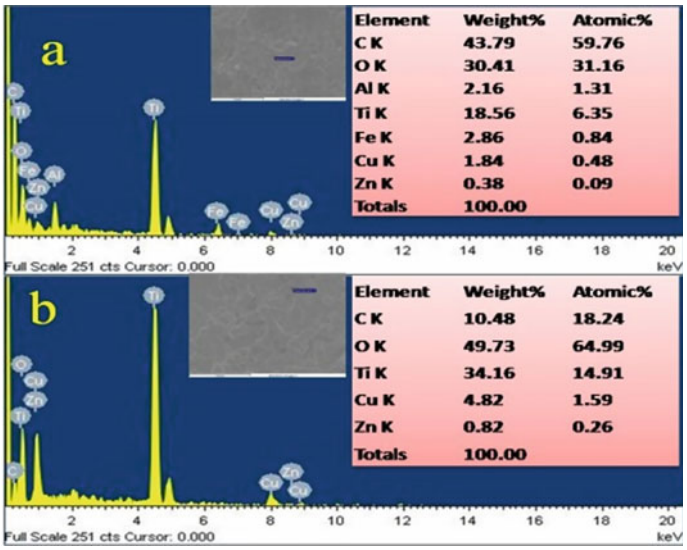

Fig. 10 Energy-dispersive X-ray (EDX) analysis

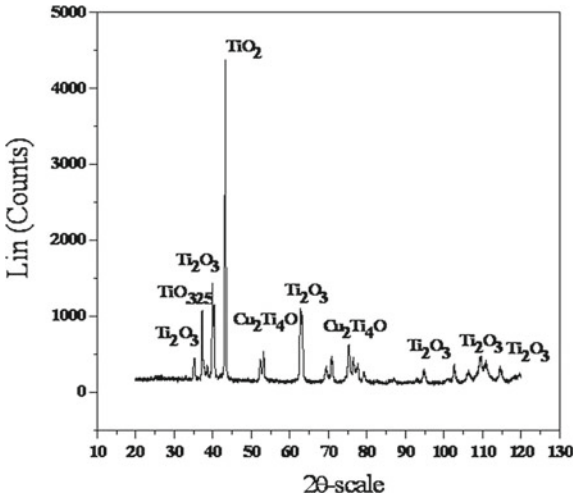

Fig. 11 X-ray diffraction of the machined surface

References

1. Shahali H, Yazadi MRS, Mohammadi A, Limanian E (2012) Optimization of surface roughness and thickness of white layer in wire electrical discharge machining of DIN1.4542 stainless steel using micro-genetic algorithm and signal to noise ratio techniques. Proc I Mech Eng Part B: J Eng Manuf 226(5):803–812
2. Kuruvila N, Ravindra HV (2011) Parametric influence and optimization of wire EDM of hot die steel. Mach Sci Technol 15:47–75
3. Ramakrishnan R, Karunamoorthy L (2006) Multi response optimization of wire EDM operations using robust design of experiments. Int J Adv Manuf Technol 29:105–112
4. Sarkar S, Mitra S, Bhattacharyya B (2006) Parametric optimization of wire electrical discharge machining of γ titanium aluminide alloy through an artificial neural network model. Int J Adv Manuf Technol 27:501–508
5. Lee JW (2003) Microstructure evaluation and phase transformation of recast layers in electrical discharge machined dual phase Fe-Mn-Al alloy. J Mater Sci 38:1679–1687
6. Hascalik A, Caydas U (2007) Electrical discharge machining of titanium alloy (Ti-6Al-4V). Appl Surf Sci 253:9007–9016
7. Spedding TA, Wang ZQ (1997) Parameter optimization and surface characteristics of wire electrical discharge machining process. Int J Prec Eng 20:5–15
8. Govindan P, Joshi SS (2012) Analysis of micro-cracks on machined surfaces in dry electrical discharge machining. J Manuf Process 14:277–288
9. Lin YC, Chen YF, Lin CT, Tzeng HJ (2008) Electrical discharge machining (EDM) characteristics associated with electrical discharge energy on machining of cemented tungsten carbide. Mater Manuf Process 23(4):391–399
10. Kumar A, Kumar V, Kumar J (2013) Investigation of machining parameters and surface integrity in wire electric discharge machining of pure titanium. Proc I Mech Eng Part B: J Eng Manuf 227(7):972–992
11. Kumar A, Kumar V, Kumar J (2014) Surface integrity and material transfer investigation of pure titanium for rough cut surface after wire electro discharge machining. Proc I Mech Eng Part B: J Eng Manuf 228(8):880–901
12. Kumar A, Kumar V, Kumar J (2013) Experimental investigation on material transfer mechanism in WEDM of pure titanium (Grade-2). Adv Mater Sci Eng 2013:1–20

13. Kumar A, Kumar V, Kumar J (2013) Microstructure analysis and material transformation of pure titanium and tool wear surface after wire electric discharge machining. Mach Sci Technol 18(1):47–77
14. Ekmekci B, Elkoca O, Tekkaya AE, Erden A (2005) Residual stress state and hardness depth in electrical discharge machining: de-ionized water as dielectric liquid. Mach Sci Technol 9(1):39–61
15. Huang CA, Tu GC, Yao HT, Kuo HH (2004) Characteristics of the rough cut surface quenched and tempered martensitic stainless steel using wire electric discharge machining. Meta Mater Trans A 35A:1351–1357
16. Kumar A, Kumar V, Kumar J (2012) An investigation into machining characteristics of commercially pure titanium (Grade-2) using CNC WEDM. Appl Mech Mater 159:56–68
17. Garg MP, Jain A, Bhushan G (2014) Multi-objective optimization of process parameters in wire electric discharge machining of Ti-6242 Alloy. Arab J Sci Eng 39(2):1465–1476
18. Montgomery DC (2002) Design and analysis of experiments, 4th edn. Wiley, New York
19. Kung KY, Chiang TK (2008) Modeling and analysis of machinability evaluation in the wire electric discharge machining (WEDM) process of aluminum oxide-based ceramics. Mater Manuf Process 23:241–250
20. Lee SH, Li XP (2003) Study of the surface integrity of the machined workpiece in the EDM of tungsten carbide. J Mater Process Technol 139:315–321
21. Lee HT, Tai TY (2003) Relationship between EDM parameters and surface crack formation. J Mater Process Technol 142:676–683
22. Patil NG, Brahmankar PK (2010) Some studies into wire electro-discharge machining of alumina particulate-reinforced aluminum matrix composites. Int J Adv Manuf Technol 48:537–555
23. Lin YC, Cheng CH, Su BL, Hwang LR (2006) Machining characteristics and optimization of machining parameters of SKH 57 high-speed steel using electrical-discharge machining based on Taguchi method. Mater Manuf Process 21(8):922–929
24. Aldrin JR, Balasubramanian K, Palanisamy D, Emmanuel AGS (2020) Experimental investigation on WEDM process for machining high manganese steel. Mater Manuf Process 35(14):1612–1621
25. Bisaria H, Shandilya P (2020) Wire electric discharge machining induced surface integrity for $Ni_{55.95}Ti_{44.05}$ shape memory alloy. Proc I Mech Part E: J Proc Mech Eng. https://doi.org/10.1177/0954408920951146
26. Jindal S, Singh H (2021) Microstructural analysis and multiresponse optimization of WEDM of Inconel 825 using RSM based desirability approach. J Mech Behav Mater 30(1):9–18
27. Kumar A, Sharma R (2020) Multi-response optimization of magnetic field assisted EDM through desirability function using response surface methodology. J Mech Behav Mater 29(1):29–35
28. Sharma A, Garg MP, Goyal KK (2014) Prediction of optimal conditions for WEDM of Al 6063/ ZrSiO4(p) MMC. Procedia Mater Sci 6:1024–1033. https://doi.org/10.1016/j.mspro.2014.07.173
29. Patil NG, Brahmankar PK (2010) Some studies into wire electro-discharge machining of alumina particulate reinforced aluminium matrix composites. Int J Adv Manuf Technol 48:537–555. https://doi.org/10.1007/s00170-009-2291-5

Polarization-Independent Broadband Metasurface Absorber for Near Infrared Spectrum

Abida Parveen, Vijay Laxmi, Keyu Tao, and Zhengbiao Oyuang

Abstract All-dielectric nanophotonics lies at a bleeding edge of nanoscience and innovation as it permits to control light at the nanoscale utilizing its electric and magnetic components. Accomplishing the broadband absorption of metamaterial absorbers is very difficult due to the narrow bandwidth. This paper includes a theoretical demonstration of the novel design of angular and polarization-insensitive ultra-broadband multi-metasurfaces-based absorber (MMBA) in the infrared spectrum of wavelength 1.8–1.95 μm for TE and TM plane-polarized wave. The absorption bandwidth of multiple layers increased more than twice in our proposed absorber as compared to previous absorbers. Using a single dielectric structure, the simulated total absorption increased by 65% at a specific wavelength. Moreover, the absorption bandwidth can be greatly prolonged up to 95% by using a multilayered dielectric structure. In addition, the proposed absorber is angle-insensitive and polarization-independent (S-polarization and P-polarization) which makes it a good candidate for spectroscopic imaging, thermal emitters, as well as thermal detectors, etc.

Keywords Metasurfaces · S-polarization-independent and P-polarization-insensitive · Broadband absorbers

1 Introduction

Recently, metamaterials have become a hot topic and well-acknowledged in the field of electronics and photonics at the nanoscale [1–7]. The first metamaterial absorber was proposed, designed, fabricated, and simulated by Landy et al. in 2008 [8], two

A. Parveen · V. Laxmi · K. Tao · Z. Oyuang (✉)
Key Laboratory of Micro-Nano Photonic Information Technology, Key Laboratory of Optoelectronic Devices and Systems of Ministry of Education and Guangdong Province, THz Technical Research Center of Shenzhen University, College of Physics and Optoelectronic Engineering, Shenzhen University, ShenzhenShenzhen 518060, China
e-mail: zbouyang@szu.edu.cn

Z. Oyuang
International Collaborative Laboratory of 2D Materials for Optoelectronic Science and Technology, Shenzhen University, Shenzhen 518060, P.R. China

K. Geetha et al. (eds.), *Recent Trends in Materials*, Springer Proceedings in Materials 18, https://doi.org/10.1007/978-981-19-5395-8_29

resonators were placed on which the top and lowest sides of the substrate. In theoretical and experimental studies of metamaterial perfect absorber, the macroscopic electromagnetic properties of surface arise at subwavelength scale due to collective response of the individual structure. Moreover, broadband absorption is attractive due to its practical applications in numerous fields such as imaging and surface-enhanced sensing. To maximize the bandwidth, multilayer structures are used [5, 9]. In recent years, terahertz absorbers have attracted great attention with the rapid development of terahertz technology. Usually, terahertz absorbers cover a huge range of spectrum from 0.1 to 10 THz. These terahertz metamaterial absorbers play a crucial role in the field of telecommunications [10–12]. These terahertz (THz) absorbers work on electromagnetic resonances to gain maximum absorption but their narrow bandwidth becomes a bottleneck for many applications and lies in security and industrial fields. Metamaterials are designed in many ways and have different categories depending on their functionalities. They are designed by alternative stacking of different materials which shows periodic nature. Metamaterial's properties strongly depend on their structure instead of the materials of which they are designed. Various metamaterials (MMs) have been realized theoretically and experimentally such as MMs absorbers that are designed by multiple stacking from bilayer to a few layers [6] including infrared or visible region.

Numerous structures have been proposed with a metallic base ground plane with a dielectric spacing periodically. Up to now, the theory of magnetic polaritons (MPs) has been effectively utilized to clarify and anticipate the resonances in a grating assembly composed of metals [13, 14], slim slit array [15, 16], double-layer nanoslit array [17], and deep grating [18, 19]. Indeed, MPs cannot just be utilized in a periodic structure with one dimension (1D), yet additionally legitimate in two dimension (2D) and three-dimension (3D) structures [17, 20]. Furthermore, because of the absence of the terahertz frequency spectrum in naturally occurring materials, high-performance terahertz metamaterial absorbers are in high demand. Nevertheless, their narrow bandwidth still limits their applications in various fields of technology. Numerous efforts have been made to extend their absorption band which includes many examples like using many resonators in the single unit cell, [21–23] dual-band absorber [24, 25], multi-band absorber [26, 27], broadband absorbers [28, 29], etc. However, the average absorptivity efficiency is not high because those absorption spectra are composed of discrete peaks. With this, there is one more thing that the single-band metasurface absorbers (MAs) are not appropriate for some particular zones such as phase imaging and spectroscopic detection where distinct absorption peaks are required and most metasurface absorbers (MAs) generally require unit cells with complex geometries, bringing about trouble and cost of manufacture. Moreover, many previous designs are sensitive to angular and polarization which may block numerous practical applications.

Here, we theoretically demonstrate the novel design of angular and S-polarization-insensitive and P-polarization-insensitive broadband multi-metasurfaces-based absorber (MMBA) in the infrared spectrum of wavelength ranging from 1.8 to 1.95 μm. The unit cell of MMBA consists of a five-layered periodic structure, in which metal and dielectrics are stacked alternatively with perfect electric conductor

(PEC) ground plane. To demonstrate the behavior of metal at infrared wavelength, two benchmarks of absorption are studied. First is to use a single dielectric structure, and second is to use a multi-dielectric resonator. In this paper, we demonstrated the broadband absorption of light with the absorption of an average of more than 60% at 1.92–1.94 μm wavelength for the single resonator. To achieve broadband absorption, a multilayered MIM resonator is used with a subwavelength period which increases the absorption up to 95%. The final proposed device of absorber shows almost double bandwidth as compared to the single resonator. Absorptivity $A(\omega)$ is calculated by using Eq. (1) given below

$$A = 1 - R(\omega) - T(\omega) \tag{1}$$

where $R(\omega)$ represents reflectivity and $T(\omega)$ shows transmissivity as functions of frequency ω, respectively.

2 Device Design and Simulation

Usually, the geometrical configuration and parameters are the special factor in deciding the resonance frequency. To achieve broadband absorption, multiple resonators of the same sizes can be used in 3D stacking configurations, which gives multiple absorption peaks, thus maximizing the absorption bandwidth. In this paper, the multi-metasurface broadband absorber (MMBBA) is demonstrated with multiple structures of different geometrical parameters as shown in Fig. 1. Figures 1a and c consist two different structures, in which a single dielectric resonator is replaced by a multi-resonator to further improve the absorptivity and absorption band of the proposed structure. A single unit cell is designed in such a way that it can cover numerous absorption peaks, by assembling different sized subunits, or sometimes they are stacked in vertical to form multilayer structures. Because of the resonance's independence, many well-defined resonant peaks are observed. To understand the concept of multi-band absorption, we first examine a single dielectric resonator as shown in Fig. 1a.

The proposed absorber is designed with a PEC on the ground plane, the top layer is gold with the conductivity of 4.10×10^7 S/m, and the dielectric is germanium (Ge) with a refractive index of 4.0. This structure is simulated for both S-polarized and P-polarized plane waves. The metal–insulator rings of identical width are periodically arranged on PEC with a period $\Lambda X = 1.5$ μm with widths $\Lambda Y = 1.5$ μm. Throughout the structure, the thickness of Ge is 0.1 μm. For a single resonator, the top metallic gold ring has thickness $t_{\text{Au(ring)}} = 0.025$ μm with a radius of 0.3 μm and the gold disk has thickness $t_{\text{Au(disk)}} = 0.1$ μm. We used PEC as a substrate and gold as a metal. The thickness of the substrate is chosen as $t_{\text{PEC}} = 0.1$ μm. Figure 1b presents the perspective view of single-band multi-sized resonators at normal incidence with the same thickness. The ring resonator of gold metal on the top of the surface has an outer radius of $R_1 = 0.3$ μm and has an inner radius of $R_2 = 0.2$ μm. Figure 1

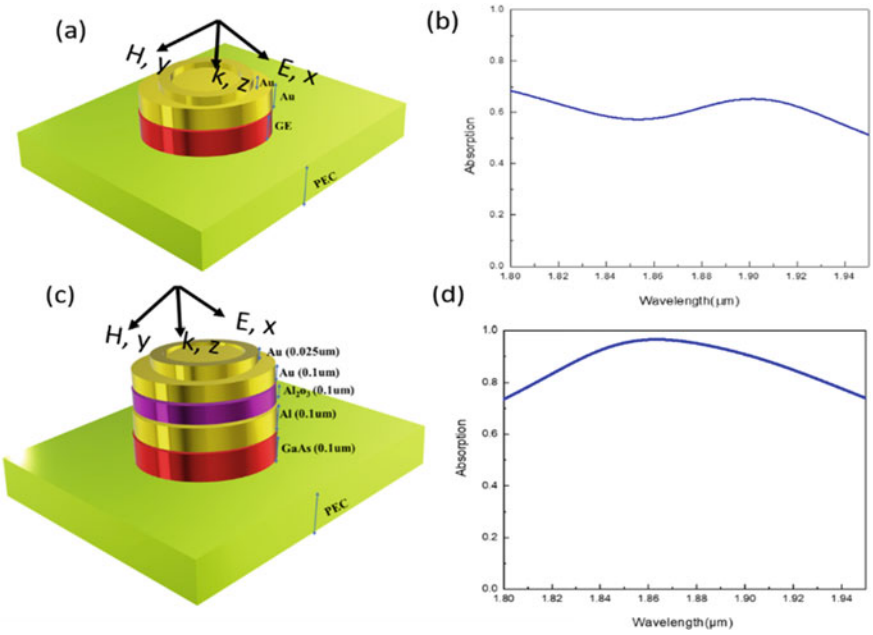

Fig. 1 **a** Perspective view of single dielectric layer resonator metasurface. **b** Absorption spectrum for structure in (**a**). **c** Perspective view of metasurface with multiple dielectric resonators. **d** The corresponding absorption spectrum for the resonator in (**c**)

has four different insets, in which Figs. 1a and c show the device structure from basic to advance at which the absorption increases up to 95% with a large absorption band. Figures 1c and d illustrate the absorption spectra corresponding to each structure shown with their respective subfigure. These absorption spectra display similar nature for S-polarization and P-polarization. The single spectrum is presented for the conciseness of the paper.

The finite-difference time-domain (FDTD) method is used to simulate and investigate the performance of the designed MM absorber, presented in Fig. 1. In the simulation arrangement, the boundary conditions are chosen according to the structure, in which *z*-direction is set as perfect matched layer (PML), and the others are set as periodic alongside the *x*- and *y*-directions. The final proposed absorber works in the range of terahertz regime with covering an ultra-high absorption in the wavelength range of 1.8–1.95 μm. The transmission is approximately zero in the whole spectrum range during simulations because of the complete inhibition of transmission due to the presence of the PEC ground plane. Therefore, the device shows minimum reflection and this eventually leads to an ultra-broadband absorption depicted in Fig. 1c. By taking the (absorption) $A > 60\%$, the range of the spectrum is varied from 1.8 to 1.95 μm for a single dielectric layer.

For further improvement in the absorption mechanism, a multilayer absorber is presented in Fig. 1c which shows the schematic arrangements of the multilayer structure and propagation configurations. The maximum absorption with this absorber is approximately more than 95%. Large broadband is achieved at a wavelength ranging from 1.85 to 1.88 μm which shows that this MMBA has a perfect bandwidth in the mid-infrared regime. This absorber shows excellent absorption including absorption bandwidth and absorption efficiency in comparison with common metallic nano-resonators-based absorbers [21]. In this proposed absorber, the calculated refractive index of GaAs is about 2.6, and the loss tangent of Al_2O_3 is 2.28. Moreover, their angle dependency and polarization dependency are investigated to make them more utilize in the field of science and technology.

3 The Absorption Characteristics

The absorption spectra as a function of incident angle are also investigated at a fixed azimuthal angle ($\varphi = 0$) and polarization angle ($\theta_p = 0$) as depicted in Figure. 2. It can be seen that the absorption spectrum remains unchanged at a different incident angles and peaks did not show any changes and show similar absorption at each angle. These results verify those surface plasmons are restricted and surface plasmonic resonance is not responsible for the excitation of these absorption peaks. There are no absorption dips which shows that our device is responding to the condition of destructive interference [30]. Figure 2a shows the absorption spectra of the MM absorber, in which the incident angle (θ) varies from 10° to 70°, and absorption is calculated. A similar absorption peak at each angle identifies that the proposed structure is angular insensitive and equally responds. First, Fig. 2a shows the incident angle variation for S-polarization where ($\theta_p = 0°$) and Fig. 2b displayed absorption spectra at various incident angles for P-polarization ($\theta_p = 90°$). This concludes that the proposed absorber behaves similarly for different polarized radiation with maximum absorption of up to 95%.

The absorber is further investigated to make it more effective for other applications such as photovoltaic cells where a wide angle is important to observe the radiation for maximum absorption [31, 32]. To use this absorber in various applications, absorption peaks are determined at various azimuthal angles where absorption spectra are calculated as a function of azimuthal angle (φ) at a fixed incident angle ($\theta = 0°$) and polarization angle ($\theta_p = 0°$) for S-polarization as shown in Fig. 3. Where these three angles can be defined as the angle of propagation concerning to injection axis is acts as the incidence angle (θ). The azimuthal angle (φ) is the angle of propagation concerning the angle of incidence. Figure 3a shows the absorption peaks for various azimuthal angles and keeps the incident angle the same that is 0°. Figure 3b illustrates the absorption spectra at different azimuthal ranging from $\varphi = 10°$ to $\varphi = 70°$ with the angle of incidence that is 0° for P-polarization. The polarization angle ($\theta_p = 0°$) defines the S-polarization, and polarization angle ($\theta_p = 90°$) is mentioned for P-polarization. It can be seen that absorption spectra remain unchanged at these angles.

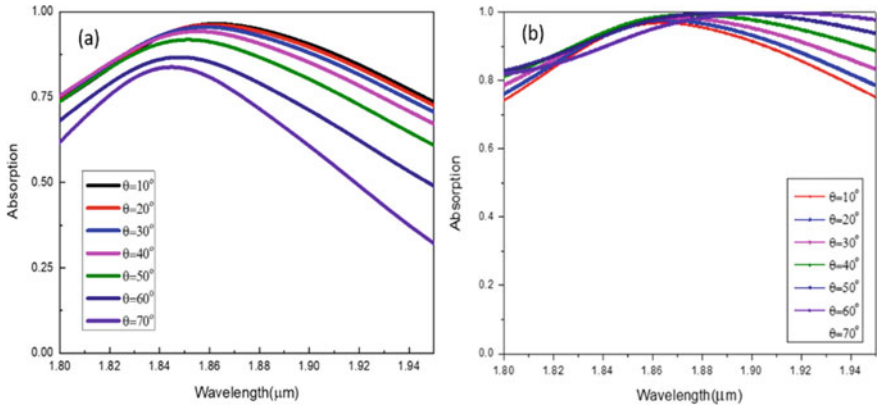

Fig. 2 **a** Absorption spectra of multi-structure at different incident angles are depicted ranging from $\theta = 10°$ to 70° at azimuthal angle $\varphi = 0°$ and polarization angle $\theta_p = 90°$ for S-polarization. **b** Absorption spectra for P-polarization

Therefore, it can be realized that our absorber shows the same absorption mechanism as that for 0° so we can realize that it is an omnidirectional and polarization-insensitive perfect absorber.

As a Function of Polarization Angle

For metamaterials, polarization insensitivity is an essential factor for their practical applications. To achieve this, we investigated a polarization-independent absorber for the different polarization angles. Absorption spectra are investigated and plotted at various polarization angles keeping the other two angles (incident angle and

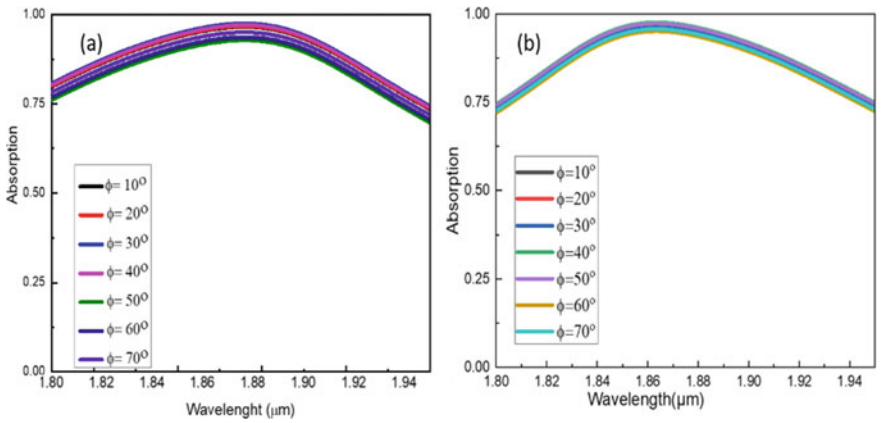

Fig. 3 **a** Absorption spectrum of MMBBA at different azimuthal angles extending from $\varphi = 10°$ to 70° for S-polarization. **b** Absorption spectra for $\varphi = 10°$ to $\varphi = 70°$ at a fixed incident angle of 0° for P-polarization

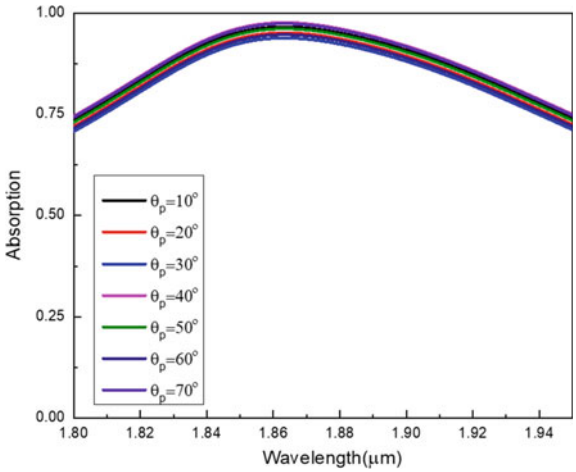

Fig. 4 Absorption spectra for multi-metasurface absorber as a function of wavelength for different polarization angle at a fixed azimuthal angle ($\varphi = 0°$) and incident angle ($\theta = 0°$). The black line shows the absorption spectra at $\theta_p = 10°$, red line shows at $\theta_p = 20°$, the blue line shows absorption spectra at $\theta_p = 20°$, etc.

azimuthal angle) constant that is 0° as shown in Fig. 4 for the proposed light absorber. The absorber shows similar bandwidth from 1.8 to 1.95 μm for TE and TM polarized light. It is found that in Fig. 4 both the absorption spectra are consistent with each other which shows the polarization insensitivity of the proposed absorber. When the multi-resonators are combined into a one-unit cell into the subwavelength period, the total absorption exceeds 90% from 1.8 to 1.95 μm. The simulation also reveals that our structure exhibits less absorption 1.8–1.95 μm for the single-layered structure, and for dual-layered structures, 95% absorptance is approximately in the 1.8–1.95 μm spectral range. The proposed device covers a wide range of applications such as biomedical, telecommunications, imaging, polarizer, modulator, photodetector, electromagnetic cloaks, and phase shifter [33–37].

4 Conclusion

In conclusion, an infrared broadband absorber based on dual-band multi-metasurface is proposed. Originally, a multi-structure single resonator with the same dielectric spacing layer is demonstrated to calculate the absorption spectra. A large absorption band is observed with around 65% absorptivity. To maintain the absorption band as large as it was with high absorptivity, the structure was modified and the final device is composed of a dual-band multilayer structure of the equivalent thickness and dielectric spacing layer. The absorption is increased twice by using a dual-band multilayer structure. That is, the absorption FWHM of single-layered is 65 and 95% (from 1.8 to 1.95 μm) for multilayered structure. The device shows much better performance than previously reported. This absorption is very robust to the incident angle, azimuthal angle, and polarization angle. Additionally, this also provides us with the omnidirectional behavior at each angle and also remains the same at each

polarization. By tuning geometric scalability, it can also work efficiently at another frequency regime. Due to the ultra-broadband property of the multilayered structure, it is helpful and can be used in spectroscopic imaging, thermal emitters, as well as thermal detectors, etc.

Acknowledgements This research was funded by the National Natural Science Foundation of China, grant numbers: 61275043, 61307048, 60877034, and 61605128. Moreover, it was partially funded by the Natural Science Foundation of Guangdong Province, grant number: 2020A1515011154 and the Natural Science Foundation of Shenzhen City, grant numbers: JCYJ20190808151017218, JCYJ20190808161801637, JCYJ20180305124247521, and 20180123.

References

1. Lu Y, Li J, Zhang S, Sun J, Yao JQ (2018) Polarization-insensitive broadband terahertz metamaterial absorber based on hybrid structures. Appl Opt 57(21):6269–6275
2. Liu Y, Huang R, Ouyang Z (2021) Terahertz absorber with dynamically switchable dual-broadband based on a hybrid metamaterial with vanadium dioxide and graphene. Opt Express 29(13):20839–20850
3. Barzegar-Parizi S, Ebrahimi A, Ghorbani K (2021) Dual-broadband and single ultrawideband absorbers from the terahertz to infrared regime. J Opt Soc Am B 38(9):2628–2637
4. Ding F, Cui Y, Ge X, Jin Y, He S (2012) Ultra-broadband microwave metamaterial absorber. Appl Phys Lett 100(10):103506
5. Liu S, Chen H, Cui TJ (2015) A broadband terahertz absorber using multi-layer stacked bars. Appl Phys Lett 106(15):151601
6. Zhu P, Guo LJ (2012) High performance broadband absorber in the visible band by engineered dispersion and geometry of a metal-dielectric-metal stack. Appl Phys Lett 101(24):241116
7. Wang B-Y et al (2014) A novel ultrathin and broadband microwave metamaterial absorber. J Appl Phys 116(9):094504
8. Landy NI, Sajuyigbe S, Mock JJ, Smith DR, Padilla WJ (2008) Perfect metamaterial absorber. Phys Rev Lett 100(20):207402
9. Zhu J et al (2014) Ultra-broadband terahertz metamaterial absorber. Appl Phys Lett 105(2):021102
10. Zhang B, Zhang Y, Duan J, Zhang W, Wang W (2016) An omnidirectional polarization detector based on a metamaterial absorber. Sensors 16(8):1153
11. Zheng X, Xiao Z, Ling X (2017) Broadband visible perfect absorber for sensor based on ultra-thin metamaterial. J Mater Sci: Mater Electron 28(11):7739–7744
12. Paul O et al (2009) Polarization-independent active metamaterial for high-frequency terahertz modulation. Opt Express 17(2):819–827
13. Lee BJ, Wang L, Zhang Z (2008) Coherent thermal emission by excitation of magnetic polaritons between periodic strips and a metallic film. Opt Express 16(15):11328–11336
14. Sakurai A, Zhao B, Zhang ZM (2014) Resonant frequency and bandwidth of metamaterial emitters and absorbers predicted by an RLC circuit model. J Quant Spectrosc Radiat Transfer 149:33–40
15. Chen C-J, Chen J-S, Chen Y-B (2011) Optical responses from lossy metallic slit arrays under the excitation of a magnetic polariton. J Opt Soc Am B 28(8):1798–1806
16. Wang L, Zhang Z (2009) Resonance transmission or absorption in deep gratings explained by magnetic polaritons. Appl Phys Lett 95(11):111904
17. Wang H, Wang L (2013) Perfect selective metamaterial solar absorbers. Opt Express 21(106):A1078–A1093

18. Wang L, Zhang ZM (2010) Effect of magnetic polaritons on the radiative properties of double-layer nanoslit arrays. J Opt Soc Am B 27(12):2595–2604
19. Wang L, Zhang Z (2011) Phonon-mediated magnetic polaritons in the infrared region. Opt Express 19(102):A126–A135
20. Cheng D, Xie J, Zhang H, Wang C, Zhang N, Deng L (2012) Pantoscopic and polarization-insensitive perfect absorbers in the middle infrared spectrum. J Opt Soc Am B 29(6):1503–1510
21. Tao H et al (2008) Highly flexible wide angle of incidence terahertz metamaterial absorber: design, fabrication, and characterization. Phys Rev B 78(24):241103
22. Cong L, Tan S, Yahiaoui R, Yan F, Zhang W, Singh R (2015) Experimental demonstration of ultrasensitive sensing with terahertz metamaterial absorbers: a comparison with the metasurfaces. Appl Phys Lett 106(3):031107
23. Tao H, Landy NI, Bingham CM, Zhang X, Averitt RD, Padilla WJ (2008) A metamaterial absorber for the terahertz regime: design, fabrication and characterization. Opt Express 16(10):7181–7188
24. Koechlin C et al (2011) Total routing and absorption of photons in dual color plasmonic antennas. Appl Phys Lett 99(24):241104
25. Yahiaoui R et al (2015) Trapping waves with terahertz metamaterial absorber based on isotropic Mie resonators. Opt Lett 40(13):3197–3200
26. Yahiaoui R, Guillet JP, de Miollis F, Mounaix P (2013) Ultra-flexible multiband terahertz metamaterial absorber for conformal geometry applications. Opt Lett 38(23):4988–4990
27. Wang B-X, Wang G-Z, Sang T, Wang L-L (2017) Six-band terahertz metamaterial absorber based on the combination of multiple-order responses of metallic patches in a dual-layer stacked resonance structure. Sci Rep 7(1):1–9
28. Beeharry T, Yahiaoui R, Selemani K, Ouslimani HH (2018) A dual layer broadband radar absorber to minimize electromagnetic interference in radomes. Sci Rep 8(1):1–9
29. Beeharry T, Yahiaoui R, Selemani K, Ouslimani HH (2018) A co-polarization broadband radar absorber for RCS reduction. Materials 11(9):1668
30. Pan H, Zhang H, Tian X, Zhang D (2021) Design, simulation, and analysis of an ultra-broadband polarization-insensitive terahertz metamaterial absorber. J Opt Soc Am B 38(1):95–103
31. Rufangura P, Sabah C (2015) Dual-band perfect metamaterial absorber for solar cell applications. Vacuum 120:68–74. https://doi.org/10.1016/j.vacuum.2015.05.033
32. Rufangura P, Sabah C (2016) Polarisation insensitive tunable metamaterial perfect absorber for solar cells applications. IET Optoelectron 10(6):211–216. https://doi.org/10.1049/iet-opt.2016.0003
33. Charola S, Patel SK, Parmar J, Jadeja R (2022) Multiband Jerusalem cross-shaped angle insensitive metasurface absorber for X-band application. Journal of Electromagnetic Waves and Applications 36(2):180–192
34. Huang Y, Feng Y, Jiang T (2007) Electromagnetic cloaking by the layered structure of homogeneous isotropic materials. Opt Express 15(18):11133–11141
35. Watts CM et al (2014) Terahertz compressive imaging with metamaterial spatial light modulators. Nat Photonics 8(8):605–609
36. Islam M, Rao S, Kumar G, Pal BP, Chowdhury DR (2017) Role of resonance modes on terahertz metamaterials based thin film sensors. Sci Rep 7(1):1–8
37. Han Z et al (2017) Thin terahertz-wave phase shifter by flexible film metamaterial with high transmission. Opt Express 25(25):31186–31196

Natural Frequency of Overhead Water Tanks Using Shaking Table

M. B. Vikram, G. P. Chandradhara, and J. Abdul Bari

Abstract The response of elevated water tanks to dynamic loading is more complex and harder to be studied due to the complex fluid structure interaction. The objective of the study is to find the natural frequency of overhead water tanks using shaking table by one-mass and two-mass idealizations. Four tanks of various *h*/*L* ratios have been considered during the study. The natural frequency of the water along with the tank is determined during shaking for different combinations of frequency, amplitude and height of water in the tank have been determined experimentally. The value of natural frequency is determined experimentally and analytically by one-mass and two-mass idealizations for all the four models with impulsive and convective frequency. It is observed that the natural frequency obtained by one-mass idealization irrespective of fixity and hinge base shows that the natural frequency increases and then decreases with *h*/*L* ratio.

Keywords Natural frequency · Amplitude · Over head tank · Shaking table

1 Introduction

Water tanks are the most vital structures in a community which are used to store water for domestic and industrial purposes. Failure of water tanks during an earthquake can be disastrous as it caters to various needs of the community. Failure of water tanks may result in water crisis among the public and makes it difficult to fight fires caused during the earthquake. Most of the water tanks in the world are designed and constructed

M. B. Vikram (✉) · G. P. Chandradhara
Department of Civil Engineering, JSS Science and Technology University, Mysore, Karnataka, India
e-mail: vikrampalegar@gmail.com

G. P. Chandradhara
e-mail: chandradhara_gp@sjce.ac.in

J. A. Bari
Department of Civil Engineering, K.S.Rangasamy College of Technology, Tiruchengode, Tamilnadu, India
e-mail: abdulbari@ksrct.ac.in

K. Geetha et al. (eds.), *Recent Trends in Materials*, Springer Proceedings in Materials 18, https://doi.org/10.1007/978-981-19-5395-8_30

without the use of the latest available seismic design procedures and therefore are susceptible to damage and eventually fails during the occurrence of an earthquake. Elevated water tanks are structures constructed at a required height from the ground level to accommodate the water needs of a large area. The analysis of the structure considering the seismic forces prove to be crucial to assure safety during earthquakes and make sure the tanks remain functional even after the calamity. Elevated water tanks are of irregular shape with a huge mass on top of a lean supporting structure making it prone to the seismic forces.

The response of elevated water tanks to dynamic loading is more complex and harder to be studied due to the complex fluid structure interaction. The walls of the tank, in addition to the hydrostatic pressure, experience hydrodynamic forces when the structure experience a seismic load [1]. During seismic analysis, the impulsive hydrodynamic pressure is of more prominence than the convective hydrodynamic pressure when the tank is full, but when the tank is partially full the convective hydrodynamic pressure is of more prominence [2], which implies that the effect of sloshing is minimum when the tank is full and more when the tank is partially filled. Liquid sloshing is as kind of wave motion in partially filled containers [3]. Under the action of external vibrations of large amplitude and at resonance, the liquid inside a partly filled tank is subjected to vicious oscillations which have large, localized impact pressure on the tank walls and the base [4]. This localized impact pressure on the walls of the tank may result in structural damage. When the frequency of the external shaking is near to one of the natural frequencies of the tank with liquid, i.e., impulsive in case of one-mass approximation and impulsive and convective in two-mass approximation [5], large sloshing amplitudes may be anticipated. Sloshing even at small excitations is not a gentle phenomenon. The liquid motion can become very nonlinear, and the surface slopes can reach infinity, and the liquid may encounter the tank top in case of an enclosed tank [6, 7]. Hence, the natural frequency of the elevated water tanks is of key factor in the analysis.

2 Dynamic Model Idealization

The water structure interaction makes dynamic analysis a complex problem. Based on several studies, simple spring-mass models shown in Fig. 1b has been proposed to represent the tank-liquid system and to calculate the hydrodynamic forces [8]. If a closed tank is completely full of water or completely empty, it is essentially to do modelling by one-mass idealization shown in Fig. 1c. If the tank has a free water surface, there will be sloshing of the water during an earthquake, and this makes the tank essentially a two-mass structure [9–12]. In this case, the dynamic behavior of an elevated tank may be quite different. For elevated tanks [13–15], the two-mass idealization is shown in Fig. 1d and can be treated as two uncoupled single degree of freedom systems [16, 17]. Figure 1e represents the impulsive plus structural mass behaving as an inverted pendulum with lateral stiffness equal to that of the staging, Ks and the other representing the convective mass with a spring of stiffness, Kc.

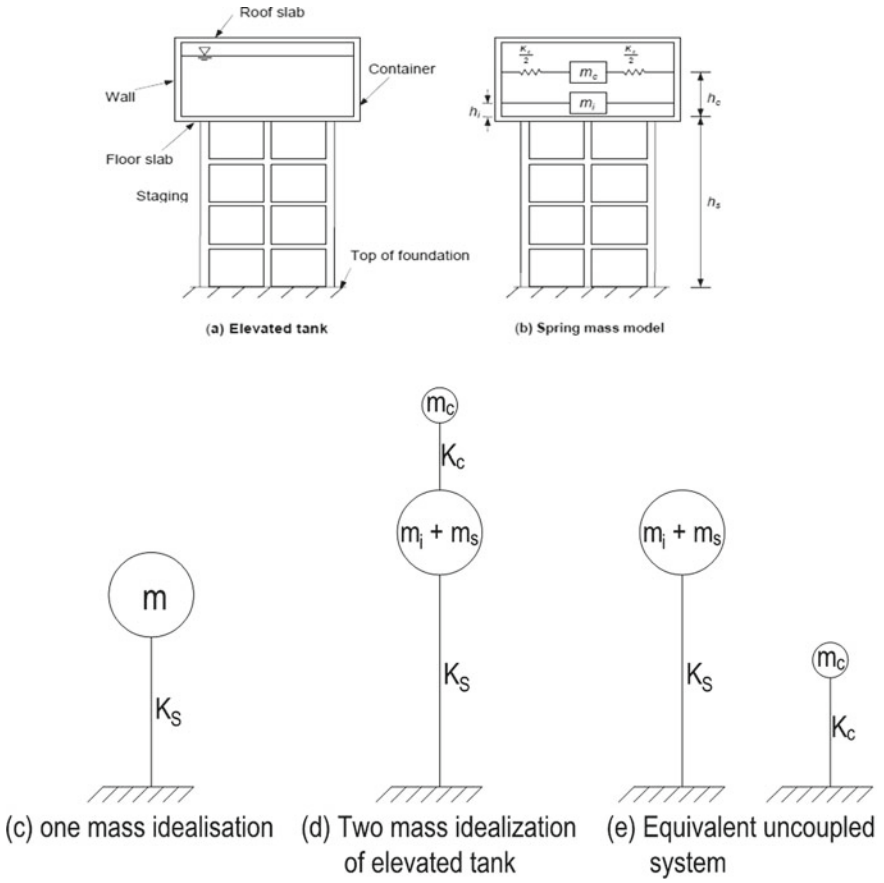

Fig. 1 Mass model idealization of elevated water tank

3 Methodology

For the present study of dynamic behavior of overhead tanks, four scaled models of different aspect ratio have been fabricated using acrylic for the container and aluminium strips and plates for the staging columns and base plate; the tests are carried out on the shaking table apparatus; various response parameters at various heights are recorded using acceleration sensors; the signals from the sensors are processed and stored using a data acquisition software and system called DEWE-SOFT [18, 19]; natural frequencies of the water along with tank are determined experimentally and compared with the values obtained analytically and using ETABS software package [20].

4 Experimental Study

The most effective method of determining the exact response of structures is through experimental investigation. In comparison with their scale models, full-size models produce better results. However, due to their robust nature, full-scale model testing may not always be feasible. In the present study, an attempt is made to study the natural frequencies of elevated rectangular overhead water tank models using shaking table tests.

4.1 Shaking Table Apparatus

Figure 2 shows the shaking table apparatus mounted with a DC-powered motor, flywheel and cam arrangement. It can produce only sinusoidal vibration at the base in the horizontal direction. But it has a provision to apply the vibrations at any desired horizontal angle with the help of a rotating disc mounted on the table. The amplitude of base motion can be varied with the help of flywheel and radial scale arrangement, but this aspect is not crucial in the conduct of the experiment. The maximum payload of the shake table is 30 kg. The operating frequency is limited to 25 Hz with a least count of 0.05 Hz and the amplitude range lies between 0 and 10 mm with a least count of 1 mm. The size of the table is 400 × 400 mm.

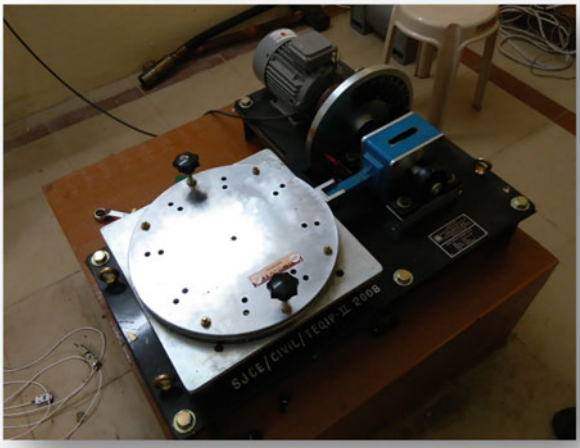

Fig. 2 Horizontal shaking table apparatus

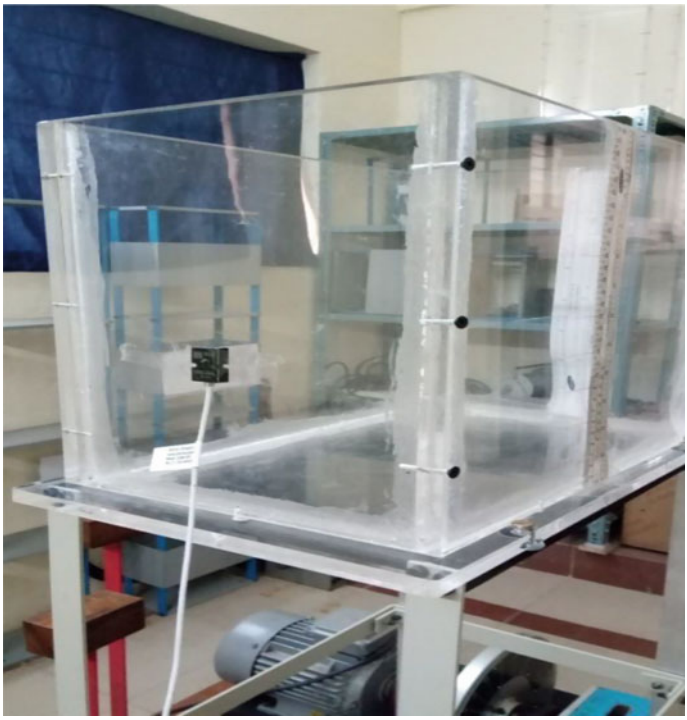

Fig. 3 Acceleration sensor mounted on tank

4.2 Piezoelectric Acceleration Sensors

In this experiment, piezoelectric acceleration sensors are used to collect the acceleration time history. These devices measure changes in acceleration and transform them into electrical charge via the piezoelectric effect. Piezoelectric converts one form of energy into another and provides an electrical signal in response to a quantity, property, or condition that is being measured. Figure 3 shows acceleration sensor mounted on tank, the capacity of the acceleration sensor is 6.25 g. The device is calibrated in such a way that the voltage signals are converted into an equivalent acceleration. The conversion factor of the sensors used in the present study is in the range of 790–810 mV/g.

4.3 Experimental Model Description

The dimensions of the model is fixed base on the natural frequency of the model to be within the operating frequency range of shaking table, and the total mass of the structure should lie within the maximum payload (30 kg). For achieving lightweight

of the model, the containers are made of acrylic plates of thickness 12 mm. The staging is made of aluminium in which the columns are made of aluminium flats of thickness 3 mm, and the base plate is made of aluminium plates of thickness 8 mm.

Four models of the tank with different aspect ratio are considered for the study (Fig. 4), and the dimensions of the tank are shown in Table 1. Aspect ratio and mass are interrelated as the ratio increases (keeping the height and width constant) the mass increases and frequency decreases and vice versa.

The tank is supported on a staging of height 400 mm, and there are no braces. The staging consists of 4 aluminium columns of cross section 25 mm × 3 mm. An aluminium base plate of thickness 8 mm corresponding to the size of the tank is used to provide platform so as to rest water tank. The thickness of the container mainly depends on the capacity of tank. İn the present study, the thickness of plate is chose based on fabrication point of view and the limitations of the shaking table (payload capacity 30 kg). The setup is shown in Fig. 5.

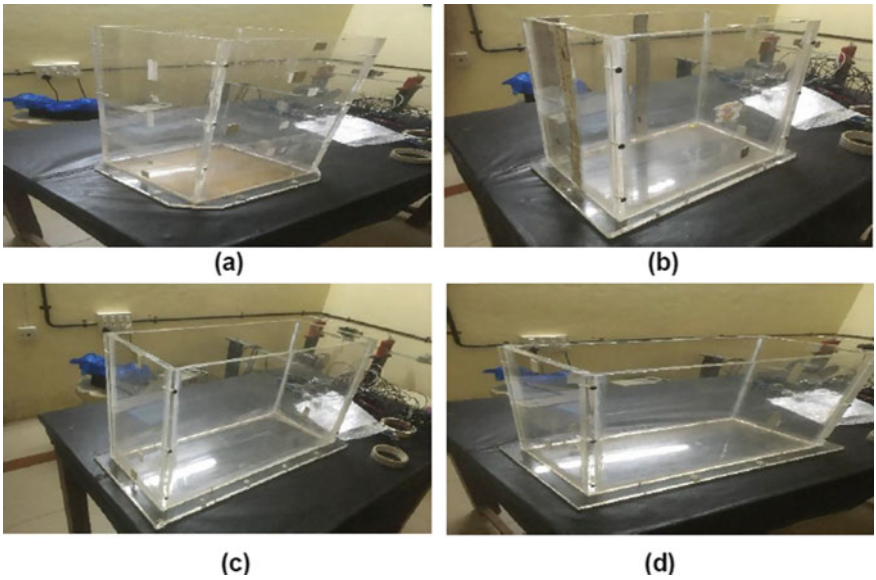

Fig. 4 Model containers of different aspect ratios

Table 1 Dimensions of the water tank

Model no	Aspect ratio	Length (mm)	Width (mm)	Height (mm)	Mass (kg)
1	1	200	200	500	12.53
2	1.5	350	200	300	10.54
3	2.0	400	200	350	13.56
4	2.5	450	200	350	15.28

Fig. 5 Elevated water tank on shaking table

5 Natural Frequency of Models

The concept of natural frequency applies to a huge range of natural and man-made systems. The frequency which produces maximum response amplitude is known as the resonant frequency or natural frequency. At this frequency, even small periodic driving forces can produce large amplitude oscillations. Thus, natural frequency plays a vital role in any dynamic analysis. Some complex systems possess more than one natural frequency and are referred as multi-degrees of freedom systems.

One of the greatest ways to describe resonance is to use the example of a swing. Small pushes performed over time build up significant amplitude of motion in a swing. This is due to the fact that each push is timed to the swing's natural momentum. The swing has a natural frequency, similar to that of a pendulum. It is feasible to create a huge motion by delivering little pushes at a frequency that matches the natural frequency. Resonance is created by the combination of the recurring pushes and the swing's natural motion. The swing's motion becomes huge even though the pushes are little as a result of the resonance. Resonance is not a single thing. Resonance is an interaction between a wave, a driving force, and the boundaries of the system.

The natural frequency of the structure is a function of mass of the structure, material damping properties, stiffness of the structure, rigidity of joints, etc.

In the present work, the natural frequencies of models have been obtained by considering one-mass and two-mass idealizations.

5.1 *Natural Frequency of the Model by One-Mass Idealization*

Elevated tanks shall be regarded as systems with a single degree of freedom with their mass concentrated at their centre of gravity. Figure 1c represents the idealization of the model. Since the damping is very small, the model is idealized as un-damped system. Figure 6 shows finite element analysis (FEA) model of the tank before and after loading.

The tank is filled with 100 and 150 mm of water, and natural frequency in the first mode is obtained. The natural frequency of the model is obtained by considering the base as fixed and hinge. The natural frequency of all the models using one-mass approximation is obtained using finite element software ETABS [8] and is shown in Table 2.

From Table 2, it is evident that the natural frequency of the structure decreases with the increase in mass of the structure. Figure 7 shows the variation of frequency

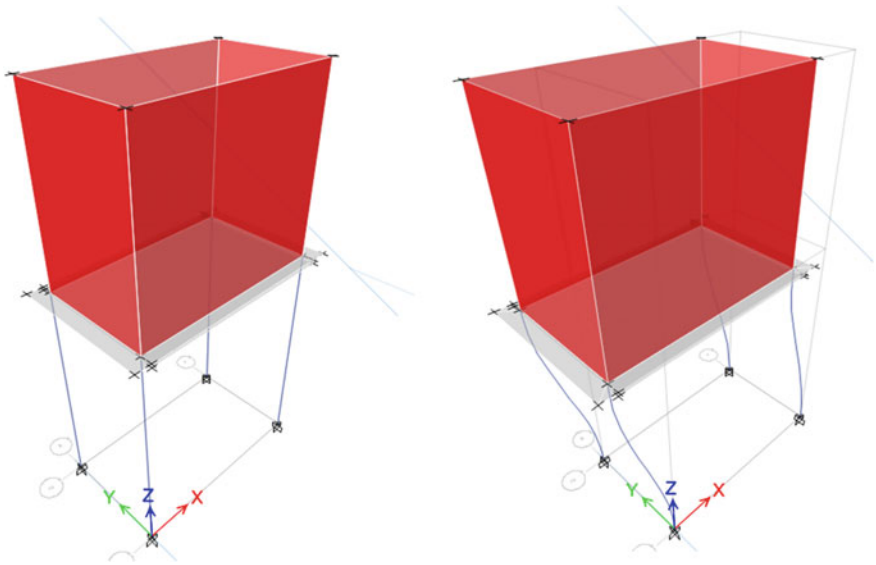

Fig. 6 FEA model of undeformed and deformed shape of staging

Table 2 Natural frequency by one-mass approximation

Model no.	Height of water in tank (mm)	*h*/*L*	Mass (kg)	Natural frequency, Hz (ETABS)	
				Fixed	Hinged
1	100	0.5	14.57	2.53	1.27
	150	0.75	18.57	2.33	1.05
2	100	0.33	15.17	2.84	1.42
	150	0.45	18.47	2.63	1.31
3	100	0.25	18.68	2.58	1.28
	150	0.37	22.68	2.44	1.22
4	100	0.2	22.40	2.41	1.21
	150	0.3	27.4	2.32	1.16

Note: h = maximum depth of liquid in tank, L = inside length of rectangular tank parallel to direction of seismic force

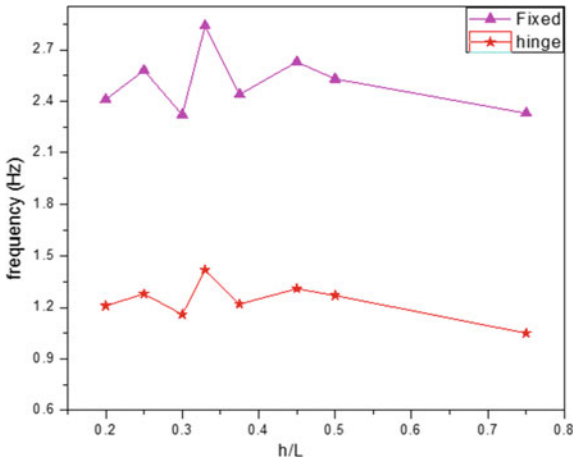

Fig. 7 Variation of frequency with respect to *h*/*L* in one-mass idealization

with respect to the *h*/*L* ratio for both fixed and hinge bases. It is observed that with the fixed and hinge base, natural frequency increases and then reduces.

5.2 Natural Frequency of the Model by Two-Mass Idealization

The natural frequency of the model is obtained using experimental approach. Initially fabricated models are placed on horizontal shaking table; then, the acceleration sensors are calibrated. The sensors are placed at the base to know the input motion

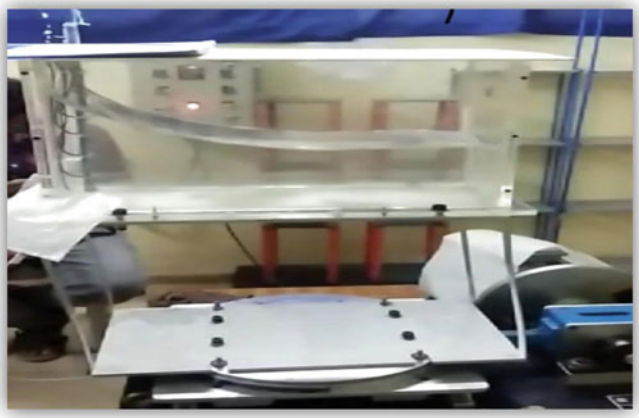

Fig. 8 Resonance at convective frequency

and top of the tank to determine response. Acceleration sensors are then connected to channels in data acquisition system DEWE-43 [5]. The amplitude in the horizontal shaking table is made fixed, and frequencies are controlled or altered using frequency controller from lowest to highest value. It is observed during shaking that when the frequency of base motion is gradually increased; two types of behavior are observed. To capture this behavior, frequency domain analysis is made. Figures 8 and 9 show the behavior at two different intervals.

The data or values obtained from sensors are stored in the data acquisition system. The stored values are then transferred to origin [6] software for further analysis. Using the acceleration time history, the predominant frequency is obtained by fast Fourier transform (FFT). Figure 10 shows time history of acceleration plot and the Fourier spectra. It is observed that two predominant frequencies exist indicating the natural frequencies at Impulsive and Convective mode of model-3 with height of water 100 mm. Similarly, for all the models, the impulsive frequency and convective frequency are obtained and shown in Table 3.

The two-mass idealization gives us two natural frequencies, namely the convective and the impulsive frequency. The primary frequency is the convective frequency which at resonance causes periodic sloshing at top portion of the liquid. The second frequency is called the impulsive frequency at resonance, and the behavior of the liquid is impulsive and unpredictable in nature. It does not exhibit a definite pattern of behavior unlike the convective component.

During the test, video recording was also taken and from the slow motion, the frequencies of convective and impulsive motion are obtained for model-3 with height of water 100 mm. It is found that in convective motion, the time taken for 20 cycles was found to be 20.51 s and the frequency was 1.02 Hz. Also, in impulsive motion, the time taken for 20 cycles was found to be 11.43 s and the frequency was 1.74 Hz. The

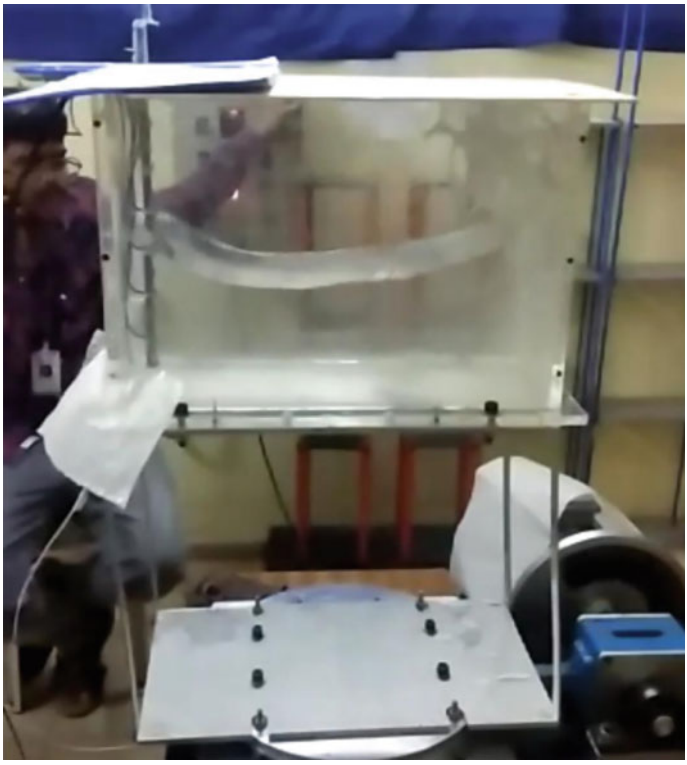

Fig. 9 Resonance at impulsive frequency

corresponding values obtained from FFT are 1.05 and 1.74 Hz. Thus, the frequencies obtained by FFT match well with the measured frequency from the time history graph.

From Tables 2 and 3, it is evident that the natural frequency obtained by FEM analysis (one-mass idealization) is in the same range as obtained by the experimental method (two-mass idealization).

Figure 11 shows the variation of frequency (impulsive and convective) with the h/L ratio. The impulsive frequency is higher as it contains bottom mass and the convective frequency is lower as it is having upper-mass which is usually lower. Figure 12 shows the variation of frequency with one-mass and two-mass idealization (impulsive) for different h/L ratios. It is interesting to observe that the impulsive frequency obtained by the experimental method lies between the values of frequency obtained by FEM analysis with one-mass idealization with supports fixed and hinged. This indicates that the fixity at the bottom of the tank during experiment is neither completely fixed nor hinged and exhibits partial fixity.

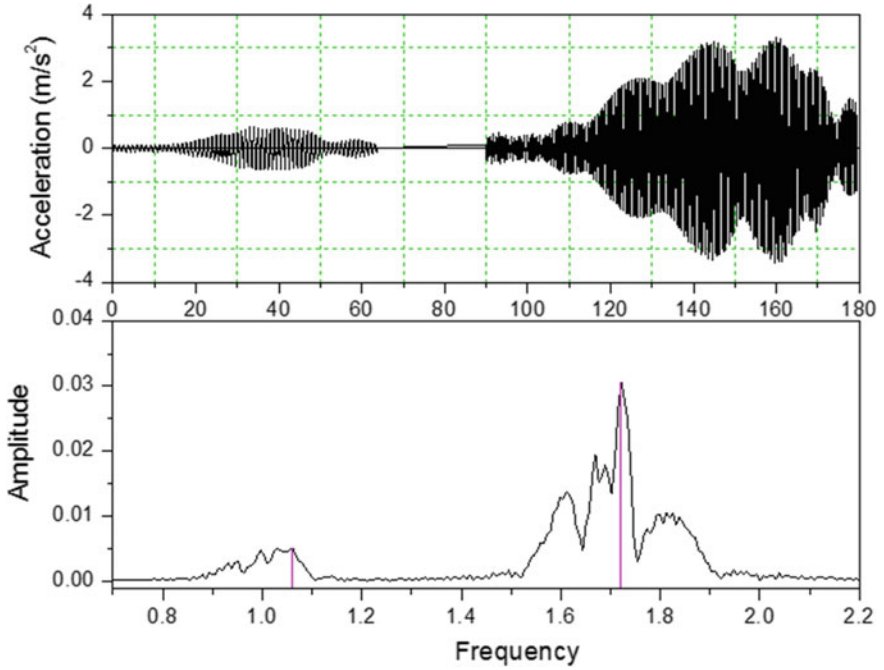

Fig. 10 Acceleration time history and frequency domain analysis of model-3 with height of water 100 mm

Table 3 Natural frequency by two-mass idealization (experimental)

Model no.	*h*/*L*	Height of the water, mm	Impulsive frequency, Hz	Convective frequency, Hz
1	0.5	100	2.45	1.5
	0.75	150	2.2	1.55
2	0.33	100	2.3	1.25
	0.45	150	2.15	1.35
3	0.25	100	1.74	1.05
	0.375	150	1.9	1.15
4	0.2	100	1.75	0.95
	0.3	150	1.65	1.10

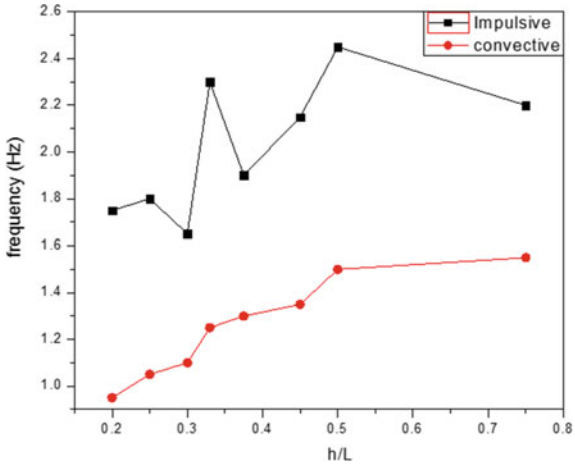

Fig. 11 Natural frequency variation with respect to *h*/*L* in two-mass idealization

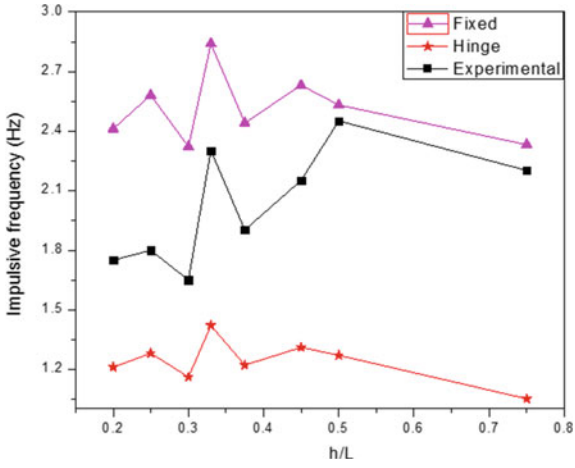

Fig. 12 One-mass and two-mass idealization with respect to *h*/*L*

6 Conclusions

The experimental and numerical study resulted in the following conclusions:

- The natural frequency obtained by one-mass idealization irrespective of fixity and hinge base shows that the natural frequency increases and then decreases with *h*/*L* ratio.
- The natural frequency obtained by experimental method (two-mass idealization) shows the increasing tendency with the increase in *h*/*L* ratio.
- In the experimental study, it is observed that two frequencies, namely convective and impulsive frequencies, are identified based on the behavior of liquid mass movement.

- In impulsive behavior, larger mass moves along with the container at higher frequency and the top mass shows the sloshing phenomenon with lower frequency.
- The convective and impulsive frequencies obtained from fast Fourier transform matches well with the frequency obtained by actual measurement from the response time history.
- The impulsive frequency obtained by experimental method lies between the values of frequency obtained by finite element analysis with one-mass idealization with supports fixed and hinge.

References

1. Housner GW (1963) The dynamic behaviour of water tank. Bull Seismol Soc Am 53(2):381–387
2. Dona Rose KJ, Sreekumar M, Anumod AS (2015) A study of overhead water tanks subjected to dynamic loads. International Journal of Trends and Technology 28(7):344–348
3. IITK-GSDMA (2007) Guidelines for seismic design of liquid storage tanks. National Information Centre for Earthquake Engineering, IIT Kanpur
4. Minowa C (1980) Dynamic analysis for rectangular water tanks. Recent advances in lifeline earthquake engineering in Japan, pp 135–142
5. Vijay PM, Prakash A (2014) Analysis of sloshing impact on overhead liquid storage structures. International Journal of Research in Engineering and Technology 2(8):127–142
6. Chen JZ, Kianoush MR (2004) Response of concrete liquid containing structures in different seismic zones. In: 13th World conference on earthquake engineering Vancouver BC, Canada, Paper No. 1441, 1–6 Aug 2004
7. Patil SA, Kumbhar AH, Mujawar TF (2016) Elevated water tank under sloshing effect. International Journal of Scientific Research and Development 4(05)
8. Hirde S, Bajare A, Hedaoo M (2011) Seismic performance of elevated water tanks. International Journal of Advanced Engineering Research and Studies I(I):78–87
9. Waghmare MV, Madhekar SN (2013) Behaviour of elevated water tank under sloshing effect. International Journal of Advanced Technology in Civil Engineering 2(1):51–54
10. Ronad U, Raghu KS, Guruprasad TN, Seismic analysis of circular elevated tank. International Research Journal of Engineering and Technology (IRJET) 3(9):903–907
11. IS 1893 (Part 2) (2014) Criteria for earthquake resistant design of structure. Liquid retaining tanks
12. Malhotra PK, Wenk T, Wieland M (2000) Simple procedure for seismic analysis of liquid storage tanks. Struct Eng Int 10(3):197–201
13. Patel CN, Vaghela SN, Patel HS (2012) Sloshing response of elevated water tank over alternate column proportionality. International Journal of Advanced Engineering Research and Studies III:60–63
14. Gaikwad MV, Mangulkar MN (2013) Comparison between static and dynamic analysis of elevated water tank. International Journal of Civil Engineering and Technology (IJCIET) 4(3):12–29. ISSN Print: 0976-6308, ISSN Online: 0976-6316
15. Falguni A, Vanza MG (2012) Structural control system for elevated water tank. International Journal of Advanced Engineering Research and Studies I(III):325–328
16. Avval IT, Kianoush MR, Ghaemmaghami AR (2012) Effect of three dimensional geometry on sloshing behavior of rectangular water tank. Presented paper on 15th conference of World conference on earthquake engineering at LISBOA 2012, pp 1–10
17. Godderidge B, Turnock S, Tan M, Earl C (2009) An investigation of multiphase CFD modeling of a lateral sloshing tank. Comput Fluids 38:183–193

18. DEWESoft V7.0.3 (2011) User manual for DEWESoft, DEWE Organisation, Trbovlje Slovenia
19. OriginPro (2017) User guide for OriginPro. Origin Lab Corp. Northampton, USA
20. ETABS 16.2.0 (2016) CSI analysis reference manual. Computers and structures, Inc, Berkeley, California, USA

Metamaterial-Based Biomedical Antenna for Low SAR Applications

G. V. Naveen Kumar, D. K. Kavitha, and P. Kiran Babu

Abstract In this paper, by analysing the ISM frequency bands, a biomedical antenna for on-body sensor has been designed. The proposed antenna has been designed over a frequency range of 2.3–3.5 GHz and 5.1–6.8 GHz with fractional bandwidth of 41% and 28%. The range of ISM frequency bands are 2.45 and 5.8 GHz. Obtaining the dual-band applications using split ring resonators is responsible for analysation. Polyamide substrate of dielectric constant of 3.5 and loss tangent of 0.008, which is a flexible substrate, has been designed. To analyse the flexible nature of antenna, bending analysis is required. This antenna serves as a stable dipole along with omnidirectional patterns.

Keywords Omnidirectional patterns · Biomedical applications · ISM frequency bands · SAR applications

1 Introduction

From past years, microwave antennas in the field of biomedical have been concentrated majorly on evolving physical parameter monitoring and hyperthermia [1]. Significantly, antennas that are placed in either inside or outside of human body help in evaluating the temperature of cancer cells. For this purpose, antennas having less weight and height with monopole or dipole having feed at centre are utilized and will be treated as sensors and exchange information in order to transfer physiological parameters for analysing [2, 3]. These antennas must have tolerance for biocompatibility tissues and should be small scale. Antenna designing which can be capable of operating is challenging in current scenarios. Some of the parameters which need to be considered are low power requirements, impedance matching, tissue conductivity should be high, size of the antenna and finally biocompatibility takes part a major

G. V. N. Kumar · D. K. Kavitha (✉) · P. K. Babu
Department of ECE, PACE Institute of Technology and Sciences, Ongole, Andhra Pradesh, India
e-mail: Kavitah_dk@pace.ac.in

P. K. Babu
e-mail: kiran_p@pace.ac.in

K. Geetha et al. (eds.), *Recent Trends in Materials*, Springer Proceedings in Materials 18, https://doi.org/10.1007/978-981-19-5395-8_31

role [4, 5]. Geometry of tissues and dielectric constants are considered for simulation. The coverage of ISM band application frequencies is required for this antenna. There is an availability of numerous frequency bands. One of the most widely used frequency bands is MIC bands which range from 402 to 405 MHz [6]. There are some additional frequency bands which are suggested for biotelemetry like 433.1, 434.8 MHz, from 868 to 868.6 MHz, from 902.8 to 928 Hz and from 2.45 to 2.48 GHz [7].

With the help of Rogers-3210 substrate, stacked antenna was designed for medical devices majorly. For studying reflection coefficient characteristics, the antenna was tested with de-ionized water and cellulose solution. Another antenna was designed for glucose monitoring applications with dual-band characteristics. The antenna worked at 402–405 MHz and 2.4–2.48 GHz, and for in-body testing, it was experimented with skin mimicking gel. Small antennas with electrical properties are appropriate for medical purposes [8]. So, under downsizing approaches, having a high directed substrate and current flow on the patch are benefits [9, 10]. The antenna was created and implanted inside the lossy medium, particularly in the human body. The near field power of an antenna increases with rising temperature, and it may also be utilized for therapeutic treatment, which has a negative impact [11]. Temperature will be raised on human tissues in the vicinity of implants for high-frequency operations. To generate radiation properties effectively in implantable antennas, the meander line structure antenna with reconfigurable frequency characteristics was used. For some important applications like patient's data monitoring and transmitting data to external device, MICS band antenna was composed.

Antennas are useful for sensor applications such as dielectric, moisture readings and sensing owing to dielectric objects. Antennas employed in therapeutics have a wide range of uses, including cancer therapy using hyperthermia [12–15], cardiac oblation and angioplasty and many more. Various antennas were built to provide inductive coil wire around dielectric ferrite, which were utilized for biomedical telemetry services such as wireless implanted communication [16–18]. The main disadvantage of this antenna was that it produced poor data rates in coil damaged devices in biocompatible tissue dipole and microstrip installed on the human body, as measured by FTDT [19].

In this article, a tiny dual-band antenna has been constructed for on-body usage. For developing and analysing, a polyamide substrate is employed. The assembled model is encircled by circular patch antenna that may be generated iteration by iteration. The body-centric antenna, as well as SAR applications, has all been developed in a sequential manner. There is a strong link between the simulated and real-world outcomes.

2 Construction of Antenna and Result Analysis

Antenna has been constructed using polyamide structure with rectangular patch orientation having dielectric constant of 3.5 and loss tangent of 0.02. The dimensions

of antenna are 40 × 30 × 0.1 mm^3. The metamaterial-inspired split ring resonator is used as patch for the required structure (Figs. 1 and 2).

The antenna is placed on various body areas to know the SAR values within the body area networks. At 5 GHz frequency, the antenna produces 0.204 W/kg SAR value, and at 5.8 GHz, it produces 0.157 W/kg SAR value (Fig. 3).

The results are analysed by varying the distance of the SAR characteristics in CST software. The current distributions of antenna are seen in Fig. 4 which shows the slot acting smartly to change the radiation of the antenna. CPW fed antenna radiation patterns are simulated with 'HFSS software'. To characterize the energy radiated from antenna, the radiation patterns are used. The radiated power is characterized graphically as shown in below figures. The designed elliptical curved fed CPW antenna radiation features in E-plane and H-plane which are plotted at resonant frequencies of 2.9, 6.9, 9.0 and 13.4 GHz, respectively. Figure 5 demonstrates the

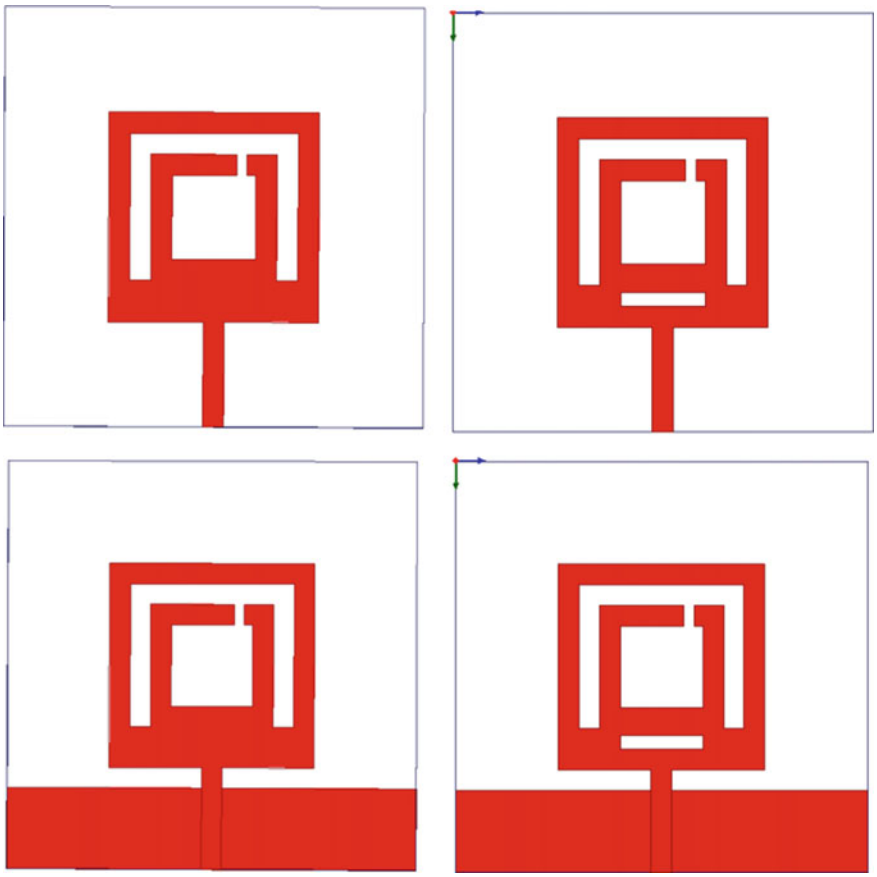

Fig. 1 Iterations of the designed antenna

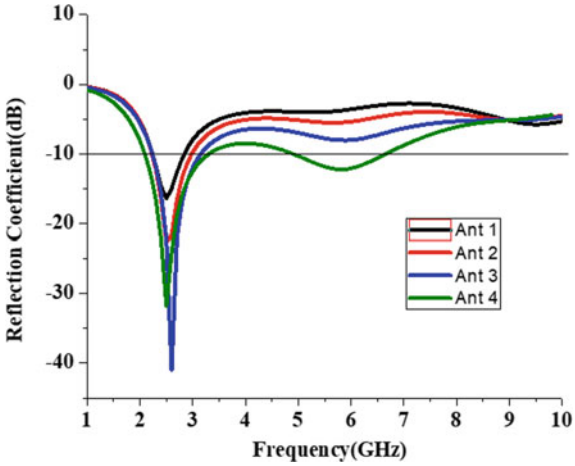

Fig. 2 Reflection coefficient of the proposed antenna

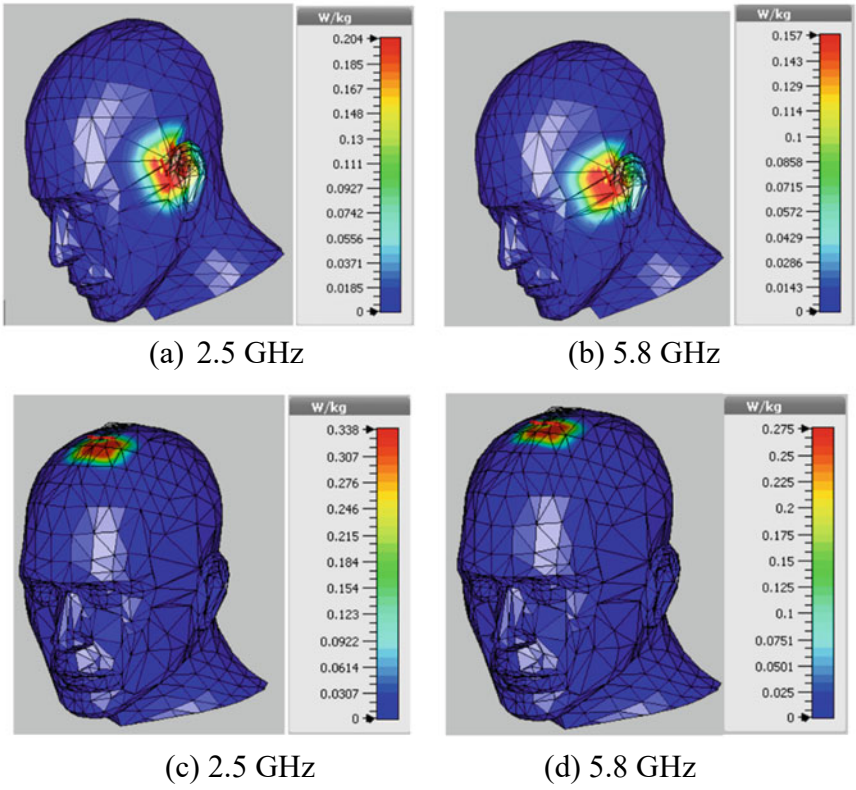

Fig. 3 Antenna SAR results at various parts near the body

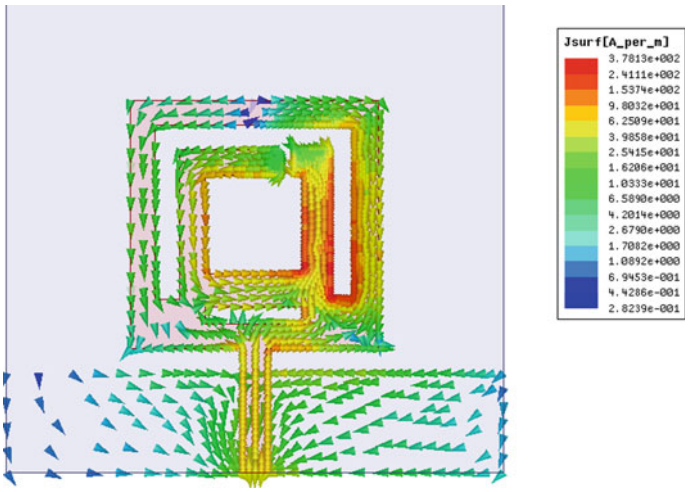

Fig. 4 Current distributions of antenna

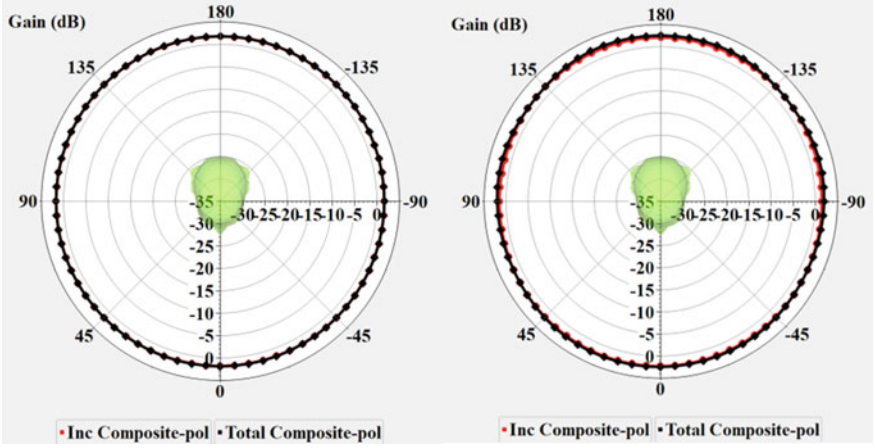

Fig. 5 2D radiation designs

2D radiation designs at the resonant frequencies, where phi = 0° is indicated by the red colour line and phi = 90° is indicated by blue colour line.

3 Conclusion

In this article, antenna working at dual band for biomedical applications has been designed. Antenna is of dimensions 40 × 30 × 0.1 mm^3. With the help of

CST microwave studio, on-body analysing of antenna is performed. At operating frequency, 3D gain is observed for antenna. When the antenna is placed on the peak of head, maximum gain can be detected of 7.24 dBi. While undergoing SAR analysis, antenna produces lower values of 0.157 W/kg which is obtained when the antenna is on the ear of human head. The antenna surrounds LTE2300, WLAN, WiMAX and ISM bands from 2.45 to 2.48 GHz and from 5.725 to 5.825 GHz.

References

1. Kim J, Rahmat-Samii Y (2004) Implanted antennas inside a human body: simulations, designs, and characterizations. IEEE Trans Microw Theory Tech 52(8):1934–1943
2. Sondas A, Ucar MH (2013) An implantable microstrip antenna design for biomedical telemetry. In: 2013 international conference on electronics, computer and computation (ICECCO), IEEE, pp 32–35
3. Soontornpipit P, Furse CM, Chung YC (2004) Design of implantable antenna for communication with medical implants. IEEE Trans Micr Theo Tech 52(8):1944–1951
4. Karacolak T, Hood AZ, Topsakal E (2008) Design of a dualband implantable antenna and development of skin mimicking gels for continuous glucose monitoring. IEEE Trans Micr Theo Tech 56(4):1001–1008
5. Fernandez CJS, Teruel OQ, Carrion JR, Sanchez LI, Iglesias ER (2010) Dual-band microstrip patch antenna based on short-circuited ring and spiral resonators for implantable medical devices. IET Micr Ant Propag 4(8):1048–1055
6. Asimina K, Konstantina SN (2012) A review of implantable patch antennas for biomedical telemetry: challenges and solutions. IEEE Antennas Propag Mag 54(3):210–228
7. Kiourti A, Nikita KS (2012) Miniature scalp-implantable antennas for telemetry in the MICS and ISM bands: design, safety considerations and link budget analysis. IEEE Trans Antennas Propag 60(8):3568–3575
8. Lee CM, Yo TC, Luo CH, Tu CH, Juang YZ (2007) Compact broadband stacked implantable antenna for biotelemetry with medical devices. Electron Lett 43(12):660–662
9. Bhattacharjee S, Maity S, Metya SK, Bhunia CT (2016) Performance enhancement of implantable medical antenna using differential feed technique. Engineering Science and Technology, an International Journal 19(1):642–650
10. Deffendol C, Furse C (1999) Microstrip antennas for dielectric property measurement. IEEE AP/URSI Int Symp Dig 3:1954–1957
11. Bahl IJ, Stuchly SS (1980) Analysis of a microstrip covered with a lossy dielectric. IEEE Trans Microwave Theory Tech 28:104–109
12. Johnson D, Cherkaev E, Furse C, Tripp A (2001) Cross-borehole delineation of a conductive ore deposit—experimental design. Geophysics 66(3):824–835
13. Johnson D, Furse C, Tripp A (2002) FDTD modeling and validation of EM survey tools. Microwave Opt Technol Lett 34(6):427–429
14. Prudhvi Nadh B, Madhav BTP, Siva Kumar M, Venkateswara Rao M, Anilkumar T (2018) Asymmetric ground structured circularly polarized antenna for ISM and WLAN band applications. Progress in Electromagnetics Research 76:167–175
15. Debroux PS (1996) Modeling of the electromagnetic response of geophysical targets using the (FDTD) method. Geophys Prospecting 44(3):457–468
16. Nevels RD, Arndt D, Carl J, Raffoul G, Pacifico A (1995) Microwave antenna design for myocardial tissue ablation applications. In: IEEE antennas and propagation society international symposium digest, vol 3, Newport Beach, CA, June 1995, p 1572
17. Manolis AS, Wang PJ, Estes NA (1994) Radio frequency catheter ablation for cardiac tachyarrhythmias. Annu Int Med 121(6):452–461

18. Prudhvi Nadh B, Madhav BTP, Siva Kumar M, Venkateswara Rao M, Anilkumar T (2019) Circular ring structured ultra-wideband antenna for wearable applications. International Journal of RF and Microwave Computer-Aided Engineering 29(4):e21580
19. Rosen A (1990) Microwave applications in cancer therapy, cardiology and measurement techniques: a short overview. IEEE MTT-S Newslett 17–20
20. Furse CM (1998) A meander antenna used as a human proximity sensor. Mission Res Inc Logan, UT, Final Report, July 1998
21. Madan N (2001) Imbedded antennas for the measurement of electrical properties of materials. MS thesis, Department of Electrical and Computer Engineering, Utah State University, Logan, UT
22. Soontornpipit P, Furse CM, Chung YC (2004) Design of implantable microstrip antenna for communication with medical implants. IEEE Trans Microw Theory Tech 52(8):1944–1951

Performance Investigations of Partially Shaded Solar Photovoltaic Modules with Cell-Level Configurations

V. BalaRaju and Ch. Chengaiah

Abstract Solar photovoltaic (PV) modules are made up of with 32, 36, 48, 60, 72, and 90 number of series connected solar cells, depending on the size and maximum power output of the module. When one solar cell or group of solar cells in PV module (PVM) are partially or fully shaded, the output power gets reduced due to power mismatches, and which can also cause a hotspot heating problem in a PV modules. This research paper focuses on the development of new PV modules (based on arrangement of solar cells within a PVM) with cell-level configurations (PVM-CLC) such as series connection module (SCM), series–parallel connection module (SPCM), total cross-tied connection module (TCTCM), bridge-linked connection module (BLCM), and honey-comb connection module (HCCM) with number of bypass diodes (BDs) to minimize the partial shading effect on PV modules. For this investigation, 36 solar cells were used to develop the new 40 W PV modules. And MATLAB/Simulink software was used to analyze the performance of developed PVM in terms of global maximum peak power and mismatch losses under different cell-level shading cases/conditions. The maximum power results are obtained under considered cell-level shading cases shows that the TCTCM outperforms other cell-level configuration modules. The main objective of this study is to get more power output under shading conditions by developing new PV modules. The proposed PVM-CLC not only reduces the mismatch power loss but also makes installation easier and less complicated when compared to array configurations.

Keywords Solar PV module · Cell-level configurations · Cell-level shading cases · Bypass diode · Global maximum peak power · Mismatch loss

1 Introduction

The majority of the energy required by the world's population is provided by fossil fuels. However, fossil fuels are rapidly depleting, and moreover also burning fossil

V. BalaRaju (✉) · Ch. Chengaiah
Department of EEE, SV University College of Engineering, Tirupati, India
e-mail: vbrajuu@gmail.com

K. Geetha et al. (eds.), *Recent Trends in Materials*, Springer Proceedings in Materials 18, https://doi.org/10.1007/978-981-19-5395-8_32

fuel will cause severe environmental damage. In recent years, the worldwide need for energy has also grown. As a result, solar energy becomes one of the most commonly employed renewable energy sources to meet the need for energy. Solar energy conversion devices such as photovoltaic (PV) cells are widely utilized to generate electricity directly from sunlight. When solar cells are partially shaded, their efficiency is lowered [1–4]. Partial shading effect is more common due to the passing clouds, surrounding buildings, trees, bird drops, tall structures, and dust [5–7]. With partial shading, the solar PV system can only produce less power when compared to the expected power value. Henceforth, partial shading is remaining as a significant factor in lowering the efficiency of a PV module (PVM) [8, 9]. When PV cells in modules are partially shaded, they get varying amounts of solar irradiation. As a result, the I–V and P–V characteristics show several peaks, resulting in mismatch losses in each PVM. For example, 36 cell solar PVM is made up of 36 number of single solar cells that are arranged in a series configuration and if any cell is shaded in the module, and the power output will be reduced due to mismatch losses. According to the literature [10–16], different PV array configurations that is module-level configurations have been presented in order to reduce the mismatch losses caused by shading/partial shading conditions. To reduce mismatch losses under partial shadings, previous studies are primarily focused on different module-level configurations of PV arrays and concluded that the configurations like total cross-tied (TCT) and bridge-linked (BL) can provide better performance in shading conditions. In larger solar PV arrays, the advantages of these configurations may be diminished due to the increased system cost, complexity, and installation time due to the presence of a larger number of connections.

To minimize the aforementioned challenges, different cell-level configurations/connections (CLC) in a single PVM (PVM-CLC) are proposed in this paper. The proposed PVM-CLC reduces the hotspot heating problems and mismatch losses, and it improves the output power of PVM compared to conventional solar PV modules (Solar cells in a conventional PV modules are connected in series). The proposed PVM with cell-level configurations include: Solar PVM with simple series configuration i.e., solar cells in a PVM are connected in series (called as series connection module: SCM), PVM with series–parallel configuration i.e., solar cells in a PVM are connected in series-parallel connection (series parallel connection module: SPCM), PVM with total cross-tied configuration i.e., solar cells in a PVM are connected in total-cross-tied connection (TCT connection module: TCTCM), PVM with bridge-linked configuration i.e., solar cells in a PVM are connected in bridge-linked connection (BL connection module: BLCM), PVM with honeycomb configuration i.e., solar cells in a PVM are connected in honey-comb connection (HC connection module: HCCM). In the literature, all studies have explored partial shading conditions at the module level alone, rather than at the cell level. The novelty of this research work is to investigate the performance of PVM-CLC under cell-level shadings (single or group of solar cells in a PVM are shaded), which is not yet reported. For this study, new PV modules using 36 solar cells with a power rating of approximately 40W have been developed and tested under a different cell level shading conditions. The MATLAB/Simulink tool was used to model and

test the developed solar PV module with proposed cell-level configurations under varied cell level shading conditions. The performance of PVM-CLC was examined in terms of global maximum peak power, mismatch losses, and the number of BDs connected across the solar cells in a PVM. When compared to alternative PVM-CLC schemes, the findings show that the TCTCM delivers superior performance with the highest maximum power and lowest mismatch losses. To simulate the partial shades of a PVM-CLC, this study uses the "solar cell" package component of MATLAB/Simulink which was built and proven to operate the basic PV modules under standard test conditions (STC).

The following describes the overall structure of this paper: Mathematical modeling of a PV cell and module is presented in Sect. 2. In Sect. 3, the performance of PVM with cell-level configurations (PVM-CLC) is analyzed under different cell-level shading cases. Section 3.5 compares the performance of several PVM-CLCs in terms of global maximum peak powers, mismatch losses, and number of bypass diodes (BDs) connected across the solar cells in PVM. Section 4 concludes the proposed research work.

2 Mathematical Modeling of Solar PV Cell and Module

2.1 Modeling of a Double-Diode PV Cell

A single current source with two anti-parallel diodes, as well as series resistance and shunt resistance [17–20] is used in the equivalent circuit of the double-diode PV cell model, as shown in Fig. 1.

Apply Kirchhoff's current law to the PV cell model presented in Fig. 1 to find the current value of the cell. The current of a PV cell is provided in Eq. (1).

$$I_{\text{pv}} = I_{\text{photo}} - I_{d1} - I_{d2} - I_p \tag{1}$$

The photocurrent generated by a PV cell when it is exposed to sunlight is denoted as I_{photo}, and it varies linearly with the solar irradiation at a fixed temperature, the shunt resistor current represented by I_p. A PV cell's nonlinearity is caused by the current flowing through the anti-parallel diodes (D1, D2), which is measured as I_{d1}, I_{d2}. Substitute the formula for I_{d1}, I_{d2}, and I_p in Eq. 1. As a result, the cell current

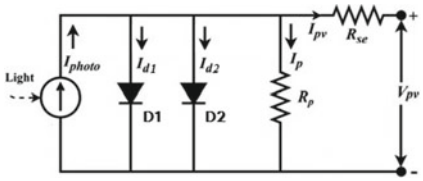

Fig. 1 Equivalent double-diode PV cell model

is calculated using Eq. 2.

$$I_{\text{pv}} = I_{\text{photo}} - I_{s1}\left[exp\left(\frac{q(V_{\text{pv}} + I_{\text{pv}}R_{\text{se}})}{a_1.kT}\right) - 1\right] - I_{s2}\left[\exp\left(\frac{q(V_{\text{pv}} + I_{\text{pv}}R_{\text{se}})}{a_2.kT}\right) - 1\right] - \left(\frac{V_{\text{pv}} + I_{\text{pv}}R_{\text{se}})}{R_p}\right) \quad (2)$$

where I_{s1}, I_{s2}: reverse saturation currents of the two diodes, $\boldsymbol{q}$: electron charge, and its value is 1.602×10^{-19} C, $\boldsymbol{a_1}$,$\boldsymbol{a_2}$: ideality factor of diodes D1 and D2, Boltzmann constant is written as $k = 1.3806503 \times 10^{-23}$ J/K, T is the cell temperature, R_p, R_{se}: shunt and series resistances, respectively.

2.2 Modeling of a Single PV Module

A single PVM is made up of with a number of series connected solar PV cells and is denoted by the symbol N_{se}. When N_{se} cells are connected in series, the output current (I_M) of the PVM is expressed as a module output voltage (V_P). Equation 3 represents the total PVM current.

$$I_M = I_{\text{photo}} - I_{s1}\left[\exp\left(\frac{q(V_P + I_M R_{\text{se}})}{N_{\text{se}}a_1 KT}\right) - 1\right] - I_{s2}\left[\exp\left(\frac{q(V_P + I_M R_{\text{se}})}{N_{\text{se}}a_2 KT}\right) - 1\right] - \left(\frac{V_P + I_M R_{\text{se}} N_{\text{se}}}{N_{\text{se}} R_p}\right) \quad (3)$$

Equation (3) is applicable to all PVMs and can be applied to any number of series connected PV cells in a PVM. Figure 2 illustrates a single PVM with a total of 36 solar cells connected in series. Generally, one Solar cell yield around 0.6 V on average, and the BDs are linked in each solar PVM to bypass the solar cells when they are exposed to shade.

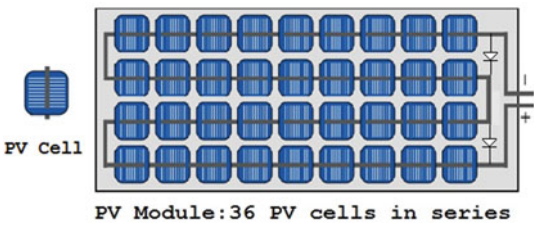

Fig. 2 Single PV cell and Single PV module with 36 series connected PV cells

3 Performance Investigation of Solar PV Module with Cell-Level Configurations

3.1 Solar PV Module with Cell-Level Configurations (PVM-CLC)

In this paper, new 40 W solar PV Modules were designed and developed by converting the conventional 36 cell series structure PV module into a 9 × 4 series–parallel design with various cell-level configurations. The schematic diagram of 36 cell solar PVM with cell-level configurations (PVM-CLC) is shown in Fig. 3. In this paper, five possible cell-level configurations (within a PVM) are reported, they are, PVM with simple series configuration (Series connection module: SCM), PVM with total cross-tied configuration (TCT connection module: TCTCM), PVM with series–parallel configuration (SP connection module: SPCM), PVM with bridge-linked configuration (BL connection module: BLCM), and PVM with honey-comb configuration (HC connection module: HCCM). Despite the fact that the research literature provides many configurations for solar PV arrays at the module level [12–15], the authors of this study have constructed and modeled various configurations at the cell level within a PVM. The developed PVM has a power output of approximately 40 W and is made up of with 36 solar cells. The illustration of proposed PVM-CLC are shown in Fig. 3b–f , where C1, C2, ……. C35, C36 represents the solar cells and V_{md}, I_{md} denotes the output voltage and currents of the PV Module.

- The PVM with 9 × 4 cell arrangement (36 cells) is illustrated in Fig. 3a. In this arrangement, total 36 cells are divided into four cell strings and each cell string consists of nine number of series connected solar cells.
- The PVM with cell level series configuration (Series connection module: SCM) is the most simple and fundamental cell-level configuration, as illustrated in Fig. 3b. SCM connects all four cell strings in a series. While the output voltage is high, the output current is equally low in this design. In order to address this disadvantage, a variety of different configurations are presented.
- Figure 3c shows the PVM with cell level series–parallel configuration (SP connection module: SPCM). In SPCM, all solar cell strings (each cell string consists of nine series connected solar cells) are connected in parallel.
- Figure 3d shows the PVM with cell level total cross-tied configuration (TCT connection module: TCTCM). To form TCTCM, cross ties across each cell row are connected in SPCM.
- Figure 3e shows the PVM with cell level bridge-link configuration (BL connection module: BLCM). There is a four cells bridging unit available. In a bridge, two cells are first connected in series and then in parallel. Cross ties are used to connect bridges.
- Figure 3f shows the PVM with cell level honey-comb configuration (HC connection module: HCCM). HCCM is a modified version of the BLCM, with the addition of a changeable bridge size.

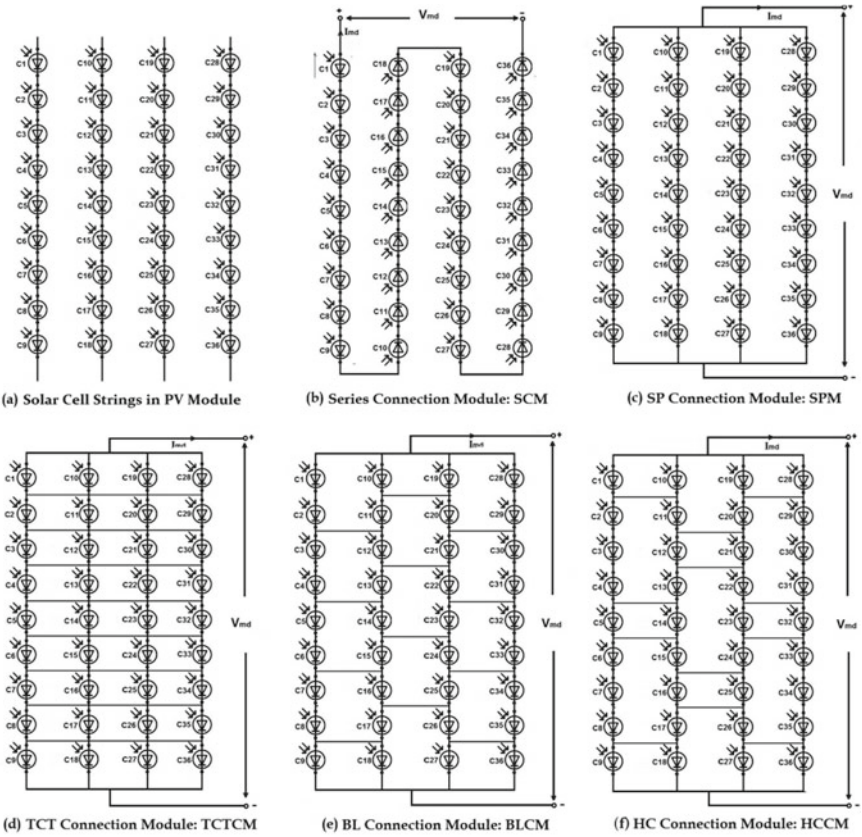

Fig. 3 Development of a new solar PV modules with CLC

- In this study, new PV modules (without BDs) are developed with CLC as illustrated in Fig. 3. The number of BDs is connected across each or group of solar cells within a PVM and modeled using MATLAB/Simulink software.

3.1.1 Bypass Diodes (BD)

Bypass diodes are typically installed in anti parallel (reverse biassed) to small groups of series connected cells in order to avoid shadowing cells from limiting the current path in a string, degrading the performance of other cells in series, and reducing the power output of the entire string. When a module is shaded, bypass diodes are used to maintain output voltage and to reduce hot spot heating and the possibility of cell failure [9]. In this research work, the number of BDs such as 0, 1, 4, 12, and 36 is connected across each solar cell or a group of solar cells within a single PVM and investigate the performance under different cell-level shading cases. The number of BDs connected in the developed PVM-CLC using 36 cells as follows: 0 BD: no

bypass diode is connected in a 36 cell PVM, 1 BD: one bypass diode is connected across entire PVM i.e., only one bypass diode is connected across 36 solar cells, 4 BDs: one bypass diode is connected for every group of 9 solar cells, 12 BDs: one bypass diode is connected for every group of 4 solar cells, 36 BDs: one bypass diode is connected to each solar cell in a PVM.

3.2 Cell-Level Shading Effects on Solar PVM-CLC

Partial Shading Effect: A single shaded cell out of a 36 or 72 cells solar module can significantly lower the majority of the power output, making partial shading extremely problematic for solar modules. The shaded cell functions as a load, wasting energy on itself, which may create hot spots and ultimately harm the cells. Mismatch losses are seen to rise as the fraction of single cell shading does. Generally, shading happens as a result of a variety of reasons like clouds, trees, surrounding buildings, and other natural phenomena, and it has an impact on the PVM power output. In the literature, all researchers have focused on elucidating partial shading conditions at the module level, rather than at the cell level. The novelty of this research work is to investigate the performance of PVM-CLC under cell-level shading cases, which is not before reported. The considered cell-level shadings in a 36 cell PVM are illustrated in Fig. 4. The performance of the PVM-CLC is examined under eleven different cell-level shading cases and one un-shaded case (Case-U).

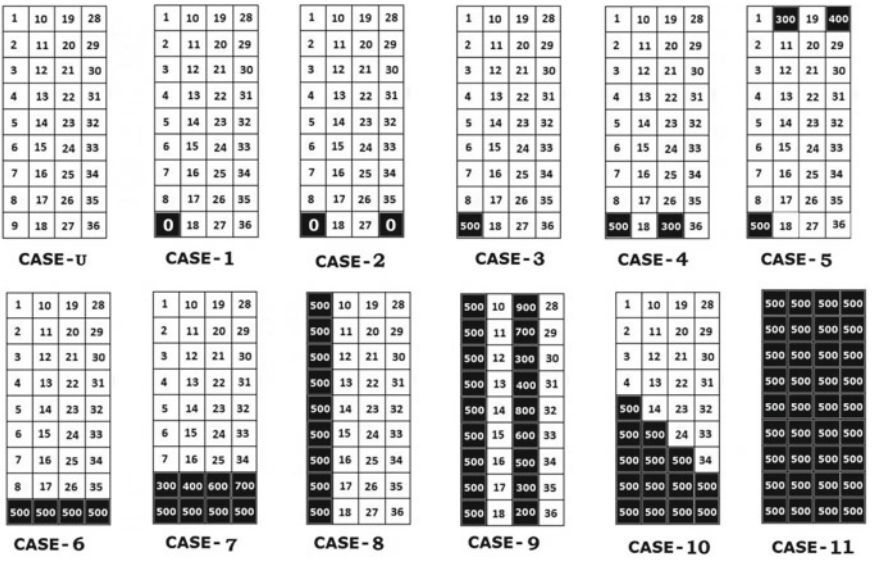

Fig. 4 Cell-level shading cases in a 36 cell solar PVM-CLCs

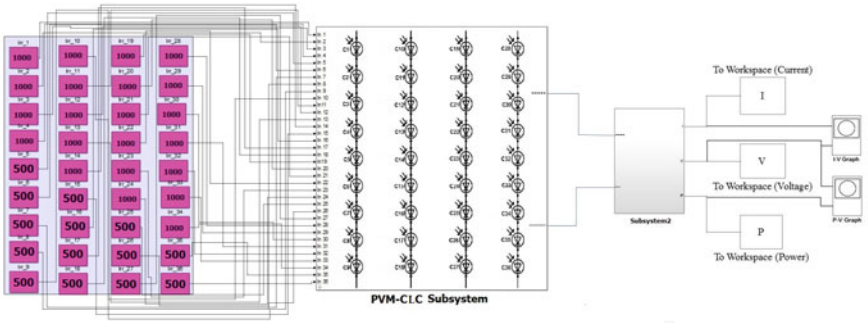

Fig. 5 MATLAB/Simulink model of PVM-CLC under cell-level shading Case-10

3.3 MATLAB/Simulink Model of PV Modules with Cell-Level Configurations

The simulation model of proposed PVM-CLCs with cell-level shading case-10 is shown in Fig. 5. The PVM-CLC subsystem is composed of a single PVM with 36 solar cells that are connected in various cell-level configurations, including SCM, SPCM, TCTCM, BLCM, and HCCM type with BDs. For this study, PV modules with a power rating of 40 W have been developed and tested. In this research work, the number of BDs such as 0, 1, 4, 12, and 36 is connected across each solar cell or a group of solar cells within a single PVM and investigate the performance under different cell-level shading cases.

3.4 Simulation Parameters

3.4.1 Parameters of a Single Solar PV Cell

This study describes the development of a new solar PVM with various cell-level configurations, which was accomplished by using 36 single solar cells. The short-circuit current I_{sc} and open-circuit voltage V_{oc} of each solar cell is 2.45 A and 0.6083 V, respectively and the series resistance (R_s) is 0.0079 Ω and shunt resistance (R_{sh}) is set to infinity (default value) in Simulink tool. The new developed solar PVM produces a maximum output power of approximately 40 W under a full irradiance of 1000 W/m^2 and temperature of 25 °C at STC. The parameters of a solar cells used in the implementation of proposed PVM-CLC are given in Fig. 6. The main parameters are short-circuit current (I_{sc}), open-circuit voltage (V_{oc}), irradiance (Ir0), quality factor (N), and series resistance (R_s). The solar cell was built on the validated double-diode substitute PV cell model in MATLAB/Simulink software.

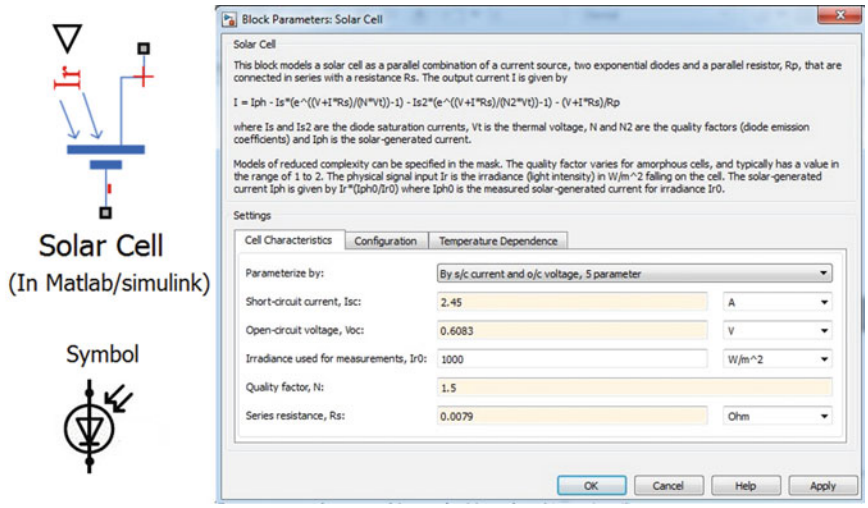

Fig. 6 Solar cell parameters used in simulation

3.5 Results and Discussion

The obtained results from a simulation of a 36 cell PVM-CLC under cell-level shadings with varying irradiances and with the equal irradiances falling on the PVM are given in Tables 1 and 2, respectively, for all the proposed cell level configurations. The power output of PVM-CLC with different number of BDs under un-shaded case (Case-U) is approximately 40 W. If the uniform irradiance falling on the entire PVM, all PVM-CLCs give the same global maximum peak power (GMPP) output in all cell-level shading cases. Mismatch Losses (ML): The interconnection of solar cells or modules with varied characteristics or under various environmental conditions results in mismatch losses. Under certain conditions, mismatch losses can be a major problem for PV modules and arrays because, in the worst-case scenario, the output of the entire PV module is controlled by the solar cell with the lowest output. For example, when one solar cell in the module is shaded while the others are not, the power produced by un-shaded solar cells may be wasted by the lower-performing cell rather than being used to power the load. This can then result in extremely localised power loss, and the local heating that follows may harm the module permanently. The mismatch losses under considered eleven cell-level shading cases are given in Table 3. The mismatch losses are calculated by using the following Eq. (4).

$$\text{Mismatch Losses (ML) in Watts} = \text{GMPP}_{\text{un-shadedcase}} - \text{GMPP}_{\text{shadingcases}} \quad (4)$$

Table 1 Comparison of GMPP of PVM-CLC under different cell-level shading (CLS) cases

CLS cases	No. of BDs connected across solar cells in PVM-CLC	Global Maximum Peak Powers (GMPP) of PVM-CLC in Watts					Best PVM-CLC w.r.t GMPP
		SCM	SPCM	TCTCM	BLCM	HCCM	
U	0	40.02	40.02	40.02	40.02	40.02	ALL
	1	40.02	40.02	40.02	40.02	40.02	ALL
	4	40.02	40.02	40.02	40.02	40.02	ALL
	12	40.02	40.02	40.02	40.02	40.02	ALL
	36	40.02	40.02	40.02	40.02	40.02	ALL
1	0	0	30.02	34.51	32.93	33.24	TCTCM
	1	0	30.02	34.51	32.93	33.24	TCTCM
	4	28.84	30.02	34.51	32.93	33.24	TCTCM
	12	35.51	30.02	34.41	32.93	33.24	TCTCM
	36	*37.73*	34.53	34.51	32.93	33.24	TCTCM
2	0	0	19.99	33.65	31.82	31.94	TCTCM
	1	0	19.99	33.65	31.82	31.94	TCTCM
	4	17.65	19.99	33.65	31.82	31.94	TCTCM
	12	30.99	23.51	33.49	31.82	31.94	TCTCM
	36	35.44	32.75	33.65	31.82	31.94	TCTCM
3	0	24.88	35.42	39.52	37.53	37.95	TCTCM
	1	24.88	35.42	39.52	37.53	37.95	TCTCM
	4	28.86	35.42	39.52	37.53	37.95	TCTCM
	12	35.53	35.42	38.01	37.53	37.95	TCTCM
	36	37.76	35.42	39.52	37.53	37.95	TCTCM
4	0	15.41	28.77	32.56	32.15	32.55	TCTCM
	1	15.41	28.77	32.56	32.15	32.55	TCTCM
	4	17.97	28.77	32.56	32.15	32.55	TCTCM
	12	31.04	28.77	32.46	32.15	32.55	HCCM
	36	35.48	32.83	32.56	32.15	32.55	TCTCM
5	0	15.41	23.45	31.9	31.88	31.9	TCTCM/HCCM
	1	15.41	23.45	31.9	31.88	31.9	TCTCM/HCCM
	4	15.41	23.45	31.9	31.88	31.9	TCTCM/HCCM
	12	26.55	23.45	31.9	31.88	31.9	TCTCM/HCCM
	36	33.22	31.73	31.9	31.88	31.9	TCTCM/HCCM
6	0	24.13	24.17	33.65	33.32	33.65	TCTCM/HCCM
	1	24.13	24.17	33.65	33.32	33.65	TCTCM/HCCM
	4	24.13	24.17	33.65	33.32	33.65	TCTCM/HCCM
	12	24.13	24.17	33.49	33.32	33.65	HCCM
	36	30.98	30.92	34.26	33.32	33.65	TCTCM

(continued)

Table 1 (continued)

CLS cases	No. of BDs connected across solar cells in PVM-CLC	Global Maximum Peak Powers (GMPP) of PVM-CLC in Watts					Best PVM-CLC w.r.t GMPP
		SCM	SPCM	TCTCM	BLCM	HCCM	
7	0	15.37	20.4	32.21	31.34	30.45	TCTCM
	1	15.37	20.4	32.21	31.34	30.45	TCTCM
	4	15.37	20.4	32.21	31.34	30.45	TCTCM
	12	22.08	21.89	32.19	31.34	30.45	TCTCM
	36	22.01	21.94	32.21	31.34	30.45	TCTCM
8	0,1,4,12,36	34.8	34.8	34.8	34.8	34.8	ALL
9	0	10.03	26.91	29.26	28.84	28.64	TCTCM
	1	10.03	26.91	29.26	28.76	28.64	TCTCM
	4	17.69	26.91	29.26	28.76	28.64	TCTCM
	12	15.15	26.91	29.26	28.65	28.64	TCTCM
	36	17.64	26.91	29.26	28.65	28.64	TCTCM
10	0	22.26	22.1	30.94	28.32	30.12	TCTCM
	1	22.26	22.1	30.94	28.32	30.12	TCTCM
	4	22.26	22.1	30.94	28.32	30.12	TCTCM
	12	22.26	22.1	30.94	28.32	30.12	TCTCM
	36	22.26	22.1	30.94	28.32	30.12	TCTCM
11	0, 1, 4, 12, 36	19.29	19.29	19.29	19.29	19.29	ALL

Table 2 Comparison of GMPP of PVM-CLC under equal irradiances falling on a single PVM

Irradiance: W/m^2	No. of BDs connected across solar cells in PVM-CLC	Global Maximum Peak Powers (GMPP) of PVM-CLC in Watts					Best PVM-CLC w.r.t GMPP
		SCM	SPCM	TCTCM	BLCM	HCCM	
0	0, 1, 4, 12, 36	0	0	0	0	0	–
50	0, 1, 4, 12, 36	1.602	1.602	1.602	1.602	1.602	ALL
100	0, 1, 4, 12, 36	3.412	3.412	3.412	3.412	3.412	ALL
200	0, 1, 4, 12, 36	7.226	7.226	7.226	7.226	7.226	ALL
300	0, 1, 4, 12, 36	11.17	11.17	11.17	11.17	11.17	ALL
400	0, 1, 4, 12, 36	15.21	15.21	15.21	15.21	15.21	ALL
500	0, 1, 4, 12, 36	19.29	19.29	19.29	19.29	19.29	ALL
600	0, 1, 4, 12, 36	23.4	23.4	23.4	23.4	23.4	ALL
700	0, 1, 4, 12, 36	27.52	27.52	27.52	27.52	27.52	ALL
800	0, 1, 4, 12, 36	31.69	31.69	31.69	31.69	31.69	ALL
900	0, 1, 4, 12, 36	35.83	35.83	35.83	35.83	35.83	ALL
1000	0, 1, 4, 12, 36	40.02	40.02	40.02	40.02	40.02	ALL

Table 3 Comparison of mismatch losses of PVM-CLC under different cell-level shading (CLS) cases

CLS Cases	No. of BDs connected across solar cells in PVM-CLC	Mismatch Losses (ML) in Watts					Best PVM-CLC w.r.t ML
		SCM	SPCM	TCTCM	BLCM	HCCM	
Global Maximum Peak Power (GMPP) under un-shaded case (Case-U) with irradiance of 1000 W/m^2 is 40.02 W							
1	0	40.02	10	5.51	7.09	6.78	TCTCM
	1	40.02	10	5.51	7.09	6.78	TCTCM
	4	11.18	10	5.51	7.09	6.78	TCTCM
	12	4.51	10	5.61	7.09	6.78	TCTCM
	36	2.29	5.49	5.51	7.09	6.78	TCTCM
2	0	40.02	20.03	6.37	8.2	8.08	TCTCM
	1	40.02	20.03	6.37	8.2	8.08	TCTCM
	4	22.37	20.03	6.37	8.2	8.08	TCTCM
	12	9.03	16.51	6.53	8.2	8.08	TCTCM
	36	4.58	7.27	6.37	8.2	8.08	TCTCM
3	0	15.14	4.6	0.5	2.49	2.07	TCTCM
	1	15.14	4.6	0.5	2.49	2.07	TCTCM
	4	11.16	4.6	0.5	2.49	2.07	TCTCM
	12	4.49	4.6	2.01	2.49	2.07	TCTCM
	36	2.26	4.6	0.5	2.49	2.07	TCTCM
4	0	24.61	11.25	7.46	7.87	7.47	TCTCM
	1	24.61	11.25	7.46	7.87	7.47	TCTCM
	4	22.05	11.25	7.46	7.87	7.47	TCTCM
	12	8.98	11.25	7.56	7.87	7.47	HCCM
	36	4.54	7.19	7.46	7.87	7.47	TCTCM
5	0	24.61	16.57	8.12	8.14	8.12	TCTCM/HCCM
	1	24.61	16.57	8.12	8.14	8.12	TCTCM/HCCM
	4	24.61	16.57	8.12	8.14	8.12	TCTCM/HCCM
	12	13.47	16.57	8.12	8.14	8.12	TCTCM/HCCM
	36	6.8	8.29	8.12	8.14	8.12	TCTCM/HCCM
6	0	15.89	15.85	6.37	6.7	6.37	TCTCM/HCCM
	1	15.89	15.85	6.37	6.7	6.37	TCTCM/HCCM
	4	15.89	15.85	6.37	6.7	6.37	TCTCM/HCCM
	12	15.89	15.85	6.53	6.7	6.37	HCCM
	36	9.04	9.1	5.76	6.7	6.37	TCTCM
7	0	24.65	19.62	7.81	8.68	9.57	TCTCM
	1	24.65	19.62	7.81	8.68	9.57	TCTCM
	4	24.65	19.62	7.81	8.68	9.57	TCTCM

(continued)

Table 3 (continued)

CLS Cases	No. of BDs connected across solar cells in PVM-CLC	Mismatch Losses (ML) in Watts					Best PVM-CLC w.r.t ML
		SCM	SPCM	TCTCM	BLCM	HCCM	
	12	17.94	18.13	7.83	8.68	9.57	TCTCM
	36	18.01	18.08	7.81	8.68	9.57	TCTCM
8	0,1,4,12,36	5.22	5.22	5.22	5.22	5.22	ALL
9	0	29.99	13.11	10.76	11.18	11.38	TCTCM
	1	29.99	13.11	10.76	11.26	11.38	TCTCM
	4	22.33	13.11	10.76	11.26	11.38	TCTCM
	12	24.87	13.11	10.76	11.37	11.38	TCTCM
	36	22.38	13.11	10.76	11.37	11.38	TCTCM
10	0	17.76	17.92	9.08	11.7	9.9	TCTCM
	1	17.76	17.92	9.08	11.7	9.9	TCTCM
	4	17.76	17.92	9.08	11.7	9.9	TCTCM
	12	17.76	17.92	9.08	11.7	9.9	TCTCM
	36	17.76	17.92	9.08	11.7	9.9	TCTCM
11	0, 1, 4, 12, 36	20.73	20.73	20.73	20.73	20.73	ALL

where $GMPP_{\text{un-shaded case}}$ is the global maximum peak power under un-shaded case (Case-U) and $GMPP_{\text{shading cases}}$ is the global maximum peak power under different cell-level shading cases.

From the above obtained simulation results, it can be concluded that:

- Under un-shaded case (Case-U), the maximum powers of PVM-CLCs are same. Un-shaded case indicates that the PVM receives irradiance of 1000 W/m^2. Under Case-U, the power output of a PVM-CLC is approximately 40 W.
- When the same irradiance falling across the each PVM that is when all PV cells in the module receive the same amount of sunlight and its range from 50 to 900 W/m^2, the global maximum peak power (GMPP) of PVM-CLC is same for all considered cell-level shading cases.
- The performance of TCTCM is best in the majority of cell-level shading cases under varying irradiance conditions, i.e., each solar cell in a PVM receives a different irradiance. The proposed TCTCM illustration in Fig. 7d.
- Accordingly, the TCTCM offers the best overall performance in terms of highest global maximum peak power (GMPP) and lowest mismatch losses (ML) under considered cell-level shading cases. Power output from TCTCM and HCCM is same in 5th and 6th cell-level shading scenarios.

The illustration of proposed developed solar PV Modules made from single solar PV cells is visualized in Fig. 7. As shown in Fig. 7a, the developed module is composed of 36 solar cells, with nine cells connected in series to form solar cell

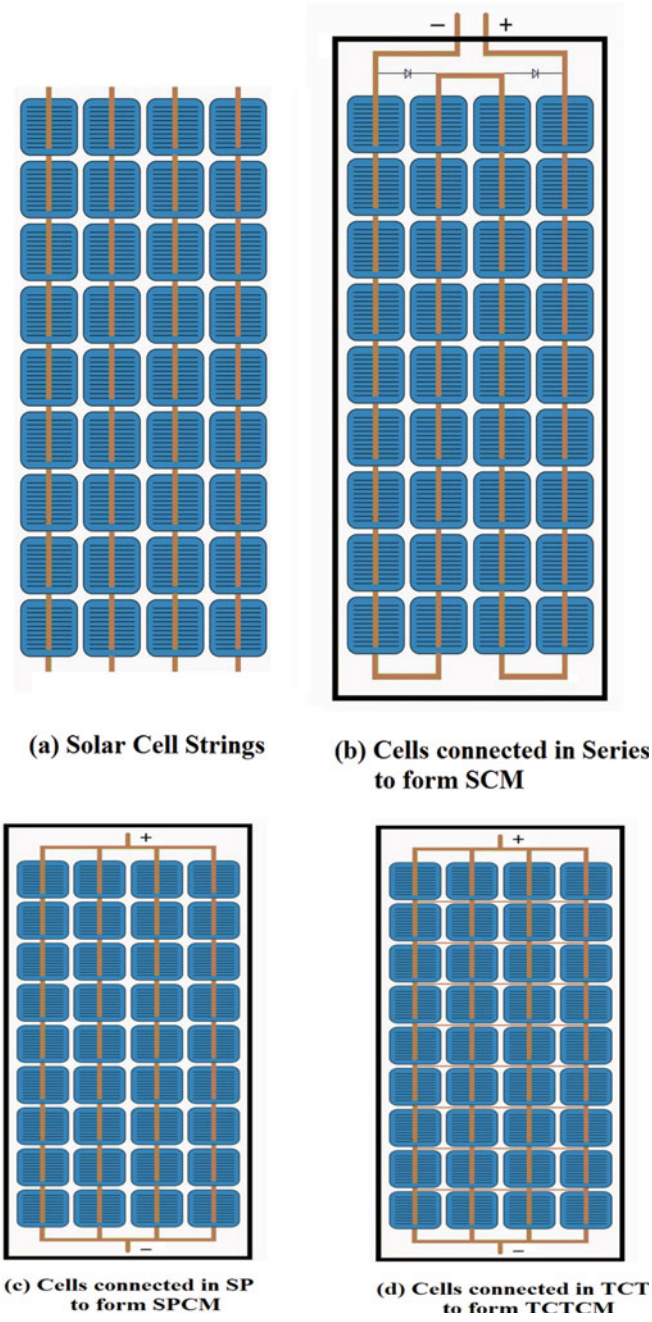

Fig. 7 Illustration of developed solar PV modules

Fig. 7 (continued)

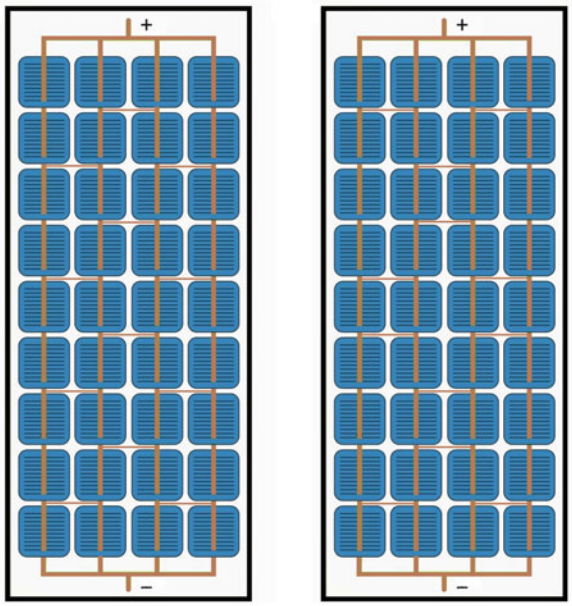

(e) Cells connected in BL to form BLCM **(f) Cells connected in HC to form HCCM**

strings and these cell strings being combined in varying configurations to build the proposed PVM-CLC. Figure 7b shows a standard PVM, which is a SCM, in which all 36 cells are connected in series. Figure 7c–f show how the cells are joined in various configurations to construct proposed solar PV modules with cell-level configurations (PVM-CLC). In SCM, two BDs are connected across a set of solar cells, however, in the proposed PVM-CLC, essentially the same GMPP is generated with 0 or 1 or 4 or 12 or 36 number of BDs. The GMPP of PVM-CLC is listed in Table 1. The PV modules that have been developed can be used in a wide range of applications, including small and large-scale PV systems. It is preferable to utilize a PVM-CLC with a single bypass diode (BD) for standalone or grid-connected applications because it provides better protection of the PVM under shading conditions by bypassing the PVM.

4 Conclusion

This research presents the results with a thorough investigation on PVM with cell-level configurations (PVM-CLC) such as simple series connection module (SCM), series–parallel connection module (SPCM), bridge-linked connection module (BLCM), total cross-tied connection module (TCTCM), and honey-comb connection

module (HCCM) types under various cell-level shadings. From the results, it can be concluded that the proposed TCTCM outperforms the other developed PV modules under considered cell-level shading cases. Furthermore, the developed PV modules with proposed cell-level designs need fewer BDs (which bypass a set of solar cells under shading conditions), which is a significant consideration when the cells are connected in series. The optimal and acceptable configuration selection is largely reliant on the strength of shading, shading pattern, location of shading pattern, and type of shading (uniform or not) influencing the PVM, according to a thorough examination on each cell-level configuration under various cell-level shading cases.

References

1. Mekhilef S, Saidur R, Safari A (2011) A review on solar energy use in industries. Renew Sustain Energy Rev 15:1777–1790
2. Bany J, Appelbaum J, Braunstein A (1977) The influence of parameter dispersion of electrical cells on the array power output. Trans Electron Dev 24(8):1032–1040
3. Bucciarelli LL (1979) Power loss in photovoltaic arrays due to mismatch in cell characteristics. Sol Energy 23:277–288
4. Gonzalez C, Weaver R (1980) Circuit design considerations for photovoltaic modules and systems. In: Proceedings of 14th IEEE photovoltaic specialists Conference, pp 528–535
5. Swaleh MS, Green MA (1982) Effect of shunt resistance and bypass diode on the shadow tolerance of solar cell modules. Solar Cells 5(2):183–198
6. Bishop JW (1988) Computer simulation of the effects of electrical mismatches in photovoltaic cell interconnection circuits. Solar Cells 25:73–89
7. Belhachat F, Larbes C (2015) Modeling, analysis and comparison of solar photovoltaic array configurations under partial shading conditions. Sol Energy 120:399–418
8. Kaushika ND, Gautam NK (2003) Energy yield simulations of interconnected solar PV arrays. IEEE Trans Energy Conversion 18
9. Kaushika ND, Rai AK (2007) An investigation of mismatch losses in solar photovoltaic cell networks. Energy 32:755–759
10. Peled A, Appelbaum J (2016) Minimizing the current mismatch resulting from different locations of solar cells within a PV module by proposing new interconnections. Sol Energy 135:840–847
11. Deline C, Dobos A, Janzou S, Meydbray J, Donovan M (2013) A simplified model of uniform shading in large photovoltaic arrays. Solar Energy 96:274–282
12. Mao M, Cui L, Zhang Q, Guo K, Zhou L, Huang H (2020) Classification and summarization of solar photovoltaic MPPT techniques: a review based on traditional and intelligent control strategies. Energy Reports 6:1312–1327
13. Tam LTM, Duong NV, Tien NT, Ngu NV (2014) A study on the output characteristic of photovoltaic array under partially shaded conditions. Appl Mech Mater 472:198–205
14. Orozco-Gutierrez ML, Spagnuolo G, Ramos- CA, Ramirez- JM, Ospina-Agudelo B (2019) Enhanced simulation of total cross tied photovoltaic arrays. Math Comput Simul 158:49–64
15. Mohammadnejad S, Khalafi A, Ahmadi SM (2016) Mathematical analysis of total-cross-tied photovoltaic array under partial shading condition and its comparison with other configurations. Sol Energy 133:501–511
16. Balaraju V, Chengaiah C (2020) Mathematical analysis of solar photovoltaic array configurations with partial shaded modules. Trend Renewable Energy 6(2):131–155. https://doi.org/10.17737/tre.2020.6.2.00115

17. Pachauri RK, Babu TS, Alhelou HH (2021) Power losses reduction of solar PV systems under partial shading conditions using re-allocation of PV module-fixed electrical connections. IEEE Access 9
18. BalaRaju V, Chengaiah C (2019) Power enhancement of solar PV arrays under partial shading conditions with reconfiguration methods. Innovations in Power and Advanced Computing Technologies (i-PACT)
19. Seyedmahmoudian M, Mekhilef S, Rahmani R, Yusof R, Renani ET (2013) Analytical modeling of partially shaded photovoltaic systems. Energies 6:128–144. https://doi.org/10.3390/en6010128
20. Premkumar M, Subramaniam U, Babu TS, Elavarasan RM, Mihet-Popa L (2020) Evaluation of mathematical model to characterize the performance of conventional and hybrid PV array topologies under static and dynamic shading patterns. Energies 13:3216. https://doi.org/10.3390/en13123216

Biocompatibility of Poly(3-Hydroxybutyrate)/Nano-Magnetite Composite Material for Bone Tissue Engineering Applications

Daria Travnikova, Dariana Chesnokova, Irina Zharkova, Garina Bonartseva, Tatiana Makhina, Yulia Mukhortova, Artem Pryadko, Roman Chernozem, Maria Surmeneva, Roman Surmenev, and Anton Bonartsev

Abstract The development of orthodontics and orthopedics requires new materials for guided bone regeneration. These materials must meet certain requirements for affinity with surrounding tissues and the ability to induce osteogenesis. Poly-3(hydroxybutyrate) (PHB) is a biocompatible and biodegradable material, actively used in different biomedical applications. Recent studies have shown piezoelectric properties of PHB. Since electrical signals have a huge impact on differentiation and cell growth, novel materials with piezoelectric properties could be effective tool for tissue regeneration. To enhance this effect in PHB polymer was combined with magnetic nanoparticles (MNs). The main component of MNs was magnetite (Fe_3O_4) synthesizing under different conditions using the magnetic separation method. Assessment of toxicity was obtained with composite films on mesenchymal stem cells (MSCs). Our work demonstrates that composites PHB/MNs have a potential to be used as a smart new material for bone tissue engineering applications.

Keywords Biopolymers · Poly-3(hydroxybutyrate) · Magnetite nanoparticles · Composite material · Tissue regeneration

1 Introduction

Tissue engineering is an interdisciplinary field involving fundamental knowledge and effective strategies from biomedical and engineering disciplines [1]. A number

D. Travnikova (✉) · D. Chesnokova · I. Zharkova · A. Bonartsev
Faculty of Biology, Moscow State University, Moscow, Russia
e-mail: darija-travnikova@yandex.ru

G. Bonartseva · T. Makhina
Federal Research Center, Fundamentals of Biotechnology, Russian Academy of Sciences, Moscow, Russia
e-mail: bonar@inbi.ras.ru

Y. Mukhortova · A. Pryadko · R. Chernozem · M. Surmeneva · R. Surmenev
National Research Tomsk Polytechnic University, Tomsk, Russia

K. Geetha et al. (eds.), *Recent Trends in Materials*, Springer Proceedings in Materials 18, https://doi.org/10.1007/978-981-19-5395-8_33

of requirements are put forward to materials used in regenerative medicine [2]. It includes such aspects as an absence of toxicity both material and its products processing in the body; biocompatibility including the ability to interact with biological tissues to achieve the optimal therapeutic effect without causing adverse reactions; non-traumatic form of the product. For the engineering of bone tissue, material required to induce osteogenesis and its physical properties must be close to natural bone such as porosity, rigidity and elasticity [3]. Titanium alloys and various forms of bioceramics are currently used as biomaterials for bone tissue regeneration. However, inorganic materials have disadvantages such as poor resorption, brittleness and low plasticity [4]. In addition, a large number of synthetic and natural polymers are being investigated for this role. Among them, polyhydroxyalkanoates (PHAs) are a convenient chemical family that meets all aforementioned requirements [5]. PHA is an extensive group of polymers of microbiological origin capable of biodegradation [6]. Engineering products made from these polymers may provide a number of opportunities for restoring damaged skin, filling defects in soft and bone tissues, creating tissue-engineered equivalents of blood vessels and heart valves and many others [7, 8]. The most studied chemical of the PHA family is the polymer of 3-hydroxybutyric acid (poly-3(hydroxybutyrate) (PHB). Since 3-hydroxybutyrate is a natural product of cell and tissue metabolism, biodegradability products made from this polymer are highly biocompatible [9]. Bacteria capable of synthesizing PHB, such as Azotobacter sp., accumulates this polymer under starvation conditions as a reserve substance [10]. By selecting the compounds proportion of the culture medium, it is possible to reach from highly effective strains such as Azotobacter croococcum 7B, the accumulation of more than 80% of the polymer per dry weight [11].

In addition, PHB has piezoelectric properties that allow electromechanical stimulation [12] of cells and accelerates the recovery of damaged tissues, especially with the usage of 3D scaffolds that mimic extracellular matrix [13]. The bone is a highly renewable tissue [14] and naturally the pressure during elastic deformation causes a piezoelectric effect [15]. It contributes to the synthesis of collagen fibers, which are later overgrown with mineral substances. Also piezoelectric stimuli affect cell differentiation and enhance osteogenesis [16]. Therefore, the piezoelectric effect is a crucial feature for a novel smart material in bone reconstruction. However, the crystal structure of PHB, which determines its piezoelectric properties, is still insufficiently studied. It is assumed that PHB has a piezoelectric response due to its non-centrosymmetric crystal structure [17]. PHB is able to transform electrical energy into mechanical energy and vice versa, which is an important property for regenerative tissue engineering. Moreover, piezoelectric materials, in particular PHB, are able to inhibit the growth of bacteria that increases their attractiveness as materials for tissue engineering [18].

To control and enhance this piezoelectric effect in PHB, the polymer was combined with nanoparticles of magnetite (Fe_3O_4). Magnetite nanoparticles (MNs) have a great potential in different fields of biomedicine [19].

Magnetites can be loaded into biocompatible scaffolds for creation of magnetically responsive materials for bone tissue engineering [20]. Through magnetic or ultrasound, stimulation such scaffolds could become a promising biomaterial for

quick and effective bone healing. Recent studies demonstrate the biocompatibility of composite scaffolds based on piezoelectric polymer as poly(vinylidene fluoride) (PVDF) with addition of magnetostrictive particles of $CoFe_2O_4$ [21]. Another similar to this theme research is devoted to the low cytotoxicity of magnetic nanoparticles in a polydopamine shell [22]. Nevertheless, at the moment, little is known about the cytotoxicity of magnetites in PHB composite. Due to this fact, the novelty of the work included assessment of cytotoxic effects provoked by magnetites in PHB/MNs composite material. Technical betterment of the proposed design over the previous ones comprised the utilization of highly biocompatible PHB polymer to construct original composite supplemented with Fe_3O_4 nanoparticles.

The aim of this study was to characterize biocompatibility of poly(3-hydroxybutyrate)/nano-magnetite composite material for bone tissue engineering applications. Investigation included comparisons between six variants of MNs differ in composition, method of synthesis and in size, and then PHB/MN composite films to choose the most appropriate for biomedical needs. Despite the fact that, the application of 3D scaffolds and films is not the most satisfactory method in regenerative medicine, such techniques are convenient as an in vitro models. However, for bone tissue regeneration in vivo, it would be more appropriate to use individual constructions obtained by 3D printing.

2 Materials and Methods

2.1 Materials

Synthesis of composite material included the following chemicals: poly-3-hydroxybutyrate (PHB, natural origin, Mr = 350 kDa [23]), trichloromethane (EKOS-1, Russia), six type of magnetite nanoparticles, which were provided by colleges from National Research Tomsk Polytechnic University. MNs were produced using three various methodologies of co-precipitation [24]. To reduce or eliminate aggregation of some types of MNs, during synthesis, citric acid (CA) was introduced into the solution of the reaction [25]. Additionally, a part of MNs was covered with reduced graphene oxide (rGO) to increase biocompatibility [26] (Table 1).

2.2 Obtaining Films via the Evaporation Method

A solution of PHB [ρ = 6% (m/w)] in chloroform was filtered through a paper filter. One of 6 samples of magnetite (M0, M1, M3, M7, M8, M11) was added to PHB solution in one of concentrations (0.02 mg/ml or 0.05 mg/ml). That composite suspension was subjected to ultrasonic stimuli during 4 h to disperse the particles uniformly. Films were obtained by casting composite suspension on petri dish for

Table 1 Main characteristics of MNs

Composition	Atmosphere of synthesis	Abbreviation	Proportion (Fe_3O_4/rGO)	Particle size, nm
Fe_3O_4	Air	M0	–	74 ± 12
Fe_3O_4	Argon with CA	M1	–	47 ± 9
Fe_3O_4	Air	M3	–	200–420
Fe_3O_4	Nitrogen	M7	–	46 ± 10
Fe_3O_4/rGO	Argon with CA	M8	6:1	46 ± 9
Fe_3O_4/rGO	Nitrogen	M11	6:1	61 ± 10

complete chloroform evaporation. After it, films were obtained, cut to the size of the well of a 96-well plate, sterilized in 96% ethanol for 24 h and rinsed three times with PBS (phosphate buffered saline, Serva, Germany).

2.3 Biocompatibility in Vitro

2.3.1 Cytotoxicity of MNs on MSCs

Mesenchymal stem cells (MSCs) are susceptible to non-standard cultivation conditions and able to differentiate into osteogenic cell line. Due to these facts, MSCs were chosen as a convenient in vitro model for biomaterial investigation and were used in the experiments. To determine the magnetite's cytotoxic effect, solutions of each sample of magnetites were made in a growth medium (α-MEM with 10% FBS and 1% penicillin–streptomycin) at various concentrations. A stock solution was obtained with a concentration of 0.1 mg/ml. Further dilutions were made 3 and 10 times, at concentrations of 0.03 mg/ml, 0.01 mg/ml, respectively. To assess the effect of magnetites on cell line, a cytotoxicity test was performed. Cells at the rate of 2000 cells per well were planted in a 96-well plate, and after a day, the growth medium was removed and wells were placed with magnetite solutions (6 magnetite types in 3 different concentrations). Cell viability in the presence of magnetites was assessed on 1st and 3rd days of incubation by the standard MTT assay. This method is based on recording the activity of mitochondrial enzymes by reducing MTT tetrazolium salts (3-(4,5-dimethylthiazol-2-yl)-2,5-diphenyl tetrazolium bromide) to insoluble formazan. To determine cell viability, 50 μl of α-MEM medium and 50 μl of MTT reagent (5 mg/ml) were supplemented to wells. After 3 h of incubation at 36.6 °C, the medium was replaced, and crystals of formazan were dissolved in 150 μl of dimethyl sulfoxide. After 10-min long incubation for complete dissolution, spectrophotometric analysis results were measured at 595 nm wavelength with spectrophotometer (Zenyth 3100 Microplate Multimode Detector). Measurement of non-specific readings was carried out at a wavelength of 620 nm.

Cells incubated without magnetites were used as a control sample. Absorption values for those samples were taken as 100%.

2.3.2 MSCs Growth on Composite Films

MSC growth on composite films was assessed using standard XTT assay. This method is based on recording the activity of mitochondrial enzymes by staining them with XTT tetrazolium salts. MSCs were placed in the amount of 2000 cells per well. Cells were cultured for 7 days on the surface of composite films in a flat 96-well plate ($n = 4$). XTT testing was performed on days 1, 3, 5 and 7. For testing, films with MSCs were transferred to clean wells in 100 μl of α-MEM. 50 μl of activated XTT solution was added and samples were incubated during 2 h at 36.6 °C, then the films were removed from the wells, and the optical density of the solutions was counted on a spectrophotometer at a wavelength of 450 nm. Measurement of non-specific readings was carried out at a wavelength of 620 nm. Value calibration was carried out preliminarily: Optical density was measured for a fixed number of cells (1, 2, 3, 5, 7, 10 and 15 thousand cells/well). Based on the measurement results, the equation of the calibration curve was obtained. This equation was used to convert the experimental values of the optical density into the direct number of cells in the samples.

2.4 Statistical Analysis

Statistical analysis was obtained using GraphPad Prizm 6.01 computer program package. Comparison between groups was obtained with one-way ANOVA analysis. In figures the data are illustrated as mean and standard error of the mean ($p < 0.05$).

3 Results and Discussion

3.1 Cytotoxicity of MNs on MSCs

According to the result, MNs in general do not have a cytotoxic effect on MSCs. However, at the highest concentration (0.1 mg/ml), samples M7 (Fe_3O_4, 46 nm) and M11 (Fe_3O_4/rGO, 61 nm) were showed cytotoxicity of more than 50% and 30% on third day, respectively. Nevertheless, cytotoxicity is not observed at lower concentrations. In other samples, even at maximum concentrations, the cell viability did not decrease below 80%. Since CA is normal metabolic products in human cells, CA-coated MNs (M1 and M8) are noticeably biocompatible, which allow them become expectable applicant for biomedical needs (Fig. 1).

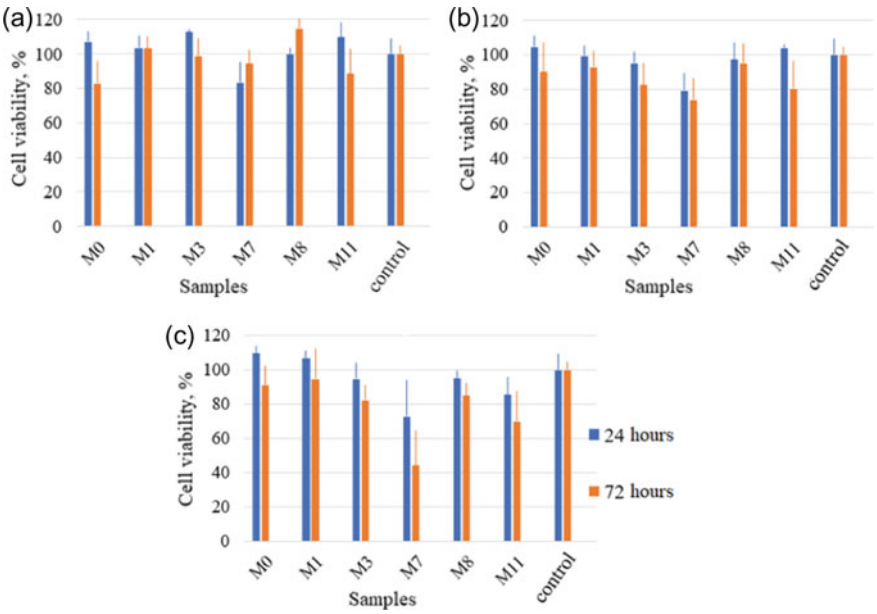

Fig. 1 Cell viability in the presence of MNs of various concentrations: **a** −0.01 mg/ml, **b** − 0.03 mg/ml, **c** −0.1 mg/ml. $N = 4$

3.2 MSCs Growth on Composite Films

The results of the MSCs growth on composite films are exhibited in Fig. 2. In the experiment, steady cell growth has been achieved for all composite films. The results for composite PHB/MN films were not lower than for control PHB samples. Thereby MN additive was not toxic for cells. The PHB/M8 (Fe_3O_4/rGO, 47 nm) composite film has shown the highest cell grow from first to seventh day. This film, presumably, has greater biocompatibility due to the additional coating of particles with citric acid and the presence of reduced graphene oxide in the composition.

4 Conclusion

During the work, it was shown that composites of PHB and magnetic nanoparticles are biocompatible materials. Magnetic nanoparticles, synthesized in argon atmosphere with citric acid, showed the best results in biocompatibility in the experiment with MSCs. We consider that citric acid prevents magnetite nanoparticles from oxidation and conglomeration after synthesis. The selection of the most biocompatible sample was allowed by detailed study of MNs and composite films properties.

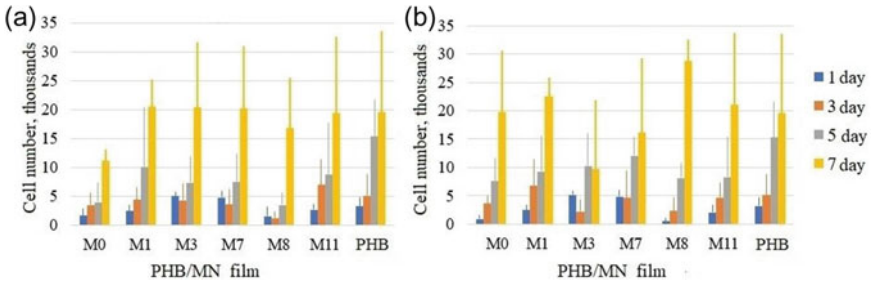

Fig. 2 Number of viable cells on films with different concentrations of MNs: **a** −0.02 mg/ml, **b** − 0.05 mg/ml

Chosen materials were used for the development of magnetically responsive electrospun scaffolds. These scaffolds could be applied as a smart biomaterial with precise control of their function. In the future, experiments are planned with constant and alternating magnetic fields to investigate a piezoelectric effect in scaffolds and study its effect on the growth and differentiation of MSCs.

Acknowledgements This work was supported by the Russian Science Foundation, project No 20-64-47008. The equipment used in this work was from the User Facilities Center of M.V. Lomonosov Moscow State University and the User Facilities Center of Research Center of Biotechnology of Russian Academy of Sciences.

Author Contributions Conceptualization, Bonartsev A., Surmenev R.; methodology, Bonartsev A., Surmeneva M.; validation, Bonartsev A.; investigation, Travnikova D., Chesnokova D., Zharkova I.; resources, Makhina T, Bonartseva G., Mukhortova Y., Chernozem R., Pryadko A.; data curation, Bonartsev A.; writing, Travnikova D., Chesnokova D., Zharkova I.; review, Bonartsev A.; supervision, Bonartsev A.; project administration, Bonartsev A., Surmenev R.

References

1. Murugan R et al (2007) Design strategies of tissue engineering scaffolds with controlled fiber orientation. Tissue Eng 13(8):1845–1866
2. Ikada Y (2006) Challenges in tissue engineering. J R Soc Interface 3(10):589–601
3. Turnbull G et al (2018) 3D bioactive composite scaffolds for bone tissue engineering. Bioactive Materials 3:278–314
4. Elgali I et al (2017) Guided bone regeneration: materials and biological mechanisms revisited. Eur J Oral Sci 125(5):315–317
5. Bonartsev AP, Bonartseva GA, Reshetov IV, Kirpichnikov MP, Shaitan KV (2019) Application of polyhydroxyalkanoates in medicine and the biological activity of natural poly(3-hydroxybutyrate). Acta Naturae 11/2(41):4–16
6. Poirier Y et al (1995) Production of polyhydroxyalkanoates, a family of biodegradable plastics and elastomers, in bacteria and plants. Biotechnology 13(2):142–150
7. Zhang J et al (2018) Polyhydroxyalkanoates (PHA) for therapeutic applications. Mater Sci Eng 86:144–150

8. Pryadko A et al (2021) Review of hybrid materials based on polyhydroxyalkanoates for tissue engineering applications. Polymers 13(11):1738
9. Bonartsev AP et al (2007) Biosynthesis, biodegradation, and application of poly (3-hydroxybutyrate) and its copolymers-natural polyesters produced by diazotrophic bacteria. Communicating Current Research and Educational Topics and Trends in Applied Microbiology 1:295–307
10. Kadouri D et al (2005) Ecological and agricultural significance of bacterial polyhydroxyalkanoates. Crit Rev Microbiol 31(2):55–67
11. Myshkina VL et al (2008) Effect of growth conditions on the molecular weight of poly-3-hydroxybutyrate produced by Azotobacter chroococcum 7B. Appl Biochem Microbiol 44(5):482–486
12. Chernozem RV et al (2018) Hybrid biodegradable scaffolds of piezoelectric polyhydroxybutyrate and conductive polyaniline: piezocharge constants and electric potential study. Mater Lett 220:257–260
13. Kapat K et al (2020) Piezoelectric nano-biomaterials for biomedicine and tissue regeneration. Adv Func Mater 30(44):190–195
14. Soundarya S et al (2018) Bone tissue engineering: scaffold preparation using chitosan and other biomaterials with different design and fabrication techniques. Int J Biol Macromol 119:1228–1239
15. Gautschi G (2006) Piezoelectric sensorics: force strain pressure acceleration and acoustic emission sensors materials and amplifiers. Springer Science & Business Media
16. Carter A et al (2021) Enhancement of bone regeneration through the converse piezoelectric effect, a novel approach for applying mechanical stimulation. Bioelectricity 3(4):255–271
17. Chernozem RV et al (2019) Piezoelectric 3-D fibrous poly (3-hydroxybutyrate)-based scaffolds ultrasound-mineralized with calcium carbonate for bone tissue engineering: inorganic phase formation, osteoblast cell adhesion, and proliferation. ACS Appl Mate Interfaces 11(21):19522–19533
18. Vatlin IS et al (2020) Bacteriostatic effect of piezoelectric poly-3-hydroxybutyrate and polyvinylidene fluoride polymer films under ultrasound treatment. Polymers 12(1):240
19. Li X et al (2016) Current investigations into magnetic nanoparticles for biomedical applications. J Biomed Mater Res 104(5):1285–1296
20. Hao Z et al (2021) Biophysical stimuli as the fourth pillar of bone tissue engineering. Frontiers in Cell and Developmental Biology 9. https://doi.org/10.3389/fcell.2021.790050
21. Fernandes MM et al (2019) Bioinspired three-dimensional magnetoactive scaffolds for bone tissue engineering. ACS Appl Mater Interfaces 11(48):45265–45275
22. Woźniak A et al (2017) In vitro genotoxicity and cytotoxicity of polydopamine-coated magnetic nanostructures. Toxicology In Vitro 44:256–265
23. Myshkina VL et al (2010) Biosynthesis of poly (3-hydroxybutyrate-co-3-hydroxyvalerate) copolymer by Azotobacter chroococcum strain 7B. Appl Biochem Microbiol 46(3):289–296
24. Mukhortova YR et al (2022) Fabrication and characterization of a magnetic biocomposite of magnetite nanoparticles and reduced graphene oxide for biomedical applications. Nano-Structures & Nano-Objects 29:100843
25. Cheraghipour E et al (2013) PEG conjugated citrate-capped magnetite nanoparticles for biomedical applications. J Magn Magn Mater 328:91–95
26. Wai M et al (2019) Optimization and characterization of magnetite–reduced graphene oxide nanocomposites for demulsification of crude oil in water emulsion. RSC Adv 9(4):24003–24014

Angle Detection of Steering in a Self-Driving Car

Vipul Devnani, Chandan Panjwani, Navin Kachhela, Abha Tewari, and Neeraj Gwalani

Abstract An exciting new era that has come into focus is the age of self-learning and automation, where one of its application is the self-driven vehicles. In present era, humans have to no longer care about the obstacles in the driving paths or the stressful rush hour traffics, since the automated vehicles can help reach the destination fast and efficiently. Udacity has provided a dataset containing a set of images with steering wheel angle recorded during driving. With the help of the dataset provided, prediction of the steering wheel rotation angle can be done. In order to predict the angle, computer vision is used. It is the main technology facilitating self-driven vehicles. In this project, a system is created to drive a vehicle automatically without any human input requirement. ML models like CNN and OpenCV are used for certain application to detect an object, vehicle, traffic sign, etc. The project is deployed as a simulation software that provides the output in a frame. There are two frames: one that consists the steering wheel and other that consists the road.

Keywords Autonomous cars · CNN · Machine learning · Computer vision

V. Devnani (✉) · C. Panjwani · N. Kachhela · A. Tewari · N. Gwalani
Computer Science and Engineering, Vivekanand Education Society's Institute of Technology, Mumbai, India
e-mail: 2018vipul.devnani@ves.ac.in

C. Panjwani
e-mail: 2018chandan.panjwani@ves.ac.in

N. Kachhela
e-mail: 2018navin.kachhela@ves.ac.in

A. Tewari
e-mail: abha.tewari@ves.ac.in

N. Gwalani
e-mail: 2018neeraj.gwalani@ves.ac.in

K. Geetha et al. (eds.), *Recent Trends in Materials*, Springer Proceedings in Materials 18, https://doi.org/10.1007/978-981-19-5395-8_34

1 Introduction

The concept of self-driving cars came into existence much behind than today's new technology developed by google and NVidia. In fact, an exhibition was held in 1939 in New York Fair. General Motors created the exhibition to show the world about how in the future the autonomous self-driving cars will look like in 20 years, and this system included highway system that would guide self-driving cars. Meanwhile, continuous work was carried out to construct a full-fledged autonomous vehicle. With the goal of making the car safer and simpler in coming years, experiments have been conducted since 1920 and the trials were started in early 1950s. The first trail was conducted in 1920 on automated driving systems; researchers first presented a research paper for autonomous vehicles using neural networks. In year 1958, General Motors made their futuristic vision into reality. The model of car's front side was embedded with sensors called pick-up coils which could detect the current flowing on wires that were embedded on roads.

The motivation of the project is to remove the human input required to drive a car and to develop a system that learns how to drive by observing. Predicting steering angle which is an important part of the self-driving car and which allow us to explore the power and capability of neural networks. Even if the angle detection is used as the training signal, deep CNNs can automatically extract features to help self-driven vehicles to make the prediction for angle of rotation. Desired rotation of a steering wheel angle is computed using CNN and the weight adjustment on the nodes to reduce the error rate according to the command received from the steering. The electronic system communicates with the model to achieve the goal. Different layers included in the network help to reduce the error rate, and various processing are done by different layers carried out to provide desired results.

Udacity is on a mission to create an open-source self-driving car. In their mission, they have released a dataset of images taken while driving car, steering wheel angle and ancillary senor records for training set. The goal of this mission is to develop a model, from the image taken while driving to reduce the root mean square error (RMSE) between what the model predicts, and in reality how the rotation of angle takes place. In order to design this system, technology like CNN is used to achieve the end result.

2 Related Work

Employing Neural Network (NN) for self-driven cars was proposed by Pomerleau [6]. He also built a self-driven land vehicle using CNN. The model structure was simple and comprised an interconnected neural network which is small in today's standard. It predicted actions from pixels inputs applied to simple driving scenarios with few obstacles. However, it demonstrated the potential of a neural network for end-to-end autonomous navigation (Table 1).

Table 1 Comparison of existing techniques

S. No.	Previous papers		
	Authors	Methodology	Inference
1	Shuyang Du, Haoli Guo, Andrew Simpson	Usage of 3D convolutional layers followed by recurrent layers using LSTM	The two models discussed were the model that used 3D convolutional layers and followed by recurrent layers using LSTM (long short-term memory)
2	Md Najmus Saquib1, Mr.Javed Ashraf2 and Col. (Dr) O.P.Malik3	Usage of 3D camera to manage the steering wheel of the car	It navigated across the road using GPS. The steering angle was regulated by a stepper motor that was linked to a computer. The CPU and GPU were already trained using millions of photographs from real-world road transportation in all traffic and climatic conditions
3	Praval Kumar, Shivam Shandilya, Tushar Sachan and Mr. Nizam Uddin Khan	Paper focused on algorithmic "brain" and powerful sensors, "senses" using Deep Q-learning	The learning model learned by experimentation in this case. The agent in a certain state environment has a set of actions that it can perform, and after executing those actions, it receives a reward that tells it how excellent that action was and records the correct actions in "Brain." The graph is used to determine whether or not this car receives a positive or negative reward

3 Methodology

- Road Detection: The initial phase in face processing is road detection. The major goal of this stage is to detect the road from the dataset's photographs. Individual photographs from the dataset are extracted, scanned, and validated to see if they contain a road or only the background image. The road determination system determines whether or not the input data (picture) represents a road. Following this, the result is transmitted for preprocessing.
- Feature Extraction: This step is critical as it extracts important features using the applied algorithm. The steps perform compression of image information, reducing

irrelevant features. After analysis of the features is done, the model is trained and tested against a given input image.

4 Proposed System

CNN shown in Fig. 1 is the technology that helps to collect the images generated by the camera and map them to the steering wheel. The images generated by the dashcam will be passed to the CNN. Using this technique of CNNs, it ensures that the training steps required in the training of the ML model are very less with the least amount of image preprocessing tasks. This is helpful to evaluate the image that the car dashcam provides to the neural network. The design of a neural network is inspired from the neurons present in the human brain and the organization of the visual cortex. Through relevant filters applied to the image, a CNN successfully captures the spatial/temporal dependencies in the image.

The basic idea behind the implementation is to use the dataset that was collected by the Nvidia team using the Dave2 system and use it to train the machine learning model using the CNN. Deep learning technique helps in getting the correct steering rotation angle based on the current road condition. Since this will be a simulation of the technique, a video of a car dashboard is used to simulate a driver's view and the steering rotates based on the output received from the driving system.

Figure 2 shows a detailed diagram of the simulator. Images of the road are provided as an input into a CNN which gives the desired rotation angles for the car after performing computations. The generated output is compared to the required result for that image, and in order to have an identical output generated, the weights of the CNN are modified through backpropagation.

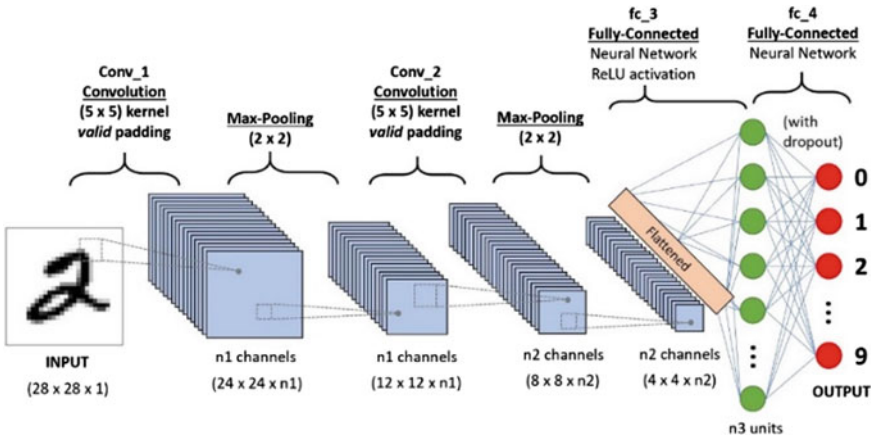

Fig. 1 CNN

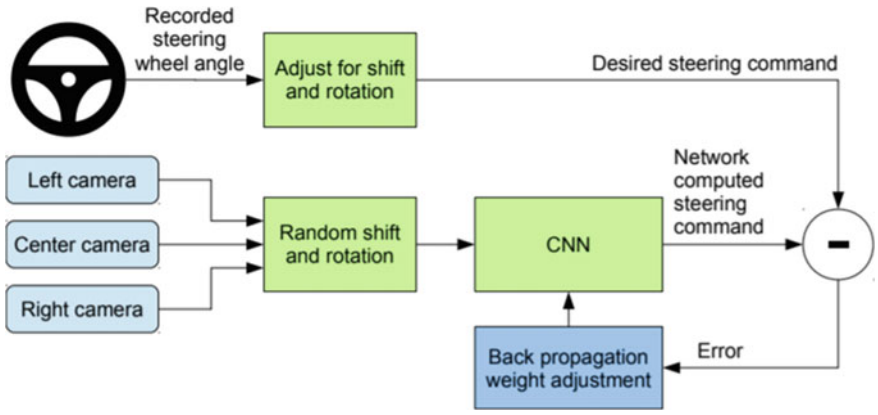

Fig. 2 Simulator block diagram

4.1 Architecture

To reduce the MSE between the human driver command and the steering input, training the weight of the network is done. The architecture of the model is described in Fig. 3. The total number of layers in the network is nine which comprises of three fully connected and five convolution layers. The input image from the camera is passed through the network after being divided into YUV planes. The task of normalization is performed by the initial layer of the network. With the help of GPU processing, the process of performing normalization is accelerated. By keeping in mind the feature extraction, the convolutional layers are made after going through the series of experiments of the layered configurations. The use of stride convolutions is made in the initial three layers with 2×2 strided convolution with a 3×3 kernel size in the last two convolution layers.

4.2 Training Details

Data Selection: Initial step for training a CNN is selecting the frame to use. The image data is labeled with weather condition, driver's activity, and the road type. To train, the images where the driver is not staying in the lane are discarded and the rest are accepted. Then, the video is sampled to ten frames.

Data collection: Data collection is done by the Nvidia team using a test vehicle driven by wire. The model that can be used is 2016 Lincoln mkz, or a 2013 Ford Focus. A particular vehicle make or model has no effect on the functioning of the system. Full attention while driving is required by the drivers, i.e., drive like they normally do. About 72 h of the driving, the data are collected.

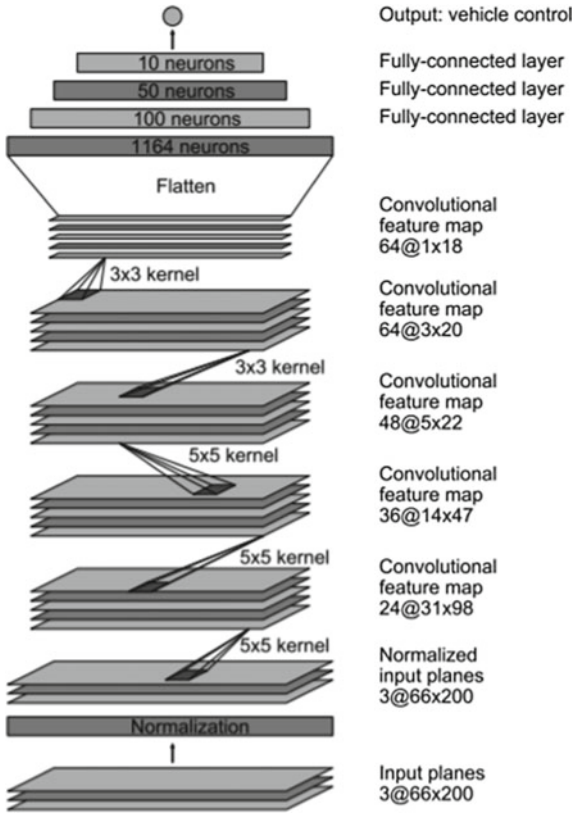

Fig. 3 Conceptual architecture

Data augmentation: Augmentation of the data is done after selecting the initial frames by adding rotations and artificial shifts, so that the network can be taught how to recover from mistakes or bad orientations. The distribution has zero mean, and the standard deviation is twice the standard deviation that is measured with human drivers. In this process, some undesirable artifacts are added as the magnitude increases.

4.3 Keras, NumPy, OpenCV

Keras:

Keras is a big machine learning library created by Google. It is implemented in Python and is used for creating and training neural network models. Usage of Keras in the project is to accomplish various preprocessing tasks like adding the Lambda preprocessing layer, 2D convolution layer, max pooling operation for 2D spatial data, etc. For adding the Lambda layer, the following snippet is used.

```
model.add(Lambda(lambda x: x / 127.5 - 1.,
input_shape=(image_x, image_y, 1)))
```

```
model.add(Conv2D(32, (3, 3), padding='same'))
```

NumPy:

NumPy is a library for the Python programming language, adding support for large multi-dimensional arrays and matrices, along with a large collection of high-level mathematical functions to operate on these arrays. Usage of NumPy is done to create arrays of features and labels present in the image. These arrays are basically portable, serialized representations of Python objects. For creating arrays for features and labels, the following snippet is used.

```
features = np.array(pickle.load(f))
labels = np.array(pickle.load(f))
```

OpenCV is a large library for image processing, computer vision and machine learning. Reading the frames from the input image and using them to do the preprocessing task of resizing the image, requires the use of OpenCV. The resize function is used to resize the source image down to or up to the specified size; the initial destination and size are not taken into account. To resize the image, the following snippet is used.

```
resized = cv2.resize((cv2.cvtColor(img,
cv2.COLOR_RGB2HSV))[:, :, 1], (100, 100))
```

5 Results

5.1 Demonstration

For demonstration of the project, the following are the implementation screenshots. There are two frames used in the project, one for the steering wheel as shown in Fig. 4b and other for the video of the dashcam as shown in Fig. 4a.

The previous approaches require the usage of 3D cameras or non-practical mechanisms that are inefficient or cannot be used in the real world. This approach achieves an accuracy of 90% (accuracy provided by the CNN). By the usage of CNN, the need of extensive efforts in training the model and image preprocessing tasks is minimized.

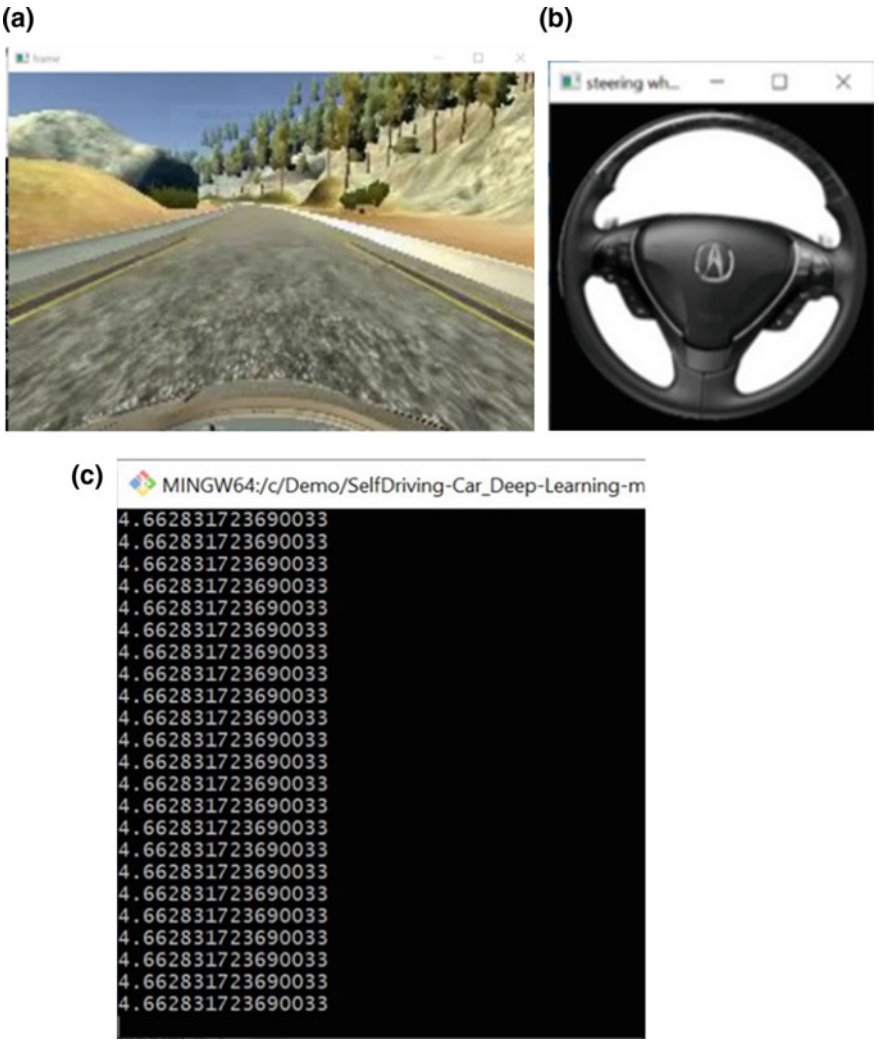

Fig. 4 **a** Frame of dashcam video. **b** Frame of steering wheel. **c** Angle estimation

5.2 Result Evaluation

Evaluation of networks is done through simulation. In simulation, the network provides steering commands in the simulator to an ensemble of pre-recorded video that consists of a road condition considered to be a normal situation, i.e., in normal lighting conditions with lanes and adequate traffic in the city.

The proportion of time the network might drive the car (autonomously) is estimated in order to determine precision. The metric is calculated by counting the number of simulated human interventions. When the simulated vehicle deviates from

the center line by more than one meter, these interventions occur. Assuming that in real life an actual intervention would take 6 s, which is the time it takes for a human to resume control of the car, it is re-centered and then the self-steering mode is restarted. The percentage autonomy is then computed by counting the number of interventions, multiplying by 6 s, dividing by the time elapsed during the simulated test, and subtracting the result from 1.

$$\text{autonomy} = \left(1 - \frac{(\text{number of interventions}) \cdot 6\,\text{s}}{\text{elapsed time [s]}}\right) \cdot 100$$

6 Future Scope and Conclusion

This project demonstrates one of the most effective ways of creating a self-driving car system using the techniques of machine learning, deep learning, and convolutional neural networks. It is one of the most basic systems for creating a self-driven car and is cost effective. The technique does not require much preprocessing tasks for image processing which is very crucial while creating a system that is going to run in a constrained environment with respect to processing capabilities. Although this technique is workable, there is still scope for more improvement which will help reach the level 5 of autonomous cars. The current system guarantees level 4 of automation. Safety of the passengers in a car is an overarching concern. Many thousands of people die in motor vehicle crashes every year in the world (more than 1,51,417 in 2018); and therefore, self-driving vehicles could, hypothetically, reduce that number since software could prove to be less error-prone than humans.

References

1. LeCun Y, Boser B, Denker JS, Henderson D, Howard RE, Hubbard W, Jackel LD (1989) Backpropagation applied to handwritten zip code recognition. Neural Comput 1(4):541–551
2. Krizhevsky A, Sutskever I, Hinton GE (2012) Imagenet classification with deep convolutional neural networks. Advances in Neural Information Processing Systems 25
3. Jackel LD, Sharman D, Stenard CE, Strom BI, Zuckert D (1995) Optical character recognition for self-service banking. AT&T Technical Journal 74(4):16–24
4. Large scale visual recognition challenge (ILSVRC). http://www.image-net.org/ challenges/LSVRC/
5. Net-Scale Technologies, Inc. Autonomous off-road vehicle control using end-to-end learning, July 2004. Final technical report. http://net-scale.com/doc/net-scale-dave-report.pdf
6. Pomerleau DA (1989) ALVINN, an autonomous land vehicle in a neural network. Technical report, Carnegie Mellon University. http://repository.cmu.edu/cgi/viewcontent.cgi?article=2874&context=compsci
7. Wikipedia.org. DARPA LAGR program. http://en.wikipedia.org/wiki/DARPA_LAGR_Program

8. Wang D, Qi F (2001) Trajectory planning for a four-wheel-steering vehicle. In: Proceedings 2001 ICRA. IEEE international conference on robotics and automation (Cat. No. 01CH37164), IEEE, vol 4, pp 3320–3325
9. DAVE 2 driving a Lincoln. https://drive.google.com/open?id=0B9raQzOpizn1TkRIa241ZnBEcjQ
10. Akey Sungheetha RSR (2021) Classification of remote sensing image scenes using double feature extraction hybrid deep learning approach. J Inf Technol 3(02):133–149
11. Raj JS, Joe CV (2021) Wi-Fi network profiling and QoS assessment for real time video streaming. IRO Journal on Sustainable Wireless Systems 3(1):21–30
12. Sai Pavan EJ, Ramya P, Valarmathi B, Chellatamilan T, Santhi K (2021) Object detection for autonomous vehicles using deep learning algorithm. Computational vision and bio-inspired computing. Springer, Singapore, pp 327–339
13. Kumar P, Shandilya S, Sachan T, Khan NU (2019) Self-driving car using soft computing. https://www.ripublication.com/irph/ijisaspl2019/ijisav11n1spl_24.pdf
14. George T, Zacharia S, Rufus E, Alex ZC (2015) Design and development of LabVIEW based steering wheel angle sensor system. IJET 7:577–582
15. Saquib MN, Ashraf J, Malik CDO (2017) Self driving car system using (AI) artificial intelligence. Asian Journal of Applied Science and Technology (AJAST) 1(6):85–88
16. Tewari A, Khan S, Krishnan A, Rauth T, Singh J (2018) Smart driver assistant. In: 2018 second international conference on electronics, communication and aerospace technology (ICECA), pp 1127–1131. https://doi.org/10.1109/ICECA.2018.8474760
17. Tewari A, Sarguroh N, Kingrani P, Shetty T, Motwani R (2021) AI-based autonomous driving assistance system. In: 2021 5th international conference on computing methodologies and communication (ICCMC), pp 1491–1498. https://doi.org/10.1109/ICCMC51019.2021.9418403
18. Self-driving car—a computer will park for you, Yair Wiseman. https://u.cs.biu.ac.il/~wisemay/autonomousm.pdf
19. Caicedo F, Robuste F (1956) Lopez-Pita A (2006) Parking management and modeling of car park patron behavior in underground facilities. Transp Res Rec 1:60–67
20. Wiseman Y (2017) Self-driving car-a computer will park for you. IJETAS 1(1):9–16

Dielectric Properties of Barium Titanate Using Different Preparation Techniques

N. Preetha, S. Padmavathi, and B. Mahalakshmi

Abstract Barium Titanate, a ferroelectric material which is mostly found in perovskite structure is well known for its dielectric ceramic. It is used in many electronic applications such as electro-optical, electromechanical and electro ceramic applications due to its low dielectric loss and high dielectric constant. These electrical properties can be easily tuned by a simple substitution technique which has a great impact in today's modern electro ceramics. This has motivated the scientists to choose an appropriate cation to be substituted at cationic sites. This work shows a brief review over the various preparation techniques of $BaTiO_3$ with different dopants and its effect of grain size and dielectric properties at different temperatures are deliberated.

Keywords Barium titanate · Preparation methods · Electrical properties · Dielectric constant · Dielectric loss

1 Introduction

Barium Titanate ($BaTiO_3$) is a ferroelectric compound with perovskite structure having general formula ABO_3. They can be synthesized using various techniques suitable for different applications. Doped Barium Titanate has turn out to be one of the greatest significant ferroelectric ceramics due to its widespread applications in

N. Preetha (✉) · S. Padmavathi
Department of Physics, Karpagam College of Engineering, Coimbatore, India
e-mail: gsrpreetha@gmail.com

S. Padmavathi
e-mail: padmavathi.s@kce.ac.in

N. Preetha
Research Scholar, Karpagam Academy of Higher Education, Coimbatore, India

B. Mahalakshmi
Department of Physics, Hindustan College of Engineering and Technology, Coimbatore, India

Department of Science and Humanities, Nehru Institute of Engineering and Technology, Coimbatore, India

K. Geetha et al. (eds.), *Recent Trends in Materials*, Springer Proceedings in Materials 18, https://doi.org/10.1007/978-981-19-5395-8_35

semiconductors, positive temperature coefficient resistors, ultrasonic transducers and piezoelectric devices. It is well recognized that the property of ceramics and residues of barium Titanate sturdily depend on the method of preparation as reported previously by numerous scientists [1–3]. In order to obtain improved positive temperature coefficient of resistivity (PTCR) property for the host Titanate, addition of dopants is needful. For this purpose, it is conceivable to substitute some trivalent rare earth elements in order to produce semiconducting behavior in the perovskite lattice. There are several approaches for preparation of $BaTiO_3$ powders that has its own advantages and drawbacks. In general, the crystallographic form of $BaTiO_3$ is classified into 5 types namely, cubic, orthorhombic, hexagonal and tetragonal. In nature, the cubic and hexagonal are paraelectric where the other 3 are ferroelectric [4–7]. In order to obtain the required characteristics for different applications, it is significant to choose the right doping technique for $BaTiO_3$. The electrical properties of $BaTiO_3$ can be modified using the dopants (A- and B-site). Since it is perovskite in structure, the materials have the ability to host particles of various size so that the $BaTiO_3$ lattice can be accommodated with greater number of different dopants which makes the material semiconducting [8–10]. In the current work, a brief review of various preparation techniques for the development of improved dielectric properties has been studied.

2 Grain Size

From the most studied temperatures, it is found that the grain size increases with the decrease in dielectric constant. The impact of particle size over the dielectric properties of Barium Titanate composites were reported, where they found that the particle size of Barium Titanate composite changes with dielectric loss and dielectric constant when the applied frequency is varied [1]. When the $BaTiO_3$ particles are smaller than 58 nm, the dielectric constant of the composite ($BaTiO_3$/PVDF) is increased greatly at frequencies below 1 kHz. As the particles became larger than 58 nm, the difference of dielectric constant with frequency became smooth for composites with the same size of $BaTiO_3$ particle as shown in Fig. 1.

From the previous reported studies of pure and doped $BaTiO_3$ nanopowders with various concentration of La synthesized by Polymeric Precursor Method (PPM), it is concluded that this technique can be used for the preparation of $BaTiO_3$ (20–40 nm) [10]. After sintering, these investigates recognized very much extended grain size and lastly found that, the increase in Lanthanum concentration impact over grain development, resulting in smaller grain size. Table 1 gives the variation of density and average grain size for pure and La subo0stituted different $BaTiO_3$ ceramics. BTL1 (0.1 mol%), BTL3 (0.3 mol%) and BTL5 (0.5 mol%) speaks to, La substitution in $BaTiO_3$.

Further, it was seen that dielectric constant is sturdily reliant on grain size. They stated that PPM technique is an advanced process for the preparation of nano sized

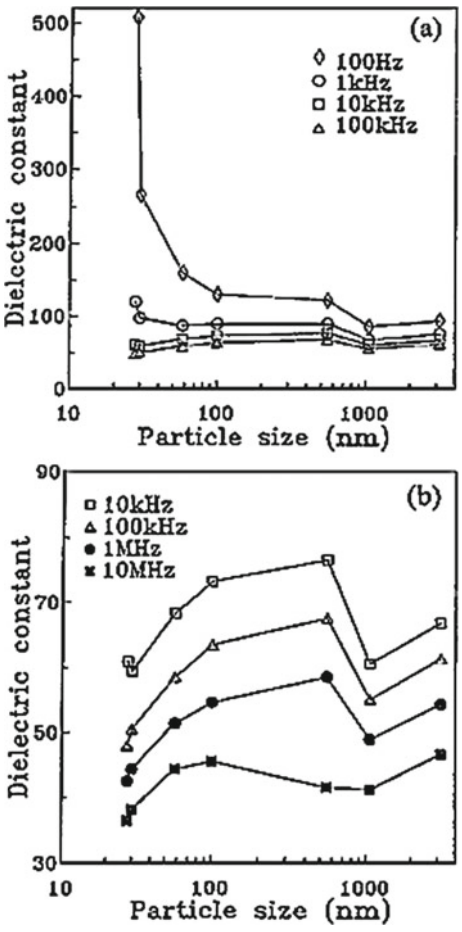

Fig. 1 Variations of dielectric constant in the $BaTiO_3$ composites at different frequency with size **a** within 100 Hz and 100 kHz **b** between 10 kHz and 10 MHz

powders. The addition of different concentration of Lanthanum is a viable method to adjust dielectric behavior and control grain size.

3 XRD Analysis

The XRD investigation of the powders synthesized at 350 °C in the water–vapor atmosphere over the periods of 0–20 h demonstrated that the powders comprised crystalline $BaTiO_3$ [3] (Fig. 2).

The crystalline phase of the Hydrothermally prepared nano-composite was examined using XRD [4]. The diffraction patterns of powdered Barium Titanate calcined at varied calcination temperature are revealed in Fig. 3. There exists a change in XRD

Table 1 Density value and average grain size for different samples of $BaTiO_3$ ceramics

Sample	Frittage time (h)	DSEM (mm)	Density (g/cm^3)
BT	2	2.0–4.0	85.2
	4	1.5–2.0	88.3
	8	1.0–2.5	90.1
BTL 1	2	0.7–0.8	69.5
	4	1.2–1.5	70.2
	8	1.5–1.8	74.6
BTL 3	2	0.6–0.8	75.1
	4	0.8–1.0	78.3
	8	0.75–1.0	85.1
BTL 5	2	0.3–0.6	81.3
	4	0.3–0.65	83.6
	8	0.2–0.4	87.0

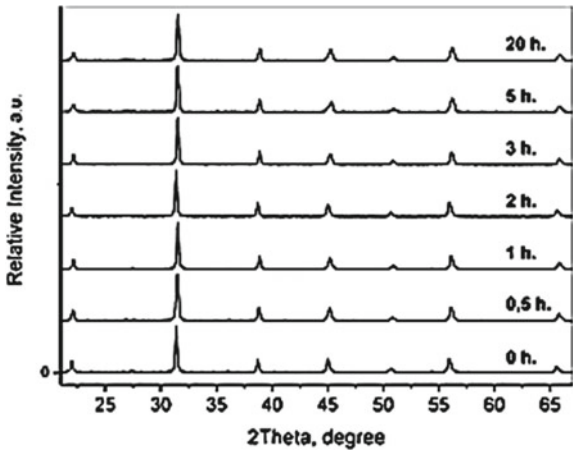

Fig. 2 XRD patterns of BTO powders prepared at 350 °C in water vapor and 16 MPa for 0–20 h

patterns of composites when compared with nano powders, where the intensity peak of Polyvinylidene fluoride (PVDF) is absent in all the composites.

XRD patterns of Ni doped $BaTiO_3$ and Nb doped $BaTiO_3$ were recorded by Rachna et al. [7]. A sharp and well characterized peak were obtained for all bends, demonstrating great crystalline character (Fig. 4 and Table 2). The Tetragonal phase of $BaTiO_3$ changes to hexagonal phase when doping with Ni.

The synthesis of $BaTiO_3$ (with Strontium and Deuterium dopants) shows the XRD which has a great improvement in the development of $BaTiO_3$ phases with great purity and gives perfect peaks for tetragonal $BaTiO_3$ [8].

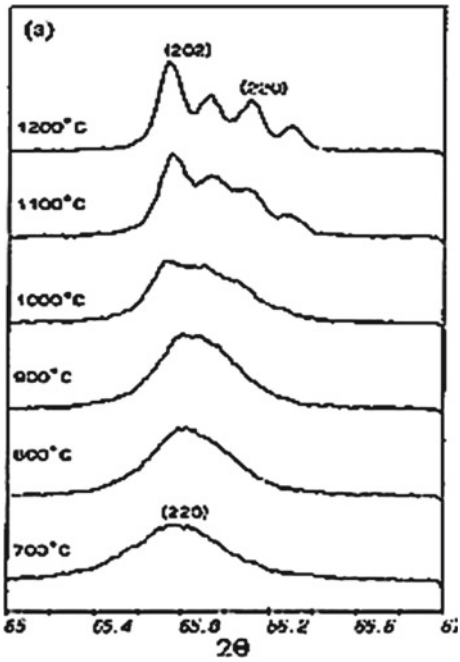

Fig. 3 XRD patterns of the $BaTiO_3$ powders calcined at various calcination temperatures

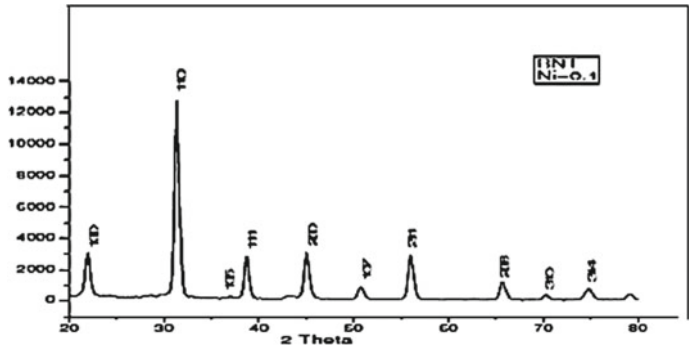

Fig. 4 XRD patterns Ni doped $BaTiO_3$

Table 2 Crystallite size of barium titanate doped with nickel

Investigated line (d)	2ϑ (deg.)	ϑ (deg.)	Full width at half maximum	Crystalline size (nm)
001	22.9	10.95	0.6	14
110	31.4	15.7	0.5	11

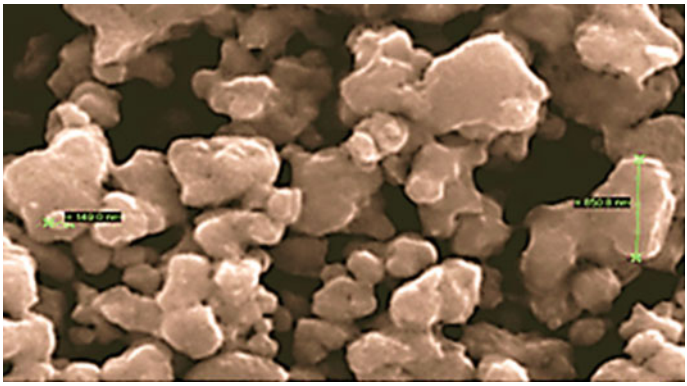

Fig. 5 Morphology of Ni doped $BaTiO_3$

4 Morphological Studies

The Morphology for the crystals of Thermo Vapors Barium Titanate ceramics show a narrow size distribution. The average crystal size somewhat changes in a range of 150–188 nm without a particular connection to the duration of the synthesis as reported in [3].

The impact of zirconia accumulation in Barium Titanate is noteworthy. The grain size of untainted Barium Titanate is around 50 μm. When 22 mol% of TZ3Y is added, a large portion grains are around 5 μm. But when 22 mol% of ZrO_2 is added, the vast majority grains are around 3 μm. [5].

SEM picture of untainted$BaTiO_3$ and$BaTiO_3$doped with Ni are shown in Fig. 5 and Fig. 6 respectively. There is also an indication of uniform spreading in grain size with a lesser amount of sponginess in untainted$BaTiO_3$but greater sponginess in $BaTiO_3$when doped with nickel. It is also observed that the consistent grains have sufficient energy to join with the adjacent grains [7].

5 Dielectric Properties

The dielectric constant value relies upon the preparation technique, which implies purity, density, grain size and so on. The relative permittivity is additionally reliant on temperature, rate of recurrence and material dopants [1].

Variations in dissipation factor and dielectric constant with frequency for Barium Titanate/PVDF composites of different size of $BaTiO_3$ particles are shown in Fig. 1 [4]. The dielectric constants of Barium Titanate/PVDF composites at frequencies below 1 kHz increased significantly with frequency when the Barium Titanate particle were reduced to 58 nm. As the particle increases greater than 58 nm, the change in

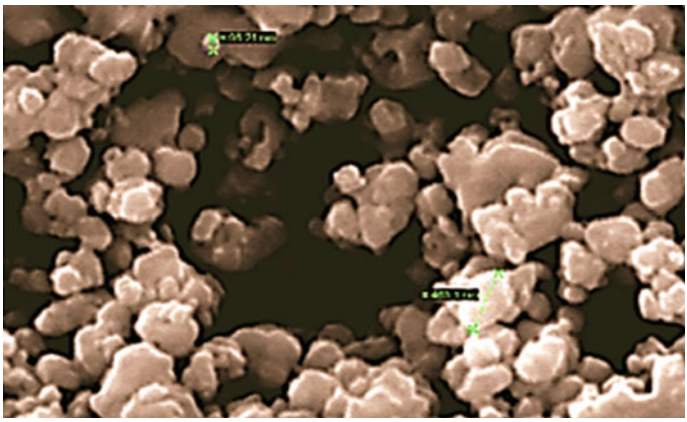

Fig. 6 Morphology of $BaTiO_3$ ($Ba_{1x}Nb_xTi_{0.99}O_3$ where $x = 0.0$)

dielectric constant with frequency got smooth for composites with the similar size of $BaTiO_3$ particle.

The pure NiO, $BaTiO_3$ and Nb_2O_5 doped $BaTiO_3$ ceramics have outstanding properties, low dielectric loss, high dielectric constant for their application in super capacitors. The values of dielectric loss are directly proportional to frequency. This condition is reversed when related to that of ($Ba_{1-x}Nb_xTiO_3$ where $x = 0.0$) as reported in [7].

Figure 7 represents the difference of dielectric constant with temperature for $BaTiO_3$ doped by Eu_2O_3 at (1 kHz) [8], It creates the impression that.

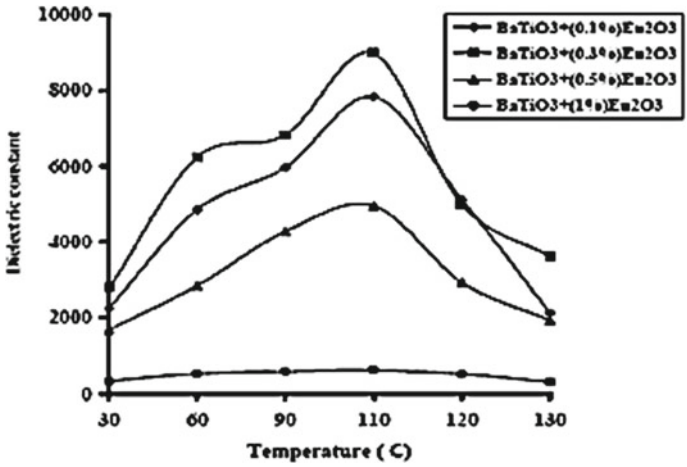

Fig. 7 Graph for dielectric constant versus temperature (°C) for as prepared sample doped with (Eu_2O_3)

- (0.1%) addition results to dielectric constant having (7832.82) by shifting the Curie point (Tc) at (10 °C) toward (110 °C).
- (0.3%) addition results to increasing in a dielectric constant to reach (8979.17) by shifting the Curie point (Tc) at (10 °C) toward (110 °C).
- (0.5%) addition results to decreasing in a dielectric constant about (0.1, and 0.3%) to reach (4949.27) by shifting Curie point (Tc) at (10 °C) toward (110 °C), and
- The (1%) addition results in decrease in a dielectric constant about (0.1, 0.3 and 0.5%) to reach (622.68) by shifting the Curie point (Tc) at (10 °C) toward (110 °C).

6 Conclusion

Barium Titanate ($BaTiO_3$) is an adaptable material displaying multidimensional properties. The great qualities viz. piezoelectric, ferroelectric and dielectric properties settle on it an outstanding choice for applications.

The new preparation techniques of $BaTiO_3$ utilizing new innovation by the different analysts relies upon the ideal features for final application. New approaches of preparation using addition of dopants at A- and B-site cations and utilization of substitute cations effects both structural and physiochemical properties of $BaTiO_3$.

Whenever there is a particle transformation, it influences the dielectric property of $BaTiO_3$. The change is critical with change in sintering time, concentration of substitute or dopant.

The scientists have featured the change in crystalline structure exposed to various pressure and temperature with the assistance of XRD and furthermore by utilizing pictures of SEM.

References

1. Vijatović MM, Bobić JD, Stojanović BD (2008) History and challenges of barium titanate: part II. Sci Sinter 40:235–244
2. Ertug B (2008) The overview of the electrical properties of Barium Titanate. Ame J Eng Res 02:01–07
3. Kholodkova A, Danchevskaya M, Popova N, Pavlyukova L, Fionov A (2015) Preparation and dielectric properties of Thermo-vaporous BaTio3ceramics. Mater Technol 49:447–451
4. Hsiang HI, Lin KY, Yen FS, Hwang CY (2001) Effects of particle size of BaTio3 powder the dielectric properties of BaTio3 & polyvinylidene fluoride composites. J Mater Sci 36:3809–3815
5. Abdelal OA, Othman KI, Elshazly ES (2014) International Journal of Advances in Engineering. Sci Technol 3:132–143
6. Lu SW, Lee BI, Wang ZL, Samuels WD (2000) Hydrothermal Synthesis and structural charecterization of BaTio3 nanocrystals. J Cryst Growth 219:269–276
7. Rachna MU (2015) Auwalu. Solid state properties of Ni and Nb doped Barium Titanate. Res J Eng Sci 4:1–10
8. Merza AS, Jameel WW, Muhammed KR (2010) "Preparation and studying the physical and electrical properties of barium titanate doped with strontum and euterium"

9. Vijatović MM, Stojanović BD, Bobić JD, Ramoska T, Bowen P (2010) Properties of lanthanum doped BaTio3 produced from nanopowders. Ceram Int 36:1817–1824
10. Kotlyarchuk A, Klymenko V, Dubovitskaya N, Lobunets T, Shatskikh S, Ragulya A (2012) Proceedings of the International conference on nanomaterials; applications and properties, vol 1, pp 1–3

Modeling Effective Maintenance Strategy for Rotodynamic System Using RCM and AHP

P. T. Elijah and M. Obaseki

Abstract This study was done with the aim of modeling effective maintenance strategy using reliability centered maintenance integrated with multi-decision analytic hierarchy process (AHP). The need for developing the new model is to ease the implementation of RCM on complex system such as process plant which also helps to deal with the equipment based on their risk levels. The primary data obtained (through questionnaire and professional discussions with personnel at the case study) was analyzed partly in the MS Excel and MATLAB computational environment in line with the modeled equations of reliability and availability and obtained the current reliability and applicability condition of a selected rotodynamic system (pump) of a particular petrochemical firm in Rivers State. AHP algorithm was then applied to obtain the most effective maintenance to be adopted for each component of the pump. The selection criteria used are equipment criticality (EC), mean time to failure (MTTF), mean time to repair (MTTR) and applicability. The analysis shows that the highest-ranking criterion is applicability of maintenance alternative on each component which ranked at 55.79%, followed by the MTTF and EC at respective rankings of 26.33% and 12.19% while the least was MTTR with ranking percentage of 5.69%.

Keywords Modeling · Effective maintenance strategy · Reliability centered maintenance · Multi-decision · Analytic hierarchy process

Nomenclature

$\underline{A}_0$	Operational availability
A_A	Achieved availability
A_t	Inherent availability
AHP	Analytical hierarchy process

P. T. Elijah (✉) · M. Obaseki
Applied Mechanics and Design/Production Research Group, Department of Mechanical Engineering, Nigeria Maritime University, Okerenkoko, Delta State, Nigeria
e-mail: paul.elijah@nmu.edu.ng

K. Geetha et al. (eds.), *Recent Trends in Materials*, Springer Proceedings in Materials 18, https://doi.org/10.1007/978-981-19-5395-8_36

EC	Equipment criticality
MATLAB	Matrix Laboratory
MDT	Mean down Time (year)
MS Excel	Microsoft Excel
MTBMA	Mean time between maintenance action (year)
MTTF	Mean time to failure (year)
MTTR	Mean time to repair (year)
n	Subsystem number
R	Reliability (s)
λ	Failure rate (s^{-1})

1 Introduction

Process plants are made up of variety of equipment which is complex in volume and size, and equipment operates under rigorous conditions. Aging of equipment, wear, corrosion of equipment component, erosion and fatigue condition on equipment weaken and deteriorate the finery leading to its failure [9, 15, 17]. For continuous operation of process plant and for the plant to continue to deliver required output, from time to time, the components of the plant need to be replaced, repaired overhauled or removed [8, 14, 18]. Failure of the plant or equipment of the plant has negative safety, environmental and economic impact to plant owner and host community. Reliability, operation and maintainability of process plant are what determine its performance [21]. Deterioration of equipment that results from wear, tear, and aging increases chance of failure and leads to decreased performance and reliability of equipment. Increased cost of operation, technical aging, poor quality and low-level production are a result of gradual regression of operational life of equipment [16, 19]. Cost minimization and reliability-centered maintenance enhance safety and reliability [2, 20]; reliability-centered maintenance is among the best known and commonly used tool to preserve the operating efficiency in critical sectors; these sectors include power plant, artillery system, aviation industry, railway networks and gas industry and marine industry [1, 13], stated that the technique provides a better failure management policy that maintains focus on each equipment health [6], pointed out limitations of call for reliability-centered maintenance new model in petroleum refineries and that include similar oil and gas or petrochemical processing plant and other process plant Idhammer [11], provided useful information to users on accurate equipment life prediction and required data to collect for analysis and to assess risk level for a particular maintenance frequency [10] noted that petrochemical plant and refinery device failure may lead to huge financial impacts for the company owing to fact that the devices operate at high pressures and temperature [7], suggested six steps involved in application of an AHP [5], implemented use of AHP in maintenance selection in oil refinery, and the factors they considered in the maintenance selection are as follows: economic, applicability, costs and safety [23], worked on a fuzzy

AHP model for effective maintenance strategy selection, and [22], worked on AHP model for maintenance selection, and four factors were taken into consideration as selection criteria: reliability, reparability, cost and availability. There is serious challenge of implementing a maintenance strategy which ensures equipment availability at optimum level and equipment/system efficiency, decreases the deterioration rate of components, ensures safety and environmentally friendly operation, and reduces total cost of operation. Although there are many maintenance strategy selection process plant and other sector of industry, these models are associated with a lot of limitations. The static nature of RCM calls for new models that provide continuous review and improvement of equipment maintenance that will remain relevant even as equipment health state changes with time as well as provide continuous reliability improvement of process plant equipment. The model in this study introduces dynamism into the RCM to provide for the limitation. It also simplifies RCM by eliminating the rigorous and time-consuming FMECA analysis. Application of AHP in maintenance selection decision-making introduces quantitative analysis in RCM rather than only experience and decision logic. This work therefore models effective maintenance strategy using RMC integrated multi-decision analytic hierarchy process (AHP), with purpose of continuous reliability improvement and quick implementation thereby eliminate bottleneck associated with reliability-centered maintenance. The objectives includes: perform reliability audit and analysis using information obtained from the history file, perform risk base criticality analysis to obtain critical equipment and perform AHP on the critical component.

2 Material and Methods

2.1 Materials

Figure 1 shows a RCM diagram with modification sketch to accommodate AHP when deciding appropriate maintenance strategy for particular component of the system.

System Selection and Data Collection

A centrifugal pump from petrochemical process plant is selected for case study. The pump takes its suction from butane 1 plant reactor and discharges into the pump around pump coolers and from there back to the reactor inlet at the top. The primary data for this study is obtained from the equipment history file, and other data is obtained through professional discussion and questionnaire with plant personnel.

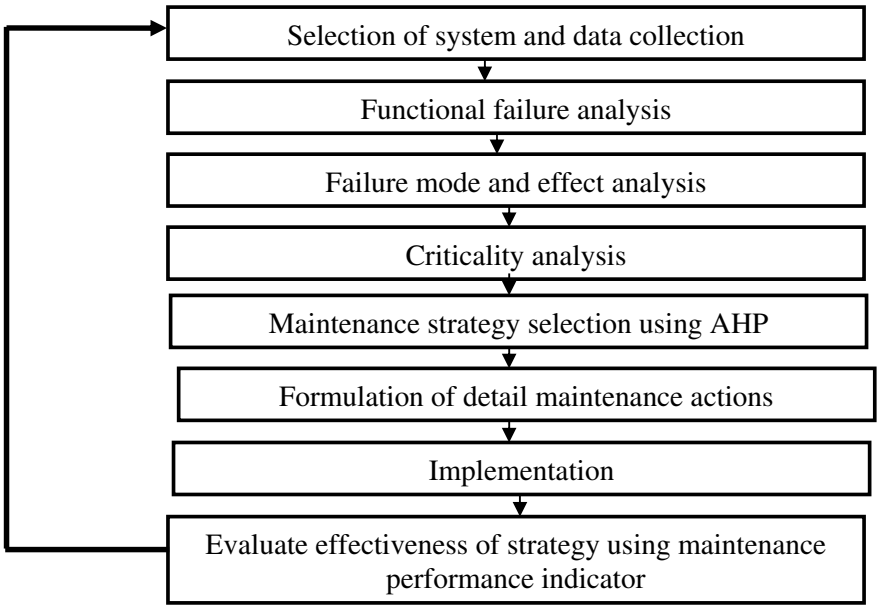

Fig. 1 Model algorithm

2.2 Methods

2.2.1 Functional Failure Analysis

The failure analysis carried out is based on the failure rate, MTTF, MTTR and availability.

Failure Rate

The failure rate is given by Eq. 1:

$$\lambda = \frac{\text{Items failure}}{\text{Total Operating Time}} = \frac{1}{\text{MTTF}} \tag{1}$$

Mean Time to Failure (MTTF) Computation

Mean time to failure [or mean time between failure (MTBF)] is considered the reciprocal of failure rate and is shown in Eq. 2

$$\text{MTTF}(\theta) = \frac{\text{Total Time}}{\text{Total No. of Failures}} = \frac{1}{\lambda} \tag{2}$$

Furthermore, the relationship between MTTF and reliability is given in Eq. 3 as:

$$\theta = \int_0^\infty R(t)\mathrm{d}t = e^{-\lambda t} \tag{3}$$

where t is time (hours), λ is failure rate (items/hour), and $R(t)$ is measured reliability at time (t) in percentage

Mean time to repair (MTTR) computation

This is used to measure the maintainability of the system, which is the time taken to restore or retain a system to a specific operation condition. MTTR is simply considered as system down-time, and it is given by [3] as:

$$\mathrm{MTTR}(\phi) = \frac{\text{Total Maintenance Downtime}}{\text{Total Number of maintenance Actions}} \tag{4}$$

Considering subsystems, we have that:

$$\phi \text{ subsystems} = \frac{\sum_i^n = 1\lambda_i R_{Pi}}{\sum_i^n = {}_1\lambda_i} \tag{5}$$

where n is the number of subsystems, λ_i is failure rate of the ith system, and R_{Pi} is repair time for ith unit.

Furthermore, to obtain the probability of completing a maintenance action within allowable time interval we use the expression.

$$M(t) = 1 - e^{-t/\phi} \tag{6}$$

where t is allowable downtime (hours), φ is MTTR or expected downtime, and $M(t)$ is probabilistic maintenance within time (t).

Availability Computation

Availability as considered is the probability that an equipment is available when required to perform its stipulated function. There are three common measures of availability which are inherent availability (A_t), achieved availability (A_A) and operational (actual) availability (A_0). The first two consider repair or maintenance action to commence immediately as failure occurs without any delay, but this is often not the case in real-life scenarios; therefore, the application of operational availability accommodates the fact that maintenance actions often do not start immediately after a failure occurs. There is often delay due to facts like unavailability of spares, maintenance engineers and some other unforeseeable circumstances. This availability also considers the time for preventive and corrective maintenance. Mathematically, the operational availability is given as:

$$A_0 = \frac{\mathrm{MTBMA}}{\mathrm{MTBMA} + \mathrm{MDT}} \tag{7}$$

where A_0 is operational availability, MTBMA is mean time between maintenance actions both preventive and corrective, and MDT is mean downtime, obtained as MTTR × Failure.

This is modified as:

$$A_0 = \frac{\text{MTTF}}{\text{MTTF} + (\text{MTTR} \times \text{Failure})} \tag{8}$$

2.2.2 Criticality Analysis of the System Equipment

The evaluation of the equipment criticality (EC) is done using the formula:

$$EC = \frac{(30P + 30S + 25A + 15V)}{3} \tag{9}$$

where EC is equipment criticality %, P is the production index, S is the safety index, A is the equipment availability (standby) index, and V is the value or capital cost index of equipment; the criticality analysis is used to determine the degree to which equipment failures affect performance of organization, and this will help to place asset or equipment in orderly manner for work prioritization, material classification and allocation, PM/PdM formulation and reliability improvement processing. The effect of equipment fault is used to assess its criticality group ranging from A through D, and it is assigned numeric score of 1, 2 and 3 as given by Table 1 and Fig. 2.

Figure 2 shows the algorithm for calculation of EC and classification of each equipment or component into groups A, B, C and D based on the criticality value of each equipment or component. The classification is done using D < 45%; 45 ≤ C < 60% ≤ B 74%; A ≥ 74%. Class A items are maintenance significant items, that is,

Table 1 Equipment component criticality table [4]

Criteria	Symbol	Weight (%)	Levels
Impact of production	P	30	(3) very important (2) important (1) normal
Impact of safety	S	30	(3) very important (2) important (1) normal
Availability of standby	A	25	(3) without safety (2) with standby and medium availability (1) with standby and high availability
Equipment value	E	15	(3) high value (2) normal (1) low value

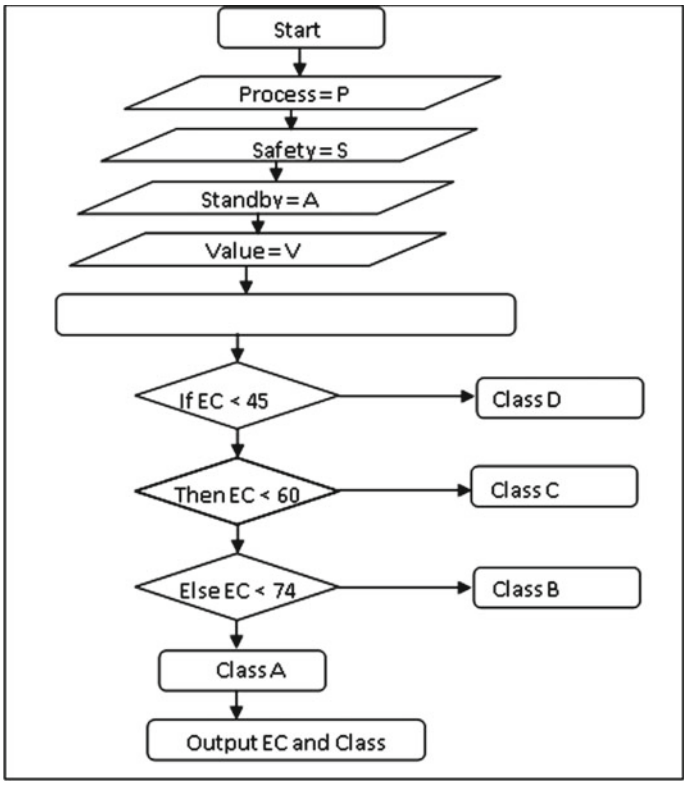

Fig. 2 Algorithm for calculation of equipment criticality (*source* [12])

items which its failure affects production or safety or both. AHP will be applied on this class of component to select appropriate maintenance.

2.2.3 Analytical Hierarchical Process

The class A equipment is maintenance significant items, which require appropriate maintenance action to ensure its failure does not affect neither the production nor the safety. The appropriate maintenance action will also enhance the profitability of the system.

To select appropriate maintenance strategies, AHP is applied to each of class A equipment separately. From the result of EC calculation, maintenance, production and management, personnel are asked to make choice of preferred maintenance approach. Run-to-failure and preventive strategies are considered pair wise comparison. Scheduled Maintenance (SM), Condition-Based Maintenance (CBM), Proactive Maintenance (PrM) and Design-out Maintenance (DoM) are classified as preventive maintenance.

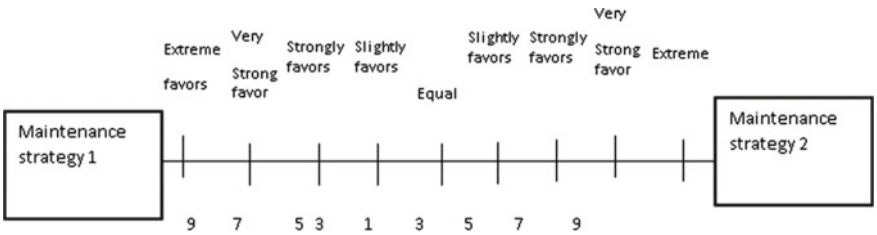

Fig. 3 Criteria ranking scale

Criteria for selection of maintenance strategy according to [5], using AHP for oil refinery, are economic, costs, applicability and safety. Triantaphyllou et al. [22], in their AHP maintenance model, presented four criteria for maintenance selection as cost, reparability, reliability and availability from the EC, cost, economic factor and safety which have been considered. The criteria yet to be taken into consideration are reparability, reliability, availability and applicability, but reparability and reliability are somewhat connected to MTTR and MTTF. The more MTTF means the more the availability, also the more the reliability. In the other hand, the lower the MTTR means high reparability. With reference to MTTF, MTTR, EC and the applicability of the given maintenance approach, a nine-point scaling is used to indicate preferred maintenance strategy for given equipment. The methodology is applied to all equipment, and it produces appropriate maintenance strategies (Fig. 3).

The Applied AHP Model

The AHP model applied herein is formulated by considering a general equation:

$$C * x = \lambda_{\max} * x \tag{10}$$

where

C is the comparison matrix of size $n * n$, for n criteria also known as the priority matrix, x is the eigenvector (or priority vector) of size $n * 1$, and $\lambda_{\max}$ is the eigenvalue.

The actual AHP process is applied sequentially as itemized from steps 1 through 8.

Step 1: List the Overall Goal, Criteria and Decision Alternative

The major goal which is to select the most effective maintenance task is given as the Level 1 element, followed by Level 2 elements which are the criteria (MTTF, MTTR, applicability and equipment).

Step 2: Development of Pairwise Comparison Matrix

Each pair of decision alternatives is rated based on relative importance as shown in Table 2. The alternative is placed horizontally and vertically in matrix form, and

Table 2 The relative pairwise rating of importance alternatives

Relative importance pairwise comparison	Numerical rating
Extremely preferred	9
Very strongly preferred	7
Strongly preferred	5
Moderately preferred	3
Equally preferred	1

the matrix has numerical ratings comparing alternative in horizontal (first) with the alternative in vertical (second).

Even numeric ratings of 8, 6, 4 and 2 can also be assigned. A reciprocal of the numerical rating is assigned when the second alternative is judged to be better than the first. The value of I is always allotted when comparing an alternative with same alternative.

Pairwise comparison matrix:

$$C = \begin{bmatrix} C_{11} & C_{12} & C_{13} \\ C_{21} & C_{22} & C_{23} \\ C_{31} & C_{23} & C_{33} \end{bmatrix} \tag{11}$$

Step 3: Normalized Matrix Development

Each number in a column of the pairwise comparison matrix is divided by its column sum.

Sum of the values in each column:

$$C_{ij} = \sum_{i=1}^{n} C_{ij} \tag{12}$$

Normalized pair-wise matrix:

$$X = \frac{C}{\sum_{i=1}^{n} C_{ij}} = \begin{bmatrix} X_{11} & X_{12} & X_{13} \\ X_{21} & X_{22} & X_{23} \\ X_{31} & X_{23} & X_{33} \end{bmatrix} \tag{13}$$

Step 4: The Priority Vector Development

The each normalized matrix row is averaged. The averaged rows form the priority vector of alternative preferences with respect to the particular criterion. The values in the priority vector sum to 1.

Weighted matrix:

$$W = \frac{\sum_j^n = 1X_{ij}}{n} = \begin{bmatrix} W_{11} \\ W_{12} \\ W_{13} \end{bmatrix} \tag{14}$$

Step 5: Calculate a Consistency Ratio

The consistency ratio is used to measure consistency of the inputted subjective pairwise comparison matrix. When the consistency ratio is less than 0.1, the consistency is good. When the ratios are greater than 0.1, the input has to be re-evaluated.

Consistency vector:

$$\begin{bmatrix} C_{11} & C_{12} & C_{13} \\ C_{21} & C_{22} & C_{23} \\ C_{31} & C_{23} & C_{33} \end{bmatrix} * \begin{bmatrix} W_{11} \\ W_{12} \\ W_{13} \end{bmatrix} = \begin{bmatrix} Cv_{11} \\ Cv_{12} \\ Cv_{13} \end{bmatrix} \tag{15}$$

$$Cv_{11} = \frac{1}{W_{11}}[C_{11}W_{11} + C_{12}W_{12} + C_{13}W_{13}] \tag{16}$$

$$Cv_{12} = \frac{1}{W_{21}}[C_{21}W_{21} + C_{22}W_{22} + C_{23}W_{23}] \tag{17}$$

$$Cv_{13} = \frac{1}{W_{31}}[C_{31}W_{31} + C_{32}W_{32} + C_{33}W_{33}] \tag{18}$$

Step 7: Development Criteria Pairwise Matrix

The criteria are subjected to pairwise comparison by using subjective ratings, and matrix is formed.

The matrix is normalized as in (step 3), and a criteria priority vector is formed as in (step 4).

Step 8: Development of Overall Priority Vector

The criteria priority vector in step 7 is multiplied by the priority matrix in step 6.

Determining the Consistency Ratio

Step 1: In each row of the pairwise comparison matrix, the weighted sum is of the multiples of the entries by the priority of its corresponding (column) alternative.

Step 2: In each row, divide its weighted sum by the priority of its corresponding (row) alternative.

Step 3: The average $\lambda_{\max}$ of the results of step 2 is determined.

Step 4: The consistency index, CI, of the n alternatives is computed by Eq. (19)

$$CI = \frac{\lambda_{\max} - n}{n - 1} \tag{19}$$

Table 3 Random index values for *n* alternatives

Alternative (*n*)	3	4	5	6	7	8
Random index (RI) value	0.58	0.90	1.12	1.24	1.32	1.41

Step 5: Determine the Random Index (RI) from the standard RI tables as given in Table 3.

Step 6: Determine the consistency ratio, **CR** as given by Eq. (18).

3 Results and Discussion

3.1 Results

The failure data for the selected system is collected over a period of three years as given in Table 4.

Table 4 gives the number of failures of the different components in different years ranging from 2010 to 2013. The data was obtained from the maintenance log record of one of the petrochemical industries.

Table 5 gives the MATLAB computed values from applying Eq. (9). It shows different EC values and class for all the subsystems of the pump system.

Table 6 shows the MATLAB computed values for failure rate, MTTF, MTTR and availability by applying Eqs. (1), (2), (5) and (8), respectively.

3.1.1 AHP Results of the Major Criteria

Table 7 shows AHP results of the major criteria, while Fig. 4 displays the relation between criteria and weights.

Table 4 Amount of component failures in three years

S/N	Component name	No. of failure in Year 1	No. of failures in Year 2	No. of failures in Year 3	Total failures over 3 years
1	Shaft	0	0	1	1
2	Bearing	4	4	3	11
3	Mechanical seal	5	4	5	14
4	Impeller	1	0	1	2

Table 5 Table of results of inputs

Component	Equipment criticality	Group
EC of shaft	90.00	Shaft belongs to Group A
EC of bearing	100.00	Bearing belongs to Group A
EC of seal	91.67	Seal belongs to Group A
EC of impeller	90.00	Impeller belongs to Group A

D < 45%; C < 60%; B < 74%; A ≥ 74%

Table 6 Failure analysis table

Failure rate results	
Component	**Failure rate (in 3 years)**
Shaft	0.000139
Bearing	0.001528
Mechanical seal	0.001944
Impeller	0.000278
Mean time to failure results	
Component	**MTTF (h)**
Shaft	7200.00
Bearing	654.55
Mechanical seal	514.29
Impeller	3600.00
Mean time to repair results	
Component	**MTTR (h)**
Shaft	5.00
Bearing	55.00
Mechanical Seal	70.00
Impeller	10.00
Availability	
Component	**Availability (%)**
Shaft	99.98
Bearing	97.28
Mechanical seal	95.66
Impeller	99.95

Table 7 Major criteria AHP table

Step 1: Pairwise comparison matrix for major criteria					
	EC	**MTTF**	**MTTR**	**Applicability**	
EC	1.00	0.33	3.00	0.20	
MTTF	3.00	1.00	5.00	0.33	
MTTR	0.33	0.20	1.00	0.14	
Applicability	5.00	3.00	7.00	1.00	
COL_SUM	9.33	4.53	16.00	1.68	
Step 2: Normalized pairwise comparison matrix					
	EC	**MTTF**	**MTTR**	**Applicability**	**Criteria weight**
EC	0.1071	0.0735	0.1875	0.1193	0.1219
MTTF	0.3214	0.2206	0.3125	0.1989	0.2633
MTTR	0.0357	0.0441	0.0625	0.0852	0.0569
Applicability	0.5357	0.6618	0.4375	0.5966	0.5579
Step 3: Weighted sum table					
	EC	**MTTF**	**MTTR**	**Applicability**	**Weight sum**
EC	0.1219	0.0878	0.1707	0.1116	0.4919
MTTF	0.3656	0.2633	0.2844	0.1860	1.0994
MTTR	0.0406	0.0527	0.0569	0.0797	0.2299
Applicability	0.6094	0.7900	0.3982	0.5579	2.3555
Step 4: Weighted ratios					
Weighted sum	**Criteria weight**	**Ratios**			
0.4919	0.1219	4.0362			
1.0994	0.2633	4.1747			
0.2299	0.0569	4.0408			
2.3555	0.5579	4.2222			
Step 5: Decision outputs					
Lambda max		**C.I**	**CR**		
4.2222		**0.0741**	**0.0823**		

3.2 Discussion

This work obtained the effective maintenance strategies for different components of centrifugal pump of a typical petrochemical process plant. The effective maintenance strategy for each component was obtained using AHP model; the effective maintenance strategy is ranking maintenance alternative between SM, Condition-Based Maintenance, PrM and DoM. The EC, mean time failure, MTTF, to repair and applicability maintenance strategy to individual component are used as decision criteria. In Table 5, all the components of the pump are group A and are maintenance significant items; therefore, AHP model was applied on all the four components

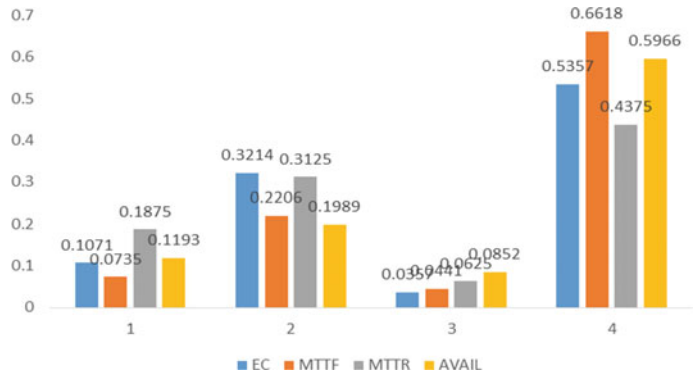

Fig. 4 Relationship between criteria weights

to select the effective maintenance strategy for each of the component using the stated decision criteria. Table 6 shows the calculated values of failure rate, MTTF and MTTR with respect to each component of the system. The table shows that the *n* descending order as: mechanical seal—bearing—impeller—shaft. For components MTTF in descending order is as the MTTR in order of highest to the lowest shaft at values of 70, 55, 0 and 5 h, respectively. For the availability; the higher the failure rate the lower the availability therefore, we could see the availability *t* as shaft—impeller—bearing—mechanical seal with corresponding availability rating of 99.98%, 99.95%, 97.28% and 95.66%, respectively. Table 7 shows the major criteria for determining maintenance method for the system. The AHP table shows in step 5 that criticality ratio (CR) is 0.0823 which is less than the standard value of 0.1; therefore, we accept that the AHP analysis is consistent. From step 2 in Table 4, the criteria weights for applicability rank highest at 55.79%, followed by MTTF at 26.33%, while EC ranks third at 12.19% and MTTR ranks least at 5.69%.

From Fig. 4, it can be seen that the relationship between the fundamental criteria for this study (i.e., EC, MTTF, MTTR and applicability) is nonlinear. However, the actual behavior of the different criteria is further studied through the analysis of the alternatives which in this study are considered sub-criteria, which are SM, CbM, PrM and DoM.

4 Conclusion

This study was done to ascertain the current reliability, availability and maintainability condition of the selected rotodynamic system (pump) of a selected petrochemical firm in Rivers State. The primary data obtained from the data case study was analyzed partly in the MS Excel and MATLAB computational environment, in line with the modeled equations of reliability, maintainability, and applicability. Furthermore, the AHP algorithm was then applied to solve for the optimal decision in

terms of effective maintenance for each component of the pump. The analysis showed that in different criteria considered in this study, the highest-ranking criteria were found to be the applicability of the maintenance strategy on each components which ranked at 55.79%, followed by the MTTF and EC at respective rankings of 26.33 and 12.19% while the least was MTTR which had a negligible ranking percentage of 5.69%.

The RCM integrated multi-decision AHP and Risk-Based Maintenance model should therefore be applied in oil and gas sector in order to evaluate performance index of their rotodynamic units and thereby create effective maintenance strategy.

Acknowledgements The researchers wish to acknowledge all authors and other contributors whose educational materials were utilized in the course of this work.

References

1. Abid M, Ayub S, Wall H, Tariq MN (2014) Reliability centered maintenance plan for the utility section of a fertilizer industry: a case study. International Journal of Science and Advanced Technology 4(3):9–16
2. Akpan NP, Bassey NA (2021) Modelling complete power outage data using reliability. American Journal of Operations Research 11:87–99. https://doi.org/10.4236/ajor.2021.112005
3. Akuno AO, Ndonye TM, Nthiwa MJ, Orawo LA (2016) Regression approach to parameter estimation of an exponential software reliability model. Am J Theor Appl Stat 5(3):80–86
4. Azadeh A, Ebrahimipour V, Bavar P (2009) A fuzzy inference system for pump failure diagnosis to improve maintenance process: the case of a petrochemical industry. Expert Syst Appl 37(1):627–639. https://doi.org/10.1016/j.eswa.2009.06.018
5. Bevilacqua M, Braglia M (2000) The analytic hierarchy process applied to maintenance strategy selection. Reliab Eng Syst Saf 70:71–83
6. Deepak PP, Jagathy RVP (2013) A new model for reliability centered maintenance in petroleum refineries. Int J Sci Technol Res 2(5):56–64
7. Dolan JG, Boohaker F, Allison J, Imperiale TF (2013) Patients' preferences and priorities regarding colorectal cancer screening. Med Decis Making 33:59–70. https://doi.org/10.1177/0272989X12453502
8. Elijah PT, Obaseki M (2021) Application of linear regression maintenance models on rotodynamic systems. Nigerian Research Journal of Engineering and Environmental Sciences 6(2):695–705
9. Filz M-A, Herrmann C, Thiede S (2020) Simulation-based assessment of quality inspection strategies on manufacturing systems. Procedia CIRP 93:777–782
10. Hameed A (2016) Risk-based shutdown inspection and maintenance for a processing facility. A thesis submitted to the School of Graduate Studies in partial fulfillment of the requirements for the degree of Doctor of Philosophy, Faculty of Engineering and Applied Science Memorial University of Newfoundland
11. Idhammer C (2008) Preventive maintenance optimization. http://www.idcon.com/resourcelibrary/articles/preventivemaintenance/541-preventive-maintenance-optimization.html
12. Islam HA (2010) Reliability-centered maintenance methodology and application: a case study. Eng 2:863–873
13. Khanis BH (2000) Use of reliability centered maintenance (RCM) analysis in petroleum development Oman (PDO) for maintenance rationalization. SPE Paper 87249, Tn: Proceeding soft the 2000 Abu Dhabi International Petroleum Exhibition and Conference

14. Kolawole A, Agbola OO, Ikubanni PP, Raji OG, Osueke CO (2019) Reliability and power loss analysis: a case study of a power plant in Nigeria. Cogent Engineering, 6, Article ID: 1579426. https://doi.org/10.1080/23311916.2019.1579426
15. Labib AW, Williams GB, O'Connor RF (1998) An intelligent maintenance model (system): an application of the analytic hierarchy process and a fuzzy logic rule-based controller. Journal of the Operational Research Society 49:745–757
16. Lindemann B, Jazdi N, Weyrich M (2020) Anomaly detection and prediction in discrete manufacturing based on cooperative LSTM networks. In: Proceedings of the 2020 IEEE 16th international conference on automation science and engineering (CASE), Hong Kong, China, 20–21 Aug 2020; IEEE: Piscataway, NJ, USA; pp 1003–1010
17. Liu Q, Ma L, Wang N, Chen A, Jiang Q (2021) A condition-based maintenance model considering multiple maintenance effects on the dependent failure processes. Reliability Engineering and System Safety 220. https://doi.org/10.1016/j.ress.2021.108267
18. Martinez P, Ahmad R (2021) Quantifying the impact of inspection processes on production lines through stochastic discrete-event simulation modeling. Modelling 2:406–424. https://doi.org/10.3390/modelling2040022
19. Ren L, Meng Z, Wang X, Zhang L, Yang LT (2021) A data-driven approach of product quality prediction for complex production systems. IEEE Trans Ind Inform 17:6457–6465
20. Selvik JT, Aven I (2011) A framework for reliability and risk centered maintenance. Reliab Eng Syst Saf 96(2):59–70
21. Shorrocks P, Labib AW (2000) Towards a multimedia-based decision support system for word class maintenance. In: Proceedings of the 14th ARTS (advances in reliability technology symposium), IMechE, University of Manchester
22. Triantaphyllou E, Kovalerchuk B, Mann L, Knapp GM (1997) Determining the most important criteria in maintenance decision making. J Qual Maint Eng 30:16–28
23. Wang I, Chu J, Wu J (2007) Selection of optimum maintenance strategies based on a fuzzy analytical hierarchy process. International Journal of Production Economics l07:151–163